SF2A 2017
C. Reylé, P. Di Matteo, F. Herpin, É. Lagadec, A. Lançon, Z. Meliani, F. Royer (eds)

Proceedings of the annual meeting of the French Society of Astronomy & Astrophysics Paris, July 4-7, 2017

Credit: Sylvain Cnudde

Contents

Foreword

The annual meeting of the French Society of Astronomy and Astrophysics (*Société Française d'Astronomie et d'Astrophysique* - SF2A) has become a tradition, cherished by many permanent, doctoral and post-doctoral researchers. The 2017 edition took place from July 4th to July 7th in the center of Paris, having been efficiently prepared by members of the *Observatoire de Paris*, little after the celebrations of its 350th anniversary. This meeting, called both "*Semaine de l'astrophysique française*", or "*Journées de la SF2A*" (and just "SF2A" by many colleagues) included the general assembly of our society, plenary sessions aimed at a large audience of professionals, workshops dedicated to various scientific issues, the young researcher and thesis price ceremony, events for schools and the public, discussions concerning societal subjects. Above 300 colleagues participated in at least some of these moments.

During the plenary sessions, we enjoyed several presentations proposed by the various *Programmes Nationaux* and *Actions Spécifiques* of INSU-CNRS. We learned among other subjects about the legacy of the Planck satellite, the observation of evolved stars with high angular resolution instruments, or the amazing landscapes and properties of Pluto. Representatives of institutions (G. Perrin for INSU, O. La Marle for CNES, B. Devost for CFHT) and the "*sections*" of CNRS (B. Mosser) and CNAP (H. Wozniak) addressed us in a frank and honest manner that sometimes lacks in more official contexts. Eduardo Unda-Sanzana was invited to present astronomy in Chile and the Chilean astronomy society (SOCHIAS). He gave a very interesting presentation, during which we learned that the Chilean government believe and invest in astronomy. An example for other countries. Finally, we hold our general assembly where the moral and financial reports were presented, and possible changes were discussed (concerning, e.g., the prices awarded by the society). A vote from the members will complement these presentations by the end of 2017.

Afternoons were dedicated to parallel workshops covering all branch of astronomy. These 15 workshops were selected among propositions from the *Programmes Nationaux* and *Actions Spécifiques*, but also from individual members of the society. These workshops thus covered the interests of our whole community, in good accordance with the topicality of the field (the first exo-planet detection by the SPHERE instrument was announced during one of them).

A very nice moment every year is the SF2A prize ceremony (followed by a cocktail, almost as nice) that occurred this year in the historical Cassini room of the *Observatoire de Paris*. The laureate of the Thesis prize was Jean-Baptiste Fouvry who presented his brilliant work concerning galaxy dynamics after a dynamic introduction by B. Famey. D. Bockelée-Morvan introduced the laureate of the young researcher price: Benoît Carry, who then presented his work on asteroids in a very lively manner.

Most of the above concerns our science. It is, however, important to keep in mind that we are not isolated in ivory domes with our telescopes. Society evolves and our community is not unaffected by this evolution. Two lunch-meetings were the occasion to discuss some of these societal issues. The first one (organized by M.-J. Goupil and M. Deleuil) focused on questions related to gender and career, a regular topic in our meetings. The second one, concerning outreach, was co-organized by E. Lagadec, member of our board, and colleagues from the Canada France Hawaii Telescope. In a time of fast communication and fake news, we discussed about how we, scientists, journalists, youtubers, can provide to the public quality information and prevent people from being tricked (like it was the case in the recent "super-moon" frenzy). We thank warmly the journalists who accepted our invitation: S. Brunier, P. Henarejos, P. Pajot. Also concerning the diffusion of astronomy (and the role of professional astronomers for this goal), prices were given to three classes of local schools in the context of the competition "*découvrir l'univers*"; and D. Rouan gave a public talk, "*Le compte des mille et une exoplanètes*" at the *Institut d'Astrophysique de Paris*. In the recent years, the links between astronomy and society have also been encouraged through an increasing activity of the SF2A board on social networks.

The SF2A is also concerned by the well-being and the future of young researchers. As it has been the case for many years, PhD students were exempted of inscription fees, and we distributed grants to help the participation of several post-docs. We co-organized with the AUDDAS association an experience-sharing event for young researchers. Finally, board member O. Berné announced the coming survey of a generation of doctors that the SF2A will follow to obtain a better view of their conditions, aspirations, and future.

Several sponsors made these *Journées* possible. Especially in a time when it is difficult to raise funds for meetings such as our, the organizers and myself are very grateful for the financial help of INSU-CNRS, CNES, the *Service d'Astrophysique du CEA/DSM/IRFU*, the *Institut d'Astrophysique Spatiale*, and the PN and AS of INSU-CNRS that have supported the organization of the workshops. We thank the sponsors of the research prize (DELL) and school competition (EDP-Science). We acknowledge the help of the *Observatoire de Paris* for the global organization and the *Institut d'Astrophysique de Paris* who let us use its theater for the public conference. I would like to thank all the members of the SF2A board who were all very active for preparing the meeting, and end with the local organizing committee: Sylvain Cnudde, Francoise Combes, Misha Haywood, Zakaria Meliani, Noel Robichon, Myriam Rodrigues, Frédéric Royer, Stephane Thomas, with a very special mention for Paola di Matteo who chaired this LOC with *maestria*. They all made this meeting a success. In addition to the rich program mentioned above (and somewhat detailed in these proceedings), embracing all of the astronomy research performed in France, the work of the LOC has also offered to all the participants many opportunities to meet and discuss beyond the limits of their own field of expertise. One more reason to pursue the tradition of our annual meetings.

We will meet again next year, in Bordeaux.

Samuel Boissier, President of the SF2A

List of participants

ACERO Fabio (e-mail: fabio.acero@cea.fr)
ALBERTAZZI Bruno (e-mail: b.albertazzi@hotmail.fr)
ALEXANDROVA Alexandra (e-mail: alexandra.alexandrova@lpp.polytechnique.)
ALEXANDROVA Olga (e-mail: olga.alexandrova@obspm.fr)
AMODEO Stefania (e-mail: stefania.amodeo@obspm.fr)
AMSIF Kader (e-mail: kader.amsif@cnes.fr)
ANDRE Nicolas (e-mail: nicolas.andre@irap.omp.eu)
ANDRÉ Quentin (e-mail: quentin.andre@cea.fr)
AOUINA Ayoub (e-mail: ayoubaouina@outlook.com)
ARENOU Frédéric (e-mail: Frederic.Arenou@obspm.fr)
ARNOLD Luc (e-mail: luc.arnold@osupytheas.fr)
ARNOUTS Stephane (e-mail: stephane.arnouts@lam.fr)
ASTOUL Aurélie (e-mail: aurelie.astoul@cea.fr)
ATHANASSOULA Lia E. (e-mail: lia@lam.fr)
AUCLAIR-DESROTOUR Pierre (e-mail: pierre.auclair-desrotour@u-bordeaux.fr)
AUNAI Nicolas (e-mail: nicolas.aunai@lpp.polytechnique.fr)
BABUSIAUX Carine (e-mail: carine.babusiaux@obspm.fr)
BALANÇA Christian (e-mail: christian.balanca@obspm.fr)
BALLET Jean (e-mail: jballet@cea.fr)
BARDET Déborah (e-mail: bardetdeborah@gmail.com)
BAUDINO Jean-loup (e-mail: jean-loup.baudino@physics.ox.ac.uk)
BELLI Alexandre (e-mail: belli@geoazur.unice.fr)
BEHAR Etienne (e-mail: etienne.behar@irf.se)
BELGACEM Ines (e-mail: ines.belgacem@u-psud.fr)
BELKACEM Kévin (e-mail: kevin.belkacem@obspm.fr)
BENBAKOURA Mansour (e-mail: mansour.benbakoura@gmail.com)
BERGER Jean-Philippe (e-mail:)
BERNARD Edouard (e-mail: ebernard@oca.eu)
BERTRAND Tanguy (e-mail: tanguy.bertrand@lmd.jussieu.fr)
BEUZIT Jean-luc (e-mail: Jean-Luc.Beuzit@univ-grenoble-alpes.fr)
BIASUZZI Barbara (e-mail: biasuzzi@ipno.in2p3.fr)
BITEAU Jonathan (e-mail: biteau@in2p3.fr)
BIZOUARD Marie Anne (e-mail:)
BIZOUARD Christian (e-mail: christian.bizouard@obspm.fr)
BLANC Michel (e-mail:)
BLAZÈRE Aurore (e-mail: aurore.blazere@obspm.fr)
BLELLY Pierre-louis (e-mail: pierre-louis.blelly@irap.omp.eu)
BOCCALETTI Anthony (e-mail: anthony.boccaletti@obspm.fr)
BOCCHIALINI Karine (e-mail: karine.bocchialini@ias.u-psud.fr)
BOISSE Isabelle (e-mail: isabelle.boisse@lam.fr)
BOISSIER Samuel (e-mail: samuel.boissier@lam.fr)
BOLANOS Simon (e-mail: simon.bolanos@polytechnique.edu)
BOLMONT Emeline (e-mail: emeline.bolmont@cea.fr)
BONIFACIO Piercarlo (e-mail: Piercarlo.Bonifacio@obspm.fr)
BONNET-BIDAUD Jean-Marc (e-mail:)

BOQUIEN Médéric (e-mail: mederic.boquien@uantof.cl)
BORG Janet (e-mail: borgjanet@gmail.com)
BOSELLI Alessandro (e-mail: alessandro.boselli@oamp.fr)
BOSKRI Abdelkarim (e-mail: aboskri@oca.eu)
BOT Caroline (e-mail: caroline.bot@astro.unistra.fr)
BOUCHET François (e-mail:)
BOULANGER Francois (e-mail: francois.boulanger@ias.u-psud.fr)
BOURDELLE DE MICAS jules (e-mail: jules.bourdelledemicas@obspm.fr)
BOURRIER Vincent (e-mail: bourrier@iap.fr)
BOUVIER Jerome (e-mail: Jerome.Bouvier@univ-grenoble-alpes.fr)
BRAINE Jonathan (e-mail: jonathan.braine@u-bordeaux.fr)
BREUILLARD Hugo (e-mail: hbreuill@gmail.com)
BRIAND Carine (e-mail: carine.briand@obspm.fr)
BRIOT Danielle (e-mail: danielle.briot@obspm.fr)
BRUGGER Bastien (e-mail: bastien.brugger@lam.fr)
BUAT Véronique (e-mail: veronique.buat@lam.fr)
BUCHLIN Éric (e-mail: eric.buchlin@ias.u-psud.fr)
BUGNET Lisa (e-mail: lisa.bugnet@cea.fr)
BURGARELLA Denis (e-mail: denis.burgarella@lam.fr)
BUSSCHAERT Clotilde (e-mail:)
CABRAL Nahuel (e-mail: nahuel.cabral@utinam.cnrs.fr)
CAFFAU Elisabetta (e-mail: Elisabetta.Caffau@obspm.fr)
CALABRO' Antonello (e-mail: nillo2412@gmail.com)
CAMBRÉSY Laurent (e-mail: laurent.cambresy@astro.unistra.fr)
CAPITAINE Nicole (e-mail: nicole.capitaine@obspm.fr)
CAPITANIO Letizia (e-mail: letizia.capitanio@obspm.fr)
CARRY Benoit (e-mail: benoit.carry@oca.eu)
CASSE Fabien (e-mail: fcasse@apc.univ-paris7.fr)
CATAPANO Filomena (e-mail: menacata3@gmail.com)
CAVALIÉ Thibault (e-mail: thibault.cavalie@obspm.fr)
CHANTEREAU William (e-mail: william.chantereau@unige.ch)
CHARBONNEL Corinne (e-mail: Corinne.Charbonnel@unige.ch)
CHARLOT Stephane (e-mail: charlot@iap.fr)
CHARLOT Patrick (e-mail: charlot@obs.u-bordeaux1.fr)
CHARNAY Benjamin (e-mail: benjamin.charnay@obspm.fr)
CHASTENET Jérémy (e-mail: jeremy.chastenet@astro.unistra.fr)
CHATAIN Audrey (e-mail: audrey.chatain31@gmail.com)
CHAUVIN Gaël (e-mail: gael.chauvin@univ-grenoble-alpes.fr)
CHOPLIN Arthur (e-mail: arthur.choplin@unige.ch)
CHRISTOPHE Steven (e-mail: steven.christophe@obspm.fr)
CHUARD Dimitri (e-mail: dimitri.chuard@cea.fr)
CIARDI Andrea (e-mail: andrea.ciardi@obspm.fr)
CIESLA Laure (e-mail: laure.ciesla@cea.fr)
COLLIN-ZAHN Suzy (e-mail: suzy.collin@obspm.fr)
COMBES Francoise (e-mail: francoise.combes@obspm.fr)
COOGAN Rosemary (e-mail: r.coogan@sussex.ac.uk)
CORBEL Stéphane (e-mail: stephane.corbel@cea.fr)
CORSIN Enora (e-mail: enora.corsin-salussolia@etu.upmc.fr)
COUSIN Agnes (e-mail: agnes.cousin@irap.omp.eu)
COZZANI Giulia (e-mail: giulia.cozzani@lpp.polytechnique.fr)
CREEVEY Orlagh (e-mail: orlagh.creevey@oca.eu)
CRIFO Françoise (e-mail: francoise.crifo@obspm.fr)
CROUZET Nicolas (e-mail: ncrouzet@iac.es)
DADDI Emanuele (e-mail: edaddi@cea.fr)
DAGONEAU Nicolas (e-mail: nicolas.dagoneau@cea.fr)

DAMÉ Luc (e-mail: luc.dame@latmos.ipsl.fr)
DASGUPTA Aayush (e-mail: aayush.dasgupta@outlook.com)
DEAL Morgan (e-mail: morgan.deal@obspm.fr)
DEFRÈRE Denis (e-mail: ddefrere@ulg.ac.be)
DELEUIL Magali (e-mail: magali.deleuil@lam.fr)
DELVA Pacôme (e-mail: pacome.delva@obspm.fr)
DEMIDEM Camilia (e-mail: demidem@apc.in2p3.fr)
DEVIN Justine (e-mail: justine.devin@etu.umontpellier.fr)
DEVOST Daniel (e-mail: devost@cfht.hawaii.edu)
DI MATTEO Paola (e-mail: paola.dimatteo@obspm.fr)
DIMAURO Paola (e-mail: paola.dimauro@obspm.fr)
DINTRANS Boris (e-mail: boris.dintrans@irap.omp.eu)
DONATI Jean-francois (e-mail: jean-francois.donati@irap.omp.eu)
DOUGADOS Catherine (e-mail: catherine.dougados@univ-grenoble-alpes.f)
DUBUS Guillaume (e-mail: Guillaume.Dubus@univ-grenoble-alpes.fr)
DUC Pierre-alain (e-mail: pierre-alain.duc@astro.unistra.fr)
DUMONT Thibaut (e-mail: tdumont@irap.omp.eu)
DUPUY Rémi (e-mail: remi.dupuy@obspm.fr)
DURRET Florence (e-mail: durret@iap.fr)
EL MELLAH Ileyk (e-mail: ileyk.elmellah@kuleuven.be)
ELBAZ David (e-mail: delbaz@cea.fr)
ELYAJOURI Meriem (e-mail: meriem.el-yajouri@obspm.fr)
FALIZE Emeric (e-mail: e.falize@cea.fr)
FAUROBERT Marianne (e-mail: marianne.faurobert@unice.fr)
FEAUTRIER Nicole (e-mail: Nicole.Feautrier@obspm.fr)
FENSCH Jérémy (e-mail: jeremy.fensch@gmail.com)
FERNANDEZ TRINCADO Jose (e-mail: jfernandezt@astro-udec.cl)
FERRIÈRE Katia (e-mail: katia.ferriere@irap.omp.eu)
FORGET Francois (e-mail: forget@lmd.jussieu.fr)
FORTIN Morgane (e-mail: fortin@camk.edu.pl)
FOUCHER Frédéric (e-mail: frederic.foucher@cnrs.fr)
FOUCHET Thierry (e-mail: Thierry.Fouchet@obspm.fr)
FOUESNEAU Morgan (e-mail: fouesneau@mpia.de)
FOUQUÉ Pascal (e-mail: fouque@cfht.hawaii.edu)
FRAGKOUDI Francesca (e-mail: francesca.fragkoudi@obspm.fr)
FRAIX-BURNET Didier (e-mail: didier.fraix-burnet@univ-grenoble-alpes.)
FRANCO Maximilien (e-mail: maximilien.franco@cea.fr)
FREISSINET Caroline (e-mail: caroline.freissinet@latmos.ipsl.fr)
FREUNDLICH Jonathan (e-mail: jonathan.freundlich@obspm.fr)
GARCIA Rafael A. (e-mail: rgarcia@cea.fr)
GASNAULT Olivier (e-mail: Olivier.Gasnault@irap.omp.eu)
GATTANO César (e-mail: cesar.gattano@obspm.fr)
GAUDEL Mathilde (e-mail: mathilde.gaudel@cea.fr)
GAUDIN David (e-mail: david.gaudin@estaca.eu)
GEHAN Charlotte (e-mail: charlotte.gehan@obspm.fr)
GILET Nicolas (e-mail: nicolas.gilet@cnrs-orleans.fr)
GILLOT Jonathan (e-mail: jonathan.gillot@obspm.fr)
GOMEZ Ana (e-mail: ana.gomez@obspm.fr)
GOMEZ LOPEZ Jesus Alberto (e-mail: jesus.gomez-lopez@lam.fr)
GONNEAU Anaïs (e-mail: gonneau@astro.rug.nl)
GONZALEZ Matthias (e-mail: matthias.gonzalez@cea.fr)
GOUPIL Mariejo (e-mail: mariejo.goupil@obspm.fr)
GOURGOULHON Eric (e-mail: eric.gourgoulhon@obspm.fr)
GRAVET Romaric (e-mail: romaric.gravet@cnrs-orleans.fr)
GRITON Léa (e-mail: lea.griton@obspm.fr)

GROSSET Lucas (e-mail: lucas.grosset@obspm.fr)
GRY Cécile (e-mail: cecile.gry@lam.fr)
GUÉPIN Claire (e-mail: claire.guepin@iap.fr)
GUERLET Sandrine (e-mail:)
GUIDERDONI Bruno (e-mail: bruno.guiderdoni@univ-lyon1.fr)
GUILET Jérôme (e-mail: jerome.guilet@cea.fr)
GUIOT Pierre (e-mail: pierre.guiot@ias.u-psud.fr)
HALBWACHS Jean-louis (e-mail: jean-louis.halbwachs@astro.unistra.fr)
HALLOIN Hubert (e-mail: hubert.halloin@apc.in2p3.fr)
HARDY Emilie (e-mail: emilie.hardy@onera.fr)
HAYWOOD Misha (e-mail: misha.haywood@obspm.fr)
HERPIN Fabrice (e-mail: fabrice.herpin@u-bordeaux.fr)
HILL Vanessa (e-mail: Vanessa.Hill@oca.eu)
HOTTIER Clément (e-mail: clement.hottier@obspm.fr)
HUBY Elsa (e-mail:)
HUYNH Phuong-anh (e-mail: phuong-anh.huynh@onera.fr)
INCHAUSPE Henri (e-mail: henri.inchauspe@onera.fr)
JANVIER Miho (e-mail: miho.janvier@ias.u-psud.fr)
JOUVE Laurène (e-mail: ljouve@irap.omp.eu)
KATZ David (e-mail: david.katz@obspm.fr)
KAZERONI Rémi (e-mail: kazeroni@mpa-garching.mpg.de)
KERVELLA Pierre (e-mail: pierre.kervella@obspm.fr)
KHAN Saniya (e-mail: saniya.khan@obspm.fr)
KHOPERSKOV Sergey (e-mail: sergey.khoperskov@obspm.fr)
KLEIN Ludwig (e-mail:)
KOECHLIN Laurent (e-mail: laurent.koechlin@irap.omp.eu)
KORDOPATIS Georges (e-mail: gkordo@oca.eu)
KOTERA Kumiko (e-mail: kotera@iap.fr)
KRETZSCHMAR Matthieu (e-mail: matthieu.kretzschmar@cnrs-orleans.fr)
KULENTHIRARAJAH Logithan (e-mail: lkulenthirar@irap.omp.eu)
KUNDU Anu (e-mail: anu.kundu@astro.unistra.fr)
L'HARIDON Jonas (e-mail: jonas.lharidon@univ-nantes.fr)
LA MARLE Olivier (e-mail: olivier.lamarle@cnes.fr)
LADJELATE Bilal (e-mail: bilal.ladjelate@cea.fr)
LAGADEC Eric (e-mail: elagadec@oca.eu)
LAGAGE Pierre-olivier (e-mail: pierre-olivier.lagage@cea.fr)
LAGARDE Nadège (e-mail: nadege.lagarde@utinam.cnrs.fr)
LALLEMENT Roselyne (e-mail: roselyne.lallement@obspm.fr)
LAMBERT Sébastien (e-mail: sebastien.lambert@obspm.fr)
LANÇON Ariane (e-mail: ariane.lancon@astro.unistra.fr)
LAVRAUD Benoit (e-mail: Benoit.Lavraud@irap.omp.eu)
LAYCHAK Mary Beth (e-mail: laychak@cfht.hawaii.edu)
LE BERTRE Thibaut (e-mail: thibaut.lebertre@obspm.fr)
LE COROLLER Hervé (e-mail:)
LE PETIT Franck (e-mail: Franck.LePetit@obspm.fr)
LE PONCIN-LAFITTE Christophe (e-mail: christophe.leponcin@obspm.fr)
LEBLANC Francois (e-mail: francois.leblanc@latmos.ipsl.fr)
LEBRETON Yveline (e-mail: yveline.lebreton@obspm.fr)
LECONTE Jeremy (e-mail: jeremy.leconte@u-bordeaux.fr)
LEIBACHER John (e-mail: john.leibacher@ias.u-psud.fr)
LEFEBVRE Eric (e-mail:)
LESTRADE Jean-françois (e-mail: jean-francois.lestrade@obspm.fr)
LIGI Roxanne (e-mail: roxanne.ligi@lam.fr)
LILENSTEN Jean (e-mail: jean.lilensten@univ-grenoble-alpes.fr)
LOH Alan (e-mail: alan.loh@obspm.fr)

LOUIS Corentin (e-mail: corentin.louis@obspm.fr)
MAKSIMOVIC Milan (e-mail: milan.maksimovic@obspm.fr)
MARCEL Grégoire (e-mail: gregoire.marcel@univ-grenoble-alpes.fr)
MARCOWITH Alexandre (e-mail: alexandre.Marcowith@umontpellier.fr)
MARIN Frederic (e-mail: frederic.marin@astro.unistra.fr)
MARSHALL Douglas (e-mail: douglas.marshall@cea.fr)
MARTIN Thomas (e-mail: thomas.martin.1@ulaval.ca)
MARTIN Jean-michel (e-mail: jean-michel.martin@obspm.fr)
MARTIN Nicolas (e-mail: nicolas.martin@astro.unistra.fr)
MARTIN-LAGARDE Marine (e-mail: marine.martin-lagarde@obspm.fr)
MARTINET Sébastien (e-mail: sebastien-martinet@gmail.com)
MARTINS Fabrice (e-mail: fabrice.martins@umontpellier.fr)
MASNOU Jean-louis (e-mail: jean-louis.masnou@malix.univ-paris1.fr)
MASTROBUONO-BATTISTI Alessandra (e-mail: mastrobuono@mpia.de)
MATTEINI Lorenzo (e-mail: lorenzo.matteini@obspm.fr)
MATAR Jessy (e-mail: jessym13@hotmail.com)
MATTER Alexis (e-mail: Alexis.Matter@oca.eu)
MAłEK Katarzyna (e-mail: kasia.malek@lam.fr)
MEI Simona (e-mail: simona.mei@obspm.fr)
MEIN Nicole (e-mail: nicole.mein@obspm.fr)
MELIANI Zakaria (e-mail: zakaria.meliani@obspm.fr)
METRIS Gilles (e-mail: Gilles.Metris@geoazur.unice.fr)
MEYNADIER Frédéric (e-mail: frederic.meynadier@obspm.fr)
MICHEL Eric (e-mail: eric.michel@obspm.fr)
MICHEL Thibault (e-mail: thibault.michel@polytechnique.edu)
MIGNOT Shan (e-mail: shan.mignot@obspm.fr)
MINAZZOLI Olivier (e-mail: ominazzoli@gmail.com)
MIRABEL Felix (e-mail: felix.mirabel@cea.fr)
MIROUH Giovanni (e-mail: gmirouh@sissa.it)
MIVILLE-DESCHêNES Marc-antoine (e-mail: mamd@ias.u-psud.fr)
MODOLO Ronan (e-mail: ronan.modolo@latmos.ipsl.fr)
MONARI Giacomo (e-mail: giacomo.monari@fysik.su.se)
MONIER Richard (e-mail: Richard.Monier@obspm.fr)
MONTARGÈS Miguel (e-mail: miguel.montarges@obspm.fr)
MONTILLAUD Julien (e-mail: julien@obs-besancon.fr)
MONTMERLE Thierry (e-mail: thierry.montmerle@iap.fr)
MOSSER Benoit (e-mail: benoit.mosser@obspm.fr)
MOUILLET David (e-mail:)
MOUCHET Martine (e-mail: martine.mouchet@obspm.fr)
MOUROT Audrey (e-mail: audreymourot@gmail.com)
MOUSIS Olivier (e-mail: olivier.mousis@lam.fr)
MUSSET Sophie (e-mail: sophie.musset@obspm.fr)
NASELLO Guillaume (e-mail: guillaume.nasello@obs-besancon.fr)
NOIROT Gaël (e-mail: gael.noirot@obspm.fr)
OU Ziwei (e-mail: ziwei.ou@ipno.in2p3.fr)
OUAZZANI Rhita-maria (e-mail: rhita-maria.ouazzani@obspm.fr)
OWIS Ashraf (e-mail: aowis@cu.edu.eg)
PAGANI Laurent (e-mail: laurent.pagani@obspm.fr)
PALACIOS Ana (e-mail: ana.palacios@umontpellier.fr)
PARIAT Etienne (e-mail: etienne.pariat@obspm.fr)
PARRONI Carolina (e-mail: carolina.parroni@obspm.fr)
PAWLOWSKI Marcel (e-mail:)
PERRAUT Karine (e-mail: karine.perraut@univ-grenoble.fr)
PERRIN Guy (e-mail: guy.perrin@obspm.fr)
PERRONE Denise (e-mail: denise.perrone@esa.int)

PERROT Clément (e-mail: clement.perrot@obspm.fr)
PESCHKEN Nicolas (e-mail: npeschken@camk.edu.pl)
PETIT Pascal (e-mail: ppetit@irap.omp.eu)
PETITEAU Antoine (e-mail: petiteau@apc.univ-paris7.fr)
PETRUCCI Pierre-olivier (e-mail: pierre-olivier.petrucci@obs.ujf-grenoble)
PICQUENOT Adrien (e-mail: adrien.picquenot@cea.fr)
PIHAN-LE BARS Hélène (e-mail: helene.pihan-lebars@obspm.fr)
POLYCARPE William (e-mail: william.polycarpe@obspm.fr)
POMMIER Mamta (e-mail: mamtapan@gmail.com)
PRANTZOS Nikos (e-mail: prantzos@iap.fr)
PRUGNIEL Philippe (e-mail: philippe.prugniel@univ-lyon1.fr)
RAMBAUX Nicolas (e-mail: Nicolas.Rambaux@obspm.fr)
RANJAN Adarsh (e-mail: ranjan@iap.fr)
RANNOU Pascal (e-mail: pascal.rannou@univ-reims.fr)
REESE Daniel (e-mail:)
RENAUD Florent (e-mail: florent.renaud@gmail.com)
REYLÉ Céline (e-mail: celine@obs-besancon.fr)
RIGON Gabriel (e-mail: gabriel.rigon@polytechnique.edu)
RIGUCCINI Laurie (e-mail: riguccini@astro.ufrj.br)
RIU Lucie (e-mail: lucie.riu@ias.u-psud.fr)
ROBIN Annie (e-mail: annie.robin@obs-besancon.fr)
RODRIGUEZ Jerome (e-mail: jrodriguez@cea.fr)
ROELENS Maroussia (e-mail: maroussia.roelens@unige.ch)
ROJAS LOBOS Patricia Andrea (e-mail: parltes@gmail.com)
ROUX Wilhem (e-mail: wroux@irap.omp.eu)
ROYER Frédéric (e-mail: frederic.royer@obspm.fr)
RUIZ-DERN Laura (e-mail: laura.ruiz-dern@obspm.fr)
SALABERT David (e-mail: david.salabert@cea.fr)
SALOME Philippe (e-mail: philippe.salome@obspm.fr)
SALOMON Jean-baptiste (e-mail: salomon@camk.edu.pl)
SAMADI Réza (e-mail: reza.samadi@obspm.fr)
SCEPI Nicolas (e-mail: nicolas.scepi@univ-grenoble-alpes.fr)
SCHIRMER Thiébaut-antoine (e-mail: schirmer.thiebaut@gmail.com)
SCHMIDT Frédéric (e-mail: frederic.schmidt@u-psud.fr)
SELSIS Franck (e-mail:)
SGATTONI Andrea (e-mail: andrea.sgattoni@obspm.fr)
SIMON-PETIT Alicia (e-mail: alicia.simon-petit@ensta-paristech.fr)
SOUCHAY Jean (e-mail: jean.souchay@obspm.fr)
SOURIE Aurélien (e-mail: aurelien.sourie@obspm.fr)
SPALLICCI Alessandro (e-mail: spallicci@cnrs-orleans.fr)
SPOTO Federica (e-mail: fspoto@oca.eu)
STEE Philippe (e-mail: philippe.stee@oca.eu)
STEHLE Chantal (e-mail: chantal.stehle@obspm.fr)
STOLARCZYK Thierry (e-mail:)
SZOPA Cyril (e-mail: cyril.szopa@latmos.ipsl.fr)
TABONE Benoit (e-mail: benoit.tabone@obspm.fr)
TALAI Mohamed Cherif (e-mail: talai.mc@univ-annaba.org)
TALLON-BOSC Isabelle (e-mail: bosc@obs.univ-lyon1.fr)
TCHANG Lydia (e-mail: lydia.tchang-brillet@obspm.fr)
TERRIER (e-mail:)
THÉVENIN Frédéric (e-mail: frederic.thevenin@oca.eu)
TOBIE Gabriel (e-mail: gabriel.tobie@univ-nantes.fr)
TRESSE Laurence (e-mail: laurence.tresse@univ-lyon1.fr)
TRIAUD Amaury (e-mail: aht34@cam.ac.uk)
TUCKEY Philip (e-mail: philip.tuckey@obspm.fr)

TURBET Martin (e-mail: `mturbet@lmd.jussieu.fr`)
TURCO-LIVERI Roberto (e-mail: `pavesan@yahoo.com`)
TURON Catherine (e-mail: `catherine.turon@obspm.fr`)
UNDA SANZANA Eduardo (e-mail:)
VALS Margaux (e-mail: `margaux.vals@gmail.com`)
VAN BOX SOM Lucile (e-mail: `lucile.vanboxsom@obspm.fr`)
VAN DER SWAELMEN Mathieu (e-mail: `swaelmen@oca.eu`)
VARNIERE Peggy (e-mail: `varniere@apc.univ-paris7.fr`)
VAUGLIN Isabelle (e-mail: `isabelle.vauglin@univ-lyon1.fr`)
VEILLET Roméo (e-mail: `romeo.veillet@free.fr`)
VIDAL GARCIA Alba (e-mail:)
VILLEBRUN Florent (e-mail: `florent.villebrun@univ-grenoble-alpes.fr`)
VILMER Nicole (e-mail:)
VISO Michel (e-mail: `michel.viso@cnes.fr`)
WESTALL Frances (e-mail: `frances.westall@cnrs-orleans.fr`)
WILLIGER Gerard (e-mail:)
WOLF Peter (e-mail: `peter.wolf@obspm.fr`)
WOZNIAK Hervé (e-mail: `herve.wozniak@umontpellier.fr`)
YGOUF Marie (e-mail: `mygouf@ipac.caltech.edu`)
YU Louise (e-mail: `louise.yu@irap.omp.eu`)
ZARKA Philippe (e-mail: `philippe.zarka@obspm.fr`)
ZILLES Anne (e-mail: `zilles@iap.fr`)

Session SF2A

Plenary session

SF2A 2017
C. Reylé, P. Di Matteo, F. Herpin, É. Lagadec, A. Lançon, Z. Meliani, F. Royer (eds)

FIRST RESULTS FROM THE MAGNETOSPHERIC MULTISCALE MISSION

B. Lavraud[1]

Abstract. Since its launch in March 2015, NASA's Magnetospheric Multiscale mission (MMS) provides a wealth of unprecedented high resolution measurements of space plasma properties and dynamics in the near-Earth environment. MMS was designed in the first place to study the fundamental process of collisionless magnetic reconnection. The two first results reviewed here pertain to this topic and highlight how the extremely high resolution MMS data (electrons, in particular, with full three dimensional measurements at 30 ms in burst mode) have permitted to tackle electron dynamics in unprecedented details. The first result demonstrates how electrons become demagnetized and scattered near the magnetic reconnection X line as a result of increased magnetic field curvature, together with a decrease in its magnitude. The second result demonstrates that electrons form crescent-shaped, agyrotropic distribution functions very near the X line, suggestive of the existence of a perpendicular current aligned with the local electric field and consistent with the energy conversion expected in magnetic reconnection (such that $\mathbf{J} \cdot \mathbf{E} > 0$). Aside from magnetic reconnection, we show how MMS contributes to topics such as wave properties and their interaction with particles. Thanks again to extremely high resolution measurements, the lossless and periodical energy exchange between wave electromagnetic fields and particles, as expected in the case of kinetic Alfvén waves, was confirmed. Although not discussed, MMS has the potential to solve many other outstanding issues in collision-less plasma physics, for example regarding shock or turbulence acceleration, with obvious broader impacts in astrophysics in general.

Keywords: collision-less magnetic reconnection,kinetic Alfvén waves, electron stochastic dynamics

1 Introduction

With the advent of the space era, it has become possible to study astrophysical plasma processes in situ. Although the plasma regime (density, temperature, magnetic field magnitude) in near-Earth space is not necessarily comparable to those in more remote astrophysical objects such as active galactic nuclei or just the Sun, it remains that near-Earth space is the only accessible astrophysical plasma from which we can hope to extrapolate our knowledge to more exotic environments. From already several decades of in situ space measurements we have increased our understanding of many key plasma processes, such as magnetic reconnection, shocks, wave-particle interactions and turbulence, among others. The Earth's magnetosphere, depicted in Figure 1, constitutes for that purpose a perfect natural laboratory. The interaction between the solar wind and the magnetosphere indeed results in the formation of various regions and boundaries where these fundamental processes are at work. The first interaction with the solar wind occurs at the fast mode wave shock, which slows down, heats and deflects the solar wind plasma along the magnetospheric flanks in a region known as the magnetosheath. This often turbulent medium is the region in direct contact with the magnetosphere at the magnetopause. The magnetopause is thus the location where plasma and energy transfer between the solar wind and the magnetosphere occurs, and magnetic reconnection is the key process at work in that respect. The process of magnetic reconnection is ubiquitous in the plasma universe. Although it has major large-scale implications on the surrounding media, the processes that control magnetic reconnection occur at very small scales in a region known as the diffusion region (where magnetic fields diffuse and reconnect with a new topology) (e.g., Priest & Forbes 2000). In proton-electron plasmas, as observed near-Earth for instance, the vastly different particle masses lead to a structured region wherein the ions (with larger gyro-radius) decouple from the magnetic field farther from the X-line (where the topology changes) than electrons. This separation leads

[1] Institut de Recherche en Astrophysique et Planétologie, Université de Toulouse, France

to the formation of an ion diffusion region with characteristic Hall currents and magnetic fields embedding a much smaller electron diffusion region (e.g., Øieroset et al. 2001; Mozer et al. 2002). While missions such as the multi-spacecraft Cluster mission have instrumentation and inter-spacecraft separation on the order of the typical ion scales at the Earth's magnetopause, the Magnetospheric Multiscale (MMS) mission has been designed to understand the electron-scale physics associated with magnetic reconnection (Burch et al. 2015). In this paper we highlight a few selected MMS results that pertain to particle dynamics, and their interaction with waves, at spatio-temporal scales that were way beyond reach before the MMS era.

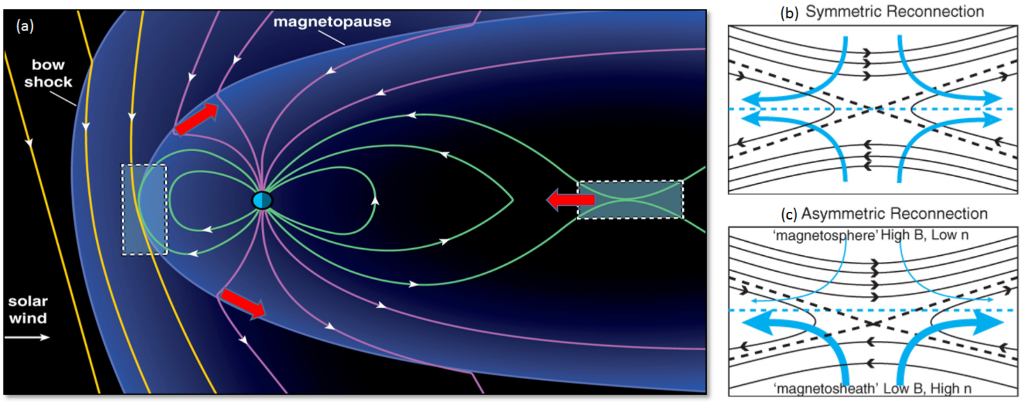

Fig. 1. (a) Schematic of the Earth's magnetosphere with its main surrounding boundaries. Two rectangles are highlighted where magnetic reconnection is known to occur; at the dayside magnetopause and in the magnetotail. The main flow patterns resulting from reconnection, and driving magnetospheric convection in the magnetosphere, are shown with red arrows. (b) Schematic of the magnetic reconnection topology and flows for symmetric plasma properties on each side of the X line. (c) Similar to (b) but for asymmetric plasma properties. Adapted from Eastwood et al. (2013).

2 The MMS mission

The four NASA MMS (Burch et al. 2015) spacecraft were launched together on March 12, 2015 on an Atlas V launch vehicle into a highly elliptical 28°-inclination orbit with perigee at 1.2 Earth radii (RE) and apogee at 12 RE. The results reviewed here are based on ion and electron measurements from the Fast Plasma Instruments (FPI, Pollock et al. 2016)), magnetic field measurements from the FluxGate Magnetometers (FGM, Russell et al. 2016)), and electric field data from the Electric Double Probe instrument, which consists of the Spin Plane Double Probe (SDP, Lindqvist et al. 2016)) and the Axial Double Probe (ADP, Ergun et al. 2016)). With a 12 RE apogee, the first 2 years of the MMS mission were dedicated to the study of magnetic reconnection at the dayside magnetopause (Figure 1a, left rectangle). Magnetic reconnection there takes place between two plasmas with very different properties (density, temperature and magnetic field in particular); magnetic reconnection is said to be asymmetric (cf. Figure 1c). After 2 years, the apogee of the MMS spacecraft has recently been increased to 25 RE so as to focus on the process of magnetic reconnection in the magnetotail (right-hand side rectangle in Figure 1c). In the magnetotail, reconnection occurs between the south and north lobe regions, which have very similar properties; magnetic reconnection is said to be symmetric. In addition to a smart orbit design, permitting to sample various types of reconnection properties, the main requirements for meeting the MMS mission objectives were: (1) four spacecraft in a close tetrahedron formation with adjustable separations down to less than 10 km, (2) accurate three-axis electric and magnetic field measurements for estimating spatial gradients and time variations, and (3) three-dimensional electron and ion distribution functions at the highest time resolution ever achieved (30 ms for electrons and 150 ms for ions). Requirement (1) is particularly critical to discriminate spatial from temporal variations in in situ measurements. Indeed, with a single spacecraft it is essentially impossible to determine if a signature in the time series is due to a spatial structure passing by the spacecraft (e.g., back and forth motion of a boundary) or the result of a temporal variation (e.g., a propagating wave). Requirement (2) stems from the fact that the calculation of gradients, e.g. the electric current using Ampère's law in the Curlometer technique (Robert et al. 1998), across the tetrahedron at such small scales requires high fidelity electromagnetic field measurements to limit the propagation of errors (in the gradient method). Then, a major leap forward brought by MMS is the unprecedentedly high temporal resolution of full three-dimensional particle measurements. It is a factor 100 higher than past measurements for electrons, consistent with the requirement (3) to study electron dynamics at the electron scale.

3 Electron dynamics in highly curved magnetic fields

Among all MMS first amazing results, many have come from its 30 ms electron measurements, which permit the study of electron dynamics in unprecedented details. Electron dynamics in collisionless magnetic reconnection has been studied mostly using test particle (Speiser 1965) and particle-in-cell (PIC) simulations (e.g., Hoshino et al. 2001; Hesse et al. 2014). For the present topic, of particular interest is the prediction that particle pitch angle scattering should occur when the gyroradius of a particle is on the order of the scale of the local magnetic field curvature. With RC the local magnetic field curvature and RG the particle gyroradius, one can define an adiabatic parameter κ such that $\kappa^2 = RG/RC$. Based on this parameter, theory predicts that particle scattering (of ions or electrons) occurs when κ^2 approaches 25, and that particle dynamics becomes chaotic for values below 10 (Büchner & Zelenyi 1989; Sergeev et al. 1983). Although there have been a few observations of non-adiabatic proton and electron dynamics in the tail region of the Earth for high energy particles (Egedal et al. 2005; Shen et al. 2014), only theory and numerical modeling were so far able to study the complex behavior of thermal electrons at electron scales (Ng et al. 2011; Hesse et al. 2014; Wang et al. 2016). No appropriate spacecraft observations were available before MMS. Such small-scale electron dynamics is illustrated in Figure 2. This Figure shows a typical anti-parallel magnetic reconnection geometry with reconnecting field lines in purple and an example electron trajectory in black. The underlying red and blue colors represent the out-of-plane magnetic field (generally called the Hall magnetic field). A spacecraft trajectory is shown with a red arrow. It is taken as representative of the crossing of a reconnecting magnetopause that occurred on 16 October 2015 (shown in Figure 2b). Apart from the magnetic field lines and spacecraft trajectory (both drawn for context) the Hall field and electron trajectory are direct outputs from a kinetic simulation made by Bessho et al. (2015). The key signature to note in Figure 2a is the non-adiabatic electron behavior. Indeed, as the example electron moves from point 1 to point 2 toward the X line, the magnetic field magnitude decreases significantly (not shown). In addition, as a result of reconnection a strong current sheet is formed along points 2 to 7 where the Hall magnetic field switches sign. The magnetic field is thus lower but also highly curved all along this current sheet. This combination of low and curved magnetic field leads to a non-adiabatic behavior such that when the electron reaches point 2 it is scattered back toward the same side of the current sheet. Had the electron behaved adiabatically, it would have crossed towards the other side of the current sheet. The same behavior is observed at points 4 and 5, while the electron traverses the current sheet at points 3, 6 and 7. Figure 2b shows data from MMS spacecraft # 4 on 16 October 2015 during a crossing of the dayside magnetopause. The spacecraft are traversing from the magnetosphere (to the left) to the magnetosheath (to the right). Although not shown, all plasma parameters are consistent with such a crossing (cf. Lavraud et al. 2016). We only focus here on the pitch angle distribution (i.e., the angle between the velocity of the electron and the magnetic field direction) of 100 eV electrons in the upper panel, and on the magnetic field curvature in the second panel. The magnetic field radius of curvature (RC) is measured thanks to a four-spacecraft gradient method, as described in more detail in Shen et al. (2003). On the magnetospheric side of the magnetopause (to the left) electrons are strongly magnetized, as demonstrated by the strong anisotropy with much larger fluxes in the field-aligned (0°) and anti-field-aligned (180°) directions. Similarly, electrons are fully magnetized in the magnetosheath (right-hand side), with a highly structured pitch angle distribution. By contrast, electrons are very isotropic in the center of the region, close to the location where the magnetic field is most curved. Together with some other signatures, not detailed here, these observations are consistent with the scattering observed in the simulation of Figure 2a. These are the first observations of thermal electron pitch-angle diffusion associated with magnetic reconnection.

4 Currents and crescent electron distributions

Another major, recent observation is that of crescent electron distribution functions (Burch et al. 2016) in the electron diffusion region of magnetic reconnection. This naming comes from the representation shown in Figure 3a. It shows a cut of the three-dimensional distribution function of electrons in the plane perpendicular to the magnetic field. The distribution function shown corresponds to a time when it is believed that the spacecraft crossed the electron diffusion region of magnetic reconnection very close to the X line of the dayside magnetopause (also on 16 October 2015, but at a time different from the event of Figure 2). This highly non-gyrotropic (i.e., not axially symmetric in the plane perpendicular to the magnetic field) distribution carries a

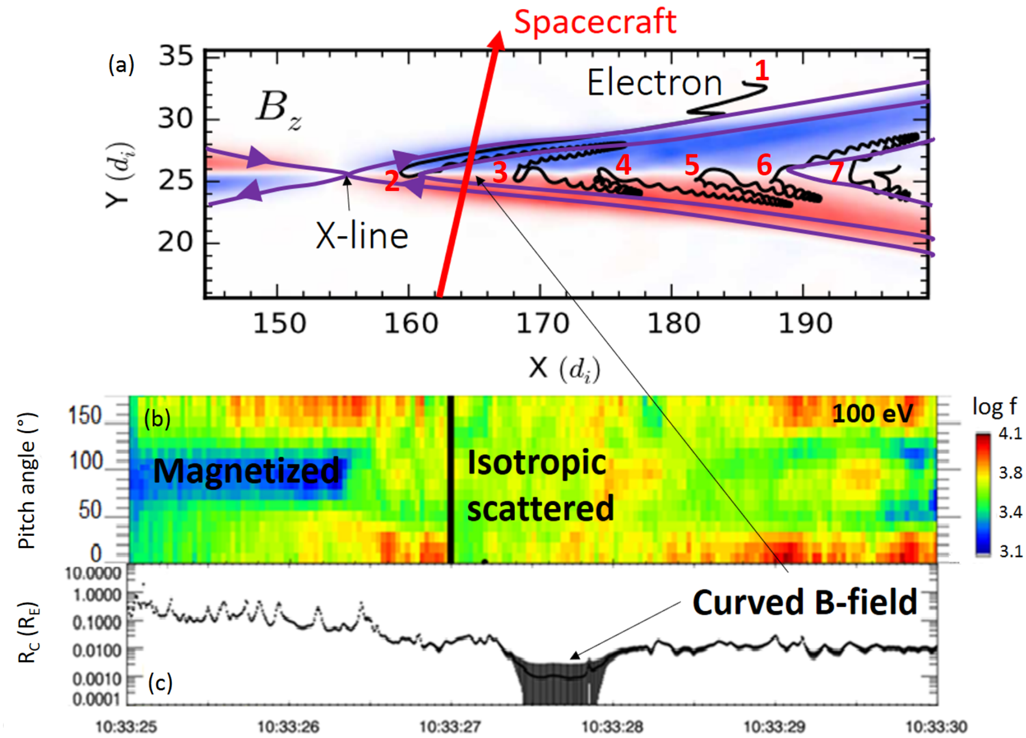

Fig. 2. (a) Illustration of an electron trajectory (black line) in the magnetic field geometry (purples lines) near a magnetic reconnection X line. Red and blue colors show the out-of-plane (Hall) magnetic field component. Seven specific locations of the electron trajectory are marked with red numbers. These are further discussed in the text. We also illustrate the rough trajectory of the MMS spacecraft that is consistent with the observations shown in panels (b) and (c). Panel (a) is adapted from a simulation by Bessho et al. (2015). Panels (b) and (c) are adapted from Lavraud et al. (2016). They show, respectively, (b) the pitch angle distribution of 100 eV electrons as a function of time during a crossing of the MMS spacecraft near an X line, together with (b) the magnetic field radius of curvature as estimated using a multi-spacecraft technique Shen et al. (2003) during the same interval. The time at which electrons become isotropic is shown with a vertical line in panel (b).

strong perpendicular current. This perpendicular current has the same orientation as the local electric field $\mathbf{E}$ (as measured by the EDP instrument) so that $\mathbf{J}\cdot\mathbf{E}$ is positive as observed in Figure 2b ($\mathbf{J}$ is the current density vector). It should be noted that this signature is confirmed by the independent calculations of the current based on the multi-spacecraft curlometer method and the direct particle measurements, i.e., $\mathbf{J} = Nq(\mathbf{V_i} - \mathbf{V_e})$ (where N is the plasma density, q the electric charge, and $\mathbf{V_i}$ and $\mathbf{V_e}$ respectively the ion and electron velocity vectors). Such direct current estimations using ion and electron data (velocity and density) had never been achieved before the high resolution, high accuracy MMS measurements. The interpretation is that such crescent electron distributions appear exactly at the X line as a result of Speiser-type (Speiser 1965) meandering electron orbits in the local inversion of the magnetic field, and that the resulting current is consistent with that expected from a dissipative process such as magnetic reconnection (with $\mathbf{J}\cdot\mathbf{E} > 0$).

5 Electromagnetic field and particles interaction in kinetic Alfvén waves

Although MMS was specifically tailored for the study of magnetic reconnection, the mission is able to tackle many other plasma physics questions. Among these is the exact mechanics of waves and wave-particle interactions. The Alfvén wave is the most ubiquitous wave mode in plasma physics (Alfvén 1942). When the wavelength is large compared to the thermal ion scale, no energy is transferred between the field and the plasma. However, when the wave's perpendicular spatial scale approaches this scale, the Alfvén wave propagates obliquely and can support a significant parallel electric field. This property means the existence of a transfer of energy between the wave and the particles (Hasegawa & Chen 1976). Such kinetic Alfvén waves (KAW) are of critical importance both in laboratory (e.g., Wong 1999) and space environments (e.g., Louarn et al. 1994). Thanks

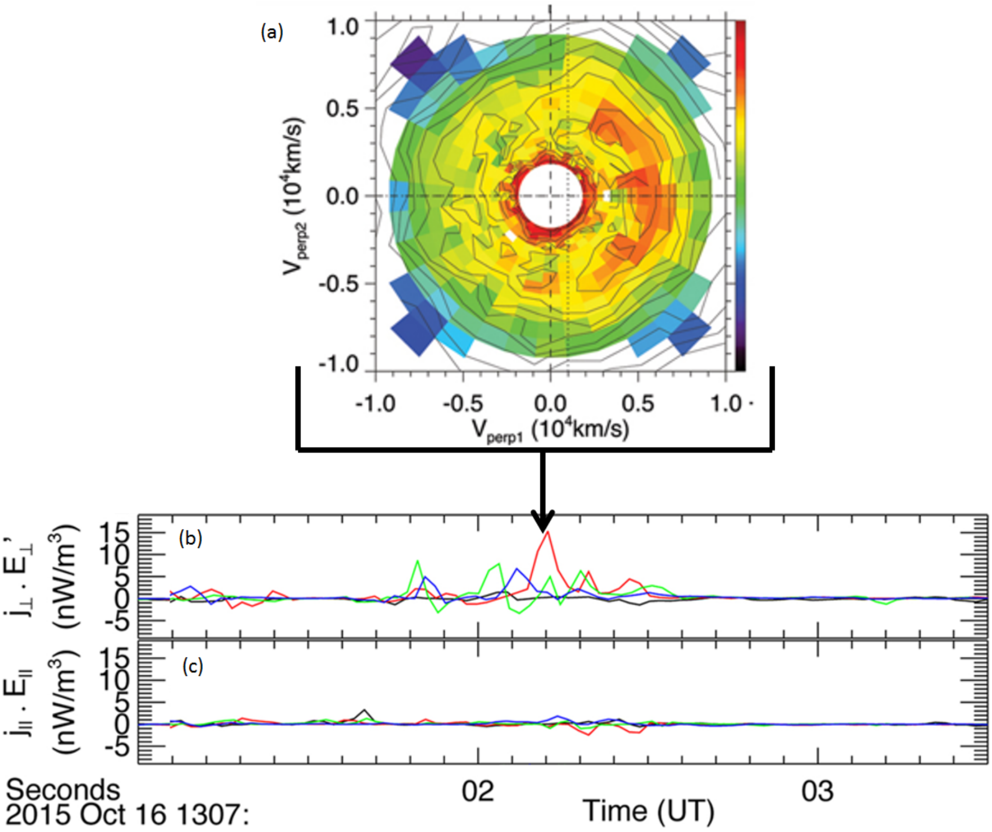

Fig. 3. (a) Cut of a three-dimension electron distribution function in the plane perpendicular to the local magnetic field during an X line crossing (electron diffusion region) on 16 October 2015. The color coding shows the phase space density of electrons. (b) Perpendicular and (c) parallel components of $\mathbf{J} \cdot \mathbf{E}$, the plasma heating term. Adapted from Burch et al. (2016).

to high resolution MMS data in the Earth's magnetosphere, Gershman et al. (2017) recently demonstrated the direct exchange of energy between plasma particles and fields in a marginally stable KAW train.

The current ($\mathbf{J}$) and electron-pressure-gradient-driven electric field ($\mathbf{Ep} = -\nabla \cdot \mathbf{Pe}/(nee)$) are perpendicular to each other in regular Alfvén wave fluctuations. $\mathbf{J} \cdot \mathbf{E}$, the plasma heating term, is thus equal to zero throughout the entire wave. Gershman et al. (2017) recently studied MMS observations of low frequency ($\sim$ 1 Hz) fluctuations akin to a KAW train in the dayside magnetosphere close to the magnetopause. The observations showed that the perpendicular and parallel components of $\mathbf{J}$ and $\mathbf{Ep}$ were $\sim 90°$ out-of-phase with respect to each other, as shown in Figure 4. This phase difference implies a non-zero value of $\mathbf{J} \cdot \mathbf{E}$ throughout the wave train, thereby demonstrating for the first time the instantaneous and very local nature of energy exchange between electromagnetic fields and particles within KAW.

Although not shown, Gershman et al. (2017) also uncovered an unpredicted population of electrons trapped within the wave fluctuations. The unprecedented high resolution measurements by the MMS spacecraft thus also open the door to a whole new unexplored territory in wave-particle interaction physics.

6 Conclusions

We have reviewed a few chosen results from NASA's recent Magnetospheric Multiscale (MMS) mission. Thanks to its unprecedented high-resolution measurements, the intricate dynamics of electron populations and associated currents in the vicinity of the diffusion region of magnetic reconnection at Earth's dayside magnetopause are revealed. This review only mentions three results: (1) the demagnetization and scattering of electrons at very small scales (and energies) owing to highly curved magnetic field lines, (2) the formation of crescent-shaped electron distribution functions at the X line, and whose perpendicular current is consistent with the conversion of magnetic energy into particle energy ($\mathbf{J} \cdot \mathbf{E} > 0$), and (3) the lossless and periodical energy exchange between

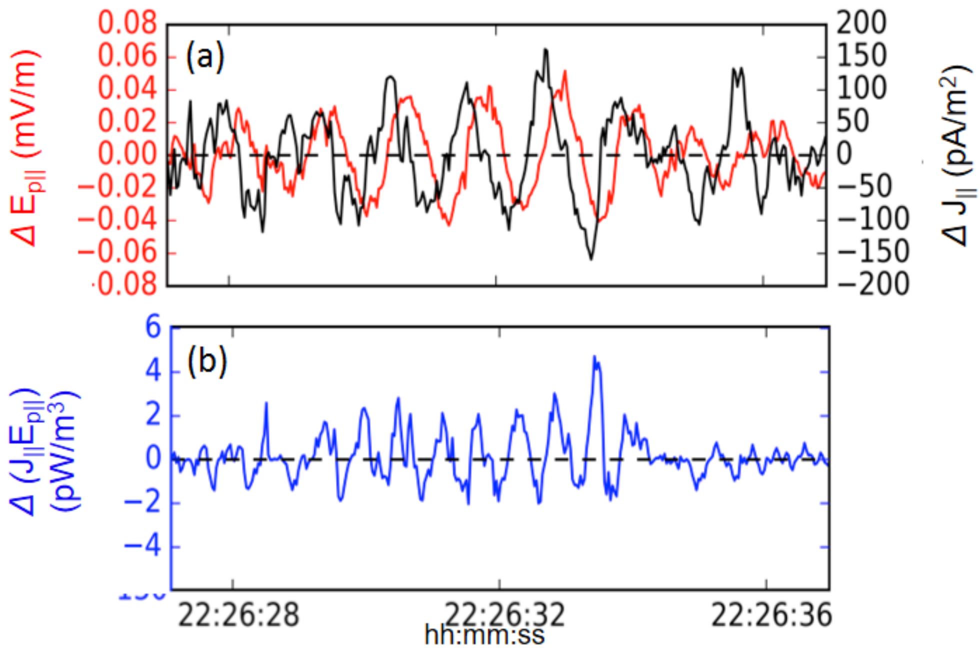

Fig. 4. (a) Parallel components of the current (**J**) and electron-pressure-gradient-driven electric field ($\mathbf{E_p}$) during a kinetic Alfvén wave fluctuation. Panel (b) shows the non-zero variations of $\mathbf{J}_{\|} \cdot \mathbf{E}_{\mathbf{p},\|}$, the plasma heating term, which demonstrates the direct exchange of energy between plasma particles and fields in this KAW train. Adapted from Gershman et al. (2017).

electromagnetic fields and particles in kinetic Alfvén waves. There are already many other results compiled, for instance, in two special sections of Geophysical Research Letters and Journal of Geophysical Research, in 2016 and 2017, respectively. The topics addressed also involve shocks and turbulence, two domains in which MMS will undoubtedly shed important new lights in the coming years.

For MMS data visit `https://lasp.colorado.edu/mms/sdc/public/`. We thank all the MMS teams for their remarkable work and great hardware accomplishments. Work at IRAP and LPP was performed with the support of CNRS and CNES.

References

Alfvén, H. 1942, Nature, 150, 405

Bessho, N., Chen, L.-J., Germaschewski, K., & Bhattacharjee, A. 2015, Journal of Geophysical Research (Space Physics), 120, 9355

Büchner, J. & Zelenyi, L. M. 1989, in Proceedings of an international Workshop on Reconnection in Space Plasma, ed. C. I. Meng, M. J. Rycroft, & L. A. Frank, Vol. 2, Europen Space Agency, Paris, 21

Burch, J. L., Moore, T. E., Torbert, R. B., & Giles, B. L. 2015, Space Sci. Rev.

Burch, J. L., Torbert, R. B., Phan, T. D., et al. 2016, Science

Eastwood, J. P., Phan, T. D., Drake, J. F., et al. 2013, Physical Review Letters, 110, 225001

Egedal, J., Øieroset, M., Fox, W., & Lin, R. P. 2005, Physical Review Letters, 94, 025006

Ergun, R. E., Tucker, S., Westfall, J., et al. 2016, Space Sci. Rev., 199, 167

Gershman, D. J., F-Viñas, A., Dorelli, J. C., et al. 2017, Nature Communications, 8, 14719

Hasegawa, A. & Chen, L. 1976, Physical Review Letters, 36, 1362

Hesse, M., Aunai, N., Sibeck, D., & Birn, J. 2014, Geophys. Res. Lett., 41, 8673

Hoshino, M., Mukai, T., Terasawa, T., & Shinohara, I. 2001, J. Geophys. Res., 106, 25979

Lavraud, B., Zhang, Y. C., Vernisse, Y., et al. 2016, Geophys. Res. Lett., this issue

Lindqvist, P.-A., Olsson, G., Torbert, R. B., et al. 2016, Space Sci. Rev., 199, 137

Louarn, P., Wahlund, J. E., Chust, T., et al. 1994, Geophys. Res. Lett., 21, 1847

Mozer, F. S., Bale, S. D., & Phan, T. D. 2002, Physical Review Letters, 89, 015002

Ng, J., Egedal, J., Le, A., Daughton, W., & Chen, L.-J. 2011, Physical Review Letters, 106, 065002

Øieroset, M., Phan, T. D., Fujimoto, M., Lin, R. P., & Lepping, R. P. 2001, Nature, 412, 414

Pollock, C., Moore, T., Jacques, A., et al. 2016, Space Science Rev., 199, 331

Priest, E. & Forbes, T., eds. 2000, Magnetic reconnection : MHD theory and applications

Robert, P., Dunlop, M., Roux, A., & Chanteur, G. 1998, in Analysis Methods for Multi-Spacecraft Data, ed. G. Paschman & P. Daly, ISSI Scientific Report SR-001 (European Space Agency), 395–418

Russell, C. T., Anderson, B. J., Baumjohann, W., et al. 2016, Space Sci. Rev., 199, 189

Sergeev, V. A., Sazhina, E. M., Tsyganenko, N. A., Lundblad, J. A., & Soraas, F. 1983, Planet. Space Sci., 31, 1147

Shen, C., Li, X., Dunlop, M., et al. 2003, Journal of Geophysical Research (Space Physics), 108, 1168

Shen, C., Yang, Y. Y., Rong, Z. J., et al. 2014, Journal of Geophysical Research (Space Physics), 119, 2458

Speiser, T.-W. 1965, J. Geophys. Res., 70, 4219

Wang, S., Chen, L.-J., Bessho, N., et al. 2016, Journal of Geophysical Research (Space Physics), 121, 2104

Wong, K.-L. 1999, Plasma Physics and Controlled Fusion, 41, R1

SF2A 2017
C. Reylé, P. Di Matteo, F. Herpin, É. Lagadec, A. Lançon, Z. Meliani, F. Royer (eds)

GALACTIC AND EXTRAGALACTIC SCIENCE WITH SITELLE

T. B. Martin[1], L. Drissen [1,2] and A.-L. Melchior[3]

Abstract. We present in this paper some recent results obtained with SITELLE, an imaging Fourier transform spectrometer (iFTS) attached to the Canada-France-Hawaii telescope, in link with which the latest improvements in terms of data analysis.

Keywords: SITELLE, Imaging Fourier Transform Spectrometry, M31, M57, planetary nebulae, diffuse ionized gas, nova shell, AT Cnc, ORCS

1 Introduction

SITELLE is an imaging Fourier transform spectrometer (iFTS) designed to obtain the spectrum, in selected bands of the visible range, of each source of light present in the 4 million pixels covering an 11'×11' field of view. It is attached to the Canada-France-Hawaii 3.6-m telescoope. Its spectral resolution R can be chosen between 1 and 10000. We will show some of the observing capabilities of SITELLE, which are closely related to the last improvements in terms of data analysis, through some of the science studies based on its data.

2 M31's Central Region, Planetary Nebulae and Diffuse Ionized Gas

The first study of the centre of M31 in the SN3 filter (649-484 nm: Hα, [NII]6548,6584, [SII]6716,6731) was dedicated to the calibration of the data and the creation of a catalogue of nearly 800 Hα emission line point-like sources (Martin et al. 2017). The best available catalogues of planetary nebulae are based on the observation of the much brighter [OIII] lines obtained with an instrument dedicated to the observation and the detection (PN.S, Merrett et al. 2006) and a multi-fibre spectrograph (Halliday et al. 2006). In table 1, we compare the catalogue obtained with SITELLE with these catalogues. We can see that, in their study based on SITELLE data, Martin et al. (2016) have been able to detect twice more emission-line point-like sources. Note that, even if these sources are believed to be mostly planetary nebulae, another study involving the observation of the [OIII] lines is needed to confirm this assessment. The attained precision in terms of velocity and astrometry is about twice better and the flux calibration precision is about the same. Note also that the detection of emission lines over the very strong background of M31 is, in a certain way, a worst-case scenario for SITELLE since the multiplex disadvantage Martin et al. (2017); Drissen et al. (2014); Maillard et al. (2013) generates a noise about $\sqrt{400}$ times higher than a dispersive technique.

The quality of the velocity calibration has been obtained with the development of a simple model of the interferometer. This model allows the wavelength calibration of the entire field of view based only on a few calibrated points (e.g. background spectra with OH sky lines, emission-line sources with known velocity). Up to now, the robustness of this model has shown to be very good (see figure 1). The astrometric calibration has also been enhanced. It now relies on a 3-step calibration process which uses the optical distortion field computed from a calibration image of a field crowded with stars to fit a WCS solution on a data cube containing only some stars (Martin et al. 2017).

The diffuse ionized gas component can also be studied with great precision. We show in Figure 2 a preliminary version of one of the two velocity components that can be seen in the Hα emission of the diffuse gas in the centre of M31.

[1] Université Laval, Québec, Québec, Canada
[2] Department of Physics and Astronomy, University of Hawai'i at Hilo, Hilo, USA
[3] LERMA, Sorbonne Universits, UPMC Univ. Paris 6, Observatoire de Paris, PSL Research University, CNRS, 75000, Paris, France

Table 1. Comparison of the precision of the catalogued emission line point like sources obtained with SITELLE (Martin et al. 2017) and the precision of the planetary nebulae catalogues of Merrett et al. (2006) (Me06) and Halliday et al. (2006) (Ha06). Note that, in the case of the data obtained with SITELLE it is still unclear how much planetary nebulae have really been detected since the [OIII] emission line study has not yet been published. The absolute and relative errors have been quadratically summed.

	SITELLE	Ha06	Me06
Velocity ($\mathrm{km\,s^{-1}}$)	2.21	5	17.72 – 19.72
Astrometry (arcsec)	0.21	1.1	0.37
Flux (mag)	0.08	—	0.07
Number of cataloged PN	>700	154	330
Completness	—	96 %	92 %

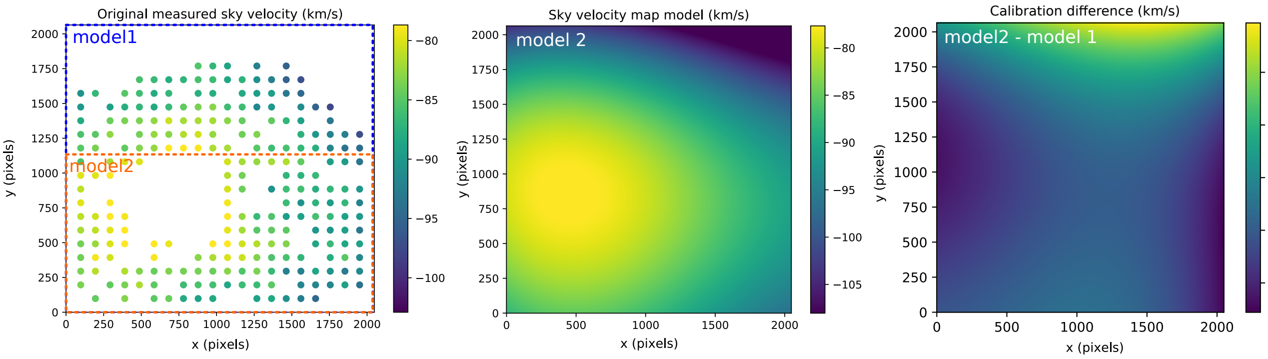

Fig. 1. Comparison of the velocity calibration models obtained considering the measured velocity of the sky lines in the whole field of view (model 1) and in a subregion (model 2). *Left:* Velocity measured at some points in the field of view. All the velocity points are considered to fit the model 1 and only the orange subregion is considered when fitting the model 2. The precision on the measurement is smaller than 2 km/s. *Center:* velocity calibration model 2. *Right:* Velocity difference between model 1 and model 2. We can see that, in most of the field, and particularly the upper part where model 2 is unconstrained, the difference between both model is smaller than 4 km/s.

3 Reconstruction of the ionized shells of the Planetary Nebulae M57

In the case of an ionized gas shell, the two lines emitted by the blue shifted and red shifted parts of the shell can be modelled, at low resolution, as one broadened Gaussian line. Its broadening is directly related to the velocity difference between both components. The observed emission-line shape is always the convolution of the real line shape and the instrumental line shape (ILS). The precise knowledge of the ILS gives the possibility to deconvolve its effect and measure very small broadening. This deconvolution is based on model fitting. The model of the observed emission-line shape, i.e. the convolution of a Gaussian emission line and a cardinal sinus ILS is a well-known result but we were lacking a numerically robust formulation. (Martin et al. 2016) have developed such a formulation and implemented a model in the data processing module ORCS(Martin et al. 2015). This model has been used to measure the broadening of the [NII]6548,6584 and Hα emission lines and partially recover, at a resolution of 2700, the data obtained with an echelle spectrograph at a resolution of 47 000 (O'Dell et al. 2013). Note that this level of precision can only be achieved at high SNR. For example, the minimum measurable broadening at a resolution of 2700 is around 15 km/s if the SNR is around 300.

4 Very Faint Emission of a Galactic Nova Shell in ATCnc

Detecting one emission line on a low background mostly eliminates the multiplex disadvantage, i.e. the SNR of the emission line is essentially the same as the SNR which would have been obtained with a dispersive technique in the same observing condition (same integration time). In this case the advantage of a large field of view (120 times larger than MUSE) clearly dominates.

A classical nova outburst produces a very thin shell of ionized gas which is still visible, though very dim, even after a few hundred years after the explosion. Shara et al. (2016) have observed the classical nova shell

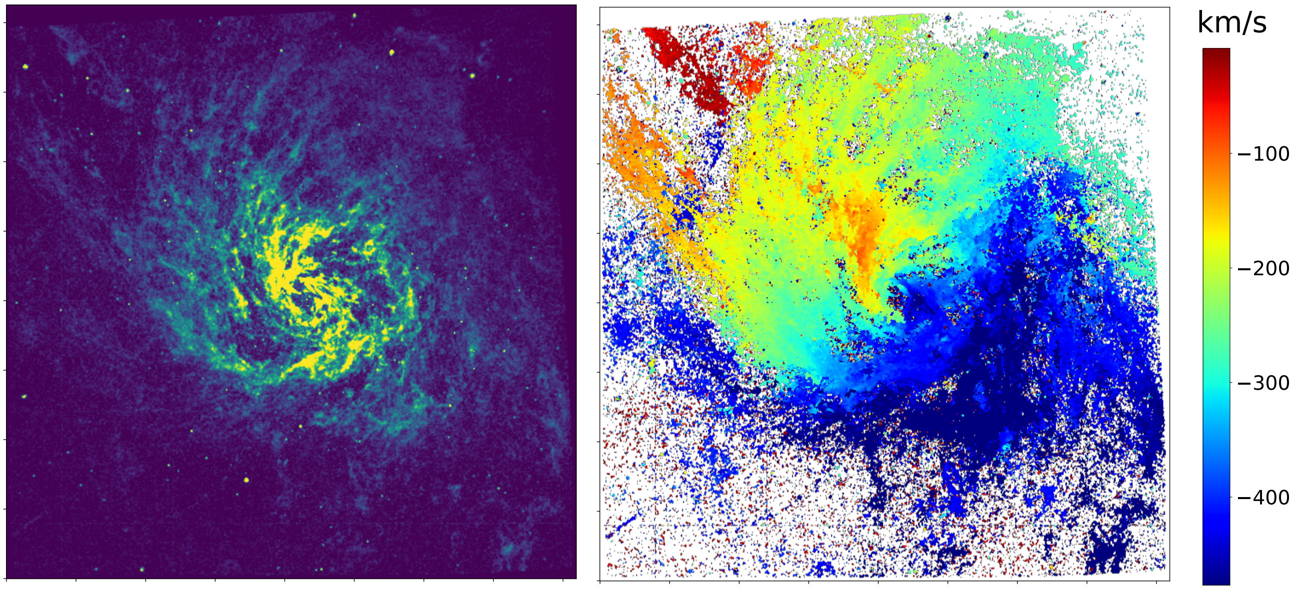

Fig. 2. Emission (left, arbitrary unit) and velocity (right) of the first velocity component of the diffuse ionized gas in the centre of M31.

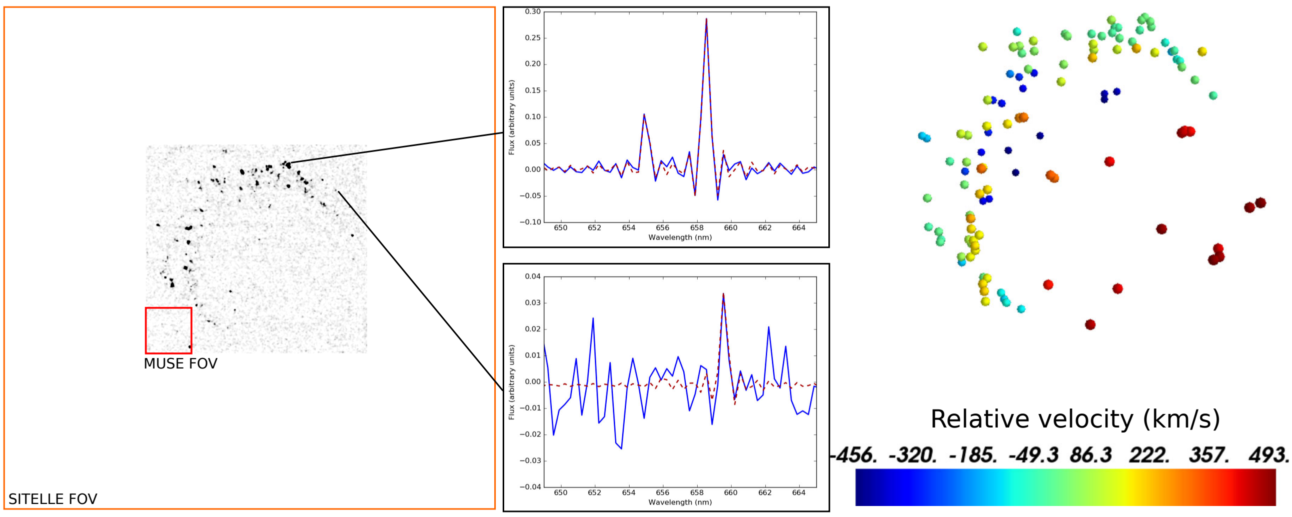

Fig. 3. *Left:* Emission of the faint nova shell observed with SITELLE. The whole SITELLE field of view and the MUSE field of view are shown. Two spectra obtained on a dim node and a bright node are also shown. *Right:* Measured velocity of the nodes.

surrounding the AT Cnc dwarf nova. This shell is essentially observable through its densest and most luminous nodes (also referred as blobs, see Figure 3). The smallest of them being point-like sources. 115 blobs were observed with a minimum flux, leading to a precise enough velocity measurement, of $6\,10^{-17}$ erg/s/cm^2. Note that the real detection limit is smaller than this flux, but a simple detection was not sufficient here (and could be better achieved through narrowband imaging). The total integration time of the cube was 3.9 hours.

Based on observations obtained with SITELLE, a joint project of Université Laval, ABB, Université de Montréal and the Canada-France-Hawaii Telescope (CFHT) which is operated by the National Research Council (NRC) of Canada, the Institut National des Science de l'Univers of the Centre National de la Recherche Scientifique (CNRS) of France, and the University of Hawaii. LD is grateful to the Natural Sciences and Engineering Research Council of Canada, the Fonds de Recherche du Québec, and the Canada Foundation for Innovation for funding.

References

Drissen, L., Rousseau-Nepton, L., Lavoie, S., et al. 2014, Advances in Astronomy, 2014, 1

Halliday, C., Carter, D., Bridges, T. J., et al. 2006, Monthly Notices of the Royal Astronomical Society, 369, 97

Maillard, J. P., Drissen, L., Grandmont, F., & Thibault, S. 2013, Experimental Astronomy, 35, 527

Martin, T., Drissen, L., & Joncas, G. 2015, Astronomical Data Analysis Software an Systems XXIV (ADASS XXIV), 495

Martin, T. B., Drissen, L., & Melchior, A.-L. 2017, Monthly Notices of the Royal Astronomical Society

Martin, T. B., Prunet, S., & Drissen, L. 2016, Monthly Notices of the Royal Astronomical Society, 463, 4223

Merrett, H. R., Merrifield, M. R., Douglas, N. G., et al. 2006, Monthly Notices of the Royal Astronomical Society, Volume 369, Issue 1, pp. 120-142., 369, 120

O'Dell, C. R., Ferland, G. J., Henney, W. J., & Peimbert, M. 2013, The Astronomical Journal, 145, 92

Shara, M. M., Drissen, L., Martin, T., Alarie, A., & Stephenson, F. R. 2016, Monthly Notices of the Royal Astronomical Society, 465, 739

SF2A 2017
C. Reylé, P. Di Matteo, F. Herpin, É. Lagadec, A. Lançon, Z. Meliani, F. Royer (eds)

THE WEAK LENSING ANALYSIS OF THE CFHTLS AND NGVS REDGOLD GALAXY CLUSTERS

C. Parroni[1], S. Mei[1,2], T. Erben[3], L. Van Waerbeke[4], A. Raichoor[5], J. Ford[6], R. Licitra[1], M. Meneghetti[7], H. Hildebrandt[3], L. Miller[8], P. Côté[9], G. Covone[10], J.-C. Cuillandre[11], P.-A. Duc[12], L. Ferrarese[9], S. D. J. Gwyn[9] and T. H. Puzia[13]

Abstract. An accurate estimation of galaxy cluster masses is essential for their use in cosmological and astrophysical studies. We studied the accuracy of the optical richness obtained by our RedGOLD cluster detection algorithm (Licitra et al. 2016a,b) as a mass proxy, using weak lensing and X-ray mass measurements. We measured stacked weak lensing cluster masses for a sample of 1323 galaxy clusters in the Canada-France-Hawaii Telescope Legacy Survey W1 and the Next Generation Virgo Cluster Survey at $0.2 < z < 0.5$, in the optical richness range 10-70. We tested different weak lensing mass models that account for miscentering, non-weak shear, the two-halo term, the contribution of the Brightest Cluster Galaxy, and the intrinsic scatter in the mass-richness relation. We calculated the coefficients of the mass-richness relation, and of the scaling relations between the lensing mass and X-ray mass proxies.

Keywords: weak lensing, galaxy clusters, scaling relations

1 Introduction

Galaxy clusters are the largest and most massive gravitationally bound systems in the universe and have proven to be fundamental tools to probe the current ΛCDM model and structure formation scenarios. The study of their properties, such as their correlation function and power spectrum, their baryonic fraction, the halo mass function and its evolution, requires accurate mass measurements and a full understanding of the systematics and biases involved in the analysis to better calibrate the scaling relations between cluster mass and observables that correlate with it. Because cluster masses cannot be measured directly, we need to rely on mass proxies. The

[1] LERMA, Observatoire de Paris, PSL Research University, CNRS, Sorbonne Universités, UPMC Univ. Paris 06, F-75014 Paris, France, University of Paris Denis Diderot, University of Paris Sorbonne Cité (PSC), F-75205 Paris Cedex 13, France
[2] Jet Propulsion Laboratory, Cahill Center for Astronomy & Astrophysics, California Institute of Technology, 4800 Oak Grove Drive, Pasadena, California, USA
[3] Argelander-Institut für Astronomie, University of Bonn, Auf dem Hügel 71, D-53121 Bonn, Germany
[4] Department of Physics and Astronomy, University of British Columbia, 6224 Agricultural Road, Vancouver, B.C., V6T 1Z1, Canada
[5] Institute of Physics, Laboratory of Astrophysics, Ecole Polytechnique Fédérale de Lausanne (EPFL), Observatoire de Sauverny, 1290 Versoix, Switzerland
[6] *e*Science Institute, University of Washington, Campus Box 351570, Seattle, WA 98195, USA
[7] INAF - Osservatorio Astronomico di Bologna, Bologna, Italy & INFN, Sezione di Bologna, Bologna, Italy
[8] Department of Physics, University of Oxford, Denys Wilkinson Building, Keble Road, Oxford OX1 3RH, U.K
[9] National Research Council of Canada, Herzberg Astronomy and Astrophysics Program, 5071 West Saanich Road, Victoria, BC, V9E 2E7, Canada
[10] INAF Osservatorio Astronomico di Capodimonte, Dipartimento di Fisica, University of Naples Federico II, INFN, Via Cinthia, I-80126 Napoli, Italy
[11] CEA/IRFU/SAp, Laboratoire AIM Paris-Saclay, CNRS/INSU, Université Paris Diderot, Observatoire de Paris, PSL Research University, F-91191 Gif-sur-Yvette Cedex, France
[12] AIM Paris-Saclay Service d'astrophysique, CEA-Saclay, F-91191 Gif sur Yvette, France, Université de Strasbourg, CNRS, Observatoire astronomique de Strasbourg, UMR 7550, F-67000 Strasbourg, France
[13] Institute of Astrophysics, Pontificia Universidad Católica de Chile, Av. Vicuña Mackenna 4860, 7820436 Macul, Santiago, Chile

aim of our work was to infer galaxy cluster masses using weak lensing measurements, through the reconstruction of their stacked shear profiles, and to calibrate the precision of the RedGOLD optical richness (Licitra et al. 2016a,b) as a mass proxy.

For our analysis, we used our own data reduction (Raichoor et al. 2014) of the Canada-France-Hawaii Telescope Legacy Survey (CFHT-LS; Gwyn 2012) Wide 1 (W1) field and of the Next Generation Virgo Cluster Survey (NGVS; Ferrarese et al. 2012). Galaxy clusters were detected using the RedGOLD optical cluster finder of Licitra et al. (2016a,b). The shear measurements come from the CFHTLenS W1 (Heymans et al. 2012; Erben et al. 2013) and NGVSLenS (Raichoor et al. 2014) catalogs and were obtained using the *lens*fit algorithm (Miller et al. 2013). Photometric redshifts were determined by Raichoor et al. (2014), using the bayesian codes BPZ (Benítez 2000) and *LePhare* (Arnouts at al. 1999). In order to have the most clean and complete sample, we restricted the analysis to clusters with redshift $0.2 < z < 0.5$ and richness $10 < \lambda < 70$, bringing the final catalog to a total of 1323 clusters. For the calculation of the scaling relations between lensing masses and X-ray mass proxies, we used Gozaliasl et al. (2014) X-ray catalog, based on the *XMM-Newton* observations in the ~ 3 deg^2 overlapping the CFHT-LS W1 field.

2 Weak lensing analysis

We calculated the mean shear radial profiles, stacking clusters binned according to their optical richness and averaged the tangential shear in logarithmic radial bins, applying lens-source pairs weights that depend on the lensing efficiency and on the quality of background galaxy shape measurements. We calculated the errors on each profile point using the bootstrap technique, taking clusters with replacements within each richness bin.

We fitted these profiles assuming a *Basic Model* that consists in a halo model (Seljak 2000), with an NFW (Navarro, Frenk & White 1996) surface density contrast, and correction terms that take into account cluster miscentering (Johnston et al. 2007; George et al. 2012), non-weak shear (Mandelbaum et al. 2006; Johnston et al. 2007) and the two halo term (Seljak 2000; Seljak & Warren 2004; Johnston et al. 2007). We then considered extensions of this model including the intrinsic scatter in the mass-richness relation, in the *Added Scatter Model*, and the contribution of the Brightest Cluster Galaxy (BCG), in the *Two Component Model*. In all cases, we used the concentration-mass relation of Dutton & Macció (2014), to reduce the dimensionality of the problem. The study of these models allowed us to constrain the contribution of each corrective term and to better understand the biases and systematics involved in the analysis.

In order to estimate the error bars on the fitting parameters, we run Markov Chains Monte Carlo (MCMC; Metropolis et al. 1953) with the Python package *emcee* (Foreman-Mackey et al. 2013), which allowed us to efficiently sample the model likelihood. In Fig. 1, on the left, we find the shear profiles, with the data (in black), the fit results (in green), the ideal profiles we would get in case all the clusters in the stack were perfectly centered (in red), and the opposite case (in blue). On the right, we can see the lensing signal-to-noise ratio map for the corresponding stack of clusters, obtained using aperture mass statistics (Schneider 1996; Schirmer et al. 2006; Du & Fan 2014).

3 Results

3.1 Mass–richness relation

We performed a fit to a power law to infer the mass–richness relation for all three models, using the lensing masses calculated for each richness bin: $\log M_{200} = \log M_0 + \alpha \log \lambda/\lambda_0$, with a pivot richness $\lambda_0 = 40$. We show the results in Fig. 2, on the left.

Because the *Basic* and the *Two Component Models* do not include the intrinsic scatter in the mass–richness relation as a free parameter in the fit, we applied an a posteriori correction as in Ford et al. (2015) to take this effect into account. Starting from the mass–richness relation inferred from the *Basic Model* and from the *Two Component Model*, we assigned a mass to each cluster in the sample, then we scattered them assuming a log-normal distribution centered on $\log M_{200}$ and with a width $\sigma_{\ln \mathrm{M}|\lambda} = 0.39$, based on the scatter measured by Licitra et al. (2016a). We then fitted the mass-richness relation using the new mean mass values in each richness bin, obtaining a difference in normalization between the original models and their scattered versions that is less than 1%. In Table 1, we summarize the slope and the normalization values obtained with the different models. All results are consistent within 1σ.

Having verified the impact of each model term on the final results, we consider as our *Final Model* the model that takes into account all the parameters considered so far, the *Two Component Model* with the a posteriori

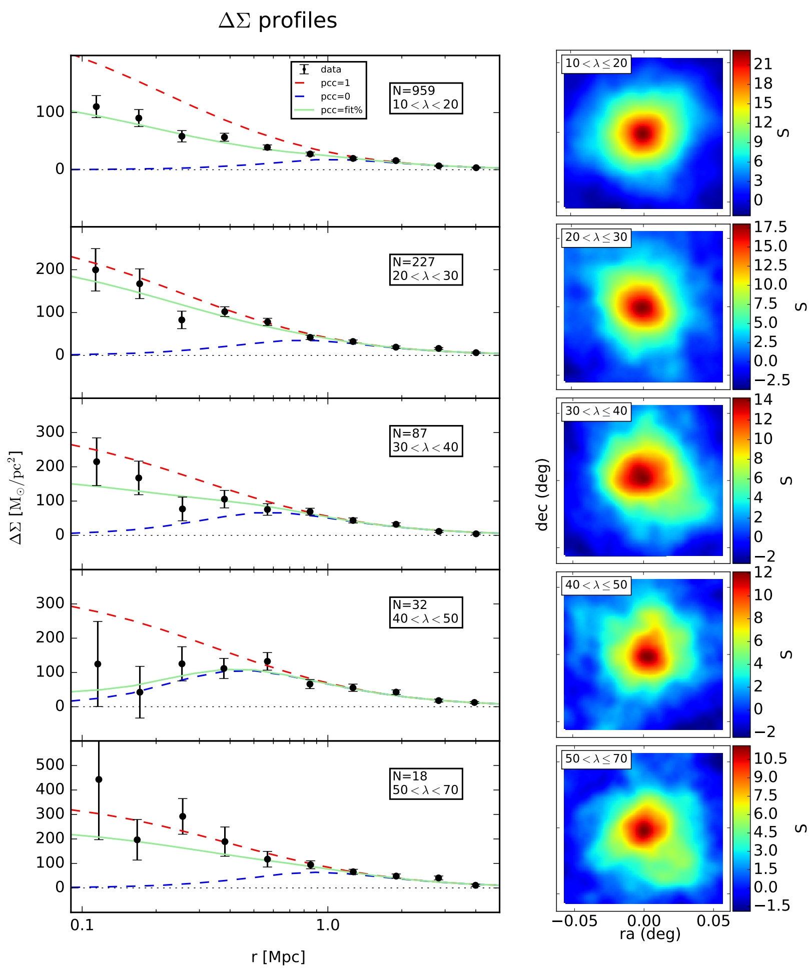

Figure 1. Left: Shear profile measurement (black), the fit results (green), the ideal profiles that we would obtain in the case in which all the clusters in the stack were perfectly centered (red) and when they would have been all miscentered (blue). The fits were obtained using the *Basic Model*, and we get similar results using the *Added Scatter* and the *Two Component Models*. **Right:** Lensing signal-to-noise ratio maps in each richness bin for our weak lensing selected sample. We applied aperture mass statistics.

intrinsic scatter correction. Our final mass–richness relation is then: $\log M_0 = 14.46 \pm 0.02$ and $\alpha = 1.04 \pm 0.09$.

Table 1. Results of the fit of the mass–richness relation obtained using the three models. For the Basic and Two Component Models, we also show the results after applying the a posteriori intrinsic scatter correction (ISC).

Model	$\log M_0$	α
Basic	14.43 ± 0.01	1.05 ± 0.07
Basic + ISC	14.47 ± 0.02	1.05 ± 0.09
Added Scatter	14.42 ± 0.03	0.97 ± 0.14
Two Component	14.43 ± 0.01	1.05 ± 0.07
Two Component + ISC	14.46 ± 0.02	1.04 ± 0.09

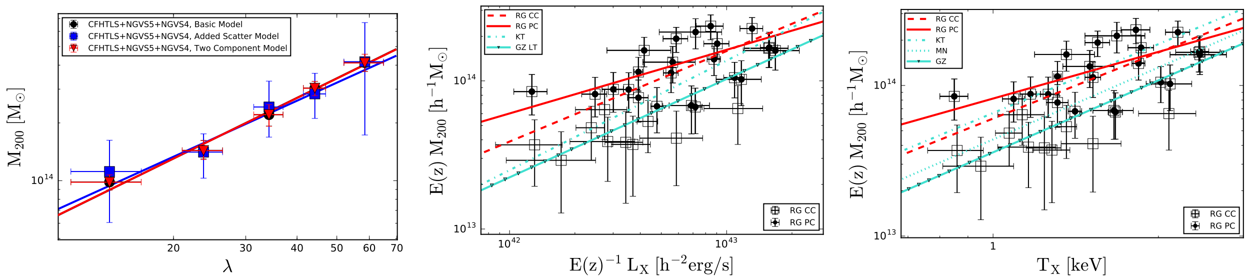

Figure 2. Left: The weak lensing mass–richness relations obtained using the *Basic Model* (black line and black dots), *Added Scatter Model* (blue line and blue squares), and *Two Component Model* (red line and red triangles). **Center:** The weak lensing mass vs X-ray luminosity relation, in red, derived matching our cluster sample with Gozaliasl et al. (2014) (GZ) X-ray catalog, compared with those of Leauthaud et al. (2010) (LT) and Kettula et al. (2015) in cyan. **Right:** The weak lensing mass vs X-ray temperature relation, in red, compared with those of Kettula et al. (2015) (KT) and Mantz et al. (2016) (MN).

As shown in Licitra et al. (2016a,b), our richness estimator λ is defined in a similar way as the richness from redMaPPer (Rykoff et al. 2014). We can then compare our results with others obtained through a similar stacking lensing analysis or different techniques (i.e. velocity dispersions, abundance matiching), using the redMaPPer cluster sample (Rykoff et al. 2012; Saro et al. 2015; Farahi et al. 2016; Melchior et al. 2016; Simet et al. 2016). Our normalization is in perfect agreement with all the works cited above ($< 1\sigma$). On the other hand, there is a slight tension between our slope and those of Simet et al. (2016) and Farahi et al. (2016) ($1.5-2\sigma$), but not with Rykoff et al. (2012), Saro et al. (2015), and Melchior et al. (2016) ($< 1\sigma$).

3.2 Lensing mass versus X-ray mass proxies relations

In order to compare our lensing mass estimates with X-ray mass proxies, we used Gozaliasl et al. (2014) X-ray catalog. We applied a logarithmic linear fit, in the form: $\log\left(\frac{M_{200}E(z)}{M_0}\right) = a + b\log\left(\frac{L_X}{L_0 E(z)}\right)$ and $\log\left(\frac{M_{200}E(z)}{M_0}\right) = a + b\log\left(\frac{T_X}{T_0}\right)$, where $E(z) = H(z)/H_0$, $M_0 = 8\times10^{13}\ h^{-1}M_\odot$ for the $M_{200}-L_X$, $M_0 = 6\times10^{13}\ h^{-1}M_\odot$ for the $M_{200}-T_X$, $L_0 = 5.6\times10^{42}\ h^{-2}erg/s$, and $T_0 = 1.5\ keV$.

For the mass–luminosity relation, we find $a = 0.10\pm0.03$ and $b = 0.61\pm0.12$, with a scatter $\sigma_{\log M_{200}|L_X} = 0.20$ dex. For the mass–temperature relation, we find $a = 0.23\pm0.03$ and $b = 1.46\pm0.28$, with a scatter $\sigma_{\log M_{200}|T_X} = 0.20$ dex. In Fig. 2, we show the mass–luminosity (center) and mass–temperature relations (right), and compare them to those of other works in literature (Leauthaud et al. 2010; Kettula et al. 2015; Mantz et al. 2016). Our results are consistent with those of the other works cited within $< 1\sigma$, in normalization and slope, except for Leauthaud et al. (2010) normalization ($< 2.5\sigma$).

4 Conclusions

We tested different profile models and different fitting techniques, obtaining results in good agreement with each other. In particular, the miscentering correction resulted to be the one that most affects the halo mass measurements ($10-40\%$), while including or not the BCG mass does not make a difference in the recovered parameters. The intrinsic scatter in the mass-richness relation is not constrained by the data, and we applied an a posteriori correction to take this factor into account.

We derived our mass–richness relation and compared it with others from the literature finding results in agreement within 1σ in most of the cases. The small slope discrepancy that we found, comparing our results to those of Farahi et al. (2016) and Simet et al. (2016), could be due to the different samples that were used (i.e. different survey depth, mean redshift, and richness estimation) and to the different analyses performed (i.e. fitting techniques, number of parameters).

Matching our sample with Gozaliasl et al. (2014) X-ray catalog, we derived the coefficients of the mass–luminosity and mass–temperature relations, and compared them with previous results, finding good agreement. In particular, the slope values found are in perfect agreement with the predicted deviations from the self-similar mass–luminosity and mass–temperature relations, confirming the role of hydrodynamical processes, such as radiative cooling, feedback from star formation, AGN activity, in the standard structure formation scenario (Böhringer et al. 2011).

In order to increase the accuracy of this kind of weak lensing mass estimates, it will be important to increase the number density of background sources to achieve a higher S/N in the shear profile measurements, either using deeper observation or increasing the cluster sample size. In the future, this will be possible with ground- and space-based large-scale surveys such as the LSST*, *Euclid*† and WFIRST‡ that will detect around 100,000 galaxy clusters, allowing us to constrain their masses with even higher accuracy.

This work is based on observations obtained with MegaPrime/MegaCam, a joint project of CFHT and CEA/IRFU, at the Canada-France-Hawaii Telescope (CFHT) which is operated by the National Research Council (NRC) of Canada, the Institut National des Sciences de l'Univers of the Centre National de la Recherche Scientifique (CNRS) of France, and the University of Hawaii. This research used the facilities of the Canadian Astronomy Data Centre, operated by the National Research Council of Canada with the support of the Canadian Space Agency. CFHTLenS data processing was made possible thanks to significant computing support from the NSERC Research Tools and Instruments grant program. R.L., S.M., and A.Ra. acknowledge the support of the French Agence Nationale de la Recherche (ANR) under the reference ANR10-BLANC-0506-01-Projet VIRAGE (PI: S.Mei). S.M. acknowledges financial support from the Institut Universitaire de France (IUF), of which she is senior member. H.H. is supported by the DFG Emmy Noether grant Hi 1495/2-1. We thank the Observatory of Paris and the University of Paris D. Diderot for hosting T.E. under their visitor programs.

Facilities: CFHT.

References

Arnouts, S., Cristiani, S., Moscardini, L., et al. 1999, MNRAS, 310, 540

Benítez N. 2000, ApJ, 536, 571

Böhringer, H., Dolag, K., Chon, G. 2011, A&A, 539, A120

Du, W. & Fan, Z. 2014, ApJ, 785, 57

Dutton, A. A. & Macció, A. V. 2014, MNRAS, 441, 3359

Erben, T., Hildebrandt, H., Miller, L., et al. 2013, MNRAS, 433, 2545

Farahi, A., Evrard, A. E., Rozo, E., Rykoff, E. S., Wechsler, R. H. 2016, MNRAS, 460, 3900

Ferrarese, L., Cote, P., Cuillandre, J.-C., et al. 2012, ApJS, 200, 4

Ford, J., van Waerbeke, L., Milkeraitis, M., et al. 2015, MNRAS 447, 1304

Foreman-Mackey, D., Hogg, D. W., Lang, D., Goodman, J. 2013, PASP, 125, 925

George, M. R., Leauthaud, A., Bundy, K., et al. 2012, ApJ, 757, 2

Gozaliasl, G., Finoguenov, A., Khosroshahi, H. G., et al. 2014, A&A 566, 140

Gwyn, S. D. J. 2012, ApJ, 143, 38

Heymans, C., van Waerbeke, L., Miller, L., et al. 2012, MNRAS, 427, 146

Hildebrandt, H., Erben, T., Kuijken, K., et al. 2012, MNRAS, 421, 2355

Johnston, D. E., Sheldon, E. S., Wechsler, R. H., et al. 2007, arXiv:0709.1159

Kettula, K., Giodini, S., van Uitert, E., et al. 2015, MNRAS, 451, 1460

Leauthaud, A., Finoguenov, A., Kneib, J.-P., et al. 2010, ApJ, 709, 114

Licitra, R., Mei, S., Raichoor, A., et al. 2016, ApJ, 829, 44

Licitra, R., Mei, S., Raichoor, A., Hildebrandt, H. 2016, MNRAS, 455, 3020

Mandelbaum, R., Seljak, U., Cool, R. J., et al. 2006, MNRAS, 372, 758

Mantz, A. B., Allen, S. W., Morris, R. G., et al. 2016, MNRAS, 463, 3582

Melchior, P., Gruen, D., McClintok, T., et al. 2016, arXiv:1610.06890v1

Metropolis, N., Rosenbluth, A. W., Rosenbluth, M. N., et al. 1953, JChPh, 21,1087

Miller L., Heymans, C., Kitching, T. D., et al. 2013, MNRAS, 429, 2858

Navarro J. F., Frenk C. S., White S. D. M. 1996, ApJ, 462, 563

Raichoor, A., Mei, S., Erben, T., et al. 2014, ApJ, 797, 102

Rykoff, E. S., Koester, B. P., Rozo, E., et al. 2012, ApJ, 746, 178

Rykoff, E. S., Rozo, E., Busha, M. T., et al. 2014, ApJ, 785, 104

---

*https://www.lsst.org/

†http://euclid- ec.org

‡http://wfirst.gsfc.nasa.gov

Saro, A., Bocquet, S., Rozo, E., et al. 2015, MNRAS, 454, 2305
Schirmer, M., Erben, T., Hetterscheidt, M., Schneider, P. 2006, A&A, 462, 875
Schneider, P. 1996, MNRAS, 283, 837
Seljak, U. 2000, MNRAS. 318, 203
Seljak, U. & Warren, M. S. 2004, MNRAS, 355, 129
Simet, M., McClintock, T., Mandelbaum, R., et al. 2016, arXiv:1603.06953v1

SF2A 2017
C. Reylé, P. Di Matteo, F. Herpin, É. Lagadec, A. Lançon, Z. Meliani, F. Royer (eds)

A QUESTION OF MASS : ACCOUNTING FOR ALL THE DUST IN THE CRAB NEBULA WITH THE DEEPEST FAR INFRARED MAPS

J. Matar[1], C. Nehmé[1,2] and M. Sauvage[2]

Abstract. Supernovae represent significant sources of dust in the interstellar medium. In this work, deep far-infrared (FIR) observations of the Crab Nebula are studied to provide a new and reliable constraint on the amount of dust present in this supernova remnant. Deep exposures between 70 and 500 μm taken by PACS and SPIRE instruments on-board the Herschel Space Telescope, compiling all observations of the nebula including PACS observing mode calibration, are refined using advanced processing techniques, thus providing the most accurate data ever generated by Herschel on the object. We carefully find the intrinsic flux of each image by masking the source and creating a 2D polynomial fit to deduce the background emission. After subtracting the estimated non-thermal synchrotron component, two modified blackbodies were found to best fit the remaining infrared continuum, the cold component with $T_c = 8.3 \pm 3.0$ K and $M_d = 0.27 \pm 0.05\ M_\odot$ and the warmer component with $T_w = 27.2 \pm 1.3$ K and $M_d = (1.3 \pm 0.4) \times 10^{-3}\ M_\odot$.

Keywords: *Dust, Supernova Remnant, Crab Nebula, FIR, SED, Herschel, Synchrotron.*

1 Introduction

It is well established that dust is efficiently formed in regions around asymptotic giant branch (AGB) stars. Thus AGB stars are classically considered as the primary source of dust grains in galaxies. Nevertheless, they cannot inject enough dust in the interstellar medium to compensate for the known destruction rates. Supernova (SN) explosions in the interstellar medium (ISM) trigger shock waves that are considered the dominant mechanism of dust destruction. Yet there is increasing evidence for the formation of non-negligible quantities of dust grains in the ejecta of SNe (Bocchio et al. 2016). The Spitzer and Herschel space telescopes have thus observed supernovae remnants (SNRs), currently known to be major sources of dust. Such is the case of the Crab Nebula, a young, bright and well resolved SN at a distance of 2 kpc (Trimble 1973), where large amounts of dust have been reported. Unlike other remnants, there is almost no interstellar material in front of or behind the Crab Nebula, so the possibility that the observed dust is simply the local ISM swept up by the expanding shockwave is disfavoured. Therefore, it represents an ideal case for deriving the total dust mass produced by a SNR. Previous studies using Herschel deduced masses ranging between 0.12-0.25 $M_\odot$ (Gomez et al. 2012) and 0.019-0.13 $M_\odot$ (Temim & Dwek 2013). These results consistently indicate that dust is formed in the ejecta, but their variability shows that much work is still needed to get a reliable estimate of the dust yields by SN. We also note that the Crab Nebula is ionized by non-thermal radiation (MacAlpine & Satterfield 2008) thus measuring accurately the synchrotron emission is important to correctly derive the dust thermal emission.

2 Observations

The Crab Nebula was observed using Herschel (Pilbratt et al. 2010) between September 2009 and September 2010. The PACS (Poglitsch et al. 2010) and SPIRE (Griffin et al. 2010) instruments performed photometry (Figure 1) at 70, 100, 160, 250, 350 and 500 μm (see Table 1). The PACS data were first reduced using HIPE, the Herschel Interactive Processing Environment (Ott 2010). Then the "unimap" software (Piazzo et al. 2015), a generalized least-squares map maker for Herschel data, was used to get rid of low frequency noise in the maps.

[1] Department of Physics & Astronomy, Notre Dame University, Lebanon; cnehme@ndu.edu.lb
[2] Laboratoire AIM, CEA/IRFU/Dep. d'Astrophysique, CNRS, Université Paris Diderot, 91191 Gif-sur-Yvette, France

All PACS observations were combined in one map per photometer band. For SPIRE, the standard pipeline HIPE version 14.0.0 was used (Griffin et al. 2010). Note that in this study, we have included for the first time data that was obtained on the Crab Nebula during the testing and qualification of PACS observing modes, thus nearly doubling the depth of the resulting maps.

Table 1. Photometric observations of the Crab Nebula using Herschel Space Observatory.

Obs. ID	**Obs. Date**	**Obs. Duration** (s)	**Instrument**	**Filter set** λ (μm)
1342183905	2009-09-15	2221	PACS	(70, 160)
1342183906	2009-09-15	2221	PACS	(70, 160)
1342183907	2009-09-15	2221	PACS	(70, 160)
1342183908	2009-09-15	2221	PACS	(70, 160)
1342183909	2009-09-15	2221	PACS	(100, 160)
1342183910	2009-09-15	2221	PACS	(100, 160)
1342183911	2009-09-15	2221	PACS	(100, 160)
1342183912	2009-09-15	2221	PACS	(100, 160)
1342191181	2010-02-25	4555	SPIRE	(250, 350, 500)
1342204441	2010-09-13	1671	PACS	(70, 160)
1342204442	2010-09-13	1671	PACS	(100, 160)
1342204443	2010-09-13	1671	PACS	(70, 160)
1342204444	2010-09-13	1671	PACS	(100, 160)

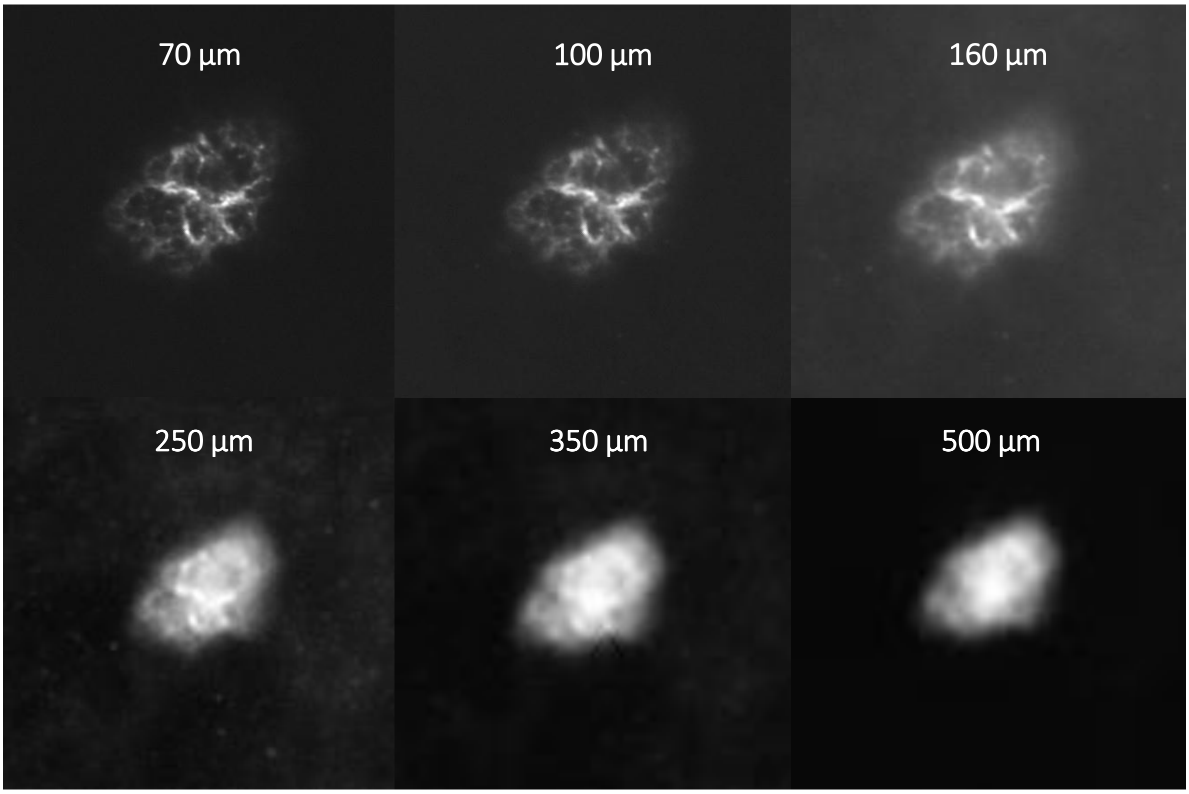

Fig. 1. *Top:* Herschel PACS 70, 100 and 160 μm images. *Bottom:* Herschel SPIRE 250, 350 and 500 μm images.

3 Analysis

3.1 Aperture Photometry and Background Subtraction

To build the overall SED of the Crab Nebula, we performed aperture photometry on the maps. We defined a single aperture that contains the full extent of the Crab Nebula at all observed wavelengths. Since the apparent size of an object increases with the wavelength when observed with the same telescope, we define the aperture on the longest wavelength image, the 500 μm map. The same circular aperture was used for the six images. In the infrared, there is always more emission than simply the objects we are interested in. Any pixel inside the aperture will see flux from the object and flux from the background. Therefore, we need to estimate the background level and subtract it. For that purpose, we designed a 2D Polynomial Fit Model to estimate the background from the emission outside the circular aperture.

3.2 Synchrotron Emission

The Crab Pulsar B0531+21 is the strongest source of synchrotron radiation in the Galaxy. We estimated the non-thermal synchrotron component by applying a least-squares fit to the Herschel (our data), Spitzer, WISE and Planck data from (Gomez et al. 2012). This produces a power law with a spectral index $\alpha = 0.413 \pm 0.085$.

4 Results

4.1 Flux Determination

In table 2, we list the fluxes extracted from our maps using the analysis method presented above.

Table 2. The background and synchrotron contribution to the fluxes.

λ (μm)	S_{Total} (Jy)	$S_{Background}$ (Jy)	$S_{Synchrotron}$ (Jy)	S_ν (Jy)	$\Delta\, S_\nu$ (Jy)
70 μm	220.696	2.523	45.719	172.454	0.186
100 μm	225.227	5.189	52.992	167.047	0.178
160 μm	153.456	28.014	64.369	61.073	0.349
250 μm	214.253	104.637	77.427	32.189	0.217
350 μm	170.179	66.038	88.995	15.147	0.214
500 μm	133.745	29.172	103.15	1.423	0.129

Notes. S_ν is the total dust emission and $\Delta\, S_\nu$ is the photometric error due to background subtraction.

4.2 Spectral Energy Distribution

If all dust grains were to share the same size and composition (Bianchi 2013), the emission of the Crab would be that of a modified blackbody (MBB), i.e. a blackbody multiplied by the dust absorption cross section. We use here this simplified approach to model the excess thermal emission observed in the FIR (Figure 2), by the sum of two modified blackbodies identified with a warm and a cold component. The figure shows that the Spitzer and WISE fluxes, consistent with one another, are not reproduced by our fit. This is expected as our model does not represent very small grains able to reach, transiently, very high temperature. We defer this to future work where we will implement a more complex representation of the dust. For all the other data points, the agreement is excellent, and the best-fitting temperatures are shown in Table 3.

4.3 Total Dust Mass

From Laor & Draine (1993) and Weingartner & Draine (2001), the dust mass for each component is:

$$M_d = \frac{S_\nu D^2}{\kappa_\nu B(\nu, T)} \tag{4.1}$$

where, S_ν is the flux density, D is the distance (Earth-Crab Nebula), $B(\nu, T)$ is the Planck function and κ_ν is the dust mass absorption coefficient.

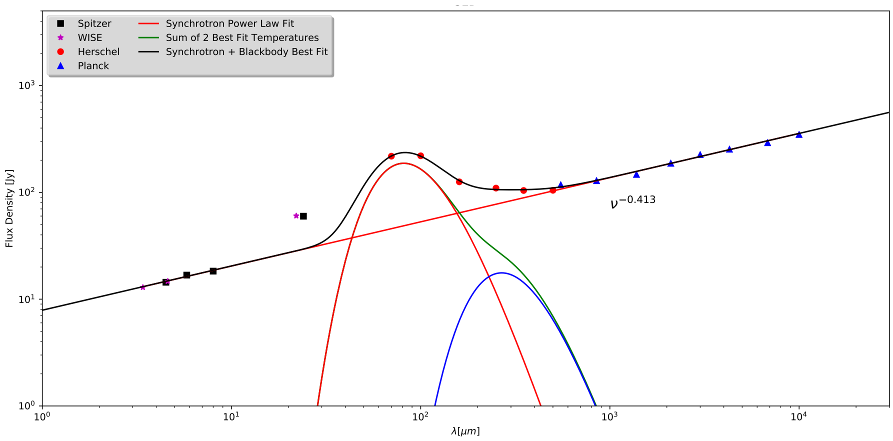

Fig. 2. SED of the Crab Nebula from the IR-radio including Herschel (red points) and Spitzer (black), WISE (purple) photometry and Planck fluxes (Planck Collaboration 2011, blue points). The black line is the total flux obtained from summing the synchrotron and the MBB.

Table 3. Result from the two-component modified black-body fit

Component	Temperature (K)	Mass ($M_\odot$)
Warm	27.3 ± 1.3	$(1.3 \pm 0.4) \times 10^{-3}$
Cold	8.2 ± 3.0	0.27 ± 0.05

5 Conclusion

In this work we present maps of the Crab Nebula with double the depth of previous PACS maps. We rederived the mass of dust using a modified black body with two temperature components fitted to the global SED. We report masses of $M_d(cold) = 0.27 \pm 0.05$ $M_\odot$, $M_d(warm) = 1.3 \pm 0.4 \times 10^{-3}$ $M_\odot$. Our results represent additional support to theoretical models predicting a total dust mass between 0.2 and 0.5 $M_\odot$ (Woosley & Weaver (1995) ; Limongi & Chieffi (2003)). Todini & Ferrara (2001) also predict between 0.1 and 0.3 $M_\odot$ of dust should form in the ejecta from the (Type-IIP) explosions of progenitor stars with initial mass < 15 $M_\odot$ such as the Crab progenitor. Nevertheless, this work is a first step of a long term project that we started on dust in the Crab nebula, to better account for the actual complexity of the source (i.e: filaments) by using the spatial information as well as the spectral information.

Acknowledgement
Dott. Elias Kammoun ... Thank you!

References

Bianchi, S. 2013, A&A, 552, A89
Bocchio, M., Marassi, S., Schneider, R., et al. 2016, A&A, 587, A157
Gomez, H. L., Krause, O., Barlow, M. J., et al. 2012, ApJ, 760, 96
Griffin, M. J., Abergel, A., Abreu, A., et al. 2010, A&A, 518, L3
Laor, A. & Draine, B. T. 1993, ApJ, 402, 441
Limongi, M. & Chieffi, A. 2003, ApJ, 592, 404
MacAlpine, G. M. & Satterfield, T. J. 2008, AJ, 136, 2152
Ott, S. 2010, in Astronomical Society of the Pacific Conference Series, Vol. 434, Astronomical Data Analysis Software and Systems XIX, ed. Y. Mizumoto, K.-I. Morita, & M. Ohishi, 139
Piazzo, L., Calzoletti, L., Faustini, F., et al. 2015, MNRAS, 447, 1471
Pilbratt, G. L., Riedinger, J. R., Passvogel, T., et al. 2010, A&A, 518, L1
Poglitsch, A., Waelkens, C., Geis, N., et al. 2010, A&A, 518, L2
Temim, T. & Dwek, E. 2013, ApJ, 774, 8
Todini, P. & Ferrara, A. 2001, MNRAS, 325, 726
Trimble, V. 1973, PASP, 85, 579
Weingartner, J. C. & Draine, B. T. 2001, ApJ, 548, 296
Woosley, S. E. & Weaver, T. A. 1995, ApJS, 101, 181

SF2A 2017
C. Reylé, P. Di Matteo, F. Herpin, É. Lagadec, A. Lançon, Z. Meliani, F. Royer (eds)

ASOV REVIEW: EXAMPLES OF VO TOOLS AND SERVICES: CASSIS, ALADIN AND ISMDB

J.-M. Glorian[1], C. Bot[2], F. Le Petit[3], T. Boch[2], M. Boiziot[1], F. Bonnarel[2], S. Bottinelli[1], E. Bron[3], M. Buga[2], C. Koragappa [2], E. Caux[1], P. Fernique[2], B. Godard[3], D. Languignon[3], N. Moreau[3], F.-X. Pineau[2] and C. Vastel[1]

Abstract. The CASSIS emission line analysis package (developed at IRAP in Toulouse) and the Aladin interactive sky atlas (developed at CDS in Strasbourg) are examples of french Virtual Observatory tools that blossomed over the past few years. We illustrate some of the interactions between CASSIS, Aladin and e-infrastructures such as VAMDC, and presents the Interstellar Medium Database (developed at Paris Observatory) that gives access to Photo-Dissociation Regions models.

Keywords: VO-tools, database

1 Introduction

The advent of high spatial and spectral resolution as well as wide band instruments has left the astronomers with an over-whelming amount of rich spectra (data cubes in the case of interferometric observations). The analysis of such datasets is tedious and time consuming, without adequate tools and databases.The International Virtual Observatory Alliance (http://www.ivoa.net) has defined sets of standards to access, in a transparent and interoperable way, to the wealth of data in astrophysics. Today, major data centers of the discipline and many data publication services in observatories and laboratories are compatible with these standards. French teams are very active in these efforts at the international level. Here, we present two of the major french VO-tools CASSIS and Aladin as well as the Interstellar Medium Database.

2 CASSIS

The advent of high spectral resolution and wide band instruments has left the astronomers with an almost over-whelming amount of rich spectra. The analysis of such datasets would be tedious and time consuming, without adequate tools. The CASSIS line analysis package (Centre d'Analyse Scientifique de Spectres Instrumentaux et Synthétiques) has been designed at IRAP to help the astronomer with these tasks (Vastel et al. 2015), with a focus on studies of emission lines. The tool can be retrieved at http://cassis.irap.omp.eu. We presented the tool during the 2017 SF2A meeting, and the link between databases and inter-operability with Aladin and ISMDB in a near future.
CASSIS uses the SSAP protocol (Single Spectral Access Protocol) to access the IVOA services in order to retrieve any spectra (Hubble, Corot, Splatalogue, ISO, etc; the complete list can be found at `http://registry.euro-vo.org`). Also CASSIS uses the SAMP messaging protocol (Simple Application Messaging Protocol) that enables astronomy software tools to inter-operate and communicate. CASSIS can visualise FITS spectra, as well as spectra obtained with the CLASS/GILDAS software, and identify any molecular species present in the JPL, CDMS, NIST etc... databases and also through the VAMDC (Virtual Atomic and Molecular Data Centre) TAP protocol.

[1] IRAP, Université de Toulouse, CNRS, UPS, CNES, Toulouse, France
[2] Université de Strasbourg, CNRS, Observatoire astronomique de Strasbourg, UMR 7550, F-67000 Strasbourg, France
[3] LERMA, Observatoire de Paris, PSL Research University, CNRS, Sorbonne Universités, UPMC Univ. Paris 06, 75014 Paris, France

Radiative transfer is also dealt with inside CASSIS. All the details on the theory can be found on the website (Formalism for the CASSIS software, author: C. Vastel). Any prediction of spectra can be done from many telescopes provided by the software, using the spectroscopic databases (frequencies, energy levels, statistical weights, Einstein coefficients). Presently a Local Thermodynamic Equilibrium (LTE) model as well as the non-LTE RADEX code (van der Tak et al. 2007) are available. Scripts for the spectral residual minimization (models vs. observations), via regular grid models or using the MCMC algorithm, are also available to retrieve best fit parameters such as the kinetic temperature, the density, the column density, the linewidth and the velocity of the observed species.
CASSIS collaborates with many tools through VO protocol. We present in Fig. 1 an example resulting from the collaboration between CASSIS and Aladin (see Section 3) Applauncher which is a product from OSUG (Jean-Marie Mariotti Centre), as well as F-VAMDC with the The Vienna Atomic Line Database (VALD). The spectrum viewed with the CASSIS interface corresponds to a hydrogen Ly$_\alpha$ transition observed with the Hubble Space Telescope (HST) towards the Quasi Stellar Object 1257+2840. VALD is then selected and the spectrum shows the Hydrogen Lyman α transition at its rest frequency (green tick) and a less intense redshifted one on the right. Selection in the database can be made based on the upper level energy and Einstein coefficient of the transitions, as well as on the V$_{LSR}$ of the source, which has an impact on the rest frequency of the transitions. A more detailed description can be found as an Euro-VO tutorial: `http://www.euro-vo.org/sites/default/files/documents/Abell1656_final.pdf`

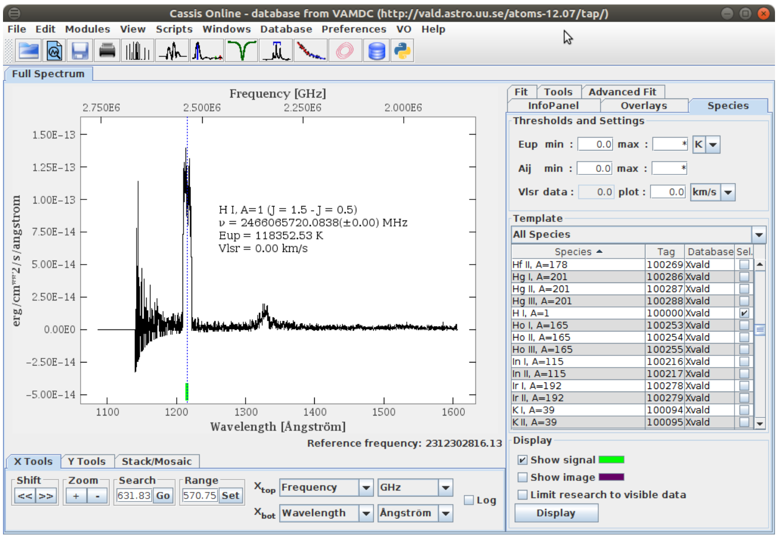

Fig. 1. CASSIS view of the hydrogen Lyman α transition observed towards QSO 1257+2840 using HST. The green tick corresponds to the line found in the wavelength range of the VALD database for HI.

3 Aladin

Aladin is an interactive sky atlas developped by the Centre de Données de Strasbourg (CDS). It focuses on visualising images, accessing data and overlaying information. As such, it is one of the portals to the Virtual Observatory. Aladin is currently ongoing a major update with v10. This new version builds on the definition and evolution of HiPS (Hierarchical Progressive Surveys) and MOC (Multi-Order Coverage) standards (Fernique et al. 2015) and their full capabilities. This translates into new possibilities to access all data available (images, catalogs, ...) and includes keyword searches in the wealth of accessible resources. A new interface for Aladin v10 has been developped to highlight these changes, but the tool remains focused on image visualisation and data access and users will still find the data they loaded in the stack on the right with a list of functionalities and the main view at the center. An example of the view in Aladin v10 is shown in Fig. 2

Thanks to the usage of the HiPS and MOC standards, new scientific uses of Aladin can be achieved with great efficiency that would be very hard to do otherwise. An example of such a usecase is the following question: given a set of observations or a set of images of interest (e.g. images from the MASH planetary nebula catalog; Parker et al. 2006), I would like to find regions among these that are at low extinction, find the sources in

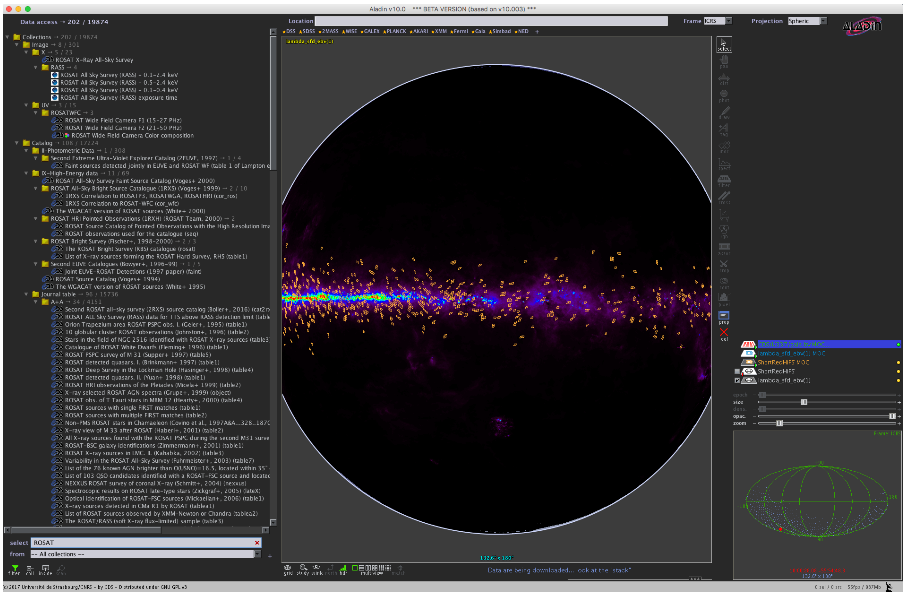

Fig. 2. The new Aladin v10 interface. The data loaded is displayed on the left in the stack and viewed at the center. On the left, a new column enables the user to search through the wealth of all available data (images, catalogs, ...). Search by keywords is shown at the bottom left.

these fields that were detected both by WISE (Cutri & et al. 2012) and Gaia DR1 (Gaia Collaboration 2016) and visualize physical quantities (e.g. a color-color diagram). Completing this scientific case requires to: 1) find the sky coverage that is the intersection of the set of MASH Short-Red images and of the sky coverage corresponding to $E(B-V) < 0.5$ as drawn from the Schlegel et al. (1998) HEALPix map, 2) load the Gaia DR1 catalog sources in the previously defined regions only (query by MOC), 3) X-match the loaded sources with WISE catalog and finally, 4) visualize the Gaia-WISE color-color diagram thanks to the interaction with other VO tools like TOPCAT. The full usecase can be done in half an hour with Aladin V10 and is described step-by-step as a tutorial available at `http://www.euro-vo.org/?q=science/scientific-tutorials`.

The presentation of this user-case is a demonstration that Aladin V10 enables an advanced scientific usage thanks to HiPS and MOC standard and their hierarchical properties on the full sky. This opens a new way to access and interact with data. Furthermore, Aladin V10 gives a fast access to the CDS X-match service. Finally, Aladin V10 keeps the same interoperability with all VO services as it previously. With all these characteristics, we believe Aladin V10 has a large potential for scientific usage that we encourage users to explore. Aladin V10 will be released in october 2017 and is currently already available as a beta version.

4 ISMDB

The Interstellar Medium Database (ISMDB) is developed at Paris Observatory (`https://ism.obspm.fr`). This service is based on the IVOA standard SimDM (Simulation Data Model). The goal of ISMDB is to publish state-of-the-art numerical models to prepare and interpret observations in the molecular interstellar medium. Presently, the system gives access to ~ 3000 PDR models (PDR: photo-dissociation region) computed with the Meudon PDR code (`http://pdr.obspm.fr`). For each model, defined by physical parameters such as the gas density and the intensity of the UV radiation field, ISMDB gives access to observables such as line intensities of atoms and molecules (C^+, C, O, H_2, CO and its isotopologs, HCN, HNC, H_2O, ...) as well as column densities. It is also possible to download the full data produced for each models to get access to the simulated structure of the PDR model: profiles of gas and grains temperature, density profiles of chemical species, ...
Compared to standard databases, the originality of ISMDB comes from the fact that we wish to build a system in which a scientist would be able to provide observed quantities (ex: atomic or molecular line intensities), and the machine would find by itself models able to reproduce these observations. So, in a certain way, we tried to bring "intelligence" on the server side. We achieved this goal moving data to metadata. A run of a PDR code computes thousands of physical quantities (ex: thousands of line intensities, thousands of column densities, in

quantum levels for hundreds chemical species when needed). Instead of using only input parameters of each run as metadata, as done usually, we added the most important data to this list of metadata. The total number of metadata per model is about 150 000. We developed our own technology to store and manage such high-dimension data. To allow the interaction between a human and a large number of physical quantities available in the system, we developed SKOS vocabularies to tag each metadata by a concept and a list of synonyms. The web interface of ISMDB contains a "google bar" in which the user type the name of a quantity he is looking for (ex: for line intensity of CO, users may start typing *I(CO ...* or *intensity CO ...*). While the user is typing the quantity name, a semantics interpreter searches for a match between this entry and the vocabulary to help him to find the name of the quantity as known by ISMDB. Once users have provided observed line intensities or column densities, possibly with errorbars, in the ISMDB web-interface, ISMDB searches in its high-dimension database the best models that match the observations. Results are provided nearly immediately since all pieces of necessary information are stored as metadata. This is an important time saving for scientists. Running grids of such models yourself and comparing the results to observations to find the best ones usually takes weeks, whereas ISMDB gives a solution in a few seconds. In the future, we will continue to develop services above ISMDB. Presently, it is only possible to provide ISMDB with observations at one spatial pixel. We are developing a new service in which it will be possible to upload files containing line intensities on several pixels of a map to reclaim the best physical parameters (such as the gas density) at each pixel.

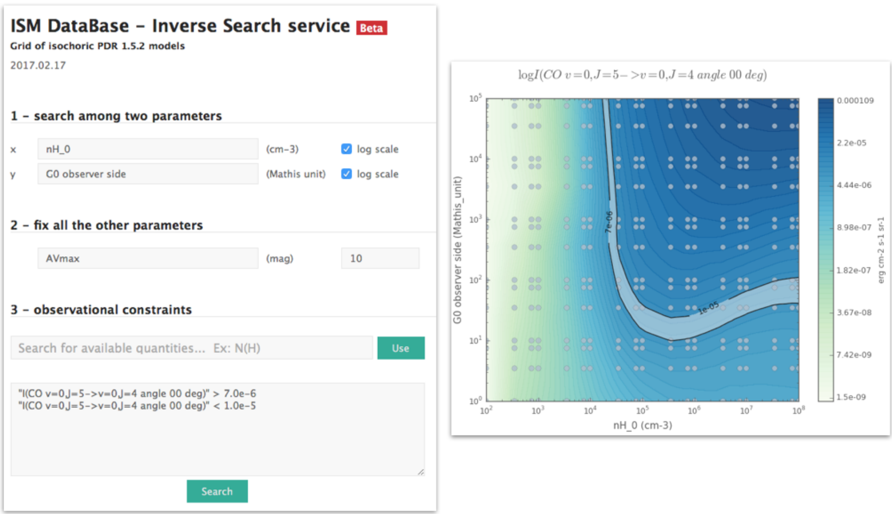

Fig. 3. ISMDB inverse search web interface. The users select the physical parameters the code will look for (ex: gas density and intensity of UV radiation field). Then, he enters some line intensities with errorbars. Finally ISMDB presents, in the relevant parameter space, the zone where models match observations best. Clicking on the bullets of the map, it is possible to download the corresponding models for further analysis.

These works were supported by the "Action Spécifique Observatoire Virtuel" of CNRS/INSU, France.

References

Cutri, R. M. & et al. 2012, VizieR Online Data Catalog, 2311

Fernique, P., Allen, M. G., Boch, T., et al. 2015, A&A, 578, A114

Gaia Collaboration. 2016, VizieR Online Data Catalog, 1337

Parker, Q. A., Acker, A., Frew, D. J., et al. 2006, MNRAS, 373, 79

Schlegel, D. J., Finkbeiner, D. P., & Davis, M. 1998, ApJ, 500, 525

van der Tak, F. F. S., Black, J. H., Schöier, F. L., Jansen, D. J., & van Dishoeck, E. F. 2007, A&A, 468, 627

Vastel, C., Bottinelli, S., Caux, E., Glorian, J.-M., & Boiziot, M. 2015, in SF2A-2015: Proceedings of the Annual meeting of the French Society of Astronomy and Astrophysics, ed. F. Martins, S. Boissier, V. Buat, L. Cambrésy, & P. Petit, 313–316

Session 01

Stellar physics

SF2A 2017
C. Reylé, P. Di Matteo, F. Herpin, É. Lagadec, A. Lançon, Z. Meliani, F. Royer (eds)

HYDRODYNAMICAL INSTABILITIES INDUCED BY ATOMIC DIFFUSION IN F AND A STARS : IMPACT ON THE OPACITY PROFILE AND ASTEROSEIMIC AGE DETERMINATION

M. Deal[1], O. Richard[2] and S. Vauclair[3,4]

Abstract. Atomic diffusion, including the effect of radiative accelerations on individual elements, leads to important variations of the chemical composition inside the stars. The accumulation in specific layers of the elements, which are the main contributors of the local opacity, leads to hydrodynamical instabilities that modify the internal stellar structure and surface abundances. The modification of the initial chemical composition has important effects on the internal stellar mixing and leads to different surface and internal abundances of the elements. These processes also modify the age determination by asteroseismology.

Keywords: stellar evolution, atomic diffusion, instabilities, opacities

1 Introduction

Atomic diffusion is a process which occurs in every star. There are internal gradients inside stars (T, P, ρ, ...) and each chemical element behaves its own way between collisions due to these gradients. The transport of chemical element by atomic diffusion depends on different effects as the one of the concentration gradient, temperature gradient, electric field and the two main processes which are the gravity and the radiative accelerations. The effect of the gravity (or gravitational settling) on the ions of the plasma depends on their atomic masses and the effect of radiative accelerations depends on their atomic structure. All of these selective processes lead to a migration of the elements inside the star to the center or to the surface depending mainly on the predominance of the gravity or of radiative accelerations. This selective motion of elements depends on their ionisation states and the same element may move to the surface in some region of the stars and to the center in others which leads to local accumulations or depletions of the elements. This could also lead to hydrodynamical instabilities as convection. It was first shown by Richard et al. (2001) with the Montreal/Montpellier code (Turcotte et al. 1998) and then the same result was found by Théado et al. (2009) with the Toulouse Geneva Evolution Code (Hui-Bon-Hoa 2008; Théado et al. 2012). This convective zone appears in F and more massive stars when the star is a slow rotator. In these stars, atomic diffusion leads to accumulations of iron and nickel around T=200000K. As the elements accumulate where they are main contributors to the opacity, the local increase of the opacity triggers convection.

An other instability may occur in the case of local accumulation of elements, the so-called *fingering convection*. This instability occurs in the case of a stable temperature gradient and an inverse mean molecular weight gradient. Fingering convection is characterised by the density ratio R_0 which is the ratio between thermal and compositional gradients:

$$R_0 = \frac{\nabla - \nabla_{ad}}{\nabla_\mu}.$$

This instability can only develop if the thermal diffusivity is larger than the molecular one. This means that a heavy blob of fluid falls in the star and keeps falling because heat diffuses more rapidly than the chemical

[1] LESIA, Observatoire de Paris, PSL Research University, CNRS, Université Pierre et Marie Curie, Université Paris Diderot, 92195 Meudon, France
[2] Laboratoire Univers et Particules de Montpellier (LUPM), UMR 5299, Université de Montpellier, CNRS, Place Eugène Bataillon, 34095 Montpellier Cedex 5, France
[3] Université de Toulouse, UPS-OMP, IRAP, 31028 Toulouse Cedex 4, France
[4] CNRS, IRAP, 14 avenue Edouard Belin, 31400 Toulouse, France

elements. Fingering convection cannot occur if the ratio of the diffusivities becomes smaller than ratio of the gradients, which leads to the following condition:

$$1 < R_0 < \frac{1}{\tau}$$

where τ is the inverse Lewis number, ratio of molecular and thermal diffusivity. For values of $R_0 < 1$ the region is dynamically convective (Ledoux criteria) and for values of $R_0 > 1/\tau$ the region is stable. This process was studied by Théado et al. (2009) for F and A type stars but only in the region of the iron/nickel convective zone.

In the following sections we describe the computation of models, then the effect of atomic diffusion on the structure of a 1.7 $M_\odot$ and finally we show the impact on the age determination using asteroseismic data of the 94 Ceti A star.

2 Models computation

All the models are computed using the Toulouse Geneva Evolution Code (TGEC) (Hui-Bon-Hoa 2008; Théado et al. 2012). This code includes the effect of atomic diffusion for several chemical elements (and isotopes) using the Chapman & Cowling equations (Chapman & Cowling 1970). We use the diffusion coefficients derived by Paquette et al. (1986) and the OPAL2001 equation of state (Rogers & Nayfonov 2002). The nuclear reaction rates are from the NACRE compilation (Angulo 1999). We use the OP opacities from the OPCD v3.3 package (Seaton 2005) to compute mean Rosseland opacity at each time step and each mesh point to take into account the local variation of abundances. In this way, the stellar structure is consistently computed all along the evolutionary tracks, as well as the individual radiative accelerations of C, N, O, Ne, Mg, Ca, and Fe. This is done by using the improved semi-analytical prescription (SVP approximation) proposed by LeBlanc & Alecian (2004).

3 Impact on the stellar structure of F and A stars

We computed a 1.7 $M_\odot$ taking into account atomic diffusion (left part of Fig. 1) and adding the effect of fingering convection (right part of Fig. 1). Atomic diffusion alone produces accumulations of iron at the surface, around $\log(\Delta M/M_*) = -6.5$ (region of the iron/nickel convective zone) and around $\log(\Delta M/M_*) = -7.8$ for the calcium (panel *a*). This is due to radiative accelerations which are larger than the gravity in these regions (panel *c*). These accumulations lead to inverse μ-gradients (panel *e*) and to local increases of the opacity because elements accumulate where they are main contributor to the opacity, ie. where the element absorbs most of the photons (panel *g*).

The regions where there are inverse μ-gradients are unstable and lead to fingering convection. The results are presented on the right part of Fig. 1. Fingering convective regions are in light grey. There is one at the bottom of the surface convective zone and one at the bottom of the calcium accumulation region. There is no fingering convection at the bottom of the iron convective zone because of the stabilising helium gradient in this region (see Deal et al. 2016 for more details). These unstable regions modify the abundance profiles and we see an increase of the calcium surface abundance and a decrease of the iron surface abundance. There is also a modification of the internal abundance profiles (panel *b*). If there is a modification of the abundance profile, there is a modification of the opacity profile and we can see panel *h* a global smoothing of the opacity profile due to the reduction of abundance gradients induced by the fingering convection mixing. These results are published in Deal et al. (2016).

4 Asteroseismology

In this section we study the effect of atomic diffusion (including the effect of radiative accelerations) on the age determination using asteroseimology. We use seismic data obtained with HARPS for the 94 Ceti A star. This is a F type star of 1.44 $M_\odot$ in which the effect of radiative accelerations are lower than the previous case (Section 3). We see that there is no effect on iron and a small effect on calcium (Fig. 2). In this case the accumulation of calcium is not large enough to triggers fingering convection.

We determine the age of the 94 Ceti A star using the asteroseimic data and a grid of models taking into account only atomic diffusion without radiative accelerations in a first time. We then did it with a model including radiative accelerations. In this case we obtain an age 4% large and a radius 1% larger when radiative

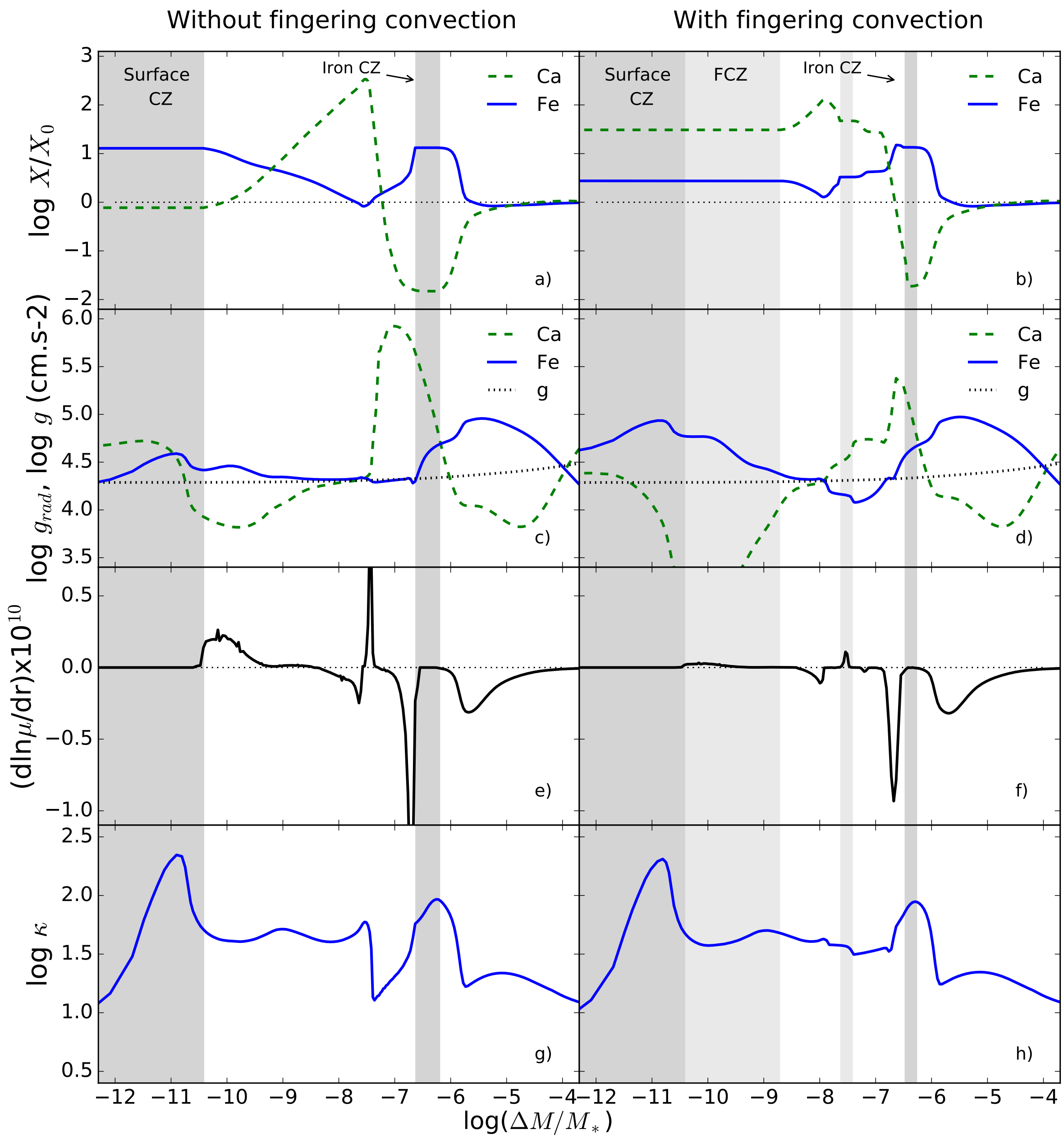

Fig. 1. Profiles of important physical quantities as a function of log($\Delta M/M_*$) in two 1.7 $M_\odot$ models at 100 Myrs with (right panel) and without (left panels) computation of fingering convection. Dynamical(CZ) and fingering (FCZ) convective zones are represented by dark and light grey regions, respectively. Panels *a* and *b* show calcium (green dashed lines) and iron (blue solid lines) abundances compare to their initial value. Panels *c* and *d* show calcium (green dashed lines) and iron (blue solid lines) radiative accelerations. The black dotted line represents the gravity. Panels *e* and *f* show the $\ln \mu$-gradient (black solid lines), panels *g* and *h* show the opacity profile (blue solid lines).

accelerations are taken into account. These differences come from the modification of the size of the surface convective zone which is deeper when element accumulates and when the mean Rosseland opacity increases. See Deal et al. (2017) for more details about this study.

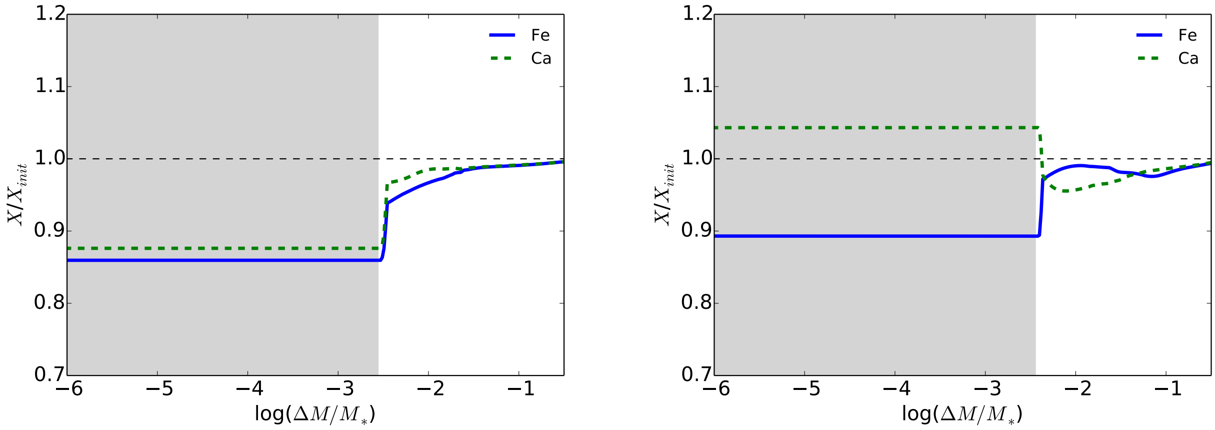

Fig. 2. Abundance profiles of calcium (green dashed lines) and iron (blue solid lines) for the model of 1.44 $M_\odot$ with $Y_{init} = 0.297$ and $Z_{init} = 0.0305$ with gravitational settling only (left panel) and including radiative acceleration (right panel). The dark grey areas represent the surface convective zone.

5 Conclusions

We saw with these two examples that atomic diffusion leads to hydrodynamical instabilities in A type stars and in both cases to a modifications of the structure of the star. This should be taken into account especially if we want to determine precise stellar parameters for the incoming space missions as PLATO and TESS. We will need, for an optimal treatment of the PLATO data, precision up to 10% on the ages, 15% in mass and 2% radius. In the case of 94 Ceti A, where radiative accelerations are not very efficient, we obtain 4% on the age and 1% on the radius which is half the precision needed. We can imagine that this difference in the parameter determination, taken into account radiative accelerations, should be larger for star where the accumulation of elements are larger. It is no longer possible to neglect the effect of atomic diffusion and the induced hydrodynamical instabilities if we want to model correctly the stars we observe with more and more precise instruments.

We thank the "Programme National de Physique Stellaire" (PNPS) of CNRS/INSU (France) for financial support.

References

Angulo, C. 1999, in American Institute of Physics Conference Series, Vol. 495, American Institute of Physics Conference Series, 365–366

Chapman, S. & Cowling, T. G. 1970, The mathematical theory of non-uniform gases. an account of the kinetic theory of viscosity, thermal conduction and diffusion in gases

Deal, M., Escobar, M. E., Vauclair, S., et al. 2017, A&A, 601, A127

Deal, M., Richard, O., & Vauclair, S. 2016, A&A, 589, A140

Hui-Bon-Hoa, A. 2008, Ap&SS, 316, 55

LeBlanc, F. & Alecian, G. 2004, MNRAS, 352, 1329

Paquette, C., Pelletier, C., Fontaine, G., & Michaud, G. 1986, ApJS, 61, 177

Richard, O., Michaud, G., & Richer, J. 2001, ApJ, 558, 377

Rogers, F. J. & Nayfonov, A. 2002, ApJ, 576, 1064

Seaton, M. J. 2005, MNRAS, 362, L1

Théado, S., Alecian, G., LeBlanc, F., & Vauclair, S. 2012, A&A, 546, A100

Théado, S., Vauclair, S., Alecian, G., & LeBlanc, F. 2009, ApJ, 704, 1262

Turcotte, S., Richer, J., Michaud, G., Iglesias, C. A., & Rogers, F. J. 1998, ApJ, 504, 539

SF2A 2017
C. Reylé, P. Di Matteo, F. Herpin, É. Lagadec, A. Lançon, Z. Meliani, F. Royer (eds)

PROPERTIES OF SIX MASSIVE BINARIES

F. Martins[1], L. Mahy⋆ [2,3] and A. Hervé[1]

Abstract. We present the analysis of six massive binaries observed with the SOPHIE spectrograph mounted on the T-193 telescope of the Observatoire de Haute Provence. The spectra are collected over the orbital period of the systems and are separated with a disentangling method. The resulting spectra are analyzed by means of atmosphere models. The stellar parameters of the components of each system are determined together with the CNO surface abundances. The degree of nitrogen enrichment and carbon and oxygen depletion is compared to theoretical predictions and to results for single stars and other binary systems. We conclude that surface abundances are not modified by binarity unless mass transfer and envelope removal takes place.

Keywords: Stars: binaries: spectroscopic – Stars: binaries: eclipsing – Stars: massive – Stars: abundances

1 Introduction

Massive stars evolve under the main influence of mass loss and rotation (Chiosi & Maeder 1986; Maeder & Meynet 2000). But a non negligible, perhaps a majority, of massive stars are also members of multiple systems (Kobulnicky et al. 2014; Sana et al. 2014). Tides induced by the presence of a companion trigger energy exchange that affects both the orbital/rotational properties but also the internal structure. When mass transfer occurs as a result of the evolution of one component and Roche lobe filling, angular momentum and material is lost/accreted. This also affects the general appearance and future evolution of stars. Of particular concern is to which level the surface abundances of massive stars are affected by binarity. High or low values of the N/C ratio sometimes escape predictions of single star evolution including rotation (Grin et al. 2017). The effect of a companion is usually quoted as a possible reason for such a discrepancy. However no quantification of such an effect has ever been performed.

In this study we present a first step towards an investigation of the effect of binarity on surface abundances of OB stars.

2 Spectral disentangling and spectroscopic analysis

We have selected massive binaries from the compilation of Gies (2003). We focussed on short-period systems in which the components are more likely to interact. We selected eclipsing binaries when possible in order to determine accurately masses and rotational velocities. We ended up with a sample of six systems: AH Cep (B0.2V+B2V), XZ Cep (O9.5V+B1III), V478 Cyg (O9.5V+O9.5V), Y Cyg (O9V+O9.5V), V382 Cyg (O6.5V((f))+O6V((f))) and DH Cep (O5.5V-III+O6V-III). The periods range from 1.77 to 5.10 d.

We used the SOPHIE spectrograph (Bouchy et al. 2013) mounted on the T-193 telescope of the Observatoire de Haute Provence. SOPHIE provides échelle spectra covering the 3900-6900Å wavelength range at a resolution of 39000. We observed each systems between 6 and 15 times depending on their period, in order to sample the orbital phase and especially the phases of maximum separation. The spectra were reduced automatically by the SOPHIE pipeline (Bouchy et al. 2009).

⋆ F.R.S.-FNRS Postdoctoral researcher

[1] LUPM, CNRS & Université de Montpellier, CC072, Place Eugène Bataillon, F-34095 Montpellier Cedex 05

[2] Space sciences, Technologies, and Astrophysics Research (STAR) Institute, Université de Liège, Quartier Agora, Bt. B5c, Allée du 6 aout, 19c, 4000, Liège, Belgium

[3] Instituut voor Sterrenkunde, KU Leuven, Celestijnenlaan 200D, Bus 2401, B-3001 Leuven, Belgium

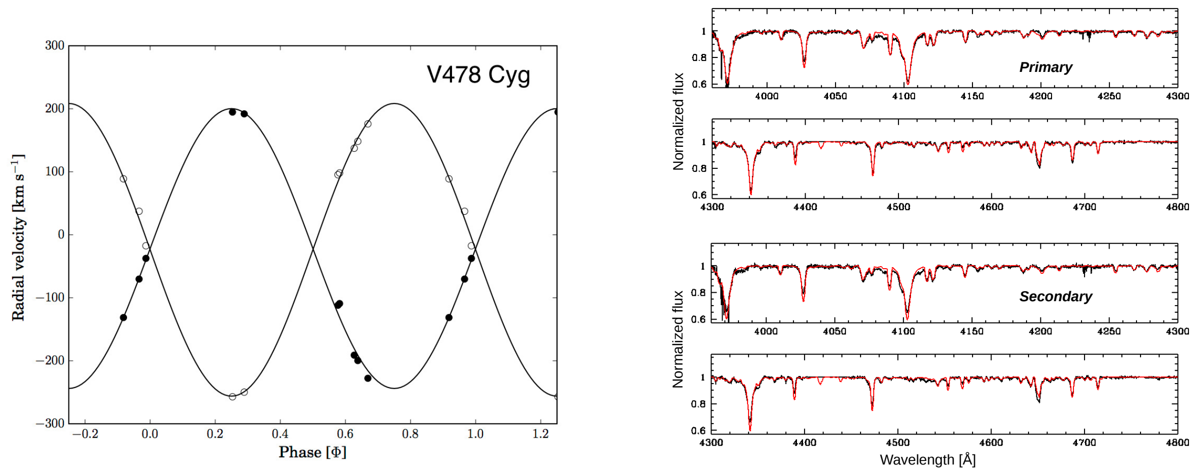

Fig. 1. Left: Radial velocity curve (circles) and orbital solution (solid line). **Right:** Best fit (red) of the disentangled spectra (black) of the primary (upper two panels) and secondary (lower two panels).

The Liège Orbital Solution Package (LOSP*) was subsequently used to perform an orbital solution. The left panel of Fig. 1 shows an example in result in the case of the system V478 Cyg. In order to separate the spectra of the two components we used a spectral disentangling method based on the method of Hadrava (1995). The orbital solution is used as an input. The resulting spectra of V478 Cyg are shown in the right panel of Fig. 1. The main difficulty is the reconstruction of the Balmer lines which are the broadest and are never totally separated from each other in the combined observed spectra.

The separated spectra were then analyzed with atmosphere models and synthetic spectra computed with the code CMFGEN (Hillier & Miller 1998). We relied on classical methods to determine the main fundamental parameters (see a summary in Martins 2011). In short, the projected rotational velocity ($V \sin i$) was determined from the Fourier transform of the OIII 5592 or HeI 4713 lines. The effective temperature was obtained from the fit of the HeI and HeII lines. The surface gravity $\log g$ was determined from the width of the Balmer lines. To constrain the surface abundances of carbon, nitrogen and oxygen we computed synthetic spectra with fixed $T_{\rm eff}$ and $\log g$ but different CNO abundances. We used a χ^2 analysis to estimate the best fit of a selection of C, N and O lines (for a description of the method see Martins et al. 2015). The right panel of Fig. 1 shows our best fit models for the primary and secondary of the V478 Cyg system.

3 Effect of binarity on surface abundances

The main results of our study are gathered in Fig. 2. First of all, we see that almost all components of our six systems have N/C ratios consistent with little enrichment. The only exception is the secondary star of XZ Cep that has log(N/C)=1.0. According to single-star evolutionary tracks, this degree of enrichment is achieved in stars with masses in the range 30-50 $M_\odot$(assuming an initial rotational velocity of 300 km s^{-1}). However the dynamical mass of this star is close to 7 $M_\odot$. This argues for a peculiar evolution of the secondary of XZ Cep (see below). For the other stars there is no obvious deviation from what is expected from single-star evolution.

Another way, rather model-independent, to reach the same conclusion is to compare the sample systems with single stars. The small symbols in Fig. 2 are such objects analyzed by Martins et al. (2015). We do not see any difference in the N/C ratios of stars in binary systems and single stars. If binarity affects surface abundances, this is with a magnitude smaller than the dispersion among single stars (dispersion that is due to different initial masses and rotational velocities).

In Fig. 2 we have added four systems known to have experienced mass transfer (Linder et al. 2008; Mahy et al. 2011; Raucq et al. 2016, 2017). Interestingly in all of them at least one component has a large N/C ratio. For LZ Cep and HD 149404 the enrichment is much larger than predicted by single-star evolutionary tracks of mass corresponding to the dynamical mass of the components. These results, combined with the

*LOSP is available at `http://www.stsci.edu/~hsana/losp.html`.

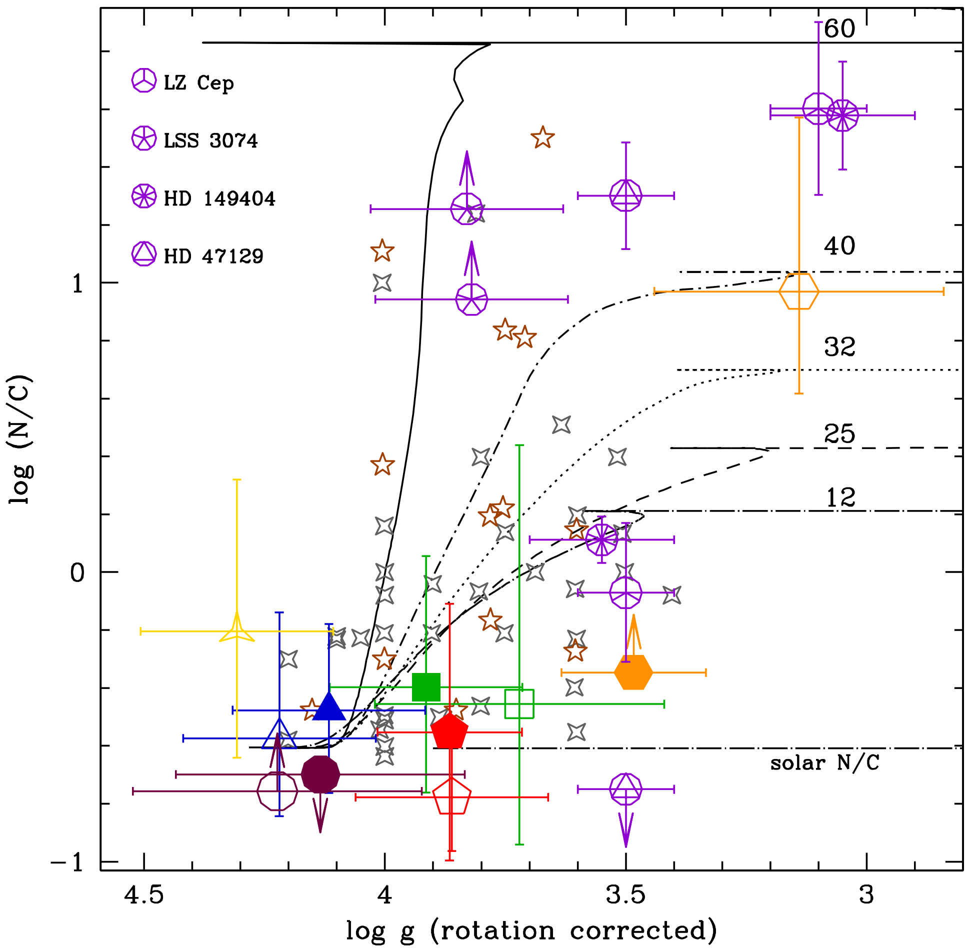

Fig. 2. log (N/C) as a function of surface gravity for the sample stars (large symbols) and other massive binaries (purple symbols). Small grey and brown symbols refer to single stars with masses below and above 28 $M_{\odot}$ respectively. Evolutionary tracks are from Ekström et al. (2012).

large enrichment of the secondary star of XZ Cep – which fills its Roche lobe according to our study – indicate that strong chemical enrichment is observed in stars that experienced mass transfer. More specifically, it is the component that lost part of its envelope through Roche lobe overflow that displays the largest chemical enrichment.

Our investigation thus shows that surface abundances in binary systems are not affected by tidal effects but can be modified in systems where mass transfer occurred. This conclusion obviously needs to be confirmed by analysis of additional massive binaries in different evolutionary states.

4 Conclusions

We have analyzed six massive binaries observed with SOPHIE at the Observatoire de Haute Provence. Individual spectra of each component have been retrieved by means of spectral disentangling. They have been subsequently analyzed with atmosphere models. The stellar parameters and surface abundances could be determined. We show that for most components of our systems surface abundances are not different from those of single stars with similar initial masses. The only case in which a larger N/C ratio is obtained is for a system that experienced Roche lobe overflow. Together with other such systems previously analyzed, this indicates that surface abundances are affected by binarity only if mass transfer (and envelope removal) occurred. In that case we observe deeper, more chemically mixed layers of the mass donor.

We thank John Hillier for making CMFGEN available to the community. We thank the Observatoire de Haute Provence for assistance with the T-193 telescope and the *SOPHIE* instrument.

References

Bouchy, F., Díaz, R. F., Hébrard, G., et al. 2013, A&A, 549, A49

Bouchy, F., Hébrard, G., Udry, S., et al. 2009, A&A, 505, 853

Chiosi, C. & Maeder, A. 1986, ARA&A, 24, 329

Ekström, S., Georgy, C., Eggenberger, P., et al. 2012, A&A, 537, A146

Gies, D. R. 2003, in IAU Symposium, Vol. 212, A Massive Star Odyssey: From Main Sequence to Supernova, ed. K. van der Hucht, A. Herrero, & C. Esteban, 91

Grin, N. J., Ramírez-Agudelo, O. H., de Koter, A., et al. 2017, A&A, 600, A82

Hadrava, P. 1995, A&AS, 114, 393

Hillier, D. J. & Miller, D. L. 1998, ApJ, 496, 407

Kobulnicky, H. A., Kiminki, D. C., Lundquist, M. J., et al. 2014, ApJS, 213, 34

Linder, N., Rauw, G., Martins, F., et al. 2008, A&A, 489, 713

Maeder, A. & Meynet, G. 2000, ARA&A, 38, 143

Mahy, L., Martins, F., Machado, C., Donati, J.-F., & Bouret, J.-C. 2011, A&A, 533, A9

Martins, F. 2011, Bulletin de la Societe Royale des Sciences de Liege, 80, 29

Martins, F., Hervé, A., Bouret, J.-C., et al. 2015, A&A, 575, A34

Raucq, F., Gosset, E., Rauw, G., et al. 2017, A&A, 601, A133

Raucq, F., Rauw, G., Gosset, E., et al. 2016, A&A, 588, A10

Sana, H., Le Bouquin, J.-B., Lacour, S., et al. 2014, ApJS, 215, 15

SF2A 2017
C. Reylé, P. Di Matteo, F. Herpin, É. Lagadec, A. Lançon, Z. Meliani, F. Royer (eds)

THE PHOTOSPHERE OF RED SUPERGIANT STARS AS SEEN BY OPTICAL INTERFEROMETRY

M. Montargès[1], P. Kervella[2], G. Perrin[2], A. Chiavassa[3], R. Norris[4], S. T. Ridgway[5] and L. Decin[1]

Abstract. During the end of their lives, massive stars become red supergiant (RSG) stars. At this stage, they are forging heavy elements in their cores that are transported up to the photosphere thanks to convection and expelled to the interstellar medium through the star's mass loss. Cooling in the outer atmosphere causes these elements to become molecules and dust that are the building blocks of future planetary systems and eventually life. One of the scenarios to explain the launch of material from the photosphere involves convection that leads to an increased scale height and facilitates mass ejection. We present here observations of several bright features on the surface of nearby RSG stars using near infrared (NIR) interferometry. They are interpreted as being the top of convective cells. We compare them with 3D convective simulation predictions. These inhomogeneities are bright and large enough to cause a photocenter displacement that might bias parallax measurements.

Keywords: stars: imaging - supergiants - stars: mass-loss - infrared: stars - techniques: interferometric

1 Introduction

The chemical enrichment of the Universe is driven by evolved stars. Red supergiant (RSG) stars represent one of the last evolutionary stages of massive stars. They experience an important mass loss (10^{-6} $M_{\odot}.yr^{-1}$ for Betelgeuse, Mauron & Josselin 2011). However, the mechanism driving this outflow has yet to be identified. A possible scenario involves convection lowering the effective gravity on the photosphere and allowing radiative pressure on molecular lines to launch the material (Josselin & Plez 2007).

The convective pattern of RSG stars has been observed for several years. Haubois et al. (2009) reconstructed the first high dynamic range image of Betelgeuse using IOTA H band observations. They observed two bright spots whose size was of the same order of magnitude as the stellar radius. These features were consistent with predictions from 3D radiative hydrodynamics (RHD) simulations (Chiavassa et al. 2010). Several inhomogeneities were observed on the photosphere of nearby RSG stars using near infrared (NIR) interferometry. With the high spectral resolution mode of VLTI/AMBER, upward and downward motions were observed in the CO shell surrounding Antares (Ohnaka et al. 2013, 2017) and Betelgeuse (Ohnaka et al. 2011). On the latter, Montargès et al. (2014) showed that their VLTI/AMBER observations were compatible with the presence of convective features on the K band photosphere.

To better understand the role of the convective cells in initiating the mass loss of RSG stars, times series need to be acquired, in order to determine the evolution timescale of the convective features and to obtain a statistics of their morphological characteristics. These elements can be used to challenge the quality of the numerical models that are unable, for now, to reproduce the molecular extension of the atmosphere of RSGs nor their terminal wind velocity. We present here observations* of the nearby RSG stars Betelgeuse and Antares that are interpreted using analytic models (Sect. 2) and preliminary reconstructed images of CE Tau, a RSG located farther away (Sect. 3).

[1] Institute of Astronomy, KU Leuven, Celestijnenlaan 200D B2401, 3001 Leuven, Belgium
[2] LESIA, Observatoire de Paris, PSL Research University, CNRS, Sorbonne Universités, UPMC Univ. Paris 06, Univ. Paris Diderot, Sorbonne Paris Cité, 5 place Jules Janssen, 92195 Meudon Cedex, France
[3] Université Côte d'Azur, Observatoire de la Côte d'Azur, CNRS, Lagrange, France
[4] Center for High Angular Resolution Astronomy, Georgia State University
[5] National Optical Astronomy Observatories, 950 North Cherry Avenue, Tucson, AZ 85719, USA
*Obtained with ESO telescopes at Paranal Observatory, under ESO programs 288.D-5035(A), 090.D-0548(A), 092.D-0366(A, B), 094.D-0869 (A), 093.D-0378(A, B, C), 093.D-0673(C), and 298.D-5005(A, B)

2 Analytic models on Betelgeuse and Antares

2.1 *Giant convective cells on Betelgeuse*

Betelgeuse (α Ori) was observed on the nights of 2012 January 31, 2013 February 09, 2014 January 11, and 2014 November 21 using ESO's Very Large Telescope Interferometer (VLTI) instrument PIONIER (Precision Integrated-Optics Near-infrared Imaging ExpeRiment, Le Bouquin et al. 2011). Squared visibilities and closure phases were obtained on the compact configuration (stations A1-B2-C1-D0) of the Auxiliary Telescopes (AT), on baselines ranging from 11.3 to 35.8 m on the ground. PIONIER sample the H band with a spectral resolution of 40. On the four epochs, the first lobe of the squared visibilities presents an unusual dependency on the position angle (PA, Fig. 1, left). This means that the fitted angular diameter for a uniform disk (UD) or a limb-darkened disk (LDD) depends on the azimuth: the difference reaches 10% for the 2013 epoch. Therefore, a classical disk model cannot reproduce these data. Presenting strong deviations from 0° and 180°, the closure phases indicate the presence of asymmetries (Fig. 1, right). This excludes an elliptical model.

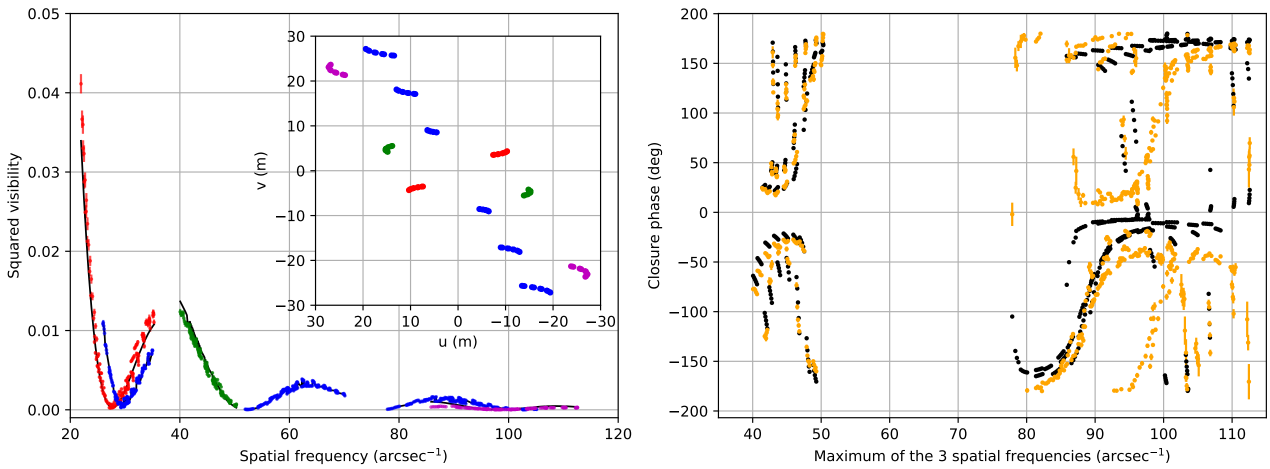

Fig. 1. Fit of the PIONIER data of Betelgeuse of February 2013 by the LDD and gaussian hotspot model. Only spatial frequencies lower than 51 arcsec^{-1} were considered. *Inset in the left image:* PA color-coded (u, v) coverage. *Left:* squared visibilities with matching colors. The black continuous line corresponds to the best fit model. *Right:* closure phases. The best fit model is represented in black.

Owing to previous observations of bright large spots on the surface of RSG stars, we fitted our observations with a power-law limb-darkened disk (Hestroffer 1997) on which we added a bright gaussian spot. The complete description of the model and of the fitting process is detailed in Montargès et al. (2016). As shown for the 2013 epoch on Fig. 1, this model fits both the squared visibilities and the closure phases. In particular, it is able to reproduce the doubling of the first lobe as a function of the PA. In this model, the resulting angular diameter of the star is correlated to the characteristics of the bright spot. This means that the presence of such structure can bias the angular diameter estimation of a star if its first lobe is probed on a single PA direction.

A bright spot can be fitted in all datasets except for the last epoch. In this case, it is necessary to introduce a second feature, dimmer and smaller. Figure 2 represents the corresponding intensity maps for the four epochs. The photocenter displacement we derived from these maps can reach up to 2 mas, more that a third of the parallax of the star (Harper et al. 2017). The position of this bright feature is consistent with spectropolarimetric measurements obtained at the Telescope Bernard Lyot with the Narval instrument (Aurière et al. 2016).

We compared our VLTI/PIONIER observations with 3D RHD simulations. Contrary to previous interferometric data (Chiavassa et al. 2010; Montargès et al. 2014), our squared visibilities and closure phases were not reproduced by the numerical models. 3D RHD simulations are unable to produce spots large and bright enough. Therefore, we proposed that Betelgeuse entered a convective regime dominated in the visible hemisphere by a large convective cell. This structure modifies the global convective pattern which can explain why the higher spatial frequencies (longer baselines, smaller convective structure on the photosphere) cannot be reproduced by the simulations either.

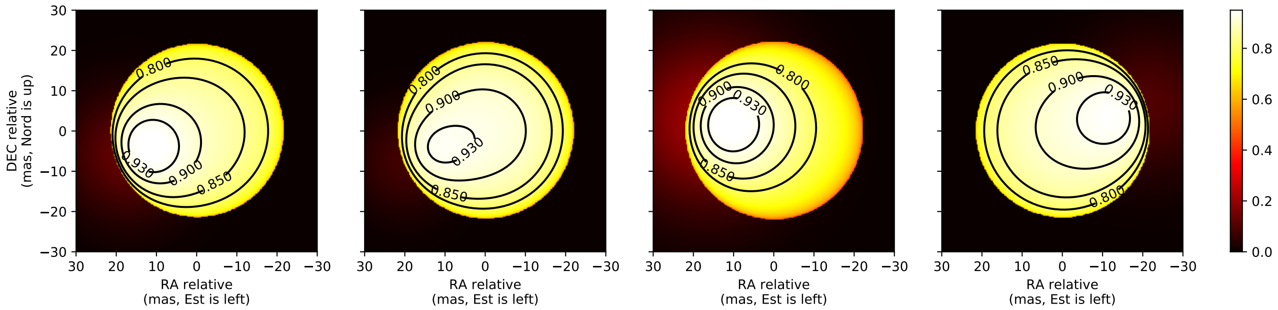

Fig. 2. Intensity maps associated to the best fit LDD and gaussian bright spot model on the PIONIER data of Betelgeuse. *From left to right:* January 2012, February 2013, January 2014, and November 2014.

2.2 *Characterizing the convective pattern of Antares*

We observed Antares with VLTI/PIONIER in its high spectral resolution mode on 2014 April 24, 29 and May 4 and 7 using the three available configuration of the AT. The spatial frequencies below 50 arcsec^{-1} cannot be reproduced by a regular disk model. However, deriving the angular diameter as a function of the PA allows to obtain a reliable estimation for each angle probed by the data. This results in an average LDD diameter of 38.27$\pm$0.37 mas at 1.61μm. Our observations probe the visibility function up to the sixteenth lobe of the visibility function. This corresponds to an angular resolution of 6% of the angular diameter. Chiavassa et al. (2011) showed that the convective pattern of RSG stars should host cells of various sizes, including small structures that should be the most numerous. Therefore, we cannot fit a single large structure on the photosphere as we did on Betelgeuse (Sect. 2.1). We adapted this previous model to derive the squared visibility and the closure phase associated to a LDD with distributions of bright spots of a fixed size. The detailed definition and expression of this model are given in Montargès et al. (2017). The deviations from the LDD model are best reproduced when using spot distributions with characteristic sizes of 17 and 2 mas, meaning 45% and 5% of the star angular diameter. With this model, the best fit angular diameter is 37.89 ± 0.10 mas at 1.61 μm. As concluded from the analysis of the VLTI/PIONIER datasets of Betelgeuse, the presence of photospheric features on a RSG star has direct consequences on the measurement of the angular diameter by optical interferometry.

This result directly affects the fit by the 3D RHD simulations. Indeed, the convective models are scaled to the angular diameter of the star. However, we demonstrated that the presence of features biases the fit of UD and LDD models. For this dataset on Antares, we set the angular diameter as a free parameter of the simulation. Figure 3 represents the best χ^2 on all the rotation angles and temporal snapshots of the simulation st35gm03n13 (Chiavassa et al. 2011) for a sample of angular diameters. The minimum χ^2 is reached for an angular diameter smaller than the value derived for a single LDD model and even a LDD with spot distributions model. The angular diameter measurement derived from NIR interferometry is strongly sensitive to the presence of features on the stellar surface, but also to their morphology. The best match was obtained for the LDD and spot distributions model. This indicates that features are present on the photosphere of Antares but that the current available 3D RHD simulations do not reproduce them correctly. This is in contradiction with previous results obtained on Betelgeuse (see references in Sect 2.1) but we stress that this Antares dataset probes previously unexplored region of the visibility function.

3 Image reconstruction on CE Tau

In September 2016, a spectropolarimetric signal was observed with the TBL/Narval instrument on CE Tau (Tessore et al. in prep.). It was the same signature as the previous observation of Betelgeuse (Sect. 2.1). This indicated the presence of photospheric features. With its ~ 10 mas angular diameter, CE Tau emerges as an interesting target for optical interferometry. Indeed, the two inner AT configurations allow to get a good sampling of the first three lobes of the visibility function, thus permitting an image reconstruction. In order to compare the feature detection with Narval with a NIR image, we observed this RSG star on 2016 November 14 and 22, and December 23 with VLTI/PIONIER. We used the high spectral resolution mode of the instrument. These observations will represent a joint diagnosis of the convective cell presence on the photosphere of CE Tau. On November 14, we used the AT in the compact configuration (A1-B2-C1-D0). On a star with the angular

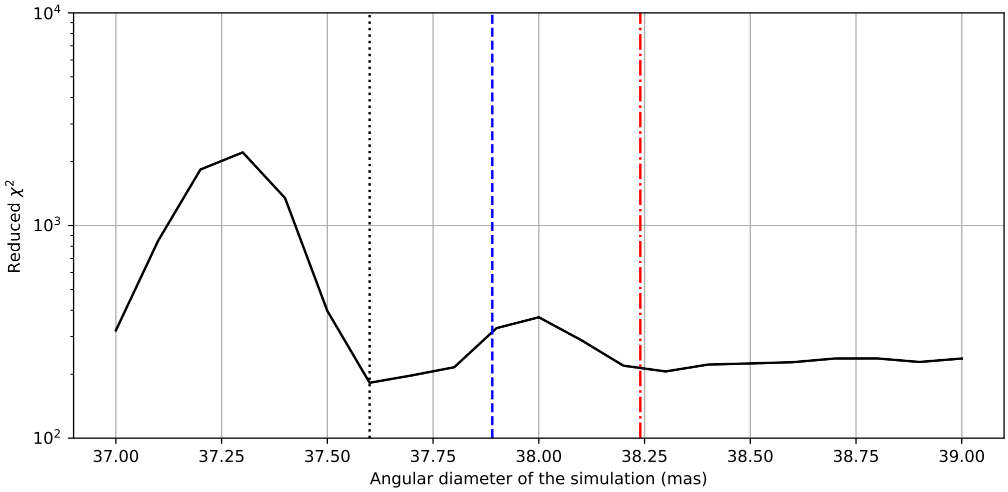

Fig. 3. Comparison of the VLTI/PIONIER squared visibilities of Antares at 1.61 μm with the 3D RHD simulation st35gm03n13. The black continuous line corresponds to the minimum χ^2 obtained over all the rotation angles and temporal snapshots of the simulation as a function of its angular diameter. The vertical black dotted line corresponds to the angular diameter giving the minimum χ^2. The red vertical dashed-dotted line corresponds to the angular diameter of the best fitted LDD model. The blue dashed line corresponds to the angular diameter of the best fitted LDD with spot distributions model.

diameter of CE Tau, these baselines probe only the first lobe of the visibility function. On November 22 and December 23, the AT were in the intermediate configuration (stations D0-G2-J3-K0). These data reach the second and third lobes: this means that features on the star are resolved. We decided to consider the November 14 data as "short spacing" observations, in an analogy with radio interferometry. With these baseline lengths, the star is not resolved and we can consider its general shape as invariant over a duration of a month. This assumption is confirmed by the intermediate configuration data: while data of the second and third lobe change between November and December, the part of the first lobe that is probed by these observations remain the same. The November 14 data were merged with the November 22 data to create a November dataset on the one hand, and with the December 23 observations on the other hand (December dataset).

For these two datasets, we reconstructed images using `SQUEEZE`, a compressed sensing based image reconstruction tool (Baron et al. 2010). `SQUEEZE` produces a mean reconstructed image that is the result of an exploration of the probability space using Monte Carlo Markov Chains. The detail of the reconstruction process as well as the images are presented in a forthcoming paper (Montargès et al. subm.).

4 Conclusions

We presented NIR interferometry observation of three nearby RSG stars. Several techniques were used to analyze these datasets: fit with classical disk models and with disk models including photospheric structures, comparisons with 3D RHD convective simulations and image reconstructions. Photospheric inhomogeneities are detected on the three stars. For Betelgeuse, we were able to follow the evolution of these structures over different epochs. The photosphere of RSG stars host a convective regime dominated by giant cells whose size reaches a significant fraction of the stellar radius. A smaller granulation is also detected on the high angular resolution data of Antares.

In the case of Antares and Betelgeuse, convective numerical simulations do not reproduce the convective pattern. These models are missing one or several ingredients: this can be for example the rotation or the magnetic field. The characterization of convection is crucial to understand its consequences on the mass loss of RSG stars but we have also shown that the presence of convective features can bias our angular diameter measurements using NIR interferometry and the parallax estimations.

We are grateful to ESOs Director-General, Prof. Tim de Zeeuw, for the allocation of observing time to our program, as well as to the Paranal Observatory team for the successful execution of the observations. This research received the support of PHASE, the high-angular resolution partnership between ONERA, Observatoire de Paris, CNRS, and University Denis Diderot Paris 7. We acknowledge financial support from the Programme National de Physique Stellaire (PNPS) of CNRS/INSU, France. This project has received funding from the European Unions Horizon 2020 research and innovation programme under the Marie Skodowska-Curie Grant agreement No. 665501 with the research Foundation Flanders (FWO) ([PEGASUS][2] Marie Curie fellowship 12U2717N awarded to MM). We used the SIMBAD and VIZIER databases at the CDS, Strasbourg (France)[†], and NASA's Astrophysics Data System Bibliographic Services. This research has made use of Jean-Marie Mariotti Center's `Aspro`[‡] service, and of the `SearchCal` service[§] (co-developed by FIZEAU and LAOG/IPAG). This research made use of IPython (Pérez & Granger 2007) and Astropy[¶], a community-developed core Python package for Astronomy (Astropy Collaboration et al. 2013).

References

Astropy Collaboration, Robitaille, T. P., Tollerud, E. J., et al. 2013, A&A, 558, A33

Aurière, M., López Ariste, A., Mathias, P., et al. 2016, A&A, 591, A119

Baron, F., Monnier, J. D., & Kloppenborg, B. 2010, in Proc. SPIE, Vol. 7734, Optical and Infrared Interferometry II, 77342I

Chiavassa, A., Freytag, B., Masseron, T., & Plez, B. 2011, A&A, 535, A22

Chiavassa, A., Haubois, X., Young, J. S., et al. 2010, A&A, 515, A12

Harper, G. M., Brown, A., Guinan, E. F., et al. 2017, AJ, 154, 11

Haubois, X., Perrin, G., Lacour, S., et al. 2009, A&A, 508, 923

Hestroffer, D. 1997, A&A, 327, 199

Josselin, E. & Plez, B. 2007, A&A, 469, 671

Le Bouquin, J.-B., Berger, J.-P., Lazareff, B., et al. 2011, A&A, 535, A67

Mauron, N. & Josselin, E. 2011, A&A, 526, A156

Montargès, M., Chiavassa, A., Kervella, P., et al. 2017, A&A, 605, A108

Montargès, M., Kervella, P., Perrin, G., et al. 2016, A&A, 588, A130

Montargès, M., Kervella, P., Perrin, G., et al. 2014, A&A, 572, A17

Ohnaka, K., Hofmann, K.-H., Schertl, D., et al. 2013, A&A, 555, A24

Ohnaka, K., Weigelt, G., & Hofmann, K.-H. 2017, Nature, 548, 310

Ohnaka, K., Weigelt, G., Millour, F., et al. 2011, A&A, 529, A163

Pérez, F. & Granger, B. E. 2007, Computing in Science and Engineering, 9, 21

[†]Available at `http://cdsweb.u-strasbg.fr/`
[‡]Available at `http://www.jmmc.fr/aspro`
[§]Available at `http://www.jmmc.fr/searchcal`
[¶]Available at `http://www.astropy.org/`

HR 7098: A NEW COOL HGMN STAR ?

R.Monier[1], M.Gebran[2], F.Royer[3] and T. Kılıcoğlu[4]

Abstract. Using one archival high dispersion high quality spectrum of HR 7098 (A0V) obtained with the échelle spectrograph SOPHIE at Observatoire de Haute Provence, we show that this star is not a superficially normal A0V star as hitherto thought. The model atmosphere and spectrum synthesis modeling of the spectrum of HR 7098 reveals real departures of its abundances from the solar composition. We report here on our first determinations of the elemental abundances of 35 elements in the atmosphere of HR 7098. Helium and Carbon are underabundant whereas the very heavy elements are overabundant in HR 7098.

Keywords: stars: individual, stars: chemically peculiar

1 Introduction

HR 7098 currently assigned an A0V spectral type, is one of the 47 northern slowly rotating early-A stars studied by Royer et al. (2014). This star has been little studied: only 47 references can be found in ADS although it is fairly bright (V= 6.63). The low projected rotational velocity of HR 7098 can either be due to i) a very low inclination angle ($i \simeq 0$) or ii) a very low equatorial velocity v_e. In this second case, the star could develop large over and underabundances and be a new Chemically Peculiar (CP) star. We have recently synthesized several lines of 35 elements present in the archival SOPHIE spectrum of HR 7098 using model atmospheres and spectrum synthesis including hyperfine structure of various isotopes when necessary. These synthetic spectra were iteratively adjusted to the archival high resolution high signal-to-noise spectrum of HR 7098 in order to derive the abundances of these elements. This abundance analysis yields underabundances of the light elements He and C, mild overabundances of the iron-peak elements and large excesses in the very heavy elements (VHE whose atomic number Z is greater than 30). This definitely shows that HR 7098 should be reclassified as a new CP star. We present here preliminary determinations of the elemental abundances in HR 7098.

2 Observations and reduction

HR 7098 has been observed at the Observatoire de Haute Provence using the High Resolution (R =75000) mode of SOPHIE in August 2009. One 20 minutes exposure was secured with a $\frac{S}{N}$ ratio of about 224 at 5000 Å. We did not observe HR 7098 ourselves but fetched the spectrum from the SOPHIE archive.

3 Model atmospheres and spectrum synthesis

The effective temperature and surface gravity of HR 7098 were first evaluated using Napiwotzky et al's (1993) UVBYBETA calibration of Stromgren's photometry. The found effective temperature Teff is 10200 ± 200 K and the surface gravity $\log g$ is 3.55 ± 0.25 dex.

A plane parallel model atmosphere assuming radiative equilibrium, hydrostatic equilibrium and local thermodynamical equilibrium has been first computed using the ATLAS9 code (Kurucz 1992), specifically the

[1] LESIA, UMR 8109, Observatoire de Paris Meudon, Place J.Janssen, Meudon, France
[2] Department of Physics and Astronomy, Notre Dame University - Louaize, PO Box 72, Zouk Mikael, Lebanon
[3] GEPI, UMR 8111, Observatoire de Paris Meudon, Place J.Janssen, Meudon, France
[4] Department of Astronomy and Space Sciences, Faculty of Science, Ankara University, 06100, Ankara, Turkey

linux version using the new ODFs maintained by F. Castelli on her website*. The linelist was built starting from Kurucz's (1992) `gfhyperall.dat` file† which includes hyperfine splitting levels. This first linelist was then upgraded using the NIST Atomic Spectra Database‡ and the VALD database operated at Uppsala University (Kupka et al. 2000)§. A grid of synthetic spectra was then computed with a modified version of SYNSPEC49 (Hubeny & Lanz 1992, 1995) to model the lines. The synthetic spectrum was then convolved with a gaussian instrumental profile and a parabolic rotation profile using the routine ROTIN3 provided along with SYNSPEC49. We adopted a projected apparent rotational velocity $v_e \sin i = 10.5$ km.s^{-1} and a radial velocity $v_{rad} = -10.84$ km.s^{-1} from Royer et al. (2014).

4 Determination of the microturbulent velocity

In order to derive the microturbulent velocity of HR 7098, we have derived the iron abundance [Fe/H] by using 36 unblended Fe II lines for a set of microturbulent velocities ranging from 0.0 to 2.5 km s^{-1}. Figure 1 shows the standard deviation of the derived [Fe/H] as a function of the microturbulent velocity. The adopted microturbulent velocity is the value which minimizes the standard deviation ie. for that value, all Fe II lines yield the same iron abundance. We therefore adopt a microturbulent velocity $\xi_t = 0.96 \pm 0.04$ km s^{-1} constant with depth for HR 7098.

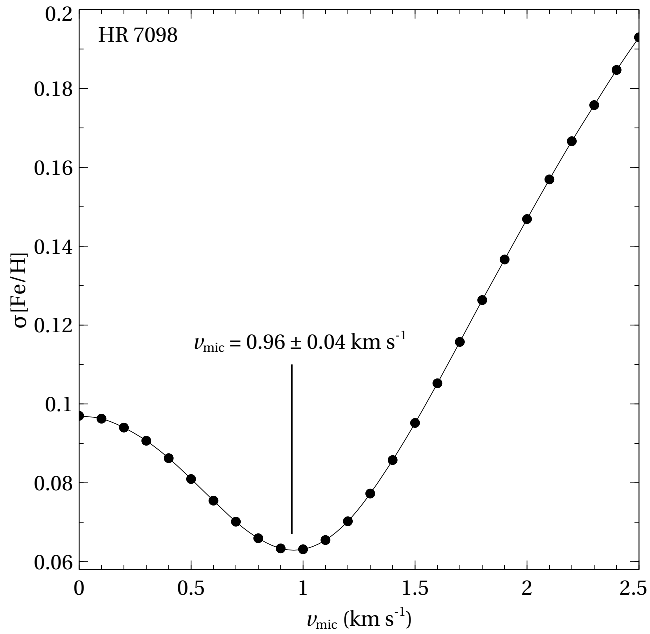

Fig. 1. The derived microturbulent velocity for HR 7098

5 The derived abundance pattern for HR 7098

The derived abundances for the 35 elements studied are displayed in Fig. 2. For a given element, we display actually the absolute abundance $\log(\frac{X}{H})$ with a representative error of $\pm$ 0.15 dex. We find that HR 7098 displays underabundances in the light elements He, C. It has solar abundances for Mg, Al, S and Ca and only mild overabundances (less than 5 times the solar values) for P, Ti, V, Cr, Mn, Fe, Ni, Sr, Y and Zr. It has large overabundances (larger than 5 times solar) in several very heavy elements: Ba, La, Pr, Nd, Sm, Eu, Gd, Dy, Ho, Er and Hg. The heaviest element Hg is the most overabundant. The abundance pattern of HR 7098 therefore resembles that of the coolest HgMn stars.

*http://www.oact.inaf.it/castelli/
†http://kurucz.harvard.edu/linelists/
‡http://physics.nist.gov/cgi-bin/AtData/linesform
§http://vald.astro.uu.se/∼vald/php/vald.php

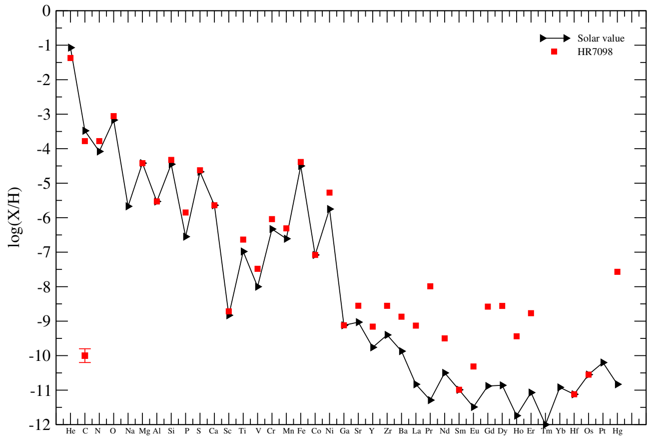

Fig. 2. The derived elemental abundances for HR 7098

6 Conclusions

The derived abundance pattern of HR 7098 departs from the solar composition which definitely shows that HR 7098 is not a superficially normal early A star but is actually another new CP star. We have already reported on the discovery of 5 new CP stars of the HgMn type in Monier et al. (2015) and Monier et al. (2016). HR 7098 has overabundances of both the rare earths and of Hg and its effective temperature and surface gravity place it at the coolest end of the realm of the HgMn stars. Hence we propose that HR 7098 be a new and very cool and mild HgMn star. We are currently planning more observations of HR 7098 with SOPHIE in order to complement the abundances derived here and search for putative line variability. This will help us adddress the relationship of HR 7098 to the coolest known HgMn stars and constrain the nature of this interesting new CP star.

The authors acknowledge use of the SOPHIE archive (`http://atlas.obs-hp.fr/sophie/`) at Observatoire de Haute Provence. They have used the NIST Atomic Spectra Database and the VALD database operated at Uppsala University (Kupka et al., 2000) to upgrade atomic data.

References

Hubeny, I., Lanz, T. 1992, A&A, 262, 501

Hubeny, I., Lanz, T. 1995, ApJ, 439, 875

Kupka F., Ryabchikova T.A., Piskunov N.E., Stempels H.C., Weiss W.W., 2000, Baltic Astronomy, vol. 9, 590-594

Kurucz, R.L. 1992, Rev. Mexicana. Astron. Astrofis., 23, 45

Monier, R., Gebran, M., Royer, F. 2015, A&A, 577A, 96M

Monier, R., Gebran, M., & Royer, F. 2016, Ap&SS, 361, 139

Napiwotzki, R., Schoenberner, D., Wenske, V. 1993, A&A, 268, 653

Royer, F., Gebran, M., Monier, R., Adelman, S., Smalley, B., Pintado, O., Reiners, A., Hill, G., Gulliver, G. 2014 , A&A, 562A, 84R

SF2A 2017
C. Reylé, P. Di Matteo, F. Herpin, É. Lagadec, A. Lançon, Z. Meliani, F. Royer (eds)

THE FLAT BOTTOMED LINES OF VEGA

R.Monier[1], M.Gebran[2], F.Royer[3] and T. Kılıcoğlu[4]

Abstract. Using one high dispersion high quality spectrum of Vega (HR7001, A0V) obtained with the échelle spectrograph SOPHIE at Observatoire de Haute Provence, we have measured the centroids of 149 flat bottomed lines. The model atmosphere and spectrum synthesis modeling of the spectrum of Vega allows us to provide identifications for all these lines. Most of these lines are due to C I, O I, Mg I, Al I, Ca I, Sc II,Ti II, Cr I, Cr II, Mn I, Fe I, Fe II, Sr II, Ba II, the large majority being due to neutral species, in particular Fe I.

Keywords: stars: individual, stars: Vega, HR 7001

1 Introduction

Vega (HR 7001), the standard A0V spectral type, is one of the 47 northern slowly rotating early-A stars studied by Royer et al. (2014). The low projected rotational velocity of HR 7001, about 24 km s^{-1} is due to the very low inclination angle ($i \simeq 0$) while the equatorial velocity $v_e \simeq 245\,\mathrm{km\ s^{-1}}$ is very large (Gulliver et al. 1994). Hence Vega is a fast rotator seen nearly pole-on whose limb almost coincides with the equator of the star. At the equator, the centrifugal force reduces the effective surface gravity which alters the ionization balance and strengthens the local I_λ profile of certain species. For these species, the distribution of the Doppler shift is bimodal, ie. arises from the two equatorial regions near the limb. We have measured all the centroids of all 149 flat-bottomed lines we could find in the high resolution SOPHIE spectrum of Vega. We have synthesized all lines expected to be present in the SOPHIE spectrum of HR 7001 in the range 3900 up to 6800 Å using model atmospheres and spectrum synthesis and an appropriate chemical composition for Vega as derived by Castelli & Kurucz (1994). The synthetic spectrum has been adjusted to the SOPHIE spectrum of HR 7001 in order to identify the flat-bottomed lines of HR 7001.

2 Observations and reduction

A search of the SOPHIE archive reveals that HR 7001 has been observed 78 times at the Observatoire de Haute Provence using SOPHIE between August 3, 2006 and August 6, 2012. We have used one high resolution (R = 75000) 30 seconds exposure secured with a $\frac{S}{N}$ ratio of about 824 at 5000 Å to search for the flat-bottomed lines.

3 Model atmospheres and spectrum synthesis

The effective temperature and surface gravity of HR 7001 were first evaluated using Napiwotzky et al's (1993) UVBYBETA calibration of Strömgren's photometry. The found effective temperature $\mathrm{T_{eff}}$ is 9550 ± 200 K and the surface gravity log g is 3.98± 0.25 dex. This temperature is in very good agreement with the fundamental temperature derived by Code et al. (1976) from the integrated flux and the angular diameter and with the mean temperature and surface gravity derived by Hill et al. (2010).

[1] LESIA, UMR 8109, Observatoire de Paris Meudon, Place J.Janssen, Meudon, France
[2] Department of Physics and Astronomy, Notre Dame University - Louaize, PO Box 72, Zouk Mikael, Lebanon
[3] GEPI,UMR 8111, Observatoire de Paris Meudon, Place J.Janssen, Meudon, France
[4] Department of Astronomy and Space Sciences, Faculty of Science, Ankara University, 06100, Ankara, Turkey

A plane parallel model atmosphere assuming radiative equilibrium, hydrostatic equilibrium and local thermodynamical equilibrium was then computed using the ATLAS9 code (Kurucz 1992), specifically the linux version using the new ODFs maintained by F. Castelli on her website*. The linelist was built starting from Kurucz's (1992) `gfhyperall.dat` file† which includes hyperfine splitting levels. This first linelist was then upgraded using the NIST Atomic Spectra Database‡ and the VALD database operated at Uppsala University (Kupka et al. 2000)§. A grid of synthetic spectra was then computed with a modified version of SYNSPEC49 (Hubeny & Lanz 1992, 1995) to model the lines. The synthetic spectrum was then convolved with a gaussian instrumental profile and a parabolic rotation profile using the routine ROTIN3 provided along with SYNSPEC49. We adopted a projected apparent rotational velocity $v_e \sin i = 24.5$ km.s^{-1} and a radial velocity $v_{rad} = -13.80$ km.s^{-1} from Royer et al. (2014).

4 Determination of the microturbulent velocity

In order to derive the microturbulent velocity of HR 7001, we have derived the iron abundance [Fe/H] by using 36 unblended Fe II lines for a set of microturbulent velocities ranging from 0.0 to 2.5 km s^{-1}. Figure 1 shows the standard deviation of the derived [Fe/H] as a function of the microturbulent velocity. The adopted microturbulent velocity is the value which minimizes the standard deviation ie. for that value, all Fe II lines yield the same iron abundance, which is [Fe/H] = -0.60 ± 0.07 dex. Hence iron is found to be underabundant in HR 7001 in agreement with previous abundance determinations (Castelli & Kurucz 1994). We therefore adopt a microturbulent velocity $\xi_t = 1.70 \pm 0.04$ km s^{-1} constant with depth for HR 7001.

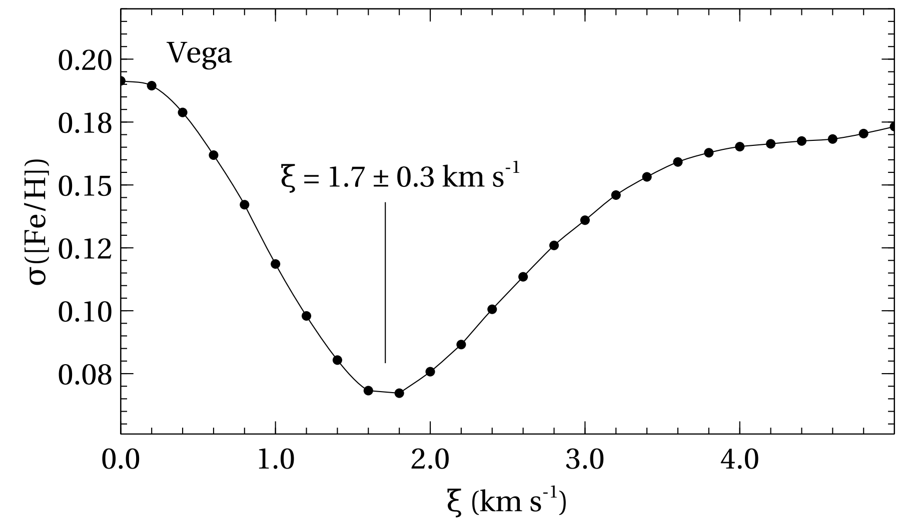

Fig. 1. The derived microturbulent velocity for HR 7001

5 The list of flat-bottomed lines in HR 7001

An example of flat-bottomed line in the spectrum of HR 7001 is the Ba II line at 4554.04 Å shown in Fig. 2. Note that the lines of Cr II at 4554.99 Å and of Fe II at 4555.99 Å have normal profiles. All the flat-bottomed lines are collected together with their identifications in Tab. 1. These lines are weak lines due to C I, O I, Mg I, Al I, Ca I, Sc II, Ti II, Cr I, Cr II, Mn I, Fe I, Fe II, Sr II, Ba II, the large majority being due to neutral species, in particular Fe I. Most of the lines we find to be flat-bottomed are also listed in the investigation of weak lines conducted by Takeda et al. (2008) in their high signal-to-noise high resolution spectrum of Vega.

*http://www.oact.inaf.it/castelli/
†http://kurucz.harvard.edu/linelists/
‡http://physics.nist.gov/cgi-bin/AtData/linesform
§http://vald.astro.uu.se/∼vald/php/vald.php

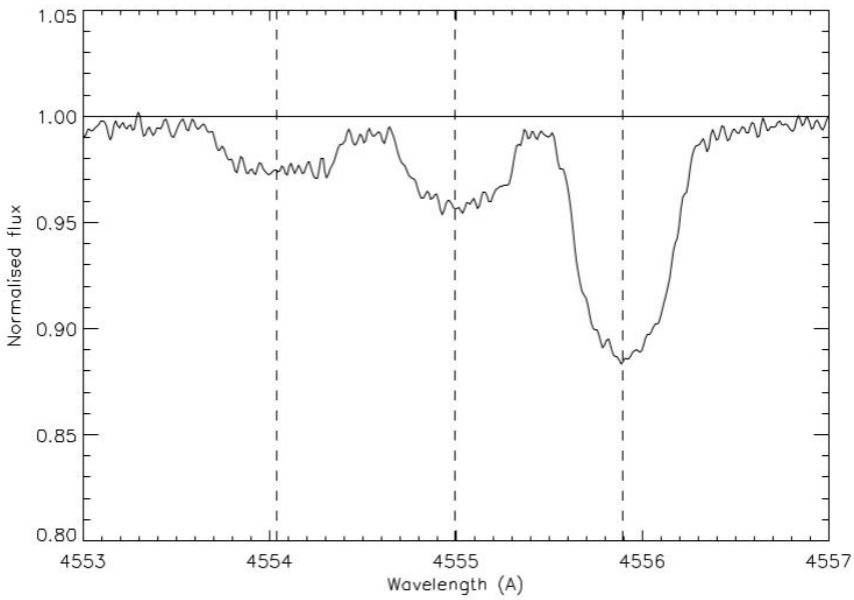

Fig. 2. The flat-bottomed line Ba II 4554.04 Å

6 Conclusions

A systematic search for flat-bottomed lines in the high resolution high quality SOPHIE spectrum of HR 7001 yields 149 lines in the range 3900 Å up to 6800 Å which complete the previous list published by Takeda et al. (2008). Most of these lines are due to C I, O I, Mg I, Al I, Ca I, Sc II,Ti II, Cr I, Cr II, Mn I, Fe I, Fe II, Sr II, Ba II, the large majority being due to Fe I.

Table 1: Identifications for flat-bottomed lines in Vega

$\lambda_{\rm obs}$ (Å)	$\lambda_{\rm lab}$ (Å)	Species	$\log gf$	E_{low}	Comments
3903.08	3902.945	Fe I	-0.47	12560.933	
3916.45	3916.45	V II	-1.060	11514.760	
3918.64	3918.642	Fe I	-0.720	24338.766	
3920.31	3920.258	Fe I	-1.75	978.074	
3922.94	3922.912	Fe I	-1.65	415.933	
3927.98	3927.920	Fe I	-1.59	888.132	
3930.31	3930.296	Fe I	-1.590	704.007	
	3930.304	Fe II	-4.030	13673.186	
3932.06	3932.023	Ti II	-1.780	9118.260	
3935.98	3935.962	Fe II	-1.860	44915.046	
3938.32	3938.289	Fe II	-3.890	13474.411	
	3938.400	Mg I	-0.760	35051.263	
3944.03	3944.006	Al I	-0.620	0.000	
3945.20	3945.210	Fe II	-4.250	13673.186	
3956.71	3956.677	Fe I	-0.430	21715.731	
3961.54	3961.520	Al I	-0.320	112.061	
4002.36	4002.483	Cr II	-2.060	42897.990	?
4005.29	4005.242	Fe I	-0.610	12560.933	
4021.88	4021.866	Fe I	-0.660	22249.428	
4034.49	4034.469	Mn I	-0.810	0.000	
	4034.502	Mn I	-0.810	0.000	
4035.67	4035.595	Fe I	-1.100	34039.315	blend
	4035.627	V II	-0.960	14461.750	

Table 1: Identifications for flat-bottomed lines in Vega

$\lambda_{\rm obs}$ (Å)	$\lambda_{\rm lab}$ (Å)	Species	$\log gf$	E_{low}	Comments
	4035.694	Mn I	-0.190	17281.999	
	4035.713	Mn I	-0.190	17281.999	
	4035.715	Mn I	-0.190	17281.999	
4043.99	4043.897	Fe I	-0.830	26140.178	blend
	4043.977	Fe I	-1.130	26140.178	
	4044.012	Fe II	-2.410	44929.549	
4057.56	4057.461	Fe II	-1.550	58668.256	blend
	4057.505	Mg I	-1.200	35031.263	
4068.01	4067.978	Fe I	-0.430	25899.986	
4070.89	4070.840	Cr II	-0.750	52321.010	
4072.38	4072.502	Fe I	-1.440	27666.345	
4118.57	4118.545	Fe I	0.280	28819.952	
4122.69	4122.668	Fe II	-3.380	20830.553	
4132.11	4132.058	Fe I	-0.650	12968.554	
4134.67	4134.677	Fe I	-0.490	22838.320	
4143.37	4143.415	Fe I	-0.200	24574.652	
4143.86	4143.868	Fe I	-0.450	12560.933	
4161.58	4161.535	Ti II	-2.360	8744.250	
4167.34	4167.271	Mg I	-1.600	35051.263	blend
	4167.299	Fe II	-0.560	90300.626	
4175.69	4175.036	Fe I	-0.670	22946.815	
4176.63	4176.566	Fe I	-0.620	27166.817	
4181.74	4181.755	Fe I	-0.180	22838.320	
4187.06	4187.039	Fe I	-0.550	19757.031	
4187.83	4187.795	Fe I	-0.550	19562.437	
4191.49	4191.430	Fe I	-0.670	19912.494	
4198.29	4198.247	Fe I	-0.460	27166.817	blend
	4198.304	Fe I	-0.720	19350.891	
4199.11	4199.095	Fe I	0.250	24574.655	
4202.02	4202.029	Fe I	-0.710	11976.238	
4210.40	4210.343	Fe I	-0.870	20019.633	
	4210.383	Fe I	-1.240	24772.016	
4215.60	4215.519	Sr II	-0.140	0.000	
4219.40	4219.360	Fe I	0.120	28819.952	
4222.30	4222.213	Fe I	-0.970	19757.031	blend
	4222.381	Zr II	-0.900	9742.800	
4226.75	4226.728	Ca I	0.240	0.000	
4227.45	4227.427	Fe I	0.230	26874.546	
4236.00	4235.936	Fe I	-0.340	19562.437	
4238.80	4238.810	Fe I	-0.280	27394.689	blend
	4238.819	Fe II	-2.720	54902.315	
4250.15	4250.119	Fe I	-0.410	19912.494	
4250.80	4250.787	Fe I	-0.710	12560.933	
4273.30	4273.326	Fe II	-3.260	21812.055	
4274.80	4274.797	Cr I	-0.230	0.000	
4275.60	4275.606	Cr II	-1.710	31117.390	
4278.20	4278.159	Fe II	-3.820	21711.917	
4282.45	4282.403	Fe I	-0.810	17550.180	blend
	4282.490	Mn II	-1.680	44521.521	
4284.20	4284.188	Cr II	-1.860	31082.940	
4287.90	4287.872	Ti II	-2.020	8710.440	
4312.90	4312.864	Ti II	-1.160	9518.060	
4325.0	4324.999	Sc II	-0.440	4802.870	

Table 1: Identifications for flat-bottomed lines in Vega

λ_{obs} (Å)	λ_{lab} (Å)	Species	$\log gf$	E_{low}	Comments
4367.6	4367.659	Ti II	-1.270	20891.660	blend
	4367.578	Fe I	-1.270	24118.816	
4369.50	4369.411	Fe II	-3.670	22469.852	
4371.4	4371.367	C I	-2.330	61981.822	
4386.9	4386.844	Ti II	-1.260	20951.600	
4394.05	4394.051	Ti II	-1.590	9850.900	
4395.08	4395.033	Ti II	-0.660	8744.250	
4400.40	4400.379	Sc II	-0.510	4883.570	
4411.10	4411.074	Ti II	-1.060	24561.031	
4417.80	4417.719	Ti II	-1.430	9395.710	
4418.40	4418.330	Ti II	-2.460	9975.920	
4450.60	4450.482	Ti II	-1.450	8744.250	
4451.60	4451.551	Fe II	-1.840	49506.995	
4454.90	4455.027	Fe I	-1.090	31307.244	
4464.50	4464.450	Ti II	-2.080	9363.620	
4466.65	4466.551	Fe I	-0.590	22856.320	
4473.00	4472.929	Fe II	-3.430	22939.357	
4476.10	4476.019	Fe I	-0.570	22946.815	blend
	4476.076	Fe I	-0.290	29732.735	
4488.40	4488.331	Ti II	-0.820	25192.791	
4494.65	4494.563	Fe I	-1.140	17726.928	
4528.70	4528.614	Fe I	-0.820	17550.180	
4529.60	4529.569	Fe II	-3.190	44929.549	
4541.60	4541.524	Fe II	-3.050	23031.299	
4554.20	4554.033	Ba II		0.000	15 hyperfine structure lines of isotopes of Ba
4582.85	4582.835	Fe II	-3.100	22939.357	
4590.0	4589.958	Ti II	-1.790	9975.920	blend
	4589.967	O I	-2.390	86631.153	
4592.10	4592.049	Cr II	-1.220	32854.949	
4616.60	4616.629	Cr II	-1.290	32844.760	
4620.50	4620.521	Fe II	-3.280	22810.356	
4666.80	4666.758	Fe II	-3.330	22810.356	
4703.00	4702.991	Mg I	-0.670	35051.263	blend
	4702.991	Zr II	-0.800	20080.301	
4731.50	4731.453	Fe II	-3.360	23317.632	
4736.82	4736.773	Fe I	-0.740	25899.986	very weak
4775.90	4775.897	C I	-2.670	18145.285	
4780.00	4779.985	Ti II	-1.370	16518.860	
4812.40	4812.468	Fe I	-5.400	22249.428	
4836.20	4836.229	Cr II	-2.250	31117.390	
4890.70	4890.755	Fe I	-0.430	23192.497	
4891.50	4891.492	Fe I	-0.140	22996.673	blend
	4891.485	Cr II	-3.040	31350.901	
4919.05	4918.994	Fe I	-0.370	23110.937	blend
	4918.954	Fe I	-0.340	33507.120	
4920.50	4920.502	Fe I	0.060	22845.868	
4932.00	4932.049	C I	-1.880	61981.822	blend
	4932.080	Fe II	-1.730	83196.488	
4934.10	4934.076	Ba II	-0.150	0.000	
4993.40	4993.565	N I	-2.860	95475.313	?
5004.20	5004.195	Fe II	0.500	82853.660	
5052.20	5052.167	C I	-1.650	61981.822	very flat bottomed
5129.20	5129.152	Ti II	-1.390	15257.430	

Table 1: Identifications for flat-bottomed lines in Vega

$\lambda_{\rm obs}$ (Å)	$\lambda_{\rm lab}$ (Å)	Species	$\log gf$	E_{low}	Comments
5133.70	5133.688	Fe I	0.140	33695.394	
5154.00	5154.070	Ti II	-1.920	12628.731	
5171.60	5171.596	Fe I	-1.790	11976.238	blend, very extended flat core
	5171.640	Fe II	-4.370	22637.205	
5185.90	5185.913	Ti II	-1.350	15265.619	
5188.70	5188.680	Ti II	-1.210	12758.110	
5192.40	5192.442	Fe II	-2.020	5192.442	
5206.00	5206.037	Cr I	0.020	7593.150	
5208.40	5208.425	Cr I	0.160	7593.150	
5217.00	5216.863	Fe II	0.610	84527.779	blend
	5216.854	Fe II	0.390	84710.686	
5226.60	5226.343	Ti II	-1.300	12628.731	
5226.84	5226.862	Fe I	-0.550	24506.914	
5227.30	5227.481	Fe II	0.800	84296.829	blend
	5227.323	Fe II	-0.030	84344.832	
5237.40	5237.329	Cr II	-1.150	32854.311	
5255.00	5254.929	Fe II	-3.230	26055.422	
5266.60	5266.555	Fe I	-0.490	24180.861	
5269.60	5269.537	Fe I	-1.320	6928.268	
5275.01	5274.964	Cr II	-1.29	32836.680	
5291.65	5291.666	Fe II	0.58	84527.779	
5313.55	5313.563	Cr II	-1.650	32854.949	
5324.20	5324.179	Fe I	-0.240	25899.986	
5325.50	5325.503	Fe II	-2.800	25981.670	
5329.70	5329.673	O I	-2.200	86627.777	blend
	5329.681	O I	-1.610	86627.777	
	5329.690	O I	-1.410	86627.777	
5330.80	5330.726	O I	-2.570	86631.453	blend
	5330.735	O I	-1.710	86631.453	
	5330.741	O I	-1.120	86631.453	
5336.80	5336.771	Ti II	-1.700	12758.110	
5337.60	5337.732	Fe II	- 3.890	26055.422	
	5337.772	Cr II	-2.030	32854.949	
5362.92	5362.869	Fe II	-2.740	25805.329	blend
	5362.957	Fe II	-0.080	84685.798	
5367.50	5367.466	Fe I	0.350	35611.622	
5370.00	5369.961	Fe I	0.350	35257.323	blend
	5370.164	Cr II	0.320	86782.011	
5371.50	5371.489	Fe I	-1.650	7728.059	blend
	5371.437	Fe I	-1.240	35767.561	
5380.35	5380.337	C I	-1.840	97770.180	
5383.30	5383.369	Fe I	0.500	34782.420	
5404.15	5404.117	Fe I	0.540	34782.420	blend
	5404.151	Fe I	0.520	35767.561	
5405.80	5405.663	Fe II	-0.440	48708.863	blend
	5405.775	Fe I	-1.840	7985.784	
5410.90	5410.910	Fe I	0.280	36079.371	
5415.20	5415.199	Fe I	0.500	35379.205	
5425.20	5425.257	Fe II	-3.360	25805.329	
5447.00	5446.916	Fe I	-1.930	7985.784	
5455.50	5455.454	Fe I	0.300	34843.934	blend
	5455.609	Fe I	-2.090	8154.713	
5526.80	5526.770	Sc II	0.130	14261.320	

Table 1: Identifications for flat-bottomed lines in Vega

$\lambda_{\rm obs}$ (Å)	$\lambda_{\rm lab}$ (Å)	Species	$\log gf$	E_{low}	Comments
5528.40	5528.405	Mg I	-0.620	35051.263	
5534.80	5534.847	Fe II	-2.940	26170.181	blend
	5534.890	Fe II	-0.690	85048.620	
5572.75	5572.842	Fe II	-0.310	27394.689	
5586.80	5586.842	Cr II	0.910	88001.361	blend
	5586.756	Fe I	-0.210	27166.817	
5588.70	5588.619	Cr II	-5.550	31117.390	
5615.70	5615.644	Fe I	-0.140	26874.547	
5669.0	5668.943	C I	-2.430	68856.328	blend
	5669.038	Sc II	-1.120	12101.499	
6147.70	6147.741	Fe II	-2.720	31364.440	
6149.30	6149.258	Fe II	-2.720	31968.450	
6162.0	6162.173	Ca I	0.100	15315.943	very weak
6238.35	6238.392	Fe II	-2.630	31364.440	
6247.45	6247.557	Fe II	-2.330	31307.949	
6417.00	6416.919	Fe II	-2.740	31387.949	

The authors acknowledge use of the SOPHIE archive (`http://atlas.obs-hp.fr/sophie/`) at Observatoire de Haute Provence. They have used the NIST Atomic Spectra Database and the VALD database operated at Uppsala University (Kupka et al., 2000) to upgrade atomic data.

References

Castelli, F., Kurucz, R.L. 1994, A&A, 281, 817

Code, A., D., Davis, J., Bless, R.C., Hanbury Brown, R. 1976, ApJ, 203, 417

Gulliver, A.F., Hill, G., Adelman, S.J. 1994, ApJ, 429L, 81G

Hill, G., Gulliver, A.F., Adelman, S.J. 2010, ApJ, 712, 250

Hubeny, I., Lanz, T. 1992, A&A, 262, 501

Hubeny, I., Lanz, T. 1995, ApJ, 439, 875

Kupka F., Ryabchikova T.A., Piskunov N.E., Stempels H.C., Weiss W.W., 2000, Baltic Astronomy, vol. 9, 590-594

Kurucz, R.L. 1992, Rev. Mexicana. Astron. Astrofis., 23, 45

Napiwotzki, R., Schoenberner, D., Wenske, V. 1993, A&A, 268, 653

Royer, F., Gebran, M., Monier, R., Adelman, S., Smalley, B., Pintado, O., Reiners, A., Hill, G., Gulliver, G. 2014 , A&A, 562A, 84R

Takeda, Y., Kawanomoto, S., Ohishi, N. 2008, ApJ, 678, 446

SF2A 2017
C. Reylé, P. Di Matteo, F. Herpin, É. Lagadec, A. Lançon, Z. Meliani, F. Royer (eds)

SYNTHETIC PHOTOMETRY OF GLOBULAR CLUSTERS

F. Martins[1], W. Chantereau[3,2] and C. Charbonnel[3]

Abstract. Color-magnitude diagrams (CMDs) of globular clusters reveal the presence of multiple sequences likely due to populations of stars with different chemical composition (variations in He, C, N, O, Na, Mg, Al). We present synthetic photometry of the globular cluster NGC 6752 based on isochrones and atmosphere models both consistently taking into account such variations of chemical composition. Theoretical CMDs based on this photometry are compared to observed CMDs. We show that CMDs based on red filters are reasonably well reproduced, while those based on blue filters suffer from a number of shortcomings.

Keywords: Globular clusters: individual: NGC 6752 – Techniques: photometric

1 Introduction

Globular clusters are among the oldest structures in the Universe. Once thought to be the result of a single star formation event, leading to the birth of stars with a uniform chemical composition and age distribution, they are nowadays considered as complex structures. This is mainly due to the discovery of multiple sequences in their color-magnitude diagrams (CMDs) thanks to the exquisite sensitivity of the Hubble Space Telescope (Bedin et al. 2004; Piotto et al. 2007). These sequences correspond to populations of stars with different chemical composition: variations in light elements are usually detected by high resolution spectroscopy among the different sequences (see review and references in, e.g. Charbonnel 2016). These variations are not random but are anti-correlated: an excess of nitrogen is associated with a lack of carbon. Similar relations exist between sodium and oxygen, and between aluminum and magnesium. These relations are typical of nucleosynthesis through the CNO cycle (Prantzos et al. 2007) encountered in massive main sequence stars or intermediate-mass Asymptotic Giant Branch stars (AGBs). Although alternative scenarios exist, the origin of multiple populations in globular clusters is thus thought to be due to one or either types of stars. The idea is that an early population of stars produced chemically processed material that was recycled in the formation of second population stars observed today in globular clusters. Depending on the nature of the first generation "polluters", a different range of helium content should be observed in multiple populations (Ventura et al. 2013; Chantereau et al. 2015). However, the helium mass fraction can only be constrained indirectly since HeI lines are not present in the spectra of GCs' stars.

This is where theoretical CMDs come to play. Using isochrones assuming different helium content, synthetic photometry can be calculated to produce such diagrams that can subsequently be compared to observed CMDs. The positions of theoretical and observed sequences are used to infer the helium content (e.g. Milone et al. 2013).

In this contribution, we investigate the ability of synthetic photometry to reproduce the observed multiple populations of the globular cluster NGC 6752. We show that a number of shortcomings usually not described in the literature affect the determination of the helium content.

[1] LUPM, CNRS & Université de Montpellier, CC072, Place Eugène Bataillon, F-34095 Montpellier Cedex 05
[2] Astrophysics Research Institute, Liverpool John Moores University, 146 Brownlow Hill, Liverpool L3 5RF, UK
[3] Observatoire de l'Université de Genève, 51 chemin des Maillettes, CH-1290, Sauverny

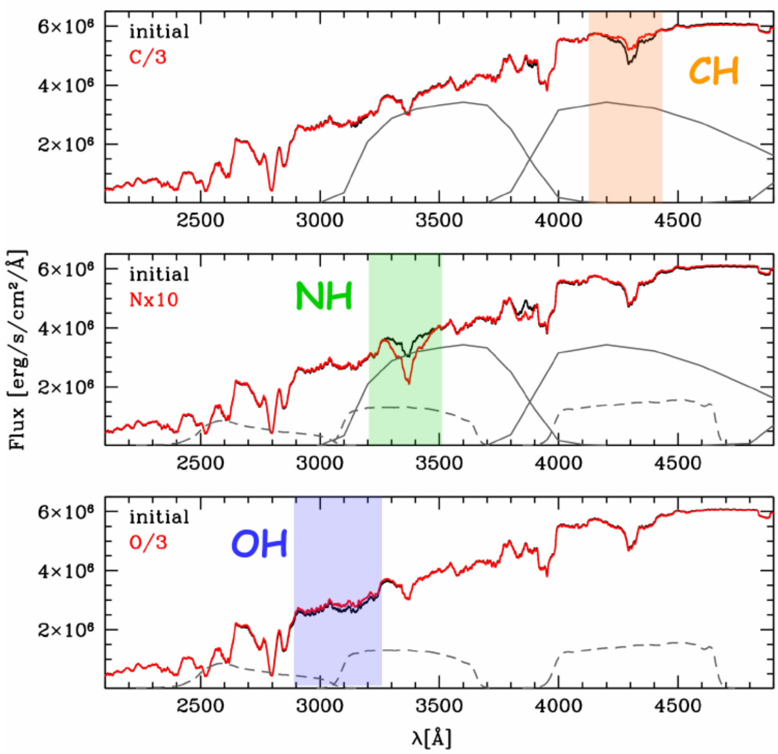

Fig. 1. Spectral energy distribution of a model with $T_{\rm eff}$=5375 K and log g=3.37. In each panel, the black solid line is the initial model. The red line corresponds to a model with a reduction of C/H by a factor 3 (upper panel), an increase of N/H by a factor 10 (middle panel) and a reduction of O/H by a factor 3 (bottom panel). The main molecular lines affected by these changes are highlighted in each panel. The grey solid (dashed) lines are the UB (F275W, F336W, F438W) filter throughputs.

2 Synthetic photometry

To build theoretical CMDs one needs to start with isochrones calculated from stellar evolution tracks. We have used the tracks of Chantereau et al. (2015) recomputed for a metallicity [Fe/H]=-1.53 corresponding to that of NGC 6752. The code STAREVOL (Decressin et al. 2009; Lagarde et al. 2012) was used for these computations. These tracks assume a chemical enrichment of the second population stars according the the scenario of fast rotating massive stars (Decressin et al. 2007). Isochrones have been built for an age of 13.4 Gyr adapted to NGC 6752. Different sets of chemical compositions, characterized by an initial helium content and associated variations in light elements, lead to different isochrones.

For each isochrone, we selected a few points at fixed luminosities (the same for all isochrones). We computed an atmosphere model and the corresponding spectral energy distribution (SED) using the effective temperature, surface gravity and chemical composition of these selected points. For that purpose the codes ATLAS12 (Kurucz 2014) and SYNTHE (Kurucz 2005) were used. Fig. 1 illustrates the dependence of the SED shape on the composition in C, N and O. Depending on the filter used to compute photometry (see below) magnitudes can thus be affected differently. For instance, a change of C/H does not affect the U photometry but modifies the B magnitude since a CH band is present around 4300 Å. A careful selection of filters is thus needed to clearly distinguish the different populations: an increase of N/H associated with a decrease of C/H is best seen in the color built from the HST F336W and F438W filters (see top and middle panels of Fig. 1).

Once SEDs were obtained for all isochrones, we computed synthetic photometry in different filters. We retrieved the transmission curves from the Virtual Observatory* and calculated zero points using the Vega reference spectrum. We reddened the SEDs using the extinction of Seaton (1979) and Howarth (1983) prior to calculation of photometry.

*http://svo2.cab.inta-csic.es/svo/theory/fps3/

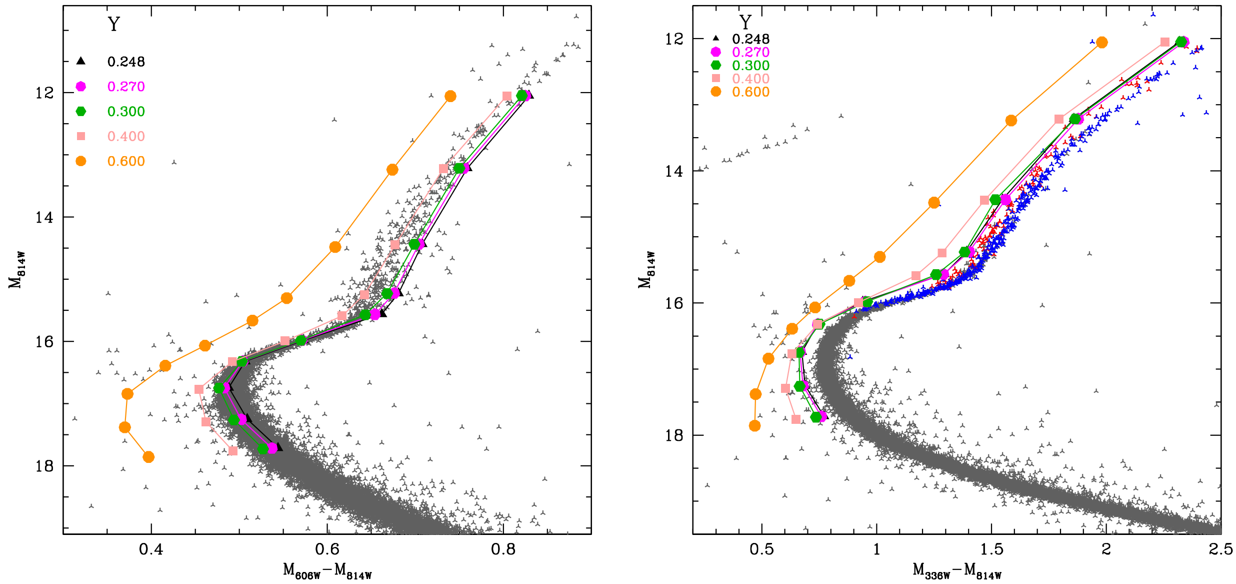

Fig. 2. Left: Magnitude in the F814W filter as a function of color defined by the magnitude difference in the F606W and F814W filters. **Right:** Magnitude in the F814W filter as a function of color defined by the magnitude difference in the F336W and F814W filters. Grey crosses are the observations of Milone et al. (2013). Red and blue crosses in the RGB correspond to two distinct populations. In both panels, different colors in the theoretical isochrones correspond to different chemical compositions, labelled by helium mass fraction.

3 Comparison to observations

In order to see if our synthetic photometry was able to reproduce observed CMDs, we focussed on NGC 6752 and used the HST data of Milone et al. (2013). We adopted a distance modulus of 13.19 (Harris 1996) and a color excess E(B-V)=0.035. Fig. 2 shows two CMDs. In the left panel, filters centered at 606 nm and 814 nm were combined. Synthetic isochrones with larger helium content are always bluer than less He-rich ones. The reason is mainly the change in $T_{\rm eff}$ when He increases. For instance a model with log $\frac{L}{L_{\odot}}$ = 0.85 has $T_{\rm eff}$ = 5375 K for Y = 0.248 and $T_{\rm eff}$ = 5427 K for Y = 0.300. The ~50 K difference affects the SED which has more flux at shorter wavelength. Consequently the associated colors are bluer. In Fig. 2 (left panel) we see that our synthetic isochrones with no or a small helium enrichment reproduce correctly the main sequence, turn-off and sug-giant branch. They may be slightly too red in the Red Giant Branch (RGB). Extreme helium enrichment (Y = 0.600) is excluded.

In the right panel of Fig. 2, the F606W filter is replaced by F336W (centered at 336 nm, see Fig. 1). In that case, all the synthetic isochrones are too blue compared to the observed sequence. The red and blue points on the RGB correspond to two populations: the red one is the less helium enriched according to Milone et al. (2013). The blue one corresponds to their two He-rich populations (grouped in a single population in our study, for clarity). In the CMD built using F336W and F814W, we see that the He-rich population is located on the right side of the He-normal sequence. This trend is weakly present in the synthetic isochrones, and only for Y=0.248 and Y=0.270 (black and magenta curves). For Y larger than 0.270, more He-rich populations are always located on the blue side of less helium enriched ones. The redder location of the Y=0.270 isochrone is due to the nitrogen enrichment associated with the increase of Y. As seen in Fig. 1 this strengthens the NH band encompassed by the F336W filter, which in turn shifts the (F336W-F814W) color towards larger values. This effect compensates for the $T_{\rm eff}$ increase due to a larger helium content. At higher Y, the increase of $T_{\rm eff}$ becomes dominant over the strengthening of the NH absorption.

Hence, the determination of the helium content using blue filters requires a good knowledge of the nitrogen content. The reason for the systematic shift towards bluer colors in synthetic isochrones is not clear and affects absolute helium abundance determinations. Alternatively, red filters not affected by nitrogen are usually preferred (Milone et al. 2013; Milone 2015). However, such filters are not optimal to separate multiple populations in CMDs since SEDs at long wavelength are much less sensitive to $T_{\rm eff}$ changes induced by helium content variations.

4 Conclusions

We have shown that synthetic photometry based on theoretical isochrones and atmosphere models cannot reproduce quantitatively all the features of CMDs. The choice of filters is crucial: filters located at short visible wavelength are sensitive to changes in $T_{\rm eff}$, Y and CNO content. They are best suited to identify multiple populations but synthetic photometry based on them suffers from the largest discrepancies when compared to observations. Filters located in the red part of the spectrum better reproduce CMDs because of their reduced sensitivity to chemical composition. As a consequence these red filters are less suited to separate multiple populations and thus to determine their helium content.

We thank A. Milone for sharing HST photometry of NGC 6752. CC acknowledges support from the Swiss National Science Foundation (SNF) for the Projects 200020-159543 "Multiple stellar populations in massive star clusters Formation, evolution, dynamics, impact on galactic evolution" and 200020-169125 "Globular cluster archeology". We thank the International Space Science Institute (ISSI, Bern, CH) for welcoming the activities of the Team 271 "Massive Star Clusters Across the Hubble Time" (2013 - 2016).

References

Bedin, L. R., Piotto, G., Anderson, J., et al. 2004, ApJ, 605, L125

Chantereau, W., Charbonnel, C., & Decressin, T. 2015, A&A, 578, A117

Charbonnel, C. 2016, in EAS Publications Series, Vol. 80, EAS Publications Series, ed. E. Moraux, Y. Lebreton, & C. Charbonnel, 177–226

Decressin, T., Charbonnel, C., Siess, L., et al. 2009, A&A, 505, 727

Decressin, T., Meynet, G., Charbonnel, C., Prantzos, N., & Ekström, S. 2007, A&A, 464, 1029

Harris, W. E. 1996, AJ, 112, 1487

Howarth, I. D. 1983, MNRAS, 203, 301

Kurucz, R. L. 2005, Memorie della Societa Astronomica Italiana Supplementi, 8, 76

Kurucz, R. L. 2014, Model Atmosphere Codes: ATLAS12 and ATLAS9, ed. E. Niemczura, B. Smalley, & W. Pych, 39–51

Lagarde, N., Decressin, T., Charbonnel, C., et al. 2012, A&A, 543, A108

Milone, A. P. 2015, MNRAS, 446, 1672

Milone, A. P., Marino, A. F., Piotto, G., et al. 2013, ApJ, 767, 120

Piotto, G., Bedin, L. R., Anderson, J., et al. 2007, ApJ, 661, L53

Prantzos, N., Charbonnel, C., & Iliadis, C. 2007, A&A, 470, 179

Seaton, M. J. 1979, MNRAS, 187, 73P

Ventura, P., Di Criscienzo, M., Carini, R., & D'Antona, F. 2013, MNRAS, 431, 3642

SF2A 2017
C. Reylé, P. Di Matteo, F. Herpin, É. Lagadec, A. Lançon, Z. Meliani, F. Royer (eds)

HYPERFINE STRUCTURE AND ABUNDANCES OF HEAVY ELEMENTS IN 68 TAURI (HD 27962)

S. Martinet[1] and R. Monier[2]

Abstract. HD 27962, also known as 68 Tauri, is a Chemically Peculiar Am star member of the Hyades Open Cluster in the local arm of the Galaxy. We have modeled the high resolution SOPHIE (R=75000) spectrum of 68 Tauri using updated model atmosphere and spectrum synthesis to derive chemical abundances in its atmosphere. In particular, we have studied the effect of the inclusion of Hyperfine Structure of various Baryum isotopes on the determination of the Baryum abundance in 68 Tauri. We have also derived new abundances using updated accurate atomic parameters retrieved from the NIST database.

Keywords: stars: abundances - stars: individual: 68 Tau - stars: chemically peculiar

1 Introduction

68 Tauri (HD 27962) is the hottest and most massive member of the Hyades open cluster (age about 700 Myrs). Previous abundance analyses of HD 27962 have revealed a distinct underabundance of scandium and overabundances of the iron-peak and heavy elements which prompted to reclassify this early A star as an Am star. The last abundance analysis dates back to 2003 (Pintado & Adelman 2003). It seems therefore justified to redetermine and expand the chemical composition of this interesting object using updated atomic data. In particular we have included the hyperfine structure (Hfs) for several lines. We present here the results for one line of Ba II and discuss the revision of the baryum abundance and other abundances in 68 Tauri.

2 Abundance Determinations

2.1 Model Atmosphere and Spectrum Synthesis

We used the observed Strömgren photometry of 68 Tauri retrieved from SIMBAD and the UVBYBETA code of T.T.Moon (1985) to determine an effective temperature of 9025 ± 200 K and a surface gravity log(g)=3.95 ± 0.25 dex for 68 Tauri. We used these parameters to compute a 72 layers plane parallel model atmosphere with the ATLAS9 code (Kurucz, 1992) assuming Local Thermodynamical Equilibrium, Hydrostatic Equilibrium and Radiative Equilibrium.

We used Hubeny's code SYNSPEC49 (1992) to compute a grid of synthetic spectra to model the observed spectrum of 68 Tauri. We first computed a synthetic spectrum adopting solar abundances as a first iteration and then altered the abundances in order to reproduce the line profiles of selected lines with accurate atomic parameters.

2.2 Baryum Hyperfine Structure

We have replaced the single line λ 5853.675Å of Ba II extracted from the NIST Atomic Spectra Database with the Hfs of the 5 major isotopes of Baryum as calculated by McWilliam(1998). We used a solar isotopic mixture to compute the grid of synthetic spectra. We find a large difference in Baryum abundance when including the full hyperfine structure. For the 5853.675Å line shown Figure 1, the inclusion of Hfs yields a Baryum abundance lower by 0.4 dex than when ignoring Hfs.

[1] Sebastien.Martinet@univ-grenoble-alpes.fr
[2] LESIA, UMR 8109, Observatoire de Paris Meudon, Place J.Janssen, Meudon, France. Richard.Monier@obspm.fr

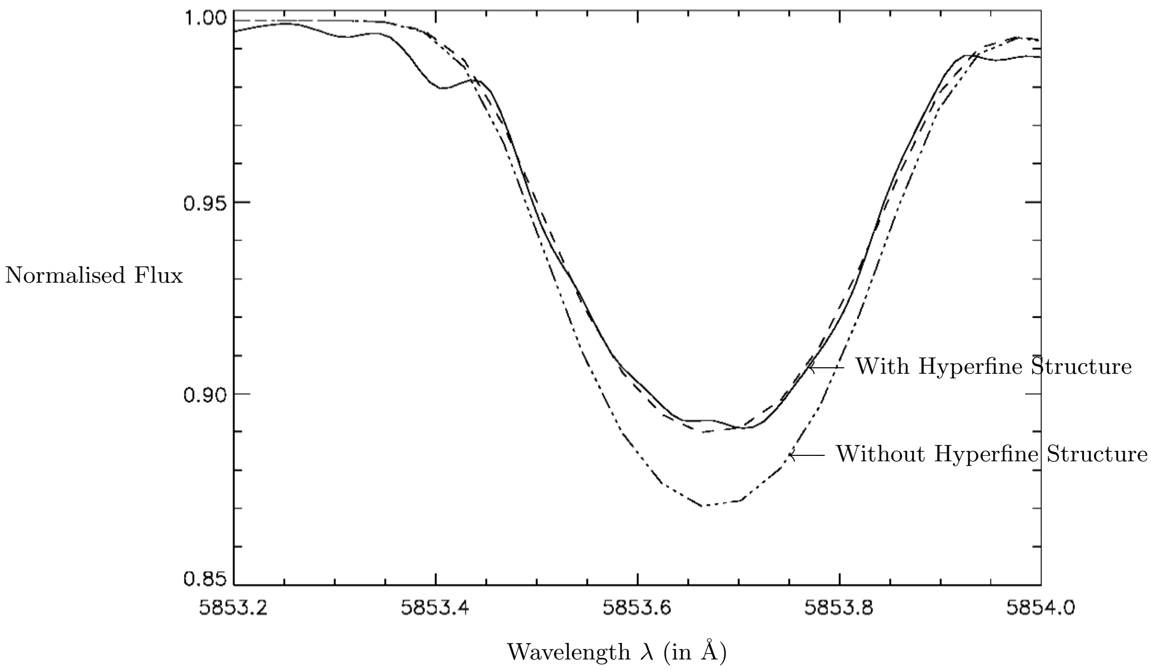

Fig. 1: The effect of including hyperfine structure on the line profile of the 5853.675 Å line of Ba II. *(observed: solid line, synthetic spectra: dashed lines).*

2.3 Abundances in the Atmosphere of 68 Tauri

For iron, we have determined abundances for each lines of Fe II and then computed a weighted mean according to the quality grades assigned to each transition in NIST.

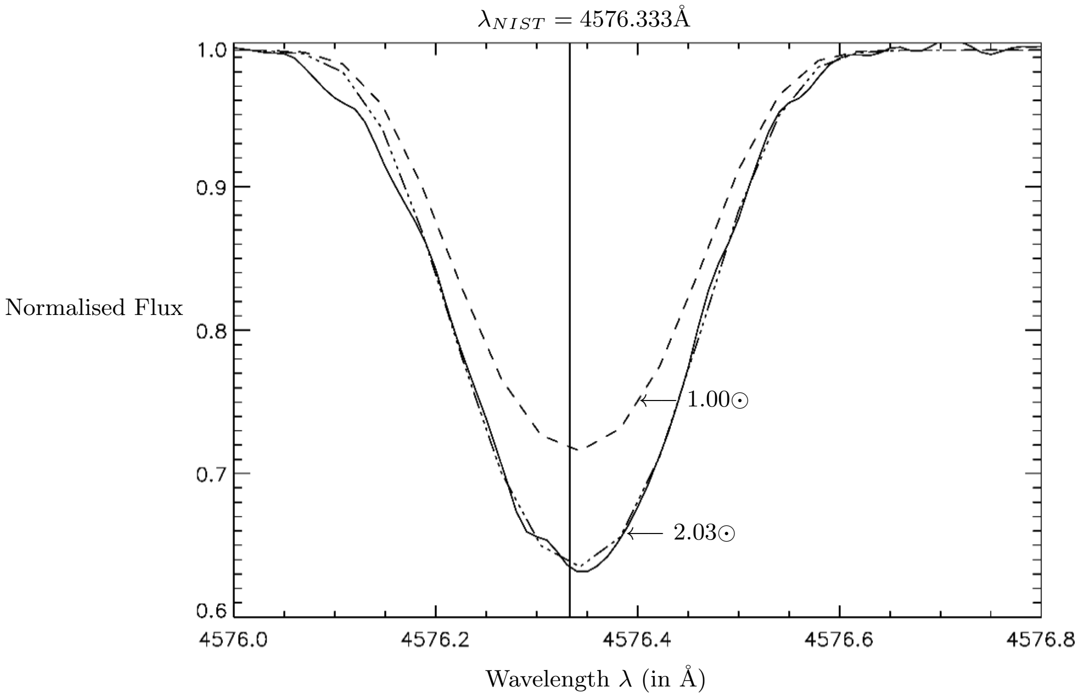

Fig. 2: Determination of Iron abundance for the 4576.33Å Fe II line *(observed: solid line, synthetic spectra: dashed lines)*

We then applied this method to determine the abundances of 21 elements. Our determinations are displayed in Figure 3 with error bars, and we compare our results to the abundances previously found by Pintado & Adelman (2003) who used the same effective temperature and surface gravity. Indeed, the parameters chosen by Pintado & Adelman differ as $\Delta T_{eff} = \pm 250$K and $\Delta \log(g) = \pm 0.25$ from our parameters. Furthermore, we used in our model atmosphere a microturbulence velocity up to $\xi_T = 2.64 \ \pm 0.66 \ km/s$ while Pintado & Adelman used $\xi_T = 2.3 \ km/s$.

Our abundance analysis yields a pronounced underabundance of Sc and slight underabundances in C, O, Mg, Si and Ca, mild overabundances of the iron-peak elements and large overabundances of the rare-earth elements. We find abundances which are consistent with the determinations of Pintado & Adelman (2003) except for Scandium. Our results differ from 0.01 dex up to 0.4 dex as we adopted new atomic data. All these new abundance determinations confirm the Am status for 68 Tauri.

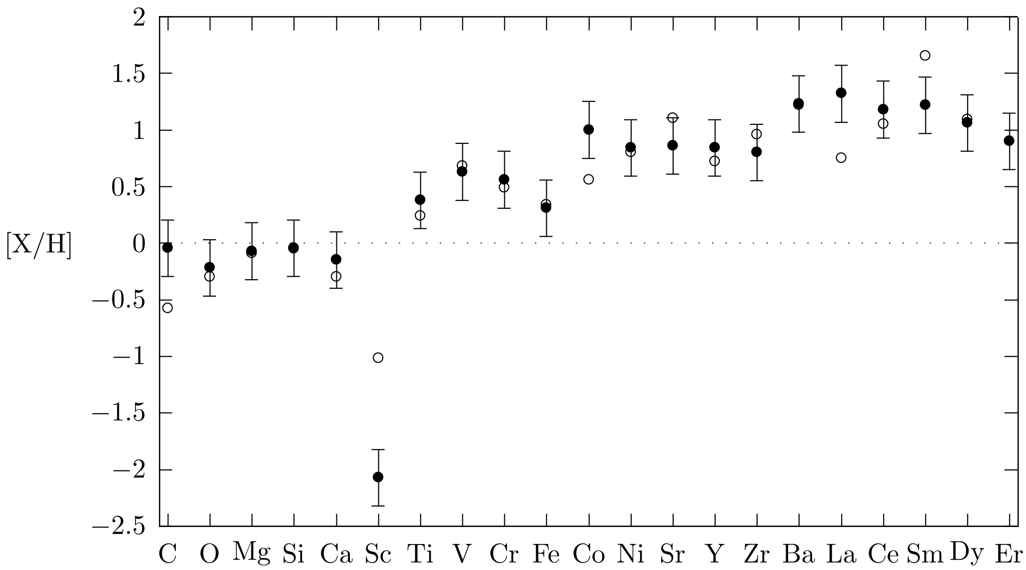

Fig. 3: The abundance pattern determined for 68 Tauri: *circles (Pintado & Adelman 2003), dots (this work).* As usual, the script [X/H] means $log(X/H)_* - log(X/H)_\odot$; the solar abundances are adapted from Grevesse and Sauval (1998).

3 Conclusions

Our abundance analysis yields a pronounced underabundance of Sc and slight underabundances in C, O, Mg, Si and Ca, mild overabundances of the iron-peak elements and large overabundances of the rare-earth elements. All these new abundance determinations confirm the Am status for 68 Tauri. Thanks to the improvement of atomic data, we have enlarged and improved the elemental abundances of 68 Tauri. The new results on the rare-earth group confirm the Am peculiarity of 68 Tauri. The inclusion of the hyperfine structure of the various isotopes of Ba II leads us to decrease the baryum abundance in 68 Tauri. We stress the importance of taking into account the Hyperfine Structure for all isotopes when available in order to derive accurate abundances.

References

Grevesse, N. & Sauval, A. J. 1998, Space Sci. Rev., 85, 161

Kurucz, R. L. 1992, in IAU Symposium, Vol. 149, The Stellar Populations of Galaxies, ed. B. Barbuy & A. Renzini, 225

McWilliam, A. 1998, AJ, 115, 1640

Moon, T. T. & Dworetsky, M. M. 1985, MNRAS, 217, 305

Pintado, O. I. & Adelman, S. J. 2003, A&A, 406, 987

SF2A 2017
C. Reylé, P. Di Matteo, F. Herpin, É. Lagadec, A. Lançon, Z. Meliani, F. Royer (eds)

IONIZATION RATIOS AND ELEMENTAL ABUNDANCES IN THE ATMOSPHERE OF 68 TAURI

A.Aouina[1] and R.Monier[2]

Abstract.
We have derived the ionization ratios of twelve elements in the atmosphere of the star 68 Tauri (HD 27962) using an ATLAS9 model atmosphere with 72 layers computed for the effective temperature and surface gravity of the star. We then computed a grid of synthetic spectra generated by SYNSPEC49 based on an ATLAS9 model atmosphere in order to model one high resolution spectrum secured by one of us (RM) with the échelle spectrograph SOPHIE at Observatoire de Haute Provence. We could determine the abundances of several elements in their dominant ionization stage, including those defining the Am phenomenon. We thus provide new abundance determinations for 68 Tauri using updated accurate atomic data retrieved from the NIST database which extend previous abundance works.

Keywords: stars: individual, stars: Chemically Peculiar, HD 27962

1 Introduction

68 Tauri (HD 27962) is the hottest and most massive member of the Hyades open cluster (age about 700 Myr). Previous abundance analyses of HD 27962 have revealed a distinct underabundance of scandium and overabundances of the iron-peak and heavy elements which prompted to reclassify this early A star as an Am star. The last abundance analysis dates back to 2003 (Pintado & Adelman, 2003). It seems therefore justified to redetermine and expand the chemical composition of this interesting object using updated atomic data.

2 Observations and reduction

HD 27962 was observed with the SOPHIE spectrograph at the Observatoire de Haute Provence on 04 October 2006 using the High Resolution (R=75000) mode . The exposure time was 600 seconds yielding a signal-to-noise ratio of about 429 at 5000 Å. There are currently about 60 high resolution spectra of 68 Tauri in the SOPHIE archive.

3 Fundamental parameters determination

In order to derive the effective temperature and surface gravity for 68 Tauri, we used Napiwotzki et al. (1993) UVBYBETA code and the observed uvby photometry from Hauck &Mermilliod (1998) for 68 Tauri. We derived $T_{\rm eff} = 9025\,\mathrm{K} \pm 200\,\mathrm{K}$ and $log\,g = 3.25 \pm 0.25$ dex.

4 Model atmospheres and spectrum synthesis

Using the stellar parameters derived in the previous section, we have computed a 72 layers plane parallel model atmosphere using the ATLAS9 code (Kurucz, 1992). We justify the use of this model by discussing the assumptions made by ATLAS9 :

[1] LESIA, UMR 8109, Observatoire de Paris Meudon, Place J.Janssen, Meudon, France
[2] LESIA, UMR 8109, Observatoire de Paris Meudon, Place J.Janssen, Meudon, France

- The thickness of atmosphere is 10^{-3} of the stellar radius, so is negligible compared to this radius, which justifies the use of plane-parallel geometry.

- 68 Tauri is an Am star so it doesn't have a large magnetic field which could influence the atmospheric structure.

- The hypothesis of local thermal equilibrium (LTE) and radiative equilibrium are justified because 68 Tauri is still near the main sequence in the HR diagram.

A plane parallel model atmosphere assuming radiative equilibrium, hydrostatic equilibrium and local thermodynamical equilibrium has been first computed using the ATLAS9 code (Kurucz 1992), specifically the linux version using the new ODFs maintained by F. Castelli on her website*. The linelist was built starting from Kurucz's (1992) `gfhyperall.dat` file† which includes hyperfine splitting levels. This first linelist was then upgraded using the NIST Atomic Spectra Database‡ and the VALD database operated at Uppsala University (Kupka et al. 2000)§. A grid of synthetic spectra was then computed with SYNSPEC49 (Hubeny & Lanz 1992) to model the lines. The synthetic spectrum was then convolved with a gaussian instrumental profile and a parabolic rotation profile using the routine ROTIN3 provided along with SYNSPEC49. We adopted a projected apparent rotational velocity $v_e \sin i = 10.5$ km.s^{-1} from Royer et al. (2007) and a radial velocity $v_{rad} = 39.43$ km.s^{-1} determined by cross-correlation of the observed spectrum with the synthetic spectrum.

5 The ionisation profiles

In order to determine the abundance of a chemical element, it is preferable to model the absorption lines of the ion corresponding to the major ionisation state in the atmosphere. To determine the dominant ionisation state for a given element, we have used Saha's equation which yields the fraction between the number of ions in two successive ionisation states versus optical depth, assuming LTE in the atmosphere of the star :

$$\frac{n_j(\tau)}{n_{j-1}(\tau)} = \frac{\phi_j(T)}{P_e}$$

where:

$$\phi_j(T) = 0.665 \frac{u_j}{u_j - 1} T(\tau)^{\frac{5}{2}} 10^{\frac{-5040I}{kT(\tau)}}$$

Using the temperature profile $T(\tau)$ from the model atmosphere, the partition function u of each ion and the ionisation potential I, we could derive the ionisation profiles of various elements.

Fig. 1 represents the run of the ionisation ratio of once ionised iron FeII over the total number of neutral and ionised iron versus optical depth in the atmosphere of 68 Tauri. We can see that FeII is the dominant ionization stage, which justifies the use of the Fe II lines rather than FeI to derive LTE abundances of iron in the atmosphere of 68 Tauri.

6 Abundances determination method

To derive the abundances of the various chemical elements in the atmosphere of 68 Tauri, we have iteratively adjusted synthetic spectra to selected observed line profiles. In SYNSPEC49 the theoretical flux in LTE is computed as:

$$F_\nu(0) = 2\pi \int_0^\infty I_\nu(0, \mu) \mu d\mu$$

where I_ν is the intensity of the radiation field from and μ the cosine of the angle between the direction of propagation and the area traversed.

---

*http://www.oact.inaf.it/castelli/

†http://kurucz.harvard.edu/linelists/

‡http://physics.nist.gov/cgi-bin/AtData/linesform

§http://vald.astro.uu.se/~vald/php/vald.php

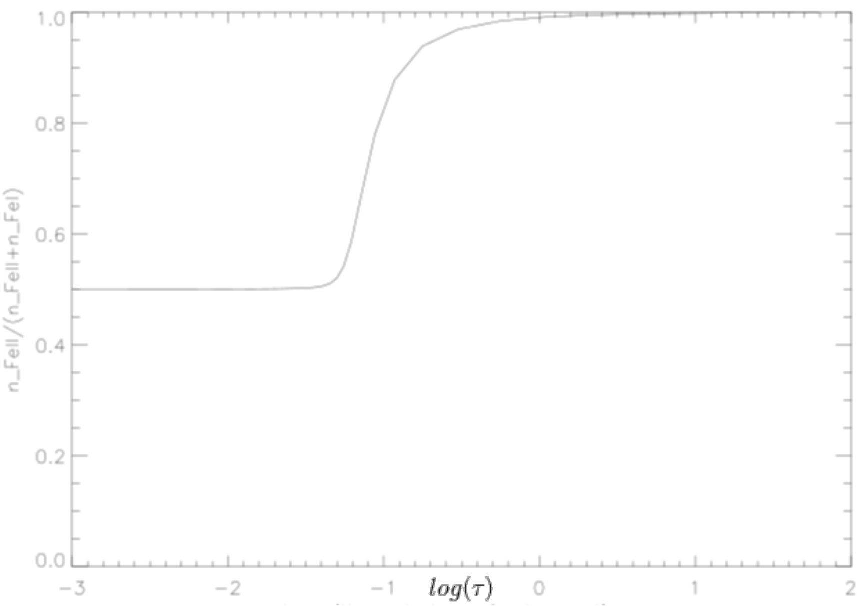

Fig. 1. Ionisation ratio of Fe II versus optical depth τ

This flux is a complex function of several parameters:

$$F = F_\nu(T(\tau_\nu), \xi, log\ gf, \gamma_i, \frac{X}{X_\odot})$$

where $T(\tau_\nu)$ is the temperature at each optical depth, ξ the microturbulent velocity assumed to be constant with depth, gf the product of the statistical weight and the oscillator strength, γ_i the damping constants and $\frac{X}{X_\odot}$ the relative abundance compared to the solar value.

We have fixed as many physical parameters as possible and left the unknown abundance as the only free parameter. Then for each line of each element we changed the abundance until the synthetic spectrum fits best the observed spectrum normalized to its local continuum. A priori, we analysed unblended lines whose atomic parameters are as accurate as possible.

7 Results and discussion

The abundance analysis of 68 Tauri yields a distinct under-abundance of Sc and over-abundances of V, Cr, Ni, Dy and Ba. These anomalies are characteristic features of hot Am stars. Pintado and Adelman (2003) obtained the abundances of 32 elements in 68 Tau. They used the same atmospheric parameters as in this work. Their results agree with ours within ± 0.25 dex for Mg, Ni, Sc, Ca, Fr, Ti, and Ba. However, the abundances of vanadium disagree because of the difference in the $log\ gf$ value of V II adopted in this work and in Pintado & Adelman (2003). Indeed we have used more recent improved $log\ gf$ value from the NIST database.

8 Conclusions

Our abundance analysis using recent atomic data confirms the Am status of HD 27962 and provides improved abundances for Fe, Ti, Cr, Mg, Ca, Sc, V, Ni, Ba, Dy, Sm and Ce. A continuation of this work will consist in using all spectra available in the SOPHIE archive to derive more elemental abundances and search for radial velocity and line variations.

The authors acknowledge use of the SOPHIE archive (`http://atlas.obs-hp.fr/sophie/`) at Observatoire de Haute Provence. They have used the NIST Atomic Spectra Database and the VALD database operated at Uppsala University (Kupka et al., 2000) to upgrade atomic data.

	O&S (1990)	P&A (2003)	This work
Fe	0.81$\odot$	1.51$\odot$	2.18$\odot$
Ti	1.31$\odot$	1.77$\odot$	2.68$\odot$
Cr	4.67$\odot$	3.98$\odot$	3.41$\odot$
Mg	1.41$\odot$	1.62$\odot$	1.50$\odot$
Ca	0.34$\odot$	0.88$\odot$	0.70$\odot$
V	5.37$\odot$	0.69$\odot$	4.42$\odot$
Ba	9.33$\odot$	21.87$\odot$	23.00$\odot$
Ni	0.75$\odot$	8.91$\odot$	8.50$\odot$
Sc	0.08$\odot$	0.12$\odot$	0.06$\odot$
Dy	$\times$	2.01$\odot$	1.60$\odot$
Sm	$\times$	2.10$\odot$	2.40$\odot$
Ce	$\times$	1.90$\odot$	1.71$\odot$

Table 1. Comparison of the derived abundances with previous works

References

Hubeny, I., Lanz, T. 1992, A&A, 262, 501

Kupka F., Ryabchikova T.A., Piskunov N.E., Stempels H.C., Weiss W.W., 2000, Baltic Astronomy, vol. 9, 590-594

Kurucz, R.L. 1992, Rev. Mexicana. Astron. Astrofis., 23, 45

Monier, R., Gebran, M., Royer, F. 2015, A&A, 577A, 96M

Monier, R., Gebran, M., & Royer, F. 2016, Ap&SS, 361, 139

Napiwotzki, R., Schoenberner, D., Wenske, V. 1993, A&A, 268, 653

Okyudo, M., Sadakane, K., 1990, PASJ, 42, 317O

Pintado, O. I.; Adelman, S. J., 2003, A&A, 406, 987

Royer, F., Zorec, J., Gomez, A.E. 2007 , A&A, 463, 671R

SF2A 2017
C. Reylé, P. Di Matteo, F. Herpin, É. Lagadec, A. Lançon, Z. Meliani, F. Royer (eds)

HOT JUPITERS AROUND YOUNG STARS

L. F. Yu[1] and J.-F. Donati[1]

Abstract. This conference paper presents the results of the MaTYSSE (Magnetic Topologies of Young Stars and the Survival of massive close-in Exoplanets) observation programme, regarding the search for giant exoplanets around weak-line T Tauri stars (wTTS), as of early 2017. The discoveries of two hot Jupiters (hJs), around V830 Tau and TAP 26, sun-like stars of respectively ∼2 Myr and ∼17 Myr, are summarized here. Both exoplanets seem to have undergone type-II migration (planet-disc interaction leading the orbit to narrow around the host) based on their low orbital eccentricity. The methods which were used are given more focus in the paper *Stellar activity filtering methods for the detection of exoplanets* in the present book.

Keywords: methods: statistical, stars: activity, stars: evolution, stars: imaging, stars: individual (V830 Tau, TAP 26), stars: magnetic fields, (stars:) planetary systems: formation, stars: pre–main-sequence, stars: rotation, stars: spots

1 Introduction

To improve the community's understanding of the formation and early evolution of solar-like planetary systems, we investigate the migration processes of hot Jupiters at the beginning of their life. Hot Jupiters are massive close-in exoplanets which have, according to the theory, formed beyond the ice line and then migrated inwards due to one of these interactions: planet-disc interaction which induces a fast (a few 0.1 Myr) and smooth (quasi circular orbit) migration, or planet-planet scattering where several already formed planets interact and one of them ends up on a highly eccentric orbit, progressively circularized by tidal effects (several ∼10 Myr). Due to their strong gravitational influence on the rest of the bodies in their system, constraining the migration process of hJs can help to elucidate the early orbital choreography of solar-like planetary systems.

The sample of the MaTYSSE (Magnetic Topologies of Young Stars and the Survival of massive close-in Exoplanets) programme, some 30+ solar-like stars of a few Myrs (33 weak-line Tauri stars – wTTS, whose disk has mostly dissipated, and 6 classical T Tauri stars – cTTS, which still have an accretion disk), therefore offers ideal targets to hunt for hJs and, in case of success, distinguish between these two processes. MaTYSSE aims at studying the role of the magnetic field in the early stages of a star's life (loss of the disc, formation of exoplanets) thanks to spectra in the optical bandwidth taken with the ESPaDOnS (Echelle SpectroPolarimetric Device for the Observation of Stars) and NARVAL instruments, mounted on the Canada France Hawaii Telescope (CFHT) and on the TBL (Télescope Bernard Lyot) respectively. The planet detection technique used here is the velocimetry method.

However, wTTSs are fast rotators (with periods of the order of the day) and thus have a high level of magnetic activity, which manifests itself in particular in a high brightness contrast on the photosphere. This contrast, added to the stellar rotation, induces distorsions in the line profiles of the stellar spectrum, which in turn add a jitter (called "activity jitter") in the stellar line-of-sight-projected velocity (radial velocity, RV), making it more difficult to detect a planet signature in the RV signal.

2 Methods

2.1 Spectra and radial velocity (RV)

The unpolarized (Stokes I) spectral lines of wTTSs, which are used to compute the stellar RV, are shaped by the Doppler effect, which causes a strong correlation between the location of spots on the surface of the

[1] IRAP, Université de Toulouse, CNRS, UPS, CNES, Toulouse, France

star (and therefore their local RV) and distorsions in the rotation-broadened line profiles. Assuming that the distorsions are the same in most spectral lines (each line being weighed by its equivalent width), Least-Squares Deconvolution (LSD) profiles have been generated for each spectrum in order to concentrate the information into one profile, the x-axis of which represents the local RV (see Fig. 1 for an illustration).

The RVs, in which one looks for a periodic signal in order to detect a planet, are computed as the centroid of the continuum-subtracted LSD profiles. Because of the brightness contrast and the stellar rotation, the RV signal one derives from a planetless wTTS is not constant and the resulting modulation, called activity jitter (typically of the order of 1 km s^{-1} of amplitude), follows the stellar rotation period (see Fig. 2).

The star's global motion, and in particular the hypothetical reflex motion it would have in the presence of a planet (typically of the order of 0.1 km s^{-1} of amplitude), does not change the shape of the line profiles, but shifts the whole spectrum according to the star's RV. As a consequence, the computed RV of the star is the sum of the activity jitter and of the actual stellar RV.

The aim of this study is to model the activity of each star in order to subtract its activity jitter from its RV curves and look for potential planet signatures in the filtered RVs.

2.2 Imaging and filtering process, example of wTTS TAP 26

This section explains the imaging and RV filtering process, using the case of wTTS TAP 26 as an illustration. The reader is invited to consult Yu et al. (2017) for a full in-depth explanation.

TAP 26 is a 17 Myr wTTS located in the Taurus region, with a 1.04±0.10 $M_\odot$ mass and a rotation period of 0.7135 d (see Table 1). Theoretical evolution models (Siess et al. 2000) suggest that its radiative core has reached a radius of at least half the stellar radius and that its magnetic field has started to evolve into a complex topology (Gregory et al. 2012).

29 observations, comprising both unpolarized (Stokes I) and circularly polarized (Stokes V) spectra, were taken with the ESPaDOnS spectropolarimeter, 16 in November 2015 and 13 in January 2016 (see Fig. 1 middle).

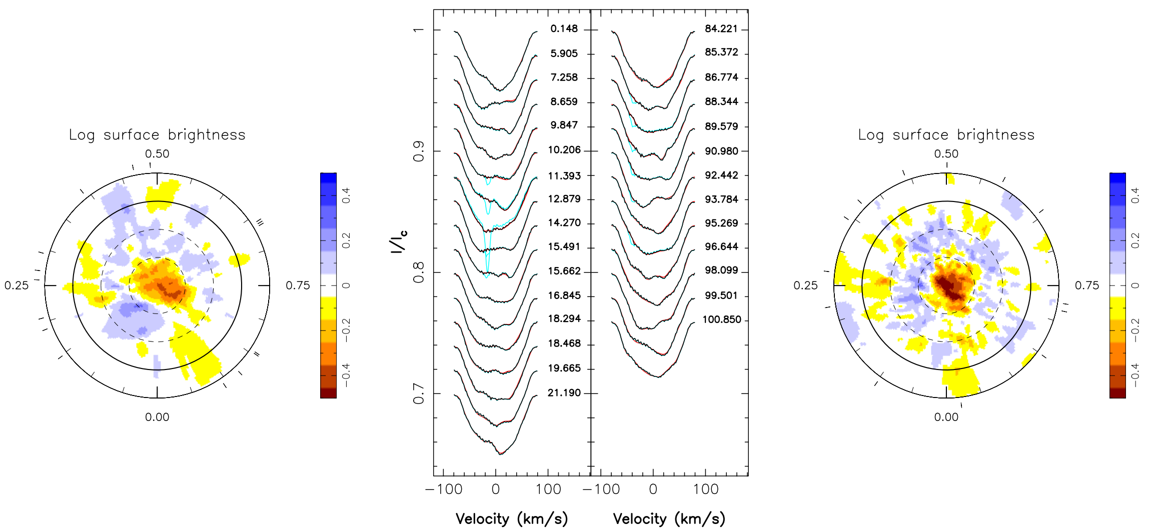

Fig. 1. Middle: maximum entropy fit (thin red lines) to the observed (thick black lines) Stokes I LSD profiles, with the 2015 Nov dataset on the left and the 2016 Jan dataset on the right (the Stokes I LSD profiles before the removal of lunar pollution are coloured in cyan). The rotational cycles are written beside their corresponding profiles, in concordance with Table 1 in Yu et al. (2017). **Left** and **right**: Flattened polar view of the surface brightness maps for the 2015 Nov dataset (left) and 2016 Jan dataset (right), with the equator, the 60°, 30° and -30° latitude parallels as solid and dashed black lines respectively. The colour scale indicates the logarithm of the relative brightness, with brown/blue areas representing cool spots/bright plages, and the outer ticks mark the phases of observation.

Zeeman-Doppler Imaging (ZDI, Donati & Brown 1997) was used to reconstruct the brightness and magnetic maps that generate the spectra which fit our LSD profiles down to noise level with the smallest amount of information. The maps are constituted of a mesh over the visible surface of the star (which depends on its inclination) where each cell has a local brightness value and the three components of the local magnetic field, which influence the local line profile through the Doppler and Zeeman effects. The synthesized line profile is then integrated over the visible surface, taking into account the local radial velocity, causing Doppler broadening (dictated by the equatorial velocity and the inclination) and limb darkening. A sine-square latitudinal differential rotation can be considered in the fitting process.

The reconstructed brightness maps are displayed on Fig. 1 (left and right). Although the main brightness features remain similar between both observation epochs, the evolution of the surface brightness distribution in the span of a few months is noticeable. The activity jitter, derived from the synthetic profiles generated from the reconstructed brightness maps, is shown on Fig. 2 and exhibits a periodicity corresponding to stellar rotation, as well as some temporal evolution, due not only to differential rotation (visible within each observing epoch), but also to intrinsic variability (visible as a difference between both observing epochs).

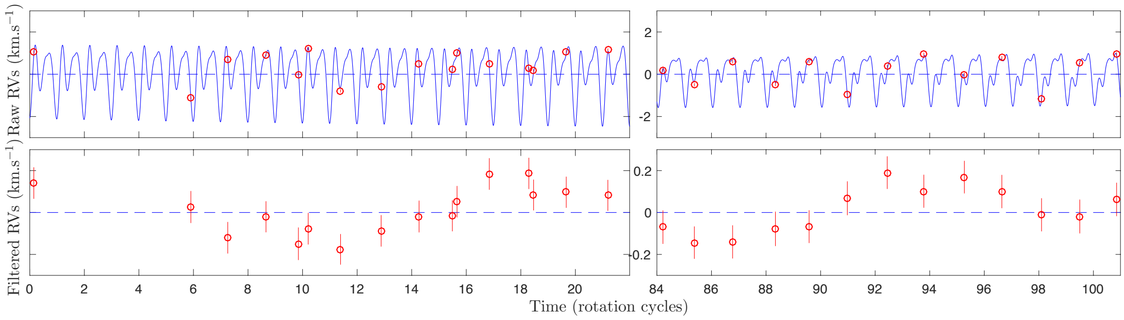

Fig. 2. Top: RV (in the stellar rest frame) of TAP 26 as a function of rotation phase, as measured from our observations (open circles) and predicted by the tomographic maps (blue line). **Bottom**: filtered RVs derived by subtracting the modelled activity jitter from the raw RVs, with a 10x zoom-in on the vertical axis.

After subtracting the activity jitter from the raw RVs (derived from the observed LSD profiles), several periods stand out in the filtered RV due to the observing window (see Fig. 3). However, the period with highest likelihood, at 13.41 d, has a false-alarm probability of 6×10^{-4}, confirming the presence of a periodic signal in the star's RVs, and therefore the presence of a planet. After subtracting the corresponding sine wave fit from the filtered RVs, the residual RVs have a rms of 51 $\mathrm{m\,s^{-1}}$, which is close to noise level. Trying to fit a keplerian curve in the filtered RVs yields an eccentricity of 0.16 ± 0.15, which favors the hypothesis of type II migration over planet-planet scattering. See Table 1 for the planet properties.

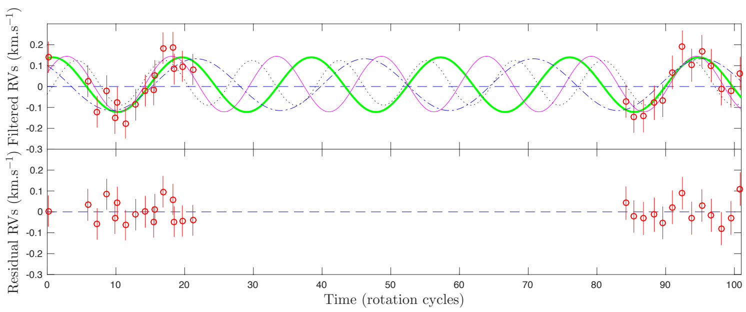

Fig. 3. Top: Filtered RVs of TAP 26 and four sine curves representing the best fits. The thick green curve represents the case $P_{\mathrm{orb}} = 18.80\ P_{\mathrm{rot}} = 13.41$ d. **Bottom**: Residual RVs resulting from the subtraction of the best fit (green curve) from the filtered RVs.

Other methods were used to analyze the spectra and RV curves of TAP 26, which confirmed the periodicities detected in the filtered RVs with the method detailed above. Simulations were also conducted in order to verify that such periods were not generated by the filtering process (Yu et al. 2017).

3 MaTYSSE results

Two hJs around TTSs have been found within the MaTYSSE programme, their properties are found in Table 1.

The formation of hJs can therefore be as fast as a few million years. In both cases, the eccentricity was found to be negligible, favoring the hypothesis of type II migration over planet-planet scattering, with the fact

	V830 Tau (Donati et al. 2016)	**TAP 26** (Yu et al. 2017)
Age [Myr]	$\simeq$2.2	$\simeq$17
$M_\star$ [$M_\odot$]	1.00±0.05	1.04±0.10
$P_{\rm rot}$ [d]	2.741	0.7135
$R_\star$ [$R_\odot$]	2.0±0.2	1.17±0.17
$v \sin i$ [km.s^{-1}]	30.5±0.5	68.2±0.5
i [°]	55±10	55±10
$P_{\rm orb}$ [d]	4.927±0.008	10.79±0.14
$M \sin i$ [$M_{\rm Jup}$]	0.57±0.10	1.66±0.31
a [au]	0.057±0.001	0.0968±0.0032
a [$R_\star$]	6.1±0.6	17.8±1.3

Table 1. Summary of the properties on both hot Jupiters found within the MaTYSSE programme. From top to bottom: age, stellar mass in terms of solar masses, stellar rotation period expressed, stellar radius in terms of solar radii, line-of-sight-projected equatorial rotation velocity, inclination of stellar rotation axis to the line of sight, orbital period, minimal mass in terms of jovian masses, semimajor axis and semimajor axis in terms of stellar radii.

that the planet did not dive into the star being explained by the presence of a magnetospheric gap at the center of the disc, caused by the magnetic field of the star (strong at a young age), and which stopped the migration from going further in.

It is not certain whether the position of the planets still mark the inner boundary of the discs at the time of dissipation, or if they have migrated due to tidal interactions in the meantime. If we assume them not to have migrated, the age of disc dissipation can be traced back by considering that the inner boundary was located at the corotation radius (due to magnetic coupling between the star and the disc), and thus finding the rotation rate of the star at the time of dissipation, leading to its age at that time by following evolutionary tracks.

If the planets have migrated however, it is important to study the star-planet system evolution by examining the interactions at play (magnetic, tidal), coupled with the temporal evolution of the stellar rotation rate, structure and magnetic field.

Finally, although the sample is still too small to be considered representative of actual statistics, finding 2 hJs in a sample of ~30 stars bears the question of the frequency of hJs around young solar-like stars compared to that of hJs around mature ones (1%), and, rejoining the object of the previous paragraph, the dynamics that could lead to a potential decrease in hJ rate as star-planet systems evolve towards the main sequence.

Further observations will be conducted within both the MaTYSSE programme and the SPIRou (SpectroPolarimètre Infra-Rouge) Large Survey, enabling the community to ensure follow-up studies on the two detected hJs as well as refine our statistics on hJs around young solar-like stars. Our numerical methods are undergoing improvements in order to improve the modelling of the activity jitter, in particular by adding the intrinsic variability aspect into ZDI.

This paper is based on observations obtained at the Canada-France-Hawaii Telescope (CFHT), operated by the National Research Council of Canada, the Institut National des Sciences de l'Univers of the Centre National de la Recherche Scientifique (INSU/CNRS) of France and the University of Hawaii. We thank the CFHT QSO team for the great work and effort at collecting the high-quality MaTYSSE data presented in this paper. MaTYSSE is an international collaborative research programme involving experts from more than 10 different countries (France, Canada, Brazil, Taiwan, UK, Russia, Chile, USA, Ireland, Switzerland, Portugal, China and Italy). We also warmly thank the IDEX initiative at Université Fédérale Toulouse Midi-Pyrénées (UFTMiP) for funding the STEPS collaboration program between IRAP/OMP and ESO. We acknowledge funding from the LabEx OSUG@2020 that allowed purchasing the ProLine PL230 CCD imaging system installed on the 1.25-m telescope at CrAO. SGG acknowledges support from the Science & Technology Facilities Council (STFC) via an Ernest Rutherford Fellowship [ST/J003255/1]. SHPA acknowledges financial support from CNPq, CAPES and Fapemig.

References

Donati, J.-F. & Brown, S. F. 1997, A&A, 326, 1135

Donati, J. F., Moutou, C., Malo, L., et al. 2016, Nature, 534, 662

Gregory, S. G., Donati, J.-F., Morin, J., et al. 2012, ApJ, 755, 97

Siess, L., Dufour, E., & Forestini, M. 2000, A&A, 358, 593

Yu, L., Donati, J.-F., Hébrard, E. M., et al. 2017, MNRAS, 467, 1342

SF2A 2017
C. Reylé, P. Di Matteo, F. Herpin, É. Lagadec, A. Lançon, Z. Meliani, F. Royer (eds)

THE MAGNETIC PROPERTIES OF THE AM STAR ALHENA

A. Blazère[1, 2], P. Petit[3, 4] and C. Neiner[2]

Abstract. Alhena (γ Gem) is a bright magnetic Am star that exhibit normal Zeeman signature with a positive and negative lobe, contrary to all previously studied Am stars that show the presence of ultra-weak (sub-Gauss) fields with peculiar Zeeman signatures with an unexpected prominent positive lobe.

We present here the result of the follow-up observations of Alhena, thanks to very high signal-to-noise data obtained with the spectropolarimeter Narval. Thanks to this data, we determine the magnetic properties of Alhena.

Keywords: stars: magnetic field – stars: early-type – stars: individual: Alhena

1 Introduction

Until recently, among the intermediate-mass stars the only known magnetic stars were the chemically peculiar Ap/Bp stars. These stars exhibit strong magnetic fields ($B_d \geq 300$ G) and the structure of the field is quite simple (usually mostly a dipole). The discovery of an ultra-weak magnetic field (longitudinal magnetic field below 1 Gauss) at the surface of the fast rotating normal star Vega (Lignières et al. 2009; Petit et al. 2010) changed this vision of the magnetic fields in intermediate-mass stars and raised the question of the existence of such kind of magnetic field in intermediate-mass stars that do not host a strong magnetic field.

In addition, ultra-weak magnetic fields have been detected in four Am stars: Sirius A (Petit et al. 2011), β UMa and θ Leo (Blazère et al. 2016b), and Alhena (Blazère et al. 2016a). The first three stars exhibit peculiar Zeeman signatures in circular polarization with a prominent positive lobe. Blazère et al. (2016b) demonstrated that this kind of ultra-weak signature have a magnetic origin, although they were not expected in the standard Zeeman effect theory. Alhena is the only Am stars that exhibit normal Zeeman signatures similar to the one of Vega. The difference between the field of Alhena and the other Am stars is puzzling. In particular, Alhena has very similar stellar parameters to θ Leo that exhibit peculiar signatures.

Alhena is a well known bright spectroscopic binary composed of a subgiant A0IVm star (Gray 2014) and a cool G star (Thalmann et al. 2014). Drummond (2014) measured the orbital elements of the binary thanks to interferometry and found a orbital period of 12.63 years with a high eccentricity (e=0.89).

2 Spectropolarimetric measurements

2.1 Observations

In the frame of the BRITE spectropolarimetric survey (Neiner et al. 2016), new observations of Alhena wer obtained with the Narval spectropolarimeter (Aurière 2003), in circular polarization mode (Stokes V). Narval is a high-resolution spectropolarimeter, very efficient to detect stellar magnetic fields thanks to the polarization they generate in photospheric spectral lines, installed at the 2-meter Bernard Lyot Telescope (TBL) at the summit of Pic du Midi in the French Pyrénées. Alhena was observed in total 25 times, once on October 27, 2014, 20 times between September 2015 and April 2016, and 5 times in April/May 2017. The journal of observations is provided in Table 1.

[1] Institut d'Astrophysique et de Géophysique, Université de Liège, Quartier Agora (B5c), Allée du 6 août 19c, 4000 Sart Tilman, Liège, Belgium

[2] LESIA, Observatoire de Paris, PSL Research University, CNRS, Sorbonne Universités, UPMC Univ. Paris 06, Univ. Paris Diderot, Sorbonne Paris Cité, 5 place Jules Janssen, 92195 Meudon, France

[3] Université de Toulouse, UPS-OMP, Institut de Recherche en Astrophysique et Planétologie, Toulouse, France

[4] CNRS, Institut de Recherche en Astrophysique et Planétologie, 14 Avenue Edouard Belin, F-31400 Toulouse, France

Table 1. Journal of 25 observations of Alhena indicating the date of observation, Heliocentric Julian Date at the middle of the observations (mid-HJD - 2450000), the number of sequences and exposure time in seconds, the mean S/N of the intensity spectrum at ∼500 nm, the longitudinal magnetic field of Alhena A (B_l), and null (N) measurements with their respective error bars, and magnetic detection status (DD = Definite Detection, MD = Marginal Detection).

#	date	mid-HJD	$T_{\rm exp}$ (s)	S/N	$B_l \pm \sigma B_l$ (G)	N$\pm\sigma$N (G)	Detection
1	27 Oct. 14	6958.6531	4 × 25	986	-3.72±2.25	-1.36 ±2.25	DD
2	18 Sep. 15	7284.6954	4 × 35	1016	-6.50±2.33	2.17±2.31	DD
3	19 Sep. 15	7285.6944	4 × 35	1093	-6.58±2.12	-1.90±2.12	DD
4	20 Oct. 15	7304.7204	4 × 35	1152	-10.34±2.06	0.54±2.06	DD
5	09 Oct. 15	7305.7266	4 × 35	1194	-6.32±1.99	-2.03±1.99	DD
6	10 Oct. 15	7306.7104	4 × 35	961	-6.50±2.42	1.72±2.43	DD
7	14 Oct. 15	7310.5895	4 × 35	938	-8.61±2.46	-2.83±2.43	DD
8	20 Oct. 15	7316.6682	4 × 35	832	-9.45±2.87	-1.94±2.85	DD
9	30 Oct. 15	7326.7289	4 × 35	1157	-6.68±2.24	0.17±2.24	DD
10	31 Oct. 15	7327.7354	4 × 35	1149	-5.43±2.06	3.32±2.04	MD
11	09 Nov. 15	7336.7300	4 × 35	935	-10.01±2.54	-1.77±2.52	MD
12	16 Nov. 15	7343.6352	4 × 35	917	-3.79±2.49	0.14±2.49	DD
13	01 Dec. 15	7358.6118	4 × 35	951	-4.53±2.47	-0.40±2.47	DD
14	06 Dec. 15	7363.6642	4 × 35	1320	-6.65±1.79	0.15±1.79	DD
15	11 Dec. 15	7368.6264	4 × 35	1170	-6.66±2.00	-2.08±2.02	DD
16	17 Dec. 15	7374.6085	4 × 35	1057	-7.19±2.38	1.15±2.39	DD
17	20 Jan. 16	7408.6078	3 × 4 × 42	2246	-8.08±1.05	1.03± 1.05	DD
18	20 Feb. 16	7439.4452	3 × 4 × 42	1323	-8.31±1.78	0.51±1.78	DD
19	20 Mar. 16	7460.4035	3 × 4 × 42	2307	-5.15±0.98	-0.16±0.98	DD
20	06 Apr. 16	7485.3300	3 × 4 × 42	2173	-8.82±1.89	1.09±1.90	DD
21	20 Apr. 17	7864.3198	3 × 4 × 42	1028	-5.15±1.40	-2.14±1.40	DD
22	21 Apr. 17	7865.3263	3 × 4 × 42	1346	-5.15±1.02	0.28±1.02	DD
23	22 Apr. 17	7866.3196	3 × 4 × 42	1203	-6.12±1.11	-0.25±1.11	DD
24	03 May 17	7877.3349	3 × 4 × 42	1141	-8.49±1.27	-0.64±1.27	DD
25	07 May 17	7881.3275	3 × 4 × 42	1347	-5.59±1.05	0.11±1.05	DD

2.2 Magnetic measurements

We applied the well-known and commonly used Least-Squares Deconvolution (LSD) technique (Donati et al. 1997) on each individual spectrum, using a mask containing 1052 spectral lines.

Thank to this mask, we extracted LSD Stokes I and V profiles for each observations as well as the null (N) polarization profiles to check for spurious signatures. Normal Zeeman signatures with positive and negative lobe are clearly seen for all nights.

Using the centre-of-gravity method (Rees & Semel 1979), we calculated the longitudinal field value (B_l) of Alhena. The values of the longitudinal magnetic field are all negative and vary between -10 G and -3 G, with typical error bars below 3 G. The values extracted from the N profiles are compatible with 0 G within 3σN, where σN is the error on N. The result are summarized in Table 1 for each night of observations.

Due to the binarity, the LSD I profiles taken in 2017 are shifted (see Fig. 1) compared to the ones taken in 2015/2016. The signature in the Stokes V profile follows this shift in radial velocity, confirming that it is the primary (the Am star) that is magnetic.

3 Magnetic modeling

3.1 Stokes V modeling

We modeled the Stokes V signatures thanks to the oblique rotator model, assuming that the magnetic field of Alhena A is a dipole and that the rotational period is 8.975 days as determined thanks to the variation of equivalent width of the LSD I profiles (see Blazère et al. in prep. for more details).

We calculated a grid of Stokes V profiles for each phase of observation by varying the five free parameters: the inclination i, the obliquity angle β, the dipolar magnetic field B_d, a phase shift ϕ, and the off-centering

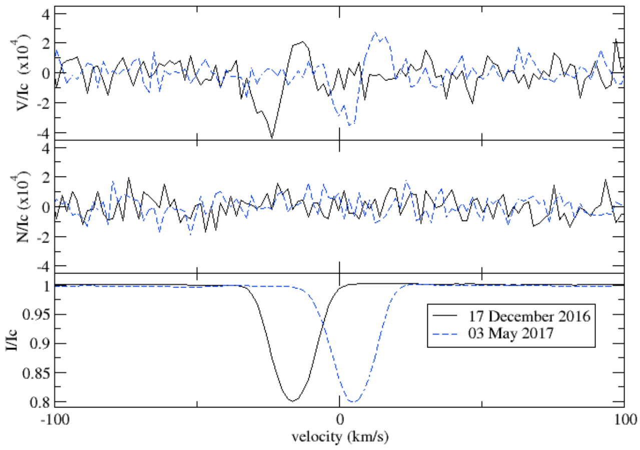

Fig. 1. Example of LSD Stokes I (bottom), Stokes V (top), and null N (middle) profiles for two different nights of observation.

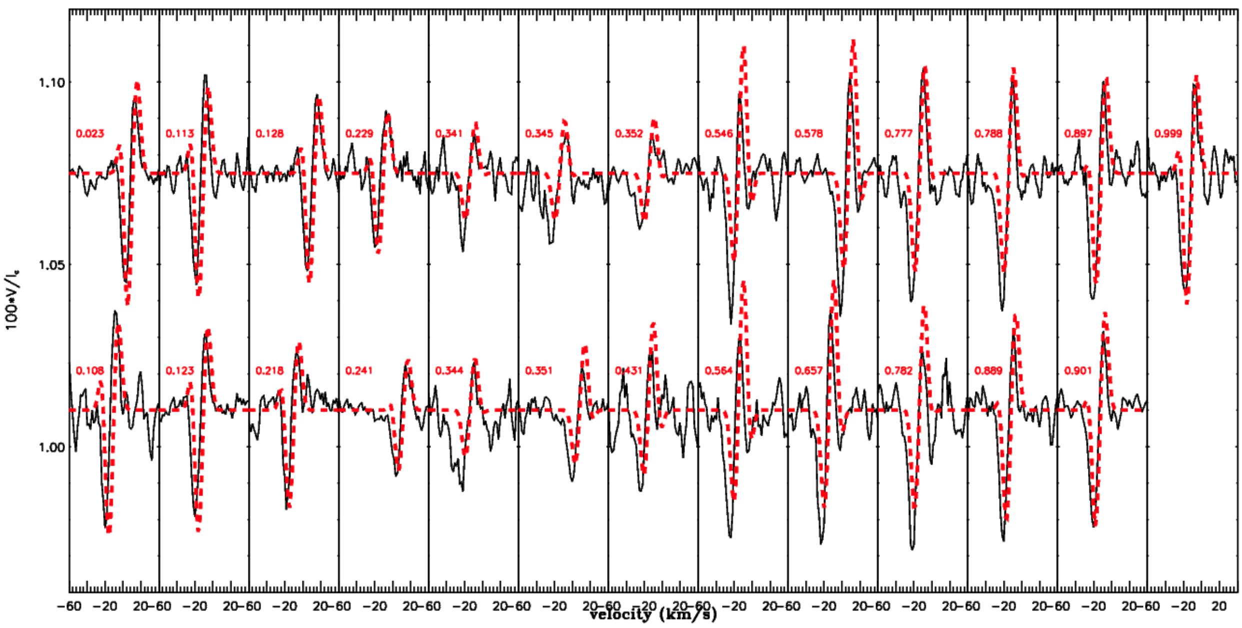

Fig. 2. Best dipolar model fit (red) of the observed Stokes V profiles (black) of Alhena A. The red numbers correspond to the rotational phase.

distance d_d of the dipole with respect to the center of the star (d_d=0 for a centred dipole and d_d=1 if the center of the dipole is at the surface of the star). We obtained the best fit of all observations simultaneously by applying a χ^2 minimization (for more details see Alecian et al. 2008). The best fit is obtained for i=22.8±4.1°, β=34.1±3.4°, ϕ=0.201±0.013, $B_{\rm pol}$=32.4±1.7G and d_d=0.007±0.014, where the error bars correspond to a 3σ confidence level.

The comparison between the observed and the best synthetic LSD Stokes V profiles for all observations is shown in Figure 2. The model fits quite well the Stokes V profiles. Nevertheless, the fit does not match perfectly with the observations, suggesting that the structure of the magnetic field is more complex than a dipole or that some variability of the magnetic field or line profile exist.

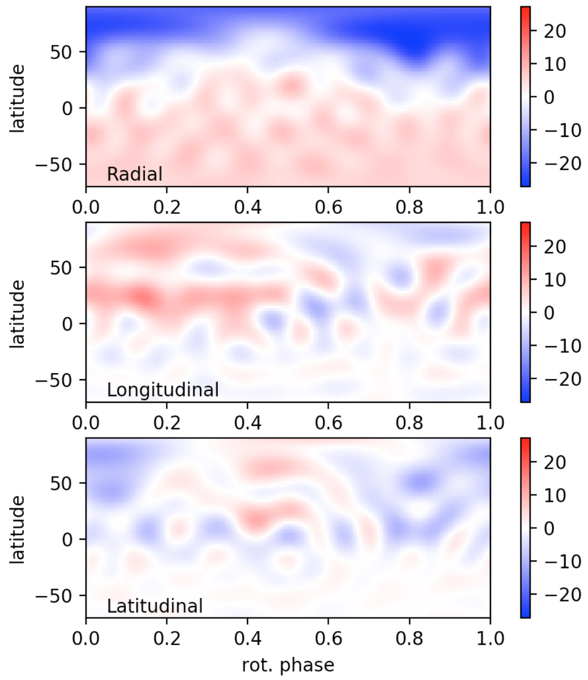

Fig. 3. Magnetic map of Alhena A. The three panels illustrate the field components in spherical coordinates (top: radial, center: azimuthal, and bottom: meridional). The magnetic field strength (colour scale) is expressed in Gauss.

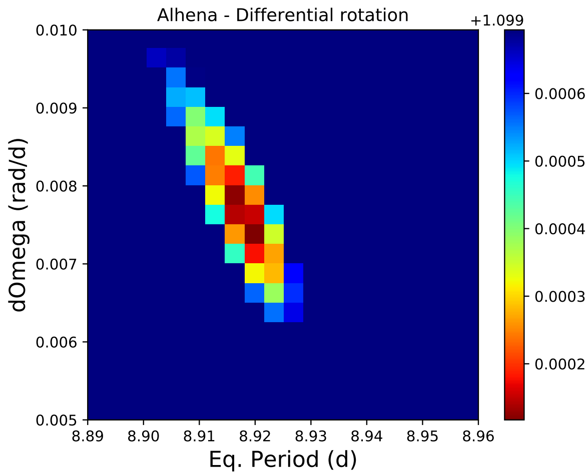

Fig. 4. Surface differential rotation of Alhena A.

3.2 *Zeeman-Doppler Imaging*

We reconstruct the magnetic map at the surface of Alhena A using the Zeeman-Doppler Imaging technique (ZDI, Donati & Brown 1997). The map of the magnetic field is shown in Fig. 3. We find that the field has a simple configuration, compatible with a dipole and we find a rotational period of 8.97 days close to the one determined with the equivalent width variations. We can also measure the surface differential rotation of the star using the method developed by Petit et al. (2002), assuming a simplified solar rotation law. We detect differential rotation at the surface of Alhena A (Fig. 4).

4 Conclusions

Alhena A is the first Am star that exhibit normal Zeeman signatures contrary to the other studied Am stars that exhibit peculiar signatures. We found a rotational period of ~ 8.97 days and a dipolar strength of ~ 30 G. This value is weak compared to the strong magnetic fields of Ap/Bp stars. However it is higher than the one of Vega. It is also the first discovery of surface differential rotation on a magnetic intermediate-mass star.

References

Alecian, E., Catala, C., Wade, G. A., et al. 2008, MNRAS, 385, 391

Aurière, M. 2003, in EAS Publications Series, Vol. 9, EAS Publications Series, ed. J. Arnaud & N. Meunier, 105

Blazère, A., Neiner, C., & Petit, P. 2016a, MNRAS, 459, L81

Blazère, A., Petit, P., Lignières, F., et al. 2016b, ArXiv e-prints

Donati, J.-F. & Brown, S. F. 1997, A&A, 326, 1135

Donati, J.-F., Semel, M., Carter, B. D., Rees, D. E., & Collier Cameron, A. 1997, MNRAS, 291, 658

Drummond, J. D. 2014, AJ, 147, 65

Gray, D. F. 2014, AJ, 147, 81
Lignières, F., Petit, P., Böhm, T., & Aurière, M. 2009, A&A, 500, L41
Neiner, C., Wade, G., Marsden, S., & Blazère, A. 2016, ArXiv e-prints
Petit, P., Donati, J.-F., & Collier Cameron, A. 2002, MNRAS, 334, 374
Petit, P., Lignières, F., Aurière, M., et al. 2011, A&A, 532, L13
Petit, P., Lignières, F., Wade, G. A., et al. 2010, A&A, 523, A41
Rees, D. E. & Semel, M. D. 1979, A&A, 74, 1
Thalmann, C., Desidera, S., Bonavita, M., et al. 2014, A&A, 572, A91

SF2A 2017
C. Reylé, P. Di Matteo, F. Herpin, É. Lagadec, A. Lançon, Z. Meliani, F. Royer (eds)

ON THE DERIVATION OF RADIAL VELOCITIES OF SB2 COMPONENTS: A "CCF VS TODCOR" COMPARISON*

J.-L. Halbwachs[1], F. Kiefer[2], F. Arenou[3], B. Famaey[1], P. Guillout[1], R. Ibata[1], T. Mazeh[4] and D. Pourbaix[5]

Abstract. The radial velocity (RV) of a single star is easily obtained from cross-correlation of the spectrum with a template, but the treatment of double-lined spectroscopic binaries (SB2s) is more difficult. Two different approaches were applied to a set of SB2s: the fit of the cross-correlation function with two normal distributions, and the cross-correlation with two templates, derived with the TODCOR code. It appears that the minimum masses obtained through the two methods are sometimes rather different, although their estimated uncertainties are roughly equal. Moreover, both methods induce a shift in the zero point of the secondary RVs, but it is less pronounced for TODCOR. All-in-all the comparison between the two methods is in favour of TODCOR.

Keywords: binaries: spectroscopic, Techniques: radial velocities

1 Introduction

The derivation of a radial velocity (RV) from a CCD spectrum is a routine operation for a single-lined spectroscopic binary (SB1), leading to an accuracy of a few m.s^{-}1, or even less. However, things are not so simple when double-lined binaries (SB2s) are considered. However SB2s allow the estimation of the masses of the stellar component when the orbital inclination may be obtained from an astrometric technique, such as interferometry or high-precision spatial astrometry, and accurate RVs are necessary to derive accurate masses. For that reason, we have applied the two most common techniques on a set of well-observed SB2s, and we compare their results hereafter.

2 The SB2 sample

We consider 24 SB2s which were observed since 2010 with the SOPHIE spectrograph installed on the 193 cm telescope of the Haute-Provence Observatory (OHP). These stars are all known spectroscopic binaries for which it could be possible to derive the masses with an accuracy around 1 % when the astrometric measurements of the Gaia satellite will be delivered (Halbwachs et al. 2014). Ten revised spectroscopic orbits were published in Kiefer et al. (2016), and the publication of 14 others is in preparation (Kiefer et al. 2017). These orbits are presented in Halbwachs et al. (2017)

* BASED ON OBSERVATIONS PERFORMED AT THE HAUTE-PROVENCE OBSERVATORY

[1] Université de Strasbourg, CNRS, Observatoire astronomique de Strasbourg, UMR 7550, F-67000 Strasbourg, France

[2] Institut d'Astrophysique de Paris, CNRS, UMR 7095, 98bis boulevard Arago, F-75014 Paris

[3] GEPI, Observatoire de Paris, PSL Research University, CNRS, Université Paris Diderot, Sorbonne Paris Cité, Place Jules Janssen, F-92195 Meudon, France

[4] School of Physics and Astronomy, Tel Aviv University, Tel Aviv 69978, Israel

[5] FNRS, Institut d'Astronomie et d'Astrophysique, Université Libre de Bruxelles, boulevard du Triomphe, 1050 Bruxelles, Belgium

3 The "CCF1" technique

The first technique we have applied makes use of the cross-correlation functions (CCFs) of the spectra with a single template. In practice, it is the numerical equivalent of the photoelectric RVs measured, for instance, with the now decommissioned CORAVEL instrument (Baranne, Mayor & Poncet 1979): each component generates in the CCF a bell-shaped dip which is assumed to obey a normal function. Therefore, the velocities are derived by computing the parameters of two normal functions which the sum is as close as possible to the CCF. For any SB2, the slope of the background is fixed to the same value for all the spectra; at the opposite, the middles, the standard deviations, and the depths of the correlation dips are calculated from a χ^2 minimisation for the CCF of each spectrum. In practice, these parameters are derived from a range restricted to a given number of standard deviations, σ, around each minimum as shown in Fig. 1. This range may be as large as 2 or even 3 σ for some stars, but, for others, even 1 σ would lead to a very approximative fit; this depends on the compatibility of the templates with the two spectra, and also on the rotation velocities of the stars. As a consequence, we may expect that the RVs of the components are affected by systematic errors when the correlation dips are closer than approximately 3 times the sum of their standard deviations. However, reality is often even worse: since the template doesn't exactly correspond to the spectrum of each component, the correlation dips are often flanked by side lobes which are much less deep but as large as the main dips. Therefore, the minimum difference guaranteeing reliable RVs is in fact 6 times the sum of the standard deviations. Since the standard deviations are as large as about 3 km/s for the slow rotators with G-K spectral types, and larger otherwise, that means that, in the best case, the RVs are dubious when the difference is less than 36 km/s; this concerns a large part of the measurements obtained for our sample.

4 TODCOR

The TODCOR algorithm (Zucker & Mazeh 1994; Zucker et al. 2004) derives the CCF assuming a template for each component. This method is rather sophisticated, since the templates must be chosen carefully, as explained in Kiefer et al. (2016). For the search of the minimum of the CCF, see, e.g., Halbwachs et al. (2013). The templates are synthetic spectra extracted from the Phoenix library (Hauschild, Allard & Baron 1999). When they are really similar to the actual spectra of the components, the errors related to the CCF1 methods are avoided. However, when the templates are different, systematic errors related to the difference of RV may rise again.

The RV used to derive the published orbits were all obtained with TODCOR.

5 A comparison CCF1 vs TODCOR

Rather than comparing the RVs coming from the two techniques, we used them to derive the SB2 orbital elements, following the method presented in Kiefer et al. (2016). A systematic shift of the RVs of the secondary components is added to the classical orbital elements, in order to verify the adequacy of the templates. In this section, the results of both methods are compared, considering three points : the minimum masses of the components, the shift of the secondary RVs, and the standard deviations of the residuals of the orbits.

5.1 Minimum masses

The orbital elements of a SB2 orbit lead to the minimum masses, $\mathcal{M}_1 \sin^3 i$ and $\mathcal{M}_2 \sin^3 i$, where i is the inclination of the orbital plane and $\mathcal{M}_1$ and $\mathcal{M}_2$ the masses of the components. The minimum masses were derived from the RVs obtained with the CCF1 and with the TODCOR methods, and they are compared in Fig. 2. The error bars are represented too.

It appears that the difference has the same sign for both components, and, more important, that the minimum masses may be very significantly different. This confirms the importance of the choice of the technique. .

5.2 Shift of the secondary RVs

The shift of the secondary RVs with respect to the primary ones is presented in Fig. 3. Aside from a few exception, this difference is always positive. For the CCF1 method this comes obviously from the choice of the template which has a spectral type earliest that the secondary component.We notice also a concentration of stars along the vertical red line: these stars have a negligible shift when the TODCOR method is applied, as

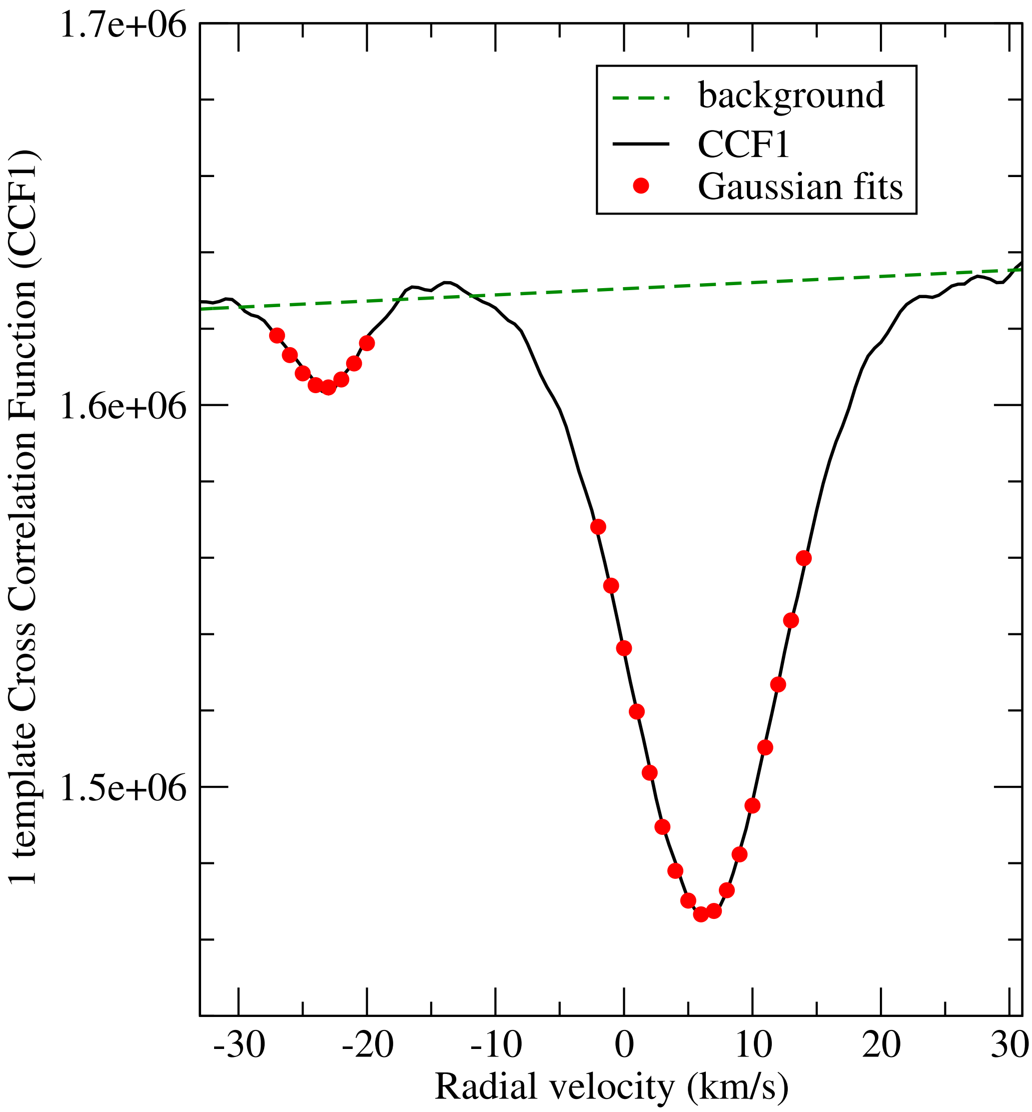

Fig. 1. The cross-correlation function of a spectrum of a SB2 with a template. The red points are the sum of two normal functions derived from a range of 1.4 σ around the RV of the components.

expected. However, we see also a lot of SB2s along the red diagonal, and for which the shift is roughly the same with TODCOR than with CCF1.

5.3 Residuals of the orbit

The residuals of the SB2 orbits are presented in Fig. 4. The stars are concentrated along the diagonal, but an excess of large residuals is visible for the CCF1 method.

6 Conclusions

We have seen that TODCOR and the CCF1 method give RVs which are clearly different, since the minimum masses derived from the orbital SB2 elements are often not compatible. It is expected that TODCOR give more reliable results than CCF1, and it is confirmed that the smallest systematic shift between the RVs of the components is obtained with TODCOR, on average. Moreover, TODCOR leads to residuals which are, on average, smaller than those obtained from CCF1. Therefore, we confirm that TODCOR is the most reliable technique. Nevertheless, it is not perfect: the shift of the secondary RVs is not systematically negligible, as it

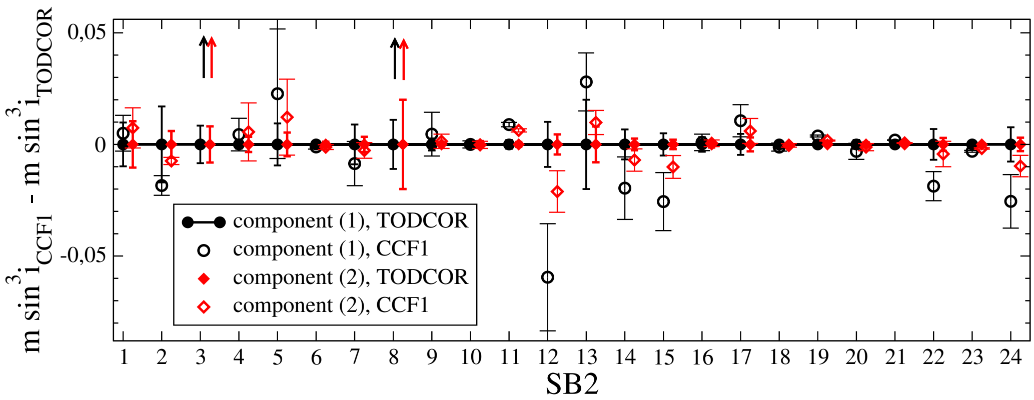

Fig. 2. Comparison of the minimum masses, $\mathcal{M}_1 \sin^3 i$ and $\mathcal{M}_2 \sin^3 i$, derived from RVs obtained with the CCF1 and with the TODCOR method. The masses coming from TODCOR are used as references. The stars are sorted according to the spectral type of the primary component, with the early-type stars at left.

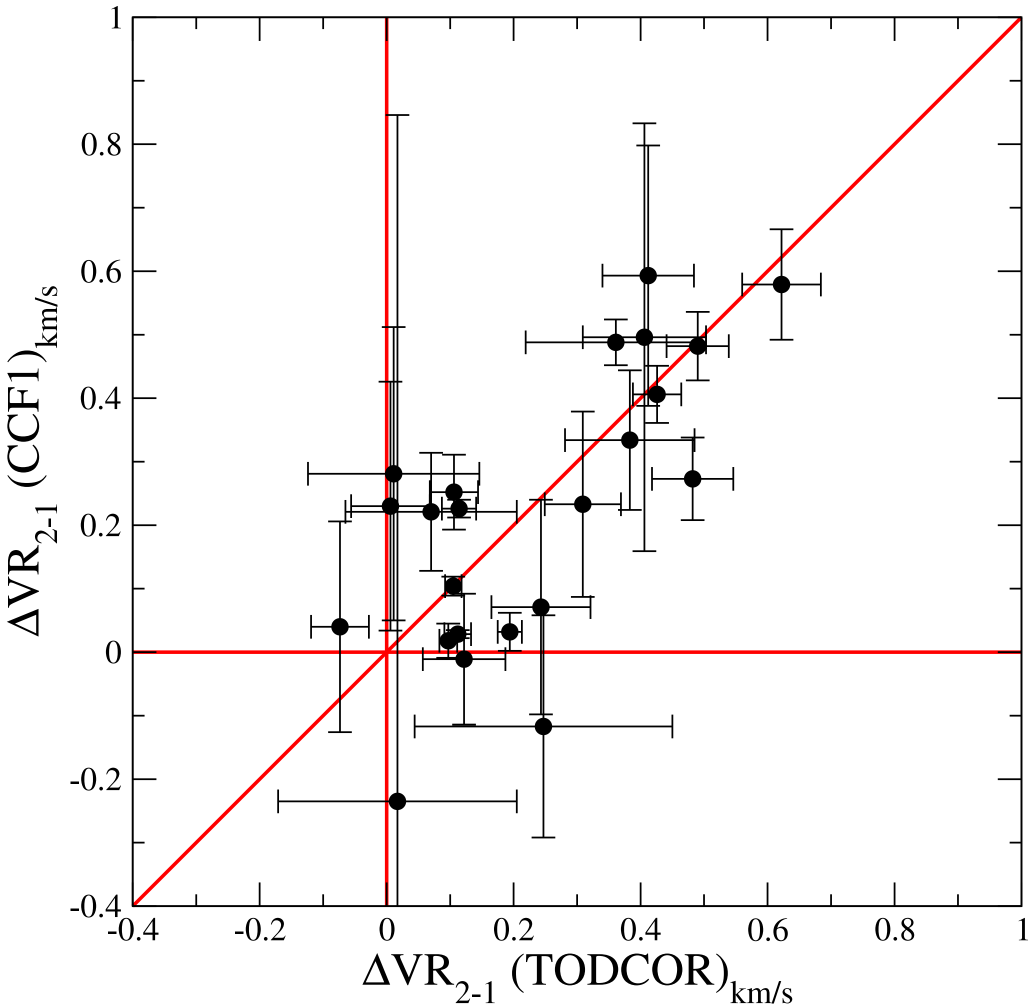

Fig. 3. Comparison of the differences between the secondary and the primary mean RVs. The points above the diagonal represent the SB2s for which the CCF1 method gives a difference larger than that obtained with TODCOR.

should be, and the residuals of TODCOR are sometimes larger than that of CCF1. This is probably due to differences between the actual spectra and the templates from the Phoenix library.

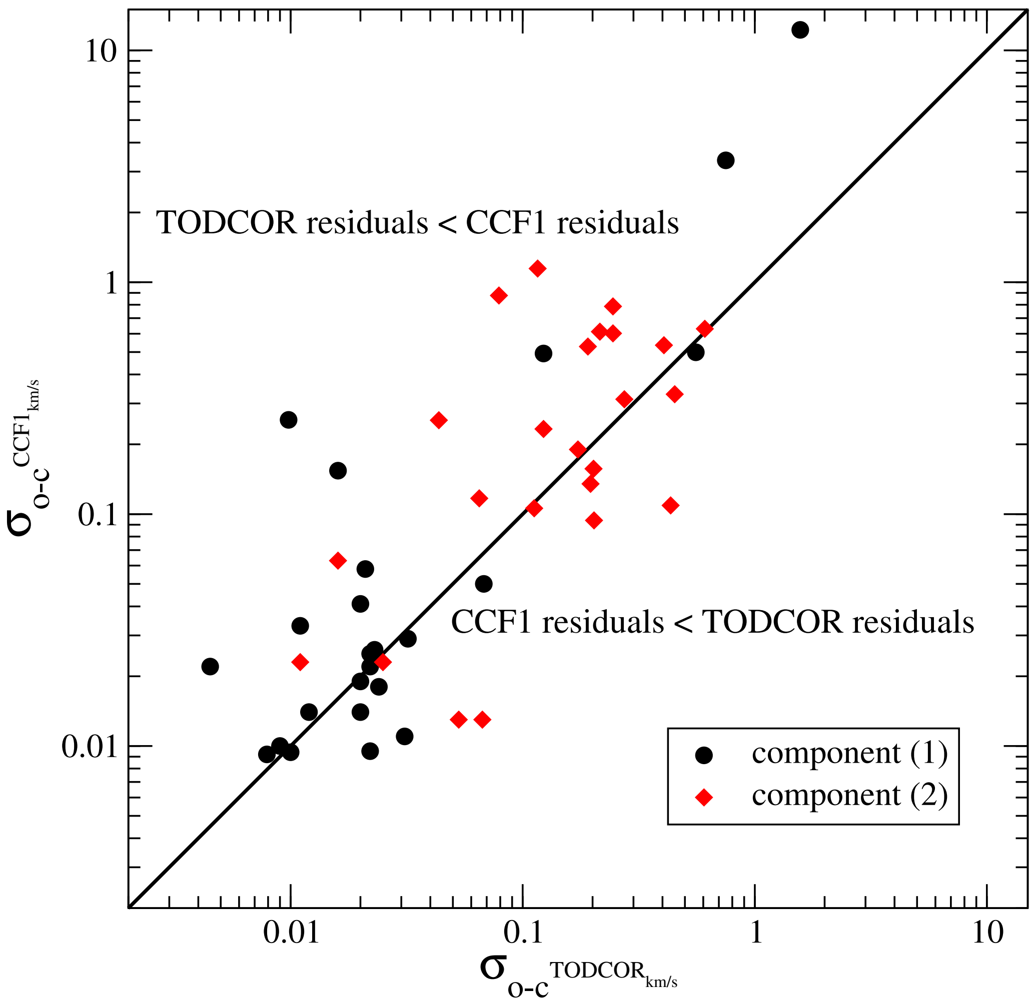

Fig. 4. Comparison of the standard deviations of the residuals of the RVs after the calculation of the SB2 orbital elements. The points above the diagonal represent the SB2s for which the CCF1 method gives residuals larger than that obtained with TODCOR.

This project was supported by the french INSU-CNRS "Programme National de Physique Stellaire" and "Action Spécifique *Gaia*". We are grateful to the staff of the Haute–Provence Observatory, and especially to Dr F. Bouchy, Dr H. Le Coroller, Dr M. Véron, and the night assistants, for their kind assistance. We made use of the SIMBAD database, operated at CDS, Strasbourg, France. This research has received funding from the European Community's Seventh Framework Programme (FP7/2007-2013) under grant-agreement numbers 291352 (ERC)

References

Baranne, A., Mayor, M. & Poncet, J.L. 1979, Vistas in A., 23, 279

Halbwachs, J.-L., Arenou, F., Guillout, P. et al. 2013, In: Cambrésy L., Martins F., Nuss E., Palacios A. edr. Proceedings SF2A 2013, 127-135, SF2A

Halbwachs, J.-L., Arenou, F., Pourbaix, D. et al. 2014, MNRAS, 445, 2371

Halbwachs, J.-L., Arenou, F., Boffin, H.M.J. et al. 2017, In: Reylé C., Di Matteo P., Herpin F., Lagadec É, Lançon A., Royer F. edr. Proceedings SF2A 2017, this volume, SF2A (arXiv:1710.02017)

Hauschild, P.H., Allard, F. & Baron, E. 1999, ApJ, 512, 377

Kiefer, F., Halbwachs, J.-L., Arenou, F. et al. 2016, MNRAS, 458, 3272

Kiefer, F., Halbwachs, J.-L., Arenou, F., et al. 2017, MNRAS, (in preparation)

Zucker, S. & Mazeh, T. 1994, ApJ, 420, 806

Zucker, S., Mazeh, T., Santos, N.C., Udry, S., & Mayor, M. 2004, A&A, 426, 695

SF2A 2017
C. Reylé, P. Di Matteo, F. Herpin, É. Lagadec, A. Lançon, Z. Meliani, F. Royer (eds)

FLIPER: CHECKING THE RELIABILITY OF GLOBAL SEISMIC PARAMETERS FROM AUTOMATIC PIPELINES

L. Bugnet[1, 2], R. A. García[1,2], G. R. Davies[3, 4], S. Mathur[5,6,7] and E. Corsaro[8]

Abstract. Our understanding of stars through asteroseismic data analysis is limited by our ability to take advantage of the huge amount of observed stars provided by space missions such as CoRoT, *Kepler*, K2, and soon TESS and PLATO. Global seismic pipelines provide global stellar parameters such as mass and radius using the mean seismic parameters, as well as the effective temperature. These pipelines are commonly used automatically on thousands of stars observed by K2 for 3 months (and soon TESS for at least $\sim$ 1 month). However, pipelines are not immune from misidentifying noise peaks and stellar oscillations. Therefore, new validation techniques are required to assess the quality of these results. We present a new metric called FliPer (Flicker in Power), which takes into account the average variability at all measured time scales. The proper calibration of FliPer enables us to obtain good estimations of global stellar parameters such as surface gravity that are robust against the influence of noise peaks and hence are an excellent way to find faults in asteroseismic pipelines.

Keywords: asteroseismology - methods: data analysis - stars: oscillations

1 Introduction

Surface gravity and global seismic parameters ($\Delta\nu$, $\nu_{\rm max}$) are related through the so-called global seismic scaling relations (Brown & Gilliland 1990; Kjeldsen et al. 1994): $\Delta\nu \propto M^{\frac{1}{2}} \times R^{\frac{-3}{2}}$ and $\nu_{max} \propto M \times R^{-2} \times {T_{eff}}^{-\frac{1}{2}}$. Hence, an accurate estimation of the seismic global parameters and the effective temperature can be used to provide an estimate of the surface gravity of stars with convective envelopes. However, most asteroseismic data obtained from *Kepler* and K2 are sampled with cadence of around 30 minutes (long cadence), leading to limited spectral information above the corresponding Nyquist frequency ($\sim$ 288 μHz). If a star pulsates at frequencies higher than the long cadence Nyquist frequency (for instance a main-sequence star, e.g. Davies et al. 2015) typical analysis methods cannot be applied to estimate seismic parameters. In some cases reliable information can be obtained (Chaplin et al. 2014) but typical automated asteroseismic pipelines are susceptible to providing unreliable estimates. Indeed, internal magnetic fields can inhibit the modes (e.g. Mosser et al. 2009; García et al. 2010; Chaplin et al. 2011), complicating the automatic characterization of seismic parameters.

Several methods have been developed to estimate the stellar parameters (e.g. surface gravity) from photometric data based on a simple measurement such as the variance of the time series (Hekker et al. 2012), the Flicker (Bastien et al. 2013, 2016), granulation characterization of the power spectrum (Mathur et al. 2011; Kallinger et al. 2014) or the autocorrelation as described in Kallinger et al. (2016). Some of these methods require the observation of acoustic modes of oscillation but those that rely on the information provided by just granulation do not. The Flicker technique is typically used for main-sequence stars, subgiants and giants down

[1] IRFU, CEA, Université Paris-Saclay, F-91191 Gif-sur-Yvette, France
[2] Université Paris Diderot, AIM, Sorbonne Paris Cité, CEA, CNRS, F-91191 Gif-sur-Yvette, France
[3] School of Physics and Astronomy, University of Birmingham, Edgbaston, Birmingham, B15 2TT, UK
[4] Stellar Astrophysics Centre, Department of Physics and Astronomy, Aarhus University, Ny Munkegade 120, DK-8000 Aarhus C, Denmark
[5] Instituto de Astrofísica de Canarias, E-38200, La Laguna, Tenerife, Spain
[6] Universidad de La Laguna, Dpto. de Astrofísica, E-38205, La Laguna, Tenerife, Spain
[7] Space Science Institute, 4750 Walnut Street Suite 205, Boulder, CO 80301, USA
[8] INAF - Osservatorio Astrofisico di Catania, Via S. Sofia 78, I-95123 Catania, Italy

to a $\log_{10}(g)$ ∼2.5 dex. With FliPer we can reach the range of application to red giants to lower log(g) by taking into account the variability at all measured frequencies in the power spectrum (Bugnet et al. *in prep.*). Thus, with this simple metric it is possible to assess in a few seconds the reliability of results obtained from automatic global seismic pipelines.

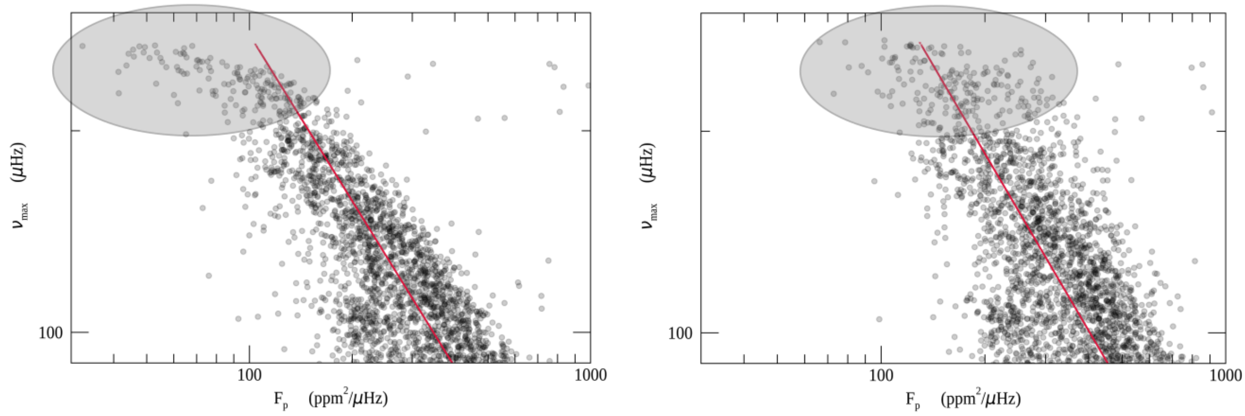

Fig. 1. $\nu_{\rm max}$ provided by the A2Z pipeline (Mathur et al. 2010) **vs** FliPer for stars with $\nu_{\rm max}$ from 90 to $300\mu Hz$ (It corresponds to a zoom on the rectangle on the left panel of Fig. 2). **Left:** Case where FliPer is computed using the mean of the high-frequency signal as the photon noise. **Right:** Case when the theoretical photon noise computed by Jenkins et al. (2010) is used. The grey-shaded circle is where the impact of the noise calculation on FliPer is important.

2 Origin and definition of FliPer

It is well known that the shape and the amount of power in the power spectrum density (PSD) of a star changes with stellar evolution as discussed above. The shape of the PSD is dominated by photometric variability caused by star spots and stellar rotation at low frequencies, a convective continuum, and a hump of power due to the stellar oscillations. All of these stellar contributions are added to the constant photon noise. As a star evolves and surface gravity decreases, so $\nu_{\rm max}$ decreases. Because granulation properties are linked to $\nu_{\rm max}$ or surface gravity, as a star evolves so the total power from granulation increases (e.g. García & Stello 2015). To account for the total power in the PSD we define the new metric FliPer (F_p) as follows:

$$F_p = \overline{\rm PSD} - P_n \tag{2.1}$$

where $\overline{\rm PSD}$ represents the mean value of the power spectrum density and P_n the photon noise. $\overline{\rm PSD}$ is computed from 0.7 μHz (corresponding to the 20 days high-pass filter used to calibrate the light curves following García et al. (2011)) to the Nyquist frequency (∼288 μHz for long cadence *Kepler* data). The photon noise is estimated following Jenkins et al. (2010) and depends on the magnitude of the star. It could also be evaluated by taking the mean power at high frequency (see Fig. 1, left panel) instead of computing the expected noise by Jenkins et al. (2010) (see Fig. 1, right panel). A comparative study showed that for most stars, the values of FliPer obtained with both methods are similar. The only important difference appears for stars in which the high-frequency part of the spectrum is dominated by stellar signal and not by noise. This is typically the case for stars with $\nu_{\rm max}$ close to Nyquist or for super-Nyquist stars. For these stars, the power contained in the modes and in the granulation profile is partially taken into account in the noise calculation because there are still power at high frequencies. The resulting photon noise value is thus higher than expected. In this case, FliPer is artificially lowered when using the high-frequency noise calculation as shown for stars in the grey circle on Fig. 1.

3 Prediction of seismic parameters

From Fig. 2 left, we get in a first approximation a logarithmic law ($\log(F_{p,ppm^2/\mu Hz}) = -1.14 \times \log(\nu_{max,\mu Hz}) + 4.88$) between FliPer and $\nu_{\rm max}$ followed by more than 90% of the 16,000 red giants analyzed here. By calculating FliPer, we used this metric to determine those stars for which the resultant seismic parameters do not follow the

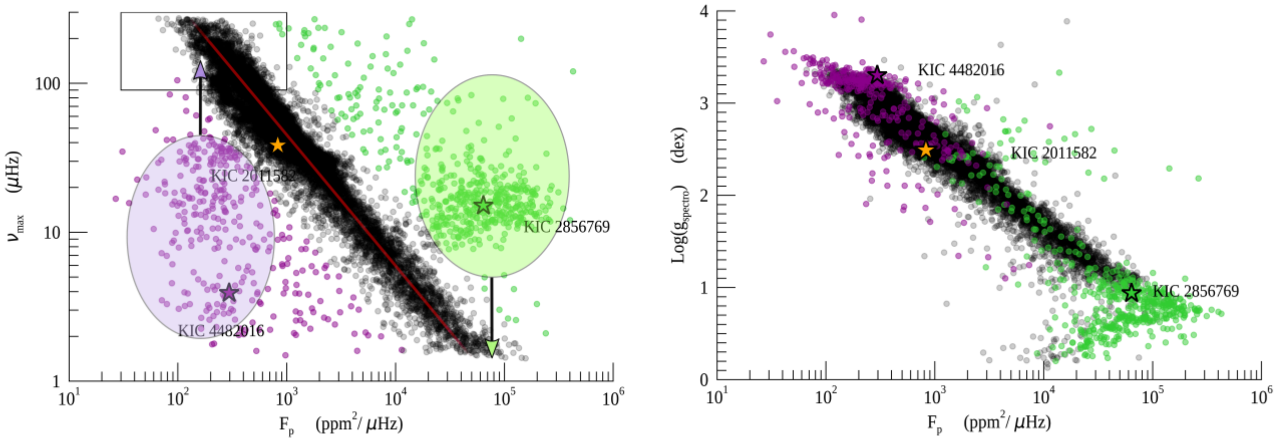

Fig. 2. Left: $\nu_{\rm max}$ provided by the A2Z pipeline (Mathur et al. 2010) for $\sim 16,000$ red giants observed by *Kepler* (data corrected and interpolated following García et al. (2011, 2014c)) VS FliPer. The red line represents the best fitting to the data. Green stars have higher FliPer than the general trend and should be replaced at lower frequencies, while violet points have lower values of FliPerand should be replaced at higher frequencies (as indicated by ellipses and arrows). These limits are located at one standard deviation from the law. The black rectangle shows the location of the zoom of Fig. 1. **Right:** $\log(g)$ provided by photometric and spectroscopic measurements from the NASA *Kepler* catalog (Mathur et al. 2017) VS FliPer for the same stars than in the left panel.

general trend. This could be a consequence of the presence of unexpected features in the PSD (e.g. pollution by spikes, etc) or because the resultant value obtained by the pipeline is incorrect.

The right panel of Fig. 2 represents the spectroscopic surface gravity from the NASA *Kepler* catalog (Mathur et al. 2017) against FliPer for the same sample of stars using the same color code than in the left panel. We observe that the purple outliers in the left panel follow the general trend with log(g), while the green data points appear to be reflected at some point. This change of slope around 0.7 dex comes from the cut in the PSD as a consequence of the high-pass filter used to calibrate the data (García et al. 2011). All stars with $\log(g)$ lower than this boundary have a biased estimation of FliPer and form a clump of green outliers stars on the left panel. This left panel show the same data from FliPer but with seismic $\nu_{\rm max}$ on the y-axis. The $\log(g)$ measurements come from spectroscopic analysis that are independent of the seismic analysis. We thus demonstrate that most outliers stars in the left panel are due to a problem in the automatic seismic determination and not in FliPer, because FliPer values are consistent with surface gravity data.

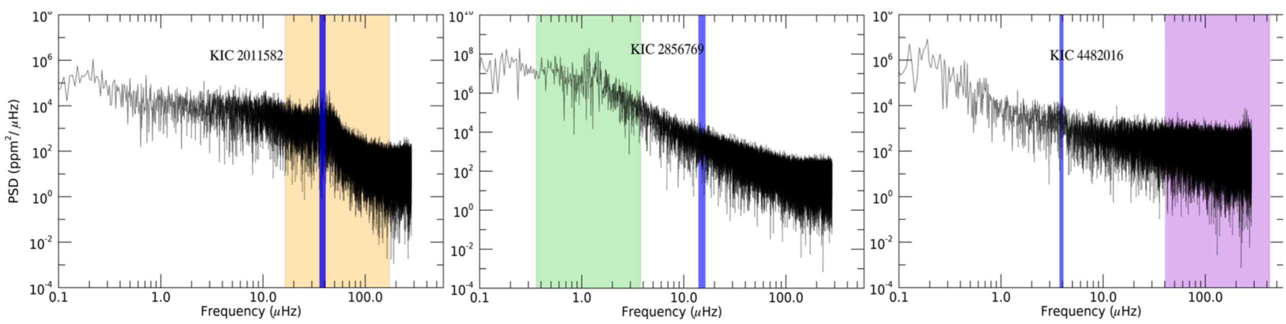

Fig. 3. PSD of the three stars represented with a star symbol on Fig. 2. The blue area corresponds to the $\nu_{\rm max}$ returned by A2Z. The yellow, green, and purple shaded regions correspond to the range of accepted values of $\nu_{\rm max}$ by FliPeras in Fig. 2. **Left:** KIC 2011582 for which the $\nu_{\rm max}$ is well determined by A2Z. **Middle:** A high F_p star (KIC 2856769). This star has lower frequency modes than obtained by A2Z. **Right:** A low F_p star (KIC 4482016). This star has higher frequency modes than obtained by A2Z.

Figure 3 represents the PSD of three stars represented with a star symbol in Fig. 2. Left panel corresponds to KIC 2011582 well characterized both by A2Z and FliPer. Stars with a higher FliPer value than expected (green stars on Fig. 2) have low surface gravities, meaning that they are highly evolved RGB stars. The $\nu_{\max}$ is too close to the frequency cut-off of 20 days used to calibrate the series. As a result, the A2Z pipeline cannot properly estimate $\nu_{\max}$ (a lower filter is needed to properly analyze these stars). An example, KIC 2856769, is presented in the middle panel in Fig. 3. Most outliers stars with a low value of FliPer (purple stars on Fig. 2) have a high $\log(g)$: they are probably main-sequence or sub-giants stars and should have a much higher $\nu_{\max}$ than the value returned automatically by A2Z. An example is KIC 4482016 represented on the right panel of Fig. 3. These stars needs to be treated independently by A2Z and FliPer helps to flag them up.

There are however about 1% of the stars that remain outliers on the right panel of Fig. 2. Among these outliers that could present however a good estimation of $\nu_{\max}$, we observe stars that present high rotation power (e.g. García et al. 2014b; Ceillier et al. 2017), spikes, pollution by another star, binaries systems, low signal-to-noise ratio stars (Mathur et al. 2016), low-amplitude dipole mode stars (e.g. Mosser et al. 2012; García et al. 2014a), etc. Not only does the FliPer metric allows to estimate surface gravity, but also to detect stars that present a particular signal in their power spectra. For example, the detection of spikes is important in the study of K2 observations which are affected by spikes at the Thrusters frequency and its harmonics.

4 Conclusions

We demonstrate that the FliPer follows a quasi-logarithmic trend with the global seismic parameters and, therefore, it is related to surface gravity. It allows us to quickly estimate the reliability of seismic parameters estimated from global pipelines. The FliPer method can be used to identify stars without detected modes, stars dominated by the harmonics of the K2 Thrusters seen as spikes in the spectrum, highly evolved stars, and super-Nyquist stars (i.e., stars for which the p-mode excess power is above the observational Nyquist frequency).

L.B. and R.A.G. acknowledge the support from CNES. S.M. acknowledge support by the National Aeronautics and Space Administration under Grant NNX14AB92G issued through the *Kepler* Participating Scientist Program. E.C. is funded by the European Unions Horizon 2020 research and innovation programme under the Marie Sklodowska-Curie grant agreement no. 664931.

References

Bastien, F. A., Stassun, K. G., Basri, G. et al. 2016, ApJ, 818, 43
Bastien, F. A., Stassun, K G., Basri, G. et al. 2013, Nature, 500, 427
Brown, T. M. & Gilliland, R. L. 1990, ApJ, 350, 939
Ceillier, T., Tayar, J. and Mathur, S. et al. 2017, A&A, 605, 111
Chaplin, W. J., Bedding, T. R., Bonanno, A. et al. 2011, ApJ, 732, 5
Chaplin, W. J., Elsworth, Y., Davies, G. R et al. 2014, MNRAS, 445, 946
Davies, G. R., Chaplin, W. J., Farr, W. M. et al. 2015, MNRAS, 446, 2959
García, R. A., Mathur, S., Salabert, D. et al. 2010, Science, 329, 1032
García, R. A., Hekker, S., Stello, D. et al. 2011, MNRAS, 414, L6
García, R. A., Pérez Hernández, F., Benomar, O. et al. 2014a, A&A, 563, 84
García, R. A., Ceillier, T., Salabert, D. et al. 2014b, A&A, 572, 34
García, R. A., Mathur, S., Pires, S. et al. 2014c, A&A, 568, 10
García R. A. & Stello, D. 2015, Asteroseismology of red giant stars in Extraterrestrial Seismology, ed. V. Tong & R. García (Cambridge University Press) (pp. 159-169)
Hekker, S., Elsworth, Y., Mosser, B. et al. 2012, A&A, 544, 90
Jenkins, J. M., Caldwell, D. A., Chandrasekaran, H. et al. 2010, ApJl, 713, L120
Kallinger, T., De Ridder, J., Hekker, S. et al. 2014, A&A, 570, A41
Kallinger, T., Hekker, S., Garcia, R. A. et al. 2016, Science Advances, 2, 1500654
Kjeldsen, H. and Bedding, T. R. 1994, A&A, 293, 87-106
Mathur, S., García, R. A., Regulo, C. et al. 2010, A&A, 511, A46
Mathur, S., Hekker, S., Trampedach, R. et al. 2011, ApJ, 741, 119
Mathur, S., García, R. A., Huber, D. et al. 2016, ApJ, 827, 50
Mathur, S., Huber, D., Batalha, N. M. et al. 2017, ApJS, 229, 30
Mosser, B., Michel, E., Appourchaux, T. et al. 2009, A&A, 506, 33
Mosser, B., Elsworth, Y., Hekker, S. et al. 2012, A&A, 537, 30

SF2A 2017
C. Reylé, P. Di Matteo, F. Herpin, É. Lagadec, A. Lançon, Z. Meliani, F. Royer (eds)

MODELING RADIAL VELOCITIES AND ECLIPSE PHOTOMETRY OF THE KEPLER TARGET KIC 4054905: AN OSCILLATING RED GIANT IN AN ECLIPSING BINARY

M. Benbakoura[1,2], P. Gaulme[3,4,5], J. McKeever[4,6], P. G. Beck[7,8], J. Jackiewicz[4] and R. A. García[1,2]

Abstract. Asteroseismology is a powerful tool to measure the fundamental properties of stars and probe their interiors. This is particularly efficient for red giants because their modes are well detectable and give information on their deep layers. However, the seismic relations used to infer the mass and radius of a star have been calibrated on the Sun. Therefore, it is crucial to assess their accuracy for red giants which are not perfectly homologous to it. We study eclipsing binaries with a giant component to test their validity. We identified 16 systems for which we intend to compare the dynamical masses and radii obtained by combined photometry and spectroscopy to the values obtained from asteroseismology. In the present work, we illustrate our approach on a system from our sample.

Keywords: asteroseismology, methods: data analysis, binaries: eclipsing, stars: evolution, stars: oscillations

1 Introduction

Over the last 10 years, asteroseismology has been the most efficient tool to probe stellar interiors. In this field, red giants are of particular interest because, on the one hand, they are solar-like pulsators, i. e., their oscillations are stochastically excited by granulation, and on the other hand, the presence of mixed-modes in their power spectrum allows to probe their core (e.g. Beck et al. 2011, 2012; Mosser et al. 2011). Moreover, the huge sample of observed red giants from *Kepler* (Borucki et al. 2010) and CoRoT (Baglin et al. 2006), including more than 30,000 stars, allows to make statistical inferences as a function of different parameters.

Obtaining masses and radii of red giants allows to know more about the fate of the Sun. These parameters can be directly obtained by measuring the effective temperature as ell as the global seismic parameters $\Delta\nu$ and $\nu_{\max}$, by applying the so-called global seismic scaling relations (Brown et al. 1991; Kjeldsen & Bedding 1995):

$$\frac{R_*}{R_\odot} = \left(\frac{\Delta\nu_\odot}{\Delta\nu}\right)^2 \left(\frac{\nu_{\max}}{\nu_{\max,\odot}}\right) \left(\frac{T_{\rm eff}}{T_{\rm eff,\odot}}\right)^{1/2} \tag{1.1}$$

$$\frac{M_*}{M_\odot} = \left(\frac{\Delta\nu_\odot}{\Delta\nu}\right)^4 \left(\frac{\nu_{\max}}{\nu_{\max,\odot}}\right)^4 \left(\frac{T_{\rm eff}}{T_{\rm eff,\odot}}\right)^{3/2} \tag{1.2}$$

These relations have been calibrated on the Sun and are based on the assumption that solar-like pulsators are homologous to our star. However, in red giants the aspect ratio (radius of the radiative zone divided by the radius of the star) may be smaller than in main-sequence stars by more than one order of magnitude. Moreover, the envelope of the former is significantly less dense because of the expansion. The departure from homology and asymptotic regime might introduce a systematic error in the seismic relations (e. g. Mosser et al. 2013;

[1] IRFU, CEA, Université Paris-Saclay, F-91191 Gif-sur-Yvette, France
[2] Université Paris Diderot, AIM, Sorbonne Paris Cité, CEA, CNRS, F-91191 Gif-sur-Yvette, France
[3] Max-Planck-Institut für Sonnensystemforschung, Justus-von-Liebig-Weg 3, 37077, Göttingen, Germany
[4] Department of Astronomy, New Mexico State University, P.O. Box 30001, MSC 4500, Las Cruces, NM 88003-8001, USA
[5] Physics Department, New Mexico Institute of Mining and Technology, 801 Leroy Place, Socorro, NM 87801, USA
[6] Department of Astronomy, Yale University, 52 Hillhouse Avenue, New Haven, CT 06511, USA
[7] Instituto de Astrofísica de Canarias, E-38200, La Laguna, Tenerife, Spain
[8] Universidad de La Laguna, Dpto. de Astrofísica, E-38205, La Laguna, Tenerife, Spain

Rodrigues et al. 2017, and references therein) Therefore, the scaling relations should be studied carefully and it is crucial to test their accuracy.

One way of testing the validity of seismic scaling relations is to compare the values of stellar mass and radii from seismology with results from independent methods. Gaulme et al. (2016) and Rawls et al. (2016) considered eclipsing binary systems with at least one giant component. For such systems, the mass and radius of both components can be accurately measured by combining photometry and spectroscopy. Indeed, the simultaneous modeling of the eclipses and the radial velocities allows to retrieve, on the one hand, the orbital parameters of the systems such as eccentricity, inclination, longitude of periastron, and semi-major axis, and on the other hand, global properties of its components. On a sample of 10 systems, Gaulme et al. (2016) compared the values of masses and radii obtained through this method (the dynamical values) with the seismic inferences. They found that the latter were systematically overestimated by $\sim 5\%$ for the radius and $\sim 15\%$ for the mass.

To investigate further this result, we aim at extending this set of stars to a larger fraction of multiple systems containing at least one pulsating red giant. Hence, we have identified 16 new binary systems with a giant component. All of them have been observed by *Kepler*. We combine the photometric light curves with spectroscopic follow-up observations from the ARCES spectrometer on the 3.5m telescope at Apache Point Observatory (APO), New Mexico, and the HERMES spectrometer (Raskin et al. 2011) on the 1.2m Mercator Telescope in La Palma to measure the dynamical masses and radii and compare them to the seismic inferences. The latter were obtained from *Kepler* data prepared with KADACS software (García et al. 2011), which was analyzed by the asteroseimic pipeline A2Z (Mathur et al. 2010).

In this work, we show our preliminary analysis of KIC 4054905. Section 2 details how we measured the dynamical mass and radius of the giant. In section 3, we explain how we prepared the light curve from which the global seismic parameters were computed. Then, we show the result of the comparison between seismic estimates and dynamical measurements. Finally, in section 4, we present the perspectives of our work and the suggestions to improve the scaling relations.

2 Measuring the dynamical masses and radii

The photometric light curves were obtained from the Target Pixel Files, which we integrated to produce time series. They were then flattened so that only the eclipses remain. We modeled the orbit with the JKTEBOP code (Southworth 2013), which uses a Markov chain Monte Carlo (MCMC) method to fit the sum of the fractional radii $\frac{R_1+R_2}{a}$, where R_1, R_2 and a are the radius of the giant, that of the companion and the semi-major axis, respectively, the ratio of the radii $\frac{R_2}{R_1}$, the orbital inclination and eccentricity, the longitude of periastron, the brightness ratio $\left(\frac{T_{\mathrm{eff},2}}{T_{\mathrm{eff},1}}\right)^4$, orbital period and reference time for the primary eclipse. Concerning the eclipses, we used the same convention as Gaulme et al. (2016), i.e., the primary eclipse refers to the companion eclipsing the giant. We set its orbital phase to 0. For the limb darkening of the companion, we assumed a linear law. We did not fit it because of the small influence it has compared to that of the giant and the resulting difficulty to converge on this parameter. Concerning the giant, we assumed a quadratic law and computed guesses with the JKTLD routine, which uses limb-darkening tables to interpolate them in the *Kepler* bandpass. We fixed the order-2 coefficient and fitted the linear one.

We combined the modeling of the eclipses with a two-year spectroscopic follow-up done mostly at APO. We used the Echelle spectrometer ARCES located at the 3.5m telescope. The data was reduced as described by Rawls et al. (2016). We used the broadening function (BF) technique as outlined by Rucinski (2002) to extract the radial velocities. This method relies on solving a convolution equation and requires a template spectrum to compare the positions of the spectral lines. In this work, we used templates from the PHOENIX stellar atmosphere model Husser et al. (2013). Since the giant is in general three to ten times more luminous than its companion, its lines are significantly easier to detect. This is why we used a template of a main-sequence star to compute the BF. Its temperature was chosen the closest to that of the companion. Combining radial velocities to the eclipses allows to break the degeneracy in the model. Thus, it is possible to obtain the semi-major axis of the system and the separate masses and radii of each component. Figure 1 illustrates the modeling of combined eclipses and radial velocities of KIC 4054905. For this star, the dynamical analysis gives $M_{\mathrm{giant}} = 1.05\ M_{\odot}$ and $R_{\mathrm{giant}} = 8.24\ R_{\odot}$.

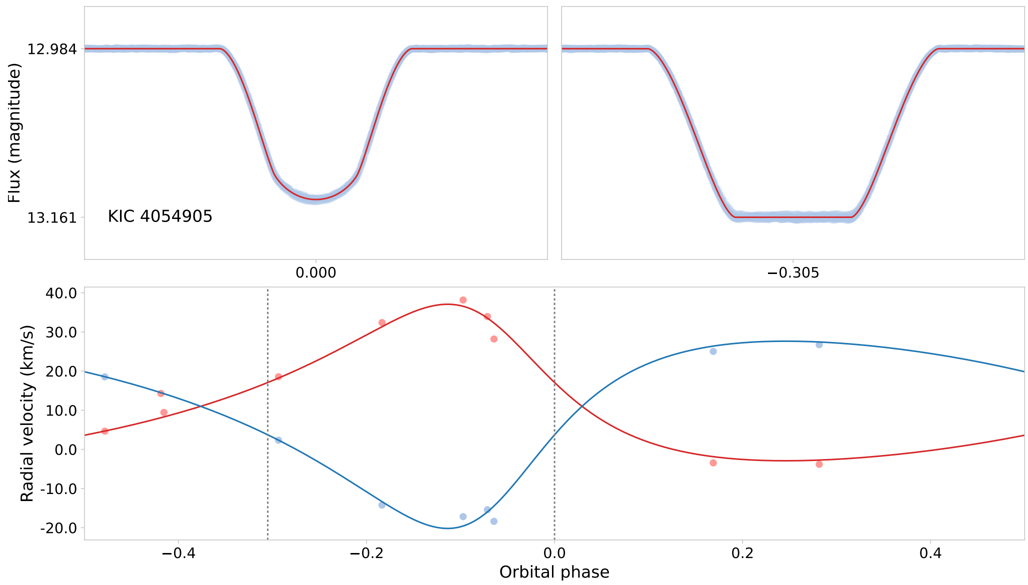

Fig. 1. Eclipses and radial velocities of KIC 4054905. *Top left panel:* Zoom on the primary eclipse (companion eclipsing the giant. The blue dots represent the processed phase-folded *Kepler* light curve and the red line, the fit of JKTEBOP. *Top right panel:* zoom on the secondary eclipse (giant eclipsing the companion). *Bottom panel:* Radial velocities of the components of the systems. The red and blue dots represent the measurements done for the giant and the companion at APO, respectively. The red and blue solid lines represent the fit of JKTEBOP for each component, respectively. The vertical dotted lines the orbital phases corresponding to the primary and second eclipse.

3 Seismic inferences

We prepared the light curves from the *Kepler* Target Pixel Files as described by García et al. (2011). In this procedure, we inserted an intermediate step to remove the eclipses from the signal. To that end, we used the Eclipsing Binary Catalog, which provides information on eclipses timing and durations (Abdul-Masih et al. 2016). Removing the eclipses in the time series generates gaps in the data. To eliminate their signature, we inpainted the light curves (García et al. 2014; Pires et al. 2015). From the obtained time series, we computed the power spectra and used the pipeline A2Z to compute the global seismic parameters $\Delta\nu$ and $\nu_{\max}$. For KIC 4054905, we obtained $M_{\rm seismo} = 1.3 \pm 0.1\ M_\odot$ and $R_{\rm seismo} = 9.3 \pm 0.7\ R_\odot$.

Figure 2 presents the comparison between dynamical measurements and seismic estimates of masses and radii for the sample of Gaulme et al. (2016) and KIC 4054905. Our preliminary result is in good agreement with their study since both mass and radius of our star are over estimated by the scaling relations.

4 Conclusion

Our preliminary result is in agreement with those of Gaulme et al. (2016), suggesting that the scaling relations systematically overestimate mass and radius. However, more spectroscopic observations of the other targets of our sample are needed to draw more robust conclusions. Extending the sample is crucial to test their accuracy. The departure of red giants from the asymptotic regime was already discussed by Mosser et al. (2013). Recently, Rodrigues et al. (2017) proposed to improve the scaling relations by taking into account that red giants depart from homology to the Sun. Other reasons for discrepancy between dynamical measurements and seismic estimates should also be investigated, such as the effect of other observables. For instance, Corsaro et al. (2017) found of metallicity influencing granulation in stellar clusters. Thus, considering new observables is important to better understand stellar dynamics and asteroseismology.

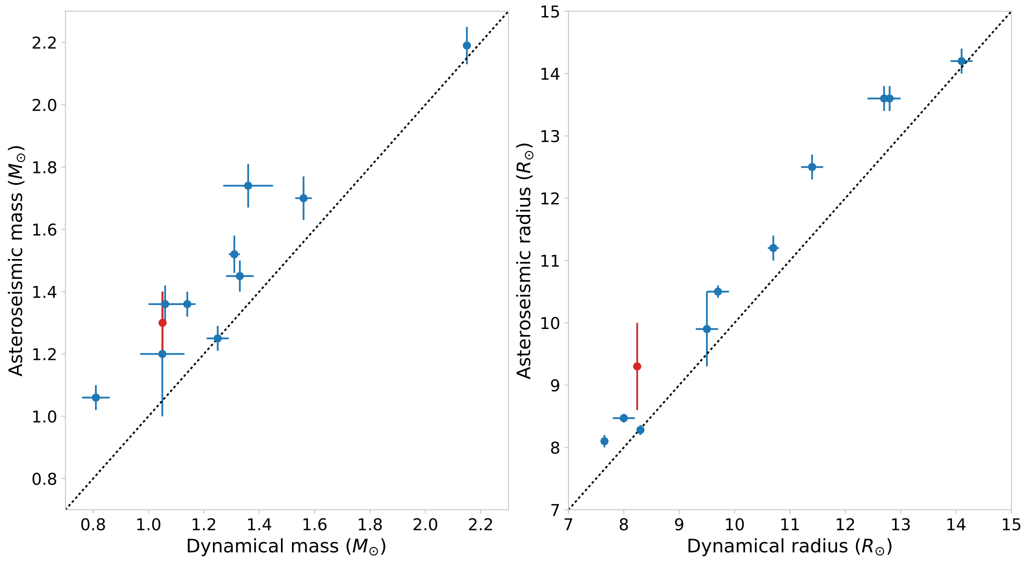

Fig. 2. Comparison between dynamical measurements and seismic inferences of masses and radii. *Left panel:* Seismic masses as a function of dynamical masses. The blue dots correspond to the sample of Gaulme et al. (2016) and the red dot, to our measurements on KIC 4054905. The grey dotted line represents the line on which $M_{\rm seismo} = M_{\rm dyn}$. *Right panel:* Seismic radii as a function of dynamical radii.

We acknowledge the work of the team behind *Kepler*. Funding for the *Kepler* Mission is provided by NASA's Science Mission Directorate. We thank the technical team as well as the observers of the HERMES spectrograph and Mercator Telescope, operated on the island of La Palma by the Flemish Community, at the Spanish Observatorio del Roque de los Muchachos of the Instituto de Astrofísica de Canarias. The authors acknowledge S. Mathur for useful comments and discussion during the project. M.B. and P.G. acknowledge support from NASA ADAP grant NNX14AR85G. M.B. and R.A.G. received funding from the CNES. PGB acknowledges the support of the Spanish Ministry of Economy and Competitiveness (MINECO) under the programme 'Juan de la Cierva' (IJCI-2015-26034).

References

Abdul-Masih, M., Prša, A., Conroy, K., et al. 2016, AJ, 151, 101
Baglin, A., Auvergne, M., Boisnard, L., et al. 2006, in COSPAR Meeting, Vol. 36, 36th COSPAR Scientific Assembly
Beck, P. G., Bedding, T. R., Mosser, B., et al. 2011, Science, 332, 205
Beck, P. G., Montalban, J., Kallinger, T., et al. 2012, Nature, 481, 55
Borucki, W. J., Koch, D., Basri, G., et al. 2010, Science, 327, 977
Brown, T. M., Gilliland, R. L., Noyes, R. W., & Ramsey, L. W. 1991, ApJ, 368, 599
Corsaro, E., Mathur, S., García, R. A., et al. 2017, A&A, 605, A3
García, R. A., Hekker, S., Stello, D., et al. 2011, MNRAS, 414, L6
García, R. A., Mathur, S., Pires, S., et al. 2014, A&A, 568, A10
Gaulme, P., McKeever, J., Jackiewicz, J., et al. 2016, ApJ, 832, 121
Husser, T.-O., Wende-von Berg, S., Dreizler, S., et al. 2013, A&A, 553, A6
Kjeldsen, H. & Bedding, T. R. 1995, Astrophysical Journal, 293, 87
Mathur, S., García, R. A., Régulo, C., et al. 2010, A&A, 511, A46
Mosser, B., Barban, C., Montalbán, J., et al. 2011, A&A, 532, A86
Mosser, B., Dziembowski, W. A., Belkacem, K., et al. 2013, A&A, 559, A137
Pires, S., Mathur, S., García, R. A., et al. 2015, A&A, 574, A18
Raskin, G., van Winckel, H., Hensberge, H., et al. 2011, A&A, 526, A69
Rawls, M. L., Gaulme, P., McKeever, J., et al. 2016, ApJ, 818, 108
Rodrigues, T. S., Bossini, D., Miglio, A., et al. 2017, MNRAS, 467, 1433
Rucinski, S. M. 2002, AJ, 124, 1746
Southworth, J. 2013, A&A, 557, A119

SF2A 2017
C. Reylé, P. Di Matteo, F. Herpin, É. Lagadec, A. Lançon, Z. Meliani, F. Royer (eds)

TOWARD THE FIRST STARS: HINTS FROM THE CEMP-NO STARS

A. Choplin[1]

Abstract. CEMP-no stars are iron-deficient, carbon-rich stars, with no or little s- and r-elements. Because of their very low iron content, they are often considered to be closely linked to the first stars. Their origin is still a matter of debate. Understanding their formation could provide very valuable information on the first stars, early nucleosynthesis, early galactic chemical evolution and first supernovae. The most explored formation scenario for CEMP-no stars suggests that CEMP-no stars formed from the ejecta (wind and/or supernova) of a massive source star, that lived before the CEMP-no star. Here we discuss models of fast rotating massive source stars with and without triggering a late mixing event just before the end of the life of the source star. We find that without this late mixing event, the bulk of observed CEMP-no stars cannot be reproduced by our models. On the opposite, the bulk is reproductible if adding the late mixing event in the source star models.

Keywords: stars: abundances – stars: massive – stars: interiors – stars: chemically peculiar – nucleosynthesis

1 Introduction

Carbon-enhanced metal-poor (CEMP) stars are iron-deficient stars with an excess of carbon compared to normal metal-poor stars. Most of these stars are also enriched in N, O, Na, Mg and other light elements. The CEMP-no stars (the term was introduced by Beers & Christlieb 2005) show no enhancements in s- (e.g. Sr) or r- elements (e.g. Eu), contrary to the CEMP-s or CEMP-r stars. The most iron-poor star known today is SMSS 0313-6708, a CEMP-no star with [Fe/H] $<$ 7.1 (Keller et al. 2014). This star, like other CEMP-no stars with almost no iron, was likely born very early in the universe. Understanding the origin of the CEMP-no stars will provide valuable clues on the first stars, early nucleosynthesis, first supernovae and early galactic chemical evolution.

It is commonly accepted that internal processes inside the CEMP-no stars (atomic diffusion, dredge-up...) cannot be fully responsible for the peculiar chemical composition of such stars. An external source is likely needed. The help of a binary companion to explain the chemical abundances of CEMP-no stars does not seem a reliable hypothesis because the binary fraction among CEMP-no stars is only about 20% (Hansen et al. 2016). An alternative is to rely on a massive *source star*, that lived before the CEMP-no star and enriched through winds and/or supernova the interstellar medium in which the CEMP-no star formed later on (this scenario has been discussed in different works, e.g. Umeda & Nomoto 2002; Meynet et al. 2006, 2010; Tominaga et al. 2014; Takahashi et al. 2014; Maeder & Meynet 2014).

Chiappini et al. (2006) and Chiappini et al. (2008) have shown that some abundances of normal metal-poor stars in the Milky Way halo can only be reproduced if there were very fast rotators among the first massive stellar generations. Here we try to see wether the ejecta of fast rotating massive source stars at very low metallicity can provide a material able to reproduce the observed chemical pattern of CEMP-no stars.

2 Results

We focus first on three source stars of 20, 32 and 60 $M_\odot$ at a metallicity $Z = 10^{-5}$ and with* $v_{\rm ini}/v_{\rm crit} = 0.7$. These models were computed with the stellar evolution code GENEC and are evolved until the end of the central silicon burning phase. The $^{12}C/^{13}C$ and [C/N] ratios in the wind ejected by the models are shown on Fig. 1

[1] Geneva Observatory, University of Geneva, Maillettes 51, CH-1290 Sauverny, Switzerland
*$v_{\rm crit}$ is the velocity at the equator at which the gravitational acceleration is exactly compensated by the centrifugal force.

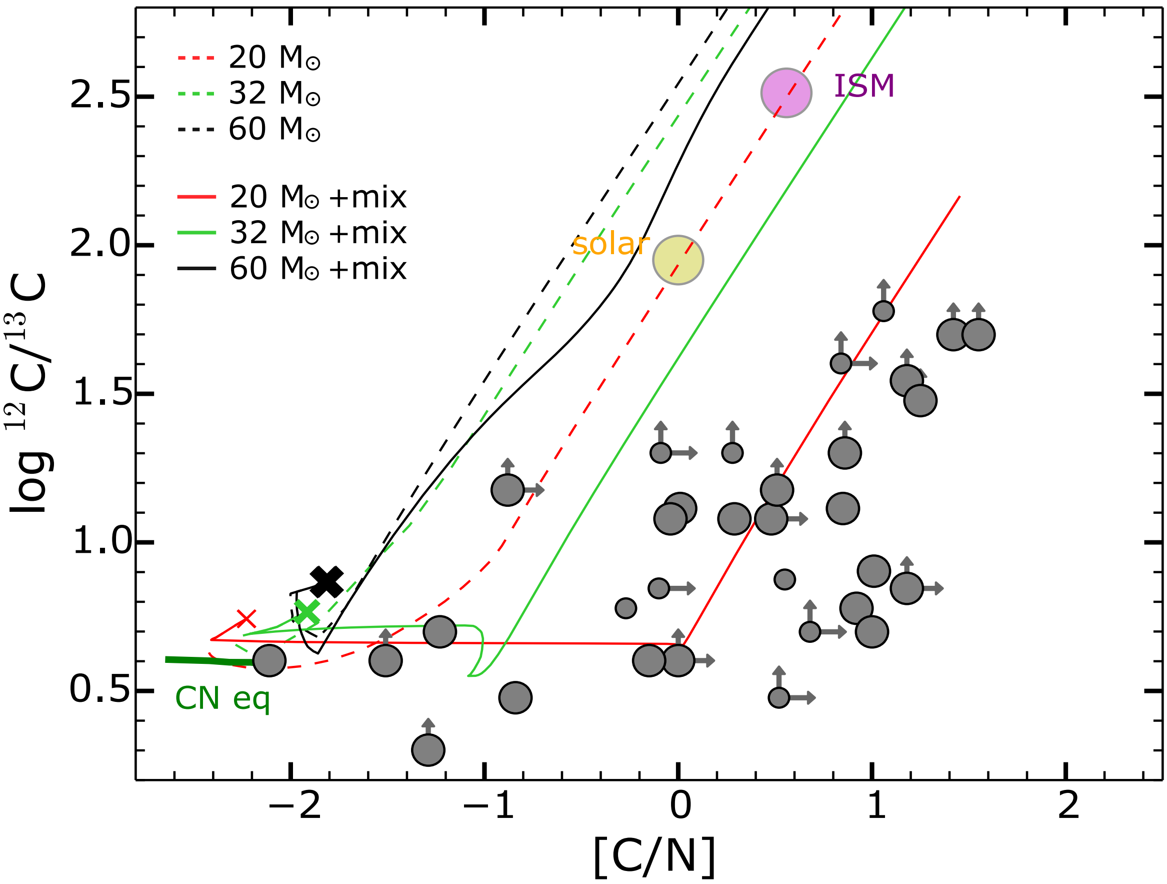

Fig. 1. Small/big grey circles are ratios observed at the surface of MS/RG CEMP-no stars with [Fe/H] < -2.5, [C/Fe] > 0.7 and [Ba/Fe] < 1 (observations from Christlieb et al. 2004; Beers et al. 2007; Johnson et al. 2007; Lai et al. 2008; Masseron et al. 2010; Allen et al. 2012; Norris et al. 2013; Spite et al. 2013; Yong et al. 2013; Cohen et al. 2013; Roederer et al. 2014; Hansen et al. 2015). The arrows indicate that only lower limits are deduced from spectroscopy. The yellow and purple circles represent the solar ratios and the ratio in an α-enhanced ISM, respectively. The crosses show the ratios in the wind at the end of evolution of 20, 32, and 60 $M_{\odot}$ fast-rotating source star models. The tracks represent the integrated ratios as more and more layers of the final structure are ejected and added to the wind. The thick green lines labelled 'CN eq' represent the ratios obtained in a single zone at CN-equilibrium for $30 < T < 80$ MK.

by the three colored crosses. The wind bears the signature of CN-processing (the crosses are close to the 'CN eq' line). This is because of the rotational mixing operating in the source star that brings the CN-processed material from inner layers to the surface of the source star. When mass loss occurs, this material is ejected. Dashed lines on Fig. 1 show the effect of the mass cut† for these models. As we move on the lines starting from the crosses, we see the effect of ejecting (and adding to the wind) deeper and deeper layer of the source star. At a given point, layers processed by helium burning are ejected. In such a region, ^{13}C and ^{14}N are depleted so that ^{12}C/^{13}C and [C/N] rise sharply.

Whatever the mass and the mass cut, the models cannot provide a material able to reproduce the bulk of observed CEMP-no stars. We have also found that slower rotators cannot reproduce the observed distribution (not shown on Fig. 1 for clarity).

A possibility to improve the fit is to rely on a late mixing event in the source star. This mixing event is described in details in Choplin et al. (2017). It intervenes during the carbon burning phase, about 200 yr before the end of the evolution, between the He- and H-burning shells of the source star. As schematically shown in Fig. 1, it suddenly brings extra ^{12}C from the He- to the H-shell, boosting the CN-cycle in the H-shell. After

†The mass cut delimits the part of the star that is expelled from the part that is locked into the remnant.

the mixing episode, it takes some time to the CN-cycle to go back to equilibrium. The ^{12}C/^{13}C ratio goes back to its equilibrium value ~ 10 times faster than C/N. The time left before the end of the evolution is sufficient for ^{12}C/^{13}C to go back to equilibrium but not sufficient for C/N. When evolution ends (nucleosynthesis is then stopped), there is a zone in the source star with log ^{12}C/^{13}C at equilibrium (about 0.6) but [C/N] above its equilibrium value of ~ -2.4. The solid lines in Fig. 1 show the same models as before but with the late mixing event in addition. Thanks to the mixing event discussed before, these models can give a material with a low ^{12}C/^{13}C and a high C/N (e.g. the solid red line). However, as the initial mass of the source star increase, the tracks are shifted to lower C/N. This is because in more massive source stars, the temperature in the H-shell is higher so that the CN-cycle is faster. Hence, at the end of the evolution, C/N in the H-shell is closer to its equilibrium value for more massive stars. In the end, only the 20 M$_\odot$ model can provide a material able to reproduce the bulk of observed CEMP-no stars.

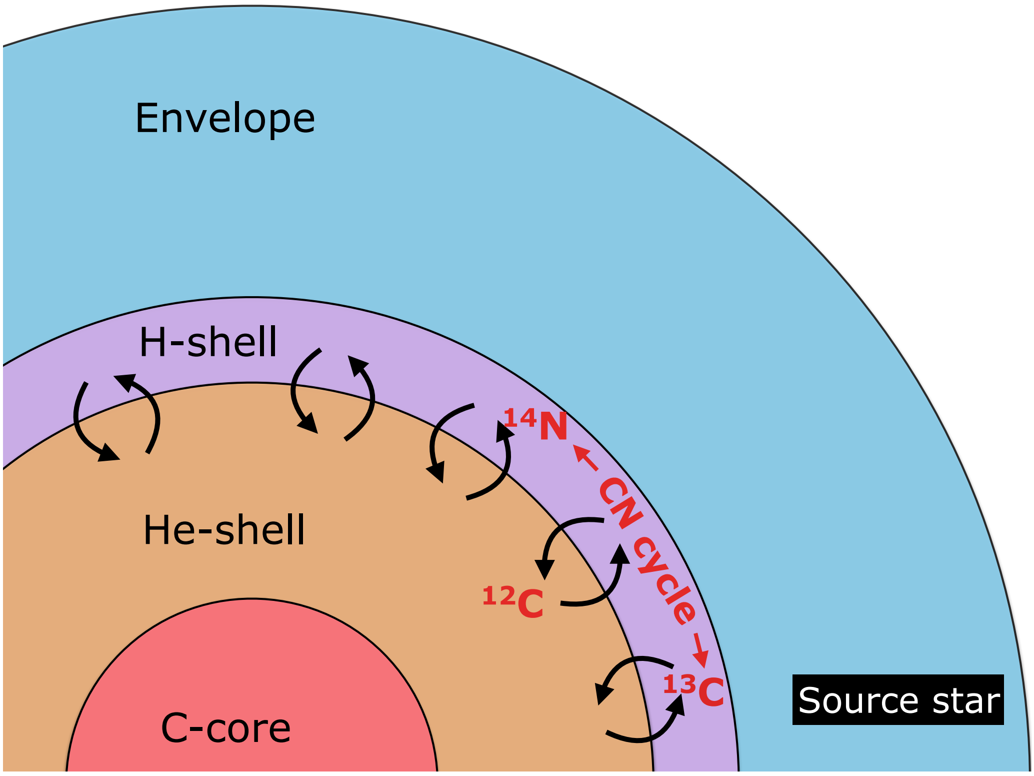

Fig. 2. Schematic view of the late mixing event in the source star, responsible for the tracks labelled '+mix' in Fig. 1.

3 Conclusions

We have investigated the origin of the CEMP-no stars through a comparison between the material ejected by fast-rotating massive source stars and the chemical composition observed at the surface of the CEMP-no stars. The 2D abundance plot ^{12}C/^{13}C vs. C/N leads to quite strong constraints on the kind of source star needed. 20-60 $M_\odot$ models of any initial rotation rate between 0 and 70 % of the critical velocity cannot provide a material able to reproduce the bulk of observed CEMP-no stars. A late mixing event operating in between the H- and He-shell of the source star, during the carbon burning phase improves the fit. However, in the end, only the 20 $M_\odot$ model gives a material with the right chemical composition, i.e. with ^{12}C/^{13}C close to equilibrium and C/N above its equilibrium value. The temperature in the H-shell of more massive source stars is higher so that the CN-cycle is faster and C/N goes back quicker to equilibrium after the mixing event.

We draw the following conclusions: (1) ~ 20 $M_\odot$ source stars might be better CEMP-no source stars than ~ 60 $M_\odot$ and (2) the late mixing event, artificially triggered in our models, might point toward a missing ingredient in current 1D stellar evolution codes. It might be that this extra mixing process just reflect a too poor description of the convective boundaries in 1D stellar evolution codes. In our code, these limits are sharp. However, multi-dimensional simulation of convective zones tend to show that these limits extend further (Meakin & Arnett 2007; Cristini et al. 2016). This might induce some extra mixing in the source star, especially between the H- and He-burning shell.

References

Allen, D. M., Ryan, S. G., Rossi, S., Beers, T. C., & Tsangarides, S. A. 2012, A&A, 548, A34

Beers, T. C. & Christlieb, N. 2005, ARA&A, 43, 531

Beers, T. C., Sivarani, T., Marsteller, B., et al. 2007, AJ, 133, 1193

Chiappini, C., Ekström, S., Meynet, G., et al. 2008, A&A, 479, L9

Chiappini, C., Hirschi, R., Meynet, G., et al. 2006, A&A, 449, L27

Choplin, A., Ekström, S., Meynet, G., et al. 2017, ArXiv e-prints

Christlieb, N., Gustafsson, B., Korn, A. J., et al. 2004, ApJ, 603, 708

Cohen, J. G., Christlieb, N., Thompson, I., et al. 2013, ApJ, 778, 56

Cristini, A., Meakin, C., Hirschi, R., et al. 2016, ArXiv e-prints

Hansen, T., Hansen, C. J., Christlieb, N., et al. 2015, ApJ, 807, 173

Hansen, T. T., Andersen, J., Nordström, B., et al. 2016, A&A, 586, A160

Johnson, J. A., Herwig, F., Beers, T. C., & Christlieb, N. 2007, ApJ, 658, 1203

Keller, S. C., Bessell, M. S., Frebel, A., et al. 2014, Nature, 506, 463

Lai, D. K., Bolte, M., Johnson, J. A., et al. 2008, ApJ, 681, 1524

Maeder, A. & Meynet, G. 2014, ApJ, 793, 123

Masseron, T., Johnson, J. A., Plez, B., et al. 2010, A&A, 509, A93

Meakin, C. A. & Arnett, D. 2007, ApJ, 667, 448

Meynet, G., Ekström, S., & Maeder, A. 2006, A&A, 447, 623

Meynet, G., Hirschi, R., Ekstrom, S., et al. 2010, A&A, 521, A30

Norris, J. E., Yong, D., Bessell, M. S., et al. 2013, ApJ, 762, 28

Roederer, I. U., Preston, G. W., Thompson, I. B., et al. 2014, AJ, 147, 136

Spite, M., Caffau, E., Bonifacio, P., et al. 2013, A&A, 552, A107

Takahashi, K., Umeda, H., & Yoshida, T. 2014, ApJ, 794, 40

Tominaga, N., Iwamoto, N., & Nomoto, K. 2014, ApJ, 785, 98

Umeda, H. & Nomoto, K. 2002, ApJ, 565, 385

Yong, D., Norris, J. E., Bessell, M. S., et al. 2013, ApJ, 762, 26

SF2A 2017
C. Reylé, P. Di Matteo, F. Herpin, É. Lagadec, A. Lançon, Z. Meliani, F. Royer (eds)

LARGE-SCALE MEASUREMENTS OF THE RED GIANT CORE ROTATION THROUGH ASTEROSEISMOLOGY

C. Gehan[1 1], B. Mosser[1] and E. Michel[1]

Abstract. Red giant stars are solar-like pulsators presenting mixed-modes. Such modes consist in a coupling between pressure waves propagating in the external convective envelope and gravity waves propagating in the radiative interior. Therefore, the red giant asteroseismology provides us with a direct view on their core and opens the possibility to monitor the evolution of their core rotation. Previous measurements of the mean core rotation revealed that angular momentum is efficiently transferred from the core to the envelope inside red giants, but the physical mechanisms at work are not yet fully understood. We thus need stronger observational constraints on the evolution of the red giant core rotation.
In this context, we developed an automated method to determine the mean core rotation of red giant branch stars observed with *Kepler*. This automated method is paving the way for the future PLATO data, representing hundreds of thousands of potential red giant oscillation spectra.
Results obtained for almost 1200 red giant branch stars indicate that the rate of the core rotation braking is lower than previoulsy estimated and does not seem to depend on the stellar mass.

Keywords: Stars: oscillations, - Stars: interior, - Stars: evolution, - Stars: rotation

1 Introduction

The *Kepler* NASA space mission has provided frequency oscillation spectra of unprecedent quality, opening the possibility to study the red giant core rotation. Red giants are evolved intermediate-mass stars, between 0.5 and 8 $M_{\odot}$. Hydrogen is exhausted in the core and is burning in a shell above the core. Red giants can lay in two evolutionary phases, the red giant branch (RGB) or the red clump. During the RGB phase, the star undergoes strong structural changes: the inert helium core contracts while the convective envelope deepens and extends, leading to a strong increase of the stellar radius and luminosity. The clump phase comes when the red giant starts burning helium in the core.
Red giant stars are solar-type pulsators: internal seismic waves are stochastically excited by the turbulent convection in the external envelope (De Ridder et al. 2009). They present mixed-modes, consisting in a coupling between pressure waves propagating in the convective envelope and gravity waves propagating in the radiative interior (Beck et al. 2011). This feature allows us to have a direct insight on their core, which is not the case for solar-type pulsators on the main sequence like the Sun.
Rotation strongly impacts the stellar structure and evolution by altering the chemical element mixing inside stars (Lagarde et al. 2012), but including rotation in stellar evolution models is still challenging. Models still predict central rotation rates at least ten times too large compared to asteroseismic measurements. It is thus of prime importance to know how internal rotation evolves in time. Moreover, measurements of the mean core rotation of almost 300 red giants have revealed that the red giant core is slowing down along the RGB, while the core is contracting (Mosser et al. 2012). This necessarily implies that a very efficient angular momentum transport from the core to the envelope is at work inside red giants. Magnetic fields, (Cantiello et al. 2014), mixed-modes (Belkacem et al. 2015a,b) or internal gravity waves (Fuller et al. 2014; Pinçon et al. 2017) stand among the physical mechanisms that can dissipate angular momentum. Nevertheless, no modelling based on such physical mechanisms can reproduce the measured orders of magnitude of the red giant core rotation. We thus need stronger observational constraints on the evolution of rotation inside evolved stars.

[1] Observatoire de Paris, LESIA, Université Pierre et Marie Curie, Université Paris Diderot, PSL

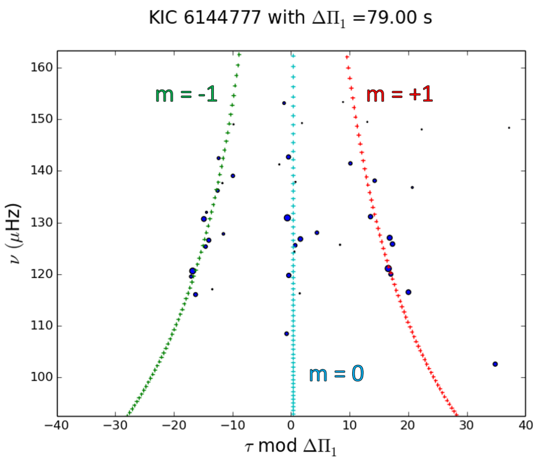

Fig. 1. Stretched period échelle diagram for a RGB star with an intermediate inclination angle. The rotational components are identified in an automatic way with a correlation of the observed spectrum with a synthetic one through Eq. 2.1. The color codes the azimuthal order: the $m = \{-1, 0, 1\}$ rotational components are represented in green, light blue and red respectively.

2 Automatic measurements of the red giant mean core rotation

Rotation has an effect on oscillation spectra which is similar to the Zeeman effect of a magnetic field on the energy levels of an atom: it lifts the degeneracy between oscillation modes having the same angular degree ℓ but different azimuthal orders m. We consider in this study dipole mixed-modes with a degree $\ell = 1$ as they mostly probe the red giant core (Goupil et al. 2013). In these conditions rotation generates three rotational components having azimuthal order values $m \in \{-1, 0, 1\}$.

We can build échelle diagrams based on stretched periods τ that reveal the rotational components (Mosser et al. 2015; Gehan et al. 2016a,b). The number of visible rotational components depends on the stellar inclination: the two components associated to $m = \pm 1$ are present when the star is seen equator-on, all the three rotational components are visible for intermediate inclination configurations, and only the rotational component associated to $m = 0$ can be observed when the star is seen pole-on.

The stretched period spacing between dipole mixed-modes having the same azimuthal order depends on the mean core rotational splitting $\delta\nu_{\mathrm{rot,core}}$ (Mosser et al. 2015). It varies as

$$\Delta\tau_{\mathrm{m}} = \Delta\Pi_1 \left(1 + 2\, m\, \zeta\, \frac{\delta\nu_{\mathrm{rot,core}}}{\nu}\right), \tag{2.1}$$

where $\Delta\Pi_1$ is the asymptotic period spacing of pure dipole gravity modes, ζ defines the stretching of the mode periods, and ν are the mode frequencies. The measurement of $\delta\nu_{\mathrm{rot,core}}$ gives an estimate of the mean core angular velocity (Goupil et al. 2013; Mosser et al. 2015) through

$$\delta\nu_{\mathrm{rot,core}} \simeq \frac{1}{2} \left\langle \frac{\Omega_{\mathrm{core}}}{2\pi} \right\rangle. \tag{2.2}$$

We developed a method allowing an automated identification of the rotational components based on the correlation of the observed spectrum with synthetic ones constructed through Eq.2.1 (Gehan et al. 2018).

3 Constraining the rate of the core braking

We applied our method to 1714 RGB stars presenting a large mass range from 1 $M_\odot$ up to 2.5 $M_\odot$ (Gehan et al. 2018). Stellar masses were estimated from the asteroseismic global parameters $\Delta\nu$ and ν_{max} (Kjeldsen & Bedding 1995; Mosser et al. 2013) through

$$\frac{M}{M_\odot} = \left(\frac{\nu_{\mathrm{max}}}{\nu_{\mathrm{max},\odot}}\right)^3 \left(\frac{\Delta\nu}{\Delta\nu_\odot}\right)^{-4} \left(\frac{T_{\mathrm{eff}}}{T_\odot}\right)^{3/2}, \tag{3.1}$$

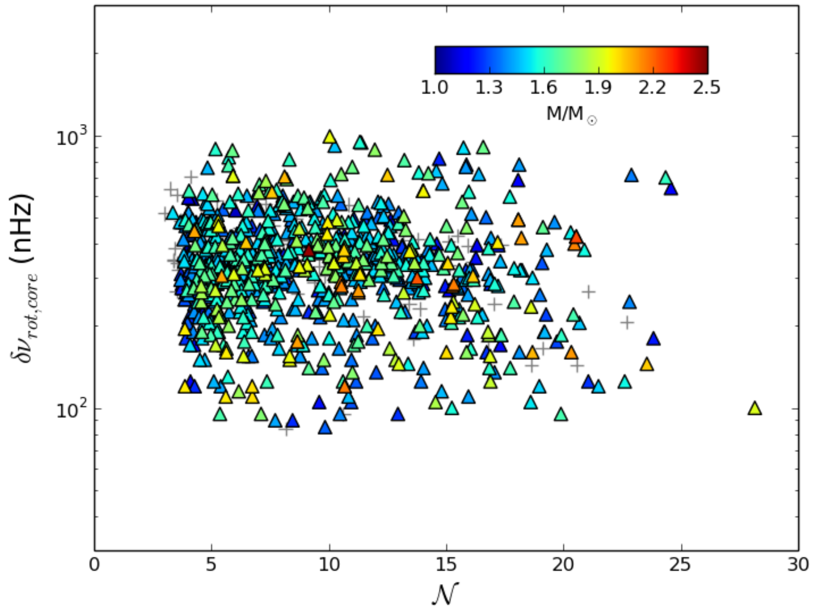

Fig. 2. Mean core rotational splitting as a function of the mixed-mode density, in semi-log scale. Gray crosses represent the measurements of Mosser et al. (2012). Colored triangles represent the measurements obtained in this study (Gehan et al. 2018), the color coding the mass estimated from the asteroseismic global parameters. The mixed-mode density increases along the evolution on the red giant branch.

where $\Delta\nu$ is the large separation of pure pressure modes, and $\nu_{\max}$ is the frequency of maximum oscillation power. $\nu_{\max,\odot} = 3050\,\mu$Hz, $\Delta\nu_\odot = 135.5\,\mu$Hz and $T_\odot = 5777\,K$ are the solar values chosen as references.
Our method led to the identification of the rotational components for 69% of cases. As it is not possible to retrieve information on the core rotation of stars seen pole-on, we obtained 875 mean core rotation measurements, with a typical uncertainty of about 10 nHz (Fig. 2).
We considered the number of gravity modes per $\Delta\nu$-wide frequency range as a proxy of stellar evolution (Gehan et al. 2018). This mixed-mode density is defined as

$$\mathcal{N} = \frac{\Delta\nu}{\Delta\Pi_1\,\nu_{\max}^2}. \tag{3.2}$$

The large dataset considered in this study covering an extended mass range allowed us to investigate how the rate of the core braking depends on the stellar mass. We thus selected stars in four different mass ranges and fitted a relonship of the type

$$\delta\nu_{\text{rot,core}} \propto \mathcal{N}^a. \tag{3.3}$$

The exponents a are summarized in Table 1 as a function of the mass range considered. The present result indicates that the braking rate of the core rotation does not seem to depend on the stellar mass (Fig. 3). When applying Eq.3.3 to the measurements for RGB stars made by Mosser et al. (2012), we obtain a mean braking rate much higher than the value measured in this study (Table 2). This discrepancy is mainly due to sample effects. Indeed, we now have a RGB sample about 10 times larger than Mosser et al. (2012), thus more significant from a statistical point of view. The result obtained provides a more precise estimate of the slope of the core braking (Fig. 3). Nevertheless, the lower slope of the core braking measured in this study does not call into question the results of Mosser et al. (2012) predicting an efficient angular momentum transport inside red giant cores.

4 Conclusions

Disentangling rotational splittings from mixed modes is now possible in a simple way, opening the era of large-scale measurements of the core rotation of red giants. We developed a method allowing an automated

Table 1. Slope of the core braking as a function of the mixed-mode density $\mathcal{N}$ for different mass ranges

M	a
$M \leq 1.4M_{\odot}$	-0.01 ± 0.05
$1.4 < M \leq 1.6M_{\odot}$	0.08 ± 0.04
$1.6 < M \leq 1.9M_{\odot}$	-0.07 ± 0.07
$M > 1.9M_{\odot}$	-0.05 ± 0.13

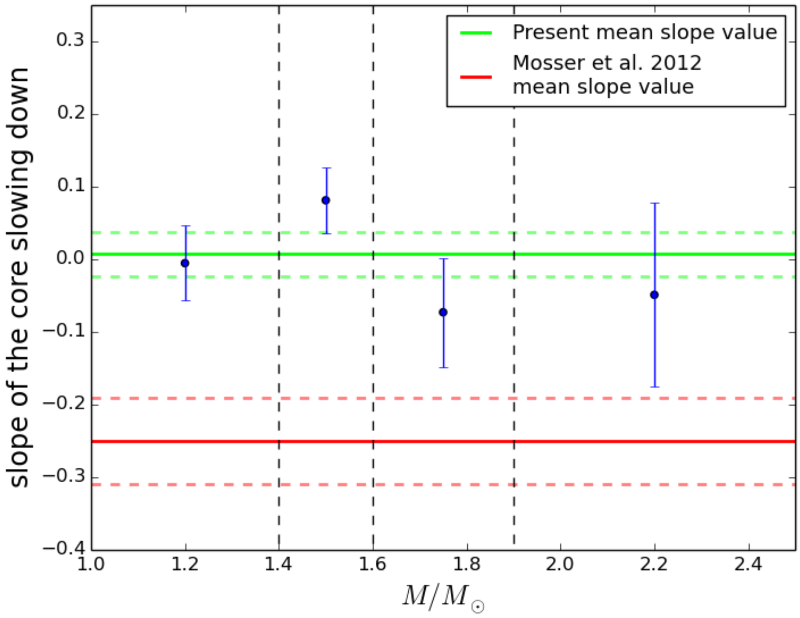

Fig. 3. Slopes of the core braking when considering the evolution of the core rotation as a function of the mixed-mode density for different mass ranges. Our measurements are represented in blue with the associated error bars. Vertical black dashed lines represent the boundaries between the different mass ranges considered. The green continuous and dashed lines indicate the mean value of the braking efficiency measured in this study and the associated error bars, respectively. The red continuous and dashed lines indicate the mean braking efficiency and the associated error bars estimated from Mosser et al. (2012) measurements, respectively.

identification of the dipole gravity-dominated mixed-modes split by rotation, providing us with a measurement of the mean core rotational splitting $\delta\nu_{\mathrm{rot,core}}$. The method satisfactorily identified the rotational components of 1181 red giant branch stars, representing a success rate of 69% and providing us with 875 $\delta\nu_{\mathrm{rot,core}}$ measurements. This large dataset including stars with masses as high as 2.5 $M_{\odot}$ allowed us to show that the slope of the core braking does not seem to depend on the stellar mass, but also that this slope is much lower than what was estimated by Mosser et al. (2012). Nevertheless, this measurement does not go against a very efficient angular momentum transport inside red giant cores. This result suggests that the efficiency of the mechanism transporting angular momentum inside red giant branch stars should increase with the stellar mass in order to compensate simultaneously the stronger differential rotation which is expected to develop in higher mass stars and their faster temporal evolution. Further investigation on the efficiency of the angular momentum transport inside red giants is necessary, through modelling of the evolution of the core inertia depending on the stellar

Table 2. Slope of the core braking as a function of the mixed-mode density $\mathcal{N}$ for Mosser et al. (2012) red giant branch stars. a_{2012} is the slope estimated from Mosser et al. (2012) measurements, a is the slope measured in this study.

a_{2012}	a
-0.25 ± 0.06	0.01 ± 0.03

mass.

We acknowledge financial support from "Programme National de Physique Stellaire" (PNPS) of CNRS/INSU, France.

References

Beck, P. G., Bedding, T. R., Mosser, B., et al. 2011, Science, 332, 205
Belkacem, K., Marques, J. P., Goupil, M. J., et al. 2015a, A&A, 579, A30
Belkacem, K., Marques, J. P., Goupil, M. J., et al. 2015b, A&A, 579, A31
Cantiello, M., Mankovich, C., Bildsten, L., et al. 2014, ApJ, 788, 93
De Ridder, J., Barban, C., Baudin, F., et al. 2009, Nature, 459, 398
Fuller, J., Lecoanet, D., Cantiello, M., et al. 2014, ApJ, 796, 17
Gehan, C., Mosser, B., & Michel, E. 2016a, ArXiv e-prints
Gehan, C., Mosser, B., & Michel, E. 2016b, ArXiv e-prints
Gehan, C., Mosser, B., & Michel, E. 2018, in prep.
Goupil, M. J., Mosser, B., Marques, J. P., et al. 2013, A&A, 549, A75
Kjeldsen, H. & Bedding, T. R. 1995, A&A, 293, 87
Lagarde, N., Decressin, T., Charbonnel, C., et al. 2012, A&A, 543, A108
Mosser, B., Goupil, M. J., Belkacem, K., et al. 2012, A&A, 548, A10
Mosser, B., Michel, E., Belkacem, K., et al. 2013, A&A, 550, A126
Mosser, B., Vrard, M., Belkacem, K., et al. 2015, A&A, 584, A50
Pinçon, C., Belkacem, K., Goupil, M. J., et al. 2017, ArXiv e-prints

SF2A 2017
C. Reylé, P. Di Matteo, F. Herpin, É. Lagadec, A. Lançon, Z. Meliani, F. Royer (eds)

NON-ADIABATIC OSCILLATIONS OF FAST-ROTATING STARS: THE EXAMPLE OF RASALHAGUE

G. M. Mirouh[1 3], D. R. Reese[2], M. Rieutord[3] and J. Ballot[3]

Abstract. Early-type stars generally tend to be fast rotators. In these stars, mode identification is very challenging as the effects of rotation are not well known. We consider here the example of α Ophiuchi, for which dozens of oscillation frequencies have been measured. We model the star using the two-dimensional structure code ESTER, and we compute both adiabatic and non-adiabatic oscillations using the TOP code. Both calculations yield very complex spectra, and we used various diagnostic tools to try and identify the observed pulsations. While we have not reached a satisfactory mode-to-mode identification, this paper presents promising early results.

Keywords: asteroseismology, stars:rotation

1 Introduction

In many early-type (O-,B- and A-type) stars, the κ-mechanism excites both pressure and gravity modes. These stars are also usually fast rotators, with an average $v \sin i \sim 100 - 200$km s^{-1} (Royer 2009). The impact of this rotation is twofold: the star is flattened by the centrifugal force, while the Coriolis acceleration modifies the mode properties. Both of those effects scramble the oscillation spectra and make mode identification much harder, requiring two-dimensional stellar models and oscillation calculations.

In this work, we extend the work by Mirouh et al. (2013) by using the so-called forward approach to model the fast rotator Rasalhague (α Ophiuchi). We model the star using the two-dimensional code ESTER that fully takes rotation into account, but leaves out mass loss and chemical diffusion in the star, and then compute the non-perturbative oscillation spectrum in the same geometry using the TOP program. Due to the high resolution used to describe the stellar interior and the modes, this typically yields several hundreds of modes, among which we need to select the most relevant candidates for identification. Another approach consists in looking for regular patterns in the oscillation spectrum: because of the effects of rotation, theoretically-predicted patterns (Lignières & Georgeot 2009) went long unnoticed, until García Hernández et al. (2015) was able to find a large separation in a small sample of stars and link it to stellar properties.

2 Rasalhague

Our study case is the A-type star Rasalhague. Interferometry showed that the star is seen almost equator-on, with a ratio between the equatorial and polar radii of 1.2, i.e. $R(\text{pole}) = 1.2R(\text{equator})$ (Zhao et al. 2009). Its mass has been constrained by means of its orbiting companion (Hinkley et al. 2011) and interferometry to $M \sim 2.18 - 2.4M_\odot$. Moreover, fifty-seven oscillation frequencies, ranging from 1.768 to 48.347 c/d, have been measured with the asteroseismology mission MOST (Monnier et al. 2010).

We compute an ESTER model (Espinosa Lara & Rieutord 2013; Rieutord et al. 2016) that fits the luminosity and the equatorial and polar radii, the properties of which are summarized in table 1. This model is the same as the one presented in Mirouh et al. (2013)

[1] SISSA - International School for Advanced Studies, via Bonomea 265, I-34136 Trieste, Italy
[2] LESIA, Observatoire de Paris, PSL Research University, CNRS, Sorbonne Universités, UPMC Univ. Paris 06, Univ. Paris Diderot, Sorbonne Paris Cité, 5 place Jules Janssen, F-92195 Meudon Cedex, France
[3] IRAP, Université de Toulouse, CNRS, UPS, CNES, 14 avenue Edouard Belin, F-31400 Toulouse, France

Ω/Ω_K	0.624	$T_{\rm eff}(p)(K)$	9177
$M/M_\odot$	2.22	$T_{\rm eff}(e)(K)$	7731
X_c/X	0.3685	$R(p)/R_\odot$	2.388
X	0.7	$R(e)/R_\odot$	2.858
Z	0.02	$V_{\rm eq}({\rm km.s}^{-1})$	240
		$L/L_\odot$	31.1

Table 1. Properties of our model for Rasalhague (α Ophiuchi). The left part of the table contains the input parameters of the model, while the right part lists the quantities matched to the quantities observed for the star.

3 Adiabatic oscillations

The eigenvalue problem of adiabatic oscillations is solved with the TOP code (Reese et al. 2009) for modes with azimuthal orders $-4 \leq m \leq 4$, in the range of frequencies in which modes are observed. We find g modes and p modes modified by rotation, and we can clearly distinguish these two populations in the spectra (see Figure 1).

To select the modes that might be seen from Earth, we compute the mode visibilities, following Reese et al. (2013). As the mode amplitudes cannot be derived from a linear calculation, we need to normalize the eigenmodes. For this purpose, we normalize all our solutions by max $||\boldsymbol{\xi}||^2 \, (\omega + m\Omega)^2$, where $\boldsymbol{\xi}$ is the Lagrangian displacement and $(\omega + m\Omega)$ the corotating mode frequency (Reese et al. 2017). We find that g modes are the least visible, as one would expect, considering they probe deep layers of the star and are usually evanescent towards the surface. Located near the surface, p modes are much more visible.

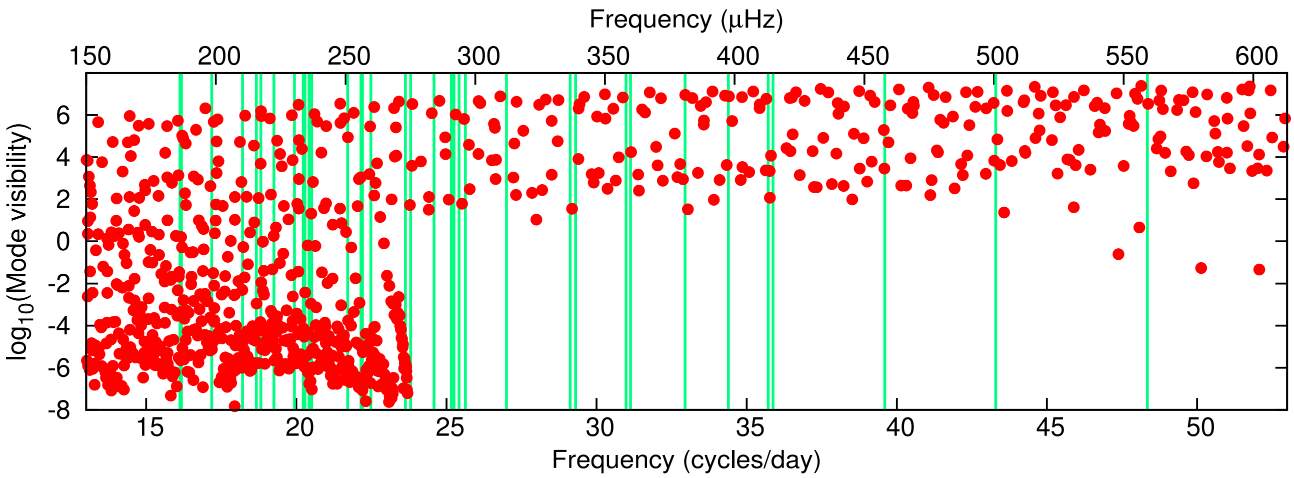

Fig. 1. Mode visibilities of $m = 0$ modes, obtained through adiabatic calculations. The low-frequency low-visibility clump corresponds mostly to g modes, while the higher-visibility strip spanning the whole frequency range corresponds to p modes. Each vertical green line corresponds to a frequency measured by Monnier et al. (2010).

We also compute the thermal dissipation rates using the quasi-adiabatic approximation (Unno et al. 1989), which yields only linearly stable modes. Using this method, the more visible p modes appear to be more damped than the g modes. This conundrum seems to prevent the identification of the modes.

4 Non-adiabatic oscillations

In an attempt to improve our description of the modes, we use the non-adiabatic version of TOP (Reese et al. 2016). This calculation is much more demanding numerically but results in complex eigenvalues that include both the modes' frequencies and growth rates. While the mode visibilities present the same properties as that of the adiabatic modes shown in figure 1, we are able to find amplified modes. Figure 2 shows the growth rates of the modes. Keeping only the most visible amplified modes does not seem to allow a direct identification of the modes, but fine tuning the models might lead to a better match. The ESTER models also suffer from a couple of limitations that may affect our calculation: as of now, the code does not implement evolution but determines the stellar structure at a given time; it also leaves aside any surface convection. As this prevents us from describing accurately the transfer of heavy elements from the core to the envelope due to core recession or diffusive effects along the main-sequence evolution, and results in a two-domain chemical composition with a depleted core and a homogeneous envelope, it may impact individual eigenmodes, and especially the g modes that probe deep layers in the star.

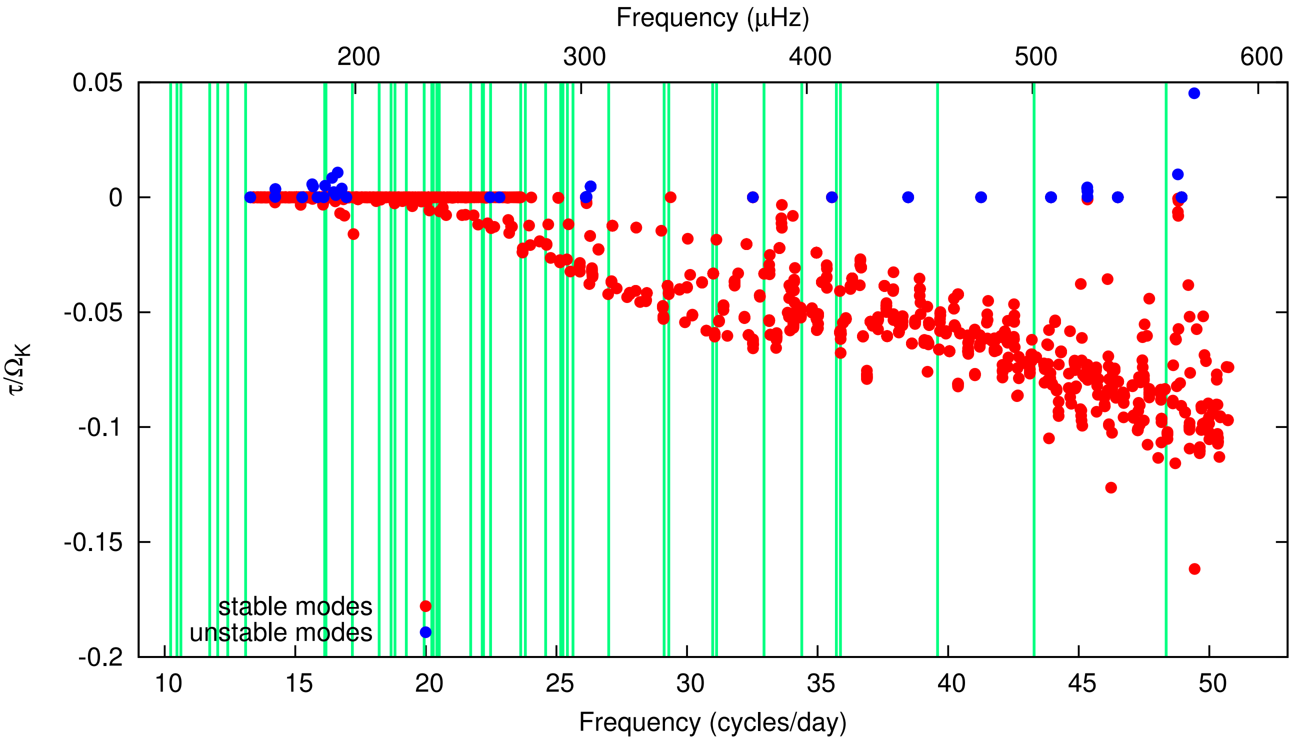

Fig. 2. Damping rates for the axisymmetric modes ($m = 0$) obtained through the non-adiabatic calculation. We find amplified g and p modes, most of the latter seem to follow a regular pattern.

We also find a series of amplified modes that seem spaced by a regular separation. However, this separation is not exactly constant ($\sim 30\mu$Hz) and does not seem to match the one uncovered by García Hernández et al. (2015) ($20 \pm 1\mu$Hz). When checking the nature of the modes, it appears that these amplified modes are high-degree gravity modes, and not the island pressure modes hypothesized by Lignières & Georgeot (2009).

Two-dimensional non-adiabatic calculations are still at an early stage, and the needed resolution, associated with the high number of variables and equations involved, impact the precision of the solutions. To improve the numerical convergence, we decide to split the star in two domains: we solve the perturbed equations using the adiabatic approximation in the inner part of the star, while the full non-adiabatic equations are solved in the outer part. For a first exploration, we set the Lagrangian perturbation of entropy to zero at the interface between the two domains. Figure 3 shows the dispersion of the solutions for various sizes of the inner adiabatic domain, for the p mode at $f = 424.378\mu$Hz when using slightly different input guesses.

We see that as we move the interface outwards, the solutions first get closer to the average value (that we suppose to be correct): this is explained by the disappearance of numerical errors, as the very small δs is no longer computed in the inner part of the star but set to zero by hand. However, when the adiabatic region becomes larger, the growth rate gradually falls to zero, as we start neglecting non-adiabatic effects that are important in outer layers.

5 Conclusions and future prospects

In this work, we computed a two-dimensional model and both the adiabatic and non-adiabatic oscillations of the fast-rotating δ Scuti star α Ophiuchi, in order to identify the observed oscillation frequencies. Because of the complexity of the oscillation spectrum, and the high number of calculated eigenmodes, we computed the

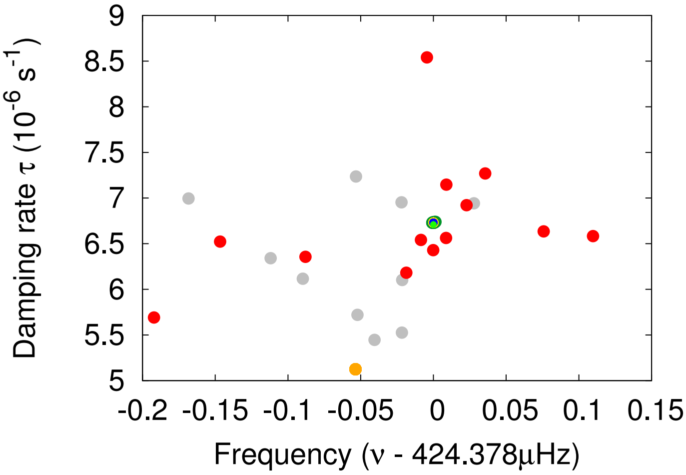

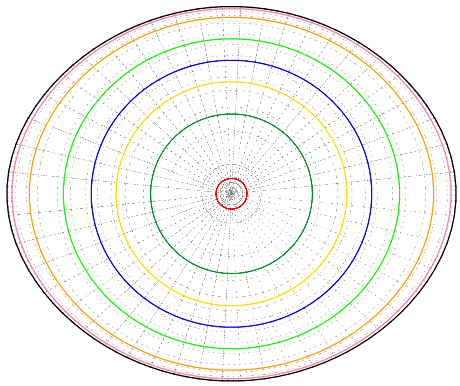

Fig. 3. The left plot shows the dispersion for the split calculation. We place the adiabatic inner domain/non-adiabatic outer domain interface at various depths, shown on the meridional cut on the right plot. The colours of the symbols correspond to those of the interfaces: the grey points corresponding to the full non-adiabatic calculation, while the dark green, yellow, blue and green dots overlap. We omit the result of the fully adiabatic calculation, which would have $\tau = 0$.

damping rates and mode visibilities in order to narrow down the range of possible matches between calculated and observed modes. The adiabatic calculation, using the so-called quasi-adiabatic approximation predicts only damped modes. This is due to a poor description of the modes near the stellar surface. Using a non-adiabatic calculation allows us to find amplified modes. As we cannot predict the amplitude of the modes, we normalize them and compute their visibilities. Using these two diagnostics, we are able to select only a reasonably small subsample of the whole synthetic spectrum, that we compare to the observations. At this point, we were unable to identify individual frequencies or find regular patterns that match the observations. This may come from the numerical issues raised by the non-adiabatic calculation or the limitations of the ESTER stellar models. Improving both of these aspects will be necessary to make the oscillation growth rates and the rotating star structures more reliable and reach a satisfying two-dimensional seismic inference for Rasalhague.

References

Espinosa Lara, F. & Rieutord, M. 2013, A&A, 552, A35

García Hernández, A., Martín-Ruiz, S., Monteiro, M. J. P. F. G., et al. 2015, ApJ Lett., 811, L29

Hinkley, S., Monnier, J. D., Oppenheimer, B. R., et al. 2011, ApJ, 726, 104

Lignières, F. & Georgeot, B. 2009, A&A, 500, 1173

Mirouh, G., Reese, D., Espinosa Lara, F., Ballot, J., & Rieutord, M. 2013, in IAU Symposium 301, Vol. 865, Precision Asteroseismology, ed. W. Chaplin, J. Guzik, G. Handler, & A. Pigulski, 1

Monnier, J. D., Townsend, R. H. D., Che, X., et al. 2010, ApJ, 725, 1192

Reese, D. R., Dupret, M.-A., & Rieutord, M. 2016, in Seismology of the Sun and the Distant Stars 2016, ed. M. J. P. F. G. Monteiro, M. S. Cunha, & J. M. T. Ferreira

Reese, D. R., Lignières, F., Ballot, J., et al. 2017, A&A, 601, A130

Reese, D. R., Prat, V., Barban, C., van 't Veer-Menneret, C., & MacGregor, K. B. 2013, A&A, 550, A77

Reese, D. R., Thompson, M. J., MacGregor, K. B., et al. 2009, A&A, 506, 183

Rieutord, M., Espinosa Lara, F., & Putigny, B. 2016, Journal of Computational Physics, 318, 277

Royer, F. 2009, in Lecture Notes in Physics, Berlin Springer Verlag, Vol. 765, The Rotation of Sun and Stars, ed. J.-P. Rozelot & C. Neiner, 207–230

Unno, W., Osaki, Y., Ando, H., Saio, H., & Shibahashi, H. 1989, Nonradial oscillations of stars (University of Tokyo Press)

Zhao, M., Monnier, J. D., Pedretti, E., et al. 2009, ApJ, 701, 209

CHARACTERIZING STELLAR PARAMETERS FROM HIGH RESOLUTION SPECTRA OF COLD/YOUNG STARS FOR SPIROU LEGACY SURVEY

L. Kulenthirarajah[1], J.-F. Donati[2], G. Hussain[3] and J. Morin[4]

Abstract. We propose to create a high resolution spectral library in the optical and infrared range with PHOENIX model atmospheres code that can compute molecular lines in order to estimate stellar parameters. The chosen grid of stellar parameters will be as follows: δT_{eff} =25K, $\delta logg = 0.05$, $\delta[M/H] = 0.05$, ranging between: $T_{\text{eff}} = [2500K, 4000K]$, $logg = [4.0, -5.5]$, $[M/H] = [-1, -1]$ but first, we need to calibrate on F to K stars. We present here the preliminary tests and calibration on the Sun and 18sco. The method yield respectively $T_{\text{eff}} = 5770 \pm 3K$, $logg = 4.458 \pm 0.006$ and $T_{\text{eff}} = 5763 \pm 3.5K$, $logg = 4.451 \pm 0.007$

Keywords: Stars, M dwarf, synthetic spectra, stellar parameters, PHOENIX

1 Introduction

Having well constrained stellar parameters is essential for deducing the properties of planets and magnetic fields from radial velocity and polarimetric data. Radiative transfer and stellar models are the key to analyze high resolution spectra in order to infer fundamental stellar parameters such as temperature, gravity, rotation, magnetic fields and composition. These initial results are necessary to analyze radial velocity and polarimetric data. The goal of this project is to construct, test and validate a high resolution synthetic spectral library using PHOENIX (Allard et al. 2011) model atmospheres with a reliable tool to estimate stellar parameters of M dwarfs. Directly fitting observed high resolution spectra to a library of synthetic ones can yield stellar parameters such as T_{eff}, $logg$ and $[M/H]$, while enabling us to make a systematic error analysis. Valenti & Fischer (2005) have carried out a similar spectroscopic analysis for over a 1000 F to K type stars, deriving successfully parameters such as T_{eff}, $logg$ and $[M/H]$ along with precise error estimates (44 K in T_{eff}, 0.03 dex in $[M/H]$ and 0.06 in $logg$). Applying the same technique on M dwarfs is difficult and has not been done on a large scale yet. The spectral transition from F to M dwarfs requires a model atmosphere code that can treat molecular lines with accuracy such as PHOENIX. It is first necessary to create a new and finely-sampled spectral library with molecular lines using state-of-the-art stellar atmosphere models as well as to calibrate it to reproduce $F - G - K$ stars spectra. In this contribution we present some preliminary tests and calibration results for solar-like stars.

2 Synthetic spectra

We used the latest version of the model atmosphere code PHOENIX to synthesize stellar spectra. It is a three-step process : model atmosphere calculation, high resolution spectral synthesis and finally a continuum computation for normalization.

The model atmosphere is computed using existing "restart" files coming from old models (Allard et al. 2012). For each of our computed models, the restart file was carefully chosen to minimize the computing time to achieve convergence. The convergence criterion is defined as the difference (in %) between the total flux emitted and σT_{eff}^4 in each layer. Convergence is assumed when this criterion is lower than 1% in radiative layers. The models

[1] Université Paul Sabatier, Toulouse, France
[2] IRAP, Toulouse, France
[3] ESO, Munich, Germany
[4] Université de Montpellier, Montpellier, France

were calculated iteratively in spherical mode with 128 layers and assuming local thermodynamic equilibrium (LTE) until either convergence was achieved, or after N iterations ($N = 20$).

Once the models were computed, they were used to produce high resolution spectra with micro-turbulent broadening and continua with PHOENIX. Allard et al. (2012) have conducted 2D radiative hydrodynamic model atmosphere simulations to estimate micro-turbulent motions as a function of $T_{\rm eff}$, which we used. As most of our observed spectra are flux normalized with the apparent continuum, it is necessary to have normalized synthetic spectra to compare against. PHOENIX can compute the actual continuum for a given set of stellar parameters. This is done by removing the discrete opacities, making any atomic and molecular data unavailable and by keeping dust and continuous opacities. As shown on Fig. 1, this yields a close to perfect continuum placement on the synthetic spectra.

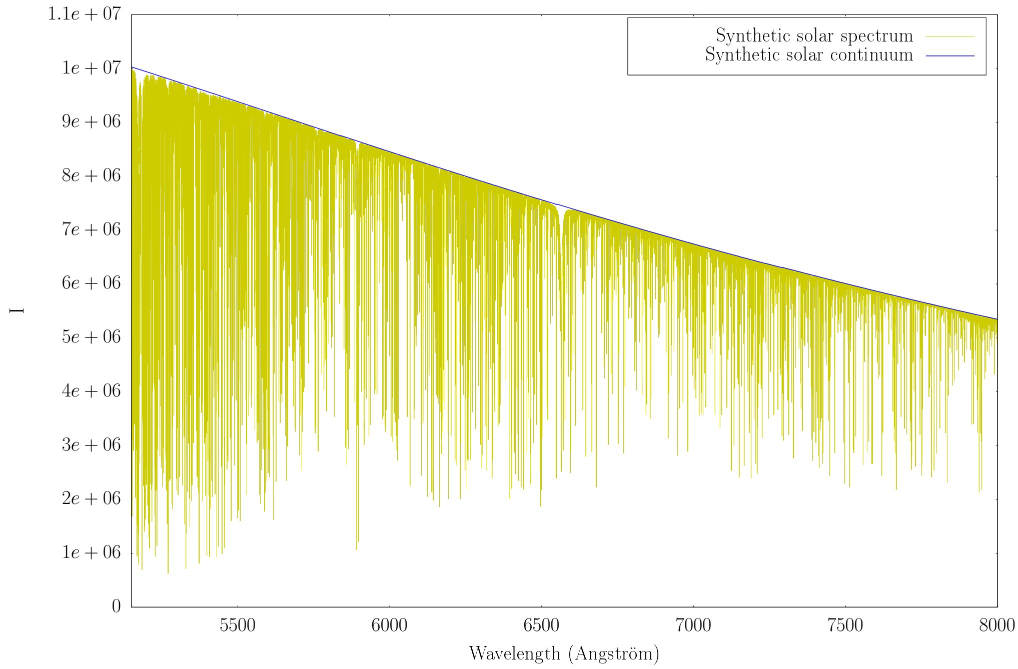

Fig. 1. Synthetic spectrum and continuum for the Sun ($T_{\rm eff} = 5775K$ and $logg = 4.440$)

3 Spectroscopic analysis tool

High resolution spectroscopy and stellar atmosphere modeling allow us to directly compare observed spectra to synthetic ones, across multiple spectral ranges in wavelength. This approach enables us to model all observed spectra uniformly and ensures self-consistency and statistical significance while estimating stellar parameters from a large sample of observed spectra.

Given a set of observations, estimating which model best fits the data is a well known problem in data modeling. The basic approach to solve this problem is generally to choose an estimator and a merit function that describes the agreement between the data and the model, and adjust the parameters of the latter to achieve close agreement. We used a maximum-likelihood estimator, also known as a χ^2 estimator, and the Levenberg-Marquardt (LM) algorithm to search through the non-linear dependencies of the model parameters. For a given observed spectrum we compared it to a synthetic spectrum with known $T_{\rm eff}$, $logg$ and $[M/H]$ by fitting the following parameters directly using the LM algorithm: rotation velocity, radial velocity, macro-turbulence, and continuum coefficients. Given the fact that we are fitting different windows in wavelength, this function is computed window by window but fitted simultaneously to the observed spectrum. The resulting χ^2 is used to map the parameter space in $T_{\rm eff}$, $logg$ and $[M/H]$ iteratively and estimate the optimum values.

4 Tests and validations

The first step of the test and validation consisted in creating a spectrum for the Sun in the optical range, as many high quality spectra have been collected with two spectropolarimeters, ESPaDOnS at CFHT and HARPS-Pol at ESO and for which high S/N high, high quality reduced spectra are available. We updated the existing PHOENIX atomic line data with the latest line data from the Vienna Atomic Line Database (Piskunov et al. 1995; Kupka et al. 1999, 2011). The database is dominated by line data from Kurucz & Bell (1995), but more recent results are incorporated periodically. We used the solar spectrum to determine empirical corrections for initial values of the oscillator strength that did not adequately reproduce observed line profiles, keeping stellar parameters fixed at known solar values. the oscillator strength of over 200 lines were corrected using the solar spectrum. We then used our spectroscopic analysis tool (SAT) to map the parameter space (keeping $[M/H] = 0$). Fig. 2 shows our results for the Sun, from which we find $T_{\rm eff} = 5770 \pm 3K$ and $logg = 4.458 \pm 0.006$. We then used SAT on a high S/N spectrum of 18 Sco (a solar analogue), on which our synthetic spectra were not calibrated, to also map the parameter space (by also keeping $[M/H] = 0$) and we obtained $T_{\rm eff} = 5763 \pm 3.5K$ and $logg = 4.451 \pm 0.007$. The latter results are in agreement with a similar analysis done by Valenti & Fischer (2005); they found $T_{\rm eff} = 5791 \pm 44K$ and $logg = 4.41 \pm 0.06$.

One should keep in mind that the given errors on the parameters are an estimate of the error bars using χ^2 formal error analysis. This only gives us a lower limit for the error bars. This method never yields really good estimates of the error bars when the uncertainties are not independent and does not follow a normal distribution. In our case, uncertainties due to photon noise are completely dominated by systematic errors, which we are attempting to quantify.

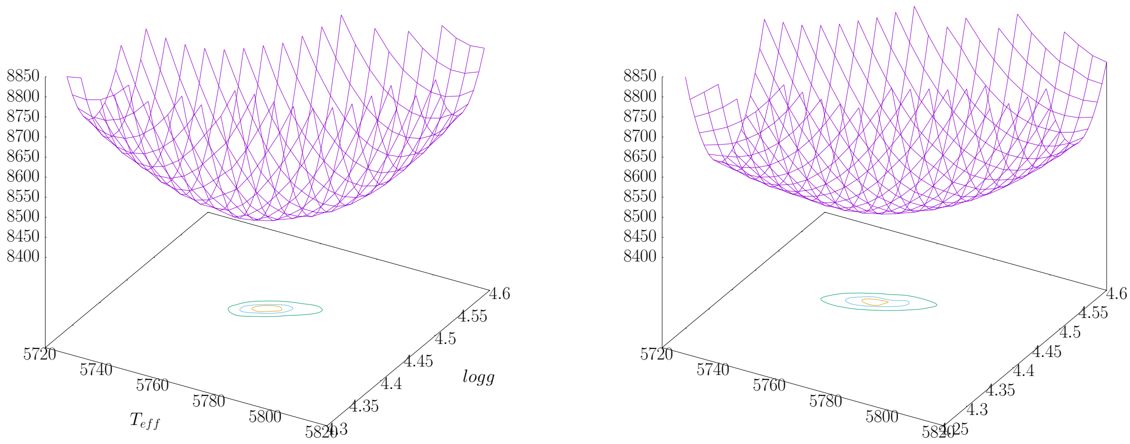

Fig. 2. Left: χ^2 map for the Sun as a function of the $T_{\rm eff}$ and $logg$ with contours delimiting 68.3%, 95.4% and 99.99% of confidence level. **Right:** χ^2 map for the 18 Sco as a function of the $T_{\rm eff}$ and $logg$ with contours delimiting 68.3%, 95.4% and 99.99% of confidence level .

5 Conclusions

Results from the first tests and validations are encouraging for the Sun and 18 Sco. Firstly, we need to extend these tests to other solar-like stars (similar $T_{\rm eff}$ and $[M/H]$) and confirm this performance as well as adding $[M/H]$ as an additional free parameter. Secondly, we need to extend our sample to a wider range of spectral types and validate the method on late G and early K type stars. The latter will probably require another empirical correction for initial values of the oscillator strength. A preliminary test on a sample spectrum from a K-type star suggested this will be necessary to once again anchor our models into standards. We also need to properly constrain the error bars on the parameters by estimating the uncertainties due to systematics.

We are indebted to France Allard and Peter Hauschildt for kindly providing the latest version of the PHOENIX code and for the various conversations that helped us a lot. We want to thank Boris Dintrans whose help was really valuable in installing PHOENIX and optimizing it on EOS (super computer at CALMIP). We also gratefully acknowledge the staff CALMIP (3 Rue Caroline Aigle, 31400 Toulouse) for providing computing time on EOS and their staff for helping the project. We thank Colin Folsom for ongoing useful conversations and for providing his customized line-list plotting software which greatly helped identifying the lines.

References

Allard, F., Homeier, D., & Freytag, B. 2011, in Astronomical Society of the Pacific Conference Series, Vol. 448, 16th Cambridge Workshop on Cool Stars, Stellar Systems, and the Sun, ed. C. Johns-Krull, M. K. Browning, & A. A. West, 91

Allard, F., Homeier, D., & Freytag, B. 2012, Philosophical Transactions of the Royal Society of London Series A, 370, 2765

Kupka, F., Dubernet, M.-L., & VAMDC Collaboration. 2011, Baltic Astronomy, 20, 503

Kupka, F., Piskunov, N., Ryabchikova, T. A., Stempels, H. C., & Weiss, W. W. 1999, A&AS, 138, 119

Kurucz, R. L. & Bell, B. 1995, Atomic line list (Kurucz CD-ROM, Cambridge, MA: Smithsonian Astrophysical Observatory, 1995)

Piskunov, N. E., Kupka, F., Ryabchikova, T. A., Weiss, W. W., & Jeffery, C. S. 1995, A&AS, 112, 525

Valenti, J. A. & Fischer, D. A. 2005, ApJS, 159, 141

Session 02

High energy and cosmic phenomena

SF2A 2017
C. Reylé, P. Di Matteo, F. Herpin, É. Lagadec, A. Lançon, Z. Meliani, F. Royer (eds)

WEBPLOTDIGITIZER, A POLYVALENT AND FREE SOFTWARE TO EXTRACT SPECTRA FROM OLD ASTRONOMICAL PUBLICATIONS: APPLICATION TO ULTRAVIOLET SPECTROPOLARIMETRY

F. Marin[1], A. Rohatgi[2] and S. Charlot[3]

Abstract. In this contribution, we present WebPlotDigitizer, a polyvalent and free software developed to facilitate easy and accurate data extraction from a variety of plot types. We describe the numerous features of this numerical tool and present its relevance when applied to astrophysical archival research. We exploit WebPlotDigitizer to extract ultraviolet spectropolarimetric spectra from old publications that used the Hubble Space Telescope, Lick Observatory 3 m Shane telescope and Astro-2 mission to observe the Seyfert-2 AGN NGC 1068. By doing so, we compile all the existing ultraviolet polarimetric data on NGC 1068 to prepare the ground for further investigations with the future high-resolution spectropolarimeter POLLUX on-board of the proposed Large UV/Optical/Infrared Surveyor (LUVOIR) NASA mission.

Keywords: physical data and processes, methods: numerical, software

1 Introduction

Astronomical spectra acquired before the era of Internet and on-line data storage are only available through papers published in physical form. Observational data, in particular those obtained by small missions and modest telescopes before the 90's, are not all stored in databases and several observations cannot be retrieved. New observations are thus required but it is a time-consuming task, especially for those who only want to fit their numerical simulations in order to test the relevance of their model. In this context, asking for observational time on new satellites and telescopes that are already facing high pressure-factors is a waste of effort. The best solution relies on digitalization of the old spectra using high resolution scanners. The digitalized plots are thus available for data extraction using modern softwares. However, many of the software tools dedicated to this task are either expensive or not very versatile. The common complaints about the existing tools are their limited features, poor compatibility with different operating systems and closed source code.

In this contribution, we present WebPlotDigitizer, a software created by Ankit Rohatgi that is distributed free of charge as an open source web-based tool. Thanks to its large adaptability, we show that the software can be easily handled to accurately extract data from any published paper in the field of astrophysics (and beyond). To show the great potential of this tool, we use it to retrieve the old ultraviolet polarimetric data of NGC 1068, a Seyfert-2 active galactic nuclei (AGN), acquired before the millennium by the Hubble Space Telescope, Lick Observatory 3 m Shane telescope and Astro-2 mission. This preliminary step will allow us to test model predictions for the high-resolution spectropolarimeter POLLUX that is proposed for the NASA mission study LUVOIR.

2 Description and application of WebPlotDigitizer

2.1 An overview of the software

WebPlotDigitizer has been continuously developed since its creation in 2011 by Ankit Rohatgi at the University of Notre Dame (Indiana, USA). This software uses affine transformations to map pixel location in the image

[1] Université de Strasbourg, CNRS, Observatoire astronomique de Strasbourg, UMR 7550, F-67000 Strasbourg, France
[2] ANSYS Inc., Austin, Texas, USA
[3] Sorbonne Universités, UPMC-CNRS, UMR7095, Institut d'Astrophysique de Paris, F-75014 Paris, France

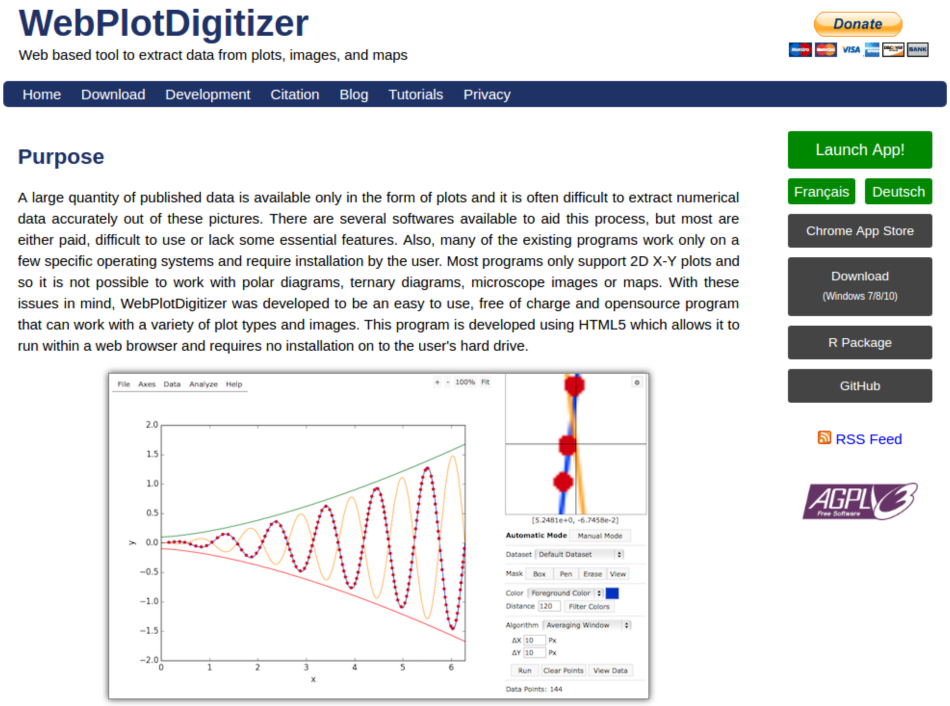

Fig. 1. WebPlotDigitizer webpage.

to data points on a figure based on the calibration points provided by the user. Various image processing algorithms included with this software can be used to extract large number of data points from uploaded figures with great precision. WebPlotDigitizer is distributed under the GNU General Public License version 3, and the latest stable version of the software (v3.12, June 2017) can be used directly from the website http://arohatgi.info/WebPlotDigitizer. Fig. 1 is a screenshot of the main web page. It shows the software launching button as well as all the recent developments of the code. A language selection is available (English, French and German). One can also download the code or donate for the code's sustainability.

2.2 Extracting data from figures

In order to extract a spectrum from an archival paper, the first step is to create an image that isolates the spectrum, including the horizontal and vertical axes. The presence of text and legends won't interfere. Once the image of the spectrum is created (see, e.g., Fig. 2), it must be loaded by the program using File > Load image. Different plot types can then be selected to map the image pixels to the corresponding data values in the image correctly (regular XY plot, but also 2D bar plots, polar and ternary diagrams, maps with scale bar and images). The next step is to quantitatively calibrate the data using axes alignment. The software will ask the user to select a few known points on the axes (2 points on the X-axis and 2 more points on the Y-axis for a 2D spectrum) and enter the corresponding values. For better accuracy during the digitization process, it is better to pick points that are as far away from each other as possible.

To acquire the data after plot axes calibration, several options are available. A tedious option is to manually select data points on the image (particularly helpful for low-resolution spectra with error bars). A zoomed view, on the top-right corner of the screen, see Fig. 2, helps to be precise and reflects actual data coordinates corresponding to the mouse position on the image. The manual mode allows for point selection, adjustment or removal by manually clicking at the desired locations. An alternative, faster method, is to use the automatic mode. In the automatic mode, the user can set up and execute an extraction algorithm that can differentiate between the data points and the image background and identify several data points in a short time. This is the method that was used to extract the total flux spectrum from NGC 1068 from Code et al. (1993) in Fig. 2.

Boxes of user-defined sizes and a virtual pen are used to define the region of interest where the spectrum resides. The user literally paints the spectrum, without spilling over the axes or legends, and the algorithms

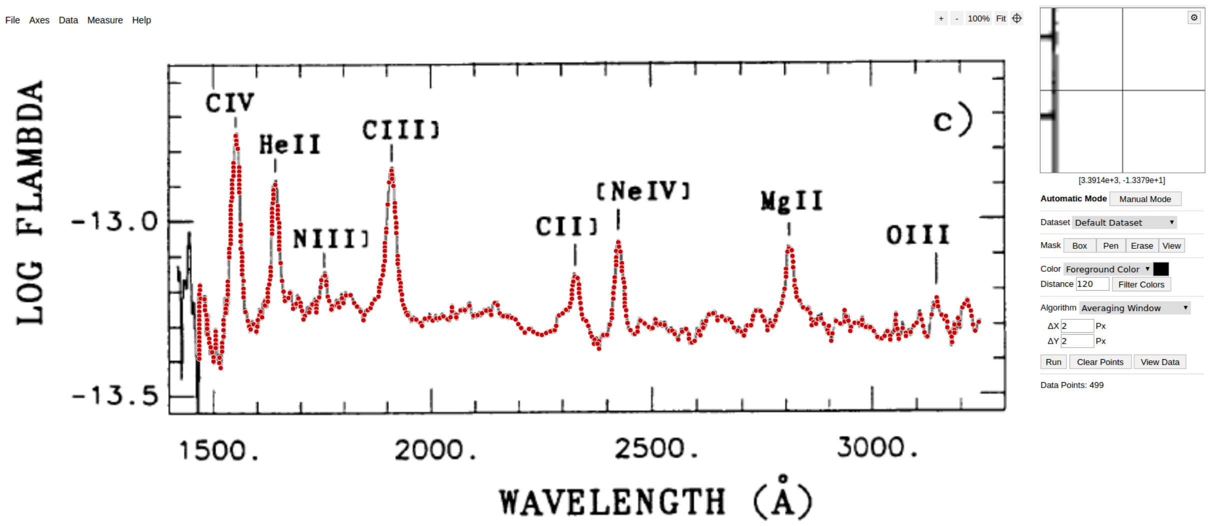

Fig. 2. On-line interface of WebPlotDigitizer. The red points are the calibrated data sampled throughout the spectrum, with a resolution ΔX and ΔY of 2 pixels (on-screen). The side panel shows the data acquisition controls. The spectrum is from Code et al. (1993).

look for the foreground color specified for the data and ignore everything else. A background mode also allows the algorithms to include everything except the background color as potential data points, a very useful feature in the case of overlapping curves/spectra of different colors. If the user paints over the axes, then it is possible to erase the erroneous parts and paint again, without limits on the number of attempts. When the spectrum is fully colored, the user simply has to press the Run button to start the auto-detection algorithm. After this is completed, the detected points appear in red over the image (see Fig. 2). If necessary, one can adjust the parameters of the extraction algorithm, the mask or the color settings and run the algorithm until satisfied.

The last stage of the operation is to download the digitized values. By clicking the View Data button, a popup window appears and the values can be sorted by their x or y coordinates, or in order of the distance between the points (Nearest Neighbor). The final values can be copied and saved*.

2.3 Application to ultraviolet spectropolarimetric data on NGC 1068

We used WebPlotDigitizer to extract the total flux spectra and polarization from old observations. Namely, we first extracted the ultraviolet flux spectrum (in $\log(F_\lambda)$) from Grimes et al. (1999). They observed the far-ultraviolet spectrum (912 – 1840 Å) of NGC 1068 using the Hopkins Ultraviolet Telescope during the 1995 March Astro-2 mission. The spectrum is represented in orange in Fig. 3. Due to the pixel resolution on screen the data are not as smooth as in the publication (resolution degradation to 0.5 Å) but all the emission lines and the absorption features are correctly duplicated, together with the proper fluxes levels. We then extracted the total flux spectrum and polarization degree and angle taken by the Lick Observatory 3 m Shane telescope mounted with a Cassegrain Pockels cell polarimeter (Miller & Antonucci 1983). The near-ultraviolet emission is shown in black in Fig. 3. Finally, we digitized the Hubble Space Telescope spectropolarimetric observation made by Code et al. (1993). These data are plotted in red. We merged the three total flux spectra by normalizing their narrow line emission fluxes and continuum emission.

The final composite polarization spectrum of NGC 1068 is shown in Fig. 3. This is a compilation of all the observed ultraviolet polarimetric data we know on this nearby, very bright type-2 AGN whose optical polarized spectrum allowed in 1985 to understand the true nature of radio-quiet AGN (Antonucci & Miller 1985). Considering the numerous gaps in wavelengths and the very low polarimetric data resolution for this source, it clearly remains a prime target for new generations of space-based polarimeters. In this regard, POLLUX, a high-resolution ultraviolet spectropolarimeter for the LUVOIR space mission at NASA (Stahl & Hopkins 2015;

*A detailed user manual is available on the software webpage: http://arohatgi.info/WebPlotDigitizer/userManual.pdf, and additional examples are shown on YouTube videos.

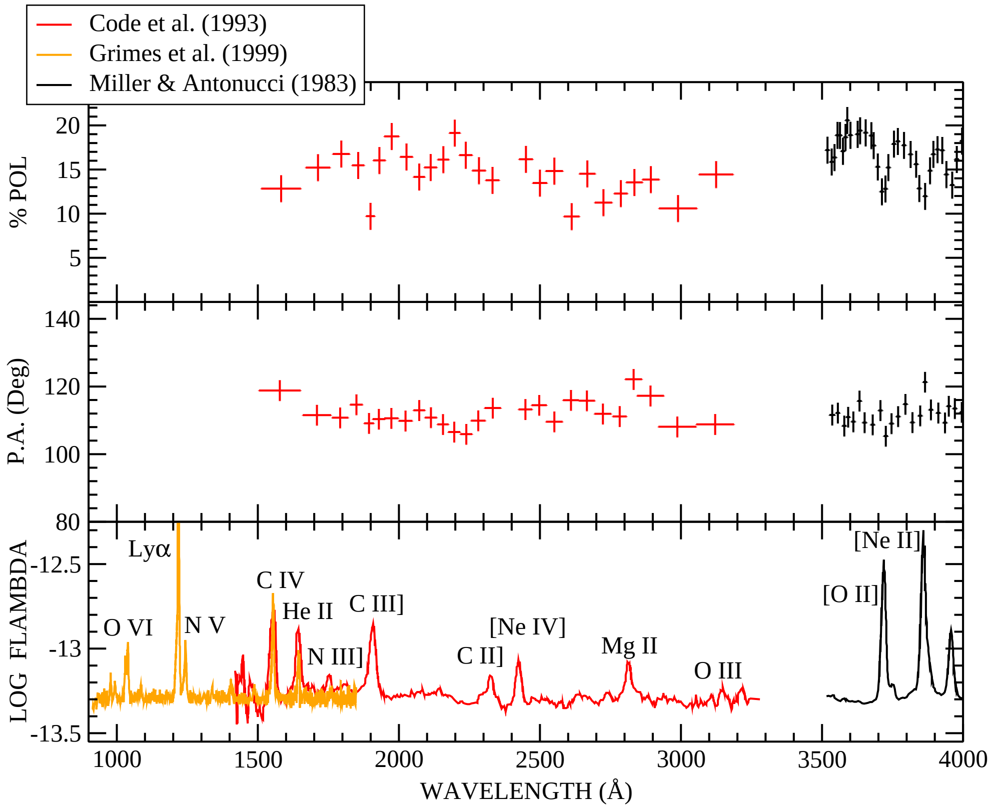

Fig. 3. NGC 1068 ultraviolet polarization degree (top), polarization position angle (middle) and total flux (bottom) extracted from Miller & Antonucci (1983), Code et al. (1993) and Grimes et al. (1999) using WebPlotDigitizer.

Bolcar et al. 2016; France 2016; Peterson et al. 2017) is the ideal instrument. Supported by CNES and developed by a European consortium, POLLUX is expected to provide very high resolution polarimetric observations of bright sources in the 900 – 4000 Å band (desired wavelength coverage). The study of AGN at high polarimetric resolution will enable us to probe the physics of outflowing winds with incredible precision. The launching site of the theoretical disk-born winds can be probed at the closest radii from the central supermassive black hole and the polarized emission line and continuum will be directly influenced by the geometry and composition of the wind (Marin & Goosmann 2013a,b,c). Additionally, the composition of the dusty material, at radii larger than the physical limits imposed by dust sublimation, could be probed in a waveband where no terrestrial or space-born polarimetric data exists with sufficient wavelength coverage and resolution (Hines et al. 2001).

3 Conclusions

We have shown the ability of the WebPlotDigitizer software to precisely and efficiently digitize graphical spectra. Such an ability has potential implications for easy model-to-data comparison in many fields of astronomy. It can help access old data in record time without going through data reduction again and can be used, for example, to compile all existing spectra of a particular object. We applied WebPlotDigitizer to the case of NGC 1068, a bright type-2 Seyfert galaxy whose ultraviolet polarization spectrum lacks a proper coverage, both in wavelength and resolution. By creating the first composite ultraviolet polarimetric spectrum of NGC 1068, we highlighted the need for a high-resolution ultraviolet spectropolarimeter such as POLLUX.

F.M acknowledges funding through the CNES post-doctoral position grant "Probing the geometry and physics of active galactic nuclei with ultraviolet and X-ray polarized radiative transfer".

References

Antonucci, R. R. J. & Miller, J. S. 1985, ApJ, 297, 621

Bolcar, M. R., Feinberg, L., France, K., et al. 2016, in Proc. SPIE, Vol. 9904, Space Telescopes and Instrumentation 2016: Optical, Infrared, and Millimeter Wave, 99040J

Code, A. D., Meade, M. R., Anderson, C. M., et al. 1993, ApJ, 403, L63

France, K. 2016, in Proc. SPIE, Vol. 9904, Space Telescopes and Instrumentation 2016: Optical, Infrared, and Millimeter Wave, 99040M

Grimes, J. P., Kriss, G. A., & Espey, B. R. 1999, ApJ, 526, 130

Hines, D. C., Schmidt, G. D., Gordon, K. D., et al. 2001, ArXiv Astrophysics e-prints

Marin, F. & Goosmann, R. W. 2013a, MNRAS, 436, 2522

Marin, F. & Goosmann, R. W. 2013b, in SF2A-2013: Proceedings of the Annual meeting of the French Society of Astronomy and Astrophysics, ed. L. Cambresy, F. Martins, E. Nuss, & A. Palacios, 475–478

Marin, F. & Goosmann, R. W. 2013c, in SF2A-2013: Proceedings of the Annual meeting of the French Society of Astronomy and Astrophysics, ed. L. Cambresy, F. Martins, E. Nuss, & A. Palacios, 479–482

Miller, J. S. & Antonucci, R. R. J. 1983, ApJ, 271, L7

Peterson, B. M., Fischer, D., & LUVOIR Science and Technology Definition Team. 2017, in American Astronomical Society Meeting Abstracts, Vol. 229, American Astronomical Society Meeting Abstracts, 405.04

Stahl, H. P. & Hopkins, R. C. 2015, in Proc. SPIE, Vol. 9602, Optics for EUV, X-Ray, and Gamma-Ray Astronomy VII, 960206

SF2A 2017
C. Reylé, P. Di Matteo, F. Herpin, É. Lagadec, A. Lançon, Z. Meliani, F. Royer (eds)

THE GIANT RADIO ARRAY FOR NEUTRINO DETECTION

K. Kotera[1] for the GRAND Collaboration

Abstract. The Giant Radio Array for Neutrino Detection (GRAND) project aims at detecting ultrahigh-energy neutrinos and cosmic rays with a $\sim 10^5$ radio antenna array over 200'000 km^2 in mountainous regions in China, in order to solve the mystery of the origin of these two linked particles. Its strategy is to detect extensive air showers of the highest energies, above 10^{17} eV, that are triggered by the interaction of high-energy particles in the atmosphere or underground. In its first stages, GRAND will be competitive to detect the first cosmogenic neutrinos for favorable source scenarios. Ultimately, GRAND aims at reaching a sensitivity and angular resolution that should launch neutrino astronomy, and that will ensure the detection of these neutrinos, even in the most pessimistic cases. We present preliminary results of our simulations, plans for the ongoing, staged approach to the construction of GRAND, and the rich research program made possible by the design of GRAND.

Keywords: air shower, radio emission, radio detection

1 Hunting ultrahigh energy neutrinos with radio antennas

Ultrahigh energy neutrinos, with energies $\sim 10^{18}$ eV, remain unchartered territory: they have not been detected yet, and their sources are unknown. Their existence is guaranteed however, as they are bound to be produced by the interaction of ultrahigh energy cosmic rays (charged nuclei that bombard the Earth with energies $> 10^{20}$ eV, and that are routinely detected), with the cosmic photon backgrounds, on their way from their source to the Earth. The sources of these ultrahigh energy cosmic rays (UHECRs) has been a long-standing enigma (Kotera & Olinto 2011). The GRAND experiment aims at unveiling these mysteries by reaching a sensitivity that ensures the detection of such neutrinos, even in the most pessimistic UHECR source models. For standard source models, it should detect enough events to launch neutrino astronomy. The project consists of an array of $\sim 10^5$ radio antennas deployed over an area of $\sim 200\,000$ km^2 in a mountainous site. GRAND will search for the radio signal emitted by the air showers of τ leptons produced by the interaction of cosmic neutrinos underground.

Earth-skimming cosmic ν_τs can produce τ particles underground through charged-current interaction. τs travel to the surface of the Earth and decay in the atmosphere, generating extensive air showers (EAS) (Fargion 1999; Bertou & et al 2002). Coherent electromagnetic radiation is associated to the shower development at frequencies of a few to hundreds of MHz at a detectable level for showers with $E > 10^{17}$ eV. The strong beaming of the electromagnetic emission combined with the transparency of the atmosphere to radio waves will allow the radio-detection of EAS initiated by τ decays at distances up to several tens of kilometers. Inclined showers can leave footprints of several kilometers on the ground after traveling such large distances in the atmosphere, allowing a sparse antenna distribution. Furthermore, radio antennas offer practical advantages (limited unit cost, easiness of deployment, ...) that allow the deployment of an array over very large areas, as required by the expected low neutrino rate.

GRAND antennas are foreseen to operate in the $30 - 200$ MHz frequency band. Short wave background prevents detection below this range, and above the coherence of the geomagnetic emission fades. Remote sites, with low electromagnetic background, should obviously be considered for the array location. In addition, mountain ranges are preferred, first because they offer an additional target for the neutrinos, and also because mountain slopes are better suited to the detection of horizontal showers compared to flat areas, parallel to the showers trajectories.

[1]Sorbonne Universités, UPMC Paris 6 et CNRS, UMR 7095, Institut d'Astrophysique de Paris, 98 bis bd Arago, 75014 Paris, France et Laboratoire AIM-Paris-Saclay, CEA/DSM/IRFU, CNRS, Université Paris Diderot, F-91191 Gif-sur-Yvette, France

2 Detector Performance

Simulation chain. We present here a preliminary simulation, based in particular on a parametrization of the radio emission process. A complete, end-to-end simulation chain is being finalized and will produce results early 2018. The area considered for the present study is a rectangle of $300 \times 300\,\mathrm{km}^2$ in the Tianshan mountain range, in China, centered on the TREND site (86°44'E, 42°57' N). The topography of the site is interpolated from a 200 m step elevation map derived from public NASA satellite data. A square grid with 800 m step size deployed over the full area is considered for the antenna layout.

For the incoming ν_τs, fixed values are considered for energies ($10^{17}\,\mathrm{eV} < E < 10^{20.5}\,\mathrm{eV}$), as well as zenith ($86° < \theta < 93°$) and azimuth angles ($0° < \phi < 360°$). For each (E, θ, ϕ) set, n_{Gen} random trajectories are generated until 100 showers with $E_{\mathrm{sh}} > 10^{16}$ eV are produced. A simplified 1D tracking of the processes is performed through a Monte-Carlo simulation process for each randomly chosen trajectory. Neutrino interaction lengths in rock are taken from Gandhi et al. (1998) and the energy-dependent interaction depths for Neutral Current (NC) or Charged Current (CC) events are sampled accordingly and located along the trajectory. The kinematic of the neutrino DIS event is delegated to Pythia6.4, using CTEQ5d probability distribution functions. If a CC interaction occurs with a rock target in the simulation volume, a τ simulation starts. The τ energy loss and proper time distributions are parametrized from GEANT4.9 simulations performed or various primary energies and depths in Standard Rock (Dziewonski & Anderson 1981). Photonuclear interactions are of prime importance for UHE leptons. They have been extended in GEANT4.9 above PeV energies following Dutta et al. (2000). If a decay of the τ occurs after it has emerged above the Earth surface, it is simulated with the TAUOLA package (Davidson et al. 2012). If the induced shower energy E_{sh} (computed as the τ final energy minus the energy of νs and μs secondaries) is above 10^{16} eV, then radio detection is simulated.

However the CPU request of computing programs simulating air shower radio emission is too large (several hours for a single shower) to allow for a full treatment of all simulated showers over the considered detection area. An end-to-end simulation chain overcoming this technical issue, called *radio morphing* (Zilles 2017) is being developed, but at present only a geometric parametrization of the EAS radio emission is used to determine if a simulated shower can be detected by the GRAND antenna array. In an agressive scenario –where means to improve the background rejection could be implemented in the GRAND DAQ system– the detection threshold of the integrated electric field amplitude in the 30-80 MHz frequency range, is taken equal to 30 μV/m, twice the background noise level expected from Galactic emission in this frequency range. A more conservative threshold value of 100 μV/m –achievable with present, standard trigger algorithm– is also considered.

Preliminary results. Assuming a 3-year observation with no neutrino candidate detected in this 60 000 km^2 simulated array, a 90% C.L. integral upper limit of 2.0×10^{-9} GeV^{-1} cm^{-2} s^{-1} can be derived for an E^{-2} all-flavor neutrino flux in our agressive scenario (4.0×10^{-9} in our conservative scenario), as displayed in Fig. 1. This preliminary analysis also shows that mountains constitute a sizeable target for neutrinos, with ∼50% of down-going events coming from neutrinos interacting inside the mountains (see Fig. 1). It also appears that specific parts of the array (large mountains slopes facing another mountain range at distances of $30 - 80\,\mathrm{km}$) are associated with a detection rate well above the average. Our simulations for such a hotspot of 7 500 km^2 for example yield an effective area about one third of the value computed for the total 60 000km^2 area. By splitting the detector into smaller subarrays of $\mathcal{O}$(10,000) km^2 each, deployed solely on such favorable *hotspots*, an order-of-magnitude improvement in sensitivity could probably be reached with only a factor-of-3 increase in detector size, compared to the 60 000 km^2 simulation area. This is the envisioned GRAND setup. The associated 2.0×10^{-10} GeV^{-1} cm^{-2} s^{-1} sensitivity limit extrapolated to the 200 000 km^2 GRAND complete configuration would then correspond to a detection rate of 1 to 60 cosmogenic neutrino events per year assuming fluxes from Kotera et al. (2010).

Background rejection. A few to a hundred cosmic neutrinos per year are expected in GRAND. The rejection of events initiated by high energy particles other than cosmic neutrinos should be manageable, as: i) the flux of atmospheric neutrinos is negligible above 10^{16} eV (Aartsen et al. 2014), ii) the rate of showers generated by muon decay above GRAND is expected to be few per century (Chirkin 2004), and iii) rejection of all trajectories reconstructed down to 1° below the horizon would strongly suppress the measured rate of EAS initiated by standard cosmic rays, without significantly affecting GRAND neutrino sensitivity. On the other hand, man-made background noise is too diverse in nature and intensity to be properly modeled. Only an experimental implementation of the event selction procedure will thus validate it. Amplitude patterns on the ground (emission beamed along the shower axis or signal enhancement along the Cherenkov ring), as

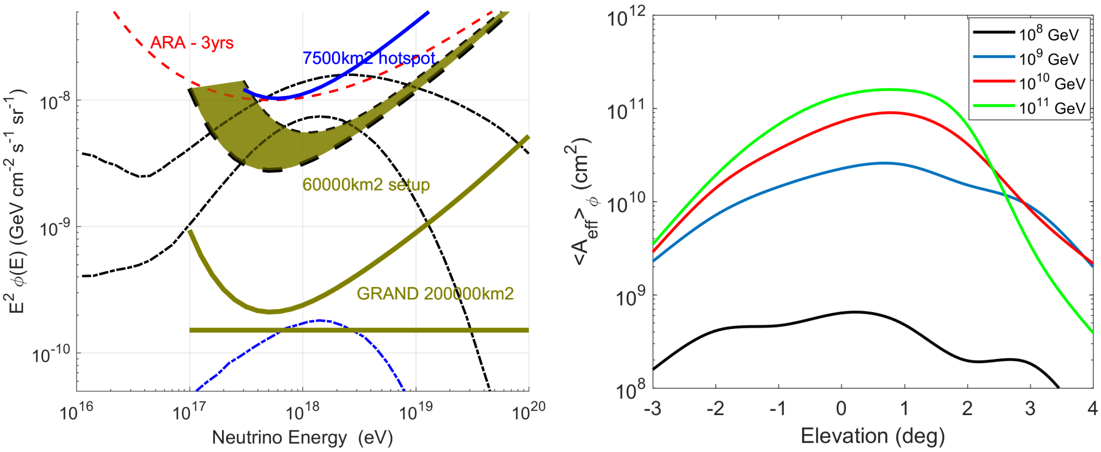

Fig. 1. *Left:* 90% C.L. differential limit on a E^{-2} ν_τ astrophysical flux for 3 years of observation with 0 candidates for aggressive (thick dashed line) and conservative thresholds (thin dashed line). Also shown are the projected limit for the envisioned 200 000 km^2 GRAND array (thick brown solid line), for the 7 500 km^2 GRAND hotspot (blue) and limits for the ARA project (Allison et al. 2016)(red dotted line), as well as the estimated theoretical cosmogenic neutrino fluxes for a single neutrino flavor (Kotera et al. 2010). *Right:* Differential effective area $\mathcal{A}_{\rm eff}^{E,\theta,\phi}$ as a function of zenith angle θ for various ν energies for the 60 000 km^2 simulated array, assuming an agressive threshold (see text). The curves are averaged over azimuth angles ϕ. Following GRAND angular conventions, $\theta < 90^\circ$ corresponds to upward-going showers.

well as wave polarization (Aab et al. 2014) are strong signatures of ν-initiated air showers that could provide efficient discrimination tools. These options are being investigated within GRAND, through simulations and experimental work. In 2017 the GRANDproto35 project (Gou 2015) in particular, will deploy an hybrid detector composed of 35 3-arm antennas (allowing a complete measurement of the wave polarization) and 24 scintillators, that will cross-check the EAS nature of radio-events selected from a polarization signature compatible with EAS. Testing the background rejection performances will also be one purpose of GRANDproto300, the subsequent prototype phase of the GRAND instrument.

3 Physics Case: High-energy neutrino astronomy, UHECRs and Fast Radio Bursts

The sensitivity of GRAND should guarantee the detection of cosmogenic EeV neutrinos produced during the propagation of UHECRs to the Earth. A 5σ identification of individual point sources out of a diffuse background requires $\sim 100-1000$ events with a sub-degree angular resolution for sources that have a local density of $10^{-9}-10^{-7}\,{\rm Mpc}^{-3}$ (Fang et al. 2016). Assuming a neutrino flux of $10^{-8}\,{\rm GeV\,cm^{-2}\,s^{-1}\,sr^{-1}}$, the GRAND neutrino sensitivity corresponds to a detection of $\sim$ 100 events after three years of observation. The unprecedented sensitivity of GRAND, the non-detection of events would strongly constrain UHECR models. The ideal way to identify high-energy neutrino sources would be to observe a point source. GRAND opens this possibility with its excellent spatial resolution and its sky coverage. In the simulation layout, the instantaneous field of view of GRAND is a band corresponding to zenith angles $80^\circ \leq \theta \leq 100^\circ$, and its integrated exposure $\sim 10^{16}\,{\rm cm^2\,s}$ for 3 years in the energy range $\sim 10^{17-20}\,{\rm eV}$, over a large portion of the sky (Fig. 2).

GRAND will observe UHECRs with an effective area that is at least an order of magnitude larger than Auger. The high statistics will resolve any small-scale anisotropies and features near the end of the cosmic ray spectrum. GRAND will also reach an UHE photon sensitivity exceeding that of current experiments. Future simulation studies will be dedicated to performance of energy and $X_{\rm max}$ reconstructions.

GRAND will contribute in a unique way to the measurement of fast radio bursts and giant radio pulses by collecting unprecedented statistics at low frequencies. For instance, GRAND could record giant pulses from the Crab pulsar above 5 Jy at 200 MHz with a rate about 200 per day. In addition, GRAND could be a preferred instrument for other science topics such as the study of the epoch of reionization.

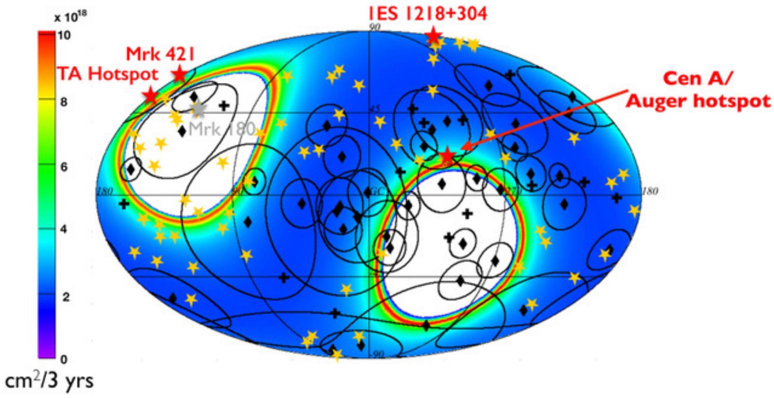

Fig. 2. Integrated 3-year exposure of GRAND to UHE neutrinos of 3×10^9 GeV. Within the GRAND field of view are known TeV-emitting AGN and starburst galaxies (yellow stars), from TeVCat. IceCube High-Energy Starting Events (HESE) from the 4-year data release are shown as diamonds (for showers) and crosses (for tracks). Circles around diamonds represent the angular uncertainty; for tracks, it is smaller than the symbol size.

4 Development plan

The GRAND project aims at building a next-generation neutrino telescope composed of a radio antenna array deployed over 200,000 km^2. Preliminary simulations indicate that 5% of the array deployed in favorable sites will improve the sensitivity over that of current-generation telescopes by an order of magnitude. The full array will offer a sensitivity that ensures a detection of cosmogenic neutrinos in the most pessimistic scenario, and an identification of individual point sources in an optimistic scenario. GRAND will also be a powerful instrument for UHECR observations with high statistics. Simulation and experimental work is ongoing on technological development and background rejection strategies. The GRAND development plan consists of several steps. Presently, deployment of a prototype array with 35 antennas and scintillator detectors is underway in the mountainous region of Ulastai, China. Following this step, a dedicated setup with a size of 300 km2 will be deployed. This array will establish the autonomous radio detection of very inclined EAS with high efficiency and excellent background rejection, as a validation for the future GRAND layout.

This work is supported by the APACHE grant (ANR-16-CE31-0001) of the French Agence Nationale de la Recherche. The GRAND and GRANDproto projects are supported by the Institut Lagrange de Paris, the France China Particle Physics Laboratory, the Natural Science Fundation of China (Nos.11135010, 11375209) and the Chinese Ministery of Science and Technology.

References

Aab, A. et al. 2014, Phys. Rev. D, 89, 052002
Aartsen, M. G. et al. 2014, Phys. Rev. D, 89, 062007
Allison, P. et al. 2016, Phys. Rev. D, 93, 082003
Bertou, X. & et al. 2002, Astroparticle Physics, 17, 183
Chirkin, D. 2004, ArXiv High Energy Physics - Phenomenology e-prints
Davidson, N., Nanava, G., Przedzinski, T., Richter-Was, E., & Was, Z. 2012, Comput. Phys. Commun., 183, 821
Dutta, S. I., Reno, M. H., & Sarcevic, I. 2000, Phys. Rev., D62, 123001
Dziewonski, A. M. & Anderson, D. L. 1981, Phys. Earth Planet. Interiors, 25, 297
Fang, K., Kotera, K., Miller, M. C., Murase, K., & Oikonomou, F. 2016, JCAP, 12, 017
Fargion, D. 1999, International Cosmic Ray Conference, 2, 396
Gandhi, R., Quigg, C., Reno, M. H., & Sarcevic, I. 1998, Phys. Rev. D, 58, 093009
Gou, Q. 2015, these proceedings
Kotera, K., Allard, D., & Olinto, A. V. 2010, J. Cos. and Astro. Phys., 10, 13
Kotera, K. & Olinto, A. V. 2011, Ann. Rev. Astron. Astrophys., 49, 119
Zilles, A. e. a. 2017, in SF2A 2017 Proceedings

SF2A 2017
C. Reylé, P. Di Matteo, F. Herpin, É. Lagadec, A. Lançon, Z. Meliani, F. Royer (eds)

UNVEILING THE PAST OF THE GALACTIC NUCLEUS WITH X-RAY ECHOES

D. Chuard[1, 2], R. Terrier[2], A. Goldwurm[1,2], M. Clavel[3], S. Soldi[2], M. R. Morris[4], G. Ponti[5], M. Walls[6] and M. Chernyakova[6, 7]

Abstract. Giant molecular clouds populating the central molecular zone have a high enough column density to reflect X-rays coming from strong compact sources in their neighbourhood, including possible powerful outbursts from the Galactic supermassive black hole Sgr A*. From observations of the molecular complex Sgr C made with the X-ray observatories *XMM-Newton* and *Chandra* between 2000 and 2014, we confirm this reflection scenario, even though the region hosts several objects (including two PWN candidates) that may be responsible for intense cosmic-ray production. By comparing data to Monte Carlo simulated reflection spectra, we are able to put the best constraints to date on the line-of-sight positions of the main bright clumps of the molecular complex. Ultimately, extending this approach by the inclusion of other molecular complexes allows us to partially reconstruct the past lightcurve of the Galactic supermassive black hole.

Keywords: Galaxy: center, ISM: clouds, X-rays: ISM

1 Introduction

Until the late 1990s, the presence of a supermassive black hole at the centre of the Milky Way (as in most nuclei of massive galaxies) was debated, mainly because the candidate radio source Sagittarius A* (Sgr A*; Balick & Brown 1974) was not detected at other wavelengths (see e.g. Goldwurm et al. 1994, for hard X-ray observations). However, the detection of stellar proper motions in the immediate vicinity of the source, followed by the orbital analysis of the so-called "S-stars" (especially S2), led to the unambiguous identification of Sgr A* as the electromagnetic counterpart of a supermassive black hole whose mass is about 4 million times that of the Sun (see Genzel et al. 2010, for a review). The source was resolved in X-rays (2–10 keV) with *Chandra* shortly afterwards, confirming that its absorption-corrected quiescent X-ray luminosity ($L_X \sim 10^{33}$ erg s^{-1}) is almost ten orders of magnitude below the Eddington limit (Baganoff et al. 2003). As a result, explaining the extreme faintness of the Galactic central black hole has become a challenge.

However, Sgr A* might only be in a transient dormant phase. There are indeed several indications that the black hole may have been more active in the past (see Ponti et al. 2013, for a review). For instance, the discovery of two large gamma-ray bubbles extending up to 50° above and below the Galactic plane suggests, among other possibilities, that an intense AGN phase occurred a few 10^6 yr ago (Su et al. 2010; Zubovas et al. 2011; Zubovas & Nayakshin 2012). Traces of potential more recent high-activity episodes can be found in the molecular material concentrated in the inner $\sim$ 600 pc of the Galaxy, known as the central molecular zone (CMZ; Morris & Serabyn 1996). While propagating through the CMZ, X-ray flares get reflected onto optically thick clouds (Sunyaev et al. 1993). This triggers echoes of the original flaring events than can be used to track the past activity of the Galactic nucleus.

[1] Irfu/Département d'astrophysique, CEA Paris-Saclay, Orme des Merisiers, 91191 Gif-sur-Yvette, France
[2] APC, Univ. Paris Diderot, CNRS/IN2P3, CEA/Irfu, Obs. de Paris, USPC, 75205 Paris Cedex 13, France
[3] Space Sciences Laboratory, 7 Gauss Way, University of California, Berkeley, CA 94720-7420, USA
[4] Dep. of Physics and Astronomy, University of California, Los Angeles, CA 90095, USA
[5] Max-Planck-Institut für extraterrestrische Physik, 85748, Garching, Germany
[6] School of Physical Sciences, Dublin City University, Glasnevin, Dublin 9, Ireland
[7] Dublin Institute of Advanced Studies, 31 Fitzwilliam Place, Dublin 2, Ireland

Table 1. Values of the spectral parameters for the two PWN candidates, obtained by fitting the *Chandra* data with an absorbed power law of photon index Γ. N_H is the value of the gas column density responsible for interstellar absorption towards the Galactic centre. Errors are given at 1σ (68% confidence) level.

Region	N_H (10^{22}cm^{-2})	Γ	χ^2/d.o.f.
G359.40–0.08	$11.1^{+2.6}_{-2.3}$	$1.33^{+0.46}_{-0.42}$	17.0/14
G359.39–0.08	$8.2^{+5.0}_{-3.9}$	$0.69^{+0.86}_{-0.73}$	7.5/11

These echoes can be identified by their spectrum, which exhibits a bright fluorescent line of neutral and low-ionised iron (Fe Kα) at 6.4 keV along with a continuum component produced by Compton scattering. Such reflected emission was first detected in the direction of Sgr B2, the most massive giant molecular cloud in the Milky Way (Koyama et al. 1996). It was interpreted as the echo of an outburst that took place at the Galactic center $\sim$ 300 yr ago. Since then, similar detections have been reported in the direction of all main molecular complexes, namely Sgr A, B, C and D, the most likely illuminating source being Sgr A* itself (see e.g. Terrier et al. 2017). Yet, no proper reconstruction of the past lightcurve of Sgr A* has been possible because the exact positions of the clouds, and hence the propagation delay of the echoes, are unknown. One way to tackle this issue is to correlate variations between multiple clumps all over the CMZ, assuming that they are illuminated by the same event (Clavel et al. 2013; Churazov et al. 2017; Terrier et al. 2017). Another is to use the properties of the reflected emission to constrain the line-of-sight positions of each cloud (Capelli et al. 2012; Ryu et al. 2013; Walls et al. 2016). Indeed, the flux and spectral shape of the reflected emission are very sensitive to the angle between the cloud, the illuminating source and the observer, referred to as the line-of-sight angle, as well as to the cloud column density (Walls et al. 2016), which makes possible the determination of these two parameters using spectral analysis. Here we focus on the reflected emission coming from the molecular complex Sgr C as it allows these two approaches to be applied together for the first time.

2 The molecular complex Sgr C

Sgr C is located approximately 0.5° away from Sgr A*, i.e. at a projected distance of $\sim$ 70 pc. It is an ideal position for studying correlations in the reflected emission from both sides of the Galactic plane, especially since Sgr B2 is located at a similar projected distance on the opposite side of Sgr A*. Sgr C is also a good candidate for line-of-sight position determination based on spectral analysis since its Fe Kα emission is well resolved into a few distinct clumps (Nakajima et al. 2009). Moreover, it allows to verify if the 6.4 keV line is produced either by X-ray echoes or by an alternative mechanism based on cosmic-ray irradiation (e.g. Yusef-Zadeh et al. 2002; Dogiel et al. 2009; Tatischeff et al. 2012). Indeed, Sgr C hosts several objects that may be responsible for intense cosmic-ray production, including the supernova remnant (SNR) candidate G359.41−0.12 and an associated chimney-like outflow structure (Tsuru et al. 2009). It is indeed critical to disentangle the two possible Fe Kα emission origins to avoid any misinterpretation.

Sgr C has been frequently observed with various X-ray observatories, during either dedicated pointings or CMZ scans. We consider here *XMM-Newton* and *Chandra* observations covering the period from September 2000 to August 2014. Exposure-corrected images and spectra are produced following the data reduction procedures detailed in Chuard et al. (2017a).

While studying the thermal diffuse emission from the Sgr C region (Chuard et al. 2017b), we report a new non-thermal cometary feature designated as G359.39−0.08 (Fig. 1). It is located within 30 arcsec of G359.40−0.08, another, brighter comet-like X-ray filament already identified by Johnson et al. (2009). This new object is revealed thanks both to *Chandra*'s unique high-resolution imaging capabilities and to the amount of cumulated exposure time ($\sim$ 200 ks). The spectra of these two structures are well fitted using a power-law model with interstellar absorption (Table 1). This, along with their morphology, suggests that they are likely pulsar wind nebulae (PWN). Their proximity to each other and to the SNR candidate is puzzling and suggests that the region might be more complex than previously thought (see also Ponti et al. 2015). Despite the possible interaction of all those structures with the 6×10^5 M$_\odot$ of molecular gas contained in Sgr C (Liszt & Spiker 1995), Terrier et al. (2017) and Chuard et al. (2017a) independently report that the Fe Kα emission from Sgr C exhibits significant variability in both space and time, which confirms its reflection origin. Paradoxically, the Sgr C2 clump, which is located close to the possible interaction site of G359.41−0.12 with molecular gas, exhibits the strongest short-term variability. This strongly confirms the reflection scenario. However, cosmic-ray irradiation may still contribute to the much fainter diffuse background emission.

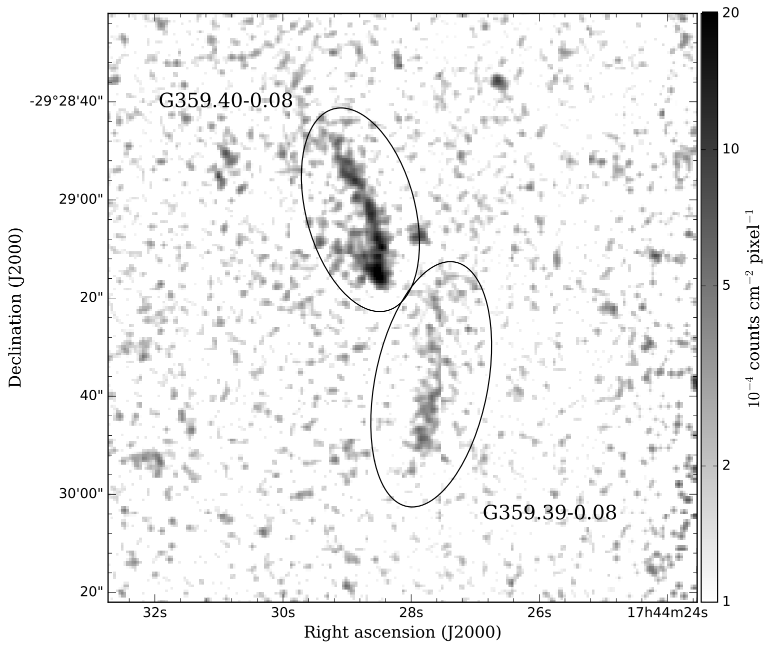

Fig. 1. Exposure-corrected image of the two non-thermal cometary features identified in Sgr C, obtained by compiling the 2005 and 2014 *Chandra* observations in the 2.0−8.0 keV band. The map is in units of counts $\mathrm{cm}^{-2}\,\mathrm{pixel}^{-1}$ with pixel size of about $0.5''$, and smoothed using a Gaussian kernel of 1-pixel radius. It is given in logarithmic scaling with north defined as up and east as left.

3 Constraints on the past activity of Sgr A*

Walls et al. (2016) have developed a Monte Carlo model computing the spectrum produced by X-ray reflection onto a spherical molecular cloud. The geometry of the phenomenon is parametrised in the model by the line-of-sight angle. The total flux in the continuum notably increases with this angle at low energies since photons only penetrate shallowly into the cloud before being scattered towards the observer. The scattered photons are thus more likely to be absorbed in the low-angle case than in the high-angle case. The strength of the 6.4 keV line and the depth of the iron edge also depends on the line-of-sight angle, as well as on the cloud column density. Both are free parameters of the Monte Carlo model that can thus be constrained through a spectral fitting procedure. This allows us to precisely determine the line-of-sight positions of the Fe Kα bright clumps, and hence to put constraints on the past lightcurve of Sgr A*.

For this purpose, we fit the data from the deepest available observations from both *XMM-Newton* and *Chandra* (taken in 2000, 2005, 2012 and 2014) with a spectral model composed of (*i*) two thermal plasmas whose temperatures are fixed at 1.0 and 6.5 keV respectively, (*ii*) the reflected emission as modelled by the Monte Carlo code and (*iii*) foreground interstellar absorption ($N_H = 7.5 \times 10^{22}$ cm^{-2}). The metallicity is set to solar values. For a given clump and a given period, the normalisation is left free to vary. The line-of-sight angle and the cloud column density (with a uniform density profile) are also left free but constant over all periods.

The best-fit values of the line-of-sight angles we obtain from the fits are used to derive the 3D positions of the clumps within the CMZ (Fig. 2). Among the three main subregions of Sgr C we study (indicated as Sgr C1, Sgr C2 and Sgr C4), two are found to be behind Sgr A*, at comparable line-of-sight distances, while the third one (Sgr C2) is in front of it. The error bars are rather small, but it should be kept in mind that some systematics affect our results (see Chuard et al. 2017a, for discussion). All clumps illuminated by the same event must be located on a parabola whose focus is Sgr A*. Given the positions we obtain, we test two hypotheses: (*i*) that all clumps (including Sgr B2; Walls et al. 2016) witness the same event and (*ii*) that the illumination in Sgr C2 is due to a second event. We fit the data with one-event and two-event models and compare the fit statistics using the F-test. The two-event scenario is found to be the best one ($p < 0.05$), with delay values (counted from the year 2000) of $\Delta t_1 = 138^{+27}_{-17}$ yr for Sgr C2 and $\Delta t_2 = 243^{+20}_{-25}$ yr for all other clouds (Sgr C1, C4 and B2). As the systematics mentioned above may affect these values, they should not be

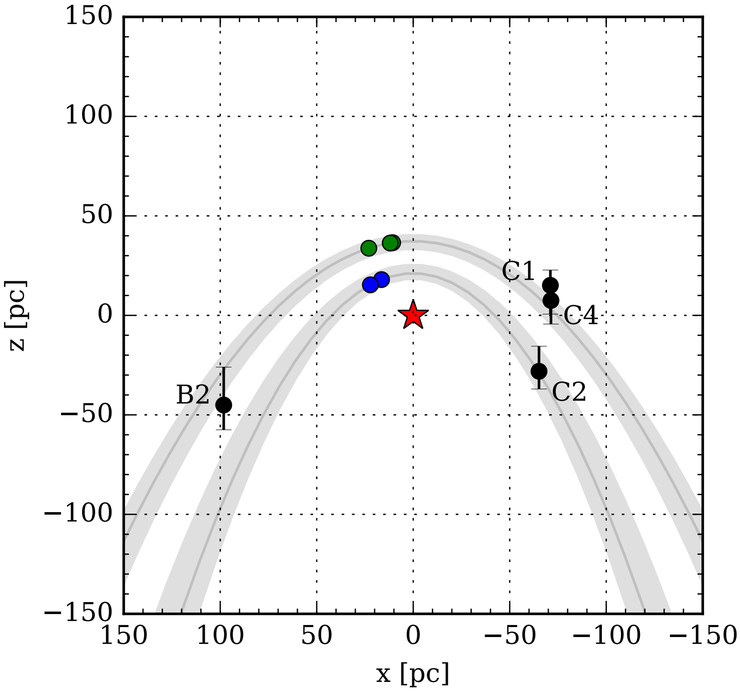

Fig. 2. Face-on view of the Galactic centre. The negative direction along the z-axis points towards the Earth. The red star marks the position of Sgr A*. The black dots show the best-fit positions for the bright clumps Sgr C1, C2, C4 (Chuard et al. 2017a) and Sgr B2 (Walls et al. 2016). The grey parabolas trace the best-fit associated wavefronts (as seen from Earth) for the two-event model. The width of the parabolas represents the uncertainty on the position, not the duration of the associated event. The green and blue dots are the predicted positions of the subregions of Sgr A (Clavel et al. 2013), assuming they witness the same two events.

considered definitive, but rather good estimates of the actual delays. Despite these limitations, our findings are confirmed by the two distinct patterns of variation seen in the lightcurves of the clumps (see Terrier et al. 2017; Chuard et al. 2017a). They are also consistent with the two-event scenario proposed by Clavel et al. (2013) for five clumps of the Sgr A complex. Indeed, their lightcurves exhibit the same two patterns of variation, which leads us to believe that they witness the same two events as the subregions of Sgr C. Based on this assumption, it is possible to predict their line-of-sight positions (Fig. 2). Testing this hypothesis by applying the Monte Carlo model to the Sgr A complex will be the subject of future work.

4 Conclusions

Sgr C is a complex region which notably hosts a SNR candidate possibly interacting with molecular material and two nearby non-thermal X-ray filaments whose spectrum and morphology suggest they are pulsar wind nebulae. These objects may be responsible for intense cosmic-ray production, which may lead to some Fe Kα emission. However, the significant variability of the emission discards this hypothesis and strongly supports the reflection scenario.

Using a Monte Carlo spectral model to determine the three-dimensional positions of the 6.4 keV bright clumps, we propose that Sgr C1, C4 and B2 are all illuminated by the same event, while Sgr C2 is likely illuminated by a second flare that took place about 100 years later. These results are supported by imaging analysis and lightcurve extraction, and are consistent with previous works based on different approaches.

This research had made use of data obtained with *XMM-Newton*, an ESA science mission with instruments and contributions directly funded by ESA Member States and NASA, and from the *Chandra* Data Archive, as well as software provided by the *Chandra* X-ray Center (CXC) in the application packages CIAO, ChIPS, and Sherpa. The authors acknowledge the Centre National d'Études Spatiales (CNES) for financial support.

References

Baganoff, F. K., Maeda, Y., Morris, M., et al. 2003, ApJ, 591, 891

Balick, B. & Brown, R. L. 1974, ApJ, 194, 265

Capelli, R., Warwick, R. S., Porquet, D., Gillessen, S., & Predehl, P. 2012, A&A, 545, A35

Chuard, D., Terrier, R., Goldwurm, A., et al. 2017a, A&A, submitted

Chuard, D., Terrier, R., Goldwurm, A., et al. 2017b, in IAU Symposium, Vol. 322, The Multi-Messenger Astrophysics of the Galactic Centre, ed. R. M. Crocker, S. N. Longmore, & G. V. Bicknell, 208–209

Churazov, E., Khabibullin, I., Sunyaev, R., & Ponti, G. 2017, MNRAS, 465, 45

Clavel, M., Terrier, R., Goldwurm, A., et al. 2013, A&A, 558, A32

Dogiel, V., Cheng, K.-S., Chernyshov, D., et al. 2009, PASJ, 61, 901

Genzel, R., Eisenhauer, F., & Gillessen, S. 2010, Reviews of Modern Physics, 82, 3121

Goldwurm, A., Cordier, B., Paul, J., et al. 1994, Nature, 371, 589

Johnson, S. P., Dong, H., & Wang, Q. D. 2009, MNRAS, 399, 1429

Koyama, K., Maeda, Y., Sonobe, T., et al. 1996, PASJ, 48, 249

Liszt, H. S. & Spiker, R. W. 1995, ApJS, 98, 259

Morris, M. & Serabyn, E. 1996, ARA&A, 34, 645

Nakajima, H., Tsuru, T. G., Nobukawa, M., et al. 2009, PASJ, 61, 233

Ponti, G., Morris, M. R., Terrier, R., & Goldwurm, A. 2013, in Astrophysics and Space Science Proceedings, Vol. 34, Cosmic Rays in Star-Forming Environments, ed. D. F. Torres & O. Reimer, 331

Ponti, G., Morris, M. R., Terrier, R., et al. 2015, MNRAS, 453, 172

Ryu, S. G., Nobukawa, M., Nakashima, S., et al. 2013, PASJ, 65, 33

Su, M., Slatyer, T. R., & Finkbeiner, D. P. 2010, ApJ, 724, 1044

Sunyaev, R. A., Markevitch, M., & Pavlinsky, M. 1993, ApJ, 407, 606

Tatischeff, V., Decourchelle, A., & Maurin, G. 2012, A&A, 546, A88

Terrier, R., Soldi, S., Clavel, M., et al. 2017, A&A, submitted

Tsuru, T. G., Nobukawa, M., Nakajima, H., et al. 2009, PASJ, 61, 219

Walls, M., Chernyakova, M., Terrier, R., & Goldwurm, A. 2016, MNRAS, 463, 2893

Yusef-Zadeh, F., Law, C., & Wardle, M. 2002, ApJ, 568, L121

Zubovas, K., King, A. R., & Nayakshin, S. 2011, MNRAS, 415, L21

Zubovas, K. & Nayakshin, S. 2012, MNRAS, 424, 666

SF2A 2017
C. Reylé, P. Di Matteo, F. Herpin, É. Lagadec, A. Lançon, Z. Meliani, F. Royer (eds)

CAN WE OBSERVE NEUTRINO FLARES IN COINCIDENCE WITH EXPLOSIVE TRANSIENTS?

C. Guépin[1] and K. Kotera[1, 2]

Abstract. The new generation of powerful instruments is reaching sensitivities and temporal resolutions that will allow multi-messenger astronomy of explosive transient phenomena, with high-energy neutrinos as a central figure. We derive general criteria for the detectability of neutrinos from powerful transient sources for given instrument sensitivities. In practice, we provide the minimum photon flux necessary for neutrino detection based on two main observables: the bolometric luminosity and the time variability of the emission. This limit can be compared to the observations in specified wavelengths in order to target the most promising sources for follow-ups. Our criteria can also help distinguishing false associations of neutrino events with a flaring source. We find that relativistic transient sources such as high- and low-luminosity gamma-ray bursts (GRBs), blazar flares, tidal disruption events, and magnetar flares could be observed with IceCube, as they have a good chance to occur within a detectable distance. Of the nonrelativistic transient sources, only luminous supernovae appear as promising candidates. We caution that our criterion should not be directly applied to low-luminosity GRBs and type Ibc supernovae, as these objects could have hosted a choked GRB, leading to neutrino emission without a relevant counterpart radiation. We treat the concrete example of PKS 1424-418 major outburst and the possible association with an IceCube event IC 35.

Keywords: Neutrinos, transients

1 Introduction

With their improved sensitivity and time resolution together with the possibility of fast follow-up, current instruments allow the observation of Galactic and extragalactic transient phenomena over a wide energy range. The recent advances in neutrino and gravitational-wave detection open promising perspectives for transient multi-messenger studies. High-energy neutrinos are expected to play a key role in this picture as undeflected signatures of hadronic acceleration.

Recently, IceCube has opened exciting perspectives in neutrino astronomy by detecting very high energy astrophysical neutrinos Aartsen et al. (2013) and has developed and enhanced methods for time-variable searches Abbasi et al. (2012). So far, no neutrino detection has been confirmed in association with a transient source. In this context, it appears timely to derive general criteria for the detectability of neutrinos from powerful transient sources.

We focus in this work on sources that are characterized by short, violent, and irregular emissions, sometimes in addition to a quiescent emission, and that are usually associated with the acceleration of leptonic and hadronic particles. Photo-hadronic and hadronic interactions can lead to a neutrino production. Here we focus on the production of neutrino flares: we aim at constraining the parameter space of bursts and flares detectable in neutrinos by providing necessary conditions on the background fields of the source. Predicting neutrino flux levels is not the scope of this study; we focus here on estimating lower limits on the photon flux of the flare, which is required for the efficient production of a neutrino flare.

We demonstrate that we can describe the large variety of existing sources with a handful of variables: the distance from the source $D_{\rm s}$, the isotropic bolometric luminosity of the flare $L_{\rm bol}$ and its peak energy $\epsilon_{\rm peak}$, the variability timescale of the emission $t_{\rm var}$, and the bulk Lorentz factor of the outflow Γ. We calculate in the

[1] Sorbonne Universités, UPMC Univ. Paris 6 et CNRS, UMR 7095, Institut d'Astrophysique de Paris, 98 bis bd Arago, 75014 Paris, France
[2] Laboratoire AIM-Paris-Saclay, CEA/DSM/IRFU, CNRS, Universite Paris Diderot, F-91191 Gif-sur-Yvette, France

$L_{\rm bol} - t_{\rm var}$ parameter-space the maximum accessible neutrino energy in these sources and the minimum flux of photons in a flare required at a specific given wavelength, in order to allow detectability of a neutrino flare with IceCube.

2 Maximum accessible proton energy and indicative maximum neutrino energy

We consider a proton* of energy $E_p = \gamma_p m_p c^2$, accelerated in a one-zone region of size $R = \beta c\,\Gamma^2 t_{\rm var}(1+z)^{-1}$, bulk Lorentz factor $\Gamma = (1-\beta^2)^{-1/2}$, and of magnetic field strength B, in a source located at redshift z. We derive the mean magnetic field strength by setting $L_B = \eta_B L_{\rm bol}$, where $L_{\rm B}$ is the magnetic luminosity, defined as $L_B \sim (1/2)\beta c\,\Gamma^2 R^2 B'^2$.†

Focussing on flares has some important theoretical consequences. $t_{\rm var}$ is related to the size of the emitting region R by a condition of causality: $R \sim \beta\Gamma^2(1+z)^{-1}ct_{\rm var}$, where βc is the velocity of the outflow, and z the redshift of the source. The particle escape time is limited by the dynamical time $t_{\rm dyn} = \Gamma^2 t_{\rm var}(1+z)^{-1}$, which corresponds to the adiabatic energy loss time. In the same way, we consider only photo-hadronic interactions of accelerated hadrons on the *flaring* radiation, as interactions with steady baryon and photon fields would produce a neutrino emission diluted over time.

The acceleration timescale can be related to the particle Larmor time $t_{\rm acc} = \eta t_{\rm L}$, regardless of the acceleration mechanism (unless one invokes peculiar non-conducting plasmas) and in most cases $\eta \gg 1$ Lemoine & Waxman (2009). Given the complexity of particle acceleration models, we consider in the following the maximally efficient acceleration timescale, with $\eta \sim 1$; therefore $t'_{\rm acc} = E'_p/c\,e\,B'$. This timescale is usually overly optimistic in terms of efficiency; it is thus conservative to derive the necessary condition for detectability.

The maximum energy of accelerated particles is set by the competition between energy gains and energy losses: $t_{\rm acc} < \min(t_{\rm dyn}, t_{\rm syn})$ where $t_{\rm syn}$ is the synchrotron energy-loss timescale. In presence of strong magnetic fields, synchrotron cooling can be stronger than adiabatic energy losses. We assume that the magnetic luminosity of the considered region is fully radiated during the flare and set $\eta_B = 1$, which is valid if the dominant emission process is synchrotron radiation. Other energy-loss processes can influence the maximum energy of particles. We choose to neglect them here, as it preserves the *maximum achievable* nature of $E_{p,\rm max}$.

Photohadronic interactions can generate neutrinos through the production of charged pions and their subsequent decay.‡ Neutrinos produced by photohadronic interactions typically carry 5% of the initial energy of hadrons. However, pions and muons can experience energy losses by adiabatic or synchrotron cooling before they decay. The muon decay time is usually the main limiting factor for neutrino production.

We find that for nonrelativistic outflows ($\Gamma \sim 1$), mild luminosities $L_{\rm bol} > 10^{36}$ erg s^{-1} and variability timescales longer than $t_{\rm var} \sim 10\,$s are required to reach $E_\nu > 100\,$TeV, which is the lower limit of the IceCube detection range. Sensitivities of future experiments such as GRAND Martineau-Huynh et al. (2016), aiming at energies $E_\nu > 1$ EeV, would be reached for higher luminosities $L_{\rm bol} > 10^{42}$ erg s^{-1} and longer variability timescales $t_{\rm var} > 10^6\,$s. We find that high-luminosity (HL) GRBs can accelerate protons up to $10^{20}\,$eV, which corresponds to classical estimates Waxman & Bahcall (2000). They could in principle produce very high energy neutrinos, with $E_\nu \lesssim 10^{18}$ eV. In this case, muon decay constitutes a very strong limiting factor and hence the maximum energy strongly depends on the variability timescale. Blazars, low-luminosity (LL) GRBs, and tidal disruption events (TDE) are also powerful accelerators with $E_\nu \lesssim 10^{18}$ eV.

3 Neutrino flux and detectability limit

We consider that the photon spectrum of the flare follows a broken power-law over $[\epsilon_{\rm min}, \epsilon_{\rm max}]$, with a break energy $\epsilon_{\rm b}$ and spectral indices $a < b$, with $b > 2$. This type of spectrum is adequate to model nonthermal processes such as synchrotron emission. However, the spectral energy distribution (SED) of explosive transients shows great diversity, and our approach could be refined by using more realistic SED. The maximum achievable neutrino flux can be estimated from the proton energy spectrum Waxman & Bahcall (1999): $E_\nu^2 F_\nu = 3/8 f_{p\gamma} E_p^2 F_p$, where $f_{p\gamma} \equiv t'_{\rm dyn}/t'_{p\gamma}$ is the photo-pion production efficiency. The photo-pion production timescale $t'_{p\gamma}$ depends

*For maximization reasons, we concentrate on the proton case, which should lead to the highest rates of neutrino production compared to heavier nuclei.

†All primed quantities are in the comoving frame of the emitting region. Quantities are labeled $Q_x \equiv Q/10^x$ in cgs units or in eV for particle energies.

‡The resulting flavor composition is $\nu_e : \nu_\mu : \nu_\tau = 1 : 2 : 0$, and the expected flavor composition at Earth is $1 : 1 : 1$ when long-baseline neutrino oscillations are accounted for. The fluxes we calculate account for all neutrino flavors.

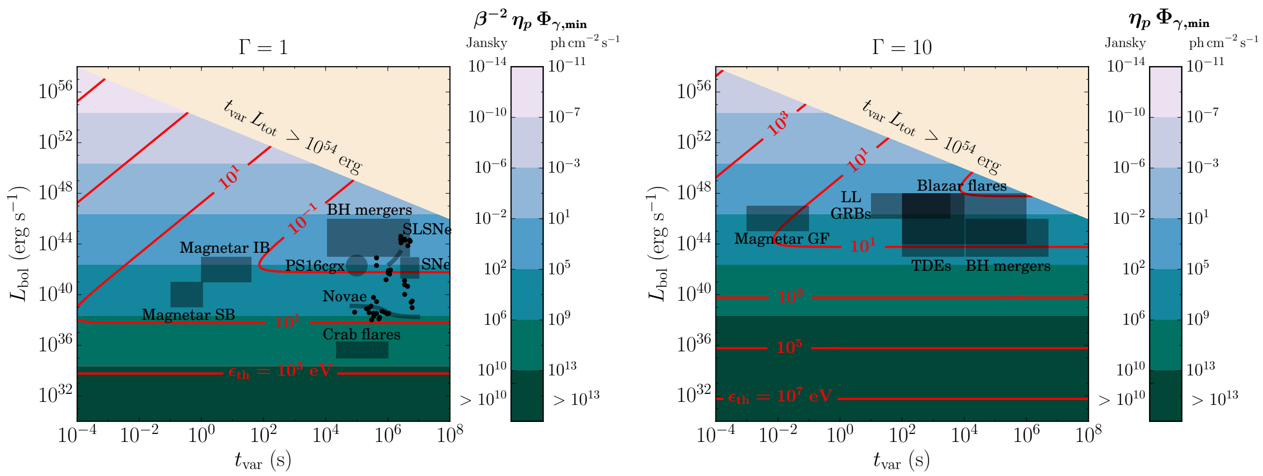

Fig. 1. Minimum photon flux $\Phi_{\gamma,\rm min}$ (color map, in Jy and ph cm^{-2} s^{-1}) as a function of $L_{\rm bol}$ and $t_{\rm var}$ for $\Gamma = 1, 10$. A neutrino flare *can* be detectable if the observed photon flux $\Phi_{\gamma,\rm obs} \gtrsim \Phi_{\gamma,\rm min}$, above $\epsilon_{\rm th}$ (red lines) for soft photon spectra, and at $\epsilon_{\rm b}$ for hard spectra. Here $\eta_B = \eta_p = 1$. Overlaid are examples of explosive transients in the $L_{\rm bol} - t_{\rm var}$ parameter space.

on the interaction threshold energy $\epsilon'_{\rm th}$, the cross-section $\sigma_{p\gamma}$ and the inelasticity $\kappa_{p\gamma}$. We assume that a fraction η_p of the bolometric source luminosity is channelled into a population of accelerated protons, with a peak luminosity $\sim \eta_p L_{\rm bol}$.

For a neutrino detector of flux sensitivity $s_{\rm exp}$ and fluence sensitivity $\mathcal{S}_{\rm exp} \sim t_{\rm var} s_{\rm exp}$, we calculate the minimum photon flux required to reach the experimental detection limit, defining $\Phi_\gamma \equiv L/(4\pi D_{\rm L}^2 \epsilon)$[§]

$$\Phi_{\gamma,\rm min} = \frac{8}{3}\frac{4\pi\beta^2 c^2 \Gamma^4 \mathcal{S}_{\rm exp}}{\langle\sigma_{p\gamma}\kappa_{p\gamma}\rangle}\eta_p^{-1} L_{\rm bol}^{-1}(1+z)^{-1} \simeq 2\,{\rm Jy}\ \eta_p^{-1}\Gamma_2^4\, L_{{\rm bol},52}^{-1}\,(1+z)^{-1}\ . \tag{3.1}$$

The flux should be estimated at the minimum threshold energy $\epsilon_{\rm th} = \Gamma\,\epsilon''_{\rm th}\, m_p c^2/(1+z)E'_{p,\rm max}$ for soft photon spectra ($a > 1$), and at the observed spectral break energy $\epsilon_{\rm b}$ for hard photon spectra ($a < 1$). For IceCube, the sensitivity is characterized by a minimum fluence $\mathcal{S}_{\rm IC} = 5 \times 10^{-4}$ TeV cm^{-2} for $E_\nu = 10\,$TeV$-10\,$PeV, which corresponds to a detection limit $s_{\rm IC} \sim 10^{-11}$ TeV cm^{-2} s^{-1} for a one-year data collection. The planned sensitivities for ARA, ARIANNA, CHANT, or GRAND are 1, 1.5, or 2 orders of magnitude better, respectively, than IceCube, at $E_\nu \sim 1$ EeV. In the following, we set the cosmic-ray loading factor $\eta_p = 1$ as a standard estimate, but most conservative limits should be obtained for $\eta_p = 100$.

We show in Figure 1 the minimum photon flux required to reach IceCube detection limit in the $L_{\rm bol} - t_{\rm var}$ parameter space for $\Gamma = 1, 10$. We set $\eta_p = \eta_B = 1$. We locate also concrete examples of explosive transients in the parameter space. The blazar case is discussed in Section 4.

In practice, here we describe how these figures can be used to determine whether an explosive transient could have a chance to be detected in neutrinos with IceCube. 1) Choose a bulk Lorentz factor Γ for the outflow.[¶] 2) Identify a broken power-law shape in the source emission, roughly measure the break energy $\epsilon_{\rm b}$ and whether the spectrum is soft ($a > 1$) or hard ($a < 1$) below the break. 3) Locate the source in the $L_{\rm bol} - t_{\rm var}$ parameter space and read the required flux $\Phi_{\gamma,\rm min}$ (colored contours). 4) Compare $\Phi_{\gamma,\rm min}$ with the observed flux of the source $\Phi_{\gamma,\rm obs}$, around the threshold energy $\epsilon_{\rm th}$ for soft spectra ($a < 1$), or at the break energy $\epsilon_{\rm b}$ for hard spectra ($a < 1$). A neutrino flare associated with the photon flare *can* be detectable if $\Phi_{\gamma,\rm obs} \gtrsim \Phi_{\gamma,\rm min}$.

We note that for many sources, $\Phi_{\gamma,\rm obs} \ll \Phi_{\gamma,\rm min}$ over the whole radiation spectrum, thus the knowledge of $\epsilon_{\rm th}$ or $\epsilon_{\rm b}$ is not necessary to conclude on the non-detectability. For more refined cases, however, we caution that $\epsilon_{\rm th}$ is a minimum value because it was derived from $E_{p,\rm max}$ (a maximum value). When checking detectability, one might wish to extend the comparison between $\Phi_{\gamma,\rm obs}$ and $\Phi_{\gamma,\rm min}$ for $\epsilon_{\rm th} > \epsilon_{\rm th,min}$, in case the actual maximum

[§] We note that Φ_γ is a directly measurable quantity

[¶] In general, for a given luminosity, a higher Γ implies a higher $\Phi_{\gamma,\rm min}$ (Eq. 3.1), and is thus worse in terms of constraints. This can be kept in mind for sources with large uncertainties on Γ.

proton energy is lower than $E_{p,\max}$. Extrapolation of spectra should be conducted with care, always trying to maximize the photon flux, in order to avoid missing a detectable case.

4 Implications for categories of transients and specific case studies

The general approach presented up to this point allows us to evaluate the detectability in neutrinos of a large variety of explosive transients. We study the implications for general source categories and examine several concrete examples. Here we discuss in detail Blazar flares, and illustrate with the case of PKS 1424-418 major outburst. We refer to our main study Guépin & Kotera (2017) for more detail about other categories of transients.

Blazars are a subset of AGN whose jet is pointed toward the observer. Unification models allow to set their mean bulk Lorentz factor to $\Gamma_{\rm j} \sim 10$. A blazar flare is a very fast and short increase in blazar luminosity, with $t_{\rm var} \sim 10^2 - 10^6\,$s. In realistic scenarii, the bulk Lorentz factor of the flare is $\Gamma \gtrsim 100$. Blazar SEDs exhibit two nonthermal peaks, at low and high energies. In some cases, Blazar flaring emissions can be described by a soft power-law from submillimeter to X-rays, with typically $L_{\rm b} \sim 10^{45}$ erg s^{-1} at $\epsilon_{\rm b} \sim 1$ keV.

The IceCube Collaboration has detected astrophysical neutrinos up to PeV energies. For the third PeV event (IC 35, $E_\nu \sim 2$ PeV), searches for coincidence with AGN flares revealed a possible association with the major outburst of the Blazar PKS 1424-418 Kadler et al. (2016). A bright γ-ray emission and an increase in X-ray, optical, and radio emissions were observed in 2012 - 2013. The flux necessary for detectability, $\Phi_{\gamma,\min} \sim 1.7 \times 10^3\,{\rm ph\,cm^{-2}s^{-1}}$, is very close to the observed flux. Therefore, neutrino flares associated with such outbursts could meet the IceCube detection requirement. However, the association between the neutrino event and the blazar outburst remains unclear. Moreover, the value of the bulk Lorentz factor can strongly influence the results: a larger value $\Gamma > 10$ would disfavor detection.

5 Conclusion

We have derived the minimum photon flux necessary for neutrino detection from explosive transients, based on two main observables: the bolometric luminosity $L_{\rm bol}$, and the time variability $t_{\rm var}$ of the flaring emission. Our minimum photon flux requirement can be compared at around the indicated energy to the observed photon flux from various transient sources, in order to assess their detectability in neutrinos.

We find that for nonrelativistic and mildly relativistic outflows, only the photon fields between IR to UV wavelengths are relevant for neutrino production. Sources flaring at very high energy with no optical counterparts will not be observed. Of the NR transient sources, SLSNe appear to be the most promising candidates. The production of very high energy neutrinos, up to $E_\nu = 1\,$EeV, requires relativistic outflows. Such neutrinos could be produced by HL GRBs, LL GRBs, blazars, or TDEs. As computed by several authors, very luminous short bursts (GRBs, magnetar flares) have a good chance of being observed. However, cooling processes could prevent detection by strongly reducing the flux at the highest energies. Pions or muons could also leave the flaring region before decaying, and thereby delay the neutrino flare.

Our criterion should not be directly applied to low-luminosity GRBs or type Ibc supernovae because these objects could be off-axis GRBs or have hosted a choked GRB, leading to neutrino emission without a relevant radiation counterpart. Nevertheless, this study can be applied to a wide range of well-known sources and sensitivities of projected instruments. Our results indicate that with an increase of one to two orders of magnitude in sensitivity, next-generation neutrino detectors could have the potential to discover neutrino flares in PeV or EeV energy ranges.

References

Aartsen, M. G., Abbasi, R., Abdou, Y., et al. 2013, Physical Review Letters, 111, 021103

Abbasi, R., Abdou, Y., Abu-Zayyad, T., et al. 2012, ApJ, 744, 1

Guépin, C. & Kotera, K. 2017, A&A, 603, A76

Kadler, M., Krauß, F., Mannheim, K., et al. 2016, Nature Physics, 12, 807

Lemoine, M. & Waxman, E. 2009, J. Cosmology Astropart. Phys., 11, 009

Martineau-Huynh, O. et al. 2016, EPJ Web Conf., 116, 03005

Waxman, E. & Bahcall, J. 1999, Phys. Rev. D, 59, 023002

Waxman, E. & Bahcall, J. N. 2000, ApJ, 541, 707

SF2A 2017
C. Reylé, P. Di Matteo, F. Herpin, É. Lagadec, A. Lançon, Z. Meliani, F. Royer (eds)

THE DEVELOPMENT OF NEUTRINO-DRIVEN CONVECTION IN CORE-COLLAPSE SUPERNOVAE: 2D VS 3D

R. Kazeroni[1,2], B. K. Krueger[2], J. Guilet[2] and T. Foglizzo[2]

Abstract. A toy model is used to study the non-linear conditions for the development of neutrino-driven convection in the post-shock region of core-collapse supernovae. Our numerical simulations show that a buoyant non-linear perturbation is able to trigger self-sustained convection only in cases where convection is not linearly stabilized by advection. Several arguments proposed to interpret the impact of the dimensionality on global core-collapse supernova simulations are discussed in the light of our model. The influence of the numerical resolution is also addressed. In 3D a strong mixing to small scales induces an increase of the neutrino heating efficiency in a runaway process. This phenomenon is absent in 2D and this may indicate that the tridimensional nature of the hydrodynamics could foster explosions.

Keywords: hydrodynamics – instabilities – accretion – shock waves – supernovae: general

1 Introduction

The explosion of massive stars in core-collapse supernovae (CCSNe) relies crucially on the action of the multi-dimensional dynamics in the core of the progenitor during the first hundreds milliseconds after the core collapses into a proto-neutron star (Foglizzo et al. 2015; Janka et al. 2016 for recent reviews). The delayed neutrino mechanism is considered as the most suitable scenario to explain a majority of core-collapse supernovae (Bethe & Wilson 1985). Detailed calculations showed that imposing spherical symmetry (1D) does not lead to an explosion (Liebendörfer et al. 2001) except for the lightest progenitors (Kitaura et al. 2006). Axisymmetric simulations (2D) revealed that two distinct instabilities can lead to a shock revival (Müller et al. 2012; Fernández et al. 2014). Both neutrino-driven convection (Herant et al. 1994; Burrows et al. 1995) and the Standing Accretion Shock Instability (SASI) (Blondin et al. 2003) break the spherical symmetry of the collapse, generate large scale non-radial motions, increase the advection timescale through the gain region and enhance the energy deposition. However in a majority of cases, 2D simulations generate under-energetic explosions (Müller 2015). Most three-dimensional (3D) simulations even produce less optimistic results with fewer explosions and a slower growth of the explosion energy (e.g. Melson et al. 2015a; Lentz et al. 2015). The different directions in which the turbulent energy cascade acts may explain the discrepancies between 2D and 3D (Hanke et al. 2012).

In this study a toy model is used to investigate the impact of the dimensionality on the dynamics of the gain region. This approach is complementary to global simulations which are still computationally challenging and for which it is complex to disentangle the hydrodynamics from other physical ingredients. We focus on the neutrino-driven convection, seen in most CCSN simulations, and develop an idealized description of the advection through the gain region. Foglizzo et al. (2006) showed that convection can be stabilized linearly by advection when the perturbations are rapidly advected outside of the heating region. Even if a perturbative analysis predicts linear stability, convection could in principle be triggered non-linearly by a perturbation with a large enough amplitude (Scheck et al. 2008).

We begin in Section 2 with a presentation of the idealized model. In section 3 we examine the linear and the non-linear onsets of convection. The impact of the dimensionality is studied in section 4. Finally we summarize our findings and conclude in section 5.

[1] Max-Planck-Institut für Astrophysik, Karl-Schwarzschild-Str. 1, D-85748 Garching, Germany
[2] Laboratoire AIM, CEA/DRF-CNRS-Université Paris Diderot, IRFU/Département d'Astrophysique, CEA-Saclay F-91191, France

2 Physical and numerical setup

The advection of matter through the gain region is modeled by a stationary and subsonic flow, parallel in the vertical direction (z), which experiences a constant gravity and heating proportionally to the density in the central region of the simulation domain. Upstream and downstream of the gain region, gravity and heating are turned off and the flow is uniform. These uniform regions alow us to place the boundaries far enough in the vertical direction to avoid numerical reflections that would impact the dynamics in the central region where convection can develop. The shock wave and the cooling layer are absent from our model which can be seen as a fraction of a realistic gain region.

A perturbative analysis similar to the one of Foglizzo et al. (2006) shows that the flow is linearly unstable to convection if

$$\chi \equiv \int_{r_{\rm g}}^{r_{\rm sh}} \omega_{\rm BV} \frac{dr}{|v_r|} \sim \frac{t_{\rm adv}}{t_{\rm conv}} > 2, \tag{2.1}$$

where $r_{\rm g}$, $r_{\rm sh}$, $t_{\rm adv}$ and $t_{\rm conv}$ respectively refer to the gain radius, the shock radius, the advection timescale across the gain region and the buoyancy timescale related to the Brunt-Väisälä frequency $\omega_{\rm BV}$.

A density perturbation is added to the stationary flow to trigger convection. Such perturbations may arise from entropy-vorticity waves produced by shock oscillations driven by SASI (Foglizzo et al. 2007), progenitor asphericites resulting from convection in Si,O shells (Müller et al. 2016) or originate from numerical artifacts such as embedded Cartesian grids using several refinement levels (Ott et al. 2013). The perturbation characteristics are set so that the unstable mode with the highest growth rate is triggered. The perturbation has a two-dimensional structure and a random noise of the order of 0.1% in density is added in the transverse direction to enable the development of the instability in 3D.

The time-dependent simulations are performed with the RAMSES code (Teyssier 2002; Fromang et al. 2006). The dimensions of the Cartesian domain are: $-150\,\mathrm{km} \leq \mathrm{x}, \mathrm{y} \leq 150\,\mathrm{km}$ for the horizontal directions and $-450\,\mathrm{km} \leq \mathrm{z} \leq 450\,\mathrm{km}$ for the vertical one. The gain region is located in the central part: $-50\,\mathrm{km} \leq \mathrm{z} \leq 50\,\mathrm{km}$. The heating and the gravity are smoothened at the edges of the gain region to avoid discontinuities. The details of the setup will be discussed in a forthcoming paper (Kazeroni et al., in preparation).

3 Competition between advection and convection

In the regime of linear stability, it was proposed that convection could be triggered by a perturbation with a high enough amplitude (Scheck et al. 2008). We test that hypothesis by performing a set of 2D simulations with different perturbation amplitudes ($\delta\rho/\rho$) and an initial value of χ below the instability threshold. We observe that the criterion of Scheck et al. (2008), giving a threshold of about 1%, is robust to predict the presence of upward motions in the gain region (Fig. 1, left). Nevertheless that is not a sufficient condition to generate self-sustained convection because buoyant motions are suppressed within an advection timescale in the case of $\delta\rho/\rho = 1\%$. Regardless the perturbation amplitude, the convective instability is always suppressed in the linear stability regime. The damping timescale increases with higher perturbation amplitudes and the proximity to the instability threshold $\chi = 2$ (Fig. 1). This shows that a single excitation by a strong perturbation is not sufficient to trigger self-sustained convection in situations where convection is linearly stabilized by advection.

The robustness of the linear instability threshold proposed by Foglizzo et al. (2006) is assessed using a second set of parametric simulations. The self-sustained instability is only obtained in cases where the χ value of the stationary flow is above the instability threshold (Fig. 1, right). This suggests that the criterion (2.1) can also be applied in the non-linear regime for which the perturbative analysis is not suitable.

4 The impact of the dimensionality

In this section, we examine the discrepancies between 2D and 3D in a case where convection is linearly unstable. The dynamics is already impacted by the dimensionality in the early non-linear phase. We observe that some 3D buoyant bubbles rise faster than their 2D counterparts. Besides, 3D simulations exhibit a higher growth of the entropy after the linear phase (Fig. 2). These discrepancies are consistent with the properties of the Rayleigh-Taylor instability. For the latter, it was shown that 3D non-linear penetration depths are higher in the case of an incompressible flow without advection (Young et al. 2001).

While the instability saturates after 4-5 advection timescales in 2D, a very distinct dynamics is observed in 3D. In the latter case, the entropy increases in a runaway process. The downflows are decelerated due to a

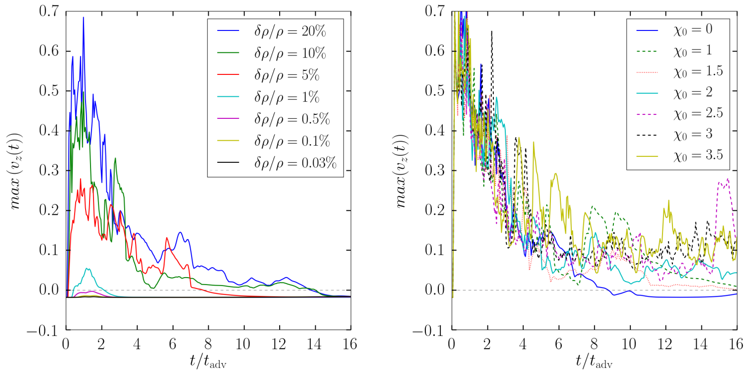

Fig. 1. Left: Time evolution of the maximum upward velocity in the gain region of 2D simulations with $\chi_0 = 1.5$. In all cases, this quantity becomes negative showing that buoyant motions are suppressed. **Right:** Time evolution of the maximum upward velocity in the gain region for a perturbation amplitude of $\delta\rho/\rho = 30\%$ and several values of χ_0. Convective motions are suppressed and the flow returns to a stable state only in cases where $\chi_0 < 2$. The instability is self-sustained beyond that threshold.

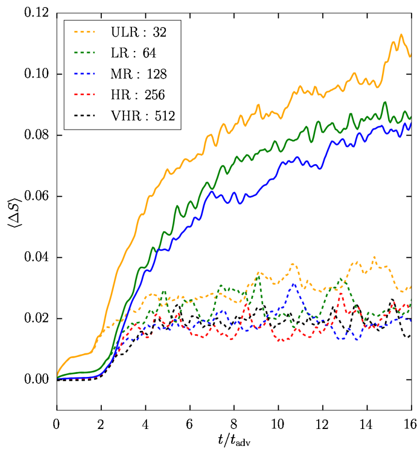

Fig. 2. Time evolution of the average entropy in the gain region of 2D (dashed curves) and 3D (solid curves) simulations. The numerical resolution is varied from 32 to 128 vertical cells in the gain region in 3D and from 32 to 512 in 2D.

more efficient mixing to small scales at their interfaces. This keeps the matter in the gain region for a longer time and thus generates more heating. On the contrary, the downflows are not disrupted in 2D and the matter is channeled more easily below the gain region (Fig. 3). Rather than being mixed, the 2D flow is stirred by large scale vortices.

The numerical resolution does not seem to affect dramatically the dynamics. An earlier growth of the instability is observed in the lowest resolution case (Fig. 2) which is rather due to the relaxation of the stationary flow on the numerical grid. Similar asymptotic entropy values are reached in 2D for the different resolutions considered. The same conclusion can be drawn from the 3D simulations keeping in mind the artificial earlier growth of in instability at low resolution. The role of the numerical resolution on global CCSN simulations is not clear yet (e.g. Janka et al. 2016). Radice et al. (2016) studied a more realistic stationary flow and concluded that despite a mixing to smaller scales with increasing numerical resolution no clear correlation exists between the evolution of global quantities, such as the shock radius and the numerical resolution.

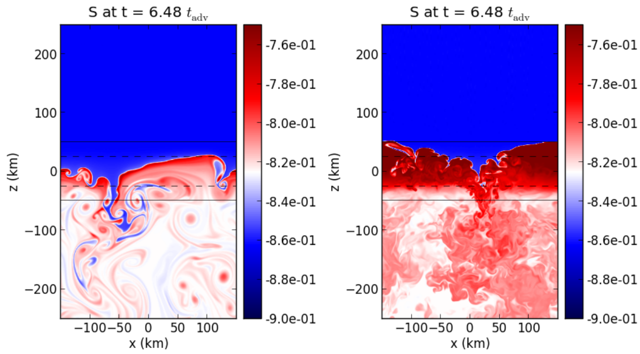

Fig. 3. Entropy snapshots of the fully turbulent dynamics. In 2D *(left)*, a downflow penetrates in the downstream layer and channels matter in a region without heating. On the contrary, the 3D *(right)* downflows are fragmented to small scales and this increases the advection time. Consequently, the heating efficiency increases in a runaway process.

5 Conclusions

The development of neutrino-driven convection was investigated using an idealized model of the gain region of CCSNe. We tested the robustness of linear and non-linear conditions to generate the instability. We found that the threshold proposed by Foglizzo et al. (2006) can be successfully applied even when the perturbed flow is already in the non-linear regime. A criterion relying on a competition between convection and advection is not sufficient to predict the development of a self-sustained instability triggered by a non-linear perturbation, because the stratification of the flow should be taken into account.

The dynamics of the gain region is severely impacted by the dimensionality. In 3D a turbulent mixing to small scales fragments the downflows. Consequently the heating efficiency increases in a runaway process. On the contrary, large scale motions in 2D channel efficiently the matter outside of the gain region preventing a continuous entropy increase as in 3D. The numerical resolution does not seem to play a significant role, at least when the instability is triggered linearly by a low perturbation amplitude.

Increasing the complexity of our model would help evaluate the relevance for global CCSN simulations of the positive 3D effects identified in this purely hydrodynamical study. The present work captures physical ingredients that seem supportive of more robust explosions in 3D as witnessed similarly by Melson et al. (2015b) and Müller (2015) in some convection-dominated low-mass progenitors. Whether these positive effects are generic characteristics of CCSNe will only be answered by performing self-consistent 3D simulations of a large set of progenitors which will become feasible within the next decade.

This work was granted access to the HPC resources of TGCC/CINES under the allocations t2014047094, x2015047094 and t2016047094 made by GENCI (Grand Équipement National de Calcul Intensif). This work is part of ANR funded project SN2NS ANR-10-BLAN-0503.

References

Bethe, H. A. & Wilson, J. R. 1985, ApJ, 295, 14

Blondin, J. M., Mezzacappa, A., & DeMarino, C. 2003, ApJ, 584, 971

Burrows, A., Hayes, J., & Fryxell, B. A. 1995, ApJ, 450, 830

Fernández, R., Müller, B., Foglizzo, T., & Janka, H.-T. 2014, MNRAS, 440, 2763

Foglizzo, T., Galletti, P., Scheck, L., & Janka, H.-T. 2007, ApJ, 654, 1006

Foglizzo, T., Kazeroni, R., Guilet, J., et al. 2015, PASA, 32, 9

Foglizzo, T., Scheck, L., & Janka, H.-T. 2006, ApJ, 652, 1436

Fromang, S., Hennebelle, P., & Teyssier, R. 2006, A&A, 457, 371

Hanke, F., Marek, A., Müller, B., & Janka, H.-T. 2012, ApJ, 755, 138

Herant, M., Benz, W., Hix, W. R., Fryer, C. L., & Colgate, S. A. 1994, ApJ, 435, 339

Janka, H.-T., Melson, T., & Summa, A. 2016, Annual Review of Nuclear and Particle Science, 66, 341

Kitaura, F. S., Janka, H., & Hillebrandt, W. 2006, A&A, 450, 345
Lentz, E. J., Bruenn, S. W., Hix, W. R., et al. 2015, ApJ, 807, L31
Liebendörfer, M., Mezzacappa, A., Thielemann, F.-K., et al. 2001, Phys. Rev. D, 63, 103004
Melson, T., Janka, H.-T., Bollig, R., et al. 2015a, ApJ, 808, L42
Melson, T., Janka, H.-T., & Marek, A. 2015b, ApJ, 801, L24
Müller, B. 2015, MNRAS, 453, 287
Müller, B., Janka, H.-T., & Heger, A. 2012, ApJ, 761, 72
Müller, B., Viallet, M., Heger, A., & Janka, H.-T. 2016, ApJ, 833, 124
Ott, C. D., Abdikamalov, E., Mösta, P., et al. 2013, ApJ, 768, 115
Radice, D., Ott, C. D., Abdikamalov, E., et al. 2016, ApJ, 820, 76
Scheck, L., Janka, H.-T., Foglizzo, T., & Kifonidis, K. 2008, A&A, 477, 931
Teyssier, R. 2002, A&A, 385, 337
Young, Y.-N., Tufo, H., Dubey, A., & Rosner, R. 2001, Journal of Fluid Mechanics, 447, 377

SF2A 2017
C. Reylé, P. Di Matteo, F. Herpin, É. Lagadec, A. Lançon, Z. Meliani, F. Royer (eds)

GIANT PULSAR GLITCHES IN FULL GENERAL RELATIVITY

A. Sourie[1,2], N. Chamel[1], J. Novak[2] and M. Oertel[2]

Abstract. We present recent numerical simulations of giant pulsar glitches, as observed in the emblematic Vela pulsar, based on a two-fluid model, including for the first time all general-relativistic effects and realistic equations of state. In particular, we focus on modelling the vortex-mediated transfer of angular momentum that takes place during the spin-up stage from the neutron superfluid to the charged particles through dissipative mutual friction forces. Taking general relativity into account does not only modify the structure of the star but also leads to a new coupling between the fluids arising from frame-dragging effects. As a consequence, general relativity can strongly affect the global dynamics of pulsar glitches : the errors on the value of the characteristic rise time incurred by using Newtonian gravity are thus found to be as large as $\sim 40\%$ for the models considered.

Keywords: pulsar glitches, neutron stars, superfluidity, general relativity, equation of state, entrainment

1 Introduction

Pulsars are neutron stars spinning rapidly with very stable periods. Nevertheless, some irregularities called glitches have been detected in the long-term evolution of the angular velocity Ω of some pulsars, during which the pulsar suddenly spins up, with relative amplitude $\Delta\Omega/\Omega$ ranging between $\sim 10^{-11}$ and $\sim 10^{-5}$, before slowly relaxing on time scales up to months or years (Espinoza et al. 2011). To date, 482 glitches have been observed in 168 pulsars*.

Since the first detections of glitches (Radhakrishnan & Manchester 1969; Reichley & Downs 1969), several mechanisms have been suggested to explain these phenomena (see the review by Haskell & Melatos (2015)). A glitch is nowadays commonly thought to be the manifestation of an internal process, except possibly for highly magnetised neutron stars for which some evidence of magnetospheric activity have been found (e.g. Antonopoulou et al. (2015)). The interior of neutron stars can thus be probed using glitch observations (Ho et al. 2015; Pizzochero et al. 2017).

The presence of superfluids inside neutron stars was first suggested by Migdal (Migdal 1959), more than sixty years ago. This idea was later supported by the very long time scales observed during post-glitch relaxations (Baym et al. 1969). Nowadays, neutron stars are expected to contain a neutron superfluid in the inner crust and in the outer core, and possibly other superfluid species in the inner core (see, e.g., Chamel (2017) and references therein). Superfluidity is likely to affect the dynamics of neutron stars. In particular, giant glitches with $\Delta\Omega/\Omega \sim 10^{-6} - 10^{-5}$, as observed in the emblematic Vela pulsar, are generally interpreted as the result of a rapid transfer of angular momentum between the neutron superfluid and the rest of the star, triggered by large-scale vortex unpinning events (Anderson & Itoh 1975). This vortex-mediated scenario is supported by both laboratory experiments (Tsakadze & Tsakadze 1980) and the ability of the vortex creep model to reproduce the post-glitch relaxations in different pulsars (Alpar et al. 1984c,a, 1996; Gügercinoğlu & Alpar 2014).

So far, most global numerical simulations of pulsar glitches have been performed in Newtonian gravity (e.g., Sidery et al. (2010); Haskell et al. (2012)). Seveso et al. (2012) and Antonelli & Pizzochero (2017) have recently developed a non-relativistic hydrodynamic model for describing the different stages of the glitch phenomenon

[1] Institut d'Astronomie et d'Astrophysique, CP-226, Université Libre de Bruxelles, 1050 Brussels, Belgium
[2] Laboratoire Univers et Théories, Observatoire de Paris, PSL Research University, CNRS, Université Paris Diderot, Sorbonne Paris Cité, 5 place Jules Janssen, 92195 Meudon, France
*See the Jodrell Bank Observatory glitch catalog : `http://www.jb.man.ac.uk/pulsar/glitches.html`.

based on the static structure of the neutron star computed in general relativity. However, general relativity is also likely to play an important role for the global dynamics of glitches.

Here, we present global numerical simulations of vortex-mediated pulsar glitches performed within a fully general relativistic framework, focusing on the spin-up stage regardless of the glitch triggering mechanism (Novak et al. 2016; Sourie et al. 2017). A glitch event can actually be decomposed into distinct stages (*i.e.* the pre-glitch evolution, the spin up, and the post-glitch relaxation), which can be – in a first attempt – modelled separately in view of the different associated time scales suggesting different physical mechanisms. During the spin up, stellar dynamics are mainly governed by the mutual friction force between the superfluid and the rest of the star. This force acts on a characteristic time scale corresponding to the glitch rise time $\tau_{\rm r}$, which has not been fully observationally resolved yet. The most stringent observational constraint on $\tau_{\rm r}$ comes from the 2000 and 2004 Vela glitch observations: $\tau_{\rm r} < 30 - 40$ s (Dodson et al. 2007). In the following, we shall assume that $\tau_{\rm r}$ is much longer than the typical time $\tau_h \sim 0.1$ ms for the star to go back to equilibrium once being driven out of it by a change in its rotation rate. Doing so, the dynamical evolution of the pulsar can be reasonably well described by a sequence of quasi-stationary equilibrium configurations.

2 Stationary configurations

2.1 Model assumptions

For years, only the neutron superfluid contained in the inner crust of the star was generally thought to be responsible for giant glitches (see, e.g., Alpar et al. (1984b, 1993); Link et al. (1999)). Still, recent studies indicate that the crust can not provide enough reservoir of angular momentum (Andersson et al. 2012; Chamel 2013; Akbal et al. 2015; Delsate et al. 2016). This suggests that the core superfluid plays a more important role than previously thought.

In this work, we thus focus on the dynamics of superfluid neutron-star cores modelled by two fluids coupled by (non-dissipative) mutual entrainment effects (Andreev & Bashkin 1976): (i) a "normal" fluid made of protons and electrons, which are locked together by magnetic effects and essentially corotate with the crust and the magnetosphere at the observed angular velocity Ω, and (ii) a neutron superfluid extending in the whole core. Quantities related to the two fluids will be labelled by indices "p" and "n" respectively. We do not account for any other effects of the magnetic field on the global dynamics of the star, which can be safely ignored for the ordinary pulsars considered here (Chatterjee et al. 2015).

Our simulations are based on the general relativistic equilibrium configurations of rotating superfluid neutron stars computed by Sourie et al. (2016), within the free and publicly available Lorene library[†]. The associated spacetime is assumed to be asymptotically flat, stationary, axisymmetric and circular. Regarding perfect fluids, this last assumption implies that the two fluids are rotating around a common axis, with possibly different rotation rates $\Omega_{\rm n}$ and $\Omega_{\rm p}$. Similarly to the model developed by Sidery et al. (2010) in Newtonian gravity, the angular velocities of the two fluids are taken to be uniform within the star. Moreover, we consider two equations of state (EoSs), DDH and DDHδ, derived from density-dependent relativistic mean-field models, including σ, ω, ρ and possibly δ mesons (Typel & Wolter 1999; Avancini et al. 2009). They were adapted to a system of two fluids at zero temperature coupled by entrainment for arbitrary compositions. More details can be found in Prix et al. (2005); Sourie et al. (2016).

2.2 Fluid couplings

Let $J_{\rm n}$ and $J_{\rm p}$ be the neutron superfluid and normal fluid angular momenta respectively (see Langlois et al. (1998) and Sourie et al. (2016) for definitions and expressions). Introducing the partial moments of inertia as

$$I_{XX} = \left(\frac{\partial J_X}{\partial \Omega_X}\right)_{\Omega_Y} \quad \text{and} \quad I_{XY} = \left(\frac{\partial J_X}{\partial \Omega_Y}\right)_{\Omega_X}, \tag{2.1}$$

where $X, Y \in \{\rm n, p\}$, any changes in the angular momentum of a fluid will be simply given by

$$\mathrm{d}J_X = I_{XX}\,\mathrm{d}\Omega_X + I_{XY}\,\mathrm{d}\Omega_Y = \hat{I}_X\,\mathrm{d}\Omega_X + \hat{\varepsilon}_X \hat{I}_X\left(\mathrm{d}\Omega_Y - \mathrm{d}\Omega_X\right), \tag{2.2}$$

[†]`http://www.lorene.obspm.fr/`.

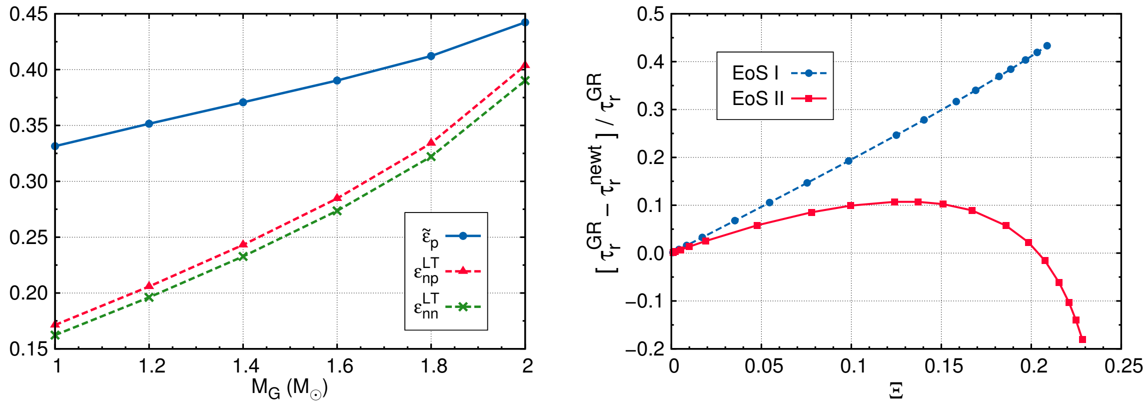

Fig. 1. Left: The quantities $\tilde{\varepsilon}_{\rm p}$, $\varepsilon_{\rm np}^{\rm LT}$ and $\varepsilon_{\rm nn}^{\rm LT}$ are plotted as functions of the gravitational mass $M_{\rm G}$ of the star for the DDH EoS, assuming $\Omega_{\rm n} = \Omega_{\rm p} = 2\pi \times 11.19$ rad.s^{-1} (which corresponds to the rotation rate of the Vela pulsar). **Right:** Relative differences between general relativistic and Newtonian rise times for a glitch amplitude $\Delta\Omega/\Omega = 10^{-6}$ as functions of the (relativistic) compactness parameter, for a star spinning at 10 Hz. Results are shown for two different polytropic EoSs described in Sourie et al. (2017).

where $\hat{I}_X = I_{XX} + I_{XY}$ and $\hat{\varepsilon}_X = I_{XY}/\hat{I}_X$. The cross moment of inertia I_{XY} (and thus $\hat{\varepsilon}_X$) contains any possible (non-dissipative) couplings between the fluids. In the Newtonian limit, entrainment happens to be the main coupling mechanism at low angular velocities. Quite remarkably, a new coupling arises in the general relativistic context from the so-called Lense-Thirring or frame-dragging effect (Carter 1975). In the slow-rotation approximation ($\Omega_{\rm n}, \Omega_{\rm p} \ll \Omega_{\rm K}$, where $\Omega_{\rm K}$ is the Keplerian angular velocity) and to first order in the lag $\delta\Omega = \Omega_{\rm n} - \Omega_{\rm p}$, the total coupling coefficient $\hat{\varepsilon}_X$ reads (Sourie et al. 2017)

$$\hat{\varepsilon}_X = \frac{\tilde{\varepsilon}_X - \varepsilon_{YX}^{\rm LT}}{1 - \varepsilon_{YX}^{\rm LT} - \varepsilon_{XX}^{\rm LT}}, \tag{2.3}$$

where the term $\tilde{\varepsilon}_X$ characterizes entrainment effects averaged over the star, whereas $\varepsilon_{YX}^{\rm LT}$ and $\varepsilon_{XX}^{\rm LT}$ represent respectively the frame-dragging effect on fluid X caused by the second fluid and fluid X itself. As can be seen from Eq. (2.3), the Lense-Thirring effect is found to act in an opposite way to entrainment in the core, where $\tilde{\varepsilon}_X > 0$ (Chamel & Haensel 2006; Sourie et al. 2016). As a consequence, in the absence of entrainment, the total coupling coefficient is still expected to be non-vanishing and negative. Although entrainment is likely to be small in the outermost regions of the core of neutron stars, its overall effect on the whole star is not necessarily negligible and therefore $\hat{\varepsilon}_X$ could be positive or negative.

The relative importance of these two effects on the total coupling parameter $\hat{\varepsilon}_{\rm p}$ is studied in the left panel of Fig. 1. Since general relativistic effects are the strongest for the most massive stars, $\varepsilon_{\rm np}^{\rm LT}$ increases with the stellar mass. Interestingly, $\tilde{\varepsilon}_{\rm p}$ and $\varepsilon_{\rm np}^{\rm LT}$ are found to be roughly of the same order of magnitude, making the Lense-Thirring contribution to the total coupling very important. Similar conclusions are reached for the two EoSs.

3 The glitch spin-up

3.1 Evolution equations

Neglecting any external torque, the dynamics of the two fluids during the spin up is simply governed by

$$\begin{cases} \dot{J}_{\rm n} = & + \, \Gamma_{\rm mf}, \\ \dot{J}_{\rm p} = & - \, \Gamma_{\rm mf}, \end{cases} \tag{3.1}$$

where overdot denotes time derivative. A covariant expression for the (relativistic) mutual friction torque $\Gamma_{\rm mf}$ was derived by Langlois et al. (1998), considering straight vortices parallel to the rotation axis. Neglecting the small contribution of the non-circular motion of the vortices and any dissipation related to chemical reactions, one has

$$\Gamma_{\rm mf} = -\bar{\mathcal{B}} \times 2\zeta \hat{I}_{\rm n} \Omega_{\rm n} \times \delta\Omega, \tag{3.2}$$

where $\delta\Omega = \Omega_{\rm n} - \Omega_{\rm p}$. The value of the quantity ζ, which reduces to 1 in the Newtonian limit, depends on the stellar structure and can be obtained from stationary configurations. Given the current lack of knowledge on the microscopic origin of the mutual friction force, the averaged mutual friction parameter $\bar{\mathcal{B}}$ is taken as a free input parameter in our numerical simulations and is moreover assumed to be time-independent for simplicity.

Plugging (2.2) into (3.1) gives the equation governing the time evolution of the lag $\delta\Omega$. Recalling that $\Delta\Omega/\Omega \ll 1$, the lag approximately evolves as $\delta\Omega(t) \propto \exp(-t/\tau_{\rm r})$, with a characteristic time scale given by

$$\tau_{\rm r} = \frac{\hat{I}_{\rm p}}{\hat{I}} \times \frac{1 - \hat{\varepsilon}_{\rm p} - \hat{\varepsilon}_{\rm n}}{2\zeta\bar{\mathcal{B}}\Omega_{\rm n}}, \tag{3.3}$$

where $\hat{I} = \hat{I}_{\rm n} + \hat{I}_{\rm p}$. Expression (3.3) is very similar to that obtained in Newtonian framework (see Sidery et al. (2010) or Sourie et al. (2017)). It should be stressed however that general relativistic effects are not only included in the coefficient ζ but also modify the moments of inertia (2.1) and the coupling coefficients (2.3).

3.2 Numerical results

To test the validity of the previous analytical approach and to assess the importance of general relativity, we have also solved Eqs. (3.1) numerically. Starting from some initial conditions at the beginning of the glitch, these equations are solved step by step so as to get the time evolution of the two angular velocities during the spin up, using the equilibrium configurations described in section 2. These simulations require the following macroscopic ingredients: the rotation rate Ω of the star, its gravitational mass $M_{\rm G}$ and the glitch amplitude $\Delta\Omega/\Omega$. In addition, the following microscopic inputs need to be specified: the EoS used to describe the interior of the star and the mutual friction parameter $\bar{\mathcal{B}}$. By fitting the time evolution of the lag $\delta\Omega$ with an exponential law, one can determine the rise time corresponding to the chosen input parameters. It should be remarked that this characteristic time corresponds indeed to the spin-up time-scale that could be measured from precise timing observations of glitches. Numerical results are found to agree with values inferred from Eq. (3.3) with a very good precision, such that the spin-up time scale can be very accurately estimated from stationary configurations only. Furthermore, since the actual value of $\tau_{\rm r}$ is found to be much longer than the hydrodynamical time scale τ_h for current estimates of the mutual friction forces, the whole dynamical evolution of the star during the spin up can be accurately computed by considering a quasi-stationary approach.

We also study the global contribution of general relativity to the glitch dynamics, by comparing the rise times obtained within both relativistic and Newtonian frameworks. For simplicity, we consider two polytropic EoSs, as implemented by Prix et al. (2005), with different entrainment contributions. These EoSs have been chosen in order to reproduce "realistic" values for the mass, radius and proton fraction of the stars. In the right panel of Fig. 1, the relative differences on $\tau_{\rm r}$ are plotted with respect to the compactness parameter Ξ (defined as the dimensionless ratio of the gravitational mass of the star to its radius), obtained for a star rotating at 10 Hz by varying its mass. As expected, general relativistic corrections vanish when the compactness parameter decreases. For values of the compactness parameter relevant for neutron stars, *i.e.* $\Xi \sim 0.15 - 0.20$, these two EoSs predict that an error of the order of $\sim 20 - 40\%$ is made on the rise time by using Newtonian gravity instead of general relativity, as can be seen in Fig. 1. It is therefore necessary to account for general relativistic effects in order to get precise results on the spin-up time scales. Furthermore, it should be mentioned that these errors depend significantly on the rotation rate and the EoS under consideration.

4 Conclusions

We have studied in detail the impact of general relativity on the global dynamics of giant pulsar glitches as observed in Vela (Sourie et al. 2017).

First, we analytically solved the dynamical equations governing the transfer of angular momentum that takes place between the core neutron superfluid and the rest of the star during the spin up, by expressing the change in the lag as $\delta\dot{\Omega}/\delta\Omega \approx -1/\tau_{\rm r}$. The characteristic rise time $\tau_{\rm r}$ can be expressed in a form similar to that obtained in the Newtonian limit (Sidery et al. 2010). Still, general relativity not only changes the structure of the star, but also impacts the fluid dynamics. In particular, frame-dragging effects induce additional fluid couplings of the same form as the entrainment arising solely from neutron-proton interactions. General relativity can thus affect significantly the glitch dynamics.

To assess the importance of general relativity, we have also solved numerically the evolution equations relative to the angular velocity of each fluid. Numerical results are found to be very well reproduced by the analytical approximation. In particular, the glitch rise time τ_r can be precisely estimated from stationary configurations only. Moreover, we have also investigated the impact of general relativity on τ_r by using two different polytropic EoSs. Both the effects of general relativity on the stellar structure and on the fluid couplings are found to be important. Realistic simulations of the global glitch dynamics should therefore be carried out in full general relativity. The errors incurred by using Newtonian gravity instead of general relativity, however, might not be the main source of uncertainties. For instance, neutron superfluid vortices may not be simply straight and aligned with the rotation axis, as assumed here. Likewise, the interactions between superfluid vortices and proton flux tubes remain poorly known and their impact on the glitch dynamics warrant further studies.

Finally, the Low Frequency Array (LOFAR) radio telescope (Stappers et al. 2011) and the future Square Kilometer Array (SKA) (Watts et al. 2015) will be able to observe the spin up with unprecedented accuracy. It would thus lead to much more stringent constraints on the characteristic time τ_r and thereby on the underlying glitch mechanism. This calls for more realistic models of glitches including the crust magnetoelasticity and superfluidity and accounting for the local dynamics of quantised vortices.

This work has been partially funded by the "Gravitation et physique fondamentale" action of the Observatoire de Paris (France), the Fonds de la Recherche Scientifique - FNRS (Belgium) under grant n° CDR J.0187.16, the PHC Tournesol (n° 35904ZJ) scientific cooperation program between France and Belgium, and the European COST action MP1304 "NewCompstar". A.S. was partially supported by the Fonds de la Recherche Scientifique - FNRS (Belgium).

References

Akbal, O., Gügercinoğlu, E., Şaşmaz Muş, S., & Alpar, M. A. 2015, MNRAS, 449, 933

Alpar, M. A., Anderson, P. W., Pines, D., & Shaham, J. 1984a, ApJ, 278, 791

Alpar, M. A., Chau, H. F., Cheng, K. S., & Pines, D. 1993, ApJ, 409, 345

Alpar, M. A., Chau, H. F., Cheng, K. S., & Pines, D. 1996, ApJ, 459, 706

Alpar, M. A., Langer, S. A., & Sauls, J. A. 1984b, ApJ, 282, 533

Alpar, M. A., Pines, D., Anderson, P. W., & Shaham, J. 1984c, ApJ, 276, 325

Anderson, P. W. & Itoh, N. 1975, Nature, 256, 25

Andersson, N., Glampedakis, K., Ho, W. C. G., & Espinoza, C. M. 2012, Physical Review Letters, 109, 241103

Andreev, A. F. & Bashkin, E. P. 1976, Soviet Journal of Experimental and Theoretical Physics, 42, 164

Antonelli, M. & Pizzochero, P. M. 2017, MNRAS, 464, 721

Antonopoulou, D., Weltevrede, P., Espinoza, C. M., et al. 2015, MNRAS, 447, 3924

Avancini, S. S., Brito, L., Marinelli, J. R., et al. 2009, Phys. Rev. C, 79, 035804

Baym, G., Pethick, C., & Pines, D. 1969, Nature, 224, 673

Carter, B. 1975, Annals of Physics, 95, 53

Chamel, N. 2013, Physical Review Letters, 110, 011101

Chamel, N. 2017, Journal of Astrophysics and Astronomy, 38, 43

Chamel, N. & Haensel, P. 2006, Phys. Rev. C, 73, 045802

Chatterjee, D., Elghozi, T., Novak, J., & Oertel, M. 2015, MNRAS, 447, 3785

Delsate, T., Chamel, N., Gürlebeck, N., et al. 2016, Phys. Rev. D, 94, 023008

Dodson, R., Lewis, D., & McCulloch, P. 2007, Ap&SS, 308, 585

Espinoza, C. M., Lyne, A. G., Stappers, B. W., & Kramer, M. 2011, MNRAS, 414, 1679

Gügercinoğlu, E. & Alpar, M. A. 2014, ApJ, 788, L11

Haskell, B. & Melatos, A. 2015, International Journal of Modern Physics D, 24, 1530008

Haskell, B., Pizzochero, P. M., & Sidery, T. 2012, MNRAS, 420, 658

Ho, W. C. G., Espinoza, C. M., Antonopoulou, D., & Andersson, N. 2015, Science Advances, 1, e1500578

Langlois, D., Sedrakian, D. M., & Carter, B. 1998, MNRAS, 297, 1189

Link, B., Epstein, R. I., & Lattimer, J. M. 1999, Physical Review Letters, 83, 3362

Migdal, A. B. 1959, Nuclear Physics, 13, 655

Novak, J., Chatterjee, D., Oertel, M., & Sourie, A. 2016, PoS, 012

Pizzochero, P. M., Antonelli, M., Haskell, B., & Seveso, S. 2017, Nature Astronomy, 1, 0134

Prix, R., Novak, J., & Comer, G. L. 2005, Phys. Rev. D, 71, 043005

Radhakrishnan, V. & Manchester, R. N. 1969, Nature, 222, 228

Reichley, P. E. & Downs, G. S. 1969, Nature, 222, 229

Seveso, S., Pizzochero, P. M., & Haskell, B. 2012, MNRAS, 427, 1089

Sidery, T., Passamonti, A., & Andersson, N. 2010, MNRAS, 405, 1061

Sourie, A., Chamel, N., Novak, J., & Oertel, M. 2017, MNRAS, 464, 4641

Sourie, A., Oertel, M., & Novak, J. 2016, Phys. Rev. D, 93, 083004

Stappers, B. W., Hessels, J. W. T., Alexov, A., et al. 2011, A&A, 530, A80

Tsakadze, J. S. & Tsakadze, S. J. 1980, Journal of Low Temperature Physics, 39, 649

Typel, S. & Wolter, H. H. 1999, Nuclear Physics A, 656, 331

Watts, A., Espinoza, C. M., Xu, R., et al. 2015, Advancing Astrophysics with the Square Kilometre Array (AASKA14), 43

SF2A 2017
C. Reylé, P. Di Matteo, F. Herpin, É. Lagadec, A. Lançon, Z. Meliani, F. Royer (eds)

CLUMPY WIND ACCRETION IN SUPERGIANT X-RAY BINARIES

I. El Mellah[1], J.O. Sundqvist[2] and R. Keppens[1]

Abstract. Supergiant X-ray binaries (sgXB) contain a neutron star (NS) orbiting a Supergiant O/B star. The fraction of the dense and fast line-driven wind from the stellar companion which is accreted by the NS is responsible for most of the X-ray emission from those system. Classic sgXB display photometric variability of their hard X-ray emission, typically from a few 10^{35} to a few 10^{37}erg·s^{-1}. Inhomogeneities (a.k.a. clumps) in the wind from the star are expected to play a role in this time variability. We run 3D hydrodynamical (HD) finite volume simulations to follow the accretion of the inhomogeneous stellar wind by the NS over almost 3 orders of magnitude. To model the unperturbed wind far upstream the NS, we use recent simulations which managed to resolve its micro-structure. We observe the formation of a Bondi-Hoyle-Lyttleton (BHL) like bow shock around the accretor and follow the clumps as they cross it, down to the NS magnetosphere. Compared to previous estimations discarding the HD effects, we measure lower time variability due to both the damping effect of the shock and the necessity to evacuate angular momentum to enable accretion. We also compute the associated time-variable column density and compare it to recent observations in Vela X-1.

Keywords: X-ray binaries - wind accretion - massive stars - computational Astrophysics - Vela X-1

1 Introduction

The donor star in sgXB is a massive O/B Supergiant. The wind-launching mechanism of those stars differs from the models for low mass stars : the resonant line absorption of ultra-violet photons by partly ionised metal ions provides net linear momentum to the outer layers of the star. As the flow accelerates, it keeps tapping previously untouched Doppler-shifted photons (Lucy & Solomon 1970; Castor et al. 1975). Due to the high resulting supersonic speed of the wind, the orbiting NS can only capture a fraction of the mass lost by the star, contrary to Roche lobe overflow configurations. The high stellar mass loss rates associated to line-driven winds partly compensates for this inefficient mass transfer and the X-ray luminosity produced by the accretion process onto the NS can reach up to a few 10^{37}erg·s^{-1} (Walter et al. 2015).

But the hard X-ray emission from classical sgXB is not constant. The discovery of Super Fast X-ray transients (Sguera et al. 2005; Negueruela et al. 2006), where the photometric fluctuations are even more dramatic, urged the community to investigate the possible origins of this time-variability. A key-source of variability may be found in the very wind which feeds accretion. Indeed, line-driven winds are prone to a strong instability (the line deshadowing instability, LDI Lucy & White 1980; Owocki & Rybicki 1984) which produces internal shocks in the wind. It gives birth to higher density regions called clumps whose serendipitous accretion by the NS could, in principle, give a flare in X-rays.

The dimensions and shapes of these clumps have been recently computed in 2D radiative-HD simulations by Sundqvist et al. (2017) in a pseudo-planar stripe between one and two stellar radii. We build up on those results to design a 3D representation of the wind where the micro-structure and the contrasts are preserved. The latter provides outer boundary conditions upstream for a 3D spherical grid centred on the accretor. As the clumps enter the simulation space, we solve the equations of HD to follow their evolution towards the NS. Thanks to a stretching of the grid, we can monitor the flow from the upper scale, where the wind is still unperturbed by the presence of the NS, down to the NS magnetosphere, one thousand times smaller. In-between these scales, the flow is beamed by the gravitational field of the NS and forms a detached bow shock.

[1] CmPA, KU Leuven, Celestijnenlaan 200B, B-3001 Leuven, Belgium
[2] Instituut voor Sterrenkunde, KU Leuven, Celestijnenlaan 200D, B-3001 Leuven, Belgium

The object of the present paper is to study the impact of a realistic inhomogeneous wind on the time-variability of the X-ray emission and the column density between the accretor and the observer. In Section 2, we detail the numerical setup we rely on to derive the results on the flow structure, the mass accretion rate and the column density described in Section 3.

2 Numerical setup

To determine the dimensions and absolute position of our simulation space in the wind, we consider 2 different configurations whose parameters are given in Table 1 : a close and a wide-configuration with a small and large orbital separation respectively. The accretion radius is the key quantity to estimate the outer radius of our 3D setup. It corresponds to the critical impact parameter below which, in the ballistic sketch drawn by Hoyle & Lyttleton (1939) and Bondi & Hoyle (1944), the planar homogeneous incoming flow is likely to be accreted (for a review of BHL accretion theory, see Edgar 2004). It defines an accretion cylinder passing by the accretor and of main axis the bulk motion of the flow at infinity, and is given by :

$$R_{acc} = 2GM/v_{\infty}^2 \quad (2.1)$$

where G is the gravitational constant, M the mass of the accretor (here the NS) and v_{∞} is the velocity of the flow before it is significantly altered by the gravitational field of the accretor (here, the speed acquired by the line-driven acceleration mechanism). Since the front shock is expected to settle at a distance from the NS given approximately by R_{acc}, we need to inject the unperturbed supersonic wind at a larger distance. We set the outer radius of the simulation space, at $8R_{acc}$. We also account for the X-ray ionising feedback from the accretor by inhibiting the line-driven acceleration within this simulation space. Indeed, for a realistic X-ray luminosity of $2 \cdot 10^{36}$erg·s^{-1} and a critical ionisation parameter of 500 (Manousakis & Walter 2015), the ionization front is approximately located at $8R_{acc}$ upstream from the accretor. Within this region, the metal ions are too ionised to sustain the line-driven acceleration (Hatchett & McCray 1977).

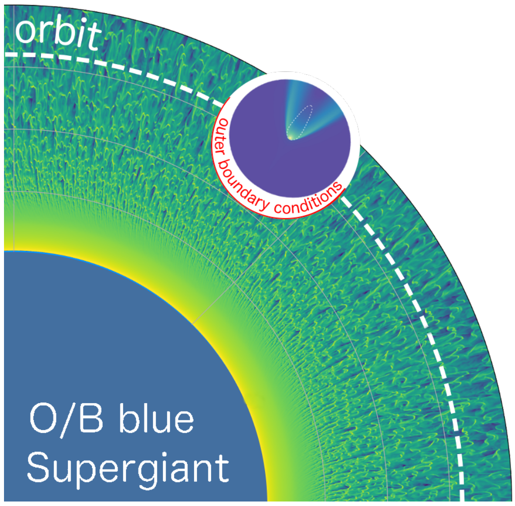

Fig. 1: Sketch of the stellar wind density map and of the position of the 3D simulation space centred on the compact object (CO), whose orbit around the Supergiant O/B star is shown. The insert in the upper right is the result of a 2D simulation of the accretion of a planar uniform flow from El Mellah & Casse (2015).

Table 1: Parameters of the two configurations considered

Parameters	Close config.	Wide config.
Stellar mass	$50M_{\odot}$	
Stellar radius R_*	$20R_{\odot}$	
Mass loss rate	$1.3{\cdot}10^{-6}M_{\odot}{\cdot}yr^{-1}$	
Orbital separation	$1.6R_*$	$2R_*$
NS mass	$1.3M_{\odot}$	$2M_{\odot}$
Effective velocity at NS	925 km·s^{-1}	1140 km·s^{-1}
Density at orb. sep.	$7.2{\cdot}10^{-15}$g·cm^{-3}	$3.6{\cdot}10^{-15}$g·cm^{-3}
Accretion radius	$\sim 4 \cdot 10^{10}$cm	

To inject the wind in the 3D simulation space, we first need to reconstruct a realistic 3D wind with the same stochastic properties. To do so, we transversely extend it (Figure 1) and compute the geometric average coefficient by coefficient of two 90-degrees rotated stripes. Once the histograms are corrected to retrieve the same distributions of values in all transverse directions, we sample this data on the surface of the spherical 3D grid embedded in the wind. It yields, as a function of time, the mass density, the speed and the pressure at the upstream outer boundary of the simulation space.

We work with a 3D spherical mesh centred on the accretor (Figure 2) and further detailed in Xia et al. (2017). To follow the flow in its journey to the NS and evaluate a representative mass accretion rate, we need to work with an inner boundary radius as small as possible. We set it to $R_{acc}/100$, deep within the shocked region. It also corresponds approximately to one thousand times the NS radius i.e. the outer rim of the NS magnetosphere ; within this region, a magnetohydrodynamical approach is required. We use a radially stretched

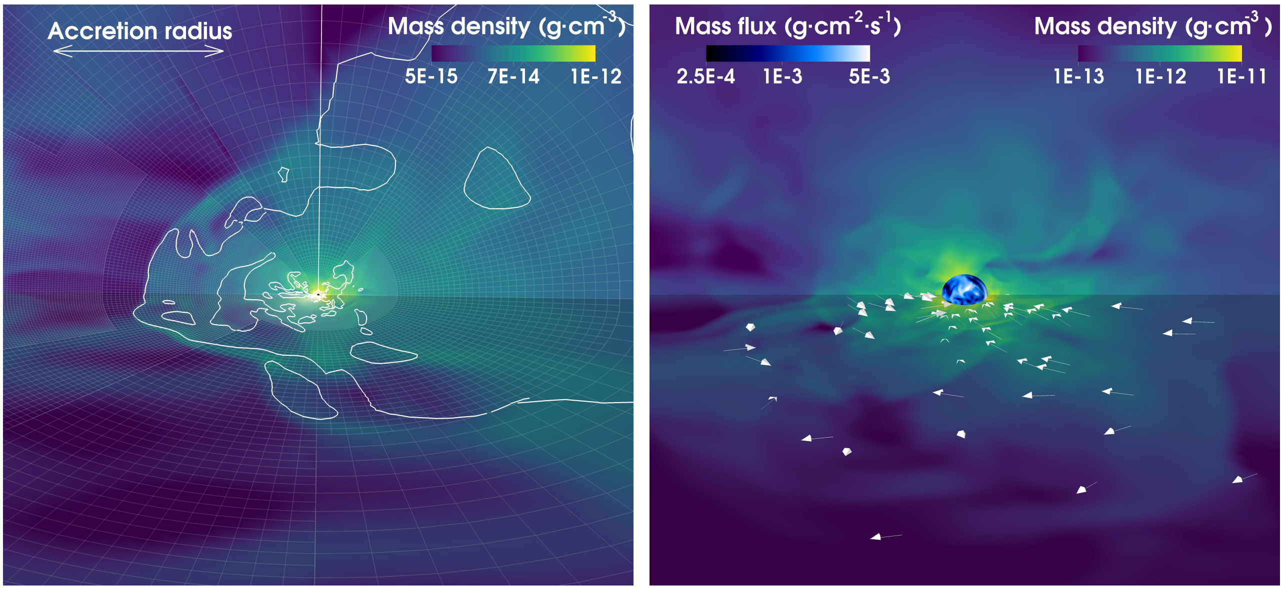

Fig. 2: Side view of a two-slice of a mass density colormap. The supersonic flow comes from the left and the polar axis is vertical. In the left panel, we zoomed in on the post-shock regions and the solid white line is the Mach-1 contour. In the right panel, we zoomed in even more and the vector field has been represented in the equatorial plane. The surface of the inner sphere, of radius $R_{acc}/100$, is colored with the local radial mass flux. See `http://homes.esat.kuleuven.be/~ileyk/clumps_HR.gif` for an animation of the inflowing clumps.

grid to span those almost 3 orders of magnitude at an affordable computational cost. Also, we enable Adaptive Mesh Refinement (AMR) in the outer regions upstream, in the aforementioned accretion cylinder, to resolve the clumps as they enter the simulation space. On the reverse, we inhibit AMR along the poles (set in the transverse plane).

3 Results

3.1 *Structure of the flow*

The flow adopts a structure qualitatively similar to the one obtained with a homogeneous inflow (El Mellah & Casse 2015). The wind with an impact parameter significantly larger than the accretion radius does not dissipate enough energy through the shock to be accreted and simply passes by the NS, flowing aways along the wake. On the reverse, the flow in the vicinity of the inflowing axis is shocked, dissipates its angular momentum in the turbulent shocked environment and flows through the inner border of the simulation space. The front shock goes back and forth, sometimes receding down to $R_{acc}/10$, but remains detached. No flip-flop instability is observed, in agreement with 3D simulations of BHL flows (Blondin & Raymer 2012).

3.2 *Mass accretion rate*

The mass accretion rate at the inner edge of the simulation space for the two configurations is plotted in Figure 3. The time-averaged values are in agreement with the order of magnitude given by the BHL approach (dashed black line in Figure 3) but it also displays an important time variability. Due to the presence of the shock, flares in mass accretion rate are not directly triggered by clumps. Sometimes, clumps with a large impact parameter pile up in the shock region before being flushed once matter with opposite angular momentum triggers dissipation. The shock tempers the influence of clumps, along with the need for clumps with a non-zero impact parameter to dissipate their angular momentum. The final time variability at the inner boundary of the simulation space is thus much smaller than what expected from accretion of purely ballistic clumps : the peak-to-peak variability we measure is of a factor of 10 in the close configuration, and 20 in the wide one. We interpret this trend of larger time variability at larger orbital separation as due to larger clumps as one moves away from the stellar surface.

An important qualitative conclusion to draw from the simulations is that an incoming large clump does

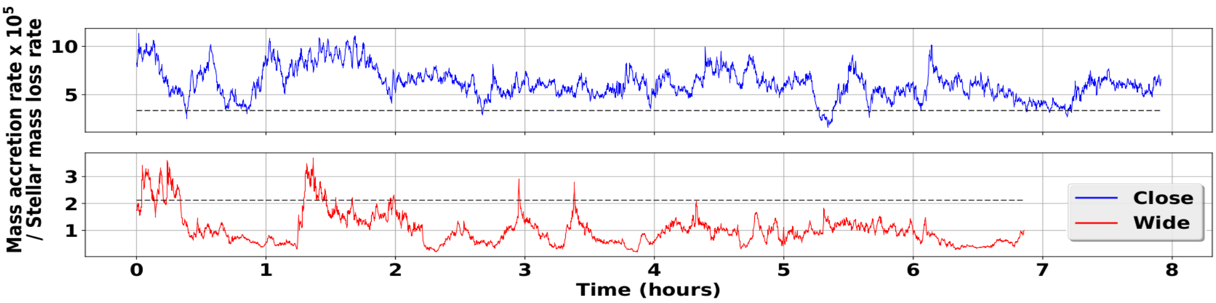

Fig. 3: Mass accretion rate at the inner boundary of the simulation space for the close ($a = 1.6\mathrm{R}_*$, third panel) and wide ($a = 2\mathrm{R}_*$, bottom panel) configurations. As a guideline, we plotted the BHL mass accretion rate for a smooth wind with the parameters from Table 1 (dashed black line).

not straightforwardly yield a flare in mass accretion rate. Conversely, it means that much caution should be taken when we try to trace back the origin of a flare to a clump mass. Between the ballistic clumps and the X-ray emission regions lie many different regions which dilute the clumps and trigger their own instabilities : time variability can be either enhance or damped depending on the physical conditions encountered by the flow as it gets accreted. If the time variability at the smaller scales is likely correlated to the one induced by the inhomogeneous wind, it is not directly related. Matter can pile up for quite long in intermediate regions (e.g. the shock or the corotation radius) before an instability which makes accretion possible is triggered.

3.3 Column density

Thanks to this numerical setup, we could also compute the column density between the NS and the observer as a function of time. Beyond the expected trend due to the orbital motion of the NS around its stellar companion, we measure a spread due to the random passing of unaccreted clumps along the line-of-sight, but also to the piling up of matter in the shocked region preceding flares. Results are given in Figure 4 for an edge-on inclination of the system and for the two configurations we considered. Grinberg et al. (2017) measured a column density varying between $0.72 \cdot 10^{22}\mathrm{cm}^{-2}$ to $5.76 \cdot 10^{22}\mathrm{cm}^{-2}$ between the orbital phases 0.21 and 0.25 (black rectangle in Figure 4. Both the close and wide configurations yield column densities lying within this range but they fail to explain this dramatic change in NH, which led Grinberg et al. (2017) to discard clumps happening to cross the line-of-sight as possible culprits. Indeed, leaving aside the uncertainty on the median value (which can be shifted by tuning, for instance, the stellar mass loss rate), the present model is unable to reach the maximal column density observed at those phases. It might be due to underlying structures within the magnetosphere that we could not study in detail with the present numerical setup. Notice however that given the orbital speeds at stake in this region, only isotropic structures could sustain such a high level of column density for so long. On the other hand, the minimal column density observed is preferentially achieved by the wide configuration, although marginally and at the end of the orbital phase interval.

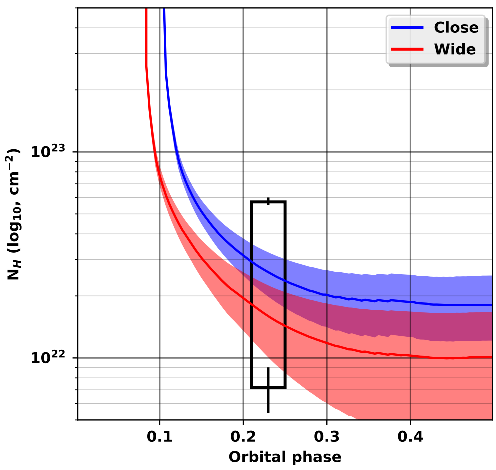

Fig. 4: Folded column density as a function of the orbital phase, for edge-on inclinations. The spread represents the 2-σ time-variability of N_H. The framed area shows the extent and the uncertainty on the variability observed by Grinberg et al. (2017), at orbital phases 0.21-0.25 (see text).

4 Conclusions

We ran 3D simulations of the accreted flow, centered on the accretor and with a mesh suitable to resolve the inhomogeneities in the upstream wind and follow them over almost 3 orders of magnitude in space. As the flow enters the sphere of influence of the NS, it is beamed toward it and forms a detached bow shock. The successive clumps cross this shock and, provided they loose enough energy and angular momentum, get accreted. As expected from the BHL approach of clump accretion (Ducci et al. 2009), the accretion proceeds mostly through the accretion cylinder. However, the present HD simulations show that the shock damps the time-variability with respect to the BHL estimation. Also, it introduces a time lag and a phase mixing since the shocked material associated to a clump is not straightforwardly accreted : it might be stored in a transient disc-like structure before accretion of matter with opposite net angular momentum triggers effective accretion.

Comparing to the X-ray luminosity diagrams at high energy, we showed that the wind micro-structure computed by (Sundqvist et al. 2017) and used in the present paper is not sufficient, per se, to retrieve the time-variability levels observed in classical SgXB such as Vela X-1 (Walter et al. 2015). The behavior at low luminosity matches the observations but the largest luminosity events require the possibility to quickly tap amounts of matter the clumps we considered here are not able to provide, even accounting for the intermediate shocked region where the flow can pile up. Other storage stages can appear once the NS magnetosphere and radiative cooling is accounted for (Illarionov & Sunyaev 1975; Bozzo et al. 2008; Shakura & Postnov 2017) or at the orbital scale (e.g. the X-ray ionizing feedback in Manousakis & Walter 2015). Also, the LDI simulations of Sundqvist et al. (2017) could yield larger clumps at a given orbital separation for a larger star or once clumping is enabled earlier on, near the stellar surface (where we know that clumps are already present, Cohen et al. 2011; Sundqvist & Owocki 2013; Torrejón et al. 2015). Given the comparative results for the wide and close configurations considered in this paper, the latter option would increase the time variability. It would also increase the time variability of the column density, bringing the results closer from what was observed by Grinberg et al. (2017) in Vela X-1.

IEM thanks the organizers of the High Energy Astrophysics session of the *Journées* of the French Astronomy Society for their interest in the present work. IEM has received funding from the Research Foundation Flanders (FWO) and the European Union's Horizon 2020 research and innovation programme under the Marie Skłodowska-Curie grant.

References

Blondin, J. M. & Raymer, E. 2012, Astrophys. J., 752, 30

Bondi, H. & Hoyle, F. 1944, Mon. Not. R. Astron. Soc., 104, 273

Bozzo, E., Falanga, M., & Stella, L. 2008, Astrophys. J., 683, 1031

Castor, J. I., Abbott, D. C., & Klein, R. I. 1975, Astrophys. J., 195, 157

Cohen, D. H., Gagné, M., Leutenegger, M. A., et al. 2011, Mon. Not. R. Astron. Soc., 415, 3354

Ducci, L., Sidoli, L., Mereghetti, S., Paizis, A., & Romano, P. 2009, Mon. Not. R. Astron. Soc., 398, 2152

Edgar, R. G. 2004, New Astron. Rev., 48, 843

El Mellah, I. & Casse, F. 2015, Mon. Not. R. Astron. Soc., 454, 2657

Grinberg, V., Hell, N., El Mellah, I., et al. 2017, submitted

Hatchett, S. & McCray, R. 1977, Astrophys. J., 211, 552

Hoyle, F. & Lyttleton, R. A. 1939, Math. Proc. Cambridge Philos. Soc., 35, 405

Illarionov, A. F. & Sunyaev, R. A. 1975, Astron. Astrophys., 39

Lucy, L. B. & Solomon, P. M. 1970, Astrophys. J., 159, 879

Lucy, L. B. & White, R. L. 1980, Astrophys. J., 241, 300

Manousakis, A. & Walter, R. 2015, Astron. Astrophys., 58, A58

Negueruela, I., Smith, D. M., Reig, P., Chaty, S., & Torrejón, J. M. 2006, Proc. X-ray Universe 2005 (ESA SP-604)

Owocki, S. P. & Rybicki, G. B. 1984, Astrophys. J., 284, 337

Sguera, V., Barlow, E. J., Bird, A. J., et al. 2005, Astron. Astrophys., 444, 221

Shakura, N. & Postnov, K. 2017, eprint arXiv:1702.03393

Sundqvist, J. O. & Owocki, S. P. 2013, Mon. Not. R. Astron. Soc., 428, 1837

Sundqvist, J. O., Owocki, S. P., & Puls, J. 2017

Torrejón, J. M., Schulz, N. S., Nowak, M. A., et al. 2015, Astrophys. J., 810, 102

Walter, R., Lutovinov, A. A., Bozzo, E., & Tsygankov, S. S. 2015, Astron. Astrophys. Rev., 23, 2

Xia, C., Teunissen, J., El Mellah, I., Chané, E., & Keppens, R. 2017, submitted

SF2A 2017
C. Reylé, P. Di Matteo, F. Herpin, É. Lagadec, A. Lançon, Z. Meliani, F. Royer (eds)

FOLLOWING THE ROSSBY WAVE INSTABILITY INTO THE KERR METRIC

P. Varnière[1, 2], F. Casse[1] and F.H. Vincent[3]

Abstract. The Rossby Wave Instability (RWI) has been proposed to explain the High-Frequency Quasi-Periodic Oscillation thought to occur in the close vicinity of black holes but this early work was done in the pseudo-Newtonian approach. Here we present the first general relativistic hydrodynamic simulations of this instability not only proving its theorized existence in a full GR environment but also studying the effect of strong gravity on the instability and how it relates to observations.

Keywords: disk, instability, GR

1 Introduction

Since their first detection there have been a long string of efforts to understand the source of the variability observed in microquasars. This is especially true for the origin of the rather elusive High-Frequency Quasi-Periodic Oscillation (HFQPO) in systems containing (or thought to contain) a black hole (BH). Indeed, their frequencies hint at a relation to the spin of the black hole. Here we focus on the model based on the Rossby-Wave Instability (Tagger & Varnière 2006; Varnière et al. 2011; Varnière et al. 2012) which is predicted to occur when the inner edge of the disk is close to the last orbit. It has been previously proposed to explain several phenomena occurring in the vicinity of black holes (Vincent et al. 2013, 2014; Casse et al. 2017) but its existence in an extreme Kerr environment had never been demonstrated.

Here we will be looking into more details at how its position closer to the last stable orbit of the black hole does influence the physics of the RWI and what changes, if any, we should be looking for in observations. For that we will be using a clean setup looking only for differences related to the GR-effects. Indeed, rather than starting with the study of the full dynamical system where it would be difficult to differentiate between GR and dynamical effects from the initial condition, we choose to follow a similar setup taken deeper and deeper in the potential well of a maximally spinning Kerr black hole to study the minute changes in the instability behavior.

2 Down the rabbit hole

The RWI requires having an extremum of $\mathcal{L} = (\nabla \times \mathbf{v})_\perp / \Sigma$ in which the instability could develop, where $\mathbf{v}$ is the velocity of the gas while Σ is its height-integrated density ($\perp$ stands for the component perpendicular the the disk plane). The position of the extremum is called the corotation radius of the wave, meaning that at this radius the wave and the gas have the same velocity. In a previous publication (Casse et al. 2017) we showed that the behavior of the instability from Newtonian to a Schwarzschild black hole stays very similar. Here, we followed the same methods but changed not only the position of the extremum of $\mathcal{L}$ located at r_b but also the spin. Having a spin closer to one allows us to get even closer to the black hole than the last stable orbit in the case of a Schwarzschild black hole.

On Fig. 1 we compare four snapshots of the developed RWI with an increasing spin/decreasing extremum position from left to right. On the far left, we have the case of a Schwarzschild metric with the inner edge of

[1] APC, AstroParticule et Cosmologie, Université Paris Diderot, CNRS/IN2P3, CEA/Irfu, Observatoire de Paris, Sorbonne Paris Cité, 10, rue Alice Domon et Léonie Duquet, 75205 Paris Cedex 13, France
[2] Laboratoire AIM, CEA/IRFU-CNRS/INSU-Université Paris Diderot, CEA DRF/IRFU/DAp, F-91191 Gif-sur-Yvette, France.
[3] Observatoire de Paris / LESIA, 5, place Jules Janssen, 92195 Meudon Cedex, France.

the disk at its last stable orbit ($a = 0, r_b = 6r_S$), then a mildly relativistic case with a spin $a = 0.5$ with the inner edge of the disk close, but not at its last stable orbit ($r_b = 5r_S$). We follow with a spin of $a = 0.95$ with the inner edge of the disk at its last stable orbit ($r_b = 1.94r_S$) and finally the extremely relativistic case of $a = 0.995, r_b = 1.45r_S$, with the inner edge of the disk close to its last stable orbit.

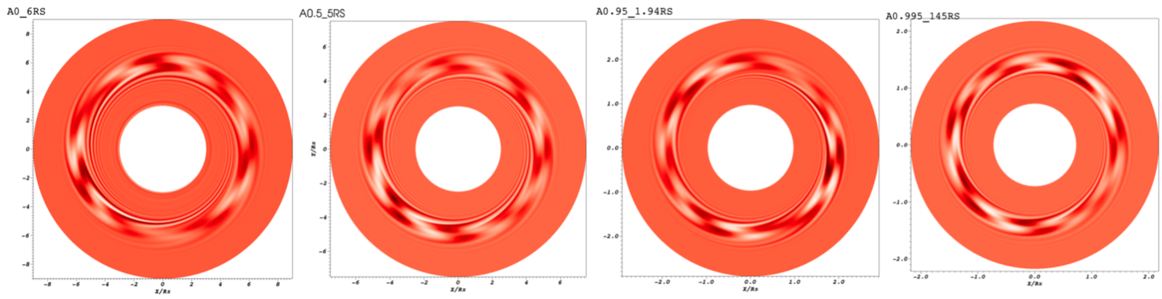

Fig. 1. Four snapshots of the developed RWI with from left to right $a = 0, r_b = 6r_S$, $a = 0.5, r_b = 5r_S$, $a = 0.95, r_b = 1.94r_S$, and $a = 0.995, r_b = 1.45r_S$

While the time, in orbital period at the corotation radius where the RWI happens, is not exactly the same for all the snapshots as it is difficult to obtain with so many different spins, we see that, qualitatively, the four disks are very similar and cannot be distinguished.

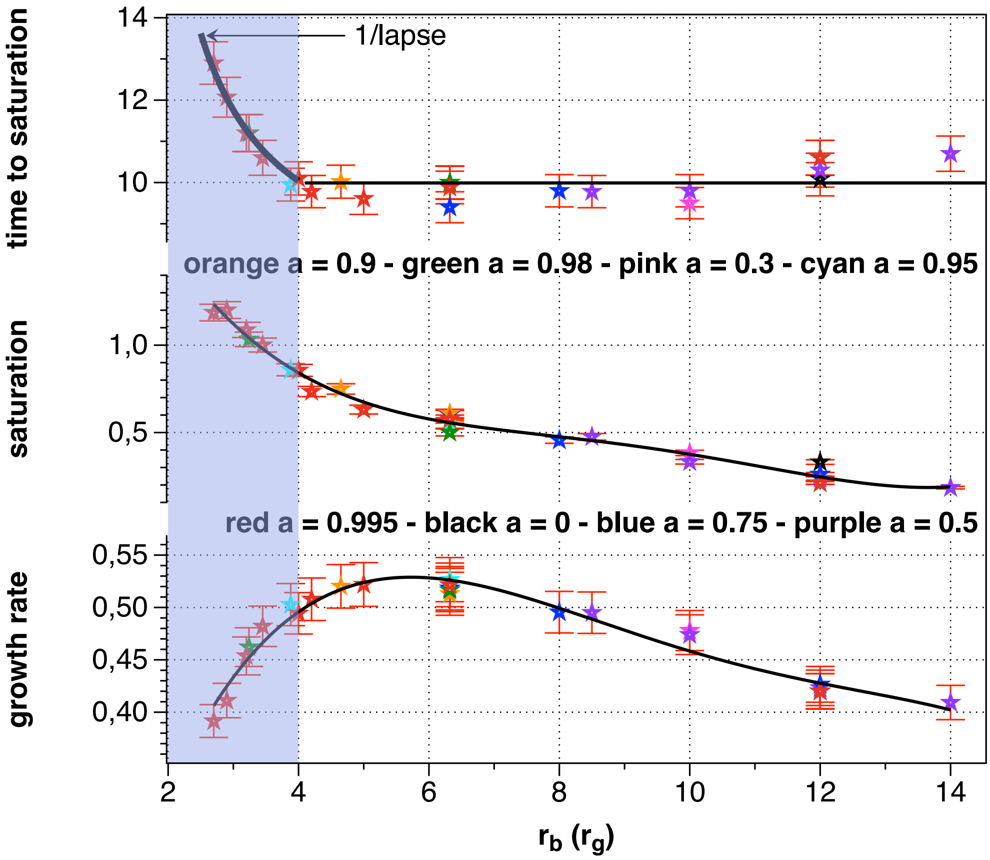

Fig. 2. Evolution of the growth rate of the instability, its saturation level and the time to reach saturation for different spin and position of the instability

To see the differences we need to look more quantitatively, namely by looking at the growth rate of the instability, its saturation level and the time required to reach saturation. On top of Fig.2 we see that the time to reach saturation, while relatively constant at larger r_b, the small differences coming mostly from the differences in the setup we used, increased rapidly when the corotation radius is inside about $4r_g$. This rise shows the impact of the lapse on the propagation of the instability. While the change is about 40% of the corotation period, the actual numerical value is extremely small as those objects are very fast. It is not possible to detect such differences in observations.

At the bottom of Fig.2 we see that the growth rate of the instability goes through a maximum for a corotation of about $5r_g$. This, once again is too small of a change to have any detectable effect as one needs too long of an observation to detect HFQPOs, so we cannot follow the 'instantaneous' evolution of its rms.

More interestingly, we see on the middle plot, that the closer to r_g the corotation is, the higher the saturation is. This quantity is related to the maximum strength a QPO can attain, hence to how much modulation there is of the observed flux. While we cannot directly test that with observations, using all the published HFQPO data we find that the higher the rms, the higher the spin of black hole. The limitation being the very low number of spin determination for HFQPO source. This is something we will be exploring, especially with NICER.

3 Looking In the time domain

Another way to look at our data is in the time-domain, which is the main way to study HFQPOs at the moment. In order to do that we created synthetic lightcurves from our simulations using the ray-tracing routine Gyoto (Vincent et al. 2011) and then performed a Fourier Transform and a 'fit' with Lorentzian as is done with real data.

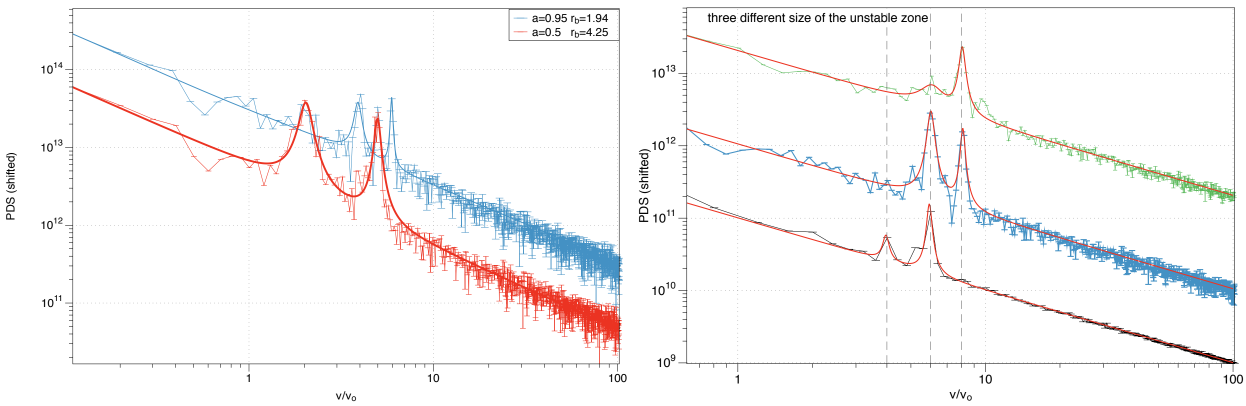

Fig. 3. Left: Two examples of synthetic PDS for two different spins and positions ($a = 0.5, r_b = 4.25$ and $a = 0.95, r_b = 1.94$) but a similar unstable zone. **Right:** Three examples of the same spin and position but with different unstable zones.

We see in on the left of Fig.3 two examples of synthetic PDS for two different spins and positions one mildly relativist ($a = 0.5, r_b = 4.25$) and one closer to maximal spin ($a = 0.95, r_b = 1.94$) but a similar unstable zone, while on the right there are three examples of the same spin and position but with different unstable zones. The abscissa of the plots are normalized to the fundamental frequency of the unstable zone so that we can compare different cases where the fundamental frequencies are different. Here we are interested in the mixture of frequencies detected and if any integer ratio exists between them. While changing the spin and position does give a different 'mix' of modes no general pattern seems to emerge as function of the spin of the central objects. Indeed, the size of the unstable zone has more impact on which modes emerge and how the ratio between the modes behaves. The three cases shown on the right of Fig.3 have at most a 30% difference in the dimension of the unstable zone (between the black and blue curve it is about 11%). Using this, a relatively small change in the local disk condition can change rapidly the dimension of the unstable zone hence creating a different observable mix of frequencies between observations.

4 Conclusions

The RWI has been previously proposed to explain the High-Frequency QPOs occurring in the vicinity of black holes (Vincent et al. 2013, 2014) but its existence in a full-GR environment had never been demonstrated up to now. Here we remedy this by performing 2D and 3D GR-HD simulations of the RWI in an extreme Kerr environment proving at the same time:

i) that, as predicted, the instability actually still exists when taking into account the full effects of a Kerr black hole.

ii) that its behaviour is only mildly affected by relativistic effects and only when the unstable zone is inside $5r_g$. Nevertheless, some of those effects might lead to observables.

iii) and that it is able to create a variety of PDS that encompass the observed one while explaining the origin of those different behaviours.

We acknowledges financial support from the UnivEarthS Labex program at Sorbonne Paris Cité (ANR-10-LABX- 0023 and ANR-11-IDEX-0005-02). Computing was done using the FACe (Francois Arago Centre) in Paris.

References

Casse, F., Varnière, P., & Meliani, Z. 2017, MNRAS, 464, 3704

Tagger, M. & Varnière, P. 2006, ApJ, 652, 1457

Varnière, P., Tagger, M., & Rodriguez, J. 2011, A&A, 525, A87

Varnière, P., Tagger, M., & Rodriguez, J. 2012, A&A, 545, A40

Vincent, F. H., Meheut, H., Varnière, P., & Paumard, T. 2013, A&A, 551, A54

Vincent, F. H., Paumard, T., Gourgoulhon, E., & Perrin, G. 2011, Classical and Quantum Gravity, 28, 225011

Vincent, F. H., Paumard, T., Perrin, G., et al. 2014, MNRAS, 441, 3477

SF2A 2017
C. Reylé, P. Di Matteo, F. Herpin, É. Lagadec, A. Lançon, Z. Meliani, F. Royer (eds)

CONSTRAINING THE EBL WITH THE 3FHL FERMI DATA

B. Biasuzzi[1], J. Biteau[1], O. Hervet[2] and D.A. Williams[2]

Abstract. The Extragalactic Background Light (EBL) is the light emitted by stars and accreting objects through the whole history of the Universe. Its spectrum is hard to measure directly due to both the presence of bright foreground emissions and magnitude limitations in galaxy surveys. Nevertheless, constraints on the EBL can be inferred by studying the absorption features in blazar spectra. By collecting a sample of 300 blazar spectra measured by *Fermi*-LAT in the energy range between 10 GeV and 2 TeV, we aim to determine the EBL scaling factor in a source-model-independent scenario. Furthermore, we want to investigate the feasibility of carring out a study on the EBL evolution as a function of redshift by using the newest 3FHL data.

Keywords: Extragalactic Background Light, Active Galactic Nuclei, Gamma-rays

1 Introduction

The Universe is permeated by a diffuse background radiation field that extends over the whole electromagnetic spectrum. The second brightest component - after the cosmic microwave radiation (CMB) - is the extragalactic background light (EBL), which is formed by the sum of the light from stars and active galactic nuclei (AGNs), emitted during all cosmic epochs. The EBL spectrum is characterized by two peaks: the first, the COB (Cosmic Optical Background, 0.1-8 μm) due to the direct light emitted by stars in the UV and optical band, and the second, the CIB (Cosmic Infrared Background, 8-1000 μm), formed by the fraction of light reprocessed and remitted in the IR band by dust and the interstellar medium.

The EBL density and its evolution as a function of redshift depend on the galaxy formation history. So, a full understanding of the EBL would provide fundamental contributions in several astrophysical fields. Unfortunately, the EBL spectrum is hard to measure directly because of the presence of strong foreground emissions, such as the zodiacal light and the diffuse light coming from the Galactic plane. Moreover, direct measurements can constrain the local background, but do not provide any information about its evolution with the cosmic epochs. Many EBL models try to reconstruct the EBL density and its evolution through different techniques: (i) models of Stecker & Scully (2006), Franceschini et al. (2008), Domínguez et al. (2011), and Franceschini & Rodighiero (2017), starting from the present galaxy luminosity functions, reconstruct the emission back in time by assuming a dependence on z (where, in turn, such a dependence is inferred by fitting the model prediction to the observed galaxy counts); (ii) models of Dwek & Arendt (1998), Razzaque et al. (2009), and Finke et al. (2010) simulate the galaxy and star formation process from the beginning of the Universe, taking into account the z-dependence of the star formation rate and models of population synthesis; and (iii) the model of Gilmore et al. (2012) follows a similar approach as in the case (i), but that uses the results provided by e.g. the *Wilkinson Microwave Anisotropy Probe* (Hinshaw et al. 2009) as initial conditions.

Another fruitful way to derive some constraints on the EBL and its evolution is through the observation of distant γ-ray sources such as AGNs. In particular the sub-class of blazars (AGNs whose relativistic jets point toward the observer) is particularly adapted for this purpose because (i) the γ-ray emission is amplified by relativistic boosting; and (ii) their presence over a large redshift range enables the study of the EBL evolution.

[1] Institut de Physique Nucléaire, IN2P3/CNRS, Université Paris-Sud, Univ. Paris/Saclay, 15 rue Georges Clémenceau, 91406 Orsay, Cedex, France
[2] Santa Cruz Institute for Particle Physics and Department of Physics, University of California at Santa Cruz, Santa Cruz, CA 95064, USA

Along their path, γ-rays emitted by blazars can interact with the photons of the EBL, generating electron-positron pairs. Such an interaction results in an observable flux decrease at very high energies in blazar spectra that depends on the EBL optical depth.

The aim of this work is to find a model-independent method to obtain the normalization factor of the EBL. A brief reminder on the EBL optical depth is introduced in Section 2. In Sections 3 and 4, we present the data sample and the analysis method, respectively. Finally, preliminary results are discussed in Section 5.

2 EBL optical depth

Along the path from the source to the observer, γ-rays can interact with EBL photons generating electron-positron pairs. This interaction results in a flux decrease in the high energy spectrum of blazars, that is strictly related to the EBL optical depth, $\tau(E_o, z_0)$. The latter, in turn, is given by integrating over (i) the source distance; (ii) the energy of the EBL photons field; and (iii) the angle θ between the EBL and γ-ray photons:

$$\tau(E_0, z_0) = \int_0^{z_0} dz \frac{\partial L}{\partial z}(z) \int_0^{\infty} d\epsilon \frac{\partial n}{\partial \epsilon}(\epsilon, z) \int_1^{-1} d\cos(\theta) \frac{1-\cos(\theta)}{2} \sigma_{\gamma\gamma}[\beta(E_0, z, \epsilon, \cos(\theta))] \tag{2.1}$$

where $\partial L/\partial z$ is the distance element in a flat ΛCDM cosmology, $n(\epsilon, z)$ is the numerical density of the EBL photon field, and $\sigma_{\gamma\gamma}$ is the pair production cross-section, given by the Bethe-Heitler formula (see Stecker et al. 1992):

$$\sigma_{\gamma\gamma}(\beta) = \frac{3\sigma_T}{16}(1-\beta^2)\left[2\beta(\beta^2-2) + (3-\beta^4)\ln\left(\frac{1+\beta}{1-\beta}\right)\right] \tag{2.2}$$

where β is:

$$\beta = \sqrt{1 - \frac{2(m_e c^2)^2}{E_0 \epsilon} \frac{1}{1+z} \frac{1}{1-\cos(\theta)}} \, . \tag{2.3}$$

As an approximation, the evolution of the EBL spectrum with redshift can be parametrized as the product between the local EBL density at $z = 0$ and an evolution term, $evol(z)$, by following Madau & Phinney (1996):

$$d\epsilon \frac{\partial n}{\partial \epsilon}(\epsilon, z) = d\epsilon_0 \frac{\partial n}{\partial \epsilon_0}(\epsilon_0, 0) \times evol(z) \, , \tag{2.4}$$

where the evolution term represents the sources contribution to the EBL photon field during the cosmic epoch.

3 Data

In this work we analyzed - by following the method described in Section 4 - the spectra of 300 blazars, taken from the preliminary release (rev. v11) of the Third Catalogue of Hard *Fermi*-LAT Sources (3FHL, The *Fermi*-LAT Collaboration 2017). Such a catalogue collects the data of 7 years of *Fermi*-LAT observations and counts 1556 objects detected between 10 GeV and 2 TeV. The improved sensitivity and angular resolution (by a factor 3 and 2, respectively with respect to the previous catalogue 1FHL, Ackermann et al. 2013), and the newest event-level analysis, Pass 8 (Atwood et al. 2013), yielded a better event reconstruction and classification together with an increased energy coverage.

We selected 300 blazar spectra with known redshift and TS > 25, including both BL Lac and Flat Spectrum Radio Quasars. The sample has been divided into three different redshift bins: 109 sources for $z \leq 0.2$, 100 for $0.2 < z \leq 0.5$, and 91 for $0.5 < z < 2.0$. Spectra contain typically from 3 to 5 significant points (most of them contains only 3 points). Upper limits have been excluded from the analysis because approximations are needed to include them in the fitting procedure.

4 Analysis method

As remarked above, the interaction between EBL photons and γ-rays, causes a flux decrease in the high energy spectrum of distant sources. Hence, the observed spectrum is attenuated according to:

$$\Phi_{obs} = e^{-\tau(E,z)} \, \Phi_{intr} \tag{4.1}$$

where Φ_{obs} and Φ_{intr} are the observed and intrinsic spectrum, respectively. The previous equation can be rewritten by multiplying the optical depth by the so-called scaling factor, α:

$$\Phi_{obs} = e^{-\alpha\,\tau(E,z)}\,\Phi_{intr} \tag{4.2}$$

that basically quantifies the agreement between the γ-ray observations and the EBL models providing $\tau(E, z, n)$. This approach has been adopted by many authors, and was e.g. applied on the *Fermi*-LAT data in Ackermann et al. (2012). In this work, we followed the same strategy, and we retrieved the scaling factor α for three different redshift bins, by combining a large number of blazar spectra. To model the intrinsic spectrum, the following functions have been taken into account: (i) power law, $\Phi_{PWL}(E) = \Phi_0\left(\frac{E}{E_0}\right)^{-\Gamma}$; (ii) exponential cutoff power law, $\Phi_{EPWL}(E) = \Phi_0\left(\frac{E}{E_0}\right)^{-\Gamma} e^{-E/E_{cut}}$; and (iii) log parabola, $\Phi_{LP}(E) = \Phi_0\left(\frac{E}{E_0}\right)^{-\Gamma-b\ln(E/E_0)}$; where Φ_0 is the flux normalization, $E_0 = \sqrt{E_{min}\,E_{max}}$ (with E_{min} and E_{max} the minimum and maximum spectrum energy, respectively) is the reference energy, Γ is the photon index at the reference energy, b is the curvature parameter, and E_{cut} is the energy corresponding to the cutoff.

A range of possible values for the scaling factor α is defined, and for equally spaced α values a fit to the data is performed in order to find the best spectral parameters describing each source. Then, the maximum likelihood value of α determines the best scaling factor according to the data. Since the emission processes of blazars are still not very well understood, it is difficult to disentangle if the spectrum curvature is due to internal emission mechanisms or to EBL absorption. So, a check on the spectral models is performed: for the best α value, a spectral model is switched into a more complex one if the latter is preferred at least at the 2σ level. A further condition to be satisfied in the fitting procedure - so that each spectral model is fully constrained - is that the degrees of freedom must be ≥ 1 (i.e., only sources whose spectrum contains strictly more than 3 significant points can be modelled with a log parabola or exponential cutoff power law). The check on the spectral models and determination of α is an iterative process, and it stops when the model-set converges.

The adopted EBL model is that of Franceschini et al. (2008), hereafter FR08. The scaling factor α has been obtained both for the full model and for an evolution template. In the latter case, we assumed that the EBL evolution term (see Equation 4.3) can be parametrized as in Raue & Mazin (2008):

$$evol(z) = (1+z)^{3-f_{evol}}\ . \tag{4.3}$$

The value of f_{evol} is set to 1.7. Such a value was demonstrated by Biteau & Williams (2015) to well reproduce the FR08 and Gilmore et al. (2012) EBL models up to $z \sim 0.6$ at least. Above this redshift, the parametrization is used, at this stage, as a toy model to study the sensitivity of our approach to the evolution of the EBL.

Finally, to test the robustness of the model selection, we run the whole procedure starting from different sets of intrinsic spectral models: (i) power law; and (ii) log parabola. Developing a model-independent approach is crucial to avoid biased results deriving from incorrect assumptions on the intrinsic spectrum (i.e., all absorption is due to the EBL in case of power law models, or most of absorption is due to internal mechanisms in case of log parabola models).

5 Results

For each redshift bin, we derived the scaling factor α (i) by assuming both the full FR08 EBL model (Figure 1), and a template evolution (Figure 2); and (i) by starting both from different initial spectral models (i.e., power law, and log parabola). Results presented in Ackermann et al. (2012) are shown for comparison, and were obtained by using the full FR08 EBL model. Their sample includes 150 blazars taken from the second *Fermi* Large Area Telescope source catalog (2FGL, Nolan et al. 2012), analyzed with the event-level analysis Pass 7. All intrinsic spectra have been modelled with a log parabola function, whose best-fit parameters were obtained by fitting the unabsorbed part of the spectrum (< 10 GeV). The uncertainties on the α-values obtained in our work are significantly reduced thanks both to the twice larger size of the source sample, and to the larger statistics and better performance in analyzing 3FHL data. We note nonetheless that more freedom is allowed in our parametrization of the intrinsic models, with both the model and parameters of each spectrum being fit jointly with the EBL normalization.

From the two plots, one can conclude that the model selection has a very similar effect both for the full and the evolution template of the FR08 EBL model: the major discrepancy occurs at low redshift, and then disappears at higher redshift. This could be due to a lack of statistics in the absorbed part of the spectrum at

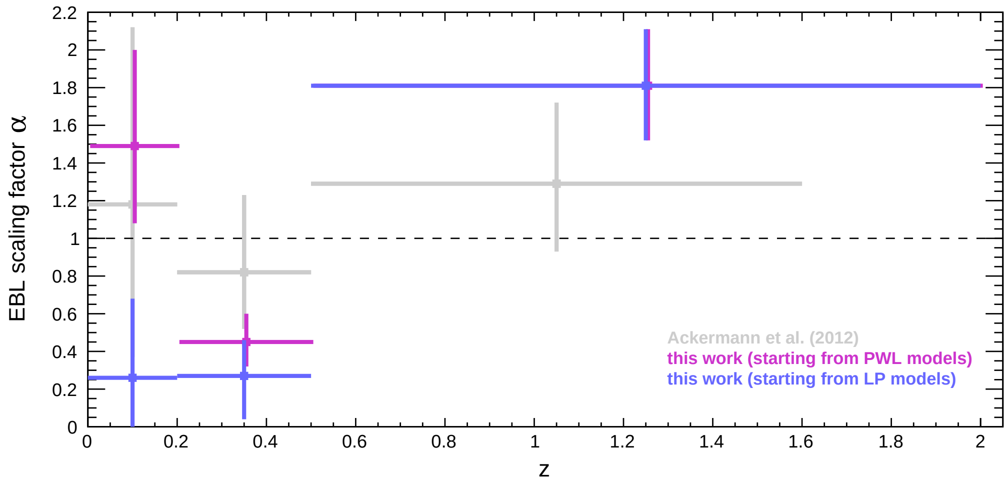

Fig. 1. EBL scaling factor as a function of redshift for the FR08 EBL model. Points were obtained for two different sets of initial spectral models: power law models (blue), and log parabola models (magenta). Results of Ackermann et al. (2012) are shown for comparison (grey).

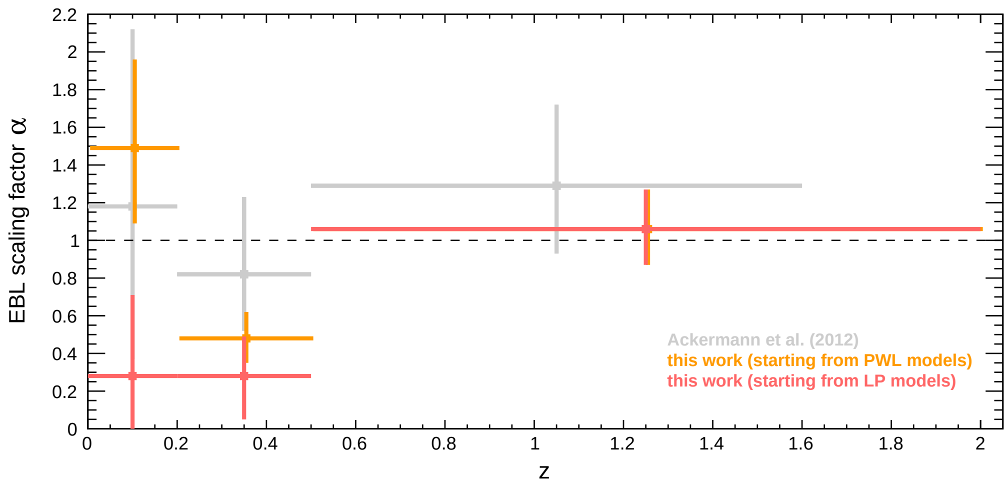

Fig. 2. Same as Figure 1, but for the evolution template of FR08 EBL model (see Equations 2.4 and 4.3), and with $f_{evol}(z) = 1.7$.

low redshift that makes the constraining power on the EBL poorer. This can lead to slightly different sets of spectral models, where the presence of few log parabola models can drive the fit to an unlikely absorption-free scenario.

What we can conclude from the inspection of the 3FHL data is that the effects of the model selection are still too large to allow us to investigate the impact of the parameter evolution. The lack of robustness at low redshifts is probably related to the fact that the intrinsic spectra are poorly constrained. To robustly evaluate the reliability of this model-independent approach, we need to broaden the investigated spectral region to lower energies, for example taking into account the spectral points contained in the third *Fermi* Large Area Telescope source catalog (3FGL, Acero et al. 2015).

Acknowledgments

This work was supported by the *Programme National Hautes Energies* with the founding from CNRS (INSU/INP3/INP), CEA, and CNES. Olivier Hervet and David Williams acknowledge support from the *Fermi*-GI Cycle 9 grant NNX16AR40G.

References

Acero, F., Ackermann, M., Ajello, M., et al. 2015, ApJS, 218, 23

Ackermann, M., Ajello, M., Allafort, A., et al. 2013, ApJS, 209, 34

Ackermann, M., Ajello, M., Allafort, A., et al. 2012, Science, 338, 1190

Atwood, W., Albert, A., Baldini, L., et al. 2013, ArXiv:1303.3514

Biteau, J. & Williams, D. A. 2015, ApJ, 812, 60

Domínguez, A., Primack, J. R., Rosario, D. J., et al. 2011, MNRAS, 410, 2556

Dwek, E. & Arendt, R. G. 1998, ApJ, 508, L9

Finke, J. D., Razzaque, S., & Dermer, C. D. 2010, ApJ, 712, 238

Franceschini, A. & Rodighiero, G. 2017, A&A, 603, A34

Franceschini, A., Rodighiero, G., & Vaccari, M. 2008, A&A, 487, 837

Gilmore, R. C., Somerville, R. S., Primack, J. R., & Domínguez, A. 2012, MNRAS, 422, 3189

Hinshaw, G., Weiland, J. L., Hill, R. S., et al. 2009, ApJS, 180, 225

Madau, P. & Phinney, E. S. 1996, ApJ, 456, 124

Nolan, P. L., Abdo, A. A., Ackermann, M., et al. 2012, ApJS, 199, 31

Raue, M. & Mazin, D. 2008, International Journal of Modern Physics D, 17, 1515

Razzaque, S., Dermer, C. D., & Finke, J. D. 2009, ApJ, 697, 483

Stecker, F. W., de Jager, O. C., & Salamon, M. H. 1992, ApJ, 390, L49

Stecker, F. W. & Scully, S. T. 2006, ApJ, 652, L9

The *Fermi*-LAT Collaboration. 2017, ArXiv: 1702.00664

SF2A 2017
C. Reylé, P. Di Matteo, F. Herpin, É. Lagadec, A. Lançon, Z. Meliani, F. Royer (eds)

ESTIMATION OF THE FLARE DUTY CYCLE OF AGNS BASED ON LOG-NORMAL RED-NOISE PROCESSES

Z.-W. Ou[1] and J. Biteau[1]

Abstract. Active Galactic Nuclei (AGN) show variability on time scales ranging from years down to minutes, e.g. in the TeV band, with outbursts often called flares. We aim at estimating the number of flares observable during a long-term monitoring campaign, depending on their flux and variability time scales. We use backward Fourier transform to construct AGN light curves as realizations of a pseudo-red-noise, log-normal process. Using a simple definition of a flare, we map their duty cycle as a function of threshold-flux and flare-duration values. The flare duty cycle can be entirely defined by two quantities: the slope of the power spectral density and the normalized variance of the process. We also produce visibility windows in order to estimate the effect of sampling on the observable number of flares.

Keywords: galaxy: nucleus, galaxies: active, gamma rays: galaxies, methods: statistical

1 Introduction

An active galactic nucleus (AGN) is a compact region in the center of a galaxy, which consists of a supermassive black hole with an accretion disk. AGNs emit relativistic jets and have strong radiation with flux variability from radio to γ-ray. However, the definition of an AGN flare, providing the amplitude and duration of flux variations, can be ambiguous. What fraction of the time does an AGN spend above a given flux with a coherent behavior? We propose a simple definition that can be used to jointly study the flux distribution and variability time scales of flares. We evaluate the duty cycle of AGN flares through simulations, assuming that the emission can be modeled as a red-noise, log-normal process.

2 Method

Long-term high-energy observations from *Fermi*-LAT reveal AGN light curves behaving as red-noise processes (Abdo et al. 2010). This means that the power spectral density (PSD) of the observed lightcurves follows a power-law spectrum as a function of frequency, $P(f) \sim f^{-\beta}$, where β is the index of the PSD and $P(f)$ is the power at frequency f. The average power-law index of FSRQs and BL Lacs was estimated by Abdo et al. (2010) to be $\beta = 1.4 \pm 0.1$ and $\beta = 1.7 \pm 0.3$, respectively.

The variations in flux are furthermore often found to have a log-normal distribution and the average amplitude of variability is proportional to the flux level (e.g. Giebels & Degrange 2009). The amplitude of flux variations is sometimes characterized by the fractional root mean square (rms) variability, $F_{\rm var}$, which is an estimator of the rms flux divided by the average flux. TeV γ-ray observations of PKS 2155$-$304 by the High Energy Stereoscopic System (H.E.S.S.) for example displayed strong flux variability with fractional rms variations between $F_{\rm var} = 0.13 \pm 0.09$ and $F_{\rm var} = 0.67 \pm 0.03$ (Abramowski et al. 2010).

In the following, we simulate light curves from log-normal flux distributions based on red-noise processes, investigating $F_{\rm var} = 0.1,\ 0.5$ and $\beta = 1,\ 2$ as test values. Timmer & Koenig (1995) propose a method for generating AGN light curves from a red-noise process. Here are the steps of our simulations:

(1) We construct a random PSD following a power-law spectrum of index β. We draw two normally distributed random numbers for each Fourier frequency f_i and multiply them by $\sqrt{P(f_i)/2} \sim f_i^{-\beta/2}$. The results are used as the real part and imaginary part of the Fourier transform. Light curves are then generated through backward

[1] Institut de Physique Nucléaire d'Orsay, Université Paris-Sud, Univ. Paris/Saclay, CNRS/IN2P3, 91406 Orsay, France

Fourier transform. We notice that such simulations can be affected by windowing and aliasing effects (Uttley, McHardy & Papadakis 2002), but we do not consider these two effects at the early stage of this study.
(2) To get a log-normal distribution, we exponentiate the flux values, $\Phi_{TK}(t)$, from the light curve obtained with the method of Timmer & Koenig (1995), noting that small distortions of the PSD are expected. $\Phi_{TK}(t)$ represents here a red-noise Gaussian process with an average of 0 and variance of 1. We rescale $\Phi_{TK}(t)$ so that the average of Φ_t is set to 1 arbitary units and its fractional rms amplitude is set to a value of $F_{\rm var}$. We obtain the corresponding log-normally distributed random flux Φ_t, using two parameters μ and σ that are the mean and standard deviation of the natural logarithm of Φ_t:

$$\Phi_t = \exp(\mu + \sigma\Phi_{TK}(t)). \tag{2.1}$$

We set $\mu = -\frac{1}{2}\ln(1 + F_{\rm var}^2)$ and $\sigma^2 = \ln(1 + F_{\rm var}^2)$, which indeed results in $<\Phi_t>= 1$ and $\sigma_{\Phi_t}/<\Phi_t>= F_{\rm var}$. In the method described above, only two parameters, β and $F_{\rm var}$, are needed to fix the statistical characteristics of the light curves and therefore to describe the flare duty cycle.
For each lightcurve, we define flares above a given flux threshold as events for which the emission remains strictly above the threshold for a given duration. We collect the start and stop times of each flare for various realizations of the lightcurves and store the duration of each flare in a 2D histogram. We define the flare duty cycle as the ratio between the sum of flare durations and the light curve duration.

3 Results

Fig. 1, left, shows a single AGN light curve simulated as a pseudo-red-noise, log-normal process. We set $\beta = 2$ and $F_{\rm var} = 0.5$ as an example that is in rough agreement with γ-ray observations from *Fermi*-LAT and H.E.S.S. We assume here an observation duration of 1 week, and a sampling of the flux every 0.5 hour.

Fig. 1, right, shows the flare duty cycle as a function of the flare duration and threshold flux obtained from simulations of 10^4 lightcurves, with the same β and $F_{\rm var}$ values as set to generate Fig. 1, left. We checked that integrating the 2D histogram over flare durations for given flux thresholds results in a 1D distribution compatible with the cumulative distribution function expected from a log-normal process.

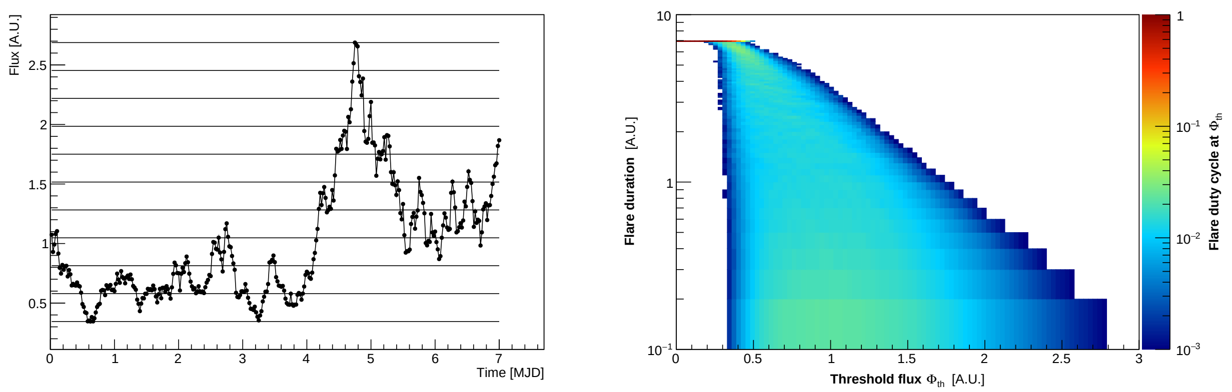

Fig. 1. Left: Example of a simulated light curve obtained with $F_{\rm var} = 0.5$ and $\beta = 2$. Horizontal lines illustrate threshold fluxes above which the start and stop times of flaring events are collected. **Right:** Flare duty cycle obtained with $F_{\rm var} = 0.5$ and $\beta = 2$.

3.1 *Varying* β *and* $F_{\rm var}$

The distribution of flare duty cycle depends on β and $F_{\rm var}$. The index of the PSD, β, reflects the ratio of long-term fluctuation power and short-term fluctuation power while the fractional rms variability, $F_{\rm var}$, reflects the average amplitude of the variations.

In Fig. 2, left, we illustrate the duty cycle obtained with $\beta = 1$ and $F_{\rm var} = 0.5$ for 10^4 simulations. In Fig. 2, right, we choose to illustrate the behavior of the duty cycle for $F_{\rm var} = 0.1$ and $\beta = 2$.
(1) The comparison of Fig. 2, left, ($\beta = 1$) and Fig. 1, right, ($\beta = 2$), shows that for larger β values, the flare duty cycle covers a wider area of the flare duration − threshold flux plane. The interpretation is that, as β is

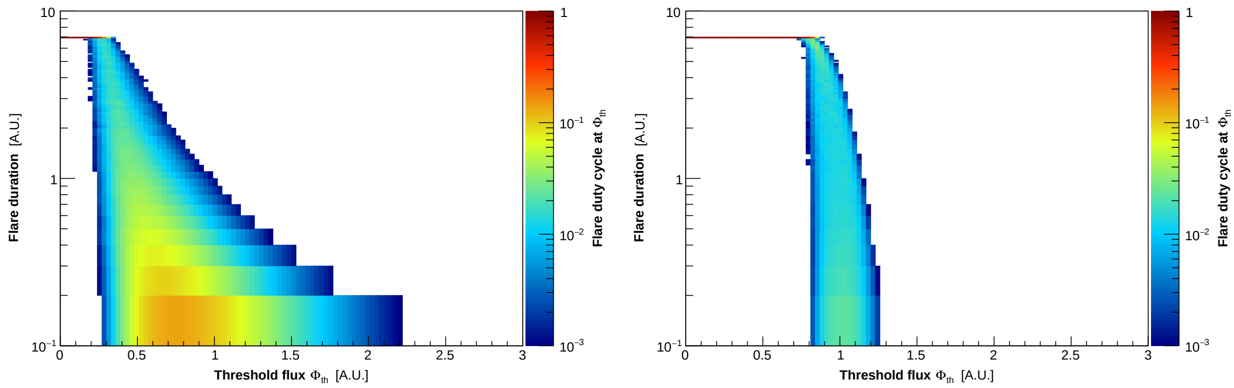

Fig. 2. Left: Flare duty cycle obtained with $F_{\rm var} = 0.5$ and $\beta = 1$. **Right:** Flare duty cycle obtained with $F_{\rm var} = 0.1$ and $\beta = 2$.

larger, more variability power is present at low frequencies. Long-duration flares are more frequent, and more time is given to build up large amplitude variations.
(2) The comparison of Fig. 2, right, ($F_{\rm var} = 0.1$) and Fig. 1, right, ($F_{\rm var} = 0.5$) also shows that for higher $F_{\rm var}$, the flare duty cycle covers a wider area of the flare duration – threshold flux plane. The interpretation is that, as $F_{\rm var}$ is larger, the flux can vary in a larger range and spread out more. Larger amplitude flares build up, but the time scale distribution remains similar to that observed in Fig. 1, right.

3.2 Simulations with observation windows

Ground-based γ-ray observations from imaging atmospheric Cherenkov telescopes such as H.E.S.S., MAGIC, and VERITAS, are usually performed during dark, moonless nights, so that realistic light curves are affected by observation windows. We illustrate in Fig. 3 the effect of windowing on a single realization of a light curve from the method discussed in Sec. 2. The red points correspond to a 5-week-long lightcurve sampled on a 0.5-hour timescale, while the black points correspond to the subsample of observations falling within H.E.S.S. visibility, assuming a source located in the direction of PKS 2155–304. We follow the visibility definition of Giomi, Gerard & Maier (2016) and exploit the code from these authors, which is based on AstroPy (`http://www.astropy.org/`). In the example chosen here, PKS 2155–304 can only be observed by H.E.S.S. in blocks of 4-5 consecutive days.

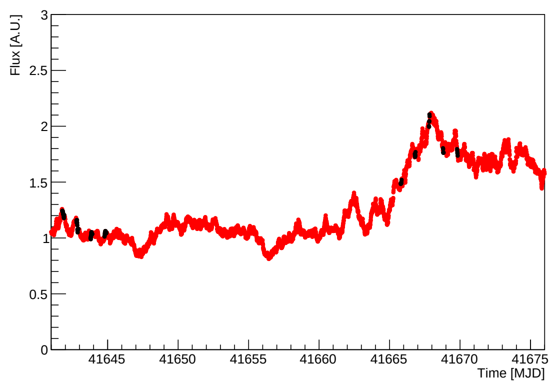

Fig. 3. Simulated light curve with $F_{\rm var} = 2$ and $\beta = 0.5$ over a 5-week term (red points) with a 0.5-hour sampling. Black points illustrate the visibility of a given source by a ground-based γ-ray observatory.

Fig. 4, left, shows the flare duty cycle obtained by simulating 10^4 lightcurves with characteristics similar to the red curve in Fig. 3 (no windowing). Fig. 4, right, shows the flare duty cycle obtained by simulating the

same lightcurves affected by windowing, i.e. lightcurves similar to the black points in Fig. 3.
The mapping of the flare duty cycle is clearly affected by the observational windowing, with characteristic time scales imprinted directly in the 2D histogram. Further studies will be dedicated to understanding how the duty cycle is distorted by the observation schedule and to how one could optimize long-term monitoring campaigns to minimize biases inherent to the windowing, e.g. in the context of long-term observations with the Cherenkov Telescope Array.

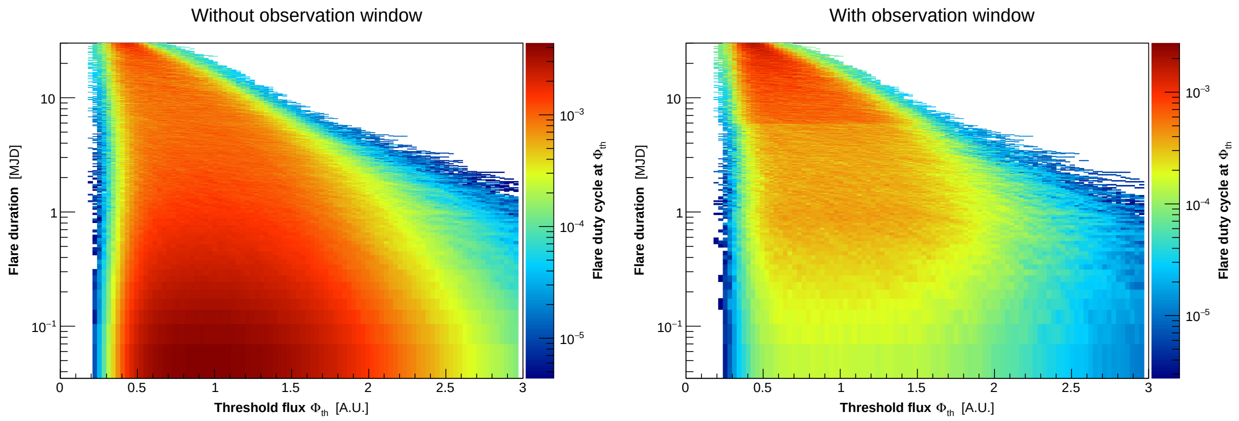

Fig. 4. Left: Flare duty cycle obtained with $F_{\rm var} = 0.5$ and $\beta = 2$ for a 5-week-long lightcurve. No observation window is considered. **Right:** Flare duty cycle obtained with the same simulations applying the observation windows illustrated in Fig. 3.

4 Conclusions and outlook

We have adopted a simple definition of flaring events from AGNs to jointly investigate the flux distribution and variability timescales of pseudo-red-noise, log-normal processes. We summarized the main conclusions here:
(1) We can estimate the duty cycle for any fractional rms variability, $F_{\rm var}$, and power spectral density index, β, as a function of the flare duration and threshold flux. All the flare information can be derived from these two parameters.
(2) Larger $F_{\rm var}$ values correspond to a wider range of flux variations, affecting the mapping of the flare duty cycle as a function of the threshold flux. Larger β values correspond to more power at low frequencies, resulting in longer flares as well as higher-amplitude flares, which have sufficient time to build up.
(3) The observational windowing affects the mapping of the duty cycle. Long-term monitoring campaigns could exploit tools such as presented in these proceedings to optimize the mapping of the duty cycle of AGN flares.
In the future, further developments for long-term γ-ray monitoring campaigns could include:
(1) A joint, unbiased, determination of $F_{\rm var}$ and β based on observations (e.g. from *Fermi*-LAT), focused on archetypal objects or populations.
(2) Simulations of long-term lightcurves to study more indepth the mapping of the duty cycle. Parallel computing appears to be a good solution to pursue such efforts.

The authors thank Matteo Giomi from DESY for the visibility code used in this study.

References

Abdo, A. et al. 2010, ApJ, 722, 520
Abramowski et al. 2010, A&A, 520, 83
Giebels, B. & Degrange, B. 2009, A&A, 503, 797
Giomi, M., Gerard, L., & Maier, G. 2016, APh, 80, 8
Timmer, J., & Koenig, M. 1995, A&A, 300, 707
Uttley P., McHardy I. & Papadakis I. 2002, MNRAS, 332, 231

SF2A 2017
C. Reylé, P. Di Matteo, F. Herpin, É. Lagadec, A. Lançon, Z. Meliani, F. Royer (eds)

RADIO MORPHING - TOWARDS A FULL PARAMETRISATION OF THE RADIO SIGNAL FROM AIR SHOWERS

A. Zilles[1], D. Charrier[2], K. Kotera[3], S. Le Coz[4], O. Martineau-Huynh[5], C. Medina[6], V. Niess[7], M. Tueros[8] and K. de Vries[9]

Abstract. Over the last decades, radio detection of air showers has been established as a detection technique for ultra-high-energy cosmic-rays impinging on the Earth's atmosphere with energies far beyond LHC energies. Todays second-generation of digital radio-detection experiments, as e.g. AERA or LOFAR, are becoming competitive in comparison to already standard techniques e.g. fluorescence light detection. Thanks to a detailed understanding of the physics of the radio emission in extensive air showers, simulations of the radio signal are already successfully tested and applied in the reconstruction of cosmic rays. However the limits of the computational power resources are easily reached when it comes to computing electric fields at the numerous positions requested by large or dense antenna arrays. In the case of mountainous areas as e.g. for the GRAND array, where 3D shower simulations are necessary, the problem arises with even stronger acuity. Therefore we developed a full parametrisation of the emitted radio signal on the basis of generic shower simulations which will reduce the simulation time by orders of magnitudes. In this talk we will present this concept after a short introduction to the concept of the radio detection of air-shower induced by cosmic rays.

Keywords: air shower, radio emission, radio detection

1 Introduction

Thanks to the development in the digital signal processing, the radio detection of air showers which are induced by cosmic rays experienced a renaissance in the last decades (Huege 2016). Especially, the results of AERA on the energy reconstruction of the primary particle (Aab et al. 2016) or LOFAR on the measurement of the mass composition (Buitink et al. 2016) show that radio detection is nowadays competitive to standard detection techniques as e.g. fluorescence light. These successes are based on the huge progress in the understanding and modeling of the radio emission mechanisms of air showers. There are several air-shower simulation programs on the market. They include modules for the calculation of the corresponding radio emission which differ in their complexity, but all of them take effects on the radio signal, e.g. due to refractive index, into account. In the last years their results started to agree with each other as well as they are consistent with radio-signal measurements under laboratory conditions (Belov et al. 2016) or by air-shower arrays, e.g. see Apel et al. (2015).

[1] Sorbonne Universités, UPMC Univ. Paris 6 et CNRS, UMR 7095, Institut d'Astrophysique de Paris, 98 bis bd Arago, 75014 Paris, France
[2] SUBATECH, IN2P3-CNRS, Université de Nantes, Ecole des Mines de Nantes, Nantes, France
[3] Sorbonne Universités, UPMC Univ. Paris 6 et CNRS, UMR 7095, Institut d'Astrophysique de Paris, 98 bis bd Arago, 75014 Paris, France et Laboratoire AIM-Paris-Saclay, CEA/DSM/IRFU, CNRS, Université Paris Diderot, F-91191 Gif-sur-Yvette, France
[4] National Astronomical Observatories, Chinese Academy of Sciences, Beijing 100012, China
[5] LPNHE, CNRS-IN2P3 et Universités Paris VI & VII, 4 place Jussieu, 75252 Paris, France
[6] APC Laboratory, Université Paris Diderot /Instituto Argentino de Radioastronomía - CONICET / CCT-La Plata, Camino Gral. Belgrano Km 40, Berazategui, Buenos Aires, Argentina
[7] Clermont Université, Université Blaise Pascal, CNRS/IN2P3, Laboratoire de Physique Corpusculaire, BP. 10448, 63000 Clermond-Ferrand, France
[8] Instituto de Física La Plata - CONICET/CCT- La Plata. Calle 49 esq 115. La Plata, Buenos Aires, Argentina
[9] Vrije Universiteit Brussel, Physics Department, Pleinlaan 2, 1050 Brussels, Belgium

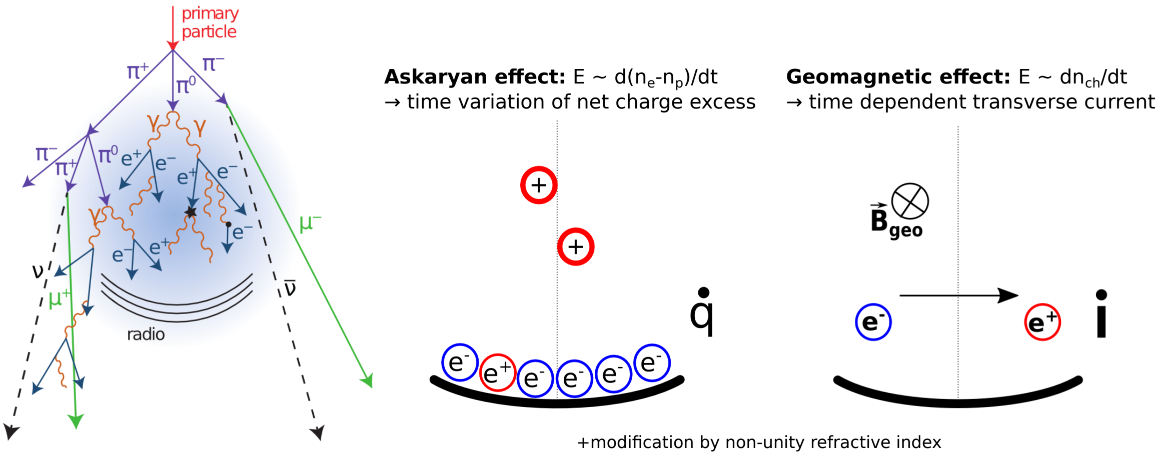

Fig. 1. Left: The particle components of an air shower Schröder (2017) (modified). **Right:** The radio-emission mechanisms of an air shower.

Nevertheless, running simulations for very high-energetic cosmic rays and arrays consisting of hundreds of antennas, e.g. in case of very large and non-flat arrays, is very CPU-time requesting so that one easily reaches the limitations of the computational resources. In the context of GRAND (Kotera & Martineau 2017), a sensitivity study shall be performed to find the locations with an enhanced detection rate of neutrino induced showers, so-called hot spots. This study will consists of running 1 Mio. antennas distributed over 1 Mio. km^2. Therefore, running massive simulations is not an option.

Within this project, we develop and test a parametrisation of the the radio signal, called radio morphing, to derive the expected electric field emitted from any air shower which is detected at any antenna position from one simulated generic shower. This will be performed by a simple scaling of the electric field amplitude and an interpolation of the pulse shape.

2 Air shower and radio emission

The cascade of ionized particles and electromagnetic radiation in the atmosphere induced by a primary cosmic particle is also called an extensive air shower. Via a nuclear interaction, a primary particle interacts with a nucleus of the Earth's atmosphere and produces secondary particles. These secondaries can be ordered in three groups: the muonic component consists of muons and neutrinos, the hadronic one of protons, neutrons, nuclear fragments, neutral and charged pions and kaons, and the electromagnetic component of electrons, positrons and photons (see fig. 1, left). The geometry of an air shower can be described by following initial shower parameters: the energy of the primary cosmic particle E with which the number of particles in the shower scales, the angles θ and ϕ which describes the direction where the showers goes to, and the injection height h which represents the vertical height of the first interaction from ground. An observable which can be linked to the mass of the primary particle initiating the extensive air shower is the atmospheric depth $X_{\rm max}$ (given in g/cm^2) at which an air shower reaches its maximum particle number in the electromagnetic component. Since the strength of the emitted radio signal scales linearly with the number of electrons and positrons, $X_{\rm max}$ can be seen at first order also as the position from where the maximum radiation comes from.

The electromagnetic component of this particle shower creates radio emission while propagating through the Earth's atmosphere or through a dense medium. Pulses of a length of tens of nanoseconds are produced, varying in amplitude between pulses hidden in the Galactic noise and pulses with amplitudes orders of magnitudes above it. The signal can be interpreted by two main mechanisms for emission of the signal, and an additional modification by the air's refractive index (Huege 2016) (compare to fig. 1, right):

The first, the so-called Askaryan effect (Askaryan 1962, 1965), can be described as a variation of the net charge excess of the shower in time ($\dot{q}$). Effectively, the surrounding medium is ionized by the air shower par-

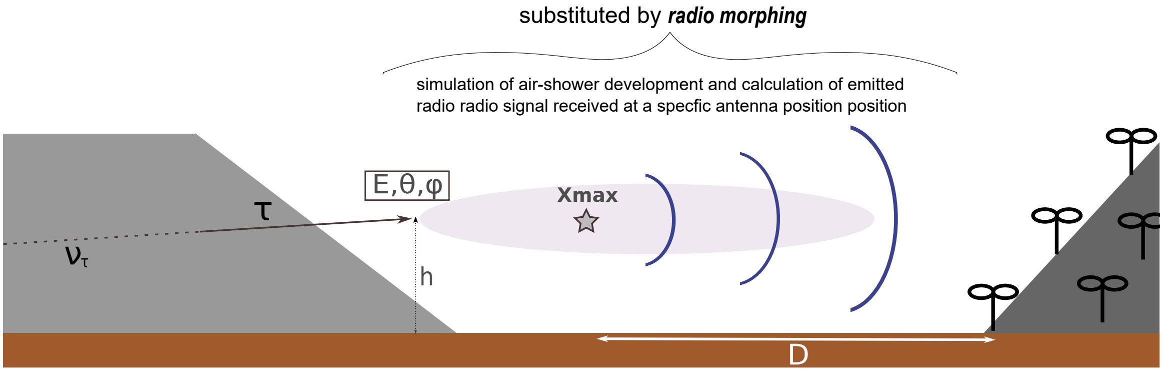

Fig. 2. The detection chain of a neutrino with GRAND: radio morphing will substitute the actual simulation of each induced air shower.

ticles passing through the Earth's atmosphere and the ionization electrons are swept into the cascade, whereas the heavier positive ions stay behind. In a non-absorptive, dielectric medium the number of electrons in the particle front varies in time and therefore the net charge excess in the cascade which develops then a coherent electromagnetic pulse.
The second mechanism and the dominant emission mechanism in an air shower is the geomagnetic effect (Huege 2016): The secondary electrons and positrons in the shower are accelerated by a geomagnetic field. They are decelerated due to the interactions with air molecules. In total, this leads to a net drift of the electrons and positrons in opposite directions as governed by the Lorentz force $F = q \cdot \vec{v} \times \vec{B}$, with q as the particle charge, $\vec{v}$ as the velocity vector of the shower and $\vec{B}$ as the magnetic field vector. As these also referred as "'transverse currents"' vary in time during the air shower development ($\dot{I}$), they lead to the emission of electromagnetic radiation.

3 Radio morphing

To be more efficient than simply running massive simulations, we are working on a parametrisation of the radio signal based on the air-shower parameters (see fig. 2), so that the expected electric field emitted from any air shower which is detected at any position can be derived from one generic shower simulated with a high antenna density. In other words the goal can be defined as following: the electric field $\vec{E}_A(t, x_i)$ at position x_i emitted from the desired target air shower A with given primary parameters $E_A, h_A, \theta_A, \phi_A$ can be derived from the simulated electric field $\vec{E}_B(t, x)$ at position x for the simulated generic air shower B with the primary parameters $E_B, h_B, \theta_B, \phi_B$. This idea is called ***radio morphing***.

Earlier simulation studies already showed that at fixed distances from the shower maximum, the strength of the radio signal solely depends on E, θ, ϕ and h of the induced air shower as well as that each of these parameter dependencies can be parametrised by simple scaling factors (e.g. $k_E = E_A/E_B$). Furthermore, each of these resulting scaling factors is independent from the others: $k_{AB} = k_E \cdot k_\theta \cdot k_\phi \cdot k_h$.

Based on these results, radio morphing consists of:

- **Producing the generic shower B**
  For the calculation of the radio emission of an air shower, the shower simulation program Aires (Sciutto 1999) and its module for the calculation of the emitted radio signal ZHAireS are used. To achieve the electric field traces at the antenna positions, the antenna positions for the simulation are arranged in planes with different distances D to the shower maximum $X_{\max}$ to account for the dependency of the air-shower development on the air density.

- **Scaling the amplitude of the reference shower A to the desired parameters of the target shower B: $\vec{E}_A(x, t) = k_{AB} \cdot \vec{E}_B(x, t)$**
  For each simulated antenna position, the scaling of the peak amplitudes of the electric field traces is performed accordingly to the desired shower parameters E_A, θ_A, ϕ_A and injection height h_A with respect

to the initial shower parameters E_B, θ_B, ϕ_B and h_B by multiplying the factor $k_{AB} = k_E \cdot k_\theta \cdot k_\phi \cdot k_h$. To account for the impact of the refractive index on the actual radio signal and therefore for another signal distribution at the specific distance to the shower maximum, the scaling procedure includes as well a stretching of the antenna positions if needed.

- **3D interpolation of the electric field trace to the desired antenna position x_i: $\vec{E}_A(x,t) \rightarrow \vec{E}_A(x_i,t)$**
  On the basis of the simulated antenna positions which are organised in planes in specific distances to the shower maximum, the electric field trace of any antenna positions which lies in-between these planes can be derived by an interpolation of the full pulse shape. The desired electric field traces are calculated in the frequency domain where the spectrum can be represented in polar coordinates: $f(r,\phi) = r \cdot e^{i\phi}$. The interpolation is performed by applying a linear interpolation of the amplitude r and the phase ϕ weighted with the distance of the desired antenna positions to the simulated antenna positions.

4 Summary

To perform a simulation study for arrays consisting of hundreds of radio antennas, more efficient simulations are needed. Therefore a parametrisation of the air-shower's radio emission is currently under development and testing. Here, the goal is to compute the expected electric field at any position emitted from any air shower on the basis of a generic air shower as reference which is simulated with a high antenna density. This so-called radio morphing is based on a pulse scaling depending on the initial shower parameters as well as a 3D interpolation of the electric field's pulse shape at any desired antenna position. Due to the gain of a very large amount of time and costs, this parametrisation will be an extremely powerful method to perform studies on the detection of air showers via their radio signal. Radio morphing will be finally applied in the sensitivity study for GRAND.

This work is supported by the APACHE grant (ANR-16-CE31-0001) of the French Agence Nationale de la Recherche.

References

Aab, A. et al. 2016, Phys. Rev. Lett., 116, 241101
Apel, W. et al. 2015, 75
Askaryan, G. 1962, Soviet Physics JETP, 14
Askaryan, G. 1965, Soviet Physics JETP, 21
Belov, K. et al. 2016, Phys. Rev. Lett., 116, 141103
Buitink, S. et al. 2016, Nature, 531, 70
Huege, T. 2016, Phys. Rept., 620, 1
Kotera, K. & Martineau, O. 2017, in SF2A 2017 Proceedings
Schröder, F. G. 2017, Prog. Part. Nucl. Phys., 93, 1
Sciutto, S. J. 1999, arXiv:astro-ph/9911331

SF2A 2017
C. Reylé, P. Di Matteo, F. Herpin, É. Lagadec, A. Lançon, Z. Meliani, F. Royer (eds)

IMPACT OF CONVECTION AND RESISTIVITY ON ANGULAR MOMENTUM TRANSPORT IN DWARF NOVAE.

N. Scepi[1], G. Lesur[1], G. Dubus[1] and M.Flock[2]

Abstract. The eruptive cycles of dwarf novae are thought to be due to a thermal-viscous instability in the accretion disk surrounding the white dwarf. This model has long been known to imply enhanced angular momentum transport in the accretion disk during outburst. This is measured by the stress to pressure ratio α, with $\alpha \approx 0.1$ required in outburst compared to $\alpha \approx 0.01$ in quiescence. Such an enhancement in α has recently been observed in simulations of turbulent transport driven by the magneto-rotational instability (MRI) when convection is present, without requiring a net magnetic flux. We independently recover this result by carrying out PLUTO MHD simulations of vertically stratified, radiative, shearing boxes with the thermodynamics and opacities appropriate to dwarf novae. The results are robust against the choice of vertical boundary conditions. In the quiescent state, the disk is only very weakly ionized so, in the second part of our work, we studied the impact of resistive MHD on transport.We find that the MRI-driven transport is quenched ($\alpha \approx 0$) below the critical density at which the magnetic Reynolds number $R_{\mathrm{m}} \leq 10^4$. This is problematic because the X-ray emission observed in quiescent systems requires ongoing accretion onto the white dwarf.

Keywords: accretion disks, convection, turbulence , magnetohydrodynamics (MHD), dwarf novae

1 Introduction

A fundamental, yet challenging, issue in accretion theory is the transport of angular momentum. Historically, the transport of angular momentum has been parametrized by the dimensionless parameter α, the ratio of the fluid stress (responsible for the transport) to the local thermal pressure (Shakura & Sunyaev 1973).

Dwarf novae (DNe) provide the best observational constrains on α (King et al. 2007). DNe are binary systems where matter is transferred by Roche lobe overflow from a solar-type star to a white dwarf. Their lightcurves show periodic outbursts during which the luminosity typically rises by several magnitudes (Warner 2003). According to the disk instability model (DIM, see Lasota 2001 for a review), these outbursts are caused by a thermal-viscous instability in the accretion disk due to the steep temperature dependence of the opacity when hydrogen ionizes around 7000 K. Outburst decay timescales imply $\alpha \sim 0.1$ (Kotko & Lasota 2012) whereas recurrence timescales imply $\alpha \sim 0.01$ in quiescence (Cannizzo et al. 1988, 2012). Although it has long been known that the DIM requires transport to be more efficient in outburst than in quiescence (Smak 1984), the physical reason for this change in α has remained elusive.

It is now widely accepted that angular momentum transport in disks is due to turbulence driven by the development of the magneto-rotational instability (MRI, Balbus & Hawley 1991). Stratified local simulations (isothermal or with an artificial cooling) with zero net magnetic flux show a universal value of $\alpha \sim 0.03$ (Simon et al. 2012, Latter & Papaloizou 2012), comparable to the value required for quiescent DNe. To properly investigate the thermal equilibrium states of DNe, Hirose et al. (2014) performed the first simulations including radiative transfer, vertical stratification and the realistic thermodynamics appropriate to DNe. They found that convection increases α to 0.1 in the hot state's low density part, in the absence of net magnetic flux, providing a tantalizing solution to the change in α in DNe (Coleman et al. 2016).

Another explanation for the difference in transport efficiency between hot and cold states was proposed by Gammie & Menou (1998). In the quiescent state of DNe, the plasma is expected to be largely neutral and thus

[1] Univ. Grenoble Alpes, CNRS, Institut de Planétologie et d'Astrophysique de Grenoble (IPAG), F-38000, Grenoble, France
[2] Jet Propulsion Laboratory, California Institute of Technology, Pasadena, California 91109, USA

the magnetic field decouples from the disk. With the electron fraction a strong function of the temperature, they pointed out that the MRI may not be able to grow or, at least, sustain fully developed turbulence in a quiescent DNe disk.

In light of these results, we have carried out numerical simulations to assess the impact of convection and resistivity on the transport of angular momentum in DNe in the hot, outburst and cold, quiescent states (respectively).

2 Framework

2.1 Model

We adopt the local, shearing-box approximation (Hawley et al. 1995), to simulate a vertically-stratified patch of accretion disk situated at a distance $R_0 = 1.315 \times 10^{10}$ cm from a $0.6\,M_\odot$ white dwarf. In the co-rotating frame, the radiative MHD equations are :

$$\frac{\partial \rho}{\partial t} + \boldsymbol{\nabla} \cdot (\rho \boldsymbol{v}) = 0 \tag{2.1}$$

$$\rho \frac{\partial \boldsymbol{v}}{\partial t} + (\rho \boldsymbol{v} \cdot \boldsymbol{\nabla}) \boldsymbol{v} = -\boldsymbol{\nabla} \left(P + \frac{B^2}{8\pi} \right) + \left(\frac{\mathbf{B}}{4\pi} \cdot \boldsymbol{\nabla} \right) \mathbf{B} + \rho \big(-2\Omega \hat{\boldsymbol{z}} \times \boldsymbol{v} + 3\Omega^2 x \hat{\boldsymbol{x}} - \Omega^2 z \hat{\boldsymbol{z}} \big) \tag{2.2}$$

$$\frac{\partial E}{\partial t} + \boldsymbol{\nabla} \cdot [(E + P_t)\boldsymbol{v} - (\boldsymbol{v} \cdot \mathbf{B})\mathbf{B}] = -\rho \boldsymbol{v} \cdot \boldsymbol{\nabla} \Phi - \kappa_P \rho c (a_R T^4 - E_R) \tag{2.3}$$

$$\frac{\partial \mathbf{B}}{\partial t} = \boldsymbol{\nabla} \times (\boldsymbol{v} \times \mathbf{B} - \frac{4\pi}{c} \eta \mathbf{J}) \tag{2.4}$$

$$\frac{\partial E_R}{\partial t} - \boldsymbol{\nabla} \frac{c \lambda(R)}{\kappa_R \rho} \boldsymbol{\nabla} E_R = \kappa_P \rho c (a_R T^4 - E_R) \tag{2.5}$$

The last three terms of Eq. 2 represent, respectively, the Coriolis force, the tidal force and the vertical component of the gravitational force.

2.2 Method

We solve the MHD equations on a 3D Cartesian grid with the conservative, Godunov-type code PLUTO (Mignone 2009). Radiative transfer is treated separately from the MHD step using an implicit time-stepping following Flock et al. (2013). In this step, we solve the coupled matter-radiation equations in the flux-limited diffusion approximation. Opacities, internal energy, mean molecular weight are computed using pre-calculated tables. For the MHD step, we use the HLLD Riemann solver and switch for HLL in region of high pressure gradient to improve the robustness of our code.

We use shear-periodic conditions in the x-direction, periodic conditions in the y-direction, and either periodic or modified outflow conditions (as in Brandenburg et al. (1995)) for the z-direction to test their influence on the results (Hirose et al. 2014 used only outflow conditions). Our boxes have a resolution of $32\times128\times256$, a size of $1.5H\times6H\times12H$ on the hot branch (see §3) and of $0.75H\times3H\times6H$ for the cold and middle branch (see §3) in x, y and z direction respectively.

We explore the parameter space in Σ and $T_{\rm eff}$ to retrieve the stability curve of the disk at R_0 and follow the evolution of α. We start from an isothermal simulation and activate radiative transfer after $\sim$ 50 orbits. For certain runs in the hot branch's low density part, we restart from previous simulations and change surface density allowing a smoother transition to capture the disk equilibrium.

For non ideal runs, resistivity is computed consistently with a pre-calculated table and we use a minimum floor to avoid dramatically small time steps.

3 Results

3.1 Ideal MHD simulations

The simulations trace an equilibrium thermal curve in the shape of an S (an S-curve) with a hot, stable branch and a cold, stable branch, providing independent confirmation of the results of Hirose et al. (2014). The S-curve from the simulations is comparable to that predicted by the vertical structure calculations using an α-prescription. These also predict a third stable branch at intermediate temperatures ($T_{\rm mid} \approx 10^4$ K).The middle branch is not as extended as the other branches and may be seen as a prolongation of the cold branch to higher temperatures.

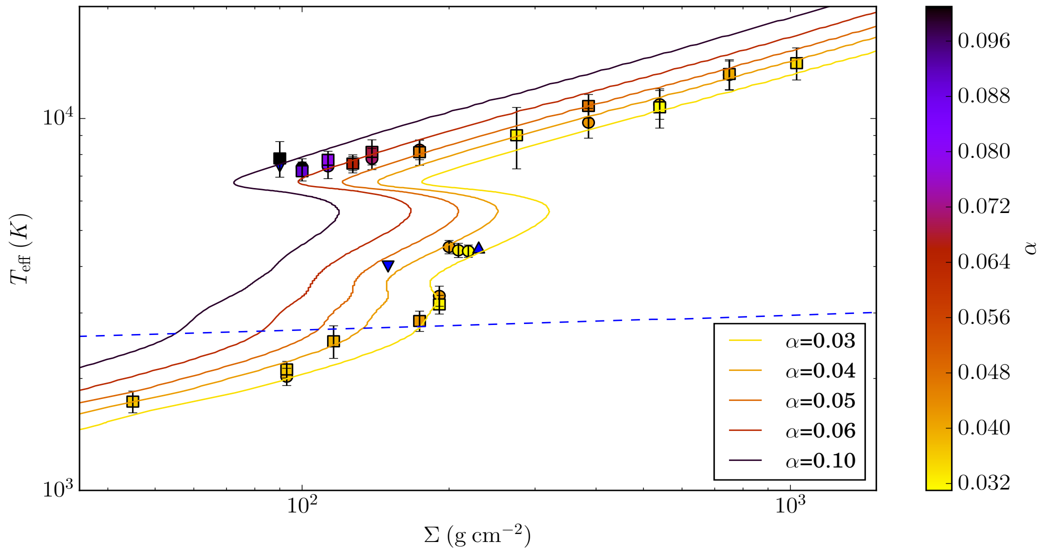

Fig. 1: Thermal equilibria in the $[T_{\rm mid}]$ vs $[\Sigma]$ (top) or $[T_{\rm eff}]$ vs $[\Sigma]$ (bottom) plane. Squares and circles are respectively for periodic and outflow runs. Triangular dots represent runs with runaway cooling (triangle facing down) or heating (triangle facing up). Error bars represent the standard deviation of the temperature fluctuations. The symbols are color-coded to the value of α. The color-coded curves are vertical thermal equilibria using an α-prescription. The dashed blue line indicates where the magnetic Reynolds number $R_m = 10^4$ based on an isothermal model.

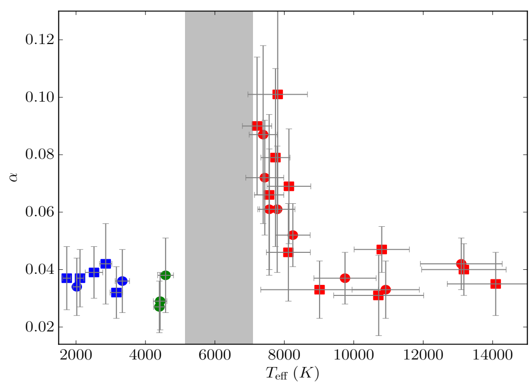

Fig. 2: α as a function of $[T_{\rm mid}]$ (top panel) and $[T_{\rm eff}]$ (bottom panel). Error bars represent the standard deviations of the fluctuations around the mean values. Blue, green and red colors are respectively for the cold, middle and hot branch. Squares and circles indicate periodic and outflow runs. The shaded area corresponds to the thermally-unstable region.

On Figure 1 and 2, we see an enhancement of α in the low Σ part of the hot branch, with a maximum value of $\alpha \approx 0.101$. Hirose et al. (2014) attributed the enhanced α to convection. We also observe that the enhanced α runs are convectively-unstable (Scepi et al. 2017) and further note that the value of α does not depend on the chosen vertical boundary conditions. Although convection plays a major role in transporting heat in the runs with an enhanced α, we find no clear relationship between α and $f_{\rm conv}$, the average fraction of the flux carried by convection. Notably, α is not enhanced on the middle branch although it is strongly convectively-unstable (Scepi et al. 2017).

3.2 Resistive simulations

Ideal MHD may not apply to the cold branch due to the very low ionization fractions. The development of the MRI can be suppressed as the resistivity due to electron-neutral collisions increase. This is quantified by the magnetic Reynolds number

$$R_{\rm m} \equiv \frac{c_s h}{\eta} \tag{3.1}$$

with η the resistivity, c_s the sound speed and $h = c_s/\Omega$ the local pressure scale-height. For $R_{\rm m} < 10^4$, it is expected that diffusion of the magnetic field becomes too important for the disk to sustain MHD turbulence (Hawley et al. 1996; Fleming et al. 2000).

We find that resistivity has a critical impact by suppressing turbulence on the cold branch below some critical density located between $\Sigma = 174\,{\rm g\,cm^{-2}}$ and $\Sigma = 191\ {\rm g\,cm^{-2}}$. The dashed blue line on Figure 1 show the limit under which MRI should be stable from an isothermal model. There is very little discrepancy between our results and the model as in the cold branch the disk is almost isothermal.

4 Conclusion

In a first part, we find that the thermal equilibrium solutions found by the simulations trace the well-known S-curve derived from α-prescription models, including a middle branch that extends the cold branch to higher temperatures and is characterized by vigorous convection. We confirm that α increases to ≈ 0.1 near the unstable tip of the hot branch as reported by Hirose et al. (2014). This increase is thus robust against the choice of numerical code and, as we investigated, against the choice of outflow or periodic vertical boundary conditions. In the second part, we show that the region of the cold branch with $\Sigma < 191\,{\rm g\,cm^{-1}}$ does not maintain the MRI-driven turbulence. This is problematic because the X-ray emission observed in quiescent DNe requires ongoing accretion onto the white dwarf.

References

Balbus, S. A. & Hawley, J. F. 1991, The Astrophysical Journal, 376, 214
Brandenburg, A., Nordlund, A., Stein, R. F., & Torkelsson, U. 1995, ApJ, 446, 741
Cannizzo, J. K., Shafter, A. W., & Wheeler, J. C. 1988, The Astrophysical Journal, 333, 227
Cannizzo, J. K., Smale, A. P., Wood, M. A., Still, M. D., & Howell, S. B. 2012, The Astrophysical Journal, 747, 117
Coleman, M. S. B., Kotko, I., Blaes, O., Lasota, J.-P., & Hirose, S. 2016, MNRAS, 462, 3710
Fleming, T. P., Stone, J. M., & Hawley, J. F. 2000, The Astrophysical Journal, 530, 464
Flock, M., Fromang, S., González, M., & Commerçon, B. 2013, Astronomy & Astrophysics, 560, A43
Gammie, C. F. & Menou, K. 1998, The Astrophysical Journal Letters, 492, L75
Hawley, J. F., Gammie, C. F., & Balbus, S. A. 1995, ApJ, 440, 742
Hawley, J. F., Gammie, C. F., & Balbus, S. A. 1996, ApJ, 464, 690
Hirose, S., Blaes, O., Krolik, J. H., Coleman, M. S. B., & Sano, T. 2014, The Astrophysical Journal, 787, 1
King, A., Pringle, J., & Livio, M. 2007, Monthly Notices of the Royal Astronomical Society, 376, 1740
Kotko, I. & Lasota, J.-P. 2012, Astronomy & Astrophysics, 545, A115
Lasota, J.-P. 2001, New Astronomy Reviews, 45, 449
Latter, H. N. & Papaloizou, J. C. 2012, Monthly Notices of the Royal Astronomical Society, 426, 1107
Mignone, A. 2009, Memorie della Societa Astronomica Italiana Supplementi, 13, 67
Scepi, N., Lesur, G., Dubus, G., & Flock, M. 2017, ArXiv e-prints
Shakura, N. I. & Sunyaev, R. A. 1973, A&A, 24, 337
Simon, J. B., Beckwith, K., & Armitage, P. J. 2012, Monthly Notices of the Royal Astronomical Society, 422, 2685
Smak, J. 1984, Acta Astron., 34, 161
Warner, B. 2003, Cataclysmic variable stars, Vol. 28 (Cambridge University Press)

SF2A 2017
C. Reylé, P. Di Matteo, F. Herpin, É. Lagadec, A. Lançon, Z. Meliani, F. Royer (eds)

ACTIVE GALACTIC NUCLEI IN THE ERA OF THE IMAGING X-RAY POLARIMETRY EXPLORER

F. Marin[1] and M. C. Weisskopf[2]

Abstract. In about four years, the National Aeronautics and Space Administration (NASA) will launch a small explorer mission named the Imaging X-ray Polarimetry Explorer (IXPE). IXPE is a satellite dedicated to the observation of X-ray polarization from bright astronomical sources in the 2 – 8 keV energy range. Using Gas Pixel Detectors (GPD), the mission will allow for the first time to acquire X-ray polarimetric imaging and spectroscopy of about a hundred sources during its first two years of operation. Among them are the most powerful sources of light in the Universe: active galactic nuclei (AGN). In these proceedings, we summarize the scientific exploration we plan in the field of AGN using IXPE, describing the main discoveries that this new generation of X-ray polarimeters is expected to make. Among these discoveries, we should see the indisputable detection of signatures of strong gravity, which will help us quantify the effects of scattering by distant cold material on the iron Kα line observed at 6.4 keV. IXPE will also be able to probe the morphology of parsec-scale AGN regions, to evaluate the magnetic field strength in quasar jets and their direction, and, among the most important results, to deliver an independent measurement of the spin of black holes.

Keywords: black hole physics, galaxies: active, magnetic fields, polarization, relativistic processes, scattering

1 Introduction

The study of cosmic polarization led to numerous discoveries in almost all astronomical fields. The first measurement of starlight polarization goes back to Hiltner (1949), who found that the light of distant stars is polarized as high as 12% due to interstellar clouds. More importantly, the position angle of the polarization was found to be close to the galactic plane, opening the way for a deeper comprehension of the nature of the interstellar medium (Davis & Greenstein 1951). The polarization of the Sun itself was measured by many astrophysicists, one of the most spectacular and earliest discoveries being the observation of the Zeeman effect in sunspots by Hale (1908), followed by the first evaluation of the solar magnetic field strength (Salet 1910). Broadband polarization was recorded for all possible astronomical objects, since it is present in radiation from coherent sources such as astrophysical masers to incoherent sources such as the large radio lobes of active galaxies. However, not all energy windows are available nowadays for a systematic exploration of astronomical polarization.

The X-ray band is a step behind in comparison to all other wavebands in this regard. The first X-ray polarization measurements go back to Tindo et al. (1970) in the case of solar flares. Extra-solar X-ray polarization observations were achieved by Novick et al. (1972), targeting the Crab nebula and several other bright X-ray sources. A unique precision measurement of the X-ray polarization of the Crab Nebula (without pulsar contamination) was achieved by Weisskopf et al. (1978) thanks to the Eighth Orbiting Solar Observator (OSO-8) graphite crystal polarimeters. Since then, only a couple of attempts were made in the hard X-ray band (Suarez-Garcia et al. 2006; Dean et al. 2008; Chauvin et al. 2017).

In these proceedings, we present the Imaging X-ray Polarimetry Explorer (IXPE), a NASA-led spatial mission that will fly in 2021 and carry, for the first time, a set of imaging X-ray polarimeters. Dedicated to the study of high energy sources, IXPE will re-open the window of X-ray polarimetric observations. Focusing on the field of active galactic nuclei (AGN), we summarize here what IXPE will be able to achieve in the first years of operation.

[1] Université de Strasbourg, CNRS, Observatoire astronomique de Strasbourg, UMR 7550, F-67000 Strasbourg, France
[2] NASA Marshall Space Flight Center, Huntsville, Alabama, United States

2 The IXPE mission

IXPE is part of the NASA's Explorer Mission project and is led by the Principal Investigator, Dr. Martin C. Weisskopf. Within a cost cap of \$ 188 M, IXPE will be comprised of three identical, grazing-incidence, X-ray mirror module assemblies that will collimate radiation to three accompanying polarization sensitive Gas Pixel Detectors (GPD). The NASA/MSFC is producing the X-ray mirror modules while the Italian Space Agency is providing the GPD, making IXPE an international mission. Ball Aerospace is taking care of the spacecraft and the services of mission integration that are also included in the cost of IXPE. The satellite will be launched from Kwajelein Atoll into a 540 km circular orbit at almost 0° inclination. The envisioned launcher is a Pegasus XL vehicle that can carry a mass of 450 kg.

The nominal lifetime of IXPE is two years and about one hundred targets will be observed, including AGN, microquasars, pulsars (plus wind nebulae), magnetars, X-ray binaries, supernova remnants, and the Galactic center. Thanks to its GPDs (Costa et al. 2001; Bellazzini et al. 2006, 2007), IXPE will be able to measure the spatial, spectral, timing, and polarization state of X-rays in the 2 – 8 keV band. NASA officially selected IXPE on January the 3rd, 2017, among fourteen proposals. As the first dedicated X-ray polarimetry observatory, IXPE will significantly enlarge the observational phase space, probing fundamental questions concerning high densities, high temperatures, non thermal particle acceleration, strong magnetic and electric fields, and strong gravity. Additional details about the mission can be found on-line at https://wwwastro.msfc.nasa.gov/ixpe/ and in Weisskopf et al. (2016).

3 Scientific goals in the field of AGN

As stated above, IXPE will observe a large variety of X-ray sources. Among them are the bright cores of active galaxies. The presence of accreting supermassive black holes can be inferred from the near-infrared to the X-ray domains but only X-ray polarization measurements can probe the geometry, composition, temperature and physics of matter at the smallest gravitational radii. In the following, we give three examples of the importance of IXPE in solving several key questions about AGN.

3.1 Spin determination

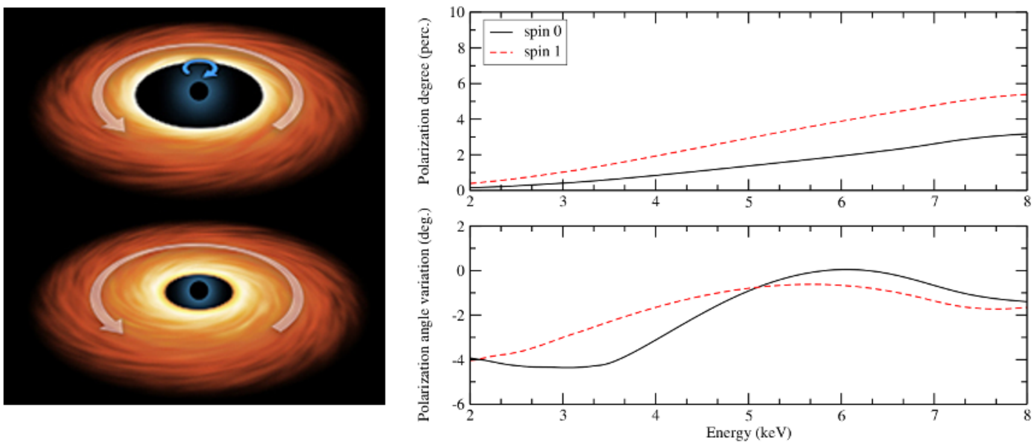

Fig. 1: Spin determination through X-ray polarization continuum measurements. The left-hand panel represents two flavors of supermassive black hole spins: a non-rotating, a=0, (or a<<1) Schwarzschild black hole at the top and a maximally rotating, a=1, Kerr black hole below. The blue arrow shows the direction of rotation, if any, for both these figures. Credits: NASA/JPL-Caltech. The right-hand panel is the polarization degree and polarization angle variation associated with the two black hole spins in the IXPE energy band. Simulations from Dovčiak et al. (2011) and Marin et al. (2017, submitted).

Measuring the spin of black holes is a long-standing problem as the spin only affects the local spacetime around the potential well. It is thus necessary to observe the central parts of the accretion disk in the X-ray band in order to determine the dimensionless angular momentum parameter, a, one of the two key parameters of black holes (with their mass). Several methods exist: one can fit the profile of the relativistically-broadened iron Kα line (e.g., Reynolds 2014) or fit the thermal X-ray continuum (e.g., McClintock et al. 2014). However the two methods do not always agree and there are many sources of possible systematic errors (e.g., intrinsic absorption, presence of a radio jet, modelling of the soft excess, role of emission from within the innermost stable circular orbit).

Measuring the X-ray polarization from AGN adds two independent quantities to the spectroscopic channel: the polarization degree and the polarization position angle. These new observational constraints remove many degrees of freedom from our current models that must fit both the spectroscopic and polarimetric data. In particular, it was shown by Schnittman & Krolik (2009) and Dovčiak et al. (2011) that the X-ray polarization from X-ray binaries and AGN is particularly sensitive to the spin, luminosity and inclination of the source. Fig. 1 illustrates the difference between a non-spinning and a maximally spinning supermassive black hole in terms of polarization degree and angle*.

3.2 Strong gravity and distant scattering

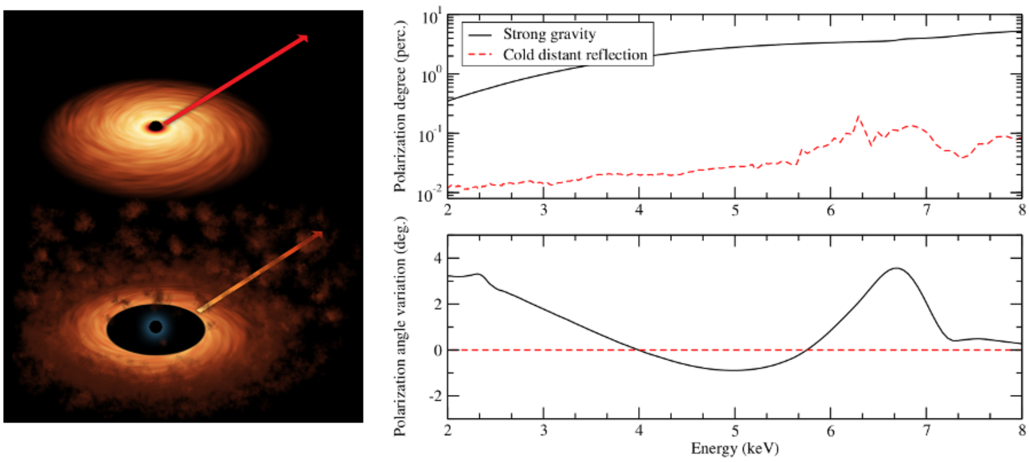

Fig. 2: Two alternative models to explain the observed asymmetrical broadening of the iron Kα line in Seyfert-1 galaxies. The left-hand panel shows that the feature can be produced by special and general relativistic effects close to the potential well (top) or by pure absorption and Compton scattering in a distant cloudy medium (bottom). Credits: NASA/JPL-Caltech. The right-hand panel is the polarization degree and polarization angle variation associated with the two models in the IXPE energy band. Simulations from Marin et al. (2012).

Another application of X-ray polarization measurements from AGN is the determination of the importance of Compton scattering by a distant cloudy medium, using the shape of the relativistically-broadened iron Kα line (Marin et al. 2012). If the broadening of the red wing of the emission line at 6.4 keV is not solely due to strong gravity effects near the black hole horizon, then the spin determined by the reflection method is probably over-estimated (Miller et al. 2008). Down-scattering of photons onto gaseous clumps along the observer's line-of-sight can significantly shift the line centroid, resulting in stronger asymmetries.

We show in Fig. 2 that the two scenarios give very different polarization signatures in the IXPE band. In particular, the polarization degree of the gravity-dominated model is more than ten times stronger than the absorption scenario and, due to the energy-dependent albedo and scattering phase function of the disk material, the relativistic model shows a non-constant polarization position angle with energy. It is quite probable that both mechanisms are happening at the same time and X-ray polarization can definitively determine the dominant process.

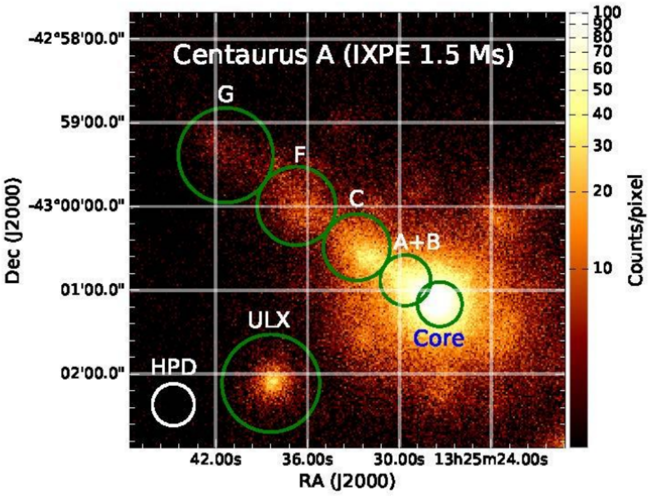

Fig. 3: IXPE-convolved Chandra image of the X-ray brightest extragalactic source Centaurus A (Cen A). The white circle indicates the half-power diameter of IXPE and the green circles (angular resolution) demonstrate the ability of the instrument to perform space-resolved X-ray polarization measurements, testing the structure of the magnetic field along the jet. An ULX, in the field of view of Cen A, can be simultaneously picked up. Credits: IXPE team.

3.3 Magnetic fields strength in jets

Radio-loud AGN, whose spectral energy distribution is dominated by jet-induced synchrotron emission in the radio-band, are also excellent targets for IXPE. For a nearby radio galaxy such as Cen A (4.6 Mpc and the X-ray brightest extragalactic source), the imaging capability of the satellite offers the possibility to perform space-resolved polarization studies, testing the structure of the magnetic field along the jet (Weisskopf et al. 2016).

Fig. 3 shows that it is possible with IXPE to map the magnetic field of resolved X-ray emitting jets close to the injection point of the electrons. Fig. 3 is a convolved Chandra image of Cen A with the IXPE response, together with a plausible model for the magnetic fields. The model consists of a transverse field in hot spots (shocks) along the jet, a longitudinal field between hot spots and, in the core, a polarization of 30% was assumed in order to estimate position-angle errors (McNamara et al. 2009). Interestingly, the imaging capabilities of the instrument allow us to simultaneously pick up ultra-luminous X-ray sources in the field, and one is shown in Fig. 3.

4 Conclusions

IXPE will revolutionize our comprehension of the energetic Universe by opening a new observational window. The measurement of X-ray polarization and/or significantly small upper limits from a large variety of sources will enable us to constrain our numerical models by reducing their degrees of freedom. It is quite probable that many of our current theories will be revised in the light of IXPE observations. In this article, we have shown three different results we expect from observations of AGN. Among others constraints, we expect to obtain precise measurements of the spin of black holes, together with a proper estimate of the impact of Compton down-scattering on the iron Kα line profile. We will also target radio-loud, jet-dominated AGN in order to probe the structure and strength of their kilo-parsec scale magnetic fields.

F.M acknowledges funding through the CNES post-doctoral position grant “Probing the geometry and physics of active galactic nuclei with ultraviolet and X-ray polarized radiative transfer”.

---

*We show the rotation of the polarization position angle with respect to a convenient average of the polarization position angles over the depicted energy band. The actual normalization of the polarization angle with respect to the disk axis is not of primary interest as we cannot determine it from these observations (Marin et al. 2012).

References

Bellazzini, R., Angelini, F., Baldini, L., et al. 2006, Nuclear Instruments and Methods in Physics Research A, 560, 425

Bellazzini, R., Spandre, G., Minuti, M., et al. 2007, Nuclear Instruments and Methods in Physics Research A, 579, 853

Chauvin, M., Florén, H.-G., Friis, M., et al. 2017, ArXiv e-prints

Costa, E., Soffitta, P., Bellazzini, R., et al. 2001, Nature, 411, 662

Davis, Jr., L. & Greenstein, J. L. 1951, ApJ, 114, 206

Dean, A. J., Clark, D. J., Stephen, J. B., et al. 2008, Science, 321, 1183

Dovčiak, M., Muleri, F., Goosmann, R. W., Karas, V., & Matt, G. 2011, ApJ, 731, 75

Hale, G. E. 1908, ApJ, 28, 315

Hiltner, W. A. 1949, Science, 109, 165

Marin, F., Goosmann, R. W., Dovčiak, M., et al. 2012, MNRAS, 426, L101

McClintock, J. E., Narayan, R., & Steiner, J. F. 2014, Space Sci. Rev., 183, 295

McNamara, A. L., Kuncic, Z., & Wu, K. 2009, MNRAS, 395, 1507

Miller, L., Turner, T. J., & Reeves, J. N. 2008, A&A, 483, 437

Novick, R., Weisskopf, M. C., Berthelsdorf, R., Linke, R., & Wolff, R. S. 1972, ApJ, 174, L1

Reynolds, C. S. 2014, Space Sci. Rev., 183, 277

Salet, P. 1910, Annales de l'Observatoire de Paris, 27, C.1

Schnittman, J. D. & Krolik, J. H. 2009, ApJ, 701, 1175

Suarez-Garcia, E., Hajdas, W., Wigger, C., et al. 2006, Sol. Phys., 239, 149

Tindo, I. P., Ivanov, V. D., Mandel'Stam, S. L., & Shuryghin, A. I. 1970, Sol. Phys., 14, 204

Weisskopf, M. C., Ramsey, B., O'Dell, S., et al. 2016, in Proc. SPIE, Vol. 9905, Space Telescopes and Instrumentation 2016: Ultraviolet to Gamma Ray, 990517

Weisskopf, M. C., Silver, E. H., Kestenbaum, H. L., Long, K. S., & Novick, R. 1978, ApJ, 220, L117

Session 03

Plasma of the heliosphere

SF2A 2017
C. Reylé, P. Di Matteo, F. Herpin, É. Lagadec, A. Lançon, Z. Meliani, F. Royer (eds)

STATISTICAL ANALYSIS OF SOLAR EVENTS ASSOCIATED WITH STORM SUDDEN COMMENCEMENTS OVER ONE YEAR OF SOLAR MAXIMUM DURING CYCLE 23: PROPAGATION AND EFFECTS FROM THE SUN TO THE EARTH.

K. Bocchialini[1], B. Grison[2], M. Menvielle[3], A. Chambodut[4], N. Cornilleau-Wehrlin[7 5], D. Fontaine[5], A. Marchaudon[6], M. Pick[7], F. Pitout[6], B. Schmieder[7], S. Régnier[8] and I. Zouganelis[9]

Abstract. From the list of 32 SSCs over the year 2002, we performed a multi-criteria analysis based on propagation time, velocity comparison, sense of the magnetic field rotation, radio waves to associate them with solar sources, identify their causes in the interplanetary medium and then look at the response of the terrestrial ionized and neutral environment to them. The complex interactions between two (or more) CMEs and the modification in their trajectory have been examined using joint white light and multiple-wavelength radio observations. The structures at L_1 after the 32 SSCs are regarded as Magnetic Clouds (MCs), ICMEs without a MC structure, Miscellaneous structures, CIRs/SIRs, and shock-only events. In terms of geoeffectivity, generally CMEs with velocities at the Sun larger than 1000 km.s-1 have larger probabilities to trigger moderate or intense storms. The most geoeffective events are MCs, since 92% of them trigger moderate or intense storms. The geoeffective events trigger an increased and combined AKR and NTC wave activity in the magnetosphere, an enhanced convection in the ionosphere and a stronger response in the thermosphere.

Keywords: Sun: CME, Solar Wind: ICME, Earth: SSC, geoeffectiveness

1 Introduction

We focus on the year 2002, a period of maximum solar activity. We propose a novel, multidisciplinary, and statistical approach to the whole chain of processes from the Sun to the Earth (Sun, L_1, magnetosphere, ionosphere, thermosphere) in order to study the geoeffectiveness of solar events (for a full description see Bocchialini et al. (2017)). In contrast to previous statistical or case studies, the starting point is neither the coronal mass ejections (CMEs) emission at the Sun, nor the value of the min(Dst) index used to evaluate the intensity of the geomagnetic storm, but the storm sudden commencements (SSCs): near-Earth signatures produced by shocks impinging on the magnetosphere and followed by geomagnetic activity. This study then aims first to associate an SSC with a possible source at the Sun (Fig. 1), and then to characterise the propagation of solar events along the entire chain from the Sun to the Earth. It exploits existing catalogs and observations of SSCs, solar activity,

[1] Institut d'Astrophysique Spatiale, Univ. Paris-Sud, CNRS, Université Paris-Saclay, Bâtiment 121, 91405 Orsay CEDEX, France
[2] Institute of Atmospheric Physics CAS, Bocni II, 1401, 141 31 Prague 4, Czech Republic
[3] Université Versailles Saint Quentin, CNRS, Laboratoire Atmosphères, Milieux, Observations Spatiales, Guyancourt, France and Univ. Paris Sud, Département des Sciences de la Terre, 91405 Orsay CEDEX, France
[4] Institut de Physique du Globe de Strasbourg, UMR7516; Université de Strasbourg/EOST, CNRS ; 5 rue René Descartes, 67084 Strasbourg CEDEX, France
[5] LPP, CNRS, Ecole Polytechnique, UPMC Univ. Paris 06, Univ. Paris Sud, Observatoire de Paris, Université Paris-Saclay, Sorbonne Universités, PSL Research University, Ecole Polytechnique, 91128 Palaiseau CEDEX, France
[6] Institut de Recherche en Astrophysique et Planétologie, Université de Toulouse, Toulouse, France and CNRS, UMR 5277, 9 avenue du Colonel Roche, BP 44346, 31028 Toulouse CEDEX 4, France
[7] Observatoire de Paris, LESIA, PSL Research University, 5 place Jules Janssen, 92195 Meudon CEDEX, France
[8] Department of Mathematics, Physics and Electrical Engineering, Northumbria University, Newcastle upon Tyne, NE1 8ST, United Kingdom
[9] European Space Agency, ESAC, Madrid, Spain

solar wind at L_1 (Fig. 2 left), magnetosphere/magnetopause, and the coupled ionosphere/thermosphere system (Fig. 2, right), using available space borne (SOHO, Wind, ACE, Cluster, Geotail, CHAMP) and ground based measurements for radio waves, geomagnetic indices and ionospheric measurements (SuperDARN).

2 Relationships between SSCs and the CMEs at their Origin

Before looking for the solar origin of the observed SSCs, we first associate SSCs to their origin at L_1, starting with the Observatori de l'Ebre/ISGI list of the 32 SSCs detected during 2002. The 32 SSCs are linked to 31 perturbations observed at L_1, two SSCs being associated with the same event. Those 31 events, relying on our observations and on existing catalogs, are identified as: 12 Magnetic Clouds (MCs), 6 Interplanetary Coronal Mass Ejections (ICMEs, non MCs), 5 CIR/SIRs, 4 miscellaneous (Misc.) or not well characterised structures and 4 isolated shocks events. On the other hand, we consider halo and non halo CMEs that have a visible source on the Sun, taken in a temporal window of 5 days before an SSC.

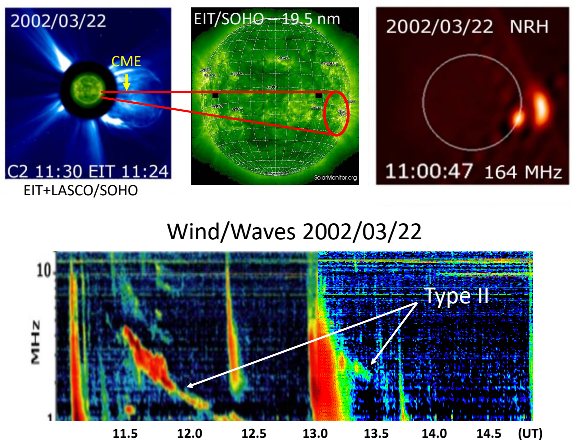

Fig. 1. Exemple of March 22, 2002. Top: Composite of EIT/SOHO image at 19.5 nm inside the LASCO C2 f.o.v showing a CME (left), EIT/SOHO image at 19.5 nm showing the source of the CME (middle), radio signature at 164 MHz measured by the NRH (right). Bottom: Dynamic spectrum from *Wind*/WAVES.

In order to further investigate the SSC/L_1 signatures/CME associations, we consider four criteria:

- propagation considerations based on the ballistic model,
- estimations from the drag-based model (DBM, (Vršnak et al. 2013)),
- radio emissions as signatures of acceleration processes linked to solar sources, and
- the compatibility of the flux rope chirality observed at L_1 with the location of the solar source. This criterion only applies to MCs.

As a first approach we start with the ballistic model and a time window to account for propagation uncertainties. In addition, we also use the drag-based-model (DBM) and calculate the drag coefficient. 85 % of the leading CME show a DBM coefficient $0.11 \times 10^{-7} < \gamma < 2.2 \times 10^{-7}$ km^{-1}, included in the range predicted by Vršnak et al. (2013) between 0.1×10^{-7} and 100×10^{-7} km^{-1}. Both mean and median values are not far from the commonly used value in the model of 0.2×10^{-7}km^{-1}, which validates the resulting association between most L_1 events and their solar source.

As a result, we can associate 28 SSCs to 44 CMES, out of an original list of 60 CMEs. The 3 SSCs with no solar source identified are due to events followed by SIR/CIRs at L_1.

The statistical analysis of the 44 CMEs, including 21 halo CMEs possibly responsible for the 28 SSCs leads to the following results:

- We confirm that the solar sources of these 44 CMEs are active regions (AR), mainly located in the central part of the disk, with filament in 60 % of the cases. The presence of a filament indicates that the magnetic

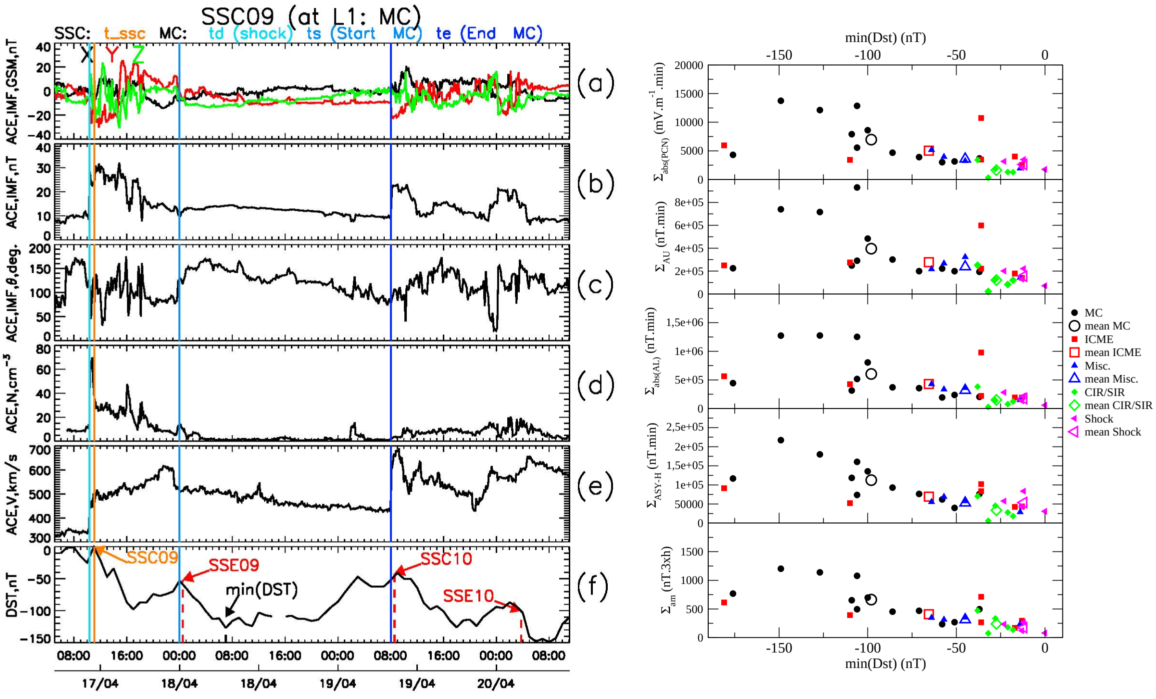

Fig. 2. Left: Observation at L_1 (ACE data) of an example of an MC together with ground-based observations of the Dst-index, on 17 April 2002. The IMF is described in the three top panels by its three components in the GSM coordinate system (a), the IMF intensity (b), and the IMF inclination with respect to the Z-axis (c). The solar-wind properties are described in the next two panels by its density (d) and velocity (e). The simultaneously observed variations of the Dst-index are displayed on the bottom panel along with the indication by dashed lines of the other SSC observed during the time window, the SSE events (see text) and the min(Dst) associated with the SSC09 event. Right: Minimum of Dst as a function of integrals of different indices over event duration (from top to bottom: PCN, AU, AL, ASY-H, am), for all events.

field of the region is strongly sheared which is a good indicator of destabilisation and eruption. CMEs are associated with small, medium, large X-ray flares with no preferences.

- In 54 % of the cases (15/28 SSCs), a single CME is related to one SSC and in 46 % of the cases, 2 CMEs at least are related to one SSC. Twenty-one are halo CMEs *i.e.* 75 % of the 28 halo CMEs –with a visible source on the Sun referenced in 2002– induce an SSC in the Earth environment, most of the time the faster the more geoeffective. According to the CDAW list, more than 500 front-side non-halo CMEs were recorded in 2002 (1.5 per day on average). Half of them are front-side and only 23 (5%) could be associated with an SSC.

- Radio observations allowed us to classify the events at the Sun in three categories, the largest group gathers events displaying Type IV radio emissions. The presence of the Type IV burst component that we call B (a long-duration radio continuum detected in a frequency range typically from decimetric to decametric wavelengths), which is physically linked with the development of the CME current sheet, is statistically the most important factor for SSC prediction. Taking only this B-components (observed by ground base instruments, and forming the first radio group) would have led in the present study to predicting 85 % of the SSC-led events with a minimum value of Dst less than -30 nT. A second group assembles the four events related to shocks only at L_1. *Wind*/WAVES observed only four Type IV radio emissions in 2002; those correspond to CME–SSC associations that are related to an MC. Globally, 25/31 events are associated with a Type II event, which is indicative of electrons accelerated by a shock.

Our analysis also underlines the importance of joint white-light and multi-wavelength-radio observations, in particular of the radio imagery, for revealing and explaining the complex interactions between different CMEs or between a CME and the ambient medium.

Most shocks observed in 2002 at L_1, either isolated or part of other events, cause an SSC. This is the case for 80 % of the 35 IP shocks listed by Gopalswamy et al. (2010). Conversely, only 5 out of 41 CIRs/SIRs reported by Jian et al. (2006) in 2002 were associated with SSCs, and for 3 of them there are no CME candidates.

For 28 SSC-led events observed at L_1, a plausible solar source is identified. Concerning MCs and ICMEs, different catalogs and studies exist. We identified a common core of 11 MCs and of 10 non-MCs ICMEs listed by respectively 3 (2) or more studies. All 11 MCs (100 %) and 6 ICMEs (60 %) caused SSCs. There is no obvious correlation between the solar source properties and the L_1 categories.

Finally, we emphasise that 14 of the 28 associations mentioned above fulfil all the relevant criteria for the considered category (*i.e.* 4 criteria for the MCs, 3 for the other categories). In particular, the criterion based on the ballistic velocity is not satisfied in 7 cases. These mismatching cases result not only from the complexity of the ICME velocity evolution during its propagation (interaction with the ambiant solar wind and/or with other ICME) but also from the lack of direct observation of the radial velocity along the Earth–Sun direction.

3 Propagation between the Sun and L_1

The propagation in the ambient medium from the Sun to L_1 is an important source of uncertainties due to the acceleration/deceleration of CMEs.

We calculate the propagation delay from the Sun to L_1 using different simple propagation models (Huttunen et al. 2005; Schwenn et al. 2005; Vršnak et al. 2013) for shock propagation (25 events) and for the ICME and MC propagation (18 events). We compare the results with our observations. There are roughly as many negative as positive delays. Half of them are longer than ± 14 hours, which is considered as the uncertainty of the models. These statistics are not improved by restricting the event base to halo CMEs or to isolated CMEs.

The results demonstrate the need for a reliable propagation tool to properly relate an ICME observed at L_1 and a CME detected within the five days preceding their arrival at L_1.

4 Geoeffectiveness

The geoeffectiveness is first discussed as a function of the minimum in Dst-values, generally used as an indicator of the storm strength (intense, -200 nT $<$ min(Dst) ≤ -100 nT; moderate, -100 nT $<$ min(Dst) ≤ -50 nT). The analysis of the SSC-related events in 2002 shows that:

- If the CME velocity $V_\odot$ is larger than 1000 km s^{-1} there is a greater probability to trigger moderate or intense storm. No particular rule is found with the nature of the CME source (halo or not, single or multiple, flare class), but the most geoeffective events are associated with Type IV radio bursts.
- The most efficient storm drivers are MCs, followed by ICMEs: 11 out of the 12 (92 %) MCs cause storms (7 intense and 4 moderate). The 2 other intense storms that follow an SSC were caused by ICMEs.
- The 3 most geoeffective MCs induce a sudden secondary event (SSE) with a magnetic signature similar to an SSC.
- Among the 6 moderate storms that follow an SSC, 4 are due to MCs and 2 to the so-called miscellaneous events. Our statistics differ from those of Echer et al. (2013) who reported that the interplanetary structure (CIRs and pure high-speed stream) are responsible for 30 % of these storms, ICMEs being the second major cause. Our study shows that when the storm is preceded by an SSC, the main driver of moderate storms remains globally ICMEs (including MCs, non-MCs, and Misc.).
- The presence of a southward IMF component and its duration are generally considered as favorable conditions for geomagnetic activity. In order to account for it, we computed a normalised and time-integrated parameter ($B^*_{z<0}$) and we found that this is a good indicator of the potential geoeffectiveness of a solar-wind structure.
- For geoeffective ICMEs (11 MCs and 2 non-MCs) triggering intense and moderate storms, we separate the effects of their sheath and central core. These statistics are limited but globally, the central core is responsible for the minimum values of the Dst. We note that for events related to intense storms, the sheath plays an important role in about half events and that this role becomes dominant for three (33 %) events since it results in the most negative min(Dst). The sheaths causing intense storms show limited

variations and low values of the β parameter ($0.4 < \beta < 0.75$ and of the Alfven Mach number $3.6 < M_A < 6.5$).

For each of the 31 SSC-led events, we considered different indices for which we computed the time integral of their absolute value, from the shock arrival time until the time of the final recovery of Dst. The results are plotted with respect to min(Dst) in Figure 2 (right) *i.e* polar cap (PCN), auroral zone (AU, AL), low-latitude (ASY-H), and sub-auroral latitude (am). The integrated indices follow some kind of slope increasing with decreasing values of the min(Dst) and reach a kind of plateau for min(Dst) < -100 nT.

The analysis of the perturbations at L_1 and their associated geomagnetic response enabled us to estimate the power that the solar wind provided to the Earth's magnetosphere by means of two coupling functions: we find that their correlation with the different magnetic indices remains relatively weak. The function proposed by Newell et al. (2007), $[\frac{\mathrm{d}\Phi_{MP}}{\mathrm{d}t}]$, might better account for the effect of the magnetic field within the discontinuity that hits the Earth's environment. The Akasofu parameter (Perreault & Akasofu 1978), $[\epsilon_3]$, correlates with mid-latitude and global indices better than does $\frac{\mathrm{d}\Phi_{MP}}{\mathrm{d}t}$, whereas the later correlates best with auroral indices.

Finally, the response of the magnetosphere – ionosphere – thermosphere system is expectedly enhanced with the geomagnetic activity level. Among them, we emphasise the following issues:

- A combined NTC and AKR wave activity develops in the magnetosphere during ICMEs (MCs, non-MCs and Misc.), suggesting the presence of acceleration processes over a large sector of the plasma sheet. Conversely, this effect appears more local for most CIRs/SIRs or Shock-only with the enhancement of only one of these emissions.

- All events associated with strong and moderate storms induce a thermospheric storm, mostly identified by a significant enhancement of the night time neutral density. This occurs during most ICMEs. Conversely, CIRs/SIRs and Shock-only have almost no impact on the thermosphere.

5 Concluding remarks

The most striking results of our combined analysis of the full chain between Sun and Earth ionised and neutral environment concern well-observed MCs in 2002, all of them being associated with SSCs; 11/12 MCs are associated with radio emission of Type IV and induce intense or moderate storms; the CMEs at their origin being not necessarily a halo CME, nor a unique CME source. The effects of the 9 intense magnetic storms of our study (7 MCs and 2 ICMEs) are seen both in the ionosphere and in the thermosphere.

The statistical results point out the difficulty of identifying the relevant parameters measured at the Sun to be able to forecast the arrival time of a CME at the Earth, and to estimate its probability of impacting the Earth, despite the use of a multi criteria analysis combining velocities, radio wave analysis and - when appropriate - chirality. The development of a reliable propagation tool is required to find the link between ICMEs observed at L_1 and the (halo) CMEs detected within the five days preceding their arrival at L_1.

The authors thank the PNST. All PIs of space and ground based experiments/observatory are thanked for the use of their data, as well as all data centres. The authors express their warmest thanks to C. Lathuillère and N. Vilmer for their important collaboration at the beginning of this work.

References

Bocchialini, K., Grison, B., Menvielle, M., et al. 2017, Sol. Phys, to be published

Echer, E., Tsurutani, B. T., & Gonzalez, W. D. 2013, J. Geophys. Res.(Space Physics), 118, 385

Gopalswamy, N., Xie, H., Mäkelä, P., et al. 2010, ApJ, 710, 1111

Huttunen, K. E. J., Schwenn, R., Bothmer, V., & Koskinen, H. E. J. 2005, Annales Geophys., 23, 625

Jian, L., Russell, C. T., Luhmann, J. G., & Skoug, R. M. 2006, Sol. Phys., 239, 393

Newell, P. T., Sotirelis, T., Liou, K., Meng, C.-I., & Rich, F. J. 2007, J. Geophys. Res.(Space Physics), 112, 1206

Perreault, W. K. & Akasofu, S.-I. 1978, Geophys. J. R. Astron. Soc., 54

Schwenn, R., dal Lago, A., Huttunen, E., & Gonzalez, W. D. 2005, Annales Geophys., 23, 1033

Vršnak, B., Žic, T., Vrbanec, D., et al. 2013, Sol. Phys., 285, 295

Session 04

Chemical and dynamical modelling of Milky Way type galaxies

SF2A 2017
C. Reylé, P. Di Matteo, F. Herpin, É. Lagadec, A. Lançon, Z. Meliani, F. Royer (eds)

DOES THE EXISTENCE OF A PLANE OF SATELLITES CONSTRAIN PROPERTIES OF THE MILKY WAY?

M. S. Pawlowski[1]

Abstract. According to the hierarchical model of galaxy formation underlying our current understanding of cosmology, the Milky Way (MW) has continued to accrete smaller-sized dwarf galaxies since its formation. Remnants of this process surround the MW as debris streams and satellite galaxies, and provide information that is complementary to studies of the Galaxy itself. The satellite system thus has the potential to teach us about the formation and evolution of the MW. Can the existence of a narrow, co-rotating plane of satellite galaxies (the Vast Polar Structure, VPOS) put constraints on our Galaxy's properties? Are such satellite galaxy planes more narrow around less massive hosts, more abundant around more concentrated hosts, more kinematically coherent around more early-forming halos? To address such questions, we have looked for correlations between properties of satellite galaxy planes fitted to cosmological simulations in the ELVIS suite and properties of their host dark matter halos, while accounting for realistic observational biases such as the obscuration by the disk of the MW. We find no evidence for strong correlations that would allow conclusions on the host halo properties from the mere existence of the VPOS around our Galaxy.

Keywords: galaxies: dwarf, Galaxy: halo, galaxies: kinematics and dynamics, dark matter, Local Group

1 Introduction

Both major galaxies in the Local Group host planes of satellite galaxies. The Vast Polar Structure (VPOS) of the Milky Way (MW) has a root-mean-square (rms) height of ≈ 20 kpc and extends perpendicular to the disk of the MW until at least its virial radius. Globular clusters and streams of disrupted systems show a preference for a similar orientation (Pawlowski et al. 2012). Proper motion measurements indicate that a majority of the 11 classical satellite galaxies co-orbit along the VPOS (Pawlowski & Kroupa 2013). Among the satellites of the Andromeda galaxy M31, about 50% have been identified to be part of a narrow Great Plane of Andromeda (GPoA, Ibata et al. 2013). This structure has a rms height of only ≈ 14 kpc. Its fortuitous edge-on orientation with respect to the Sun allows to identify a coherent line-of-sight velocity trend: 13 of 15 satellites are consistent with a rotating satellite plane (though tangential motions are unknown and could be high enough to quickly disperse the structure, Gillet et al. 2015; Buck et al. 2016). Furthermore, there is increasing evidence for similar correlations in more distant satellite systems (Chiboucas et al. 2013; Ibata et al. 2014a; Tully et al. 2015; Müller et al. 2016, Mueller et al. in prep).

Comparisons of satellite galaxy planes with sub-halo systems in cosmological simulations based on the ΛCDM model show that similarly anisotropic and kinematically correlated arrangements are very rare (Ibata et al. 2014b; Pawlowski et al. 2014; Pawlowski & McGaugh 2014). While most of these simulations are dark-matter-only, the existence of pronounced planes of satellite galaxies poses a fundamental problem for which even the inclusion of baryonic physics does not offer an obvious solution (Pawlowski et al. 2015; Ahmed et al. 2017; Pawlowski et al. 2017).

However, it is in principle imaginable that only a subset of halos with specific properties can host pronounced satellite planes. If this were the case, the observation of the VPOS could constrain properties the MW. Buck et al. (2015) have claimed to have found evidence that the existence of narrow, kinematically coherent satellite planes comparable to that of M31 is linked to properties of the host halo. In their analysis of 21 simulated satellite systems they see a correlation between the concentration parameter of the host halo and satellite

[1] Hubble Fellow, Department of Physics and Astronomy, University of California, Irvine, CA 92697, USA

planes, in the sense that more concentrated halos contain more narrow planes of satellites. They argue that halo concentration acts as a proxy for formation time: later-forming halos are less concentrated and thus do not contain as pronounced satellite planes.

Their analysis was confined to analogs of the M31 system, and did not take observational biases and uncertainties into account (such as the PAndAS survey footprint within which most known M31 satellites were discovered). Instead, they only selected satellites from within the virial volume. Since their argument was based on the M31 satellite plane, which consists of only a sub-sample of all M31 satellites, it is unclear whether such a signal persists for analogs of the MW system. To investigate this, we have analyzed the ELVIS simulations and compared them to the VPOS, more specifically to the positional and kinematic correlations found among the 11 classical MW satellite galaxies. This analysis is based on Pawlowski & McGaugh (2014), but now investigates whether the planes fitted to the sub-halo satellite systems in those simulations show any correlations with properties if the host halo. A more detailed comparison to the GPoA will be presented in a future publication.

2 Satellite plane fits in ELVIS: are there correlations with host halo properties?

Pawlowski & McGaugh (2014) focussed on testing for an environmental dependency of the occurrence and properties of planes of satellite galaxies. They found no pronounced differences between hosts that are isolated and hosts that are in a paired configuration similar to the MW-M31 system. The study used the Exploring the Local Volume in Simulations (ELVIS) suite of cosmological, dark-matter only simulations by Garrison-Kimmel et al. (2014). All 48 host halos in ELVIS are used, and the 11 top-ranked satellites (by peak mass) are selected as the equivalent of the 11 brightest, "classical" satellite galaxies of the MW (which are also the only ones for which proper motion measurements provide information on their orbital coherence). The effects of uneven sky coverage due to obscuration by the disk of the MW is modeled by drawing 100 realizations with randomly oriented MW disks that obscure 20 % of the sky. More details on the satellite selection and plane fitting can be found in Pawlowski & McGaugh (2014).

Using this dataset, we investigate the possibility of a dependence between properties of the host halos and properties of planes fitted to the satellite distribution. Specifically, we consider three measures of satellite plane coherence, averaged over the 100 realizations per host: (1) r_{per}, the rms height of satellites relative to the best-fit plane (an absolute measure of the flattening), (2) c/a, the rms short-to-long axis ratio of the satellite distribution (a relative measure of the flattening), and (3) Δ_{std}, the spherical standard deviation of the eight closest-clustering satellite orbital poles (a measure of the orbital coherence).

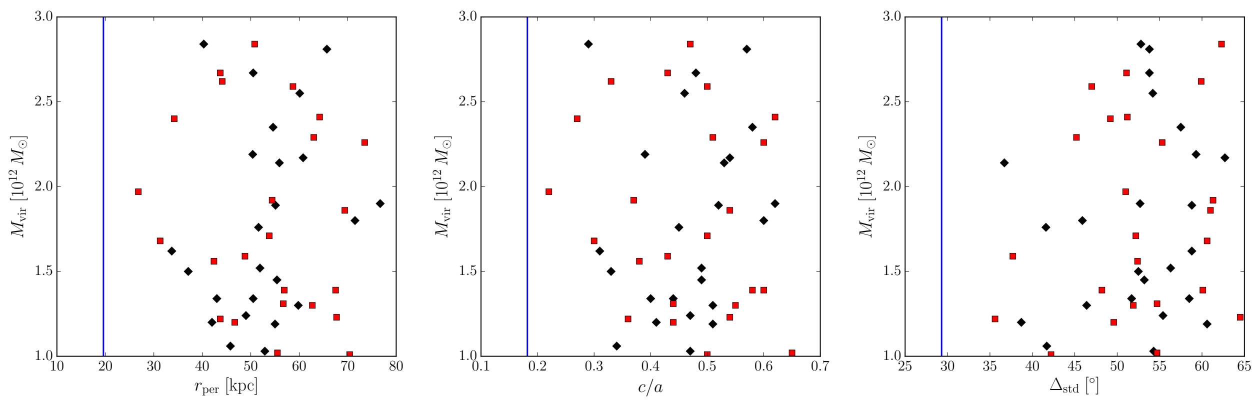

Fig. 1. Host halo virial mass M_{vir} plotted against rms height r_{per} (**left**), the short-to-long axis ratio c/a (**middle**), and the spherical standard deviation of the eight best-aligned sub-halo orbital poles (**right**) of the 11 top-ranked sub-halos. Shown are the average values for the sub-halos systems corresponding to the 48 host halos in the ELVIS suite of cosmological simulations. Isolated host halos are plotted as red squares, host halos in a paired configuration similar to that of the Local Group are plotted as black diamonds. The corresponding value for the observed system of the 11 classical MW satellite galaxies are indicated as blue lines.

Figures 1 to 4 plot these three measures against four properties of the host halos: (1) M_{vir}, the virial mass, (2) R_{vir}, the virial radius, (3) c_{-2}, the halo concentration (equivalent to an NFW halo concentration), and (4)

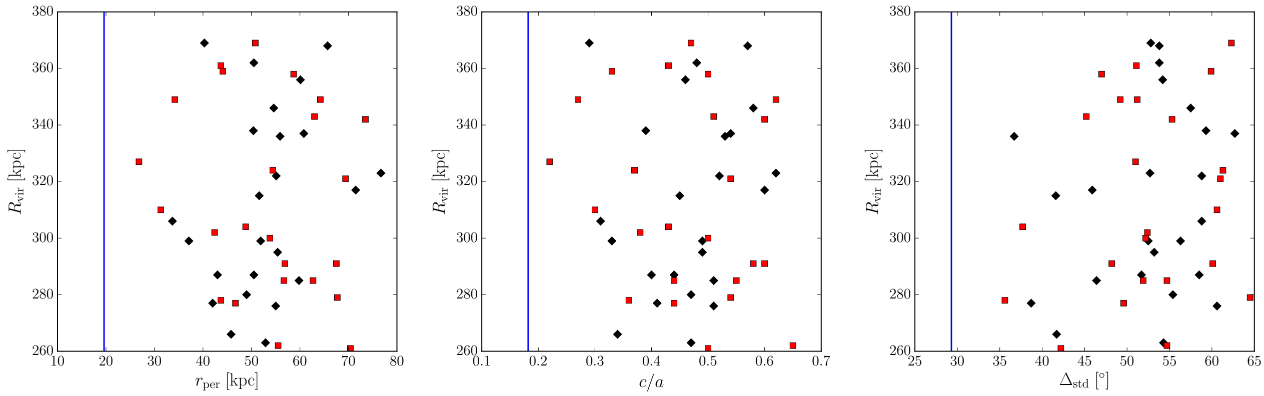

Fig. 2. Same as Figure 1, but for the host halo virial radius $R_{\rm vir}$.

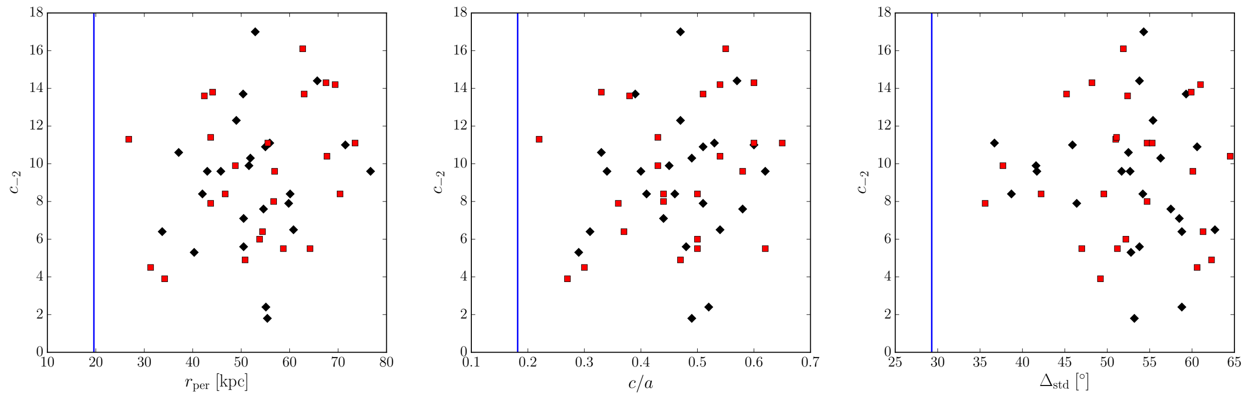

Fig. 3. Same as Figure 1, but for the host halo concentration parameter c_{-2}.

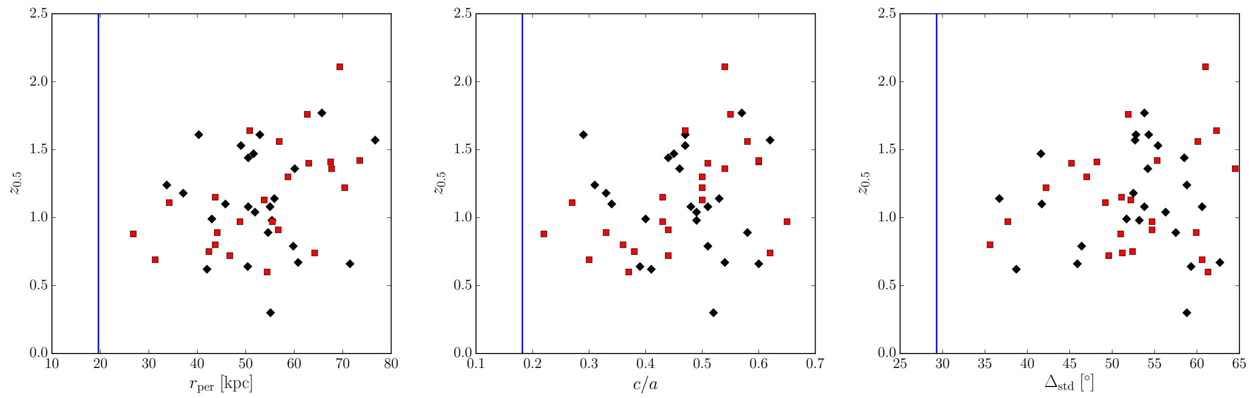

Fig. 4. Same as Figure 1, but for the host halo formation redshift $z_{0.5}$.

$z_{0.5}$, the formation redshift, defined as that redshift z where the progenitor halo first reached half of the final host halo mass.

As in Pawlowski & McGaugh (2014), each symbol in the figures represents one of the ELVIS host halos and is coded for whether it is isolated (red square) or part of a pair (black diamonds). Inspecting the figures shows that none of the 48 host halos typically contain satellite planes with properties as extreme as those observed for the 11 classical satellites (blue lines). Simulated satellite systems are wider, less flattened, and less kinematically coherent than the observed VPOS. The plots also show no difference in the plane coherence parameters between the isolated and the paired host halos, in line with the conclusion of Pawlowski & McGaugh (2014).

Most importantly, the plots demonstrate that there are no clear correlations between properties of the host halo and properties of planes fitted to their satellite system. The only possible weak trend is with the halo formation redshift $z_{0.5}$: the most narrow ($30 \leq r_{\rm per} \leq 45\,{\rm kpc}$), most flattened ($0.2 \leq c/a \leq 0.4$), and most kinematically correlated ($35^\circ \leq \Delta_{\rm std} \leq 50^\circ$) planes tend to be preferentially found for later forming halos with $0.6 \leq z_{0.5} \leq 1.3$. Other host halos with similar $z_{0.5}$ do not contain as correlated satellite planes, but the earlier forming hosts in ELVIS appear to avoid these regions of plane coherence parameters.

3 Discussion and Conclusion

Intriguingly, the tendency to find slightly more correlated satellite systems around later forming hosts is the *opposite* of the trend reported by Buck et al. (2015). It is also in tension with the formation history of the MW, which is believed to not have experienced a major merger since $z \approx 2$. As such, and in combination with the difficulty of even finding any simulated satellite systems that resemble the strong coherence found for the VPOS, it appears unlikely that the weak tendency of more correlated satellite systems living in later-forming hosts can provide a reliable constraint on the halo properties of the MW, or even solve the satellite plane problem.

However, structures of satellite galaxies can offer other constraints on their host galaxy properties. If satellite planes are found to be stable, this would require close-to spherical halo and thus constrains halo triaxiallity (Fernando et al. 2017). One proposed explanation for satellite planes is the accretion of many satellites in a common group. Identifying satellite galaxies that were accreted as one group can then constrain the MW potential since they must share similar specific angular momenta and energies. Furthermore, more exotic proposed explanations for the occurrence of apparently co-orbiting planes of satellite galaxies have implications for the history of the host galaxies. For example, if satellite galaxy planes are formed out of Tidal Dwarf Galaxies (Bournaud & Duc 2006; Kroupa 2012), this would imply a past galaxy encounter involving the host (or happening in the vicinity; Hammer et al. 2013).

Support for this work was provided by NASA through Hubble Fellowship grant #HST-HF2-51379.001-A awarded by the Space Telescope Science Institute, which is operated by the Association of Universities for Research in Astronomy, Inc., for NASA, under contract NAS5-26555

References

Ahmed, S. H., Brooks, A. M., & Christensen, C. R. 2017, MNRAS, 466, 3119
Bournaud, F. & Duc, P.-A. 2006, A&A, 456, 481
Buck, T., Dutton, A. A., & Macciò, A. V. 2016, MNRAS, 460, 4348
Buck, T., Macciò, A. V., & Dutton, A. A. 2015, ApJ, 809, 49
Chiboucas, K., Jacobs, B. A., Tully, R. B., & Karachentsev, I. D. 2013, AJ, 146, 126
Fernando, N., Arias, V., Guglielmo, M., et al. 2017, MNRAS, 465, 641
Garrison-Kimmel, S., Boylan-Kolchin, M., Bullock, J. S., & Lee, K. 2014, MNRAS, 438, 2578
Gillet, N., Ocvirk, P., Aubert, D., et al. 2015, ApJ, 800, 34
Hammer, F., Yang, Y., Fouquet, S., et al. 2013, MNRAS, 431, 3543
Ibata, N. G., Ibata, R. A., Famaey, B., & Lewis, G. F. 2014a, Nature, 511, 563
Ibata, R. A., Ibata, N. G., Lewis, G. F., et al. 2014b, ApJ, 784, L6
Ibata, R. A., Lewis, G. F., Conn, A. R., et al. 2013, Nature, 493, 62
Kroupa, P. 2012, PASA, 29, 395
Müller, O., Jerjen, H., Pawlowski, M. S., & Binggeli, B. 2016, A&A, 595, A119
Pawlowski, M. S., Dabringhausen, J., Famaey, B., et al. 2017, ArXiv e-prints
Pawlowski, M. S., Famaey, B., Jerjen, H., et al. 2014, MNRAS, 442, 2362
Pawlowski, M. S., Famaey, B., Merritt, D., & Kroupa, P. 2015, ApJ, 815, 19
Pawlowski, M. S. & Kroupa, P. 2013, MNRAS, 435, 2116
Pawlowski, M. S. & McGaugh, S. S. 2014, ApJ, 789, L24
Pawlowski, M. S., Pflamm-Altenburg, J., & Kroupa, P. 2012, MNRAS, 423, 1109
Tully, R. B., Libeskind, N. I., Karachentsev, I. D., et al. 2015, ApJ, 802, L25

SF2A 2017
C. Reylé, P. Di Matteo, F. Herpin, É. Lagadec, A. Lançon, Z. Meliani, F. Royer (eds)

NEW INSIGHTS ON THE ORIGIN OF THE HIGH VELOCITY PEAKS IN THE GALACTIC BULGE

J. G. Fernández-Trincado[1], A. C. Robin[2], E. Moreno[3], A. Pérez-Villegas[4] and B. Pichardo[3]

Abstract. We provide new insight on the origin of the cold high-$V_{\rm los}$ peaks ($\sim$200 kms^{-1}) in the Milky Way bulge discovered in the APOGEE commissioning data (Nidever et al. 2012). Here we show that such kinematic behaviour present in the field regions towards the Galactic bulge is not likely associated with orbits that build the boxy/peanut (B/P) bulge. To this purpose, a new set of test particle simulations of a kinematically cold stellar disk evolved in a 3D steady-state barred Milky Way galactic potential, has been analysed in detail. Especially bar particles trapped into the bar are identified through the orbital Jacobi energy E_J, which allows us to identify the building blocks of the B/P feature and investigate their kinematic properties. Finally, we present preliminary results showing that the high-$V_{\rm los}$ features observed towards the Milky Way bulge are a natural consequence of a large-scale *midplane* particle structure, which is unlikely associated with the Galactic bar.

Keywords: The Galaxy, bulge, disk, kinematics and dynamics, galaxies structure, numerical methods

1 Introduction

The discovery by Nidever et al. (2012) of cold high-velocity peaks ($\sim$ 200 km s^{-1}) in the Apache Point Observatory Galactic Evolution Experiment (APOGEE) commissioning data across the Galactic bulge l = {4, 14} and b = {-2, 2} and confirmed by the High-Order Kinematic Moments by Zasowski et al. (2016), suggests that there may be a significant non-axisymmetric structure that dominates the bulge regions (e.g., Robin et al. 2012; Wegg & Gerhard 2013), which has turned the study and characterization of a B/P bulge (e.g. Portail et al. 2015; Simion et al. 2017, among others) into a very active research field. Most of the models that attempt to explain the high-velocity peaks observed toward the Milky Way bulge suggest that these features are most likely bulge stars on bar orbits, i.e., orbits in a 2:1 and/or higher order resonant family (see e.g., Aumer & Schönrich 2015; Molloy et al. 2015). Recently, alternative scenarios have been proposed that do not invoke any family of bar resonant orbits linked with the building blocks of the B/P feature. Additionally, it has been suggested that the high-velocity peaks may be the product of a kiloparsec-scale nuclear stellar disk in the Galactic bulge (Debattista et al. 2015). Also, the recent study by Li et al. (2014) suggests that these kinematics features might be an artifact due to small number statistics. With these issues in mind, we expect this preliminary contribution will help improve the current understanding on the origin of the cold high-velocity peaks. In this work, we qualitatively analyzed a set of numerical simulations of a synthetic Milky Way Galaxy made up of the superposition of many composite stellar populations already described and analyzed in Fernández-Trincado (2017a). Using numerical simulations from Fernández-Trincado (2017a), we began a pilot project aimed to provide an alternative scenario for the origin of high-$V_{\rm los}$ feature in the bulge to look for possible orbital energy imprints of the cold high-$V_{\rm los}$.

[1] Departamento de Astronomía, Casilla 160-C, Universidad de Concepción, Concepción, Chile
email: jfernandezt@astro-udec.cl and/or jfernandezt87@gmail.com

[2] Institut Utinam, CNRS UMR 6213, Université Bourgogne-Franche-Comté, OSU THETA Franche-Comté, Observatoire de Besançon, BP 1615, 25010 Besançon Cedex, France

[3] Instituto de Astronomía, Universidad Nacional Autónoma de México, Apdo. Postal 70264, México D.F., 04510, México

[4] Max-Planck-Institut für Extraterrestrische Physik, Gießenbachstraße, 85748 Garching, Germany

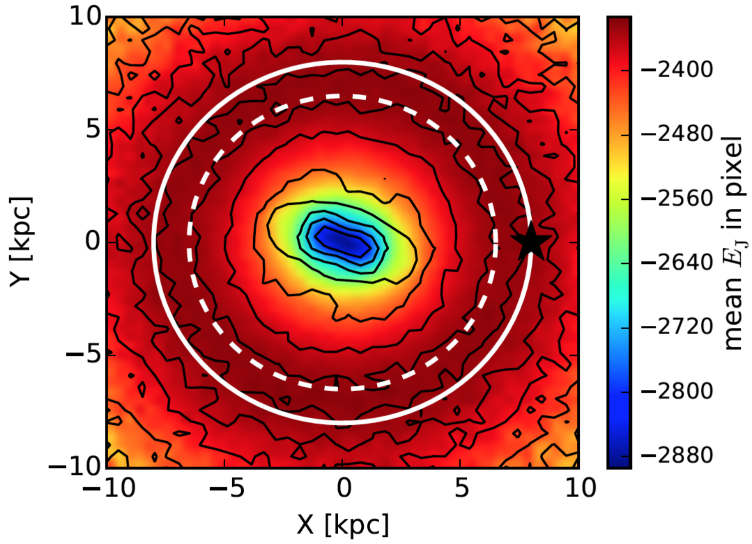

Fig. 1. Face-on view of the simulated cold stellar thin disk in the *inertial* reference frame where the bar is at an angle of 20 degrees from the Sun-GC line of sight. Colors indicate $\langle E_J \rangle$ in units of 100 km^2 s^{-2}. The white dashed circle indicates the corotation radius (6.5 kpc), which is in good agreement with results from the literature to explain the Hercules group Pérez-Villegas et al. (2017); the white circle marks the solar radius (8 kpc) and the present-day solar position is given by the black star symbol. The black contours refer to the surface density distribution for the entire sample of 1×10^6 particles in t=15 Gyr.

2 The Galactic Model

We use the galactic dynamic software *GravPot16** in order to carry out a comprehensive orbital study of particles in the inner region of the Milky Way. For a more detailed discussion about *GravPot16*, we refer the readers to a forthcoming paper (Fernández-Trincado et al. in preparation). Here we summarize the backbone of *GravPot16*. Using the new version of the Besançon Galaxy Model, in good agreement with many observations, we computed a semi-analytical steady-state 3D gravitational potential of the Milky Way, observationally and dynamically constrained. The model is primarily made up of the superposition of several composite stellar components, where the density profiles in cylindrical coordinates, ρ_i(R, Z), are the same as those proposed in Robin et al. (2003, 2012, 2014), i.e., a B/P bulge, a Hernquist stellar halo, seven stellar Einasto thin disks with spherical symmetry in the inner regions, two stellar sech^2 thick disks, a gaseous exponential disk, and a spherical structure associated with the dark matter halo. A new formulation for the global potential, Φ(R, Z), of this Milky Way density model, $\Sigma\rho_i$(R, Z), will be described in detail elsewhere (Fernández-Trincado, et al. in preparation). Φ(R, Z) has been rescaled to the Sun's galactocentric distance. The Sun is located at $R_\odot = 8.0$ kpc, and the local rotation velocity is assumed to be $\Theta_0(\mathrm{R}_\odot) = 244.5$ km s^{-1} (Sofue 2015). Here, we briefly describe the bar's structural parameters, such as recommended by Fernández-Trincado (2017a) from dynamical constraints using the BRAVA data set (Kunder et al. 2012): we assume a total mass for the bar of 1.1×10^{10} M$_\odot$, an angle of 20 degrees for the present-day orientation of the major axis of the bar and an angular velocity, $\Omega_{bar} = 35$ km s^{-1} kpc^{-1}, consistent with the recent estimate of Portail et al. (2015), and a cut-off radius $R_c = 3.28$ kpc (e.g., Robin et al. 2012). Additionally, it should be noted that the non-axisymmetric configuration of our dynamic model has been extensively employed to predict stellar orbits (Fernández-Trincado et al. 2016, 2017), and/or orbital parameters for a large set of APOGEE-TGAS sources (Abolfathi et al. 2017; Tang et al. 2017). For a more detailed discussion, we refer the readers to Anders et al. (2017, and article in preparation).

*https://fernandez-trincado.github.io/GravPot16/

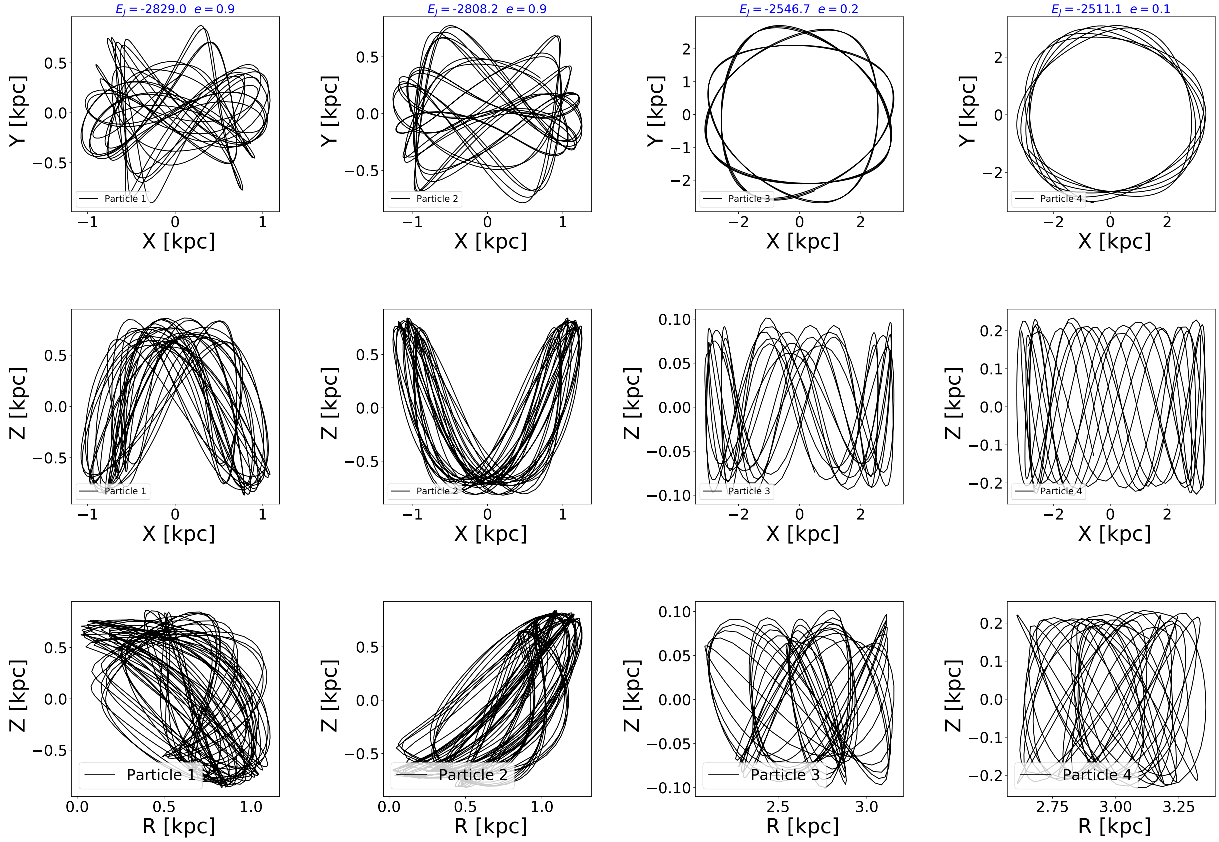

Fig. 2. Orbits viewed face-on (top), side-on (middle) and meridional (bottom) in the *non-inertial* reference frame where the bar is at rest. Column 1 and column 2 show the typical orbital configuration found for bar-trapped particles ($E_J < E_J^{boundary}$), while the column 3 and 4 show the orbital configuration for particles not trapped by the bar ($E_J > E_J^{boundary}$). The top blue label indicates the orbital eccentricity and its respective Jacobi energy (E_J).

3 Test particle simulations

First, we run controled particle simulations to mimic one of the cold stellar thin disks described in the Besançon population synthesis model (disk in the age range 7 to 10 Gyr; see e.g., Robin et al. 2003). To this purpose we use the *GravPot16* code in its axisymmetric and non-axisymmetric configuration. We adopt a strategy similar to the one described in Romero-Gómez et al. (2015) and Martinez-Medina et al. (2016). The test particles are initially involved in a steady axisymmetric potential model over long integration time (in this work we adopt an integration time of 10 Gyr) to ensure that the initial disk particle distribution reaches a state of relaxation within the background potential. Then, the boxy bar structure grows adiabatically into the simulations during a period of time of 2 Gyr. Once the bar potential is introduced into the system, we increase the integration time during a period of time long enough (> 3 Gyr) to avoid transient effects. The initial conditions for the particle velocities are assigned using the Besançon population synthesis model disc kinematics fitted to RAVE and TGAS data (Robin et al. 2017). It is important to note that our initial conditions are based on locally self-consistent recipes, but it is not guaranteed to be fully self-consistent globally, and will thus be slightly relaxed before turning on the non-axisymmetric potential (Fernández-Trincado 2017a).

Secondly, after 15 Gyr integration time in the above potential we record the Jacobi energy per unit mass, E_J[†], in the bar frame for all particles in a box of ± 3.5 kpc $\times$ 2.5 kpc $\times$ 2 kpc, which is thought to have high chance to contain orbits trapped into the bar structure as illustrated in Fig. 1 and Fig. 2 (first and second column). With the Jacobi energy distribution in the box, we determine the boundary between bar-trapped

[†]The Jacobi energy is then given by $E_J = \frac{1}{2}\vec{v}^2 + \Phi_{axi}(R,Z) + \Phi_{bar}(R,Z) - \frac{1}{2}|\vec{\Omega}_{bar} \times \vec{R}|^2$, where $\Phi_{axi}(R,Z)$ and $\Phi_{bar}(R,Z)$ are the *GravPot16* axisymmetric and non-axisymmetric potential components, respectively.

particles ($E_J < E_J^{boundary}$) and not-bar-trapped particles ($E_J > E_J^{boundary}$) by identifying the trough in the Jacobi energy distribution ($E_J^{boundary} \sim$ -2.7×10^5 km^2 s^{-2}). The results are briefly described in §4.

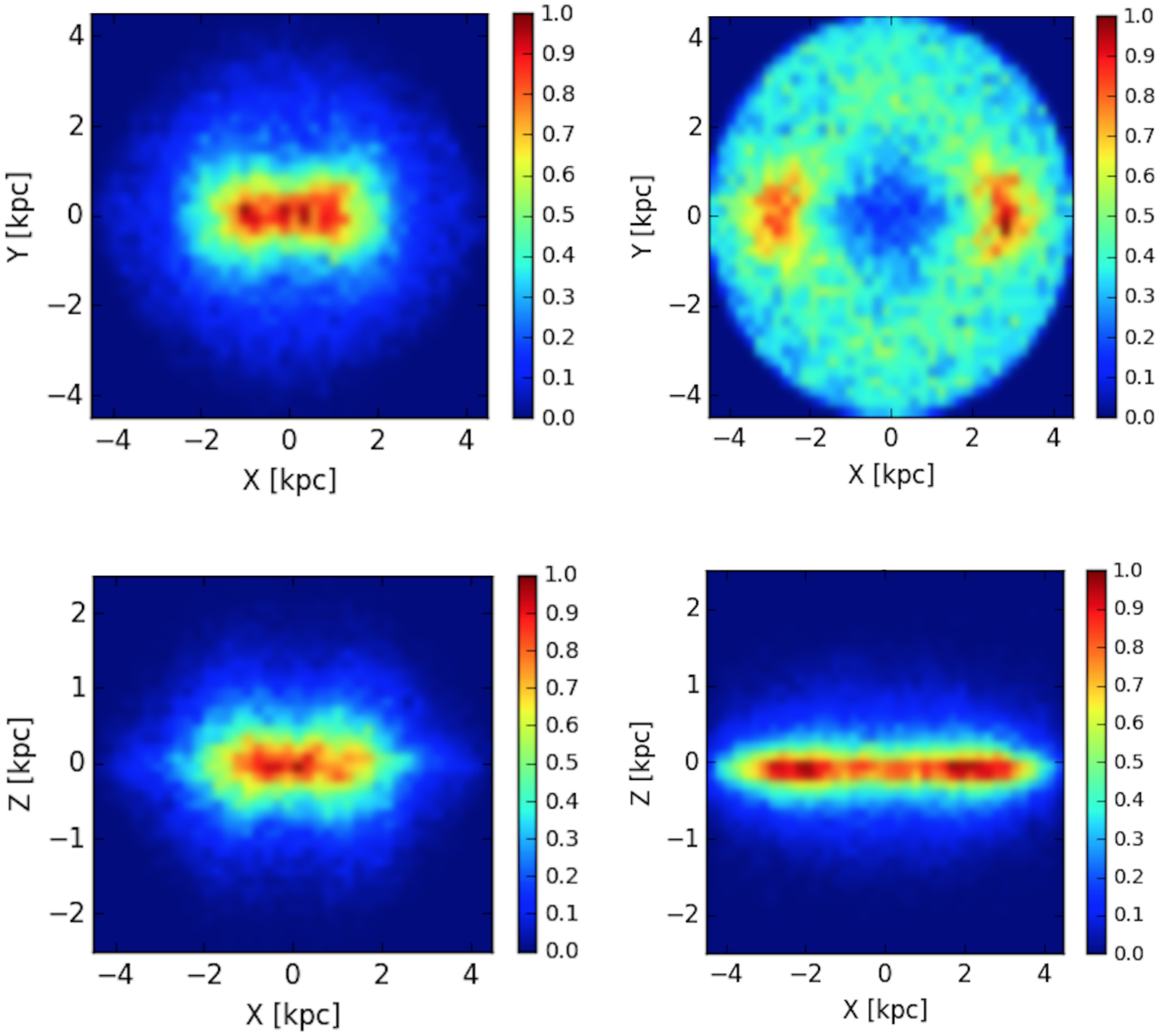

Fig. 3. Kernel Density Estimate (KDE) smoothed distributions of bar-trapped particles (left column) and not-bar-trapped particles (right column) of the simulated cold stellar thin disk in the *non-inertial* reference frame where the bar is at rest. Density distribution for the entire sample viewed face-on (first row) and side-on (second row).

4 Results and Concluding Remarks

Figure 3 plots the Kernel Density Estimate (KDE) smoothed distributions for the bar-trapped particles (first column). In particular we note that the B/P feature is carried largely by particles having a Jacobi energy $E_J < E_J^{boundary}$. In our numerical simulations, all the building blocks of the B/P bulge structure are composite of different orbits existing at energies smaller than the boundary energy, $E_J < E_J^{boundary}$, in particular diverse resonant orbits (i.e., family of tube orbits; x_1v_1: banana orbits, etc) which generate a strong peanut shape at shorter radii on the side-on projection (column 1, row 2 in the figure). This Galactic B/P structure accounts for ∼34% of the particles of the bulge (within ∼ 5 kpc; e.g., Fernández-Trincado 2017a). Figure 3 also plots the KDE smoothed distributions for the particles not trapped by the bar (second column), which do not show the B/P shape. The not-bar-trapped particles ($E_J > E_J^{boundary}$) in this model are mostly on low eccentricity orbits, which dominate the mid-plane (see column 2 and 3 in Figure 2) and account for ∼66% of the particles of the bulge.

4.1 An alternative explanation for the kinematics feature at high V_{los}

It is important to note that here we provide the kinematic predictions for orbits existing at energies smaller or greater than the boundary energy. Detailed azimuthal projections were already analyzed in Fernández-Trincado (2017a) confirming the presence of the cold high-$\mathrm{V_{los}}$ peaks extending to Galactic longitude $l \sim 10°$, which are absent a few kiloparsecs off the mid-plane, indicating that orbits with Jacobi energy (a mid-plane hosting more particles at $E_J > E_J^{boundary}$) responsible for the feature do not extend this far off-plane, as also shown in the second column of Figure 3. Figure 4 plots the predicted line-of-sight velocity distributions (LOSVDs –here called $\mathrm{V_{los}}$) in the Galacto-centric restframe. At $E_J < E_J^{boundary}$ the $\mathrm{V_{los}}$ distribution has a single peak dominated by bar-trapped-particles, hosting more particles at $V_{los} < 150$ km s^{-1}. There are also few particles that have high $\mathrm{V_{los}}$ (~ 200 km s^{-1}) and are likely associated with the high-velocity tail of the resonant bar-supporting 2:1 orbits (see Molloy et al. 2015). At $E_J > E_J^{boundary}$ the $\mathrm{V_{los}}$ have developed two peaks, with particles moving at significantly larger velocities (~ 200 km s^{-1}) in the mid-plane, dominated by not-bar-trapped particles, but remain well below the circular velocity of the galaxy. These two high velocity peaks are more prominent than the low-$\mathrm{V_{los}}$ peak developed by bar-trapped particles.

4.2 Conclusion

We have made an attempt to explain the presence of the cold high velocity peaks in the bulge. It is important to note, that we account for the composite nature of the bulge in our simulations. The dependence of $\mathrm{V_{los}}$ with l and b has not been shown in the present work, but was extensively studied by Fernández-Trincado (2017a). The right panel of Figure 4 shows color-coded maps of the average V_{los}, $\langle V_{los} \rangle$, for the entire sample of our simulated cold stellar thin disk in Galactic coordinates. In a similar manner as in Debattista et al. (2015) our numerical approach is capable of producing the peak velocities at orbit tangent points with the characteristic *winged* pattern of the velocity fields.

Lastly, we conclude that the most natural interpretation of the high velocity features towards the Galactic bulge is that they are likely not dominated by orbits at $E_J < E_J^{boundary}$ that build the B/P bulge, but may be a consequence of families of orbits at $E_J > E_J^{boundary}$ and low orbital eccentricities in the mid-plane that do not support the bar structure. Our Milky Way potential model fine-tuned to observations is able to explain the velocity distributions in most APOGEE fields in the bulge, without invoking the presence of any nuclear disk in the inner ~ 1 kpc as pointed out in Debattista et al. (2015). The advantage of our numerical approach is that the test particles have evolved in a realistic Milky Way potential inheriting the information on both density and kinematics, and the particles are in statistical equilibrium with the potential imposed (e.g., Romero-Gómez et al. 2015; Martinez-Medina et al. 2016; Fernández-Trincado 2017a). It should be noticed that we find very similar V_{los} distributions to those in APOGEE, without any adjustment parameters, but without applying the observation selection function. Hence we shall verify this point in the near future.

The high precision of the *Gaia* mission will provide the 6D phase space needed to confirm our orbital interpretations and to compute the orbital Jacobi energy beyond ~ 5 kpc from the Sun.

We thank Merce Romero Gómez, Françoise Combes and Benoît Famaey for comments on an earlier version of this paper. J.G.F-T gratefully acknowledges partial financial support from the SF2A in order to attend the SF2A-2017 meeting held in Paris in July 2017, and the Chilean BASAL Centro de Excelencia en Astrofísica y Tecnologías Afines (CATA) grant PFB- 06/2007. We also acknowledge the support of the UTINAM Institute of the Université de Franche-Comté, Région de Franche-Comté and Institut des Sciences de l'Univers (INSU) for providing HPC resources on the Cluster Supercomputer Mésocentre de calcul de Franche-Comté. E.M, A.P.V and B.P acknowledge support from UNAM/PAPIIT grant IN105916 and IN114114.

Funding for the *GravPot16* software has been provided by the Centre national d'études spatiale (CNES) through grant 0101973 and UTINAM Institute of the Université de Franche-Comte, supported by the Region de Franche-Comte and Institut des Sciences de l'Univers (INSU). The *GravPot16* Web site is at https://fernandez-trincado.github.io/GravPot16/.

References

Abolfathi, B., Aguado, D. S., Aguilar, G., et al. 2017, ArXiv e-prints

Anders, F., Queiroz, A. B., Chiappini, C., et al. 2017a, in preparation

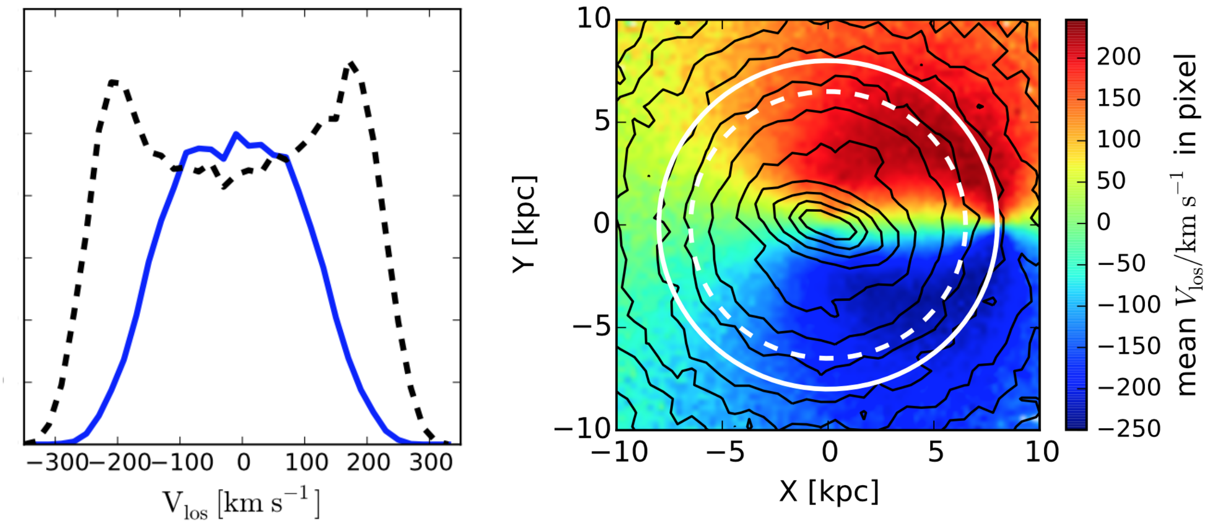

Fig. 4. *Left*: V_{los} histograms normalised to unit peak showing a dual-peak structure for the not-bar-trapped particles (black dashed line) and a unimodal distribution for the bar-trapped particles (blue line), using 20 km.s^{-1} binning. *Right*: Kinematics map of the simulated cold stellar thin disk in Galactic coordinates for the entire sample of 1×10^6 particles. The white circles and black contour levels are identical to those in Figure 1. Colors indicate $\langle V_{los} \rangle$.

Anders, F., Queiroz, A. B., Chiappini, C., et al. 2017b, in IAU Symposium, Vol. 334, Rediscovering our Galaxy, ed. C. Chiappini, I. Minchev, E. Starkenburg, & M. Valentini

Aumer, M. & Schönrich, R. 2015, MNRAS, 454, 3166

Debattista, V. P., Ness, M., Earp, S. W. F., & Cole, D. R. 2015, ApJ, 812, L16

Fernández-Trincado, J. G., Zamora, O., Garcia-Hernandez, D. A., et al. 2017b, ArXiv e-print 1707.03108

Fernández-Trincado, J. G. 2017a, Université Bourgogne Franche-Comté Phd Thesis, 1, 174

Fernández-Trincado, J. G., Robin, A. C., Moreno, E., et al. 2016, ApJ, 833, 132

Kunder, A., Koch, A., Rich, R. M., et al. 2012, AJ, 143, 57

Li, Z.-Y., Shen, J., Rich, R. M., Kunder, A., & Mao, S. 2014, ApJ, 785, L17

Martinez-Medina, L. A., Pichardo, B., Moreno, E., Peimbert, A., & Velazquez, H. 2016, ApJ, 817, L3

Molloy, M., Smith, M. C., Evans, N. W., & Shen, J. 2015, ApJ, 812, 146

Nidever, D. L., Zasowski, G., Majewski, S. R., et al. 2012, ApJ, 755, L25

Pérez-Villegas, A., Portail, M., Wegg, C., & Gerhard, O. 2017, ApJ, 840, L2

Pichardo, B., Martos, M., & Moreno, E. 2004, ApJ, 609, 144

Portail, M., Wegg, C., Gerhard, O., & Martinez-Valpuesta, I. 2015, MNRAS, 448, 713

Robin, A. C., Bienaymé, O., Fernández-Trincado, J. G., & Reylé, C. 2017, ArXiv e-print 1704.06274

Robin, A. C., Marshall, D. J., Schultheis, M., & Reylé, C. 2012, A&A, 538, A106

Robin, A. C., Reylé, C., Derrière, S., & Picaud, S. 2003, A&A, 409, 523

Robin, A. C., Reylé, C., Fliri, J., et al. 2014, A&A, 569, A13

Romero-Gómez, M., Figueras, F., Antoja, T., Abedi, H., & Aguilar, L. 2015, MNRAS, 447, 218

Simion, I. T., Belokurov, V., Irwin, M., et al. 2017, ArXiv e-print 1707.06660

Sofue, Y. 2015, PASJ, 67, 75

Tang, B., Fernández-Trincado, J. G., Geisler, D., et al. 2017, submitted, 1, 1

Wegg, C. & Gerhard, O. 2013, MNRAS, 435, 1874

Zasowski, G., Ness, M. K., García Pérez, A. E., et al. 2016, ApJ, 832, 132

ABUNDANCE ANOMALIES IN RED GIANTS WITH POSSIBLE EXTRAGALACTIC ORIGINS UNVEILED BY APOGEE-2

J. G. Fernández-Trincado[1, 2], D. Geisler[1], E. Moreno[3], O. Zamora[4, 5], A. C. Robin[2] and S. Villanova[1]

Abstract. By performing an orbital analysis within a Galactic model including a bar, we found that it is plausible that the newly discovered stars that show enhanced Al and N accompanied by Mg underabundances may have formed in the outer halo, or were brought in by satellites field possibly accreted a long time ago. However, another subsample of three N- and Al-rich stars with Mg-deficiency are kinematically consistent with the inner stellar halo. A speculative scenario to explain the origin of the atypical chemical composition of these stars in the inner halo is that they migrated to the inner stellar halo as unbound stars due to the mechanism of bar-induced resonant trapping.

Keywords: abundances, Population II, globular clusters, structure, formation, bulge, disk, kinematics and dynamics, numerical methods

1 Introduction

The classical picture of abundance anomalies as unique signatures of globular cluster environments have been challenged by the recent discoveries of field stars with globular cluster like abundance patterns, which become part of the general stellar population of the Milky Way. To date, only a handful of these chemically anomalous stars (Ramírez et al. 2012; Majewski et al. 2012; Lind et al. 2015; Fernández-Trincado et al. 2016a; Schiavon et al. 2017b; Recio-Blanco et al. 2017) exhibiting interesting variations in their light-element abundance patterns (e.g., C, N, O, Al, Mg, Si, and other) strikingly similar to those observed in the so-called *second-generation* globular cluster stars (see Mészáros et al. 2015; Tang et al. 2017; Schiavon et al. 2017a; Pancino et al. 2017, for instance) have been found in the Milky Way. Often, these stars have been hypothesised to be stellar tidal debris of surviving/defunct Galactic globular clusters (e.g., Fernández Trincado et al. 2013; Kunder et al. 2014; Fernández-Trincado et al. 2015a,b, 2016b; Anguiano et al. 2016). Following this line of investigation, Fernández-Trincado et al. (2017b) have recently discovered a new *SG-like* stellar population across all main components (bulge, disk, and halo) of the Milky Way, with atypically low Mg abundances; i.e., similar to those seen in the *second-generation* of Galactic globular cluster stars at similar metallicities. Based on the complex chemistry of these stars and their orbital properties, the authors speculate that probably most of these atypical stars may have an extragalactic origin. For example, they could be former members of dissolved extragalactic globular clusters (e.g., Mucciarelli et al. 2012) and/or the result of exotic binary systems, or perhaps former members of a dwarf galaxy (with intrinsically lower Mg) polluted by a massive AGB star.

In this work we examined the combination of proper motions from UCAC-5 (Zacharias et al. 2017), radial velocity (APOGEE-2/DR14, Abolfathi et al. 2017) and spectro-photometric distances (e.g., Anders et al. 2017) from the APOGEE survey, to determine the orbits of the enigmatic giant stars in a realistic Galactic potential.

[1] Departamento de Astronomía, Casilla 160-C, Universidad de Concepción, Concepción, Chile, email: `jfernandezt@astro-udec.cl and/or jfernandezt87@gmail.com`

[2] Institut Utinam, CNRS UMR 6213, Université Bourgogne-Franche-Comté, OSU THETA Franche-Comté, Observatoire de Besançon, BP 1615, 25010 Besançon Cedex, France, email: `jfernandez@obs-besancon.fr`

[3] Instituto de Astronomía, Universidad Nacional Autónoma de México, Apdo. Postal 70264, México D.F., 04510, México

[4] Instituto de Astrofísica de Canarias, Vía Láctea S/N, E-38205 La Laguna, Tenerife, Spain

[5] Departamento de Astrofísica, Universidad de La Laguna (ULL), E-38206 La Laguna, Tenerife, Spain

2 The Orbits

On the basis of the absolute proper motions from UCAC-5, radial velocity and distance from the APOGEE survey, we performed a numerical integration of the orbits for five of the N-, Al-rich and Mg-poor stars studied by Fernández-Trincado et al. (2017b) in a barred Milky Way model. We employ the galactic dynamic software *GravPot16** in order to carry out a comprehensive stellar orbital study. For the computations in this work, we have adopted a three dimensional potential; made up of the superposition of composite stellar populations belonging to the thin and thick disks, the interstellar medium (ISM), the stellar halo, the dark matter halo, and a rotating bar component, that fits the structural and dynamical parameters of the Milky Way (see also Fernández-Trincado et al. 2017a). For reference, the 3-dimensional solar velocity and velocity of the local standard of rest adopted by this work is: $[U_{\odot}, V_{\odot}, W_{\odot}] = [10., 11., 7.]$ km s^{-1}, $\mathrm{V_{LSR}} = 238$ km s^{-1} and the Sun is located at $R_{\odot} = 8.3$ kpc (e.g., Bland-Hawthorn & Gerhard 2016). For our computations, the bar pattern speed, $\Omega_{bar} = 45$ km s^{-1} kpc^{-1}, the total mass for the bar= 1.1×10^{10} M$_{\odot}$, and $\phi_{bar} = 20°$ for the present-day orientation of the major axis of the Galactic bar are assumed.

For each star, we time-integrated backwards half million orbits for 5 Gyr under variations of the proper motions, radial velocity and distance according to their estimated errors, assumed to follow a Gaussian distribution. The input parameters are listed in Table 1. It is important to note that the uncertainties in the orbital predictions are primarily driven by the uncertainty in the proper motions and distances with a negligible contribution from the uncertainty in the radial velocity.

Figure 1 shows the probability densities of the resulting orbits projected on the equatorial and meridional Galactic planes in the non-inertial reference frame where the bar is at rest. The red and yellow colors correspond to more probable regions of the space, which are crossed more frequently by the simulated orbits. We found that most of our stars are situated in the inner and outer halo region, which means these stars are on highly elliptical orbits (with eccentricities greater than 0.5) reaching out to a maximum distance from the Galactic plane larger than 10 kpc (outer halo) and $\sim$ 3 kpc (inner halo). The larger distances reached by 2M17535944+4708092 and 2M12155306+1431114 as well as their atypical chemical properties (see Fernández-Trincado et al. 2017b) suggest that these stars could have originated outside the Milky Way, brought in by satellites possibly accreted a long time ago, while the stars, 2M16062302-1126161, 2M17534571-2949362 and 2M17180311-2750124 could have migrated to the inner halo due to a mechanism known as *bar-induced* resonant trapping as introduced by (Moreno et al. 2015) and became part of the general stellar population of the inner stellar halo.

Table 1. Initial conditions of the stars analysed in this work.

APOGEE star	α [degrees]	δ [degrees]	distance [kpc]	$\mu_{\alpha} \times \cos(\delta)$ [mas yr^{-1}]	μ_{δ} [mas yr^{-1}]	radial velocity [km s^{-1}]
2M17535944+4708092	268.498	47.136	15.35±1.7	-4.1±2.2	-1.1±2.2	-266.02±0.02
2M12155306+1431114	183.971	14.519	14.27±1.54	0.3±3.1	-2.6±3.1	100.08±0.01
2M16062302-1126161	241.596	-11.438	3.58±0.32	-6.1±1.0	-8.5±1.0	-105.90±0.01
2M17534571-2949362	268.440	-29.827	3.38±0.75	-6.3±2.5	-8.4±2.5	-140.68±0.02
2M17180311-2750124	259.513	-27.837	4.75±1.18	-10.0±2.2	-9.0±2.2	-113.71±0.03

3 Concluding Remarks

Orbital modelling shows that two of our chemically anomalous stars (2M17535944+4708092, 2M12155306+1431114) have a large motion out of the plane of the Milky Way, with $Z_{max} > 10$ kpc. The eccentricity of the orbit and this relatively large out-of-plane motion suggest either an extra-galactic origin, or star formation at large Galactic distances. While three stars in our sample (2M16062302-1126161, 2M17534571-2949362, 2M17180311-2750124) are kinematically consistent with the inner stellar halo which is thought to have higher eccentricities, we argue that this subsample may come from stars born in the outer halo and kinematically heated into the inner Galactic halo due to perturbations by resonances with the Galactic bar (e.g., Moreno et al. 2015). The orbital projections presented here confirm the assumptions of our previous work (Fernández-Trincado et al.

*https://gravpot.utinam.cnrs.fr

2017b) that most of these atypical stars belong to the outer halo, possibly brought in by extragalactic stellar systems.

Lastly, the future *Gaia* data releases should improve the precision to which the star's orbit can be calculated by providing accurate and precise proper motions and parallax.

J.G.F-T and D.G. gratefully acknowledges partial financial support from the SF2A in order to attend the SF2A-2017 meeting held in Paris in July 2017, and the Chilean BASAL Centro de Excelencia en Astrofísica y Tecnologías Afines (CATA) grant PFB-06/2007. E.M acknowledge support from UNAM/PAPIIT grant IN105916. O.Z. acknowledge support provided by the Spanish Ministry of Economy and Competitiveness (MINECO) under grant AYA-2014-58082-P. We also acknowledge the support of the UTINAM Institute of the Université de Franche-Comté, Région de Franche-Comté and Institut des Sciences de l'Univers (INSU) for providing HPC resources on the Cluster Supercomputer Mésocentre de calcul de Franche-Comté.

Funding for the *GravPot16* software has been provided by the Centre national d'études spatiale (CNES) through grant 0101973 and UTINAM Institute of the Université de Franche-Comte, supported by the Region de Franche-Comte and Institut des Sciences de l'Univers (INSU).

References

Abolfathi, B., Aguado, D. S., Aguilar, G., et al. 2017, ArXiv e-prints

Anders, F., Queiroz, A. B., Chiappini, C., et al. 2017, ArXiv e-prints

Anguiano, B., De Silva, G. M., Freeman, K., et al. 2016, MNRAS, 457, 2078

Bland-Hawthorn, J. & Gerhard, O. 2016, ARA&A, 54, 529

Fernández-Trincado, J. G., Robin, A. C., Moreno, E., Pérez-Villegas, A., & Pichardo, B. 2017a, ArXiv e-prints

Fernández-Trincado, J. G., Robin, A. C., Moreno, E., et al. 2016a, ApJ, 833, 132

Fernández-Trincado, J. G., Robin, A. C., Reylé, C., et al. 2016b, MNRAS, 461, 1404

Fernández-Trincado, J. G., Robin, A. C., Vieira, K., et al. 2015a, A&A, 583, A76

Fernández Trincado, J. G., Vivas, A. K., Mateu, C. E., & Zinn, R. 2013, Mem. Soc. Astron. Italiana, 84, 265

Fernández-Trincado, J. G., Vivas, A. K., Mateu, C. E., et al. 2015b, A&A, 574, A15

Fernández-Trincado, J. G., Zamora, O., García-Hernández, D. A., et al. 2017b, ApJ, 846, L2

Kunder, A., Bono, G., Piffl, T., et al. 2014, A&A, 572, A30

Lind, K., Koposov, S. E., Battistini, C., et al. 2015, A&A, 575, L12

Majewski, S. R., Nidever, D. L., Smith, V. V., et al. 2012, ApJ, 747, L37

Mészáros, S., Martell, S. L., Shetrone, M., et al. 2015, AJ, 149, 153

Moreno, E., Pichardo, B., & Schuster, W. J. 2015, MNRAS, 451, 705

Mucciarelli, A., Bellazzini, M., Ibata, R., et al. 2012, MNRAS, 426, 2889

Pancino, E., Romano, D., Tang, B., et al. 2017, A&A, 601, A112

Ramírez, I., Meléndez, J., & Chanamé, J. 2012, ApJ, 757, 164

Recio-Blanco, A., Rojas-Arriagada, A., de Laverny, P., et al. 2017, A&A, 602, L14

Schiavon, R. P., Johnson, J. A., Frinchaboy, P. M., et al. 2017a, MNRAS, 466, 1010

Schiavon, R. P., Zamora, O., Carrera, R., et al. 2017b, MNRAS, 465, 501

Tang, B., Cohen, R. E., Geisler, D., et al. 2017, MNRAS, 465, 19

Zacharias, N., Finch, C., & Frouard, J. 2017, AJ, 153, 166

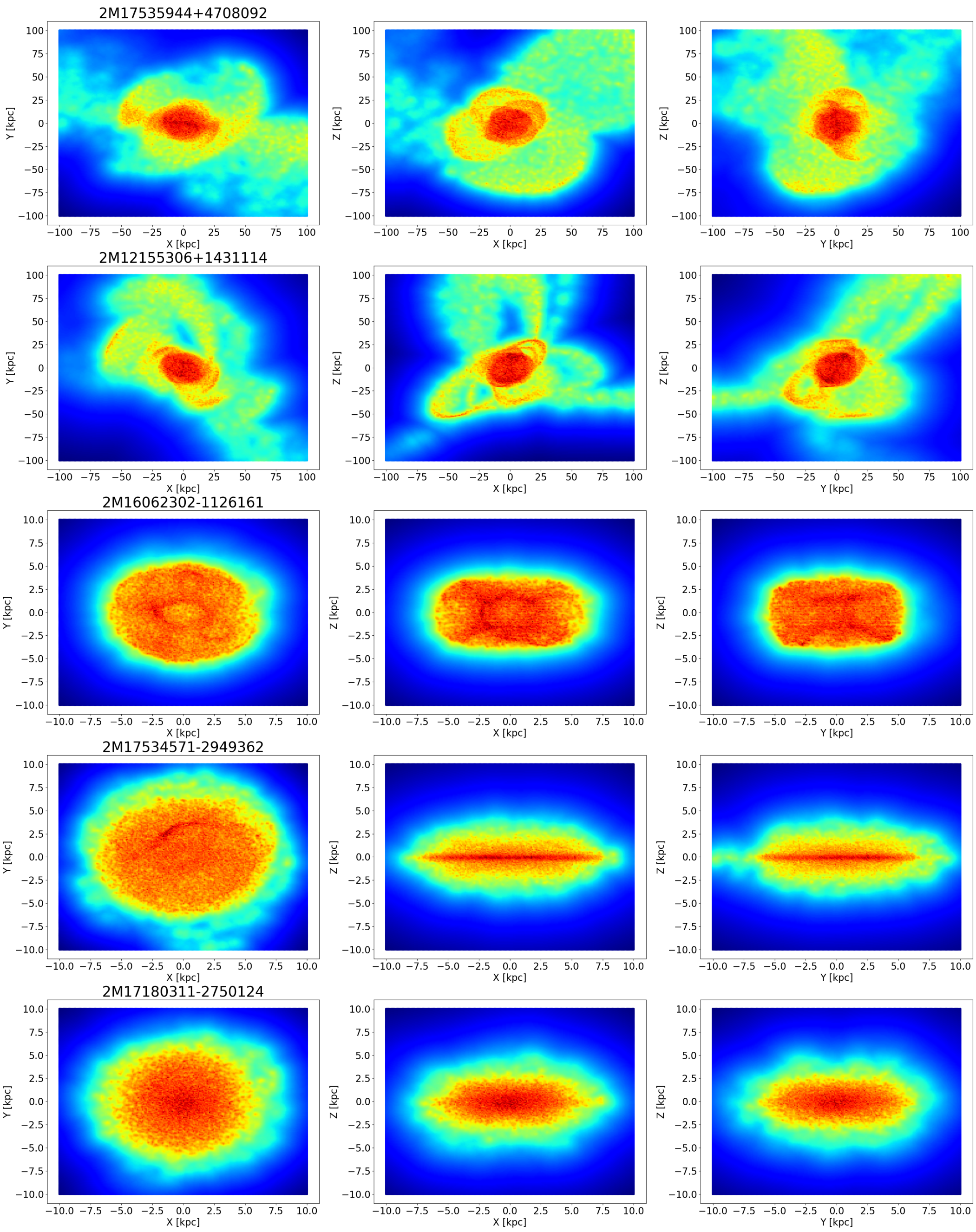

Fig. 1. Probability density in the equatorial Galactic plane (column 1) and side-on (column 2 and 3) of a half million simulated orbits of five chemically anomalous giant stars time-integrated backwards for 5 Gyr. Red and yellow colors correspond to larger probabilities.

SF2A 2017
C. Reylé, P. Di Matteo, F. Herpin, É. Lagadec, A. Lançon, Z. Meliani, F. Royer (eds)

GAIA DR1 COMPLETENESS WITHIN 250 PC AND STAR FORMATION HISTORY OF THE SOLAR NEIGHBOURHOOD

E. J. Bernard[1]

Abstract. Taking advantage of the *Gaia* DR1, we combined TGAS parallaxes with the *Tycho-2* and APASS photometry to calculate the star formation history (SFH) of the solar neighbourhood within 250 pc using the colour-magnitude diagram fitting technique. Our dynamically-evolved SFH is in excellent agreement with that calculated from the *Hipparcos* catalogue within 80 pc of the Sun, showing an enhanced star formation rate (SFR) in the past ∼4 Gyr. We then correct the SFR for the disc thickening with age to obtain a SFR that is representative of the whole solar cylinder, and show that even with an extreme correction our results are not consistent with an exponentially decreasing SFR as found by recent studies. Finally, we discuss how this technique can be applied out to ∼5 kpc thanks to the next *Gaia* data releases, which will allow us to quantify the SFH of the thin disc, thick disc and halo *in situ*.

Keywords: Hertzsprung-Russell diagram, Galaxy: disk, Galaxy: evolution, Galaxy: formation, solar neighbourhood

1 Introduction

Disc galaxies dominate the stellar mass density in the Universe, yet the details of their formation and evolution are still poorly understood. Even in the Milky Way for which we have access to a tremendous amount of information, the onset of star formation and the evolution of the star formation rate (SFR) of each Galactic component are still a matter of debate. However, the details of the formation of stellar systems are encoded in the distribution of the stars in deep colour-magnitude diagrams (CMDs). Their star formation history (SFH), that is, the evolution of both the SFR and the metallicity from the earliest epoch to the present time, can therefore be recovered using the robust CMD-fitting technique which has been extensively validated in studies of nearby Local Group galaxies. This technique requires the precise knowledge of the intrinsic luminosity of each star, and therefore its distance. In the coming years, *Gaia* will deliver distances and proper motions for over a billion stars out to ∼10 kpc, thus covering all the structural components of our Galaxy. For the first time, this opens the possibility of mapping the spatial and temporal variations of the SFH back to the earliest epochs. We illustrate this potential by exploiting the *Gaia* DR1/TGAS parallaxes for stars in the solar neighbourhood (Gaia Collaboration et al. 2016; Lindegren et al. 2016), and calculating the SFH of the Milky Way disc within 250 pc of the Sun. The main advantages of the CMD-fitting technique over other methods of recovering the SFH (e.g. chemical enrichment models, colour-function fitting, age/metallicity census of individual stars, ...) are the fact that determining the age of a population is much more robust than that of single stars, that one takes full advantage of the predictions of stellar evolution models, and the smaller number of assumptions. On the other hand, like other methods it is affected by the systematic effects due to uncertainties in the stellar models, as well as the poorly constrained amplitude of radial migrations in the disc.

2 The solar neighbourhood CMD: photometry and completeness

While TGAS provides accurate parallaxes and G-band magnitudes for over 2 million stars, no colour information is available. On the other hand, the *Tycho-2* catalogue does include B_T, V_T for all TGAS stars, but the photometric quality quickly degrades at fainter magnitudes. We thus cross-matched TGAS with the *Tycho-2*, *Hipparcos*, and APASS DR9 (Henden et al. 2012) catalogues, after transforming their photometry to the

[1] Université Côte dAzur, OCA, CNRS, Lagrange, France – email: ebernard@oca.eu

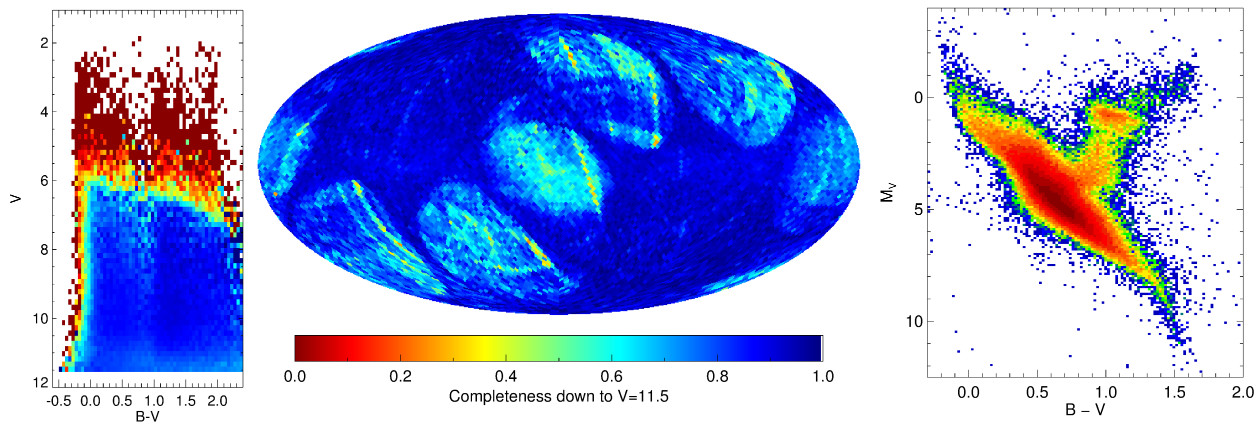

Fig. 1. Left & middle: TGAS completeness down to V=11.5 relative to *Tycho-2* in colour-magnitude space and in galactic coordinates, before the completeness corrections. Right: CMD for the solar neighbourhood within 250 pc, which is ∼94% complete down to the magnitude of the oMSTO (M_V=4.5).

Johnson B and V filters. For stars appearing in more than one catalogue, a weighted mean magnitude was calculated for each filter.

A further step before the CMD-fitting can be applied is a robust quantification of the completeness as a function of colour and magnitude. According to Høg et al. (2000), the *Tycho-2* completeness is over 90% down to $V\sim$11.5, but decreases quickly at fainter magnitudes, so we only kept stars brighter than this limit. Even though TGAS is based on *Tycho-2*, about 20% of the stars from the latter catalogue are missing in TGAS, which means that we have no robust parallaxes for these stars. This is illustrated in Figure 1, which presents the completeness of TGAS versus *Tycho-2* as a function of both colour–magnitude (left) and spatial coordinates (middle). The left panel shows that a significant fraction of the stars brighter than $V\sim$6.5 or bluer than $B-V\sim$0 are missing in TGAS; however, most of these stars have *Hipparcos* parallaxes, which we combined with those from TGAS to erase completeness variations as a function of colour and magnitude. The middle panel shows that completeness is below ∼60% in about half of the sky due to the lower number of *Gaia* transits. Unfortunately, the completeness function in these regions is too complex to correct; we therefore simply excised 57% of the sky coverage where completeness down to $V\sim$11.5 was <90%.

Finally, to obtain an accurate SFH back to the earliest epoch of star formation, a CMD reaching the oldest main-sequence turn-off (oMSTO, at M_V=4.5) is required. Given the completeness limits described above, the volume in which the SFH can be calculated is therefore limited to a distance modulus of $(V-M_V)$=7, corresponding to 250 pc. The resulting CMD, shown in the right panel of Figure 1, contains ∼148,000 stars and is mostly complete down to the oMSTO within 250 pc.

3 SFH calculation

The preliminary SFH has been calculated using the technique of synthetic CMD-fitting following the methodology presented in Bernard et al. (2012, 2015a,b). The synthetic CMD from which we extracted the simple stellar populations' CMDs is based on the BaSTI stellar evolution library (Pietrinferni et al. 2004). It contains 2×10^7 stars and was generated with a constant SFR over wide ranges of age and metallicity: 0 to 15 Gyr old and $0.0001\leq Z\leq 0.03$ (i.e. $-2.3\leq$ [Fe/H] ≤ 0.26, assuming $Z_{sun}=0.0198$; Grevesse & Noels 1993). We adopted a Kroupa (2002) initial mass function, and assumed a fraction of unresolved binary systems in TGAS of 10% with mass ratios between 0 and 1. Further tests with different fractions of binaries, a wider range of metallicity, and different prescriptions for the simulated photometric and parallactic uncertainties are necessary to better understand the possible systematic uncertainties.

While the full photometric uncertainties due to various observational effects are typically estimated using artificial stars tests on the original images (e.g. Gallart et al. 1999), this approach is impossible in the case of *Gaia* for which (most of) the images are not sent back to Earth. Instead, we relied on the distributions of photometric errors as a function of colour and magnitude provided in the *Tycho-2*, *Hipparcos*, and APASS catalogues to simulate the uncertainties in the synthetic CMD.

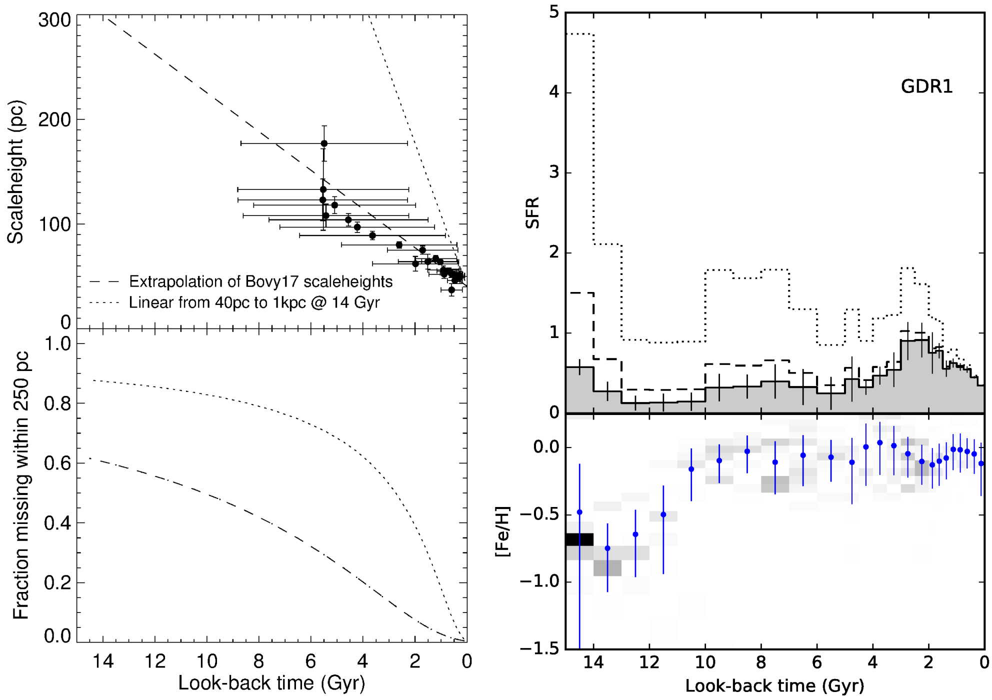

Fig. 2. Left: Evolution with time of the disc scaleheight (top) and of the corresponding fraction of stars lying beyond 250 pc (bottom, see text for details). The dashed and dotted lines correspond to the mild and the extreme corrections respectively. Right: Resulting SFH, showing the evolution of the SFR (top) and metallicity (bottom) as a function of time. In the top panel, the dashed and dotted lines represent the SFR corrected for the fraction of stars that have been heated to heights >250 pc, assuming the mild and the extreme corrections respectively.

4 Results

The SFH is presented in the right panel of Figure 2: the top and bottom plots show the evolution of the *dynamically-evolved SFR* (grey histogram) and metallicity, respectively, as a function of time. However, since the SFH was reconstructed based on the stars that are located *today* within the solar neighbourhood, the effects of secular evolution of the disc have to be taken into account. While the importance of radial migrations (e.g. Sellwood & Binney 2002) has yet to be quantified, we can correct this SFR for the disc thickening with age to obtain a SFR that is representative of the whole solar cylinder.

To quantify the thickening, we used the disc scaleheight measured by Bovy (2017) for each spectral type from A0 to G3. The mean age of each type was estimated from the synthetic CMD of the solar neighbourhood from the Besançon model (Robin et al. 2003) by selecting all the stars with a temperature within 2% of the spectral type temperature (from Pecaut & Mamajek 2013). The solid circles in the top left panel of Figure 2 show the Bovy (2017) scaleheights plotted as a function of our estimated ages, where the horizontal errorbars represent the age standard deviation. The dashed line fitted to these points – virtually the same relation as that used by Just & Jahreiß (2010) – shows a clear change of the disc thickness as a function of age, though it could either imply that the older disc formed thicker or that it thickened with time. We then used the scaleheight fit to estimate the fraction of stars of a given age that are beyond 250 pc and therefore missing from our CMD; this is shown in the bottom left panel of Figure 2. The SFR including this correction (hereafter the *mild* correction) is shown as a dashed line in the top right panel.

Note, however, that extrapolating the Bovy (2017) scaleheights to 14 Gyr ago implies an old disc that is only ∼300 pc thick, while the Milky Way thick disc is believed to be about 1 kpc thick (e.g. Jurić et al. 2008). Therefore, in the top left panel of Figure 2 we also show as dotted line a scaleheight increasing linearly from 40 pc at the present day to 1 kpc 14 Gyr ago, the corresponding fraction of missing stars in the bottom panel, and the resulting SFR in the top right panel. We label it the *extreme* correction as it clearly over-estimates the scaleheight of the intermediate-age populations; the true relation is likely more complex, possibly with a break around 10 Gyr ago corresponding to the formation of the thick disc.

The dynamically-evolved SFR (i.e. uncorrected; grey histogram) shows a constant SFR for the first 10 Gyr or so, with a slight enhancement in the past 4 Gyr. This is in excellent agreement with the SFR calculated from *Hipparcos* data within a smaller volume (∼80 pc; Vergely et al. 2002; Cignoni et al. 2006). The SFR with the *mild* correction is not significantly different, except perhaps for the slightly more pronounced enhancement at early epochs corresponding to the formation of the thick disc. On the other hand, with the *extreme* correction the SFR appears roughly constant over most of the history, but with a strong enhancement at early epochs and a decreasing SFR in the past 2–3 Gyr. This shows that even with the most extreme correction our results are not consistent with an exponentially decreasing SFR as found by several recent studies (Aumer & Binney 2009; Just, Gao, & Vidrih 2011; Bovy 2017). Instead, it favors solutions with a roughly constant star formation over 8–10 Gyr such as found by, e.g., Snaith et al. (2015).

The age-metallicity relation (AMR), shown in the bottom-right panel of Figure 2, is mostly flat for the past 10 Gyr. Only the oldest stars show a lower mean metallicity ([Fe/H]~ -0.7), which may correspond to the thick disc population. This is fully consistent with the independent results from other groups using different methods and datasets (e.g. Casagrande et al. 2011; Haywood et al. 2013; Bergemann et al. 2014).

5 Conclusions and future prospects

We have used the *Gaia* DR1 parallaxes to produce a deep CMD that is mostly complete down to the magnitude of the oMSTO within 250 pc from the Sun. We applied the CMD-fitting technique to reconstruct the dynamically-evolved SFH of the local Milky Way disc. Our results are fully consistent with those obtained previously using the *Hipparcos* data, despite the difficulty of dealing with the complex TGAS completeness function and photometric uncertainties from different catalogues. We then correct this SFR for the disc thickening with age to obtain a SFR that is representative of the whole solar cylinder, and show that even with an extreme correction our results are not consistent with an exponentially decreasing SFR. We plan to use the same technique with upcoming *Gaia* data releases. With parallaxes and homogeneous photometry in 3 bands (G, BP, RP) for $>10^9$ stars, and not limited by the poorly understood completeness function of an input catalogue like *Tycho-2* was, it will allow us to extend this analysis out to about 5 kpc, and therefore to quantify the SFH of the thin disc, thick disc and halo *in situ*, and its spatial variations. The spatial variations of the SFH within each component will also provide important constraints on the dynamical processes involved in shaping up their current stellar content.

I would like to thank Lia Athanassoula, James Binney, Cristina Chiappini, Françoise Combes, Annette Ferguson, Carme Gallart, Andreas Just, and Annie Robin for useful discussions and comments, and acknowledge support from the CNES postdoctoral fellowship program. This work has made use of data from the European Space Agency (ESA) mission *Gaia* (https://www.cosmos.esa.int/gaia), processed by the *Gaia* Data Processing and Analysis Consortium (DPAC, https://www.cosmos.esa.int/web/gaia/dpac/consortium). Funding for the DPAC has been provided by national institutions, in particular the institutions participating in the *Gaia* Multilateral Agreement.

References

Anders, F., Chiappini, C., Rodrigues, T. S., et al. 2017, A&A, 597, A30

Aumer M., Binney J. J., 2009, MNRAS, 397, 1286

Bergemann, M., Ruchti, G. R., Serenelli, A., et al. 2014, A&A, 565, A89

Bernard, E. J., Ferguson, A. M. N., Barker, M. K., et al. 2012, MNRAS, 420, 2625

Bernard, E. J., Ferguson, A. M. N., Chapman, S. C., et al. 2015a, MNRAS, 453, L113

Bernard, E. J., Ferguson, A. M. N., Richardson, J. C., et al. 2015b, MNRAS, 446, 2789

Bovy J., 2017, MNRAS, 470, 1360

Casagrande, L., Schönrich, R., Asplund, M., et al. 2011, A&A, 530, A138

Cignoni, M., Degl'Innocenti, S., Prada Moroni, P. G., & Shore, S. N. 2006, A&A, 459, 783

Edvardsson, B., Andersen, J., Gustafsson, B., et al. 1993, A&A, 275, 101

Gaia Collaboration, Brown, A. G. A., Vallenari, A., et al. 2016, A&A, 595, A2

Gallart, C., Freedman, W. L., Aparicio, A., Bertelli, G., & Chiosi, C. 1999, AJ, 118, 2245

Grevesse N., Noels A., 1993, in Origin and Evolution of the Elements, p. 15

Haywood, M., Di Matteo, P., Lehnert, M. D., Katz, D., & Gómez, A. 2013, A&A, 560, A109

Henden, A. A., Levine, S. E., Terrell, D., Smith, T. C., & Welch, D. 2012, JAAVSO, 40, 430

Høg, E., Fabricius, C., Makarov, V. V., et al. 2000, A&A, 355, L27
Jurić M., et al., 2008, *ApJ*, 673, 864-914
Just A., Gao S., Vidrih S., 2011, MNRAS, 411, 2586
Just A., Jahreiß H., 2010, MNRAS, 402, 461
Kroupa P., 2002, Sci, 295, 82
Lindegren, L., Lammers, U., Bastian, U., et al. 2016, A&A, 595, A4
Pecaut M. J., Mamajek E. E., 2013, ApJS, 208, 9
Pietrinferni A., Cassisi S., Salaris M., Castelli F., 2004, ApJ, 612, 168
Robin A. C., Reylé C., Derrière S., Picaud S., 2003, A&A, 409, 523
Sellwood, J. A., & Binney, J. J. 2002, MNRAS, 336, 785
Snaith O., et al. 2015, A&A, 578, A87
van der Kruit, P. C., & Freeman, K. C. 2011, ARA&A, 49, 301
Vergely, J.-L., Köppen, J., Egret, D., & Bienaymé, O. 2002, A&A, 390, 917

SF2A 2017
C. Reylé, P. Di Matteo, F. Herpin, É. Lagadec, A. Lançon, Z. Meliani, F. Royer (eds)

CHEMICAL EVOLUTION OF THE LMC ACROSS THE FIRST KILOPARSECS

M. Van der Swaelmen[1], V. Hill[2] and F. Primas[3]

Abstract.
The LMC provides a unique laboratory to study stellar evolution and specifically nucleosynthesis at low metallicities: with its present day metallicity of only 1/3 of solar, the chemical enrichment path followed by this galaxy gives a heavy weight to the yields of metal-poor stellar generations. In order to investigate the chemical history of the LMC and constrain formation and evolution scenarios, we performed a homogeneous detailed chemical analysis of more than 250 LMC RGB stars located in three different fields: a first field located in the bar, a second in the inner disc at $\sim 2^{\circ}$ South of the bar, and a third in the outer parts of the LMC disc, at $\sim 4^{\circ}$ from the bar. Here, we present for the first time α-element abundances for the LMC outer disc field and compare it to the other two fields already investigated in our previous works: all three fields display similar trends, thus indicating a globally homogeneous chemical composition of the LMC across the first kiloparsecs.

Keywords: Stars: abundances, Galaxies: Magellanic Clouds, Galaxies: evolution, Techniques: spectroscopic

1 Introduction

Among the satellites of the Milky Way (MW), the Small and the Large Magellanic Clouds (SMC, LMC) are of particular interest since they are the closest example of galaxies in gravitational and hydrodynamical interactions. Morphological features like the Magellanic Bridge are suspected to be the signature of an LMC-SMC interaction while circum-galactic structure like the Leading Arm and the Magellanic Stream might be the result of LMC-SMC-MW interactions (*e.g.*, Besla et al. 2012). Therefore it is a unique laboratory to study in details the effect of gravitational tides and matter exchange on the chemical evolution and the star formation history of a galaxy.

The LMC is an almost face-on, gas-rich galaxy which host a bar-shaped structure at its center, embedded into an older gazeous and stellar disc. The real nature of the bar-shaped structure is still debated as it could be a dynamically-driven bar like the one found at the MW center or it could be a stellar bulge (Zaritsky 2004). Smecker-Hane et al. (2002) have derived from deep colour-magnitude diagram (CMD) the star formation histories of field stars located in the LMC bar and LMC inner disc. They show that star formation occurs at all ages. However, while the star formation history (SFH) of the bar and the inner disc are similar and rather constant at old epochs (between 7 and 14 Gy), they show that the bar has experienced a dramatic increase of its SFH, 4 to 6 Gy ago. On the contrary, Monteagudo et al. (2017) derived SFH from VIMOS data for eleven fields sampling the LMC bar and the innermost regions of the LMC disc and claim that the bar's and disc's SFH are not significantly different. Lastly, Carrera et al. (2008) showed from age-metallicity relation that the chemical composition of the LMC disc is rather homogeneous between 3° and 8°. In order to investigate the difference between the LMC bar and disc, we present here high-resolution spectroscopic abundances obtained in an homogeneous way for three different LMC fields, sampling the bar and the disc of the LMC.

[1] Institut d'Astronomie et d'Astrophysique, Université Libre de Bruxelles, Belgium
[2] Laboratoire Lagrange, UMR 7293, Université de Nice Sophia-Antipolis, Observatoire de la Côte d'Azur, BP4229, 06304, Nice Cedex 4, France
[3] European Southern Observatory, Karl Schwarzschild Str. 2, 85748 Garching b. München, Germany

2 Data

We obtained mid-resolution ($R \sim 20\,000$) mid-S/N (S/N ~ 35) spectra of LMC red giant branch stars (RGB) with the FLAMES/GIRAFFE multi-object spectrograph (Pasquini et al. 2002) of the ESO/VLT. We used three different settings HR11 ([5590, 5830] Å), HR13 ([6110, 6400] Å) and HR14 ([6290, 6690] Å). This spectral coverage of nearly 1000 Å gives us access to numerous iron lines and other atomic lines that we used to derive the metallicity, the microturbulence velocity and elemental abundances. To reduce the spectra, we used the latest version of the GIRAFFE pipeline, available through the ESO pipeline suite, *reflex**. After the spectrum extraction with the GIRAFFE pipeline, we performed the sky-subtraction, radial velocity correction and co-addition of multi-epoch spectra thanks to our own set of scripts.

In this study, we compare the α-element abundances that we already obtained for 110 RGB stars located in the LMC bar (Van der Swaelmen et al. 2013) and 65 RGB stars located in the LMC inner disc (Pompéia et al. 2008; Van der Swaelmen et al. 2013) to our new set of abundances derived for RGB stars located in the LMC outer disc. This third field is located at $\sim 4°$ from the LMC center, in the vicinity of the globular cluster NGC 2210. About 90 stars of our observing program were observed with the three GIRAFFE setups. Our total sample consists of more than 250 LMC stars, that have been analysed in a homogeneous way (see next section).

3 Spectroscopic analysis

We used an iterative method to derive the atmospheric parameters of our objects, similar to the one explained in Van der Swaelmen et al. (2013). We briefly recall the main steps hereafter. The temperature is obtained thanks to the color-temperature-metallicity calibrations derived by Ramírez & Meléndez (2005). We use OGLE V & I (Ulaczyk et al. 2012) photometry and 2MASS J, H & K (Skrutskie et al. 2006) photometry which allowed the use of four photometric calibrations. On the other hand, the metallicity injected in the photometric calibrations is either an estimate (A. A. Cole, private communication) derived from the infrared Calcium II triplet index (if first iteration) or the high-resolution spectroscopic metallicity ([Fe/H]) derived from Fe I lines (subsequent iterations). The final photometric temperature is obtained by avergaging the four estimates. Then, we compute the $\log g$ using the photometric gravity formula using the photometric temperature, the metallicity and assuming a mass of $1.5 M_{\odot}$. Lastly, we fix simultaneously the metallicity and the microturbulence velocity by requiring that neutral iron lines of different equivalent widths give the same iron abundance, the equivalent widths of Fe I lines being measured with the automated tool DAOSPEC (Stetson & Pancino 2008). Most of the stars required two loops to reach convergence. Figure 1 shows the position of our stars in the H.-R. diagram.

We computed synthetic spectra by using the synthesis code *turbospectrum* (*turbospectrum* is described in Alvarez & Plez 1998 and improved along the years by B. Plez) together with the MARCS model atmosphere library (Gustafsson et al. 2008), the Gaia-ESO Survey atomic line list (Heiter et al. 2015) and molecular linelists for CN by Brooke et al. (2014); Sneden et al. (2014)†. We then derived elemental abundances for O, Mg, Si, Ca and Ti by absorption line fitting: we compute a grid of synthetic spectra, compare them to one observed spectrum and find the best-matching synthetic spectrum by χ^2 minimisation. The best-matching synthetic spectrum then provides the abundance of the element under study. Only two atomic lines could be used for O and Mg while about ten lines were available for Si, Ca and Ti.

4 Results & Conclusions

Figure 2 shows the abundance distributions for the five α-elements under study: O, Mg, Si, Ca and Ti. Our three LMC fields are displayed: bar (black; Van der Swaelmen et al. 2013), inner disc (red; Van der Swaelmen et al. 2013), outer disc (green; this work). The shaded area are obtained with a moving average and are an attempt to highlight the mean behaviour. We see that oxygen and magnesium have a similar behaviour: they tend to be enhanced for a metallicity $[\mathrm{Fe/H}] < -1$ and then decrease to reach a solar value at a metallicity around -0.3. On the other hand, silicon, calcium and titanium tend to have a flat distribution for metallicities higher than -1.2. This difference is expected since oxygen and magnesium are produced by type II supernovae (SNII) progenitors more massive than those producing silicon, calcium and titanium.

* `ftp://ftp.eso.org/pub/dfs/pipelines/giraffe/giraf-pipeline-manual-2.16.pdf`

† Downloadable at B. Plez's webpages at `http://www.pages-perso-bertrand-plez.univ-montp2.fr/`

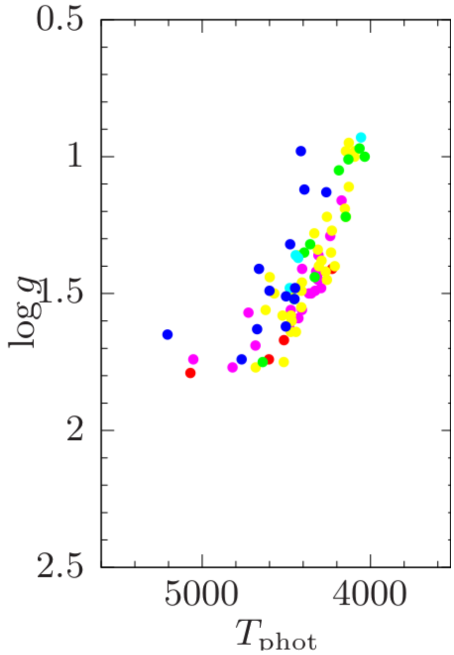

Fig. 1. Hertzsprung-Russel diagram of the LMC outer field. Metallicity bins are as follows: dark blue: [Fe/H] < -1.2; cyan: $-1.3 <$ [Fe/H] < -1.0; green: $-1.0 <$ [Fe/H] < -0.8; yellow: $-0.8 <$ [Fe/H] < -0.6; magenta: $-0.6 <$ [Fe/H] < -0.4; red: $-0.4 <$ [Fe/H].

Another feature to notice is that the abundance distributions of all fields overlap: there is no striking difference in their chemistry. This result is quite puzzling since it seems to be counterintuitive with respect to earlier results by Smecker-Hane et al. (2002) that showed a difference in the star formation history between the LMC bar and the LMC disc, which should have translated in a difference between the bar and disc α-trends. On the other hand, our abundance trends are compatible with the similar SFH derived by Monteagudo et al. (2017) for the LMC bar and disc. Thus, our results seems to speak in favour of a similar and homogeneous chemical composition of the bar and the first few kiloparsecs of the LMC disc.

Figure 3 compares our LMC α-trend (O + Mg) to that of the Milky Way (Gaia-ESO Survey Mg abundance only; see for instance Mikolaitis et al. 2014 or Kordopatis et al. 2015). Since our three LMC fields behave similary from the α-element point of view, we use a single color (red) to depict our data points. Metal-poor LMC stars possess α abundances similar to those of MW disc stars while stars with higher metallicity have α ratios smaller than that of the MW. We note also that the decrease of the [α/Fe] ratio occurs at a lower metallicity in the LMC than in the MW. This tells us that the LMC has experienced a slower chemical enrichment than that of the Milky Way and this chemical enrichment was dominated by type Ia supernovae. This could also point to a less efficient recycling of metals produced by massive SNII in the LMC. For instance, Romano & Starkenburg (2013) showed in their modelling of the Sculptor dwarf galaxy that reducing the metal recycling efficiency causes a move of the knee towards low metallicity.

To summarize, our results point at a similar and homogeneous chemical composition of the LMC bar and of the first kpc of the disc. They are compatible with the already known scenario of slow chemical enrichment of the LMC (compared to the MW) and are also compatible with a less efficient recycling of metals, which is expected for a low-mass galaxy like the LMC.

MVdS deeply thanks the SF2A for its financial support to attend "Les Journées de la SF2A". MVdS benefits from a "Fondation ULB" fellowship.

References

Alvarez, R. & Plez, B. 1998, A&A, 330, 1109

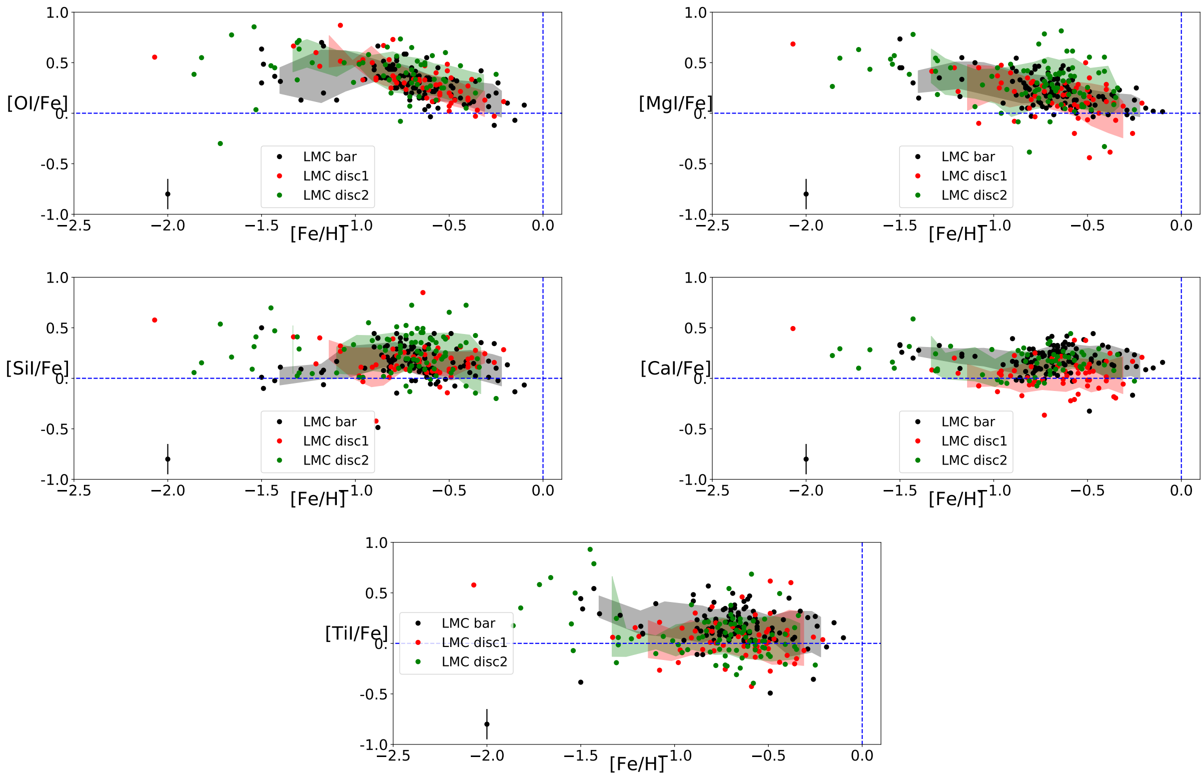

Fig. 2. Comparison of LMC O, Mg, Si, Ca, Ti trends for the three fields. Black dots: LMC bar (Van der Swaelmen et al. 2013); red dots: LMC inner disc (disc1; Van der Swaelmen et al. 2013); green dots: LMC outer disc (disc2; this work).

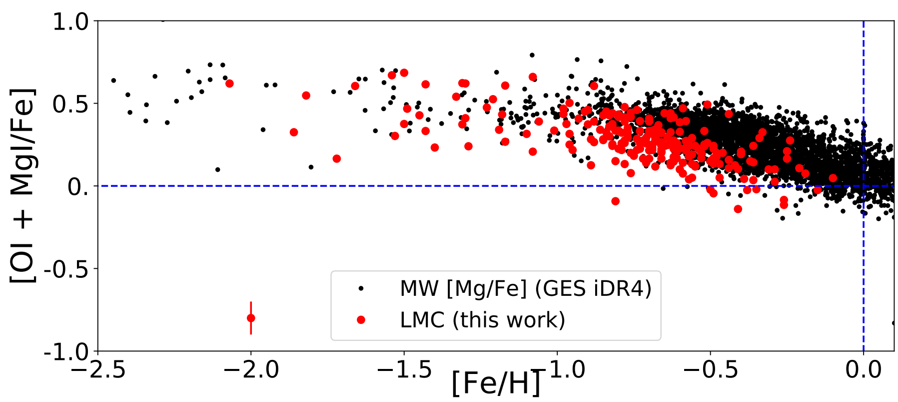

Fig. 3. Comparison of LMC [O + Mg/Fe] to MW [Mg/Fe]. Large red dots: LMC data (Van der Swaelmen et al. 2013 + this work); tiny black dots: MW GES Mg abundances.

Besla, G., Kallivayalil, N., Hernquist, L., et al. 2012, MNRAS, 421, 2109
Brooke, J. S. A., Ram, R. S., Western, C. M., et al. 2014, ApJS, 210, 23
Carrera, R., Gallart, C., Hardy, E., Aparicio, A., & Zinn, R. 2008, AJ, 135, 836
Gustafsson, B., Edvardsson, B., Eriksson, K., et al. 2008, A&A, 486, 951
Heiter, U., Lind, K., Asplund, M., et al. 2015, Phys. Scr, 90, 054010
Kordopatis, G., Wyse, R. F. G., Gilmore, G., et al. 2015, A&A, 582, A122

Mikolaitis, Š., Hill, V., Recio-Blanco, A., et al. 2014, A&A, 572, A33
Monteagudo, L., Gallart, C., Monelli, M., Bernard, E. J., & Stetson, P. B. 2017, ArXiv e-prints
Pasquini, L., Avila, G., Blecha, A., et al. 2002, The Messenger, 110, 1
Pompéia, L., Hill, V., Spite, M., et al. 2008, A&A, 480, 379
Ramírez, I. & Meléndez, J. 2005, ApJ, 626, 465
Romano, D. & Starkenburg, E. 2013, MNRAS, 434, 471
Skrutskie, M. F., Cutri, R. M., Stiening, R., et al. 2006, AJ, 131, 1163
Smecker-Hane, T. A., Cole, A. A., Gallagher, III, J. S., & Stetson, P. B. 2002, ApJ, 566, 239
Sneden, C., Lucatello, S., Ram, R. S., Brooke, J. S. A., & Bernath, P. 2014, ApJS, 214, 26
Stetson, P. B. & Pancino, E. 2008, PASP, 120, 1332
Ulaczyk, K., Szymański, M. K., Udalski, A., et al. 2012, Acta Astron., 62, 247
Van der Swaelmen, M., Hill, V., Primas, F., & Cole, A. A. 2013, A&A, 560, A44
Zaritsky, D. 2004, ApJ, 614, L37

SF2A 2017
C. Reylé, P. Di Matteo, F. Herpin, É. Lagadec, A. Lançon, Z. Meliani, F. Royer (eds)

THE MASS ASSEMBLY HISTORY OF THE MILKY WAY NUCLEAR STAR CLUSTER

A. Mastrobuono-Battisti[1] and A. Tsatsi[1]

Abstract. Nuclear star clusters (NSCs) are dense stellar clusters observed in the center of a large fraction of galaxies, including the Milky Way. Although their evolution is strictly connected to that of their host galaxy, their origin is still unknown. We explore one of the possible formation mechanisms by studying direct N-body simulations of initially randomly distributed globular clusters (GCs) that ispiral to the center of a Milky Way-like nuclear disk. We find that the NSC that forms through this process shows both morphological and kinematical properties that make it comparable with observations of the Milky Way NSC, including significant rotation, a property usually attributed to the infall of gas and following in-situ star formation. We prove that no fine-tuning of the initial orbital distribution of the infalling GCs is necessary to result in a rotating NSC. Therefore, we conclude that the cluster inspiral is a possible mechanism for the formation of the Milky Way NSC and we put constraints on the build up history of the Galactic NSC.

Keywords: Galactic nuclei, Milky Way, nuclear star cluster, formation, kinematics, morphology, globular clusters

1 Introduction

Nuclear star clusters (NSCs) are extremely dense and compact stellar systems, with masses between $\sim 10^6$ M$_\odot$ and 10^7 M$_\odot$, effective radii of a few pc and central luminosities up to $\sim 10^7$ L$_\odot$. They are commonly observed in the nuclei of galaxies along the whole Hubble sequence and they often coexist with a central supermassive black hole (SMBH, see Böker 2010, for an overview). Their properties seem to scale with those of their host galaxies suggesting a close connection between their evolution and the build up of the whole galaxy. However, their formation mechanism is not yet known. Two main hypotheses have been suggested: the in-situ star formation scenario, where gas infalls into the nucleus and forms stars (Schödel et al. 2008) and the inspiral scenario, where massive clusters, like globular clusters (GCs), decay to the galactic center via dynamical friction and merge to form a dense NSC (Tremaine et al. 1975; Capuzzo-Dolcetta 1993). Since both old and young stars are observed in galactic nuclei, these processes are not exclusive and they could work in parallel, contributing to the formation of the NSC. Here and in Tsatsi et al. (2017) we explore and test the merger scenario using detailed N-body simulations of consecutive decays of GCs into a Milky Way (MW) like nuclear disk and compare the results of the simulations to observations, using the MW NSC as a benchmark. In Section 2 we describe our simulations and the method we used for our analysis, in Section 3 we compare our results with observations and we show how kinematic misalignments and substructures could be used to disentangle the different formation mechanisms. In Section 4 we draw our conclusions.

2 Simulations and methods

The N-body simulations used in this study are described in detail in Antonini et al. (2012); Mastrobuono-Battisti et al. (2014) and Tsatsi et al. (2017). In brief, we simulate the formation of a Milky Way-like NSC through the consecutive infall of 12 identical globular clusters (GCs) with a mass of 1.1×10^6M$_\odot$ each, in the inner region of a nuclear disk ($M_{nd} = 10^8$M$_\odot$), hosting a central SMBH ($M_\bullet = 4 \times 10^6M_\odot$)), similar to Sgr A* (Genzel et al. 2010). Each GC is represented by a tidally truncated King (1966) model and is initially moving on a circular orbit with randomly chosen parameters, at a galactocentric distance of 20 pc. The time interval

[1] Max-Planck Instiut für Astronomie, Königstuhl 17, 69117 Heidelberg, Germany

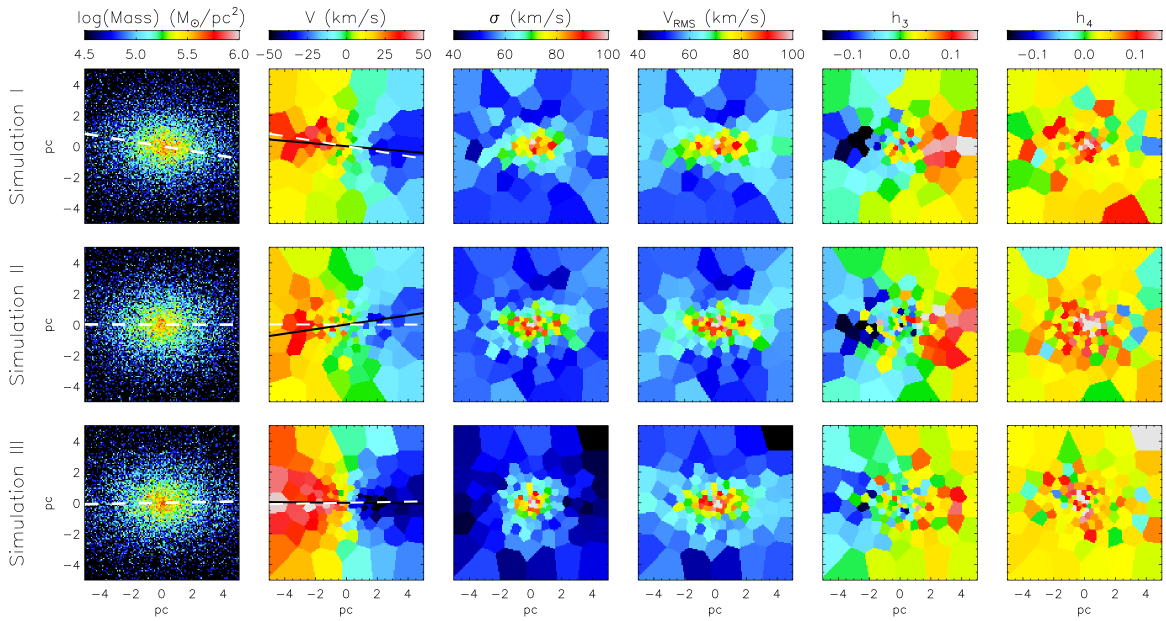

Fig. 1. LOSVD of the simulated NSC. From left to right: Projected stellar mass surface density, line-of-sight velocity v, velocity dispersion σ in km/s, and higher-order moments h_3 and h_4, comparable to the skewness and the kurtosis, respectively. The white dashed line shows the major photometric axis, while the solid black line shows the kinematic major axis of each cluster. From Tsatsi et al. (2017).

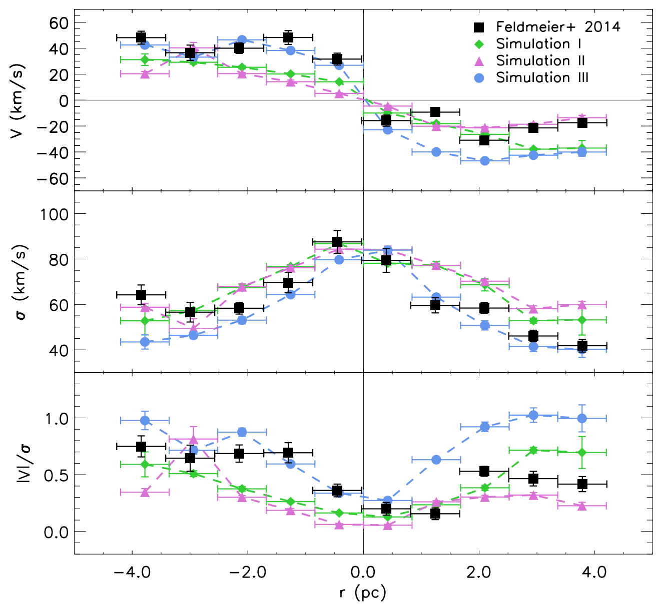

Fig. 2. Kinematic profiles (V, σ and V/σ) for the three simulated clusters (dashed lines) compared to the corresponding profiles of the Milky Way NSC (black squares) by Feldmeier et al. (2014). All profiles are extracted from a slit along the kinematic axis and the asymmetry between left and right side of the MW NSC is caused by dust extinction (Chatzopoulos et al. 2015). From Tsatsi et al. (2017).

is kept constant between each infall ($\sim$0.85 Gyr) and the times are rescaled to the real mass of the particles, as described by Mastrobuono-Battisti & Perets (2013). After the last infall the whole system is evolved in isolation for $\sim$2.2 Gyr accounting for a total time of $\sim$12.4 Gyr. The total mass of the resulting NSC is $\sim 1.4 \times 10^7 M_\odot$.

This value is in agreement on the 2-σ level with the mass of the MW NSC ($2.5 \pm 0.6 \times 10^7 M_\odot$), as estimated by Schödel et al. (2014). Here we analyse three realizations of the initial conditions described above, with different random parameters for the initial orbital parameters of the infalling GCs for the orbital parameters used in each simulation. Simulation III differs from Simulations I and II because the inclination of the orbits i is aways $<90°$, so that all the GCs inspiral on prograde orbits. This choice of initial parameters has been made to represent clusters that might have initially formed in the central molecular zone of the MW and thus will share a similar orbital spin. In order to compare the mass and orbital distribution of the simulated NSC with observable properties, we create two-dimensional mock stellar mass and kinematic maps by projecting the stellar particles along a line-of-sight which is perpendicular to the total angular momentum vector of the NSC, meaning that the line-of-sight rotation observed should be maximum. Particles are then binned on a regular grid centerd on the center of mass of the cluster, with a field-of-view (FoV) of 5 pc radius, which is approximately the half-light radius of the MW NSC (Schödel et al. 2014). The half-mass radius of our simulated NSC is approximately 10 pc for all simulation set-ups. We would expect differences between observed half-light and half-mass radius of the MW NSC if the mass-to-light ratio is not constant, as a result of the non-trivial interplay between mass segregation and the presence of young bright stars in the central region (e.g. Paumard et al. 2006). Within 5pc, the simulated NSC matches the observed shape of the surface density distribution of the MW NSC (Antonini et al. 2012). Therefore, we limit our kinematic analysis and comparison to this radial extent. The extracted kinematic maps are spatially binned using the 2D Voronoi binning method (Cappellari & Copin 2003). The mass-weighted line-of-sight velocity distribution (LOSVD) of the cluster is then extracted and fitted with the Gauss-Hermite series (van der Marel & Franx 1993; van de Ven et al. 2006). The mass and stellar LOSVD of the three simulated NSCs are shown in Figure 1.

3 Results and comparison with observations

Using the first and second moments of the intensity distribution of our mock images (see Figure 1), we find the position of the projected major axis and the flattening $q = b/a$ of our simulated NSCs within the adopted FoV of 5 pc radius. The average flattening of the NSC is $q = 0.64$ for Simulation I, and $q = 0.69$ for Simulations II and III. These values are remarkably similar to the observed flattening of the MW NSC, $q_{obs} = 0.71 \pm 0.02$ (Schödel et al. 2014). As seen from Figure 1, the NSC shows a significant amount of rotation, of an amplitude of ~ 40 km/s within 5 pc for Simulation I and II. The velocity is higher (~ 50 km/s) for Simulation III, where the infalling GCs have a similar initial orbital direction. In order to compare our results with the observed kinematic profiles of the MW NSC, we estimate the kinematic major axis of the NSC within the adopted FoV using the kinemetry method, as developed by Krajnović et al. (2006). The kinematic axis for each simulated NSC is shown in Figure 1 (solid black lines). We then place a mock slit along the kinematic axis, of width of 0.84 pc and extract the LOSVD of the simulated clusters in equal-size bins of 0.84 pc size, which corresponds to a binning similar to the one used by Feldmeier et al. (2014) to the MW NSC. The corresponding errors are calculated by Monte Carlo simulations of the extracted LOSVD (see van de Ven et al. 2006). The profiles of V, σ and V/σ for the three simulations are shown in Figure 2. The kinematic profiles show a very good agreement with the kinematic profiles observed in the MW NSC (Feldmeier et al. 2014).

3.1 Kinematic misalignments and substructures

Figure 1 shows the measured kinematic and the photometric major axes of all simulated NSCs within the adopted FoV. We find that the offset between these two axes within 5 pc is $\Delta\theta \sim 4.2°$, $8.6°$ and $0.5°$ for Simulations I, II, and III, respectively. Simulation I also shows a misalignment of about $9.2°$ between the photometric major axis within 5 pc and the projected plane, which is perpendicular to the total angular momentum vector of the NSC (the x axis of Figure 1). Simulation III, however, characterised by inspiralling GCs with similar orbital directions, shows no significant offset between the kinematic and the photometric axis of the resulting NSC. A misalignment of $\sim \Delta\theta \sim 9° \pm 3°$ between kinematics and morphology has also been recently observed in the MW center suggesting this as an evidence that cluster-inspirals may have played a role in the formation of the MW NSC (Feldmeier et al. 2014). Here we confirm that this scenario is able to produce observable misalignments between the photometry and kinematics of the resulting NSCs, which are stronger in the case where the infalling GCs have initially random orbital spin orientation (Simulations I and II), however not in the case where the GCs infall with a similar orbital direction (Simulation III). Moreover, the detailed study of the internal kinematics can provide an important tool to disentangle the possible formation mechanisms. Indeed, recent findings by Feldmeier et al. (2014) provide strong evidence for a kinematic substructure in the MW NSC,

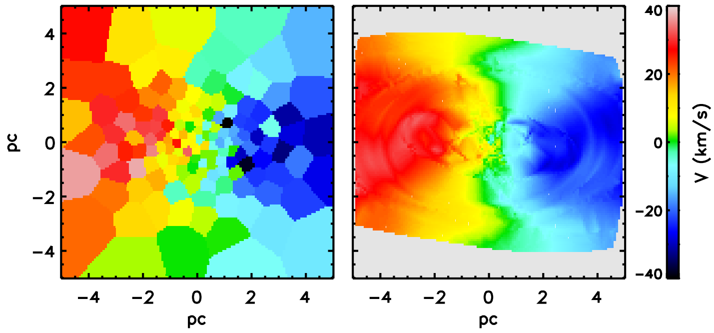

Fig. 3. Left: Mock line-of-sight velocity map of the NSC of Simulation II, after the infall of the 12th GC. Right: the corresponding kinemetric model, showing a weak polar twist at ∼3 pc. From Tsatsi et al. (2017).

rotating perpendicularly to its main body, which can be interpreted as a fossil record of a past merger event. In order to study the role of mergers in creating such kinematic substructures, we use the apply the kinemetry method to our simulated kinematic maps. In this way, we find a substructure (see Figure 3) created by a past polar merger event of a globular cluster. This is a merger signature that can be observable and long-lasting (for 3 Gyr) in the kinematics of the NSC.

4 Conclusions

We explored the possibility of a merger origin of NSCs, using N-body simulations of the consecutive inspiral of GCs in the center of a MW-like nucleus. We find that even if the GCs are initially randomly distributed around the center, the resulting NSC shows a significant amount of rotation, and that both its morphological and kinematic properties are comparable to the MW NSC. Moreover, our adopted model can account for observable kinematic misalignments and substructures in the final NSC, that can serve as long-lasting fossil records of past merger events. This is in line with recent observations of a similar substructure in the MW NSC (Feldmeier et al. 2014). According to our results, the cluster infall scenario is a viable hypothesis for NSC formation. However, the search for the dominant formation mechanism of NSCs is still ongoing, and clarifying the nature of the Milky Way and extragalactic NSCs formation requires a more detailed study of their dynamics, their stellar populations and star formation history, combined with more realistic simulations of their formation.

References

Antonini, F., Capuzzo-Dolcetta, R., Mastrobuono-Battisti, A., & Merritt, D. 2012, ApJ, 750, 111
Böker, T. 2010, in IAUS, Vol. 266, IAUS, ed. R. de Grijs & J. R. D. Lépine, 58–63
Cappellari, M. & Copin, Y. 2003, MNRAS, 342, 345
Capuzzo-Dolcetta, R. 1993, ApJ, 415, 616
Chatzopoulos, S., Gerhard, O., Fritz, T. K., et al. 2015, MNRAS, 453, 939
Feldmeier, A., Neumayer, N., Seth, A., et al. 2014, A&A, 570, A2
Genzel, R., Eisenhauer, F., & Gillessen, S. 2010, Reviews of Modern Physics, 82, 3121
King, I. R. 1966, AJ, 71, 64
Krajnović, D., Cappellari, M., de Zeeuw, P. T., & Copin, Y. 2006, MNRAS, 366, 787
Mastrobuono-Battisti, A. & Perets, H. B. 2013, ApJ, 779, 85
Mastrobuono-Battisti, A., Perets, H. B., & Loeb, A. 2014, ApJ, 796, 40
Paumard, T., Genzel, R., Martins, F., et al. 2006, ApJ, 643, 1011
Schödel, R., Merritt, D., & Eckart, A. 2008, Journal of Physics Conference Series, 131, 012044
Schödel, R. et al. 2014, A&A, 566, A47
Tremaine, S. D., Ostriker, J. P., & Spitzer, Jr., L. 1975, ApJ, 196, 407
Tsatsi, A., Mastrobuono-Battisti, A., van de Ven, G., et al. 2017, MNRAS, 464, 3720
van de Ven, G., van den Bosch, R. C. E., Verolme, E. K., & de Zeeuw, P. T. 2006, A&A, 445, 513
van der Marel, R. P. & Franx, M. 1993, ApJ, 407, 525

SF2A 2017
C. Reylé, P. Di Matteo, F. Herpin, É. Lagadec, A. Lançon, Z. Meliani, F. Royer (eds)

DISTRIBUTION FUNCTIONS FOR ORBITS TRAPPED AT THE RESONANCES IN THE GALACTIC DISC

G. Monari[2, 1]

Abstract. The present-day response of a Galactic disc stellar population to a non-axisymmetric perturbation of the potential has previously been computed through perturbation theory within the phase-space coordinates of the unperturbed axisymmetric system. Such an Eulerian linearized treatment however leads to singularities at resonances, which prevent quantitative comparisons with data. Monari et al. manage to capture the behaviour of the distribution function (DF) at a resonance in a Lagrangian approach, by averaging the Hamiltonian over fast angle variables and re-expressing the DF in terms of a new set of canonical actions and angles variables valid in the resonant region. They then follow the prescription of Binney (2016), assigning to the resonant DF the time average along the orbits of the axisymmetric DF expressed in the new set of actions and angles. This boils down to phase-mixing the DF in terms of the new angles, such that the DF for trapped orbits only depends on the new set of actions. This opens the way to quantitatively fitting the effects of the bar and spirals to Gaia data in terms of distribution functions in action space.

Keywords: Galaxy: kinematics and dynamics, Galaxy: disc, Galaxy: structure

1 Introduction

In order to fully exploit the Gaia mission (and spectroscopic follow-ups) data, we need to construct dynamical models of the Milky Way based on distribution functions (DF) – one for each stellar component of the Galaxy and even for the dark matter halo – in self-consistent equilibrium with the gravitational field that they induce. The equation that relates the DFs and the Galactic potential is the collisionless Boltzmann equation (CBE). The Jeans theorem ensures that DFs that depend on the phase-space coordinates only through integrals of motion are solutions of the CBE. Particularly convenient integrals of motion that one can choose are the 'action' variables $\mathbf{J}$ (see Binney & Tremaine 2008), so that the DF is $f_0 = f_0(\mathbf{J})$. The canonical conjugate variables to the actions $\mathbf{J}$ are the angles $\boldsymbol{\theta}$. The equations of motion of stars in the $(\mathbf{J}, \boldsymbol{\theta})$ coordinates are particularly simple, i.e $\mathbf{J} = \text{const}$ and $\boldsymbol{\theta}(t) = \boldsymbol{\Omega} t + \boldsymbol{\theta}_0$, where $\boldsymbol{\Omega}(\mathbf{J}) \equiv \partial H_0/\partial \mathbf{J}$ are the orbital frequencies and H_0 the Hamiltonian function. The actions $\mathbf{J}$ completely characterise a star's orbit, while the the angles $\boldsymbol{\theta}$ the star's phase on the orbit. A DF depending only on the actions represents a phase-mixed system. Using action based DFs, the best axisymmetric models of our Galaxy were constructed (e.g. Cole & Binney 2017).

However, it is nowadays well established that the Milky Way is not axisymmetric, since it contains large non-axisymmetric structures like the bar or the spiral arms. Moreover, the Galactic disc is externally perturbed by its satellites like the Sagittarius dwarf galaxy and the Large Magellanic Cloud. Hence, we require non-axisymmetric DFs to constrain the non-axisymmetric components of the potential, which influence the kinematics of the stars in the solar neighbourhood (see, e.g. Dehnen 1998; Famaey et al. 2005), and act as drivers of the secular evolution of the disc (see, e.g. Fouvry et al. 2015). To take in account non-axisymmetric perturbations in the DF the first step is to linearize the CBE (Monari et al. 2016), discussed here in Sect. 2, and use a special treatment for the orbits trapped at the resonances (Monari et al. 2017), which we discuss in Sect. 3. We conclude in Sect. 4.

[1] The Oskar Klein Centre for Cosmoparticle Physics, Department of Physics, Stockholm University, AlbaNova, 10691 Stockholm, Sweden
[2] Leibniz Institut für Astrophysik Potsdam (AIP), An der Sterwarte 16, D-14482 Potsdam, Germany

2 Linearisation of the CBE ('Eulerian approach')

The linearisation of the CBE ('Eulerian approach') to the problem posed by non-axisymmetry, developed in Monari et al. (2016), consists in expressing the distribution function of the perturbed system in the action/angle coordinates $(\mathbf{J}, \boldsymbol{\theta})$ of the *unperturbed* axisymmetric system.

Let Φ_1 be the perturbing non-axisymmetric potential, which is always is cyclic in the angle coordinates. We can, therefore, expand Φ_1 in a Fourier series as

$$\Phi_1(\mathbf{J}, \boldsymbol{\theta}, t) = \mathrm{Re}\left\{\mathcal{G}(t)\sum_{\mathbf{n}} c_{\mathbf{n}}(\mathbf{J})\mathrm{e}^{\mathrm{i}\mathbf{n}\cdot\boldsymbol{\theta}}\right\}, \tag{2.1}$$

where $\mathcal{G}(t)$ models the time dependence of the perturbation. In particular, $\mathcal{G}(t) = g(t)h(t)$, where $g(t)$ describe the time dependence of the amplitude of the perturbation, and $h(t)$ sinusoidal function of frequency ω_{p}, $h(t) = \exp(\mathrm{i}\omega_{\mathrm{p}}t)$. In particular, if $\omega_{\mathrm{p}} = -m\Omega_{\mathrm{p}}$ where m is the multiplicity of the perturber, $h(t)$ describes the rotation of the perturbing potential with a fixed pattern speed Ω_{p}. The indexes $\mathbf{n}$ run from $-\infty$ to ∞.

Expressing the DF as $f = f_0 + f_1$, where f_0 is the unperturbed axisymmetric DF and f_1 the linear response to the (small) perturbing potential Φ_1, the CBE to the linear order reduces to:

$$\frac{\mathrm{d}f_1}{\mathrm{d}t} = \frac{\partial f_0}{\partial \mathbf{J}} \cdot \frac{\partial \Phi_1}{\partial \boldsymbol{\theta}}. \tag{2.2}$$

Assuming that the amplitude of the perturbation and its time derivatives are null far back in time – i.e., $\forall k, g^{(k)}(-\infty) = 0$ – and that the amplitude of the perturbation is constant at the present time t – i.e. $g^{(0)}(t) = 1$, and $g^{(k)}(t) = 0$, for $k = 1, ..., \infty$ – we can integrate Eq. 2.2 and, as shown in Monari et al. (2016),

$$f_1(\mathbf{J}, \boldsymbol{\theta}, t) = \mathrm{Re}\left\{\frac{\partial f_0}{\partial \mathbf{J}}(\mathbf{J}) \cdot \sum_{\mathbf{n}} \mathbf{n} c_{\mathbf{n}}(\mathbf{J}) \frac{h(t)\mathrm{e}^{\mathrm{i}\mathbf{n}\cdot\boldsymbol{\theta}}}{\mathbf{n}\cdot\boldsymbol{\Omega} - m\Omega_{\mathrm{p}}}\right\}. \tag{2.3}$$

The linear Eulerian response obtained in this way is valid far away from resonances, but diverges at the resonances, i.e. whenever

$$\mathbf{n}\cdot\boldsymbol{\Omega} - m\Omega_{\mathrm{p}} = 0. \tag{2.4}$$

Far away from the resonances, we can compute the moments of the perturbed DFs using the linear treatment. For example, Monari et al. (2016), using the epicyclic approximation to express $(\mathbf{J}, \boldsymbol{\theta})$ as a function of the usual positions and velocities $(\mathbf{x}, \mathbf{v})$, and considering 3D spiral arms as the perturber (with corotation in the outer Galaxy) have shown that the spiral arms induce mean radial velocity gradients and vertical motions ('breathing modes') in the Galactic disc in agreement with those found in numerical experiments. Similar gradients and breathing modes have been observed in the extended Solar neighbourhood (Siebert et al. 2011; Williams et al. 2013) (see Fig. 1).

3 Treatment at the resonances ('Lagrangian approach')

The linear Eulerian treatment described in Sect. 2 is valid far from the resonances, where the orbital tori are only distorted by the small perturbing potential Φ_1. But close to resonances, the tori are completely different. For this reason, it is necessary to define an new set of actions and angles to describe the orbits near the resonances (one set for each resonance).

Monari et al. (2017) study this problem in the 2D planar case (but the method can be easily extended to the 3D case). To describe the motion of stars near the resonances it is necessary to pass through two canonical transformations. The first (time-dependent) canonical transformation 'divides' the motion in its fast and slow component. Near a resonance with $\mathbf{n} = (l, m)$,

$$\theta_{\mathrm{s}} = l\theta_R + m(\theta_\phi - \Omega_{\mathrm{p}}t), \quad \theta_{\mathrm{f}} = \theta_R, \quad J_{\mathrm{s}} = J_\phi/m, \quad J_{\mathrm{f}} = J_R - (l/m)J_\phi. \tag{3.1}$$

The angle θ_{s} is slow because, in the unperturbed case, $\Omega_{\mathrm{s}} \equiv \dot{\theta}_{\mathrm{s}} \approx 0$. It corresponds physically to the azimuth of the apocentra of the orbit in the reference frame corotating with the perturber. The Hamiltonian of the system can then be averaged over the fast variable, so to reduce the problem to the evolution of the slow angle and action, and making the fast action an approximate integral of motion. Given J_{f}, $J_{\mathrm{s,res}}$ is defined as J_{s}

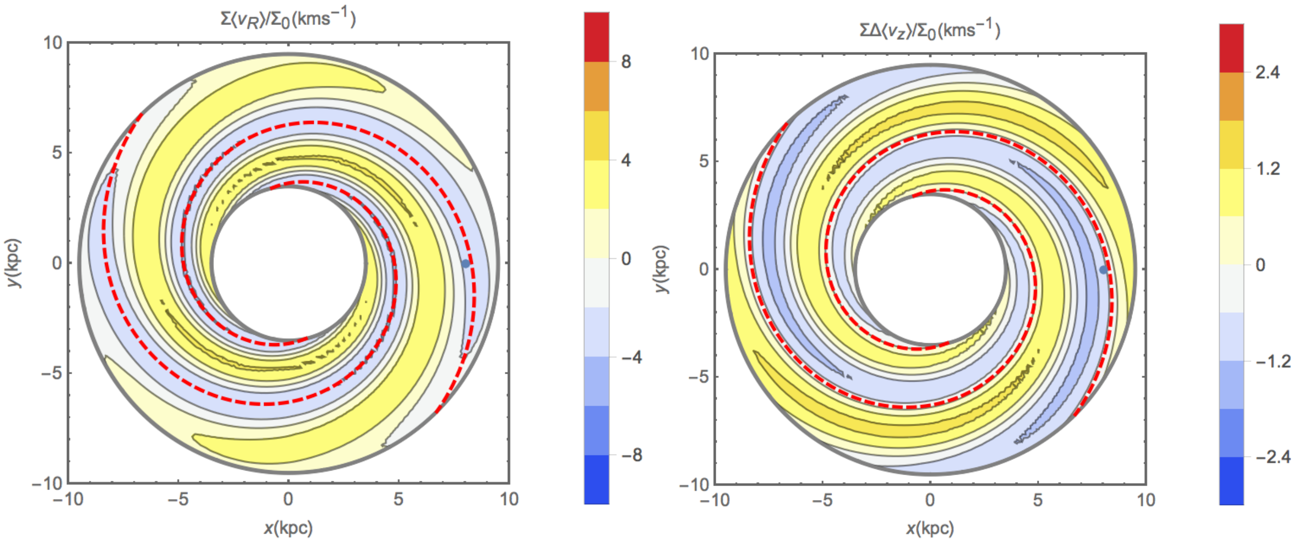

Fig. 1. Mean motions in the Galactic plane caused by 3D spiral arms. Left: mean radial velocity. Right: breathing mode. From Monari et al. (2016).

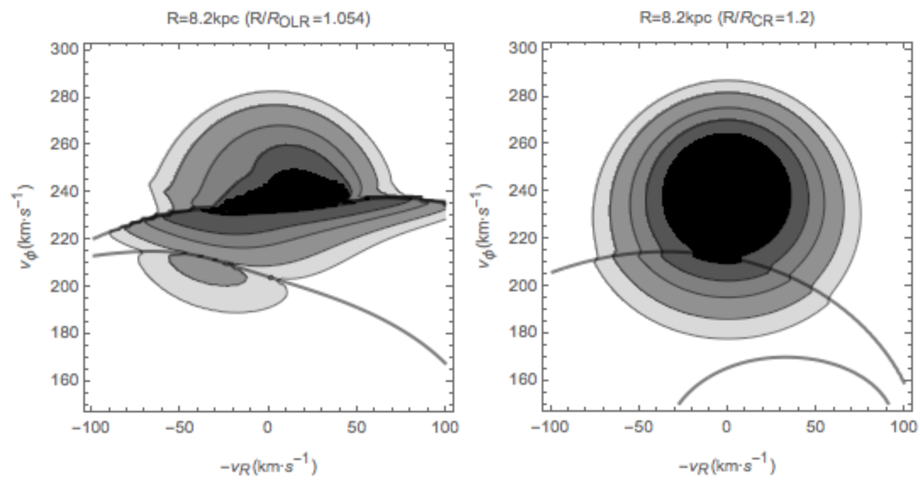

Fig. 2. Velocity distribution functions for stars nearby the Sun for models with fast and slow pattern speed bar and a flat circular velocity curve. The thick lines correspond to zones of trapping to the resonances. Left: $\Omega_\mathrm{b} = 1.8\Omega_0$, nearby outer Lindblad resonance. Right: $\Omega_\mathrm{b} = 1.2\Omega_0$, nearby corotation. From Monari et al. (2017).

where $\Omega_\mathrm{s}(J_\mathrm{s}, J_\mathrm{f}) = 0$. Expanding the averaged Hamiltonian in J_s around $J_\mathrm{s,res}$ near the resonances one obtains a one-dimendional *pendulum* Hamiltonian for the evolution of θ_s. Depending on the energy of the pendulum, this can 'circulate' or 'librate'. In the second case the orbit is trapped to a resonance.

At this point, one needs a second canonical transformation, from the slow angle and action to the actual *pendulum* action and angle $(J_\mathrm{p}, \theta_\mathrm{p})$, to express the DF for trapped orbits as $f_\mathrm{tr}(J_\mathrm{f}, J_\mathrm{p})$. Assuming that the perturbation has been present long enough for phase-mixing the pendulum orbits, a natural choice for f_tr is given byBinney (2016):

$$f_\mathrm{tr}(J_\mathrm{f}, J_\mathrm{p}) = \frac{1}{2\pi}\int_0^{2\pi} f_0(J_\mathrm{f}, J_\mathrm{s}(J_\mathrm{p}, \theta_\mathrm{p}))\mathrm{d}\theta_\mathrm{p} \qquad (3.2)$$

where f_0 is the unperturbed DF. In Monari et al. (2017) this method has been applied to study the signature of the bar perturbation on the velocity distribution of stars in the Solar neighbourhood (see Fig. 2).

4 Conclusion

The best way to extract physical information from the Gaia data is to construct action-based dynamical models of the Milky Way. However, it is necessary to take into account the non-axisymmetries in the models and this can be done through perturbation theory. The relevant formalism and methods can be found in Monari et al. (2016) and Monari et al. (2017) and they are also summarised here. In particular, Monari et al. (2016) show how we can linearize the collisionless Boltzman equation away from the resonances and solve it using the using action and angle variables of the unperturbed system. On can in this way evaluate the streaming motions caused by the non-axisymmetries, like the radial velocity gradients and vertical breathing modes caused by spiral arms, similar to those observed in the Solar neighbourhood. Monari et al. (2017) show how a Lagrangian approach allows to describe the DFs for stars trapped at resonances with the perturber, where the Eulerian linear treatment diverges. In this case the motion is described by pendulum action-angle variables and the DF is found averaging the unperturbed distribution function over the pendulum angle. Moreover, the connection with the deformed tori outside of the trapping region is smooth.

Future work on these models will require to move away from the epicyclic approximation to approximate the angle and action variables, and use more general estimates that can take into account eccentric orbits. Other challenges for these models include their extension to the time-dependence of the amplitude of perturbations and to collective effects.

References

Binney, J. 2016, MNRAS, 462, 2792

Binney, J. & Tremaine, S. 2008, Galactic Dynamics: Second Edition (Princeton University Press)

Cole, D. R. & Binney, J. 2017, MNRAS, 465, 798

Dehnen, W. 1998, AJ, 115, 2384

Famaey, B., Jorissen, A., Luri, X., et al. 2005, A&A, 430, 165

Fouvry, J.-B., Binney, J., & Pichon, C. 2015, ApJ, 806, 117

Monari, G., Famaey, B., Fouvry, J.-B., & Binney, J. 2017, MNRAS, 471, 4314

Monari, G., Famaey, B., & Siebert, A. 2016, MNRAS, 457, 2569

Siebert, A., Famaey, B., Minchev, I., et al. 2011, MNRAS, 412, 2026

Williams, M. E. K., Steinmetz, M., Binney, J., et al. 2013, MNRAS, 436, 101

SF2A 2017
C. Reylé, P. Di Matteo, F. Herpin, É. Lagadec, A. Lançon, Z. Meliani, F. Royer (eds)

SECULAR EVOLUTION OF MILKY WAY-TYPE GALAXIES

F. Combes[1]

Abstract. The internal evolution of disk galaxies like the Milky Way is driven by non-axisymmetries (bars) and the implied angular momentum transfer of the matter; baryons are essentially driven inwards to build a more concentrated disk. This mass concentration may lead to the decoupling of a secondary bar, since the orbit precessing frequency is then much enhanced. Vertical resonances with the bar will form a box/peanut bulge on a Gyr time-scale. Gas flows due to gravity torques can lead to a young nuclear disk forming stars, revealed by a σ-drop in velocity dispersion. These gas flows moderated by feedback produce intermittent accretion onto the super-massive black hole, and cycles of AGN activity. The fountain effect due to nuclear star formation may lead to inclined, and even polar nuclear disks.

Keywords: The Galaxy, secular evolution, bulge, disk, gas flows

How do we define secular evolution? It is the slow and internal evolution of a galaxy, which can be fueled by long-term gas accretion from cosmic filaments, as opposed to any violent evolution, in galaxy mergers or through interactions with a galaxy cluster. At least three types of galaxy formation and evolution schemes can be considered: (i) the monolithic scenario, in which the gas collapses and forms stars in a time shorter than the time-scale for clouds to collide and flatten into a disk; this forms a spheroidal galaxy, or a bulge that can later accrete gas to form a disk; (ii) the hierarchical scenario in which the gas flattens in disks before forming stars, leading to disky galaxies, and their interaction/merger with random angular momentum leads to the formation of spheroids; (iii) a scenario that is just a branching of (ii) in low-density environments, when mergers are rare, and the galaxy disks evolve internally to form boxy bulges from their own disk stars.

1 Two kinds of bulges, classical and pseudo (box/peanut)

Classical bulges are generally the result of major mergers, with unaligned spins: the remnant is not flattened and has little rotation. Its light profile has a Sersic index n=4 or higher. In minor mergers, disks are more easily conserved, while the classical bulge grows.

During secular evolution, bars and vertical resonances elevate stars in the inner parts into a pseudo-bulge: a component intermediate between a spheroid and a disk (Combes & Sanders 1981). It is flattened, rotating, and has an exponential light profile (n$\sim$1). Pseudo-bulges are more frequent in late-type galaxies.

Clumpy galaxies at high redshift can also form a classical bulge, through dynamical friction of the massive clumps against dark matter. The formation of classical bulges is favored, and this makes it even more difficult to form bulgeless galaxies. Observations tell us that the majority of late-type galaxies have no or little bulge today (Kormendy & Fisher 2008, Weinzirl et al 2009).

The fraction of pseudo-bulges has been quantified recently by Fisher & Drory (2016), as a function of stellar mass: classical bulges begin to dominate only for stellar masses larger than 5 10^{10} $M_\odot$. The impact of environment is important: there exists half less pseudo-bulges in centrals with respect to satellites and field galaxies (Mishra et al. 2017).

From HST images at high redshift (Goods-South) it was possible to decompose galaxies into disks and bulges, and distinguish pseudo and classicals (Sachdeva et al. 2017). Although pseudo bulges have masses about half that of classicals, both bulges double in mass since z$\sim$1: the mass fraction increases from 10 to 26%

[1] Observatoire de Paris, LERMA, Collège de France, CNRS, PSL, Sorbonne University UPMC, F-75014, Paris, France

for the pseudo, and from 21 to 52% for the classicals. This points towards secular evolution with at most minor mergers.

It might not be as easy to separate the formation of the two kinds of bulges, since the dynamical evolution implies an angular momentum transfer with the bar, ending with a spin-up of the classical bulge (Saha et al. 2012). This is particularly important for low-mass classicals, but also for higher masses (Saha et al. 2016).

2 Angular momentum transfer

Cold disks form by transferring angular momentum (AM) outwards. Bars, as negative AM waves, are amplified in the process. Stars exchange AM only at resonances (unless the potential is varying). The stars emit AM at ILR, absorb at CR and OLR (Lynden-Bell & Kalnajs 1972). The AM is also absorbed by the dark matter halo (Athanassoula 2002).

During bar growth, more and more particles are trapped along the bar, and their orbits are more elongated; the bar pattern speed Ω_b slows down, and the corotation moves outwards, the bar is longer in the disk.

When gas is present in the disk, it feels the gravity torques from the bar. It is driven inwards from CR, gives its AM to the bar, which weakens the bar (Bournaud & Combes 2002). When disks are refilled with gas and become more massive, they can reform a bar with higher Ω_b (shorter bars).

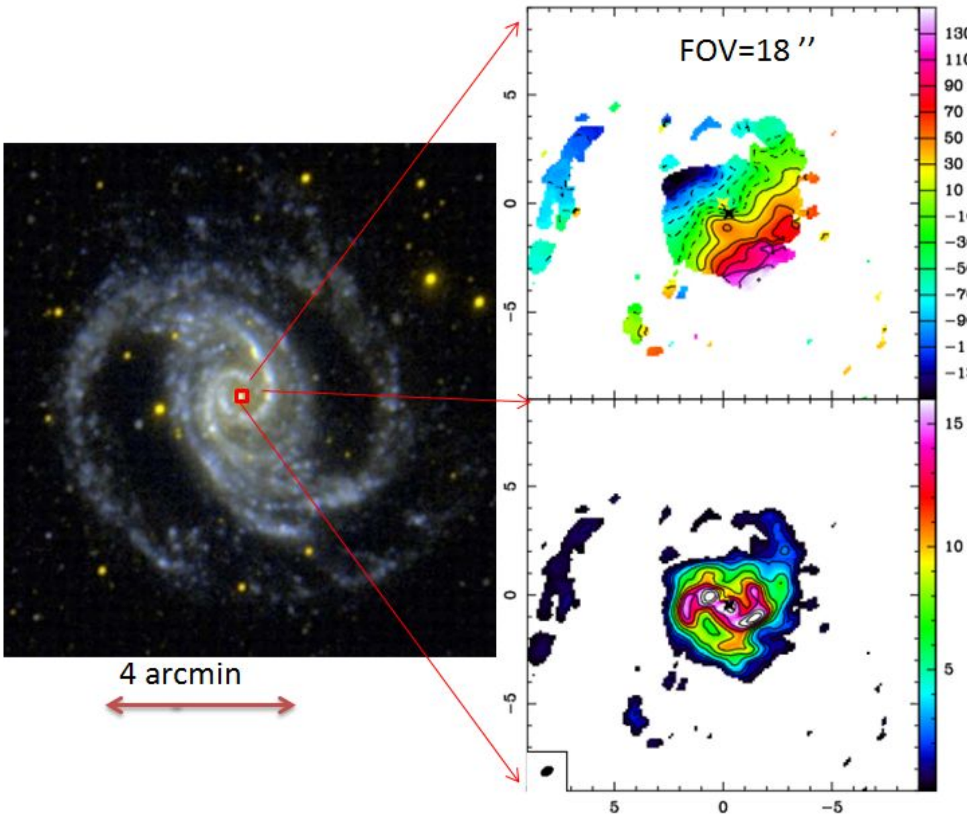

Fig. 1. ALMA CO(3-2) observations of NGC 1566 (Combes et al. 2014). The field of view of the central molecular density and velocity map is 800 pc, corresponding to the small red square in the left GALEX image. Note the conspicuous trailing nuclear spiral structure, causing the gas to fuel the Seyfert 1 nucleus.

2.1 Decoupling of a secondary bar

When the bar has slowed down and there exist two ILR, the orbits become perpendicular (x2) to the bar in between the two ILR and do not sustain the bar anymore. This produces the decoupling of a new faster bar inside the oILR ring. The z-resonance and the formation of the peanut also contribute to a weakening of the inner primary bar. The gravity torques of the second bar drive the gas to the center, forming a cool nuclear disk with young stars, which might be observed through a σ-drop, i.e. a dip in the stellar velocity dispersion (Emsellem et al. 2001, Wozniak et al 2003).

New simulations of σ-drops have been done recently (Portaluri et al. 2017; Di Matteo et al., in preparation) including spectral synthesis modelling, and chemical tagging. They show clearly that the drop is seen in luminosity-weighted images.

Embedded bars are observed in about 30% of all barred galaxies. It is also possible to form long-lived two-bar galaxies, with no resonance in common, no mode coupling (Wozniak 2015). The star formation in the gas stabilises the nuclear bar. Also the nuclear bar could form first, in an inside-out two bar formation scenario (Du et al. 2015), in clumpy high-z galaxies.

2.2 Bar gravity torques

There exists a weak correlation between bars and AGN (Schawinski et al. 2010, Cardamone et al. 2011) and certainly bars help to drive gas to the nuclear region by their gravity torques. But the situation is complex, and depends on the various time-scales.

In a survey of 20 nearby Seyferts, we have been able to compute the torques exerted by bars on the gas distribution, obtaining the gravitational potential from HST red images (NUGA project). At the scale of 10-100 pc, at which the molecular gas maps were obtained, the statistics of fueling are not high: only 35% of negative torques were measured in the center (e.g. Garcia-Burillo & Combes 2012). The rest of the times, the torques are positive, and the gas is stalled in resonant rings. The fueling phases are short, a few 10^7 yrs, maybe due to feedback. There is also star formation fueled by the torques, always associated to AGN activity, but with longer time-scales.

Embedded non-axisymmetries will occur at smaller scales to control gas accretion. Zoomed simulations of gas accretion onto a central black hole have revealed a cascade of m=2, m=1 perturbations (Hopkins & Quataert 2011), providing an intermittent inflow rate. When the gas fraction is high, the nuclear disk is unstable against warps, bending, and forms clumps, sensitive to dynamical friction, which will drive gas inwards.

High resolution (22pc) ALMA observations have been able to measure gravity torques even further towards the center. In the barred spiral NGC 1433, a second resonant ring has been discovered at 200 pc, at the ILR of the nuclear bar (Combes et al. 2013). But the torques are positive inside, and the gas is piling up at this second ring (Smajic et al. 2014). There is also a molecular outflow on the minor axis, due to the AGN feedback. This is a weak outflow of 100 km/s in velocity, and dragging 7% of the molecular gas mass.

The case of the nearby Seyfert type 1 galaxy NGC1566 is different: trailing nuclear spiral arms have been discovered within 100pc around the black hole, torques are negative, fueling the nucleus (cf Figure 1). This is due to the gravitational impact of the black hole, since the gas enters its radius of influence.

In a high-resolution simulation meant to approach the MW, peculiar hydrodynamical processes have been revealed in the central 200 pc region (Renaud et al. 2016, Emsellem et al. 2015). When sufficient gas has accumulated near the center, it becomes unstable, fragments and forms stars. Through strong supernovae feedback and its fountain effect, the gas is projected above the plane, and falls back to settle in a polar disk around the black hole (cf Figure 2).

3 Summary

Secular evolution is the dominant scenario in Milky-Way type galaxies in the second part of the age of the Universe. A stellar bar favors mass concentration, and through vertical resonance, elevates stars to form a box/peanut bulge. Primary bars drive gas from 10 kpc-scale to R $\sim$100 pc, then nuclear bars continue from 100 pc to 10 pc. Young nuclear disks are revealed by σ-drops in their velocity dispersion. The mass concentration, and inward gas flows fuel nuclear starbursts and AGN. At scales $\sim$1-10 pc, viscous turbulence, clumps, disk warps and bending, take over to fuel the super-massive black hole. The process is intermittent, moderated by feedback and gas outflows.

References

Athanassoula, E. 2002, ApJ, 569, L83

Bournaud, F., Combes, F. 2002, A&A 392, 83

Cardamone, C. N., Schawinski, K., Masters, K., Lintott, C., Fortson, L. 2011, AAS 21820603

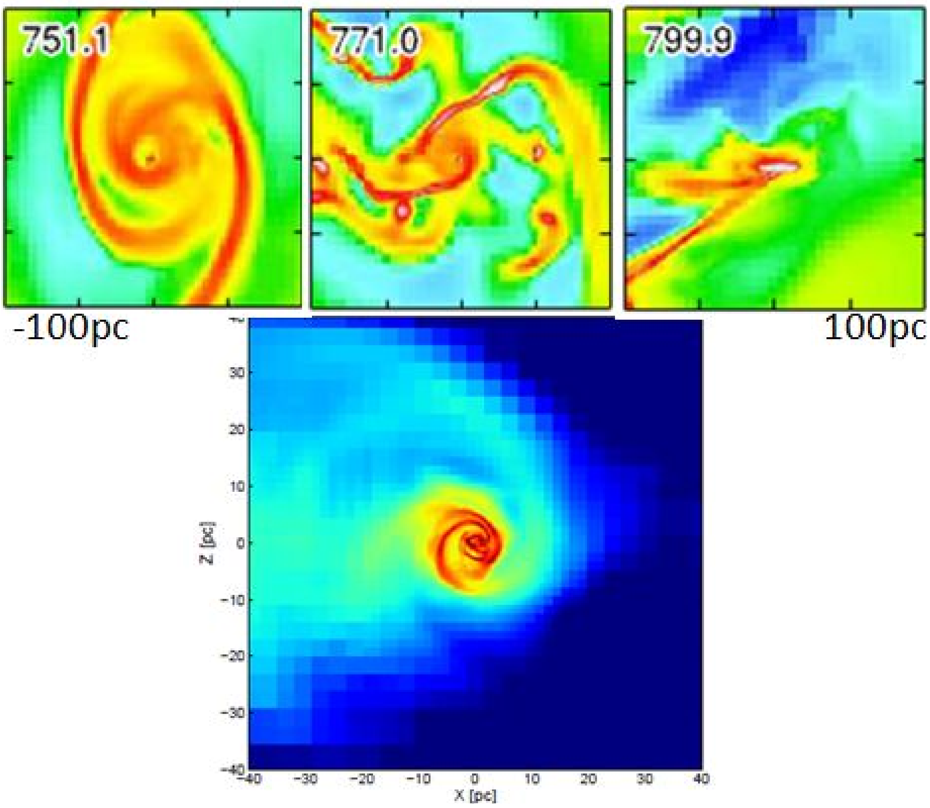

Fig. 2. Top: Three snapshots of the gas in a MW-like galaxy simulation with AMR (from Renaud et al. 2016). This is the face-on view, but the last snapshot reveals a perpendicular gas configuration (200 pc box). **Bottom:** Edge-on view of the center (80 pc box), where the gas now appears face-on, since it forms a polar nuclear disk around the black hole.

Combes, F., Sanders, R. H. 1981, A&A 96, 164
Combes, F., Garcia-Burillo, S., Casasola, V. etal. 2013 A&A, 558, A124
Combes, F., Garcia-Burillo, S., Casasola, V. etal. 2014 A&A, 565, A97
Du, M., Shen, J., Debattista, V. P. 2015, ApJ 804, 139
Emsellem, E., Greusard, D., Combes, F. et al. 2001, A&A 368, 52
Emsellem, E., Renaud, F., Bournaud, F., Elmegreen, B., Combes, F., Gabor, J. M. 2015, MNRAS 446, 2468
Fisher, D. B., Drory, N. 2016, Astr. Space Science, 418, 41
Garcia-Burillo, S. Combes, F. 2012, JPhCS 372, a2050
Hopkins, P. F., Quataert, E. 2011, MNRAS 415, 1027
Kormendy, J., Fisher, D. B. 2008, ASP Conf 396, 297
Lynden-Bell, D., Kalnajs, A. J. 1972, MNRAS 157, 1
Mishra, P. K., Wadadekar, Y., Barway, S. 2017, MNRAS, 467, 2384
Portaluri, E., Debattista, V. P., Fabricius, M. et al. 2017, MNRAS 467, 1008
Renaud, F., Bournaud, F., Emsellem, E., et al. 2016, MNRAS 463, 251
Sachdeva, S., Saha, K., Singh, H. P. 2017, ApJ 840, 79
Saha, K., Martinez-Valpuesta, I., Gerhard, O. 2012, MNRAS, 421, 333
Saha, K., Gerhard, O., Martinez-Valpuesta, I. 2016, A&A 588, A42
Schawinski, K., Urry, C. M., Virani, S. et al. 2010, ApJ 711, 284
Smajic, S., Moser, L., Eckart, A. et al. 2014, A&A 567, A119
Weinzirl, T., Jogee, S., Khochfar, S., Burkert, A., Kormendy, J. 2009, ApJ 696, 411
Wozniak, H., Combes, F., Emsellem, E., Friedli, D. 2003, A&A 409, 469
Wozniak, H. 2015, A&A 575, A7

Session 05

Habitability in low-mass star planetary systems

SF2A 2017
C. Reylé, P. Di Matteo, F. Herpin, É. Lagadec, A. Lançon, Z. Meliani, F. Royer (eds)

REPERCUSSIONS OF THERMAL ATMOSPHERIC TIDES ON THE ROTATION OF TERRESTRIAL PLANETS IN THE HABITABLE ZONE

P. Auclair-Desrotour[1], S. Mathis[2,3] and J. Laskar[4]

Abstract. Semidiurnal atmospheric thermal tides are important for terrestrial exoplanets in the habitable zone of their host stars. With solid tides, they torque these planets, thus contributing to determine their rotation states as well as their climate. Given the complex dynamics of thermal tides, analytical models are essential to understand its dependence on the structure and rotation of planetary atmospheres and the tidal frequency. In this context, the state of the art model proposed in the 60s by Lindzen and Chapman explains well the properties of thermal tides in the asymptotic regime of Earth-like rapid rotators but predicts a non-physical diverging tidal torque in the vicinity of the spin-orbit synchronization. In this work, we present a new model that addresses this issue by taking into account dissipative processes through a Newtonian cooling. First, we recover the tidal torque recently obtained with numerical simulations using General Circulation Models (GCM). Second, we show that the tidal response is very sensitive to the atmospheric structure, particularly to the stability with respect to convection. A strong stable stratification is able to annihilate the atmospheric tidal torque, leading to synchronization, while a convective atmosphere will be submitted to a strong torque, leading to a non-synchronized rotation state.

Keywords: hydrodynamics – waves – convection – planet-star interactions – planets and satellites: dynamical evolution and stability

1 Introduction

The dynamics of planetary systems over long times scales is tightly related to mutual interactions between their bodies, and particularly tides (e.g. Mathis & Remus 2013). Tides affect the rotation of planets, their distance to the star, and can generate a strong tidal heating, which is able to modify significantly the surface equilibrium of planets as observed for instance on the Jupiter's satellite Io (Lainey et al. 2009). Therefore, with the continuously growing number of discovered terrestrial planets orbiting in the habitable zone of their host stars, it is today crucial to understand physically the role played by tides for planetary dynamics. In this work, we focus on thermal atmospheric tides, namely tides generated by the stellar heating of a planetary atmosphere. These tides are of great importance for terrestrial planets close to spin-orbit synchronization because they are able to torque them *away* from this equilibrium state, in opposition to gravitationally excited tides. Typically, in the Solar system, they contribute to lock Venus at a non-synchronized rotation rate where the solid and atmospheric tidal torques exactly balance each other (Gold & Soter 1969; Dobrovolskis & Ingersoll 1980; Correia & Laskar 2001). In the absence of atmospheric tides, Venus would be today synchronized owing to the relatively small evolution timescales associated with gravitational tides. Hence, considering both the potential number of Venus-like terrestrial planets among the exoplanets discovered during the last decade and the impact that the rotation of a planet has on its atmospheric general circulation and climate, it is necessary to

[1] LAB, Université de Bordeaux, CNRS UMR 5804, Université de Bordeaux - Bt. B18N, Allée Geoffroy Saint-Hilaire CS50023, 33615 Pessac Cedex, France
[2] Laboratoire AIM Paris-Saclay, CEA/DRF - CNRS - Université Paris Diderot, IRFU/DAp Centre de Saclay, F-91191 Gif-sur-Yvette Cedex, France
[3] LESIA, Observatoire de Paris, PSL Research Université, CNRS, Sorbonne Université, UPMC Univ. Paris 6, Univ. Paris Diderot, Sorbonne Paris Cité, 5 place Jules Janssen, F-92195 Meudon, France
[4] IMCCE, Observatoire de Paris, CNRS UMR 8028, PSL Research University, 77 Avenue Denfert-Rochereau, 75014 Paris, France

understand the dependence of the atmospheric tidal response on the physical properties of planetary atmosphere and the tidal frequency.

This question was addressed recently in a numerical way by Leconte et al. (2015), who used a General Circulation Model (GCM) to compute the atmospheric tidal torque. However, this approach is limited by the high computational cost of numerical simulations that do not yet allow to explore a broad domain of the parameters space. The classical theory of atmospheric tides (see e.g. Chapman & Lindzen 1970) offers an elegant analytic approach where the tidal response is treated as a linear perturbation and written as an explicit function of the atmospheric parameters. This approach, which ignores dissipative effects, explains well the Earth's atmospheric tides and more generically the case of rapid rotators. However, it has to be adapted to the case of slowly rotating planets where dissipative processes cannot be neglected any more. Thus, we adopt in this study the linear approach and generalize it to slowly rotating planets by introducing a Newtonian cooling. We compute the tidal response and the corresponding semidiurnal tidal torque first using a global modeling, second with a local Cartesian one. We show how the atmospheric structure affects the tidal torque through the stability of stratification of the fluid with respect to convection. We provide here the main lines of results, which are detailed in Auclair-Desrotour et al. (2017a), Auclair-Desrotour et al. (2017b) and Auclair-Desrotour et al. (2017c).

2 Physical setup

We consider a spherical terrestrial planet rotating at the spin angular velocity Ω and orbiting its host star at the orbital frequency $n_{\rm orb}$ (see Fig. 1, left panel). In the absence of perturbation, the fluid is supposed to be at the hydrostatic equilibrium and radially stratified (background distributions only depend on the vertical coordinate r). The stratification of the atmosphere with respect to convection is characterized by the Brunt-Väisälä frequency given by

$$N^2 = -g \left[\frac{d \ln \rho_0}{dr} - \frac{1}{\Gamma_1} \frac{d \ln p_0}{dr} \right], \tag{2.1}$$

where g designates the gravity, Γ_1 the adiabatic exponent, and p_0 and ρ_0 pressure and density background distributions respectively. Taking into account radiative losses through a Newtonian cooling introduces an additional frequency σ_0, which is the inverse of the thermal timescale. Finally, owing to the compressibility of the fluid, the gravest horizontally propagating Lamb modes can be excited if the forcing frequency σ is greater than the characteristic acoustic cutoff frequency $\sigma_{\rm s}$. Hence, the hierarchy of the characteristic frequencies σ_0, 2Ω, N, $\sigma_{\rm s}$ and σ fully determines the nature of the tidal response and which kind of waves it is composed of (see Fig. 1, right panel): i.e. inertial, gravity and acoustic waves damped by radiative cooling.

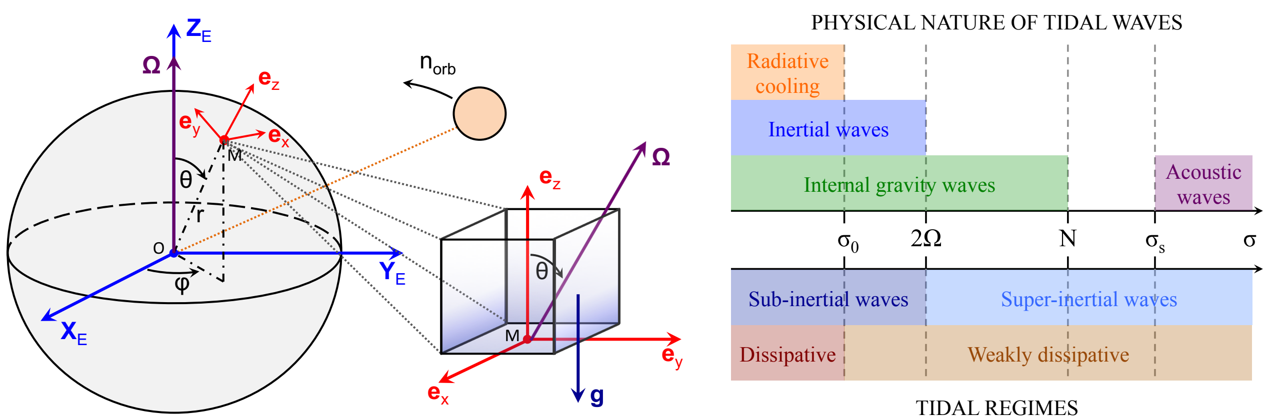

Fig. 1. Left: Spherical and Cartesian reference frames and systems of coordinates. The vectors $\mathbf{\Omega}$ and $\mathbf{g}$ designate the rotation and the gravity respectively. The notation $n_{\rm orb}$ refers to the orbital frequency of the star in the reference frame of the planet. **Right:** Frequency spectrum of tidal regimes and waves characterizing the atmospheric tidal response. The parameter σ designates the forcing frequency, 2Ω the inertia frequency, N the Brunt-Väisälä frequency, and $\sigma_{\rm s}$ the characteristic acoustic cutoff frequency.

Two types of models are used:

- Global model in spherical geometry. The background atmospheric structure only depends on the radial coordinate. We assume the *traditional approximation*, which filters out the components of the Coriolis acceleration related to the latitudinal projection of the rotation vector (we refer the reader to Auclair-Desrotour et al. 2017a, for a complete discussion).

- Local model constituted by a Cartesian local fluid section of the atmosphere (Fig. 1, left panel) (Auclair-Desrotour et al. 2017c). we assume the *f-plane* and *anelastic approximations* (where acoustic waves are filtered out). In this model, the complete Coriolis acceleration is taken into account.

3 Thermally generated atmospheric tidal torque

3.1 Global model

In Auclair-Desrotour et al. (2017a), we compute for two different atmospheric structures the tidal torque exerted on the atmosphere caused by the quadrupolar component of the thermally excited semidiurnal tide. The first structure corresponds to an isothermal atmosphere, where $N \gg \sigma$. It is strongly stably stratified with respect to convection. The second structure is an isentropic profile of temperature, which is such that $N = 0$ and thus enforces a neutral stratification. The tidal torques that we obtain in these two cases are plotted on Fig. 2 as functions of the normalized tidal frequency $\omega = (\Omega - n_{\rm orb}) / n_{\rm orb}$ using for parameters a set of values derived from the Venus case. As can be seen, we recover in the neutral stratification case the tidal torque obtained by Leconte et al. (2015) with GCM simulations for Venus. The observed behaviour corresponds to that described by the Maxwell model: a global tidal bulge follows the perturber with a delay depending of the thermal inertia of the atmosphere. In the other case, the strong stable stratification of the atmosphere prevents a net tidal bulge to form, a local density decrease being immediately compensated by the motion of denser fluid particles driven upward by the Archimedean force. As a consequence, the tidal torque is very weak and cannot balance the solid torque as in the neutral case.

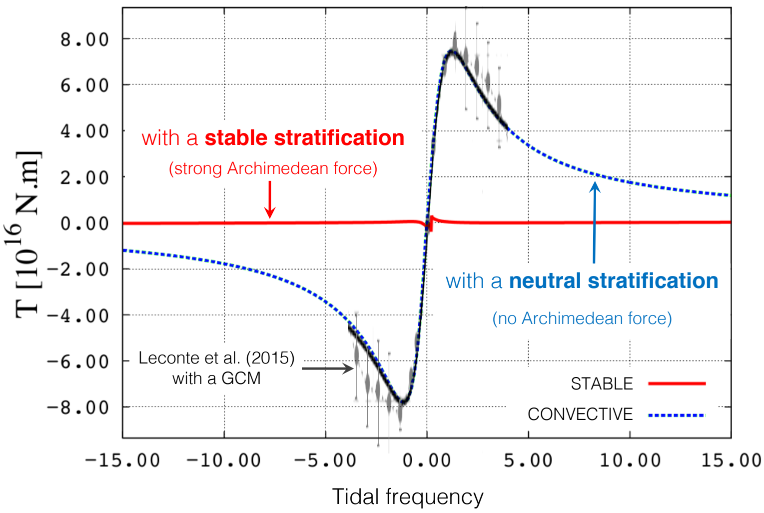

Fig. 2. Tidal torque given by the global model as a function of the tidal frequency $\omega = (\Omega - n_{\rm orb})$ for two different atmospheric structure: stably-stratified (red solid line) and neutrally-stratified (blue solid line) with respect to convection. For comparison, the shape of the tidal torque obtained by Leconte et al. (2015) using a GCM is plotted in addition to the two previous cases. Grey dots correspond to numerical simulations, the black solid line to a fit of these results with a Maxwell model.

3.2 Local model

The local model allows us to refine the diagnosis made with the global approach. Considering a planar wave propagating along the longitudinal direction, we obtain for the associated tidal torque the expression

$$\mathcal{T} = 2\sigma_0 \Im \left\{ \frac{i}{\sigma - i\sigma_0} \left[1 - \nu - \frac{\nu}{1 - K(\sigma, k_z)} \right] \right\}, \tag{3.1}$$

where $i^2 = -1$, $\Im$ is the imaginary part of a complex number, ν a function of the physical parameters of the system (forcing frequency, Brunt-Väisälä frequency, spin angular velocity, thermal frequency, colatitude, pressure height scale, horizontal wavenumber), and K a function of the forcing frequency σ and vertical wavenumber k_z of the associated tidal wave, which characterizes the contribution of internal gravity waves to the tidal torque. On the one hand, in the low-frequency range ($\sigma \to 0$), $\nu \to 0$ in the case of a neutrally-stratified atmosphere, leading to the Maxwell model identified previously. On the other hand, $\nu \to 1$ and $|K| \to +\infty$ in the stably-stratified case, which implies $\mathcal{T} \approx 0$. This suggests that the rotation rate of the planet will tend towards a *non-synchronized* state of equilibrium in the neutrally-stratified case and towards the spin-orbit synchronous rotation rate in the stably-stratified one. This is illustrated by Fig. 3 (right panel) where the normalized tidal frequency (ω) of a Venus-like terrestrial planet is plotted as a function of time for different atmospheric stratifications using Eq. (3.1) for the atmosphere and a constant tidal quality factor for the solid part of the planet.The corresponding atmospheric tidal torques are plotted as a function of ω (left panel).

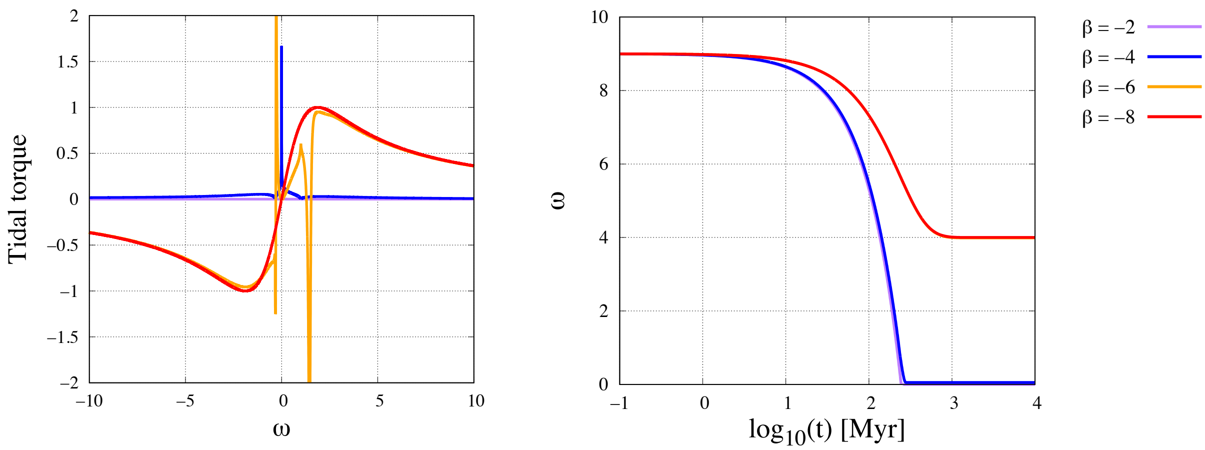

Fig. 3. Left: Tidal torque given by the local Cartesian model as a function of the frequency of the perturber $\omega = (\Omega - n_{\rm orb})/n_{\rm norb}$ for various values of the Brunt-Väisälä frequency from weak to strong stable stratification, i.e. $\beta = \log(N) = \{-8, -6, -4, -2\}$. The tidal torque is computed using Eq. (3.1). It is normalized by the maximum value of the torque of the convective case ($\beta = -8$). **Right:** Evolution of the rotation rate of a Venus-like planet for the same Brunt-Väisälä frequencies. The normalized frequency $\omega = (\Omega - n_{\rm orb})/n_{\rm orb}$ is plotted as a function of time (Myr) in logarithmic scale. The value $\omega = 0$ corresponds to spin-orbit synchronous rotation.

4 Conclusions

Motivated by the understanding of the role played by atmospheric tides in the evolution of the rotation rate of terrestrial planets, we computed the tidal torque generated by the thermally excited semidiurnal tide analytically by using an ab initio linear global model. We recovered the behaviour previously obtained with numerical simulations using GCMs, which corresponds to that described by the so-called Maxwell model. We showed evidence that the tidal response strongly depends on the structure and stability of the atmosphere through its stratification with respect to convection. In a second step, we explored this dependence by using a local Cartesian model, showing that it is determined by the hierarchy of characteristic frequencies of the system. We established the continuous transition between the stably and neutrally stratified cases, which lead to synchronized and non-synchronized rotation states of equilibrium respectively.

The authors acknowledge funding by the European Research Council through the ERC grants WHIPLASH 679030 and SPIRE 647383, and the PLATO CNES funding at CEA/IRFU/DAp.

References

Auclair-Desrotour, P., Laskar, J., & Mathis, S. 2017a, A&A, 603, A107

Auclair-Desrotour, P., Laskar, J., Mathis, S., & Correia, A. C. M. 2017b, A&A, 603, A108

Auclair-Desrotour, P., Mathis, S., & Laskar, J. 2017c, ArXiv e-prints

Chapman, S. & Lindzen, R. 1970, Atmospheric tides: Thermal and gravitational. Reidel.

Correia, A. C. M. & Laskar, J. 2001, Nature, 411, 767

Dobrovolskis, A. R. & Ingersoll, A. P. 1980, Icarus, 41, 1

Gold, T. & Soter, S. 1969, Icarus, 11, 356

Lainey, V., Arlot, J.-E., Karatekin, Ö., & van Hoolst, T. 2009, Nature, 459, 957

Leconte, J., Wu, H., Menou, K., & Murray, N. 2015, Science, 347, 632

Mathis, S. & Remus, F. 2013, in Lecture Notes in Physics, Berlin Springer Verlag, Vol. 857, Lecture Notes in Physics, Berlin Springer Verlag, ed. J.-P. Rozelot & C. . Neiner, 111–147

SF2A 2017
C. Reylé, P. Di Matteo, F. Herpin, É. Lagadec, A. Lançon, Z. Meliani, F. Royer (eds)

TOWARDS A BETTER UNDERSTANDING OF TIDAL DISSIPATION AT COROTATION LAYERS IN DIFFERENTIALLY ROTATING STARS AND PLANETS

A. Astoul[1], S. Mathis[1], C. Baruteau[2] and Q. André[1]

Abstract. Star-planet tidal interactions play a significant role in the dynamical evolution of close-in planetary systems. We investigate the propagation and dissipation of tidal inertial waves in a stellar/planetary convective region. We take into account a latitudinal differential rotation for the background flow, similar to what is observed in the envelope of low-mass stars like the Sun. Previous works have shown that differential rotation significantly alters the propagation and dissipation properties of inertial waves. In particular, when the Doppler-shifted tidal frequency vanishes in the fluid, a critical layer forms where tidal dissipation can be greatly enhanced. Our present work develops a local analytic model to better understand the propagation and dissipation properties of tidally forced inertial waves at critical layers.

Keywords: Hydrodynamics – Waves – Planet-star interactions – Planets and satellites : dynamical evolution and stability – Stars : rotation

1 Introduction

The study of tides and especially of tidal dissipation is essential to understand the secular evolution of planetary systems. Inertial waves, which are tidally excited in convective zones, carry and deposit energy and angular momentum in the envelope of low-mass stars. This dissipation can be modified by the internal dynamics of the convective envelope like differential rotation as pointed out by Baruteau & Rieutord (2013) and Guenel et al. (2016a). In a uniformly rotating fluid body, Favier et al. (2014) have also shown that differential rotation arises from non-linear evolution of inertial waves excited by tides. In the solar convective envelope, the rotation rate depends mostly on the colatitude with a difference in rotation rate of $\sim 30\%$ between the equator and the pole (e.g. García et al. 2007). Guenel et al. (2016a) and Guenel et al. (2016b), following the work of Baruteau & Rieutord (2013), examined the viscous dissipation of tidally excited inertial waves for conical solar and anti-solar rotation profiles. They found that differential rotation modifies the characteristics and amplitude of the tidal dissipation particularly at critical layers. Nevertheless, a better physical understanding is required to explain the influence of these layers and the different regimes found in numerical simulations. To reach this objective we develop a new local Cartesian model describing a small fraction of the differentially rotating convective envelope in a low-mass star. This model allows us to focus on small-scale effects, to understand how latitudinal sheared flow impacts the propagation of tidal inertial waves, as well as the role of critical layers.

2 Local Cartesian model for tidal waves propagating in a convective fluid with latitudinal shear

2.1 Presentation of the model and main assumptions

The concept of a local box to study tidal waves has been introduced by Auclair Desrotour et al. (2015) following the work of Ogilvie & Lin (2004). The box is described with a set of local Cartesian coordinates $\{x, y, z\}$ centered on a specific point M of the convective envelope, and is inclined with respect to the star's rotation axis (as illustrated in Fig. 1). The dimensions of our box are taken to be small with respect to the characteristic length scale of the convective envelope, in order to remove curvature effects. The latitudinal shear is embodied

[1] Laboratoire AIM Paris-Saclay, CEA/DRF - CNRS - Université Paris Diderot, IRFU/DAp Centre de Saclay, F-91191 Gif-sur-Yvette, France
[2] IRAP, Université de Toulouse, CNRS, UPS, Toulouse, France

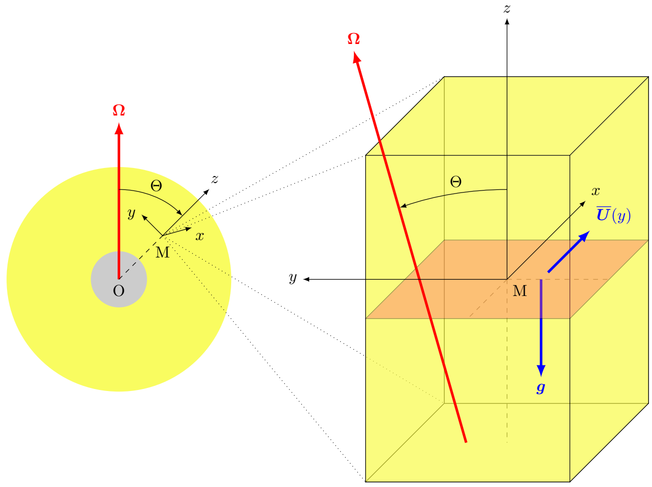

Fig. 1. Left : global view of a solar-like star. The convective envelope, depicted in yellow, lies on top of a stably stratified core (grey area). Right : the local Cartesian box, centered on a point M in the envelope, corresponding to a colatitude Θ. The local box is tilted with respect to the spin axis. Its vertical axis z, corresponding to the local radial direction, is anti-aligned with the gravity $\mathbf{g}$. The x and y axes correspond to the local azimuthal and latitudinal directions, respectively. [Adapted from André, Barker, & Mathis (2017)]

by an azimuthal mean flow velocity, $\overline{\mathbf{U}} = \overline{U}(y)\mathbf{e}_x$. In addition, the uniform rotation vector $\mathbf{\Omega}$ makes an angle Θ with our local vertical axis so that we have $2\mathbf{\Omega} = (0, 2\Omega\sin\Theta, 2\Omega\cos\Theta) = (0, \widetilde{f}, f)$. Moreover, we make the following assumptions :

- we adopt the Boussinesq approximation. Hence, the continuity equation simplifies to $\boldsymbol{\nabla}\cdot\mathbf{u} = 0$, where $\mathbf{u}$ is the local velocity of the fluid.
- we assume that in convective layers, the dissipation is driven by an effective viscous-like turbulent friction $\nu_{\rm eff}$ that leads us to neglect as a first step thermal diffusion (we refer the reader to Fig. 9 in Auclair Desrotour et al. 2015, for a detailed discussion). Furthermore, we simplify the viscous diffusion term $\nu_{\rm eff}\Delta\mathbf{u}$ as a linear (Rayleigh) friction term, which we write as $\sigma_{\rm f}\mathbf{u}$ (Ogilvie 2009) with $\sigma_{\rm f}$ homogeneous to a pulsation.
- the centrifugal acceleration is neglected. This is acceptable for not too fast rotators.
- we carry out a linear analysis, and therefore all quantities associated with the base flow remain unaltered.

2.2 System of equations

At first order, all dynamical quantities can be split into two components, an unperturbed background quantity and a small perturbation. As we study inertial waves we are interested in the dynamical tide. The equations for the perturbations of the hydrostatic balance by the companion are thus treated elsewhere (see e.g. Ogilvie 2013). All perturbed quantities are assumed to be periodic in time and along the local azimuthal axis. As a result, projected on the Cartesian basis, the Navier-Stokes and continuity equations in the rotating frame write:

$$\begin{cases} \Sigma u + \left(\dfrac{\partial \overline{U}}{\partial y} - f\right) v + \widetilde{f} w = -ik_x\Pi + F_x, \\ \Sigma v + f u = -\dfrac{\partial \Pi}{\partial y} + F_y, \\ \Sigma w - \widetilde{f} u = -\dfrac{\partial \Pi}{\partial z} + F_z, \\ ik_x u + \partial_y v + \partial_z w = 0, \end{cases} \tag{2.1}$$

where we define the quantities : $\mathbf{u} = (u, v, w)$ and $\Pi = p/\overline{\rho}$, which stand for the perturbed velocity of the fluid in the box and the local perturbed pressure divided by the mean density, respectively. Moreover, we denote by $\mathbf{F} = (F_x, F_y, F_z)$ the tidal acceleration which operates throughout the fluid. Finally, we have introduced a complex frequency $\Sigma = i\hat{\sigma} + \sigma_f$, with $\hat{\sigma} = \omega + k_x\overline{U}(y)$ the Doppler-shifted frequency, ω the frequency of the excited waves in the inertial frame and k_x the azimuthal wave number.

2.3 *The Poincaré equation*

We solve our set of Equations (2.1) by the substitution method, only keeping the second-order derivatives (i.e. the WKBJ approximation). Consequently, we derive from the system (2.1) the so-called Poincaré equation for tidally forced inertial waves propagating in a latitudinal shear :

$$\underbrace{\left(\Sigma^2 + \widetilde{f}^2\right)}_{\mathcal{A}} \partial_{y,y} v + \underbrace{\widetilde{f}\left(2f - \partial_y \overline{U}\right)}_{\mathcal{B}} \partial_{y,z} v + \underbrace{\left[\Sigma^2 + f(f - \partial_y \overline{U})\right]}_{\mathcal{C}} \partial_{z,z} v = S(x, y, z, t), \tag{2.2}$$

with $S(x, y, z, t)$ the complex source term due to the tidal forcing, which does not depend on the velocity components.

For $\mathcal{A} = \Sigma^2 + \widetilde{f}^2 \neq 0$, we introduce the transformation : $v(x, y, z, t) = \hat{V}(y) \exp\{i(k_{/\!/} z + \delta(y) + k_x x + \omega t)\}$, following Gerkema & Shrira (2005b), where δ satisfies $\frac{\mathrm{d}\delta}{\mathrm{d}y} = -k_{/\!/}\frac{\mathcal{B}}{2\mathcal{A}}$. This allows us to simplify the Poincaré equation (2.2) as :

$$\frac{\mathrm{d}^2\hat{V}}{\mathrm{d}y^2} + \underbrace{\frac{k_{/\!/}}{4\mathcal{A}^2}\left[2i\widetilde{f}\frac{\mathrm{d}^2\overline{U}}{\mathrm{d}y^2}\mathcal{A} - 4\Sigma k_x \frac{\mathrm{d}\overline{U}}{\mathrm{d}y}\mathcal{B} + k_{/\!/}(\mathcal{B}^2 - 4\mathcal{A}\mathcal{C})\right]}_{\kappa(y)^2} \hat{V} = \frac{\hat{S}(y)}{\mathcal{A}}, \tag{2.3}$$

where $S(x, y, z, t)$ has been projected on a basis of orthogonal functions (see Gerkema & Shrira 2005a; Mathis et al. 2014). From a physical point of view, this second-order ordinary differential equation is similar to a Schrödinger equation with a complex potential $\kappa(y)$.

3 The key role of critical layers

We now propose to investigate the solutions to the modified Poincaré equation (2.3) near the points where $\mathcal{A}$ cancels out, to understand waves propagation in the vicinity of such critical layers.

3.1 *The modified Poincaré equation*

In the non-rotating adiabatic case, a singularity is found for $\hat{\sigma} = 0$ (Booker & Bretherton 1967). For a vertical or inclined rotation vector, Jones (1967) and Grimshaw (1975) have shown that a singularity is obtained for $\hat{\sigma} = -2\Omega$, 0 and 2Ω. Because of differential rotation and viscosity, our critical layers are different. For a vanishing viscosity, the singularities are (i) for $\hat{\sigma}^2 = \widetilde{f}^2$, as can be noticed by setting $\mathcal{A} = 0$ in the above Poincaré equation, and (ii) for $\hat{\sigma} = 0$, which can be seen from the polarization relationships (not written here). To expand the Poincaré equation (2.3) near the critical layers $y = y_\mathrm{c}$ corresponding to $\mathcal{A} = 0$, we adopt the method used by Alvan et al. (2013) in the case of internal gravity waves propagating in a fluid with a vertical shear. Taking the Taylor expansion of $\mathcal{A}$ in the vicinity of y_c at first order, we can express the Poincaré equation (2.3) for free inertial waves around critical layers as follows :

$$\hat{V}''(y) + \frac{\chi}{(y - y_\mathrm{c})^2}\hat{V}(y) = 0, \tag{3.1}$$

where the complex variable χ gathers constant quantities evaluated at y_c. It mainly depends on the Rossby number* of the differential rotation $Ro = \overline{U}'(y_\mathrm{c})/(2\Omega)$, and the Ekman number† $E_k = \sigma_\mathrm{f}/(2\Omega)$.

*which evaluates the competition between the shear and the Coriolis acceleration.
†which describes the relative strength of viscous forces and the Coriolis acceleration.

3.2 *Applying the method by Alvan et al. (2013)*

Let us write $\hat{V}(y) = (y - y_c)^r$, where r is an unknown complex number. Injecting this function in Eq. (3.1), we obtain the index equation : $r(r-1) + \chi = 0$. If we consider the case where χ is real, two cases are possible depending on the sign of the discriminant $\Delta = 1 - 4\chi$. The ensuing criterion is similar to the one found by Alvan et al. (2013) involving the Richardson number.

3.2.1 The stable regime

We first look at the case where the discriminant Δ is negative (i.e. $\chi > 1/4$). The solution in the vicinity of y_c is:

$$\hat{V}(y) = \alpha(y - y_c)^{\frac{1}{2}+i\sqrt{\chi-\frac{1}{4}}} + \beta(y - y_c)^{\frac{1}{2}-i\sqrt{\chi-\frac{1}{4}}},$$

with α and β the amplitude of the wave function that can be seen as a combination of upward and downward-propagating waves. In order to know the behaviour of the wave getting across the critical layer, we can reconnect the solution below and above this layer. A wave propagating upward through the critical layer, is attenuated by a factor $\exp\left\{-\pi\sqrt{\chi - \frac{1}{4}}\right\}$ and dephased by an argument $\pi/2$. Likewise a wave propagating in the opposite direction, is attenuated by the same factor and has a phase difference of $-\pi/2$. As a consequence, we identify a stable regime. We plot this coefficient of attenuation in the upper panel of Fig. 2 for different colatitudes. We observe that the attenuation is greater for low Rossby numbers which correspond to fast rotating stars for a given shear, or to weak differential rotation at fixed global rotation. Moreover, at fixed Rossby number, the attenuation is larger for a weak colatitude, that is near the rotation axis.

3.2.2 The unstable regime

If $\chi < 1/4$, the solution near the critical layer is :

$$\hat{V}(y) = A(y - y_c)^{\frac{1}{2}+\sqrt{\frac{1}{4}-\chi}} + B(y - y_c)^{\frac{1}{2}-\sqrt{\frac{1}{4}-\chi}}, \tag{3.2}$$

where A and B are complex coefficients. This regime is unstable since waves can be amplified as we will show in the following discussion. The vicinity of the critical layer is decomposed as a three-zone model (see Alvan et al. 2013; Lindzen & Barker 1985). Zone II is the unstable region of prescribed length 2δ, whereas in the surrounding zones I and III the WKBJ method can be applied. Using the continuity relations between the solutions in these three regions, we are able to determine transmission and reflexion coefficients. We choose the size of zones I and III such that $\chi/(y - y_c)^2$ slowly varies and set its value to $\mathcal{K}_c \simeq \chi/\delta^2$. Furthermore, we consider that a wave going from zone I to zone II can be either reflected, or transmitted to zone III. This leads to the following expression for the wave functions in zones I and III:

$$\begin{cases} \Psi_{\rm I}(y) = \mathrm{e}^{i\mathcal{K}_c(y-y_c)} + R\,\mathrm{e}^{-i\mathcal{K}_c(y-y_c)} \\ \Psi_{\rm III}(y) = T\,\mathrm{e}^{i\mathcal{K}_c(y-y_c)} \end{cases}, \tag{3.3}$$

where R and T are the reflexion and transmission coefficients, respectively. The wave function $\Psi_{\rm I}$ is valid in the domain $y - y_c \gtrsim \delta$ while $\Psi_{\rm III}$ is valid where $y - y_c \lesssim -\delta$. In zone II, we use the solution (3.2). At both interfaces, the continuity relations for the functions Ψ and their derivatives allow us to determine A, B, R and T. We have plotted the coefficients of reflexion and transmision for a fixed Ekman number $E_k = 10^{-9}$ in the lower panel of Fig. 2. We note that for relatively high Rossby numbers, which correspond to slowly rotating stars at fixed shear or to important differential rotation at fixed global rotation, over-transmission or over-reflexion is possible. Therefore the wave can be attenuated or amplified when going across a critical layer as a function of the rotation (and shear) regime.

To summarize, when $\chi > 1/4$, waves are attenuated when going through the critical layer. They transmit their angular momentum to the stable mean flow. Conversely, when $\chi < 1/4$, the unstable mean flow provides energy to the waves allowing over-reflexion or over-transmission.

4 Conclusions

Our results show how critical layers and interactions between tidal and mean flows are crucial to understand tidal dissipation in differentially rotating stars and planets. The simple analysis that we have carried out can

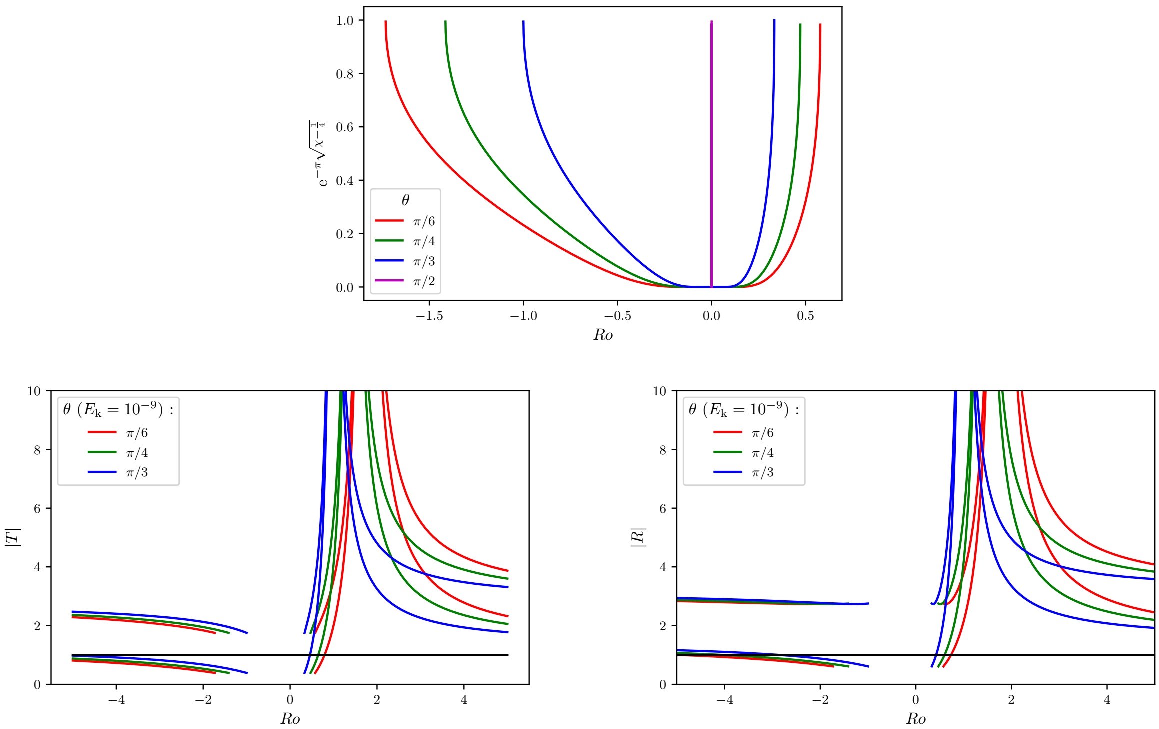

Fig. 2. Top : Attenuation coefficient as a function of the Rossby number for different values of the colatitude Θ. The Ekman number is set to $E_k = 10^{-9}$. **Bottom :** Absolute value of the transmission (left) and reflexion (right) coefficients as a function of the Rossby number. These coefficients are displayed for different colatitudes and for $E_{\rm k} = 10^{-9}$. For each colatitude there are two branches. The solid black line delimits the border between attenuation and over-transmission or over-reflexion. The possible cut in the range about $Ro \in [-1.5, 0.5]$ corresponds to the stable regime for which the attenuation coefficient is shown in the upper panel.

be used to unravel possible regimes that can be observed in direct numerical simulations. The next step will be to consider the feedbacks of the perturbed wave on the mean flow, to introduce the effects of a magnetic field (e.g. Wei 2016) and to make applications for relevant values of the different dimensionless numbers for stellar and planetary interiors.

A. Astoul, S. Mathis and Q. André acknowledge funding by the European Research Council through the ERC grant SPIRE 647383. The authors ackowledge the PLATO CNES funding at CEA/IRFU/DAp and IRAP.

References

Alvan, L., Mathis, S., & Decressin, T. 2013, A&A, 553, A86

André, Q., Barker, A. J., & Mathis, S. 2017, A&A, 605, A117

Auclair Desrotour, P., Mathis, S., & Le Poncin-Lafitte, C. 2015, A&A, 581, A118

Baruteau, C. & Rieutord, M. 2013, Journal of Fluid Mechanics, 719, 47

Booker, J. R. & Bretherton, F. P. 1967, Journal of Fluid Mechanics, 27, 513

Favier, B., Barker, A. J., Baruteau, C., & Ogilvie, G. I. 2014, MNRAS, 439, 845

García, R. A., Turck-Chièze, S., Jiménez-Reyes, S. J., et al. 2007, Science, 316, 1591

Gerkema, T. & Shrira, V. I. 2005a, Journal of Fluid Mechanics, 529, 195

Gerkema, T. & Shrira, V. I. 2005b, Journal of Geophysical Research (Oceans), 110, C01003

Grimshaw, R. H. J. 1975, Journal of Fluid Mechanics, 70, 287

Guenel, M., Baruteau, C., Mathis, S., & Rieutord, M. 2016a, A&A, 589, A22

Guenel, M., Mathis, S., Baruteau, C., & Rieutord, M. 2016b, ArXiv e-prints 1612.05071

Jones, W. L. 1967, Journal of Fluid Mechanics, 30, 439
Lindzen, R. S. & Barker, J. W. 1985, Journal of Fluid Mechanics, 151, 189
Mathis, S., Neiner, C., & Tran Minh, N. 2014, A&A, 565, A47
Ogilvie, G. I. 2009, MNRAS, 396, 794
Ogilvie, G. I. 2013, MNRAS, 429, 613
Ogilvie, G. I. & Lin, D. N. C. 2004, ApJ, 610, 477
Wei, X. 2016, ApJ, 828, 30

SF2A 2017
C. Reylé, P. Di Matteo, F. Herpin, É. Lagadec, A. Lançon, Z. Meliani, F. Royer (eds)

LAYERED SEMI-CONVECTION AND TIDES IN GIANT PLANET INTERIORS

Q. André[1], S. Mathis[1,2] and A. J. Barker[3]

Abstract. Layered semi-convection could operate in giant planets, potentially explaining the constraints on the heavy elements distribution in Jupiter deduced recently from JUNO observations, and contributing to Saturn's luminosity excess or the abnormally large radius of some hot Jupiters. This is a state consisting of density staircases, in which convective layers are separated by thin stably stratified interfaces. The efficiency of tidal dissipation in a planet depends strongly on its internal structure. It is crucial to improve our understanding of the mechanisms driving this dissipation, since it has important consequences to predict the long-term evolution of any planetary system. In this work, our goal is to study the resulting tidal dissipation when internal waves are excited by other bodies (such as the moons of giant planets) in a region of layered semi-convection. We find that the rates of tidal dissipation can be significantly enhanced in a layered semi-convective medium compared to a uniformly convective medium, especially in the astrophysically relevant sub-inertial frequency range. Thus, layered semi-convection is a possible candidate to explain high tidal dissipation rates recently observed in Jupiter and Saturn.

Keywords: Hydrodynamics, Waves, Methods: analytical, Planets and satellites : interiors, Planets and satellites: dynamical evolution and stability, Planet-star interactions

1 Context

Based on astrometric measurements spanning more than a century Lainey et al. (2009, 2012, 2017) found that the rates of tidal dissipation in Jupiter and Saturn are higher than previously thought. This has important astrophysical consequences since tidal interactions are a key mechanism for driving the rotational, orbital and thermal evolution of moons, planets and stars over very long time-scales.

Moreover, we know that this evolution, linked to the efficiency of tidal dissipation in celestial bodies, strongly depends on their internal structures, which are poorly constrained (we refer the reader to the reviews Mathis & Remus 2013; Ogilvie 2014). Several recent studies have suggested new models of giant planet interiors that significantly depart from the standard three-layers model in which a molecular H/He envelope surrounds a metallic H/He envelope, on top of a core composed of heavy elements. Among these works, some suggest that there could be regions exhibiting a stable compositional gradient, either at the core boundary due to erosion of the core (Guillot et al. 2004; Mazevet et al. 2015), or at the interface between metallic and molecular H/He due to settling of He droplets in the molecular region (Stevenson & Salpeter 1977; Nettelmann et al. 2015). These predictions seem to be corroborated by recent observations by the JUNO spacecraft, which are consistent with interior models of Jupiter in which the heavy elements of the core are diluted in the envelope (Wahl et al. 2017). Then, the presence of a stabilising compositional gradient alongside the destabilising entropy gradient (driving the convective instability) could lead to layered semi-convection (Leconte & Chabrier 2012; Wood et al. 2013), in which a large number of convective layers are separated by thin stably stratified interfaces. The associated density profile is nearly constant in the convective steps and undergoes a nearly discontinuous jump in stably stratified interfaces, giving a density staircase-like structure. Such structures are observed on Earth, for instance in the Arctic Ocean (Ghaemsaidi et al. 2016).

[1] Laboratoire AIM Paris-Saclay, CEA/DRF – CNRS – Université Paris-Diderot, IRFU/DAp Centre de Saclay, 91191 Gif-sur-Yvette, France
[2] LESIA, Observatoire de Paris, PSL Research University, CNRS, Sorbonne Universités, UPMC Univ. Paris 06, Univ. Paris Diderot, Sorbonne Paris Cité, 5 place Jules Janssen, F-92195 Meudon, France
[3] Department of Applied Mathematics, School of Mathematics, University of Leeds, Leeds, LS2 9JT, UK

In this work, we study the impact of layered semi-convection upon the efficiency of tidal dissipation. Two tidal components are usually distinguished: the equilibrium tide, a large-scale flow induced by the hydrostatic adjustment to the gravitational potential of the perturber (such as the moons of giant planets, see Zahn 1966; Remus et al. 2012), and the dynamical tide, composed of internal waves excited by the perturber (Zahn 1975; Ogilvie & Lin 2004). In this context, the latter can be called tidal waves. Their dissipation by viscosity and thermal diffusion will lead to the long-term rotational, orbital and thermal evolution of the system. This study focuses on how the dynamical tide is affected by the presence of layered semi-convection.

2 Statement of the problem

To simplify our initial study, and because tidal waves typically have very short wavelengths, we carry out our analysis in a local Cartesian box (denoted by $\mathcal{V}$) centered on a given point M of the fluid envelope, with volume V (see top left panel of Fig. 1). This allows us to study the local properties of the propagation and dissipation of internal waves in a region of layered semi-convection. Such an approach does not aim to give quantitative predictions of the rates of tidal dissipation, but instead can allow us to understand in detail the relevant physics. In addition, it allows a quantitative comparison on the rates of tidal dissipation in a local region of layered semi-convection versus a fully convective medium. We take into account rotation through the Coriolis acceleration, the rotation vector having components $2\boldsymbol{\Omega} = 2\Omega(0, \sin\Theta, \cos\Theta)$ in our local coordinate system, Θ standing for the colatitude and Ω the rotation rate.

The region of layered semi-convection is modelled by a buoyancy frequency profile, $N(z)$, that is zero in the convective regions and positive in stably stratified interfaces, as shown on the bottom left panel of Fig. 1. The mean stratification in the vertical direction is $\bar{N}$. Solutions are taken to be periodic in both time and horizontal space coordinate, defined by $\chi = x\cos\alpha + y\sin\alpha$ (see top left panel of Fig. 1). We also assume periodic boundary conditions in the vertical direction, which is equivalent to studying a small portion of a more vertically extended staircase.

We study the linear propagation of gravito-inertial waves (GIWs) under the Boussinesq approximation subject to dissipative processes, namely viscosity and thermal diffusion, and including an external forcing $\boldsymbol{F} = (F_x, F_y, F_z)$, meant to mimic tidal forcing. We refer the reader to André et al. (2017, hereafter ABM17) for the system of equations composed of the momentum, continuity and heat transport equations. The buoyancy, pressure and velocity perturbations associated to GIWs are b, p and $\boldsymbol{u}$, respectively. The energy balance satisfies the following equation,

$$\frac{\mathrm{d}\bar{E}}{\mathrm{d}t} = -\frac{1}{V}\int_S \boldsymbol{\Pi}\cdot\mathrm{d}\boldsymbol{S} + \bar{D}_{\mathrm{visc}} + \bar{D}_{\mathrm{ther}} + \bar{I}, \tag{2.1}$$

where $\bar{E}$ is the total (pseudo-)energy of the wave, sum of kinetic and potential energies (averaged over the box), and $\boldsymbol{\Pi} = p\boldsymbol{u}$ is the flux density (flux per unit area) of energy. Then the energy dissipated by viscosity and thermal diffusion have the following expressions,

$$\bar{D}_{\mathrm{visc}} = \frac{1}{V}\int_{\mathcal{V}} \rho_0\left(\nu\boldsymbol{u}\cdot\nabla^2\boldsymbol{u}\right)\mathrm{d}\mathcal{V}, \tag{2.2}$$

$$\bar{D}_{\mathrm{ther}} = \begin{cases} \dfrac{1}{V}\displaystyle\int_{\mathcal{V}} \rho_0\left(\frac{\kappa}{N^2}b\nabla^2 b\right)\mathrm{d}\mathcal{V} & \text{if} \quad N^2 \neq 0, \\ 0 & \text{if} \quad N^2 = 0, \end{cases} \tag{2.3}$$

respectively, while the energy injected by the forcing is $\bar{I} = \left(\int_{\mathcal{V}} \rho_0(\boldsymbol{u}\cdot\boldsymbol{F})\,\mathrm{d}\mathcal{V}\right)/V$. In the equations above, ν and κ are the kinematic viscosity and thermal diffusivity, respectively. To quantify the relative importance of diffusive processes, we will use the Ekman number and its equivalent for thermal diffusion,

$$\mathrm{E} = \frac{\nu}{2\Omega L_z^2} \quad \text{and} \quad K = \frac{\kappa}{2\Omega L_z^2}, \tag{2.4}$$

respectively, where L_z is the size of the box in the vertical direction. These quantify the ratio of rotational to viscous (or thermal diffusion) timescales.

Our goal is to calculate numerically* the average rates of viscous and thermal dissipation in the box, $\bar{D}_{\mathrm{visc}}$ and $\bar{D}_{\mathrm{ther}}$, respectively, and the average rate of total dissipation in the box, $\bar{D} = \bar{D}_{\mathrm{visc}} + \bar{D}_{\mathrm{ther}}$.

*This is done using a Fourier collocation method (see Boyd 2001).

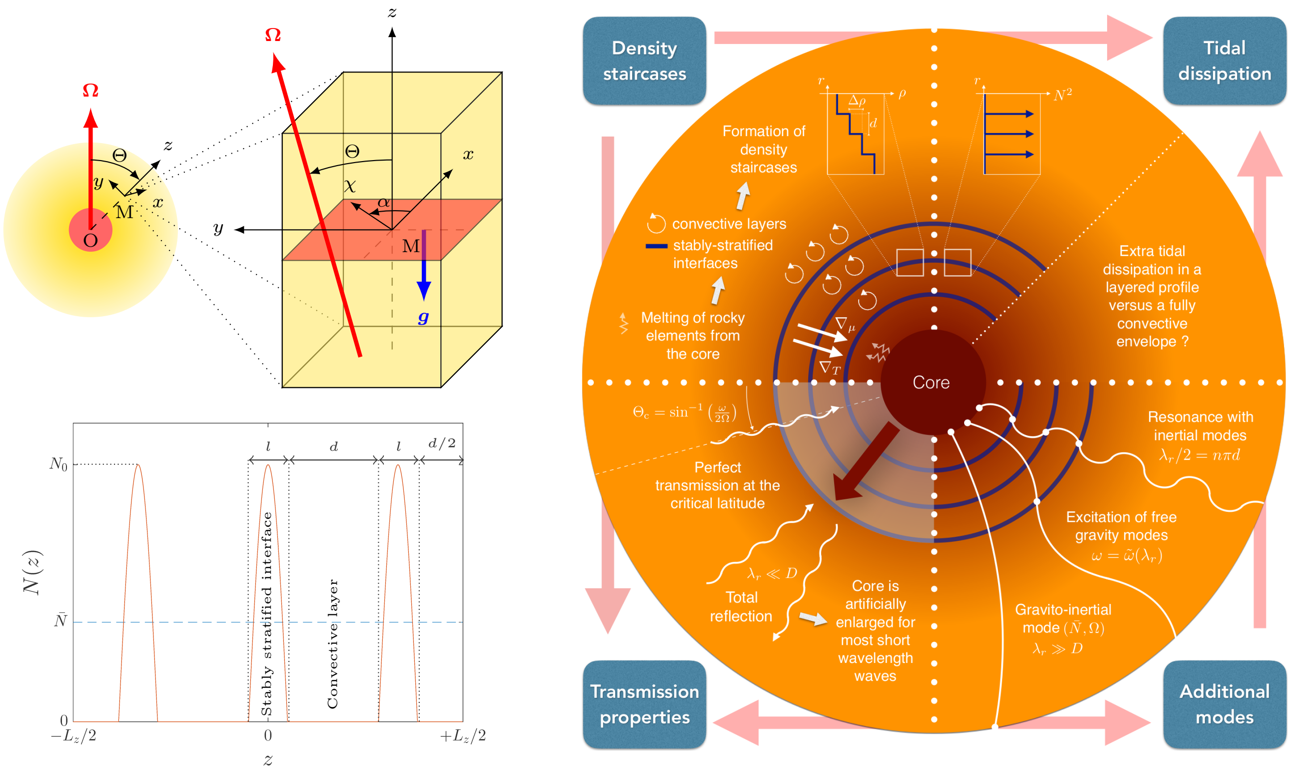

Fig. 1: **Top-left:** our local Cartesian model, centred on a point M of a giant planet envelope at a colatitude Θ. **Bottom-left:** example of buoyancy frequency profile containing three stably stratified layers. The thickness of the principal convective layers and stably stratified interfaces are d and l, respectively. **Right:** summary sketch illustrating the physical context (top-right quarter), the transmission properties found in André et al. (2017) (bottom-left quarter), the additional modes enabled by a layered structure (bottom-right quarter), and the open question of whether tidal dissipation can be enhanced in a layered profile (top-right quarter).

3 A first study of tidal dissipation in layered semi-convection

3.1 *Propagation of tidal waves*

In ABM17, we studied in detail the effect of layered semi-convection upon the propagation of internal waves. The main properties are summarised and illustrated in the bottom-left quarter of the rightmost panel of Fig. 1.

In particular, we found that an internal wave incident on a density staircase from above, will be reflected at the top unless it has a sufficiently large wavelength or is resonant with a free mode of the staircase. Thus, for most waves, the core of giant planets can be artificially enlarged by the presence of a region of layered semi-convection surrounding it. Moreover, we found that an inertial wave with frequency ω is perfectly transmitted at the location called the critical latitude, defined by $\theta_c = \sin(\omega/2\Omega)$. Finally, we were able to physically identify some specific modes that were perfectly transmitted through the staircase region. In what follows, we show that these modes correspond to resonant modes of the staircase, for which tidal dissipation is significantly enhanced.

3.2 *Dissipation rates in a layered profile*

Here, we focus on the case with one stably stratified interface in the middle of our periodic box. The dissipation rates are plotted as a function of tidal forcing frequency on Fig. 2, with the different panels corresponding to varying the diffusivity coefficients such that $\mathrm{E} = K = 10^{-3}$ and 10^{-5} in the top and bottom panels, respectively. For each panel, the total dissipation rate, $\bar{D}$, is represented by the solid orange line, while its viscous and thermal contributions, $\bar{D}_{\rm visc}$ and $\bar{D}_{\rm ther}$, are represented by the dotted blue and red lines, respectively. For comparison, we plot the corresponding quantities in a fully convective medium, $\bar{D}^{(c)}$ by the dashed light blue line. All dissipation rates are normalised by $\bar{D}^{(c)}_{\max} \equiv \max_\omega \bar{D}^{(c)}$.

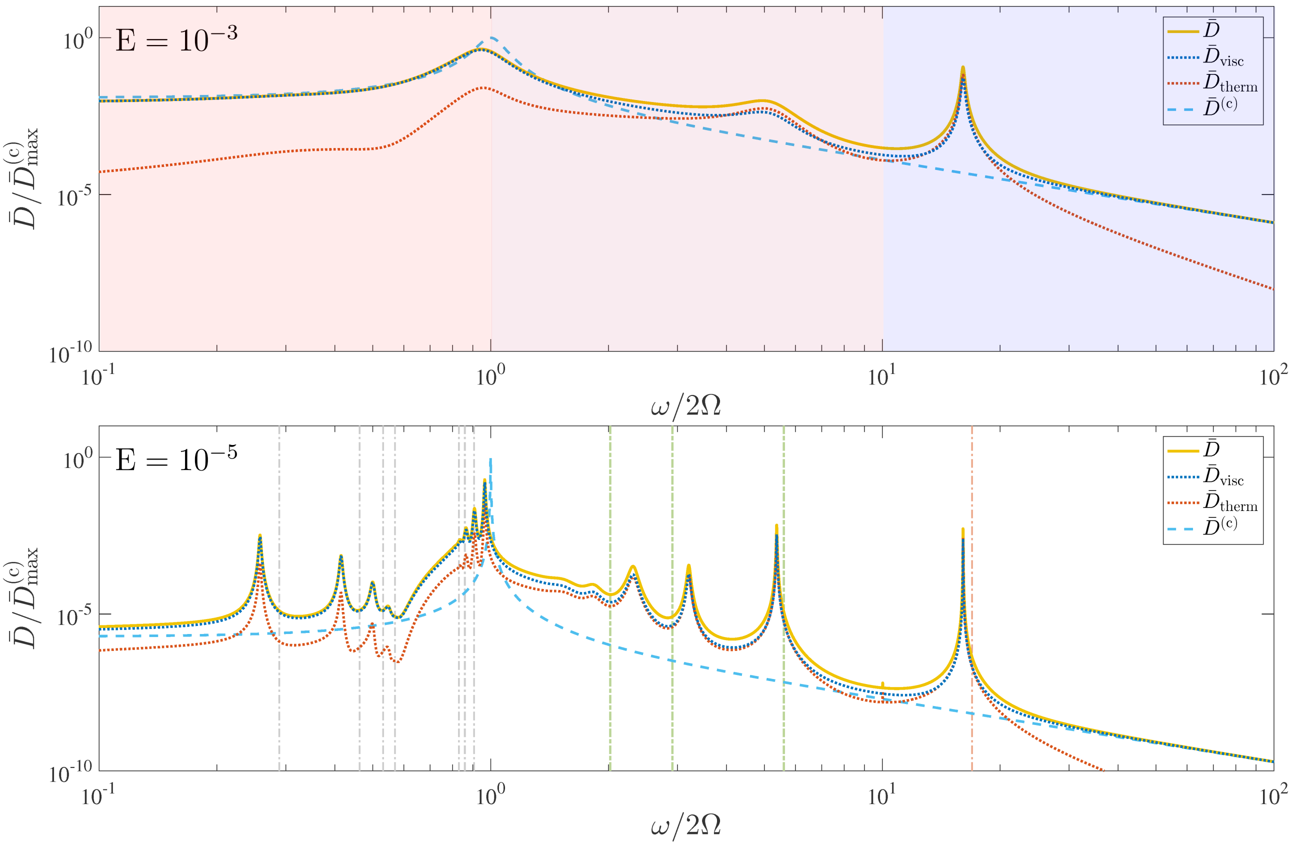

Fig. 2: Normalised dissipation as a function of tidal frequency for different Ekman numbers, $\mathrm{E} = K = 10^{-3}$ (top panel) and 10^{-5} (bottom panel), for an aspect ratio $\varepsilon \equiv l/d = 0.2$, and a colatitude $\Theta = \pi/4$. The total dissipation is represented by the orange solid line, and its viscous and thermal contributions are represented by the dotted blue and red lines, respectively. The dashed light blue line represents the average dissipation spectrum for a fully convective box, $\bar{D}^{(\rm c)}$. For each panel, the quantity represented is $\bar{D}/\bar{D}^{(\rm c)}_{\rm max}$, where $\bar{D}^{(\rm c)}_{\rm max} \equiv \max_\omega \bar{D}^{(\rm c)}$, as a function of the normalised forcing frequency $\omega/2\Omega$. In the top panel, the pink, purple and blue regions correspond to resonances with inertial, super-inertial gravito-inertial and gravity modes, respectively. In the bottom panel, the vertical dashed-dotted lines indicate the position of the characteristic frequencies; namely, from left to right: resonance with short wavelength inertial modes (in grey), resonance with short wavelength gravito-inertial modes (in light green), and resonance with a free gravity mode of the staircase (in light red).

In agreement with Ogilvie & Lin (2004) or Auclair Desrotour et al. (2015), the resonant peaks are more numerous and narrower when the viscosity (and thermal diffusivity) is decreased to reach smaller Ekman numbers that are more relevant to planetary or stellar interiors. However, while our choice of parameters would give only one resonant peak in a uniformly stably stratified or fully convective medium – centred on $\omega/2\Omega = 1$ in the latter case (see Fig. 2) – we clearly see here that the layered structure introduces new resonances. Focusing on the bottom panel, corresponding to the more relevant case with lower diffusivities, we clearly see that the total dissipation rate is higher in the layered case (orange curve) – in particular in the sub-inertial range ($\omega < 2\Omega$) relevant to tidal forcing – except near the Coriolis frequency ($\omega \sim 2\Omega$). This increase of the dissipation is allowed by the presence of new resonant peaks. Those additional resonances are broadly distributed over the frequency spectrum. Some correspond to resonances with inertial modes, corresponding to frequencies $\omega \lesssim 2\Omega$ (pink region on top panel of Fig. 2); some with super-inertial gravito-inertial modes, corresponding to frequencies $2\Omega \lesssim \omega \lesssim \bar{N}$ (purple region on top panel of Fig. 2); and finally some with gravity modes, corresponding to frequencies $\bar{N} \lesssim \omega \lesssim N_0$ (blue region on top panel of Fig. 2).

Resonance with short wavelength inertial modes. In the inertial regime ($\omega < 2\Omega$), a succession of resonant modes appears as we decrease the viscosity. We found that those correspond to inertial modes with vertical semi-wavelengths that fit inside the convective layer. The grey dashed lines on the bottom panel of Fig. 2 thus correspond to frequencies that obey the relation $\lambda_z^{(c)}/2 = nd$ or equivalently $k_z^{(c)}(\omega)d = n\pi$, for different integers n. We recall that d is the vertical extent of the convective region (see bottom left panel of Fig. 1), λ_z is the vertical wavelength and k_z is the vertical wave number. In order to draw the vertical lines on Fig. 2, we used the vertical wave number in the adiabatic limit, which can be obtained from the dispersion relation of pure inertial waves,

$$\omega^2 = \frac{(2\boldsymbol{\Omega} \cdot \boldsymbol{k})^2}{k_\perp^2 + k_z^{(c)2}}, \tag{3.1}$$

where $\boldsymbol{k} = k_\perp \hat{\boldsymbol{e}}_\chi + k_z^{(c)} \hat{\boldsymbol{e}}_z$. We have used the label $^{(c)}$ above to stress that this is the expression of the vertical wave number in a convective medium.

The discrepancy between the prediction and the actual position of those resonant modes can be partly explained twofold. First, the expression of the vertical wave number that was used corresponds to the adiabatic case. Second, the stably stratified interface in the middle of the box has a non-negligible vertical extent in which pure inertial waves become influenced by buoyancy. This differs from the simplified model that we primarily studied in ABM17, in which stably stratified interfaces were infinitesimally small.

Resonance with short wavelength super-inertial gravito-inertial modes. Based on the same idea, we looked for modes in the gravito-inertial regime with vertical semi-wavelengths that fit inside the vertical extent of the thin stably stratified layer, in which they are propagative. On the bottom panel of Fig. 2, the dotted-dashed light green vertical lines correspond to frequencies such that $k_z(\omega)d = n\pi$ for three different integers n, satisfying the dispersion relation of gravito-inertial waves,

$$\omega^2 = N_\mathrm{e}^2 \frac{k_\perp^2}{k_\perp^2 + k_z^2} + \frac{(2\boldsymbol{\Omega} \cdot \boldsymbol{k})^2}{k_\perp^2 + k_z^2}. \tag{3.2}$$

Here k_z is the vertical wave number in a stably stratified medium, characterised by the constant buoyancy frequency N_e. We note that these waves are evanescent in the convective layer surrounding the stably stratified interface (see also Mathis et al. 2014, for an extensive discussion).

The buoyancy frequency is not uniform in the stably stratified region (see bottom left panel of Fig. 1), therefore N_e was somewhat tuned so that it would match the corresponding peaks as close as possible. Its value was found to be consistent with the requirement that this effective buoyancy frequency, N_e, should lie in the range $\bar{N} < N_\mathrm{e} < \max_z N(z)$. However, following this procedure, we do not expect the vertical lines to match perfectly the position of the resonant peaks, but the agreement is sufficient to validate our interpretation.

Resonance with the free gravity mode of the staircase. In ABM17, we derived the dispersion relation for the free modes of the staircase, by extending Belyaev et al. (2015). When looking for gravity modes, we can neglect rotation so that the dispersion relation reduces to

$$\omega^2 = \bar{N}^2 \left(\frac{k_\perp d}{2\coth(k_\perp d) - 2\cos\theta \operatorname{csch}(k_\perp d)} \right), \tag{3.3}$$

where $\cos\theta$ is a root of a polynomial (see ABM17). This predicts the free modes of a layered structure in which stably stratified interfaces are modelled as discontinuous jumps. The frequency given by the equation above is displayed as the dotted-dashed light red vertical line on the bottom panel of Fig. 2. Its position matches rather well the position of the rightmost resonant peak, though we do not expect a perfect match because we have neglected the effects of rotation, viscous and thermal diffusions, and the interfaces are not infinitesimally thin.

4 Conclusions

We computed the dissipation rates in a region of layered semi-convection as a function of tidal frequency using a local Cartesian model. We found that the dissipation of tidal waves can be significantly enhanced compared to a fully convective medium in the sub-inertial frequency range, which is typically the most relevant for tidal forcing in giant planet systems. In addition, such a density structure leads to new dissipation peaks corresponding with additional resonances, for which the dissipation can be increased by several orders of magnitude. We tentatively conclude that layered semi-convection is a possible candidate to explain the high tidal dissipation rates observed by Lainey et al. (2009, 2012, 2017) in Jupiter and Saturn. Further work is required to explore and confirm the influence of layered semi-convection on tidal dissipation in global models. In a near future, other mechanisms such as differential rotation and magnetic fields should also be taken into account (Baruteau & Rieutord 2013; Barker & Lithwick 2013; Wei 2016; Lin & Ogilvie 2017).

QA and SM acknowledge funding by the European Research Council through ERC SPIRE grant 647383. AJB was supported by the Leverhulme Trust through the award of an Early Career Fellowship.

References

André, Q., Barker, A. J., & Mathis, S. 2017, A&A, 605, A117

Auclair Desrotour, P., Mathis, S., & Le Poncin-Lafitte, C. 2015, A&A, 581, A118

Barker, A. J. & Lithwick, Y. 2013, MNRAS, 435, 3614

Baruteau, C. & Rieutord, M. 2013, Journal of Fluid Mechanics, 719, 47

Belyaev, M. A., Quataert, E., & Fuller, J. 2015, MNRAS, 452, 2700

Boyd, J. 2001, Chebyshev and Fourier Spectral Methods: Second Revised Edition, Dover Books on Mathematics (Dover Publications)

Ghaemsaidi, S. J., Dosser, H. V., Rainville, L., & Peacock, T. 2016, Journal of Fluid Mechanics, 789, 617629

Guillot, T., Stevenson, D. J., Hubbard, W. B., & Saumon, D. 2004, The interior of Jupiter, ed. F. Bagenal, T. E. Dowling, & W. B. McKinnon, 35–57

Lainey, V., Arlot, J.-E., Karatekin, Ö., & van Hoolst, T. 2009, Nature, 459, 957

Lainey, V., Jacobson, R. A., Tajeddine, R., et al. 2017, Icarus, 281, 286

Lainey, V., Karatekin, Ö., Desmars, J., et al. 2012, ApJ, 752, 14

Leconte, J. & Chabrier, G. 2012, A&A, 540, A20

Lin, Y. & Ogilvie, G. I. 2017, ArXiv e-prints

Mathis, S., Neiner, C., & Tran Minh, N. 2014, A&A, 565, A47

Mathis, S. & Remus, F. 2013, in Lecture Notes in Physics, Berlin Springer Verlag, Vol. 857, Lecture Notes in Physics, Berlin Springer Verlag, ed. J.-P. Rozelot & C. . Neiner, 111–147

Mazevet, S., Tsuchiya, T., Taniuchi, T., Benuzzi-Mounaix, A., & Guyot, F. 2015, Phys. Rev. B, 92, 014105

Nettelmann, N., Fortney, J. J., Moore, K., & Mankovich, C. 2015, MNRAS, 447, 3422

Ogilvie, G. I. 2014, ARA&A, 52, 171

Ogilvie, G. I. & Lin, D. N. C. 2004, ApJ, 610, 477

Remus, F., Mathis, S., & Zahn, J.-P. 2012, A&A, 544, A132

Stevenson, D. J. & Salpeter, E. E. 1977, ApJS, 35, 239

Wahl, S. M., Hubbard, W. B., Militzer, B., et al. 2017, Geophys. Res. Lett., 44, 4649

Wei, X. 2016, ApJ, 828, 30

Wood, T. S., Garaud, P., & Stellmach, S. 2013, ApJ, 768, 157

Zahn, J. P. 1966, Annales d'Astrophysique, 29, 313

Zahn, J.-P. 1975, A&A, 41, 329

Session 06

Multi-disciplinary impact of Gaia

SF2A 2017
C. Reylé, P. Di Matteo, F. Herpin, É. Lagadec, A. Lançon, Z. Meliani, F. Royer (eds)

THE IMPACT OF GAIA ON OUR UNDERSTANDING OF THE VAST POLAR STRUCTURE OF THE MILKY WAY

M. S. Pawlowski[1]

Abstract. The Milky Way (MW) is surrounded by a Vast Polar Structure (VPOS) of satellite galaxies, star clusters, and streams. Proper motion measurements for the brightest MW satellites indicate that they are predominantly co-orbiting along the VPOS. This is consistent with a dynamically stable structure. Assuming that all satellites that are aligned with the VPOS also co-orbit along this structure allows to empirically predict their systemic proper motions. Testing predictions for individual satellite galaxies at large distances requires high-accuracy proper motion measurements such as with the Hubble Space Telescope. However, for nearby MW satellites, Gaia will allow to test these predictions, in particular for a statistical sample of satellites since proper motion predictions exist for almost all of them. This will clarify how rotationally supported the VPOS is. In addition, Gaia will discover Galactic substructure, in particular stellar streams. The degree of their alignment with the VPOS might further constrain its stability and nature.

Keywords: Milky Way, satellite galaxies, Gaia, proper motions, satellite galaxy planes, Vast Polar Structure

1 Introduction

The satellite galaxies of the Milky Way (MW) are distributed anisotropically. This was first noted by Kunkel & Demers (1976) and Lynden-Bell (1976), who demonstrated that the then-known satellites align along a common great circle, which is also shared by the Magellanic Stream. Already then this lead to the speculation that at least some of the MW satellite galaxies move along as part of a coherent structure. The subsequent discovery of additional satellite galaxies has corroborated this early finding (see Pawlowski et al. 2015 for an analysis including the most recently discovered satellite galaxies). The satellite galaxies of the MW are preferentially aligned in a flattened distribution oriented perpendicular to the Galactic disk. This Vast Polar Structure (VPOS) also contains distant globular clusters, and about half of the known stellar and gaseous streams of satellite systems disrupting in the Galactic halo are aligned with it (Pawlowski et al. 2012). Since tidal debris streams trace the orbital plane of their progenitors, this indicates a preference for satellite systems to orbit along the VPOS, whose orientation is defined by the current satellite positions. Proper motion measurements, available for all of the 11 classical satellite galaxies, reveal that this is indeed the case (Metz et al. 2008; Pawlowski & Kroupa 2013). Eight of the 11 satellites are consistent with orbiting in the VPOS, with Sculptor being the only one in a counter-orbiting orientation.

This intriguing alignment is illustrated in Figure 1, which plots the normal vectors defining the orientations of planes fitted to the positions of satellite galaxies, globular clusters, and streams, as well as the orbital poles (directions of orbital angular momentum) of individual satellite galaxies. It includes updated and new proper motion measurements for several satellite galaxies (e.g. Sohn et al. 2017; Casetti-Dinescu et al. 2017), and also the orbital poles of four stellar stream candidates discovered by Grillmair (2017). Interestingly, the two streams of these which best align with the VPOS are those with the largest pericentric distances (≥ 20 kpc): Molonglo and Murrumbidgee. The other two have pericentric distances below 7 kpc and thus their orbits can be expected to show more precession.

2 Predictions for systemic proper motions of Milky Way satellite galaxies

Since there is empirical evidence that the VPOS is, at least in part, rotationally stabilized, one can formulate the hypothesis that satellites which align with the structure also orbit along it. This in turn results in an empirical

[1] Hubble Fellow, Department of Physics and Astronomy, University of California, Irvine, CA 92697, USA

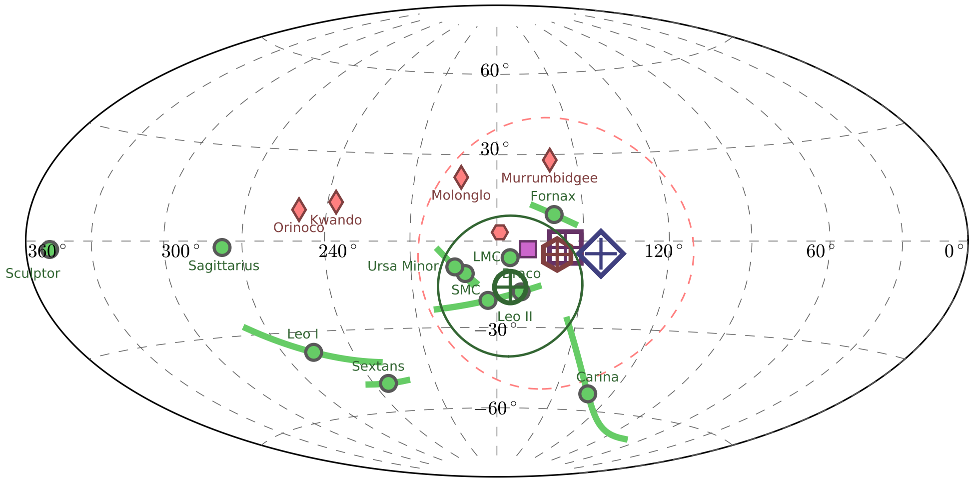

Fig. 1. All-sky plot showing the directions of the orbital poles for the 11 classical satellite galaxies for which proper motions have been measured (green dots with 1σ uncertainties). The figure is based on Pawlowski & Kroupa (2013), and has been updated with new proper motion measurements, most recently by Sohn et al. (2017) and Casetti-Dinescu et al. (2017). The normal directions to the planes fitted to the positions of satellite galaxies (magenta squares) and distant globular clusters thought to have been associated with accreted dwarf galaxies (blue diamond) lie close to the strong concentration of orbital poles, indicating that many of the satellite galaxies co-orbit in the VPOS. Also shown are the average of normal vectors to streams in the MW halo (red, from Pawlowski et al. 2012 and updated in Pawlowski & Kroupa 2014) and the Magellanic Stream (small read hexagon). The orbital poles of four stellar stream candidates recently found by Grillmair (2017) in the Galactic south (red, with names) are consistent with the finding that about half of the distant streams in the MW halos are oriented approximately along the VPOS.

prediction of the proper motion that would make a given satellite orbit as closely along the VPOS as possible. A detailed description of how these predictions are made can be found in Pawlowski & Kroupa (2013).

In brief, for a given satellite the angle between its position vector from the Galactic center and the orientation of the best-fit VPOS plane gives the best possible orbital alignment. The corresponding orbit requires that the 3D velocity of the satellite is confined to lie in this orbital plane. Since the position, distance, and line of line-of-sight velocity of the satellite is known, this results in a linear relation between the two proper motion components that constitutes the range of predicted proper motion. The maximum and minimum tangential velocities are further constrained, respectively, by requiring the satellite to be gravitationally bound to the MW (otherwise it would not be a satellite in the strict sense), and by requiring that the orbit is not predominantly radial (in which case the orbital orientation becomes meaningless). Predictions for a total of 36 MW satellite galaxies can be found in Pawlowski & Kroupa (2013), Pawlowski & Kroupa (2014), and Pawlowski et al. (2015).

3 Testing proper motions

The predicted proper motions range from $\approx 1 \mathrm{mas\,yr}^{-1}$ to less than $\approx 100 \mu\mathrm{as\,yr}^{-1}$, depending on the distance of the satellite. Such proper motion accuracy is achievable with Hubble Space Telescope (HST) measurements, and possibly also by ground-based observations given sufficiently long temporal baselines (Casetti-Dinescu et al. 2017). This is in part due to large-number statistics in the stars and background reference sources. Current measurements, several of which became available only after the satellite proper motions motion were predicted in Pawlowski & Kroupa (2013), indicate that these predictions are well met by the 11 classical satellite galaxies. In particular, more accurate measurement tend to result in a better agreement with the prediction (see Figure 2).

Figure 3 shows predicted proper motions for three examples of MW satellites. These three satellites are part of those recently discovered by Koposov et al. (2015) using data from the Dark Energy Survey (DES), and lie at different distances. Checking the Color-Magnitude Diagrams of the faint satellites in Koposov et al. (2015)

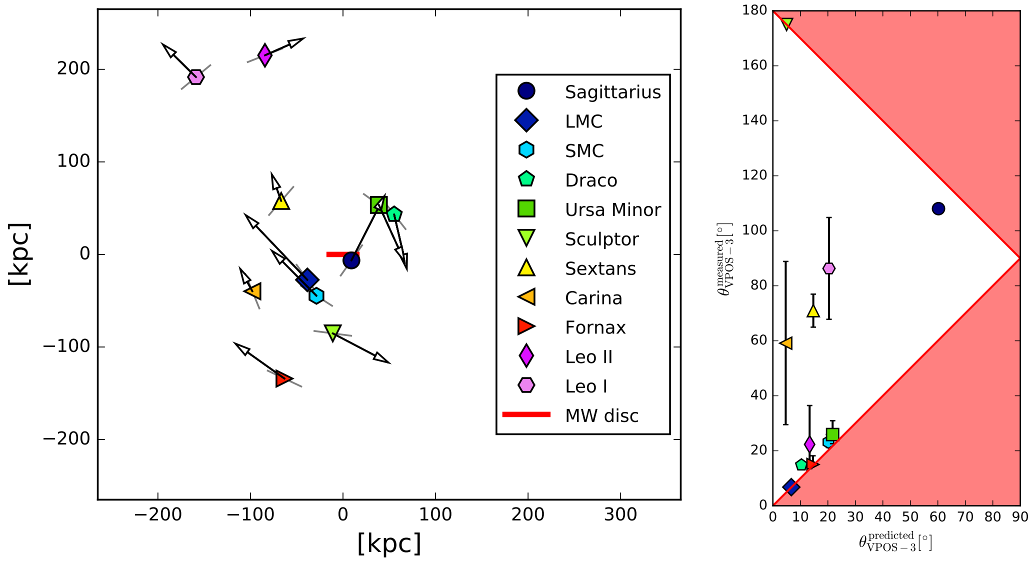

Fig. 2. Left: The distribution of the 11 classical satellite galaxies around the MW, in a view oriented face-on relative to the VPOS. The arrows show their velocities, based on the measured line-of-sight velocities and proper motions. There is a clear preference for the satellites to co-orbit, as well as for an excess of the tangential over the radial velocity component. **Right:** Predicted (minimum possible) angle between a satellite's current orbital plane and the VPOS $\theta^{\rm predicted}_{\rm VPOS-3}$, plotted against the corresponding angle $\theta^{\rm measured}_{\rm VPOS-3}$ based on the measured 3D velocity of the satellite. Most satellites with well determined proper motions (small error bars) lie close to the prediction (red lines). Same symbols as in the left panel. Both plots are updated versions based on the analysis presented in Pawlowski & Kroupa (2013).

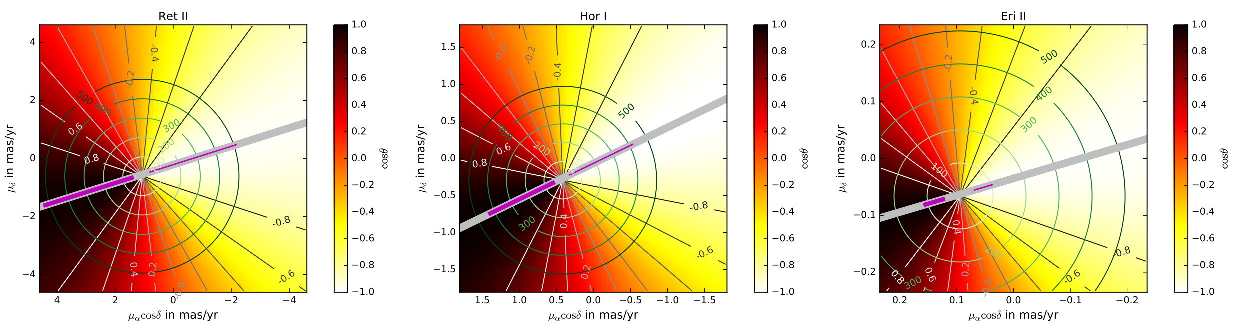

Fig. 3. Predicted proper motions and expected Gaia proper motion accuracy (cyan circle) for a single star at the detection limit of $V = 20$ mag, for three faint MW satellite galaxies discovered in the DES survey (Koposov et al. 2015): **Left:** Reticulum II at 30 kpc distance, **Middle:** Horologium I at 80 kpc distance, **Right:** Eridanus II at 380 kpc distance. Plotted are the two proper motion coordinates, with the angle between the resulting orbital plane and the VPOS plane color-coded and indicated by radial grey contours. The circular green contours indicate the resulting absolute speed for each possible proper motion combination. The predicted proper motions (resulting in the best alignment of the orbit with the VPOS) are indicated as a thick magenta line (co-orbiting with the majority of classical satellites) and thin magenta line (counter-orbiting).

shows that the more nearby satellites do potentially have a few (≤ 10) stars with apparent magnitudes above the Gaia limit of $V = 20$ mag. It might thus be possible to obtain systemic proper motions for these systems with Gaia from a few individual stars, instead of a large sample of stars from deeper HST observations and long temporal baselines. Would Gaia provide sufficient information to test the proper motion predictions and thus help us learn more about the VPOS?

As an estimate for the Gaia proper motion accuracy we use the post-launch predictions by de Bruijne et al. (2014): $\Delta\mu \approx 330 \mu\mathrm{as\,yr}^{-1}$ as expected for a single star with $V = 20$ mag and a color equivalent to a G2V star. At this accuracy, internal motions in the satellite galaxies can be neglected, in particular for the faintest satellites which have velocity dispersions of $\leq 10\,\mathrm{km\,s^{-1}}$, which is an order of magnitude smaller than their orbital velocities. A comparison of this estimated accuracy (cyan circles) with the predicted proper motions in Figure 3 illustrates that Gaia can provide good constraints on the most nearby satellite galaxies individually (left panel). For satellites at intermediate distances, Gaia proper motions will not constrain the orbits of individual satellites well. However, Gaia can provide proper motions for many such satellites. Such a larger sample of satellite galaxies with proper motions, albeit less certain, will allows to statistically test whether there are indications for a preferred kinematic correlation with the VPOS. For very distant satellites, Gaia will clearly not provide any proper motion constraints, both due to the small expected proper motions and the large distance that results in even the brightest stars in the satellites being too faint for Gaia.

In addition to testing the kinematic coherence of the VPOS via proper motions, Gaia also holds the potential to uncover stellar streams, which can be compared to the orientation of the VPOS and thus test if the preferential stream alignment persists. As discussed in Pawlowski et al. (2012), this will have to take into account the preference to detect nearby streams: since the VPOS is almost perpendicular to the Sun's position relative to the Galactic center, only streams at distances beyond $\approx 8\,\mathrm{kpc}$ can possibly align with it. Our position thus biases away from finding aligned streams, which makes the already known association of up to half of the known MW streams all the more compelling.

4 Conclusions

Known satellite galaxies, globular clusters, and streams around the MW preferentially align in a flattened distribution, the Vast Polar Structure (VPOS). The preferential alignment of streams in the MW halo indicates that objects preferentially move along this structure. This is confirmed by orbits inferred from proper motion measurements for the 11 classical satellite galaxies, most of which co-orbit along the VPOS. The existence of the VPOS thus allows to empirically predict the likely range of proper motions for most MW satellites, based on the assumption that their orbits, too, align with the structure. Testing these predictions for a sample of satellite galaxies thus allows to determine how strongly rotationally supported the VPOS is, and whether there are differences in the orbital alignment between the brightest and fainter MW satellites. While individual HST proper motion measurements can deliver accurate systemic proper motions for distant satellite galaxies, Gaia provides a complementary approach. Its extensive sky coverage and accuracy can provide proper motion constraints even for faint satellite galaxies, if the few brightest stars belonging to these objects can be accurately identified. While the accuracy for single-star proper motions will not be sufficient for precise orbit determinations for individual satellites, Gaia will allow to test how closely the full sample of satellite galaxies follows the predicted proper motions based on the assumption of orbits aligned with the VPOS.

Support for this work was provided by NASA through Hubble Fellowship grant #HST-HF2-51379.001-A awarded by the Space Telescope Science Institute, which is operated by the Association of Universities for Research in Astronomy, Inc., for NASA, under contract NAS5-26555

References

Casetti-Dinescu, D. I., Girard, T. M., & Schriefer, M. 2017, ArXiv e-prints

de Bruijne, J. H. J., Rygl, K. L. J., & Antoja, T. 2014, in EAS Publications Series, Vol. 67, EAS Publications Series, 23–29

Grillmair, C. J. 2017, ApJ, 847, 119

Koposov, S. E., Belokurov, V., Torrealba, G., & Evans, N. W. 2015, ApJ, 805, 130

Kunkel, W. E. & Demers, S. 1976, in Royal Greenwich Observatory Bulletins, Vol. 182, The Galaxy and the Local Group, ed. R. J. Dickens, J. E. Perry, F. G. Smith, & I. R. King, 241

Lynden-Bell, D. 1976, MNRAS, 174, 695

Metz, M., Kroupa, P., & Libeskind, N. I. 2008, ApJ, 680, 287

Pawlowski, M. S. & Kroupa, P. 2013, MNRAS, 435, 2116

Pawlowski, M. S. & Kroupa, P. 2014, ApJ, 790, 74

Pawlowski, M. S., McGaugh, S. S., & Jerjen, H. 2015, MNRAS, 453, 1047

Pawlowski, M. S., Pflamm-Altenburg, J., & Kroupa, P. 2012, MNRAS, 423, 1109

Sohn, S. T., Patel, E., Besla, G., et al. 2017, ArXiv e-prints

SF2A 2017
C. Reylé, P. Di Matteo, F. Herpin, É. Lagadec, A. Lançon, Z. Meliani, F. Royer (eds)

PERSPECTIVES FOR SHORT TIMESCALE VARIABILITY STUDIES WITH GAIA

M. Roelens[1], L. Eyer[1], N. Mowlavi[1], I. Lecoeur-Taïbi[2], L. Rimoldini[2], S. Blanco-Cuaresma[3], L. Palaversa[4], M. Süveges[5], J. Charnas[2] and T. Wevers[6]

Abstract. We assess the potential of *Gaia* for detecting and characterizing short timescale variables, i.e. at timescale from a few seconds to a dozen hours, through extensive light-curve simulations for various short timescale variable types, including both periodic and non-periodic variability. We evidence that the *variogram* analysis applied to *Gaia* photometry should enable to detect such fast variability phenomena, down to amplitudes of a few millimagnitudes, with limited contamination from longer timescale variables or constant sources. This approach also gives valuable information on the typical timescale(s) of the considered variation, which could complement results of classical period search methods, and help prepare ground-based follow-up of the *Gaia* short timescale candidates.

Keywords: Stars: variables: general, surveys, methods: data analysis, numerical, techniques: photometric

1 Introduction

Since the first reported discoveries of such astronomical objects, hundreds of thousands of variable stars have been identified and classified in different categories, revealing a great diversity in terms of timescales, amplitudes and phenomena at the origin of the variability.

In this work, we focus on *short timescale variability*, i.e. on sources showing variability at timescales from tens of seconds to a dozen hours. Various astronomical objects are known to exhibit such rapid variations in their light-curves, be it periodic or not, with amplitudes ranking from a few millimagnitudes (mmag) to a few magnitudes. Until a decade ago, only a relatively small number of these fast variables had been detected, due to the constraints in terms of time sampling and photometric precision when dealing with such objects. However, with the advent of Charged Coupled Devices (CCDs), and thanks to space and ground-based high cadence monitoring surveys (such as Kepler (Borucki et al. 2010) and the Optical Gravitational Lensing Experiment (Udalski et al. 1992) respectively), a deeper insight the domain of short timescale variability became accessible, and the number of known short timescale variables significantly increased.

In this context, the *Gaia* ESA cornerstone mission, launched in December 2013, offers a unique opportunity to drastically change the landscape. During its 5-year mission duration, *Gaia* will survey more than one billion objects over the entire sky, providing micro-arcsecond astrometry, photometry down to $G \approx 20.7\,\mathrm{mag}$ (where G is the *Gaia* broad-band white light magnitude) with standard errors below the mmag level for bright sources, and medium resolution spectroscopy down to $G \approx 17\,\mathrm{mag}$ (Gaia Collaboration et al. 2016). Moreover, the *Gaia* scanning law involves fast observing cadences, with groups of nine consecutive CCD observations separated by about 4.85 s from each other, followed by gaps of 1 h 46 min or 4 h 14 min between two successive groups, a group being referred to as a field-of-view (FoV) transit. Hence, *Gaia* will make a comprehensive variability search possible, enabling to investigate timescales as short as a few tens of seconds together with low amplitude variations.

[1] Observatoire de Genève, Département d'Astronomie, Université de Genève, Chemin des Maillettes 51, CH-1290 Versoix, Switzerland
[2] Observatoire de Genève, Département d'Astronomie, Université de Genève, Chemin d'Ecogia 16, CH-1290 Versoix, Switzerland
[3] Harvard-Smithsonian Center for Astrophysics, 60 Garden Street, Cambridge, MA 02138, USA
[4] Institute of Astronomy, University of Cambridge, Madingley Road, Cambridge CB3 OHA, United Kingdom
[5] Max Planck Institute for Astronomy, Königstuhl 17, D-69117 Heidelberg, Germany
[6] Department of Astrophysics / IMAPP, Radboud University, P.O. Box 9010, NL-6500GL, Nijmegen, The Netherlands

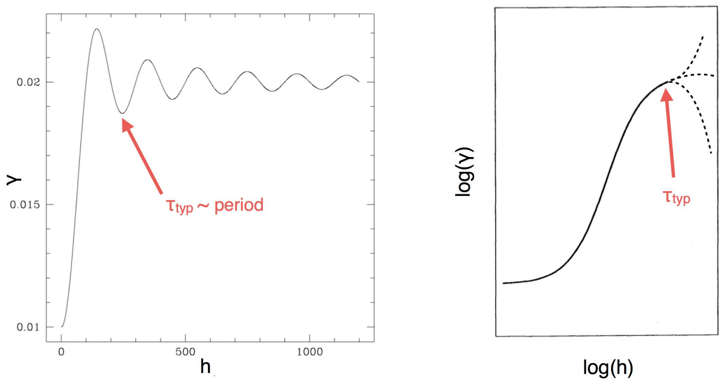

Fig. 1. Typical variogram plots. **Left:** for a periodic/pseudo-periodic variable (Eyer & Genton 1999). **Right:** for a transient variable, only exploring lags up to the first structure characteristic of variability (derived from Hughes et al. 1992). In each case, the feature used to estimate the typical timescale is pointed by a colored arrow.

In this proceeding, we estimate the *Gaia* capabilities for detecting and characterizing short timescale variability detection, using *Gaia* per-CCD photometry in the G band. Our study is based on light-curve simulations for various short timescale variable types, and relies on the *variogram method*, also known as the *structure function method*, which is extensively used in the fields of quasar and AGN studies, and in high-energy astrophysics (see e.g. Simonetti et al. 1985; MacLeod et al. 2012; Kozłowski 2016), but can also be applied to optical stellar variability (see e.g. Eyer & Genton 1999; Sumi et al. 2005). This variogram technique and its application to short timescale variability detection are detailed in Sect. 2. In Sect. 3, we describe the light-curve data sets we generated for our analysis, and summarize the expectations in the *Gaia* context. Section 4 recapitulates our conclusions.

2 Principle of the variogram analysis

The key idea of the variogram method is to investigate variability by quantifying the magnitude difference between two measurements as function of the time lag h between them. If the light-curve is defined by magnitudes $(m_i)_{i=1..n}$ observed at times $(t_i)_{i=1..n}$, then the variogram value for a time lag h is defined as (Hughes et al. 1992):

$$\gamma(h) = \sum_{i>j} \frac{(m_j - m_i)^2}{N_h} \tag{2.1}$$

and is computed on all pairs (i, j) such that $|t_j - t_i| = h \pm \epsilon_h$ where ϵ_h is the tolerance accepted for grouping the pairs by time lag (N_h is the number of such pairs).

The *variogram plot* (hereafter referred to as variogram) associated with this time series is built by exploring different lag values h_k and calculating the associated variogram values $\gamma(h_k)$. It gives information on how variable the considered source is, and on its variability characteristics if appropriate. Figure 1 shows the typical variograms for a periodic or pseudo-periodic variable (top), and for a transient variable (bottom). If the analyzed time series exhibits some variability, the expected features in its variogram are:

1. a plateau at the shortest lags,

2. towards longer lags, an increase in the variogram values, followed by a flattening phase.

When the underlying variation is periodic or pseudo-periodic, this flattening is followed by a succession of dips. In the case of a transient variation, the flattening can be followed by complex structures, e.g. other plateaus or a decrease in the variogram values, depending on the origin of variability. The lags at which those features occur allow us to estimate the characteristic variation timescales. For transient variability, the lag(s) at which the variogram flattens correspond to the typical timescale(s) τ_{typ} (see Fig. 1). For periodic variability, τ_{typ} corresponds to the lag of the first dip after the plateauing, and gives a rough estimate of the period of the variability.

In the *Gaia* context, once we retrieve the variogram associated with a given light-curve, the first think we have to do is to decide whether the considered source is a true variable or not. To answer this question, one possibility is to fix a *detection threshold* γ_{det} such that: if, for at least one lag value h_k, $\gamma(h_k) \geq \gamma_{det}$, then the source is flagged as *variable*. Otherwise, the source is flagged as *constant*. Hence γ_{det} defines the variance level above which variability in the signal is significant enough not to be due only to noise, and can be more or less restrictive. If a source is detected as short timescale candidate with this criterion, then the corresponding *detection timescale* τ_{det} is defined as the smallest lag for which $\gamma(\tau_{det}) \geq \gamma_{det}$. It quantifies the average variation rate in the investigated light-curve and is characteristic of the underlying variability. So as to focus on fast variability, we complete our detection criterion by an upper limit on the detection timescale: a detected source is flagged as a *short timescale candidate* only if $\tau_{det} \leq 0.5$ d. Finally, we estimate the typical timescales for those flagged short timescale candidates as explained above.

All in all, the interest of the variogram method lies in the fact that it enables to detect and to characterize variable candidates, handling both periodic, pseudo-periodic and non-periodic variability, though it is a complement and absolutely not a substitute to more precise period search methods, e.g. the Fourier periodograms.

3 Short timescale variability detection: what we can expect with Gaia

To evaluate the efficiency of the variogram method for detecting short timescale variables from *Gaia* data, we simulate different light-curve data sets for various types of such astronomical objects. Our sample includes eight different periodic variable types, covering a wide range of periods (from 30 s to 12 h) and amplitudes (from a few mmags to a few mags), as well as transient events, i.e. M dwarf flares and supernovae (SNe). Note that not all short-period variable types are included in this work, and that we adopt a simplified approach, simulating each periodic light-cuve with one single period P and not treating multiperiodicity. Additionally, SNe are not short timescale variables per se, since their duration is much longer than 1 d. Nevertheless, SNe can experience quite fast and significant brightening, with a variation rate of the order of 0.1 mag/d. Given the precision of the *Gaia G* photometry, if the brightening phase of a supernova is sampled by *Gaia*, then we should be able to detect significant variation at the short timescale level.

For our analysis, we generate two different types of light-curves:

1. The *Gaia-like* light-curves, with a time sampling corresponding to the expected *Gaia* observation times for a random position in the sky, over a timespan $\Delta t \approx 5$ yrs (which is the nominal duration of the *Gaia* mission), and adding noise according to a magnitude-error distribution retrieved from real *Gaia* data, similar to the distribution presented in Fig. 6 of Eyer et al. (2017).

2. The *continuous* light-curves, corresponding to the same variables as in the continuous data set (same period or duration, amplitude and magnitude), but this time without noise and with a dense and regular time sampling, for comparison purposes.

For each simulated continuous light-curve, we calculate the associated *theoretical* variogram, for the appropriate lag values defined by the underlying time sampling (i.e. explored lags are multiple of the time interval δt). Similarly, we compute *observational* variograms associated with each simulated short timescale variable *Gaia*-like light-curve. This time, the explored lags are defined by the *Gaia* scanning law, i.e. the time intervals between CCD measurements (4.85 s, 9.7 s, 14.6 s, 19.4 s, 24.3 s, 29.2 s, 34 s and 38.8 s), and those between the different FoV transits (1 h 46 min, 4 h 14 min, 6 h, 7 h 46 min, etc), up to $h \approx 1.5$ d. Note that no lag can be explored from about 40 s to 1 h 46 min, which may have consequences on the detectability and timescales estimation of some sources.

Figures 2 and 3 show examples of *continuous* and *Gaia-like* light-curves and associated variograms, for a δ Scuti star and an M dwarf flare respectively. For those two cases, the source would be detected as short timescale candidate with $\gamma_{det} = 10^{-3}$ mag^2, not only in an ideal situation but also in the *Gaia-like* context, though the detection timescale is pushed from an ideal τ_{det} of a few minutes to 1 h 46 min due to the *Gaia* lag gap mentioned above. Moreover, the estimated τ_{typ} from the observational variogram matches the simulation input period as expected. For the transient source, we can identify visualy three different timescales from the theoretical variogram, which roughly correspond to the increase, decrease and total duration of the transient event. But when turning to the observational variogram, because of the specific lag values we can explore, all we can say is that this transient has a typical timescale which is between 40 s and 1 h 46 min. For now, for the simulated transients, we retrieve the lag of the maximum observational variogram value as an estimate of τ_{typ}, which should correspond to the decrease duration of the event.

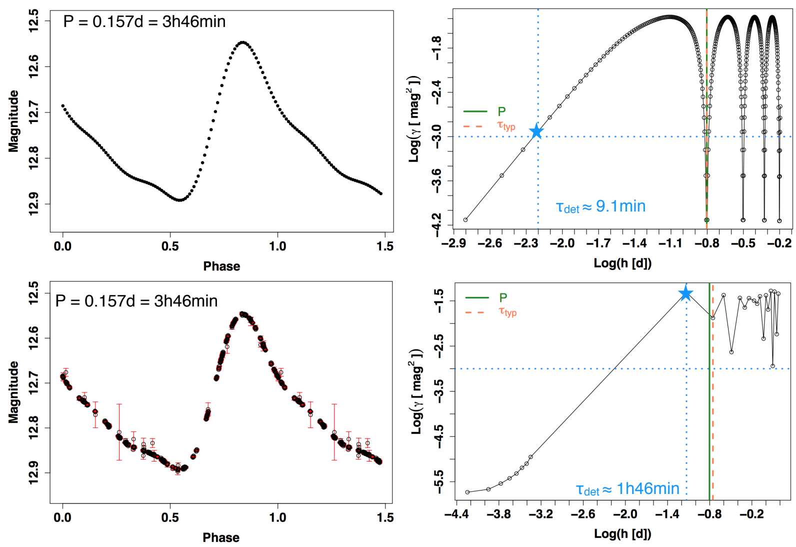

Fig. 2. Example of simulated δ Scuti light-curves. **Left:** *continuous* (top) and corresponding *Gaia-like* (bottom) light-curves, phase-folded with the input period of the simulation. **Right:** theoretical (top) and observational (bottom) variograms derived from the simulated light-curves. The blue dotted lines evidence the detection threshold (here 10^{-3} mag^2) and associated detection timescale. The green continuous line marks the simulation period, and the orange dashed line corresponds to the typical timescale estimated from the variograms.

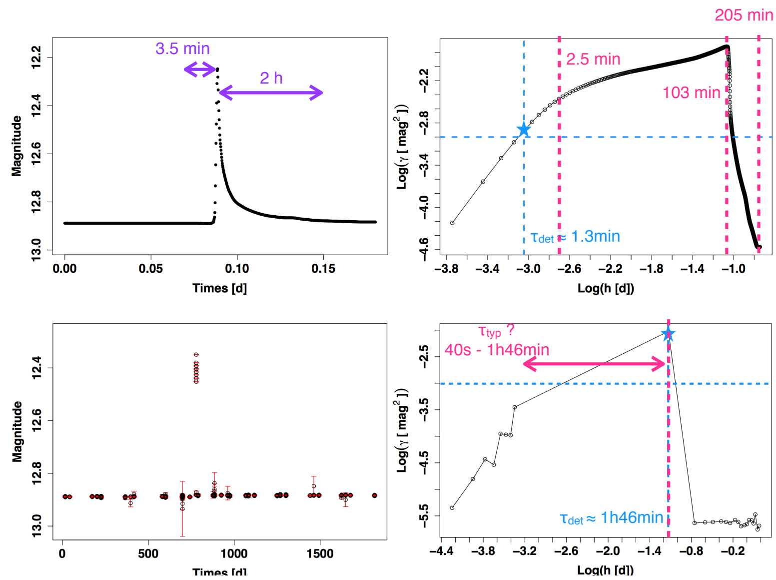

Fig. 3. Example of simulated M dwarf flare light-curves. **Left:** *continuous* (top) and corresponding *Gaia-like* (bottom) light-curves. The purple arrows indicate the approximate duration of the brightening and fading phases of the considered flare. **Right:** theoretical (top) and observational (bottom) variograms derived from the simulated light-curves. The blue dotted lines evidence the detection threshold (here 10^{-3} mag^2) and associated detection timescale. The pink dashed lines correspond to the typical timescale(s) estimated from the variograms.

Ensuring that the variogram method properly detects short timescale variables is necessary, but not sufficient. We also have to make sure that the method limits the number of unexpected detections, be it constant sources or stars showing variability on longer timescales than 12 h. Hence, we complete our *Gaia-like* data set with supplementary light-curve simulations of constant stars and sources showing sinusoidal variations with periods greater than 10 d, and calculate the corresponding observational variograms.

The short timescale detection criterion we use can be summarized as follows: a source is flagged as short timescale variable candidate if its maximum variogram value is greater than the chosen detection threshold γ_{det}, and if the associated detection timescale τ_{det} is shorter than 0.5 d. But which value of γ_{det} should we choose? Figure 4 represents the maximum variogram value as function of the mean G magnitude of the source for our full *Gaia-like* data set. As one can see, a constant threshold does not seem to be an appropriate choice: with e.g. $\gamma_{det} = 10^{-3}$ mag^2 most of the bright low amplitude variables are missed, whereas many false positive arise at the faint end. Consequently, we adopt a detection threshold depending on the mean magnitude of the source (grey continuous line in Fig. 4).

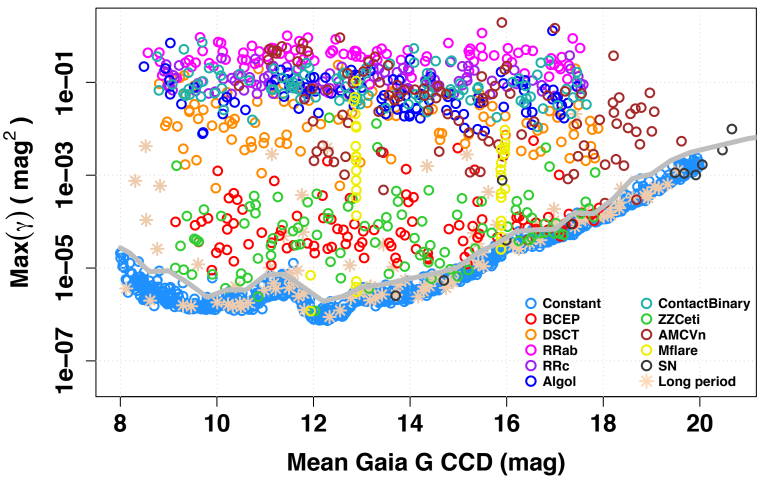

Fig. 4. Maximum variogram value as function of the mean *Gaia G* magnitude of the source, for the periodic variables and the constant sources of the *Gaia*-like data set. The grey continuous line corresponds to the definition of the detection threshold used.

With that short timescale detection criterion, about 94% of the periodic short timescale variables of the *Gaia-like* sample are recovered, as well as 30 M dwarf flares and 2 SNe. The false positive rate (i.e. contamination from constant sources) is around 0.1%, but contamination from longer period variables is as high as 16%. One way to limit that contamination could be to adopt a more restrictive definition of what short timescale variability is, e.g. with a lower detection timescale limit $\tau_{det} \leq 0.1$ d, focusing on the fastest phenomena detected. With this new upper limit on the detection timescale, the short period variable recovery rate drops from 94% to 91.9%, and we still detect 29 M dwarf flares and one supernova, whereas false positive and longer period contamination rates are significantly reduced, down to 0% and 2% respectively. Hence, with the variogram method we have a powerful criterion to identify short timescale variable candidates.

Additionally, with that approach we can further characterize our suspected variables. Figure 5 compares the typical timescale estimates for the detected short timescale candidates as function of their real characteristic timescale (i.e. input period P for the periodic sources, and decrease duration τ_{decr} for the transient ones). SNe are not treated here because their characteristic durations are longer than the maximum lag explored in the variogram analysis, thus we do not expect to retrieve a relevant timescale estimate for them. Outside the *Gaia* lag gap (brown arrows in Fig. 5) where no P or τ_{decr} good recovery is expected, we see that the typical timescale estimate, though not very precise, nevertheless gives an idea of the order of magnitude of the variation timescale. For 44% of the periodic flagged sources, τ_{typ} recovers the true period within a factor of 2. For 15% of them, our method fails to provide any typical timescale estimate. Regarding the detected M dwarf flares, for about half of them τ_{typ} recovers the decrease duration within a factor of 2. In the future, the idea would be to combine that not very precise but valuable information from the variogram with more accurate period search methods (e.g. Fourier periodograms), as well as with other variability studies performed in the *Gaia* DPAC context.

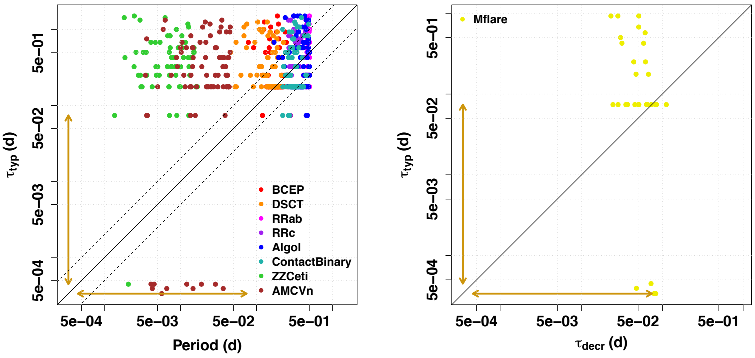

Fig. 5. Left: Typical timescale τ_{typ} as function of the input period, for the *Gaia-like* periodic simulations flagged as short timescale variables. **Right:** Typical timescale τ_{typ} as function of the decrease duration, for the *Gaia*-like transient simulations flagged as short timescale variables. The brown arrows indicate the *Gaia* lag gap.

4 Conclusions

In this proceeding, we evidence that, with an appropriate detection criterion, the variogram analysis is a very promising approach for identifying both periodic and transient short timescale variables observed by *Gaia*, from its per-CCD photometry, together with a limited contamination from non-variable and longer period variable objects. With the estimation of τ_{det} and τ_{typ}, we also retrieve valuable information on the timescale(s) and rapidity of the underlying variation. Among the perspectives it opens on the exploitation of *Gaia* data for variability analysis, in the case of periodic variability, the variogram results could be fruitfully combined with period search methods.

Nowadays, we are re-investing the knowledge and understanding we acquired on the variogram method through simulations, and are analyzing real *Gaia* data, searching for new short timescale variable candidates. We have obtained promising results, which we aim to include in the *Gaia* Data Release 2 planned for April 2018. In parallel, we have started a complementary ground-based follow-up campaign of some of our new short timescale candidates, so as to confirm the underlying supected fast variability. In the near future, we plan to further classifiy and characterize our candidates, combining all the *Gaia* data available (photometry in BP and RP, color, spectrum, parallaxes and proper motions), and exploring the performance of machine learning methods, to assess the variable type of the selected candidates.

References

Borucki, W. J., Koch, D., Basri, G., et al. 2010, Science, 327, 977

Eyer, L. & Genton, M. G. 1999, A&AS, 136, 421

Eyer, L., Mowlavi, N., Evans, D. W., et al. 2017, arXiv:astro-ph/1702.03295

Gaia Collaboration, Brown, A. G. A., Vallenari, A., et al. 2016, arXiv:astro-ph/1609.04172

Hughes, P. A., Aller, H. D., & Aller, M. F. 1992, ApJ, 396, 469

Kozłowski, S. 2016, The Astrophysical Journal, 826, 118

MacLeod, C. L., Ivezić, Ž., Sesar, B., et al. 2012, ApJ, 753, 106

Simonetti, J. H., Cordes, J. M., & Heeschen, D. S. 1985, ApJ, 296, 46

Sumi, T., Woźniak, P. R., Eyer, L., et al. 2005, MNRAS, 356, 331

Udalski, A., Szymanski, M., Kaluzny, J., Kubiak, M., & Mateo, M. 1992, Acta Astron., 42, 253

SF2A 2017
C. Reylé, P. Di Matteo, F. Herpin, É. Lagadec, A. Lançon, Z. Meliani, F. Royer (eds)

GAIA: ON THE ROAD TO DR2

D. Katz[1] and A.G.A. Brown[2]

Abstract. The second Gaia data release (DR2) is scheduled for April 2018. While Gaia DR1 had increased the number of stars with parallaxes by a factor 20 with respect to the Hipparcos catalogue, Gaia DR2 will bring another factor 500 increase, with parallaxes (and proper motions) for more than a billion stars. In addition, Gaia DR2 will deliver improved accuracy and precision for the astrometric and photometric data, G, $G_{\rm BP}$, $G_{\rm RP}$ magnitudes, radial velocities, identification and characterisation of variable stars and asteroids as well as stellar parameters for stars down to $G = 17$ mag. On behalf of the teams of the Gaia-DPAC consortium, these proceedings give a foretaste of Gaia DR2, 6 months before the release.

Keywords: Catalogues, Survey, Astrometry, Photometry, Spectroscopy

1 Introduction

Gaia was launched from Kourou on a Soyouz-Fregat rocket on 19^{th} December 2013. After a 4 week journey, Gaia was inserted on its nominal orbit around the second Lagrange point (L2) of the Sun-Earth system, on 14^{th} January 2014. There followed a 6 month commissioning phase and finally the start of the nominal mission phase on 14^{th} July 2014. For almost 4 years, Gaia has been continuously scanning the sky along 2 lines of sight simultaneously. Its two telescopes both feed 3 instruments: an astrometric instrument, a spectro-photometer and a spectrograph. The spectro-photometer uses two prisms to measure the spectral energy distribution (SED) of the sources in the blue (BP: 330-680 nm) and in the red (RP: 640-1050 nm). The spectrograph, the *Radial Velocity Spectrometer* (RVS), is a medium resolving power (R∼11 500) near infrared (845-872 nm) integral field spectrograph. The two fields of view and the 3 instruments are imaged on a single focal plane, made of 106 CCD detectors and almost a billion pixels. Gaia Collaboration et al. (2016b) provides a full description of the Gaia payload, mission and science case.

The development and operation of the ground-segment is under the responsibility of the Gaia Data Processing and Analysis Consortium (DPAC). The 450 members of the consortium are in charge of the calibration of the instruments, of the extraction of the astrophysical information and of the publication of the releases. The first Gaia data release (DR1), published a year ago on 14^{th} September 2016 (Gaia Collaboration et al. 2016a; Arenou et al. 2017) contained parallaxes and proper motions for about 2 millions stars, positions and mean G magnitudes for 1.1 billion sources and G-band light curves for about 3000 Cepheids and RR-Lyrae. Over the past 12 months, about 300 papers have already made use of the Gaia DR1. They address a large variety of science topics: e.g. open clusters (Gaia Collaboration et al. 2017b), Cepheids and RR-Lyrae (Gaia Collaboration et al. 2017a), Magellanic cloud kinematic (van der Marel & Sahlmann 2016) and structure (Belokurov et al. 2017), dynamical influence of the bar (Monari et al. 2017) and spiral arms (Hunt et al. 2017), stellar rotation (Davenport 2017) and many many others.

Coming only 1.5 years after Gaia DR1, Gaia DR2 is scheduled for April 2018. At the moment of writing these proceedings, the processing of the data has been completed and the validation is actively on-going. These proceedings present a preview of the Gaia DR2 content, 6 months before the release. Since, we are still in the validation phase, there might be some differences between this preview and the actual contents of the April release.

The second Gaia data release is the result of the collective and dedicated work of the 450 DPAC members.

[1] GEPI, Observatoire de Paris, PSL Research University, CNRS, Place Jules Janssen, F-92195 Meudon Cedex, France
[2] Leiden Observatory, Leiden University, PO Box 9513, 2300 RA, Leiden, the Netherlands

2 DR2 overview

For Gaia DR2, the 22 first months of data from the nominal mission have been processed (it was 14 months for Gaia DR1). The longer time baseline did allow for a stand alone (Gaia only) astrometric solution. From Gaia DR1 to Gaia DR2, the data processing pipelines have continued their developments and optimization, with specific attention for the instruments calibrations, leading to reduced systematics and improved precisions. The cross-match, i.e. the association of a group of observations with a given source, was also upgraded. As a consequence, the Gaia DR2 source identifiers will be independent from the Gaia DR1 ones*. A means of tracing their evolution will be provided. The pipelines have not only been upgraded, but new functionalities have also been added (G_{BP} and G_{RP} magnitudes from the photometric pipeline) and new pipelines activated: solar-system objects, spectroscopy and stellar parameters pipelines.

3 Astrometry and Photometry

For Gaia DR1, 11.2 months of data were processed. This was not enough to disentangle the parallaxes from the proper motions. In order to break this degeneracy, in Gaia DR1, a combined Tycho-Gaia Astrometric Solution (TGAS) was solved for (Michalik et al. 2015; Lindegren et al. 2016), allowing to derive the 5 astrometric parameters (positions, parallax, proper motions) for 2 million stars in common with the Hipparcos and Tycho-2 catalogues (ESA 1997; van Leeuwen 2007; Høg et al. 2000). With Gaia DR2, the longer baseline is enough to separate parallaxes from proper motions and to solve the full 5 parameter astrometric solution, using only Gaia data, for about 1 billion stars down to G=20 mag. Positions will be published for another half a billion stars. From Gaia DR1 to Gaia DR2, a lot of work has focused on improving the calibrations and in particular in the addition of colour-dependent astrometric terms as well as improved modelling of the satellite attitude and removal of the attitude disturbance (e.g. micro-meteoroids hits). The result is a reduction of the systematics and an improvement of the precision, e.g. the preliminary values for the formal errors on the parallaxes are: 30 μas at G=15, 150 μas at G=18 and 700 μas at G=20.

The number of stars with G magnitudes will increase from Gaia DR1 to Gaia DR2, from 1.1 billion (Carrasco et al. 2016; van Leeuwen et al. 2017; Evans et al. 2017) to about 1.5 billion. An important novelty of Gaia DR2 are the G_{BP} and G_{RP} magnitudes which have also been measured for 1.5 billions stars. For the bright stars the expected precision is of the order of the milli-magnitude.

4 Spectroscopy

Gaia DR2 will be the first Gaia release with radial velocities. For Gaia DR2, 235 millions of RVS spectra of stars brighter than $G_{\mathrm{RVS}} = 12$ were processed. The RVS records 3 spectra per observation (hereafter referred to as transits). The spectroscopic pipeline derives one radial velocity per transit. Therefore, about 78 millions transit radial velocities were obtained. The number of RVS transits per source is driven primarily by the Gaia scanning law and shows large excursions on the celestial sphere (figure 1) around the median which, in Gaia DR2 and for the RVS, is 7 transits per source. For Gaia DR2 the transit radial velocities will be combined to publish the median radial velocities of the 5 to 7 million stars fulfilling the following criteria: at least 2 RVS transits, T_{eff} in the range $]3500, 7000[$ K, no large dispersion of the transit radial velocities, good data quality indicators. Figure 2 shows the distribution on the sky of the stars which have passed the validation tests so far (2 months before the end of the validation phase).

Figure 3 shows the estimated radial velocity precision versus G_{RVS} magnitude and for different numbers of transits. On the bright side, the precision reaches a level of about 150 m/s. This is the current level of the wavelength calibration floor. It is about 6 times more precise than the pre-launch expectation of 1 km/s. This achievement was possible in particular because the RVS spectrograph (build by Astrium, now Airbus-DS) is a very stable instrument and Gaia has shown very smooth and stable behaviour during most of the mission. At the faint end the precision is not governed by the calibration residuals, but mostly by the photon noise. The precision therefore improves with the number of transits, from about 2.3 km/s at 4 transits to 0.9 km/s at 40

*https://www.cosmos.esa.int/web/gaia/news_20170203 transits (and $G_{\rm RVS} = 11.75$ mag).

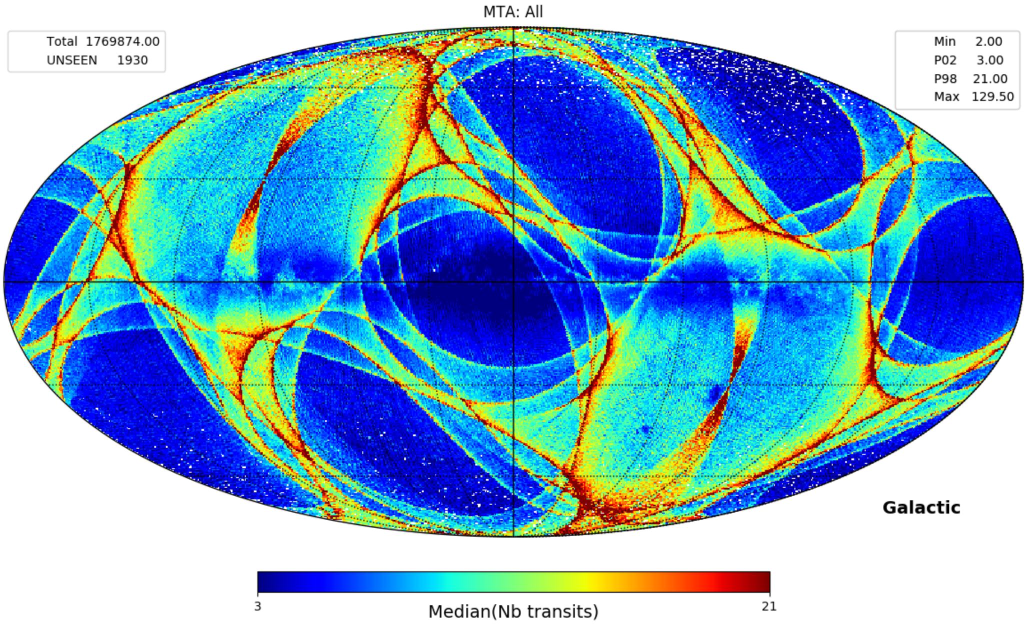

Fig. 1. Distribution on the sky (Galactic coordinates) of the median (per pixel) number of RVS transits per source. The area of the pixel is ~0.2 deg^2.

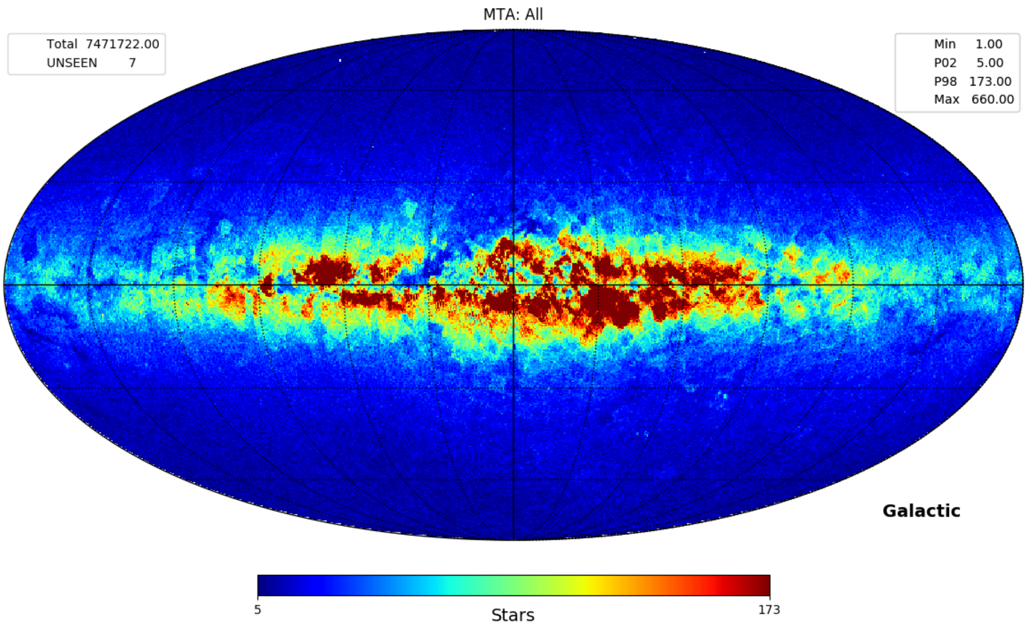

Fig. 2. Stellar density map (Galactic coordinates) of the stars for which a median velocity has been derived and which have passed the validation tests (so far). The area of the pixel is ~0.2 deg^2.

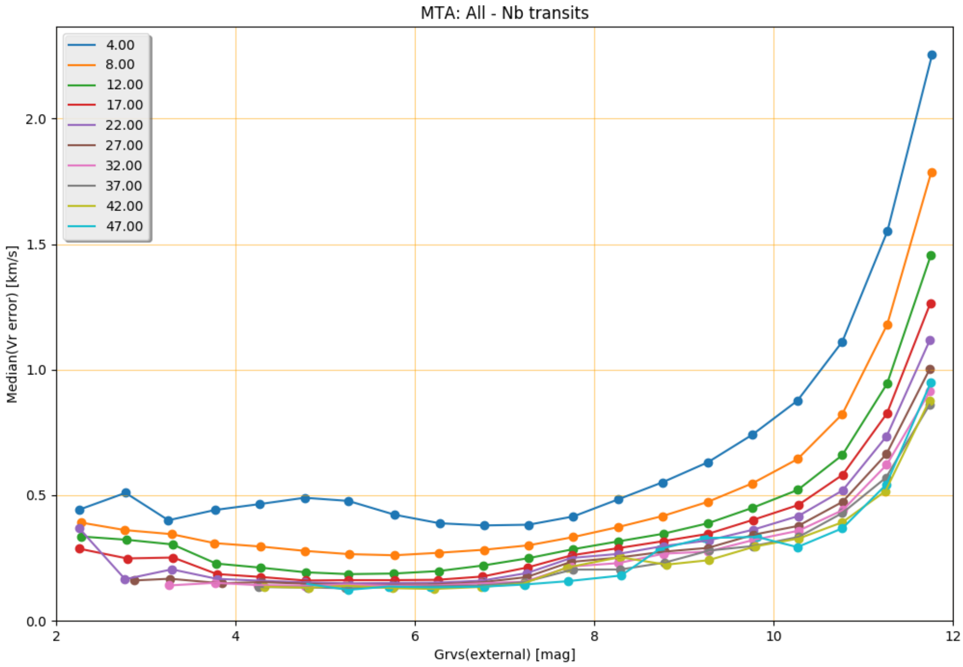

Fig. 3. Estimated radial velocity precision versus $G_{\rm RVS}$ magnitude and for different numbers of transits.

5 Asteroids, Variable stars, Stellar parameters

Another novelty of Gaia DR2 is the publication of asteroids. Several thousands of them with more than 9 transits have been detected and characterised in the 22 months of data. They include in particular: Near-Earth Objects, Main-Belt Asteroids and Trojans.

During the 2 first months of the nominal mission, Gaia followed a specific scanning law, passing through the ecliptic poles at each rotation of the satellite. The *Ecliptic Pole Scanning Law* (EPSL) yielded a large number of transits for the stars in the vicinity of the ecliptic poles. This, and the very hard work of the Gaia-DPAC variability group, resulted in the publication of a first catalogue of Gaia variable stars in Gaia DR1, ahead of the pre-launch schedule (Clementini et al. 2016; Eyer et al. 2017; Gaia Collaboration et al. 2017a). It contained 599 Cepheids and 2595 RR-Lyrae grouped in 38 deg^2 and belonging, for a large fraction, to the Large Magellanic Cloud. In Gaia DR2, the longer time baseline and therefore the larger number of transits, will enable the extension of the variability detection and characterisation pipeline to hundreds of thousands of variables over the whole sky.

The last novelty of Gaia DR2 is the publication of astrophysical parameters for stars. The G, $G_{\rm BP}$, $G_{\rm RP}$ magnitudes and the parallaxes have been used to derive the effective temperature (T$_{eff}$), absorption (A$_V$), luminosity (L) and radius (R) of stars down to $G = 17$ mag.

6 ... and beyond Gaia DR2

Two releases are already planned after Gaia DR2: `https://www.cosmos.esa.int/web/gaia/release`

The third Gaia data release (DR3) is scheduled mid/late 2020. In addition to the performance improvement, DR3 should also contain: source classification, stellar parameters derived from BP and RP spectral energy distributions and RVS spectra, radial velocities for ~40-50 millions stars brighter than $G_{\rm RVS} = 14$ mag, non-single stars as well as extended catalogues of solar system objects and variable stars.

The fourth Gaia data release (DR4) is planned at the end of 2022. It should reach the specified end-of-mission performance, contain all planned deliveries, including the exo-planets catalogue and the transit data. DR4 will be the final release for the nominal mission.

The end of the nominal mission is 2019, but Gaia's current micro-propulsion fuel supplies would allow the satellite to operate until 2024. A proposal for a 5 year extension of the mission has therefore been made. If the extension is accepted, one (or a few) catalogue(s) will follow DR4, delivering performances beyond the original mission goals.

7 Conclusions

Gaia DR2 represents a big step forward: positions, parallaxes and proper motions for a billion stars, G, $G_{\rm BP}$, $G_{\rm RP}$ for 1.5 billions stars, median radial velocities for 5 to 7 million stars as well as asteroids, variable stars and stellar parameters.

Gaia DR1 and soon Gaia DR2 are the result of more than ten years of collective work by the DPAC consortium members for designing, implementing, optimizing, testing and operating the Gaia ground-based pipelines and validating the data produced.

References

Arenou, F., Luri, X., Babusiaux, C., et al. 2017, A&A, 599, A50

Belokurov, V., Erkal, D., Deason, A. J., et al. 2017, MNRAS, 466, 4711

Carrasco, J. M., Evans, D. W., Montegriffo, P., et al. 2016, A&A, 595, A7

Clementini, G., Ripepi, V., Leccia, S., et al. 2016, A&A, 595, A133

Davenport, J. R. A. 2017, ApJ, 835, 16

ESA, ed. 1997, ESA Special Publication, Vol. 1200, The HIPPARCOS and TYCHO catalogues. Astrometric and photometric star catalogues derived from the ESA HIPPARCOS Space Astrometry Mission

Evans, D. W., Riello, M., De Angeli, F., et al. 2017, A&A, 600, A51

Eyer, L., Mowlavi, N., Evans, D. W., et al. 2017, ArXiv e-prints

Gaia Collaboration, Brown, A. G. A., Vallenari, A., et al. 2016a, A&A, 595, A2

Gaia Collaboration, Clementini, G., Eyer, L., et al. 2017a, A&A, 605, A79

Gaia Collaboration, Prusti, T., de Bruijne, J. H. J., et al. 2016b, A&A, 595, A1

Gaia Collaboration, van Leeuwen, F., Vallenari, A., et al. 2017b, A&A, 601, A19

Høg, E., Fabricius, C., Makarov, V. V., et al. 2000, A&A, 355, L27

Hunt, J. A. S., Kawata, D., Monari, G., et al. 2017, MNRAS, 467, L21

Lindegren, L., Lammers, U., Bastian, U., et al. 2016, A&A, 595, A4

Michalik, D., Lindegren, L., & Hobbs, D. 2015, A&A, 574, A115

Monari, G., Kawata, D., Hunt, J. A. S., & Famaey, B. 2017, MNRAS, 466, L113

van der Marel, R. P. & Sahlmann, J. 2016, ApJ, 832, L23

van Leeuwen, F., ed. 2007, Astrophysics and Space Science Library, Vol. 350, Hipparcos, the New Reduction of the Raw Data

van Leeuwen, F., Evans, D. W., De Angeli, F., et al. 2017, A&A, 599, A32

SF2A 2017
C. Reylé, P. Di Matteo, F. Herpin, É. Lagadec, A. Lançon, Z. Meliani, F. Royer (eds)

THE PROGRAMME "ACCURATE MASSES FOR SB2 COMPONENTS"*

J.-L. Halbwachs[1], F. Arenou[2], H.M.J. Boffin[3], B. Famaey[1], A. Jorissen[4], F. Kiefer[5], J.-B. Le Bouquin[6], D. Pourbaix[4], P. Guillout[1], R. Ibata[1], Y. Lebreton[7,8], T. Mazeh[9], A. Nebot Gómez-Morán[1] and L. Tal-Or[10]

Abstract. Accurate stellar masses are requested in order to improve our understanding of stellar interiors, but they are still rather rare. Fortunately, the forthcoming Gaia Mission will provide astrometric measurements permitting the derivation of the orbital inclinations of nearby binaries which are also observed as double-lined spectroscopic binaries (SB2s) with ground-based telescopes. A programme of radial velocity (RV) measurements was initiated in 2010 with the Sophie spectrograph of the Haute-Provence observatory in order to derive accurate SB2 orbits for a large set of stars. Therefore, combined SB2+astrometric orbits will be derived thanks to Gaia, and masses with errors around 1 % are expected for both components. The programme includes 70 SB2s, and the accurate SB2 orbits of 24 of them were already derived. In addition, two complementary programmes devoted to southern stars or to late-type dwarf stars were also initiated with the HERMES and the CARMENES spectrographs, respectively. Interferometric measurements were obtained with the VLTI/PIONIER for 7 SB2s, and were taken from other sources for 4 others. Currently, combined "visual binary" (VB) +SB2 solutions were derived for 7 binaries, leading to the masses of the components and to the parallaxes. The parallaxes from the Hipparcos 2 catalogue were corrected for orbital motion and compared to our solution, confirming the high quality of Hipparcos 2.

Keywords: binaries: spectroscopic, binaries: visual, Astrometry

1 Introduction

Mass is the most crucial input in stellar internal structure modelling. It predominantly influences the luminosity of a star at a given stage of its evolution, and also its lifetime. The knowledge of the mass of stars in a non interacting binary system, together with the assumption that the components have same age and initial chemical composition, allows us to determine the age and the initial helium content of the system and therefore to characterise the structure and evolutionary stage of the components. Such modelling provides insights into the physical processes governing the structure of the stars and gives constraints on the free physical parameters of the models, provided the masses are known with high accuracy (Lebreton 2005). Therefore, modelling stars with extremely accurate masses (at the 1 % level), in different ranges of masses, would allow to firmly anchor the models of the more loosely constrained single stars.

* BASED ON OBSERVATIONS PERFORMED AT THE HAUTE-PROVENCE OBSERVATORY

[1] Université de Strasbourg, CNRS, Observatoire astronomique de Strasbourg, UMR 7550, F-67000 Strasbourg, France
[2] GEPI, Observatoire de Paris, PSL Research University, CNRS, Université Paris Diderot, Sorbonne Paris Cité, Place Jules Janssen, F-92195 Meudon, France
[3] ESO, Av. Alonso de Cordova 3107, 19001, Casilla, Santiago 19, Chile
[4] FNRS & Institut d'Astronomie et d'Astrophysique, Université Libre de Bruxelles, boulevard du Triomphe, 1050 Bruxelles, Belgium
[5] Institut d'Astrophysique de Paris, CNRS, UMR 7095, 98bis boulevard Arago, F-75014 Paris
[6] UJF-Grenoble 1/CNRS-INSU, UMR 5274, Institut de Planétologie et d'Astrophysique de Grenoble (IPAG), F-38041 Grenoble, France
[7] LESIA, Observatoire de Paris, PSL Research University, CNRS UMR 8109, Université Pierre et Marie Curie, Université Paris
[8] Institut de Physique de Rennes, Université de Rennes 1, CNRS UMR 6251, F-35042 Rennes, France
[9] School of Physics and Astronomy, Tel Aviv University, Tel Aviv 69978, Israel
[10] Institut für Astrophysik (IAG), Friedrich-Hund-Platz 1, D-37077 Göttingen, Germany

At present, accurate masses are still rare, but the Gaia astrometric satellite could dramatically change this situation. Astrometric orbits will be obtained for several systems which are already known as spectroscopic binaries (SBs). When the radial velocities (RVs) of both components of an SB are measured, i.e. for double-lined SBs (SB2s), the products $\mathcal{M}_1 \sin^3 i$ and $\mathcal{M}_2 \sin^3 i$ may be derived from the orbital elements; therefore, when the inclination i of the orbit will be derived from Gaia observations, so will be the masses of the components, $\mathcal{M}_1$ and $\mathcal{M}_2$. In addition, the semi-major axis of a photocentric orbit is related to the luminosity ratio of the components, allowing to derive the individual magnitudes in the Gaia G band.

For all these reasons, an observational programme was initiated in 2010, using the SOPHIE spectrograph and the 193 cm telescope of the Observatory of Haute-Provence (OHP). This programme is presented in details in Sections 2 and 3. In addition, two complementary RV programmes were initiated on other telescopes, and also an interferometric programme. These related programmes are presented in Sections 4 and 5 hereafter. Thanks to the RVs and to the interferometric measurements, it was possible to derive the masses of the components of a few binaries, as well as the parallax of these systems. The Hipparcos parallaxes were thus verified, as explained in Section 6.

2 The target list

Two lists of targets are used to manage the OHP programme. The principal one, which is called the "main sample" hereafter, was extracted from a selection of about 200 SBs (single-lined or double-lined) fainter than 6th mag and for which the probability to obtain the component masses with an accuracy better than 1 % was estimated to be larger than 20 %, at least if it is possible to derive the RV of the secondary component. Seventy SB2s were eventually retained on the basis of our first observations, including 24 which were previously known as SB1s and for which the secondary component was detected with SOPHIE. The selection process is described in details in Halbwachs et al. (2014). The spectral types of the primary components are between A0 and M2. The majority of stars are on the main sequence, but 6 SB2s have a late-type giant primary component. Rough estimates of the masses of the secondary components may be derived from the spectral types of the primary components and from the mass ratios of the systems. Masses between 0.3 and 2 $\mathcal{M}_\odot$ are then obtained. The "primary spectral type vs secondary mass" diagram of the main sample is shown in Fig. 1.

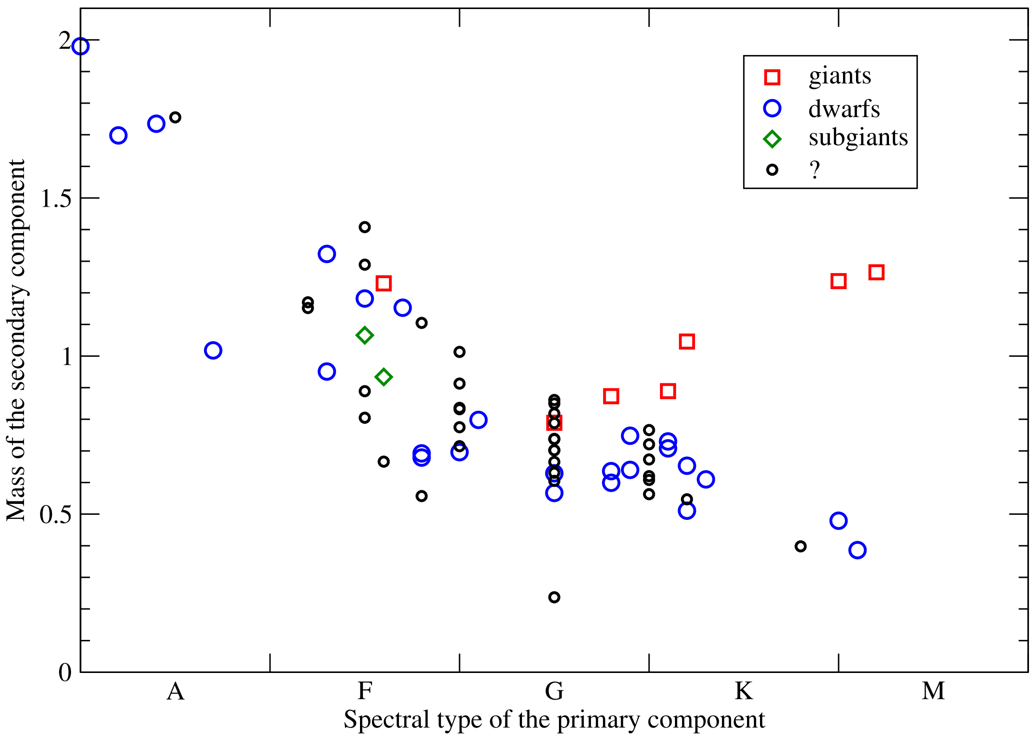

Fig. 1. The "primary spectral type vs secondary mass" diagram of the main sample.

In 2013, it was decided to observe also targets brighter than 6th mag. So bright stars are observed with Gaia, but it is expected that their astrometric measurements will be less accurate than those of the moderately faint stars. Above all, these bright targets were used as backup targets when the weather was too bad to observe the main sample. In practice, it was then possible to perform a few observations with bad weather conditions, but, fortunately, this happened rarely and the SBs of the backup sample received very few observations. In practice, however, the backup sample includes some SB1s (4 so far) for which we were able to detect the secondary spectrum.

3 Present status

In early August 2017, we had collected 1183 spectra, and we had also found 21 additional ones in the SOPHIE archive. The status of the main sample is presented in Fig. 2, which is a “orbit coverage vs number of spectra” diagram. The orbital elements of an SB2 may be reliably derived when the number of RV measurements of each component is larger than 11: this limit makes possible to derive SB1 orbits with at least 5 degrees of freedom, and therefore to estimate the weights of the RVs of each component in the computation of the elements of the SB2 orbit (see Halbwachs et al. 2016). On another side, it is requested that the orbit is covered by the observations, i.e. that the time span ΔT is longer than the period. The area delimited in the upper right corner of Fig. 2 contains the SB2s for which the orbital elements could be derived. Nevertheless, additional observations are still required for some of these stars: the secondary RV is not always measurable, and the RV measurements must also be distributed among all the phases of the orbit.

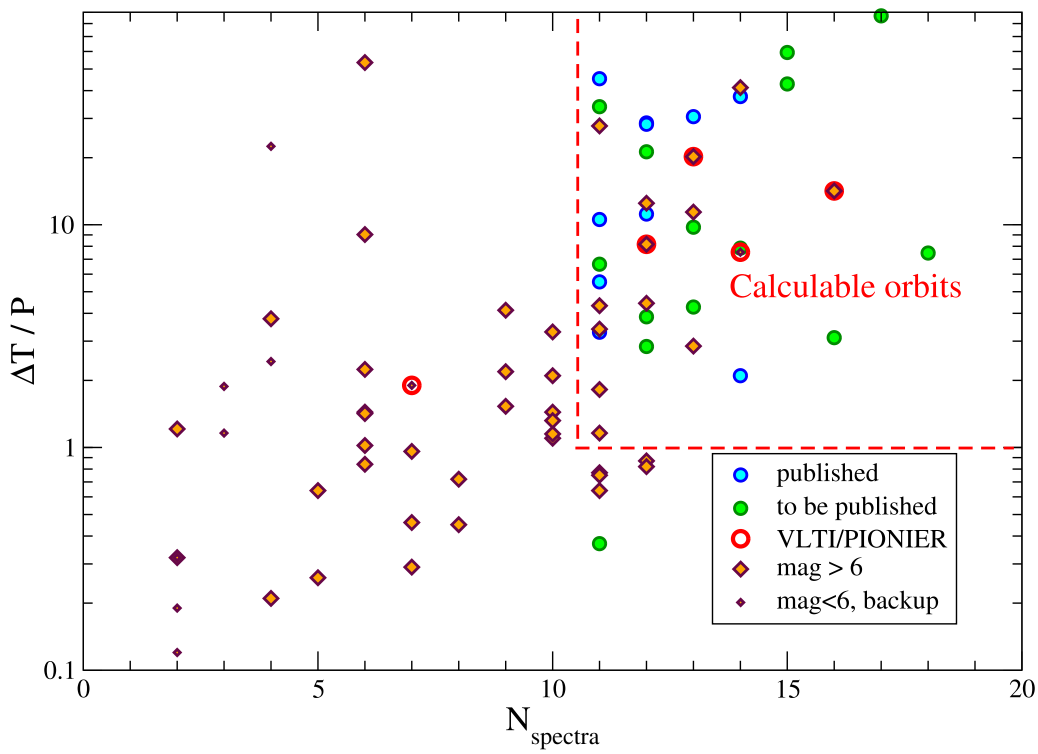

Fig. 2. The “number of spectra vs orbit coverage” diagram of the sample. The orbital elements may be calculated for the stars in the upper right corner, when the RV of the secondary was actually derived at least 11 times, and when the measurements are distributed all over the orbit.

The orbital elements of one SB2 were derived although it was not observed over a complete period: HIP 77122 has an eccentric orbit with a 11-year period, and it was observed near the periastron which is the only part of the orbit where it is possible to derive the RVs of both components. So, we have derived an accurate orbit by fixing the period to a value obtained taking into account old measurements.

The RVs of the binary components are derived twice: a preliminary estimation is computed from the cross-correlation function (CCF) of each spectrum with a template. This CCF is a product of the Sophie reduction pipe-line, and the quality of the RVs thus obtained is quite sufficient to monitor the observations: these RVs may

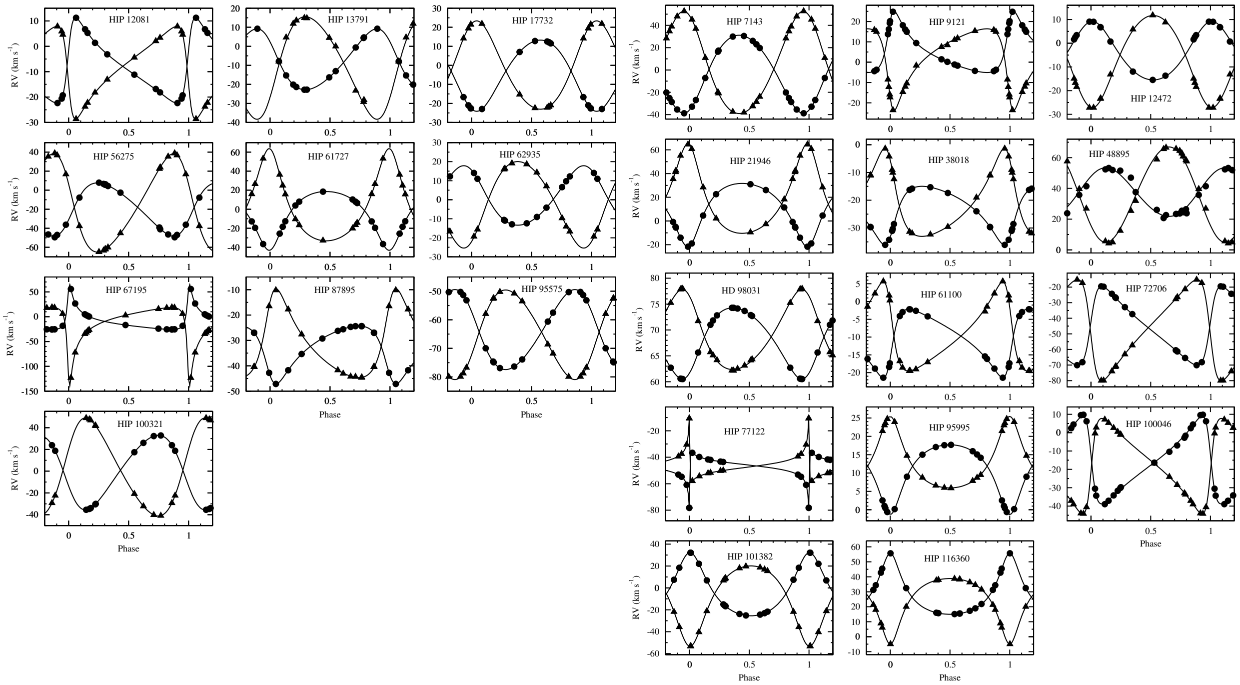

Fig. 3. Left: The 10 spectroscopic orbits derived from the RV measurements obtained with TODCOR in Kiefer et al. (2016). Right: The 14 additional spectroscopic orbits derived from the RV measurements obtained with TODCOR (Kiefer et al. 2017)

be used to improve the orbital elements used to compute ephemerides and to plan observations, and possible outliers may be detected. Nevertheless, the final RVs are derived from a new reduction using the TODCOR algorithm (Zucker & Mazeh 1994; Zucker et al. 2004). They are significantly different from the preliminary values, but more reliable, as shown in Halbwachs et al. (2017). So far, our observations lead to high-quality orbital elements for 24 SB2s: 10 SB2s in Kiefer et al. (2016), and 14 in Kiefer et al. (2017) (Fig. 3). Among the 48 components of these binaries, 32 have minimum masses more accurate than 1 %.

4 Other RV programmes

The OHP programme was complemented with two others, which are based on a similar selection. These programmes are presented hereafter:

1. **The HERMES programme**. Since the latitude of OHP is around +44 deg we had not selected SBs with declination lower than -5 deg. However, the stars with declination between -5 and -30 deg are easily observable from the La Palma Observatory (Canary Islands) with the HERMES spectrograph mounted on the Mercator telescope (Raskin et al. 2011). Fifty-height SB1s and SB2s were selected in a first step, and, after some observations, 7 of them were eventually retained.

2. **The CARMENES programme**. About 150 SB1s were observed with SOPHIE, but the secondary component was detected for only 20 of them. The CARMENES spectrograph mounted on the 3.5m telescope of Calar Alto is much more efficient than SOPHIE to detect late-type secondaries, since it is working in the infrared range. Twenty-three SB1s were selected among the OHP targets because their secondary components were expected to have spectral types at least as late as M. After one year, the secondary component was detected for 9 SBs, and it is even possible to derive an accurate orbit for 2 of them. For the 7 others, the number of RV measurements is too small to improve the orbital elements, but it is possible to derive the mass ratio.

5 SB2 resolved by interferometry

Gaia will provide astrometric orbits, i.e. the motion of the photocentre of each binary around the barycentre, in addition to the single-star parameters, which are the position, the proper motion and the trigonometric parallax. Contrarily to an astrometric orbit, an interferometric orbit is a "visual binary" (VB) orbit, describing the motion of one component (usually, the faintest one) with respect to the brightest one. However, a combined SB2+VB orbit provides most of the elements of an SB2+astrometric orbit: it includes the period and the eccentricity, the masses of the components, the three angles defining the orientation of the orbit, and also the parallax. Therefore, it is highly relevant to collect enough interferometric measurements to derive combined SB2+VB orbits for some stars of our sample. This will make possible a verification of the masses derived for our programme, but also of the parallaxes.

Among the 24 SB2s with improved orbital elements, 4 binaries were resolved by interferometry in the past, and they were sufficiently observed to derive their orbital inclinations. In addition, we obtained interferometric observations with the PIONIER instrument of the ESO Very Large Telescope Interferometer (VLTI) for 7 binaries: 3 SB2s of the OHP main sample, 2 of the OHP backup sample, and 2 of the HERMES program. The apparent relative orbits of 3 of these binaries were derived in Halbwachs et al. (2016). They are presented in Fig. 4 with three others that will be published soon (Boffin et al. 2017).

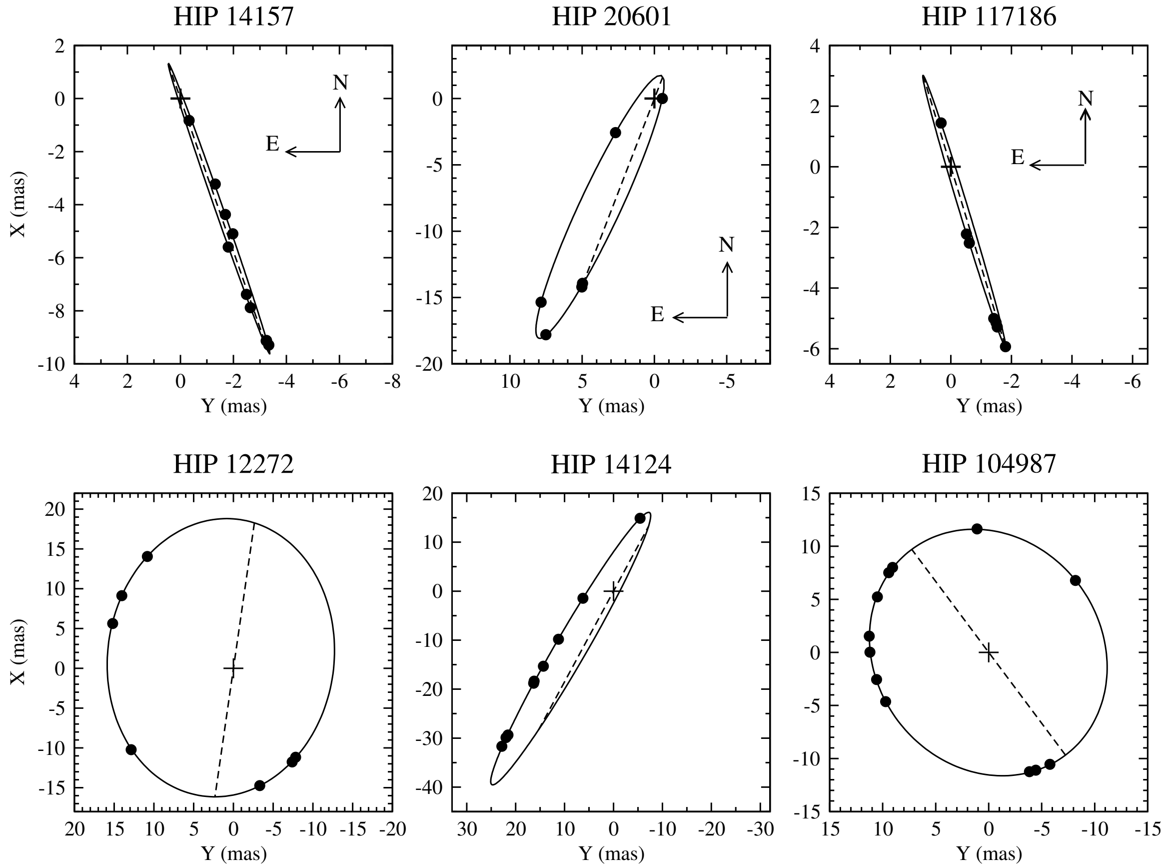

Fig. 4. Up : The 3 first interferometric orbits obtained with PIONIER (Halbwachs et al. 2016). Down : Three other PIONIER orbits (Boffin et al. 2017).

6 Verification of the Hipparcos parallaxes

It is too early to verify the Gaia parallaxes of astrometric binaries, but we can still verify the results of the Hipparcos mission. We consider the Hipparcos 2 reduction (van Leeuwen 2007), but we can't compare directly our parallaxes with those provided in the catalogue: The Hipparcos 2 parallaxes were computed ignoring the orbital motion, and they must be corrected on the basis of a combined SB2+astrometric solution. In practice, the correction is not important for most of the binaries, but it is really significant when the period is close to one year (see *e.g.* Pourbaix & Jorissen 2000)

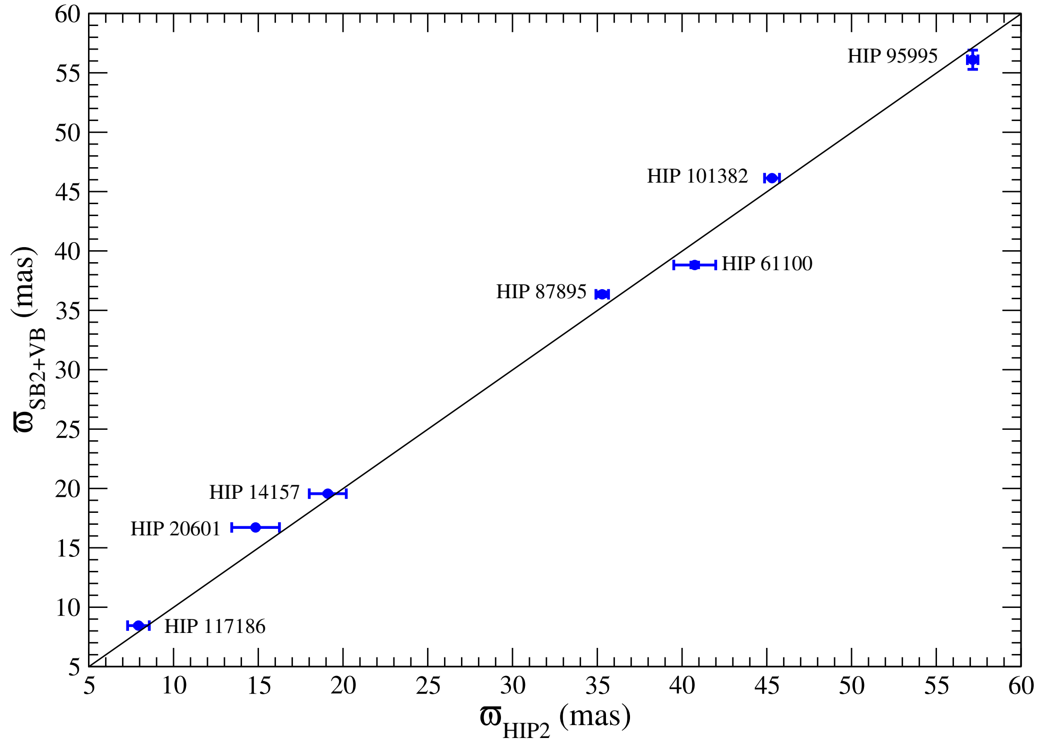

Fig. 5. Comparison of the corrected Hipparcos 2 parallaxes with the SB2+VB solutions.

We consider now the binaries for which we have an SB2+VB orbit based on accurate RV measurements. We count 7 SB2, including 1 from the HERMES programme. Among these binaries, only 3 were observed with PIONIER because the RV observations are still not completed for the binaries observed by Boffin et al. (2017). The interferometric measurements of the 4 other binaries are from other sources.

The SB2+VB parallaxes are compared to the corrected Hipparcos 2 parallaxes in Fig. 5. Since the error bars represent 1 standard deviation, it is obvious that the agreement is rather good. It is also visible that, HIP 95995 excepted, the uncertainties of the SB2+VB parallaxes are much better than that of Hipparcos 2. Therefore, they will be usable for the verification of the Gaia parallaxes, at least for the stars brighter than 6th mag.

7 Conclusions

About 80 double stars are observed through three independent programmes in order to improve their SB2 orbital elements. Thanks to this effort, it will be possible to derive the masses of several double star components with an accuracy better than 1 % when the astrometric transits of the Gaia mission will be delivered. The reliability of these masses will be verified on the basis of about a dozen interferometric binaries. For these stars, the parallax is derived from a VB+SB2 orbit, and we have verified the reliability of the Hipparcos 2 parallaxes. A similar verification will be possible for the parallaxes coming from Gaia, at least for the bright stars.

This project was supported by the french INSU-CNRS “Programme National de Physique Stellaire” and “Action Spécifique *Gaia*”. PIONIER is funded by the Université Joseph Fourier (UJF), the Institut de Planétologie et d’Astrophysique de Grenoble (IPAG), and the Agence Nationale pour la Recherche (ANR-06-BLAN-0421, ANR-10-BLAN-0505, ANR-10-LABX56). The integrated optics beam combiner is the result of a collaboration between IPAG and CEA-LETI based on CNES R&T funding. We are grateful to the staff of the Haute–Provence Observatory, and especially to Dr F. Bouchy, Dr H. Le Coroller, Dr M. Véron, and the night assistants, for their kind assistance. We made use of the SIMBAD database, operated at CDS, Strasbourg, France. This research has received funding from the European Community’s Seventh Framework Programme (FP7/2007-2013) under grant-agreement numbers 291352 (ERC)

References

Boffin, H., Le Bouquin, J.-B., Halbwachs, J.-L., et al. 2017, A&A, (in preparation)

Halbwachs, J.-L., Arenou, F., Pourbaix, D., et al. 2014, MNRAS, 445, 2371

Halbwachs, J.-L., Boffin, H., Le Bouquin, J.-B., et al. 2016, MNRAS, 455, 3303

Halbwachs, J.-L., Kiefer, F., Arenou, F., et al. 2017, in Proceedings SF2A 2017 (this volume), ed. C. Reylé, P. Di Matteo, F. Herpin, E. Lagadec, A. Lançon, & F. Royer, SF2A (arXiv:1710.02301)

Kiefer, F., Halbwachs, J.-L., Arenou, F., et al. 2017, MNRAS, (in preparation)

Kiefer, F., Halbwachs, J.-L., Arenou, F., et al. 2016, MNRAS, 458, 3272

Lebreton, Y. 2005, in The Three-Dimensional Universe with Gaia, ESA SP-576, ed. C. Turon, K. O'Flaherty, & M. Perryman (ESA), 493

Pourbaix, D. & Jorissen, A. 2000, A&AS, 145, 161

Raskin, G., van Winckel, H., Hensberge, H., et al. 2011, A&A, 526, 69

van Leeuwen, F. 2007, A&A, 474, 653

Zucker, S. & Mazeh, T. 1994, ApJ, 420, 806

Zucker, S., Mazeh, T., Santos, N.C., Udry, S., & Mayor, M. 2004, A&A, 426, 695

SF2A 2017
C. Reylé, P. Di Matteo, F. Herpin, É. Lagadec, A. Lançon, Z. Meliani, F. Royer (eds)

3D MAPS OF THE LOCAL INTERSTELLAR MEDIUM: THE IMPACT OF GAIA

L. Capitanio[1], R. Lallement[1], J. L. Vergely[2], M. Elyajouri[1], C. Babusiaux[1], L. Ruiz-Dern[1], A. Monreal-Ibero[1], F. Arenou[1] and C. Danielski[1]

Abstract. Gaia parallaxes combined with colour excess and absorption measurements from large stellar surveys will allow building increasingly precise three-dimensional maps of the interstellar matter (ISM). Reciprocally, detailed maps of the ISM will allow improving photometric calibrations of Gaia and measuring more precisely the amounts of reddening. In the future, the extraction of a diffuse interstellar band (DIB) from Gaia RVS (Radial Velocity Spectrometer) spectra will allow to build a tomography of the carrier of this DIB and compare it with dust and gas distributions. Here we show several results that illustrate current progress in local ISM mapping and a first example of the stellar-interstellar synergy linked to Gaia: a) how Gaia-DR1 parallaxes already modify the ISM maps obtained by means of a full-3D inversion of a compilation of colour excess data, b) how DIB measurements and corresponding Gaia parallaxes can complement colour excess data and improve the maps, c) new hierarchical methods combining distinct surveys, d) improved maps including APOGEE colour excess estimates deduced from the recent Gaia-based photometric calibrations of Ruiz-Dern et al (this issue), e) additional inclusion of LAMOST colour excess estimates (Wang et al, 2016).

Keywords: Interstellar medium, Milky Way, stars

1 Introduction

3D maps of the nearby and distant Milky Way Interstellar Medium (ISM) are useful multi-purpose tools that started to get developed only recently. Their construction requires very large catalogues of distance-limited absorption data to be gathered from stellar spectra, and the additional knowledge of the distances to the target stars. Both types of information are currently in significant, rapid progress: massive photometric, spectro-photometric or spectroscopic stellar surveys have started or are in preparation: they will provide dust extinction and gaseous absorption towards an increasing number of stars. In parallel, Gaia will measure parallaxes towards more than 1 billion of stars.

3D maps or pseudo-3D maps have already been produced based on photometric extinction but also diffuse interstellar bands (DIBs) (see an exhaustive list in Capitanio et al. (2017) , hereafter CLV). Each mapping technique has its advantages and limitations. The full 3D tomographic inversion methods developed by Vergely et al. (2001), Sale & Magorrian (2014) and Rezaei Kh. et al. (2017) are based on individual sightlines and have the advantages of being adapted to the nearby ISM and fully exploiting the correlations between the IS matter volume density in two locations close in space. However, whatever the technique, a major difficulty is associated with the decrease with distance of the achievable spatial resolution, due to increasing uncertainties on target distances and often due to the decrease in volume density of observed targets.

In CLV we have tested the introduction of TGAS parallaxes and presented some attempts to address the above limitations. We have analysed the changes induced in the inverted 3D maps when Hipparcos or photometric distances are replaced with parallax distances from the TGAS catalog (step1). The replacement was possible for 80% of the targets and this use of TGAS had a significant influence in some regions and removed an important discrepancy with other maps in the first quadrant at l≃70-80°. We subsequently tested the inversion of a composite dataset combining colour excess measurements based on photometry on the one hand, and colour excess estimates based on equivalent widths (EWs) of near-infrared (NIR) diffuse interstellar bands (DIBs) on

[1] GEPI, Observatoire de Paris, PSL Research University, CNRS UMR 8111 - 5 Place Jules Janssen, 92190 Meudon, France
[2] ACRI-ST, 260 route du Pin Montard, Sophia Antipolis, France

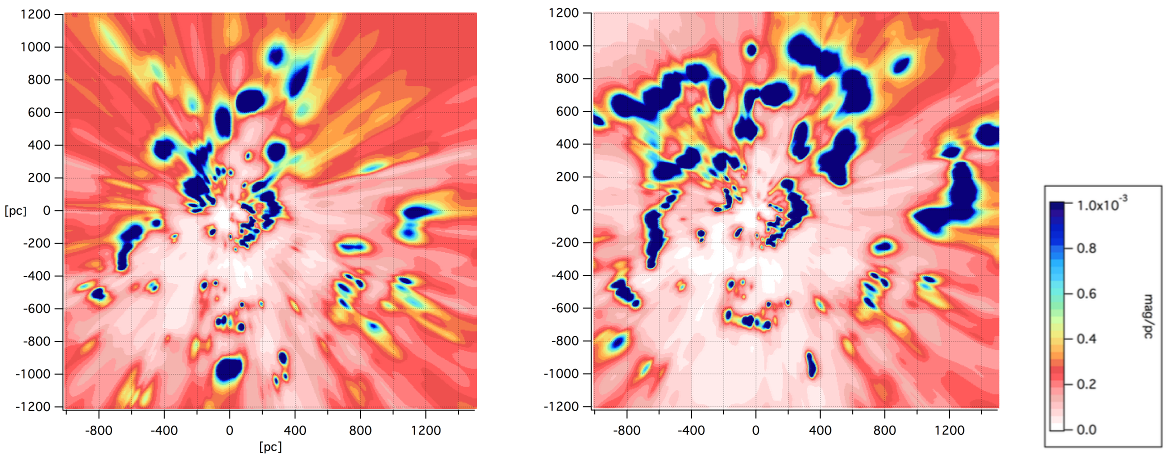

Fig. 1: Dust cloud complexes in the Galactic Plane: units are parsecs, the Sun is at (0,0), the Galactic center to the right, longitudes increase clockwise, the colour scale refers to reddening E(B-V) per parsec (mag.pc^{-1}). Left): map based on the same dataset as in Lallement et al. (2014) and a homogeneous prior distribution, but with TGAS parallaxes for 80% of the targets. Right): the latest map, with additional APOGEE data, both from DIB data and spectrophotometric color excess-distance measurements, and a PS1-based 3D pro (see CLV).

the other hand(Elyajouri et al. 2016) (step 2). The DIBs are extracted from APOGEE spectra (Majewski 2012; García Pérez et al. 2015). For the same dataset we also tested the use of a non-analytically calculated prior distribution, namely a 3D distribution inferred from the larger scale 3D distribution of Green et al. (2015) (step3). Such a use of larger scale prior distributions opens the way to hierarchical methods producing maps with a distance-dependent resolution.

In the present work we illustrate the above 3 steps and two additional improvements of the maps. The first one is based on the inclusion of $\simeq$ 20,000 distance-colour excess estimates for APOGEE red stars (step 4). These estimates utilise the G band calibration described in Ruiz-Dern et al. (2017) and Ruiz-Dern et al (this issue). This calibration could be safely made due to the low reddening of the calibration stars, a dataset selected based on our previous 3D dust maps. Such a positive feedback illustrates the potential synergy between stellar and interstellar analyses. Finally, we tested the inversion of a large target star density in a restricted area, using a fraction of the LAMOST distance-colour excess estimates of the Wang et al. (2016) catalogue. In section 2 we illustrate the effect of steps 2 to 4 in the Galactic Plane, and in section 3 we illustrate the consecutive effects of all the 5 steps in a vertical plane containing Taurus-Perseus.

2 Galactic Plane distribution

To illustrate the benefit of interstellar - stellar feedback in the frame of Gaia, we show in Fig. 1a the dust opacity in the Galactic plane based on the inversion of our previous catalogue of colour excess data (from Lallement et al. (2014)), after replacement of Hipparcos or photometric distances by Gaia parallax distances, when available (see CLV for more details). It is this map that has been used by Ruiz-Dern et al. (2017) to select Gaia targets located along sightlines that are free of dust and enter the Gaia red clump photometric calibration process. This map is compared with a more recent one obtained from an inversion with additional data from the SDSS/APOGEE survey (Fig. 1b). Two types of additional data were included -i) colour excess estimates based on photometry and spectroscopic stellar parameters and ii)-colour excess estimates deduced from the 15273A diffuse interstellar band equivalent width. As in CLV a non-analytical prior distribution deduced from Pan-STARRS 3D maps (Green et al. 2015) is used instead of an homogeneous distribution decreasing exponentially from the Plane to the halo. It is clear from the comparison between the two maps in Fig. 1 that more distant structures are now recovered, especially second ranks of clouds located beyond foreground opaque systems. This is especially visible in the third quadrant and mainly due to two effects: i) the use of more distant target stars, and ii) the use of data in the infrared. The dust clouds being less opaque in this wavelength interval than in the optical range, there are more numerous bright enough targets available beyond the closer cloud complexes and hidden clouds can be are uncovered. More granulation in structures is also seen at the Local Bubble borders, and there are less elongated "fingers-of-God" linked to scarcity of targets. Note that there are no changes in the fourth quadrant due to the distribution of APOGEE targets (observations from the Northern Hemisphere), and also that the use of a large scale prior distribution based on observation implies that maps at large distance or in locations devoid of targets are influenced by this prior (instead of our input catalogue of reddening). As said above, the APOGEE colour excess measurements included in the second map are made using a calibration based on the initial map, showing the iterative process. Work is in progress using APOGEE data and the final calibration of Ruiz-Dern et al. (2017).

3 Dust distribution in a vertical plane contain the Sun and longitudes 160°

A 3D distribution is particularly useful for the nearby structures, because the main cloud complexes in the solar neighbourhood are off-Plane. Indeed, these structures are better seen in vertical planar cuts in the 3D cube. We show in Fig. 2 the dust distribution in one of the vertical planes: the one containing the Sun, the North Galactic Pole and the Galactic sightlines at longitudes 160° and 340°. The 160° half-plane crosses the Taurus/Perseus region at negative latitudes, and the 340 ° half-plane crosses the Sco-Cen region at positive latitudes. The 5 consecutive maps from top to bottom correspond to the 5 steps described in Section 1;
-[step 0] Inversion pre-TGAS, 22467 targets, 22 % Hipparcos parallaxes, 78% photometric distances
-[step 1] Same as in step 0, 80% distances from Gaia TGAS parallaxes, 20% photometric
-[step 2] 4886 additional colour excess measurements deduced from the 15273A DIB, Gaia/TGAS distance
-[step 3] Use of the same dataset as in step 2, now with a non analytical large-scale prior 3D distribution, based on Green et al. (2015)
-[step 4] Same as step3 plus 25196 additional colour excesses of APOGEE DR13 targets. The stellar parameters are derived from APOGEE spectra and distances and colour excesses are deduced from these parameters and all available photometric data.
-[step 5] Same as step4 except for the Taurus/Perseus region, where the result of an additional local inversion based on 29359 colour excess measurements from the LAMOST DR2 catalogue of Wang et al. (2016) has been inserted at l=160 ° and -3≥b≥-35 °. At variance with all other inversions, the minimum size of the structures for this local inversion is 25pc (instead of 15pc) to take into account uncertainties on the distances.

The figure illustrates how the mapping is improved based on new data. Using the infrared range allows to map at larger distances (changes from b) to e), while the use of massive datasets allow to better define the structures (changes from e) to f)).

4 Conclusions

We have shown examples of 3D ISM mapping improvements thanks to Gaia and ground spectroscopic surveys. The next Gaia data releases in combination with current and forthcoming surveys will certainly contribute to develop the mapping in a similar way but in a much larger extent. Difficulties linked to the computation time required for the inversion of massive data need to be solved, but hierarchical techniques are under study or maps can be built region by region. The positive feedback between stellar calibrations and stellar studies in general on the one hand, and interstellar mapping on the other hand will help progressing in both ways.

L.C. acknowledges doctoral grant funding from the Centre National d'Etudes Spatiales (CNES). R.L. and A.M.-I. acknowledge support from "Agence Nationale de la Recherche" through the STILISM project (ANR-12-BS05-0016-02) and the CNRS PCMI national program. M.E. acknowledges funding from the "Region Ile-de-France" through the DIM-ACAV project.

References

Capitanio, L., Lallement, R., Vergely, J. L., Elyajouri, M., & Monreal-Ibero, A. 2017, A&A, 606, A65
Elyajouri, M., Monreal-Ibero, A., Remy, Q., & Lallement, R. 2016, ApJS, 225, 19
García Pérez, A. E., Allende Prieto, C., Holtzman, J. A., et al. 2015, ArXiv e-prints
Green, G. M., Schlafly, E. F., Finkbeiner, D. P., et al. 2015, ApJ, 810, 25
Lallement, R., Vergely, J.-L., Valette, B., et al. 2014, A&A, 561, A91
Majewski, S. R. 2012, in American Astron. Soc. Meeting Abstracts 219, 205.06
Rezaei Kh., S., Bailer-Jones, C. A. L., Hanson, R. J., & Fouesneau, M. 2017, A&A, 598, A125
Ruiz-Dern, L., Babusiaux, C., Arenou, F., Turon, C., & Lallement, R. 2017, ArXiv e-prints

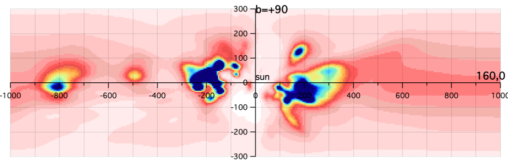

(a) *Distribution without TGAS parallaxes.*

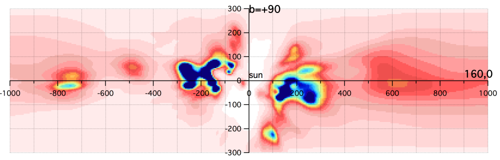

(b) *Distribution with TGAS parallaxes.*

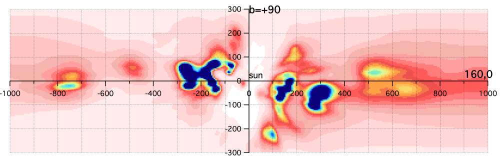

(c) *Distribution with TGAS parallaxes and DIB-based additional data.*

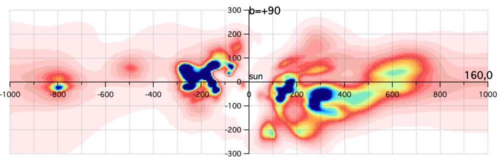

(d) *Distribution as in c) with a large-scale prior from Pan-STARRS-1.*

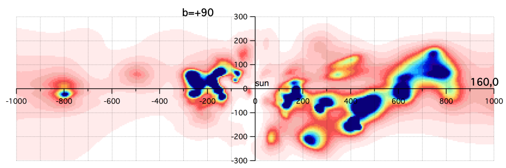

(e) *Distribution as in d) with colour excess measurements from APOGEE DR12.*

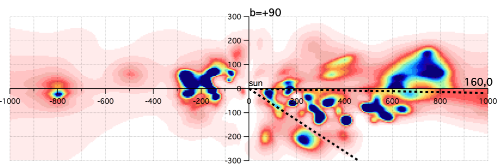

(f) *Distribution as in e) with additional LAMOST data in Taurus/Perseus region .*

Fig. 2: Dust distribution in a vertical plane along longitudes 160-340°. Units are parsecs. The colour scale is as in Fig 1.

Sale, S. E. & Magorrian, J. 2014, MNRAS, 445, 256

Vergely, J.-L., Freire Ferrero, R., Siebert, A., & Valette, B. 2001, A&A, 366, 1016

Wang, J., Shi, J., Zhao, Y., et al. 2016, MNRAS, 456, 672

SF2A 2017
C. Reylé, P. Di Matteo, F. Herpin, É. Lagadec, A. Lançon, Z. Meliani, F. Royer (eds)

THE GAIA RED CLUMP AS STANDARD CANDLE

L. Ruiz-Dern[1], C. Babusiaux[1], C. Danielski[1], F. Arenou[1], C. Turon[1] and R. Lallement[1]

Abstract. Gaia has already provided new high precision parallaxes for two million objects, allowing to recalibrate standard candles. Red Clump stars are known to be good standard candles because of their small dependency of their luminosity on their stellar composition, colour and age. We developed methods to derive some of the main physical parameters to characterise the Red Clump as standard candle.

We provide fully empirical calibrations by using visual to infrared photometry, the most up-to-date 3D extinction map, and spectroscopic atmosphere parameters. We derived new calibrations for 16 Colour-$(G - K_{\rm s})$ and Effective Temperature-$(G - K_{\rm s})$ relations and a new calibration of the RC absolute magnitude on the Gaia G and 2MASS $K_{\rm s}$ bands. These calibrations are used afterwards to estimate the G-band interstellar extinction coefficient $k_{\rm G}$. By combining of all these relations we implemented a method to determine effective temperatures and interstellar extinctions (A_0), which we will use in particular to derive asteroseismic parameters which can be directly compared with Gaia's results.

Keywords: stars: fundamental parameters, stars: abundances, stars: atmospheres, ISM: dust, extinction

1 Introduction

Standard candles play a fundamental role as a tool for distance determinations in astronomy. With the First Gaia Data Release (DR1) we have now access to new high precision parallaxes for two millions objects, with thousands of standard candles among them. In particular Red Clump (RC) stars are of special interest because we find a large number of them in the solar neighbourhood, allowing us to better characterise and parametrise them and therefore to improve distance estimations.

In this conference we briefly summarised the work detailed in Ruiz-Dern et al. (2017), Danielski et al. (in prep.) and Ruiz-Dern et al. (in prep.). In these papers we developed some methods to calibrate the RC photometrically in terms of colours, effective temperatures and absolute magnitudes, by using the Gaia G band. These calibrations were consequently used to derive the interstellar extinction coefficient in the G band (k_G). The whole set of fits is being applied to derive the effective temperatures of asteroseismic giants.

This paper first outlines the implemented methods to calibrate the colours, the effective temperatures, the absolute magnitudes and the extinction coefficient of RC stars, then focuses on the importance of high precision data to better describe the RC region, followed by the impact of our calibrations on the determination of asteroseismic distances and on the Gaia Validation process.

2 Empirical calibrations

In order to perform the calibrations, we first need to carefully select the sample. We considered several constraints to guarantee the quality of the data, and thus the quality of the final fits. The detail of the samples for each calibration may be found in Ruiz-Dern et al. (2017) for the colours, the effective temperatures and the absolute magnitudes, and in Danielski et al. (in prep.) for the k_G extinction coefficient. Nonetheless, some of the constraints are shared: the high photometric quality, the use of spectroscopic metallicities, the selection of just single stellar systems, and the cut on interstellar extinction using the most up-to-date 3D local extinction map of Capitanio et al. (2017) and the 2D map of Schlegel et al. (1998) when outside the cube. We kept only stars with $A_0 < 0.03$, where A_0 is the interstellar extinction at $\lambda = 550$ nm (Gaia reference value).

[1] [1]GEPI, Observatoire de Paris, PSL Research University, CNRS UMR 8111 - 5 Place Jules Janssen, 92190 Meudon, France
email: `laura.ruiz-dern@obspm.fr`

2.1 Colours

In addition to the general constraints, for the colour-colour (CC) calibrations we selected red giant stars following two criteria: on the colour $G - K_\mathrm{s}$ and on the parallax ϖ, to avoid contamination from other spectral types:

$$G - K_s > 1.6 \tag{2.1}$$

$$m_G + 5 + 5\ \log_{10}\left(\frac{\varpi + 2.32\ \sigma_\varpi}{1000}\right) < 4 \tag{2.2}$$

where the factor 2.32 on the parallax error σ_ϖ corresponds to the 99th percentile of the parallax probability density function.

The general fitting formula adopted was:

$$Y = a_0 + a_1\ (G - K_\mathrm{s}) + a_2\ (G - K_\mathrm{s})^2 + a_3\ [\mathrm{Fe/H}] + a_4\ [\mathrm{Fe/H}]^2 + a_5\ (G - K_\mathrm{s})\ [\mathrm{Fe/H}] \tag{2.3}$$

where Y is a given colour, and a_i are the coefficients to be estimated. The photometric bands used for Y were: Gaia G, Hipparcos $B\ V\ H_\mathrm{p}$, Tycho $B_\mathrm{T}\ V_\mathrm{T}$, 2MASS $J\ K_\mathrm{s}$, and APASS $g\ r\ i$. A Monte Carlo Markov Chain (MCMC) method was implemented to fit this formula for each colour vs $G - K_\mathrm{s}$ relation in a robust way, by accounting for all variables uncertainties. Moreover, the process penalises the complex terms by using the Deviance Information Criterion (DIC) (Plummer 2008) and it checks outliers at 3σ from the fit, one by one.

2.2 Effective Temperatures

For the T_eff vs $G - K_\mathrm{s}$ calibration we applied the same criteria as for the CC calibrations sample. We then cross-matched the sample itself with the 13th release (DR13) of the APOGEE survey (SDSS Collaboration et al. 2016) in order to have a sample with homogeneous spectroscopic effective temperatures. When no Gaia parallax information was available (i.e. APOGEE stars not present in TGAS but in DR1) we kept stars with $\log g < 3.2$, using therefore only the Schlegel et al. (1998) map to apply our low extinction criteria. For the duplicated sources a weighted mean of the parameters was computed. To fit the sample we used the same method as in Section 2.1, with Y in Equation 2.3 the normalised effective temperature $\hat{T} = T_\mathrm{eff}/5040$ instead.

2.3 Absolute Magnitudes

Besides the general constraints, to calibrate the absolute magnitudes we selected stars within $1.93 < G - K_\mathrm{s} < 2.3$ and for which M_{K_s} is brighter than -0.5, to avoid contamination by the Secondary Red Clump. We did not consider any selection on the parallax relative precision, and the photometric uncertainties were neglected.

The adopted formula was:

$$M_\lambda = \alpha + \beta\ (G - K_\mathrm{s} - 2.1) \tag{2.4}$$

where the constant 2.1, the median of $G - K_\mathrm{s}$ of the sample, allows to center the fit on the RC.

The absolute magnitude is usually estimated through a Gaussian fit. However, one must consider the strong contamination of the RC by the Red Giant Branch Bump, as well as the variation of both populations with colour. Since here we are not modelling none of these populations we instead derived the absolute magnitude through the mode of its Gaussian distribution (Ruiz-Dern et al. 2017), which is less sensitive to the sample selection function. The colour dependency was therefore modelled by looking for the maximum of $Q(\alpha, \beta)$, a kernel based distribution function of the residuals $M_\lambda - (\alpha(G - K_\mathrm{s}) + \beta)$, with M_λ the absolute magnitude of each particular band. We derived M_λ for the Gaia G, Hipparcos $B\ V$, Tycho $B_\mathrm{T}\ V_\mathrm{T}$, 2MASS $J\ K_\mathrm{s}$, and APASS $g\ r\ i$ photometric bands.

2.4 k_G Extinction Coefficient

The stars selected for this calibration follow the same colour and parallax criteria as for the CC and T_eff calibrations (Sections 2.1 and 2.2), and have effective temperature, surface gravity and metallicity information from the APOGEE DR13 and the LAMOST DR2 surveys. Since the k_G calibration uses the T_eff fit derived in Section 2.2, only stars with $3603K < T_\mathrm{eff} \pm \sigma_{T_\mathrm{eff}} < 5207K$ and $-1.5 < [\mathrm{Fe/H}] < 0.4$ were used in order to work within the T_eff and [Fe/H] ranges of applicability of that relation (see Table 2 of Ruiz-Dern et al. 2017).

The adopted formula was:

$$k_\mathrm{G} = a_1 + a_2\ X + a_3\ X^2 + a_4\ X^3 + a_5\ A_0 + a_6\ {A_0}^2 \tag{2.5}$$

with X the intrinsic colour $(G-K_\mathrm{s})_0$ or the normalised effective temperature $\hat{T} = T_\mathrm{eff}/5040$, and a_i the coefficients to be estimated.

To derive the k_G extinction coefficient, first the colour excesses $\mathrm{E}(G-K_\mathrm{s})$ and $\mathrm{E}(J-K_\mathrm{s})$ were determined through the CC calibrations of Ruiz-Dern et al. (2017) (Section 2.1). Then the theoretical k_J and k_K were computed using the Fitzpatrick & Massa (2007) extinction law and the Kurucz Spectral Energy Distributions from Castelli & Kurucz (2003). All these informations were finally introduced into a Monte Carlo Markov Chain method (similar to the CC process) developed to accurately fit the empirical relation of Equation 2.5. The significance of the coefficients a_i was also tested through the Deviance Information Criterion.

3 Gaia vs Asteroseismology

The precision that is being achieved with Gaia will allow us from release to release to significantly improve the HR diagram. Consequently the different observational features that can be found on this diagram, such as the main and secondary RCs or even the Red Giant Branch Bump, will be more clearly detected.

Indeed, already with Gaia DR1 these different populations can be better observationally differentiated (Ruiz-Dern et al. 2017). In order to check the level of detail that we can achieve with Gaia DR1, in this work we compared this data to the asteroseismic Kepler/CoRoT database. To do so in a proper way, for Gaia we used a selection of stars with the quality criteria on photometry, spectroscopy and extinction mentioned in Section 2, and applied the bolometric corrections based on the ATLAS models and our T_eff calibration. For the asteroseismology data we used the Stellar Seismic Indices (SSI, LESIA - Observatoire de Paris)* for Kepler and CoRoT, together with the spectroscopic T_eff of the APOGEE DR13 and the LAMOST DR2 surveys.

We observed that our compilation allows to have a better defined asteroseismic HR diagram with an overall agreement on the shape with the Gaia DR1 HR diagram. Gaia DR2 should allow a much detailed study of each feature on the diagram and their variations with stellar populations.

3.1 New asteroseismic distances

By combining all the photometric calibrations mentioned in Section 2 in a proper way together with asteroseismic constraints, we can derive effective temperatures, interstellar extinctions and distance modulus for all the SSI stars. Indeed, we implemented a Monte Carlo Markov Chain method in magnitude space (Ruiz-Dern et al. in prep.) and used as input ingredients the asteroseismic parameters of all the SSI database (Kepler and CoRoT), our colour-colour and T_eff vs $G-K_\mathrm{s}$ photometric calibrations, and the k_G empirical relation. The method is independent of any metallicity or effective temperature input, although if available this information is used. We obtained homogeneous distance modulus for ~ 12000 stars of the SSI database.

3.2 Asteroseismology in the context of Gaia Data Validation

One of the main points to verify the accuracy of Gaia parallaxes is to check their zero-point and their precision. A way to do this is to select stars distant enough so that their estimated distance uncertainty is better than the Gaia parallax precision. Stars detected through asteroseismology fit in fact this description for Gaia DR1.

With this purpose, within the Gaia DR1 validation process we implemented a Maximum Likelihood Estimator method (Arenou et al. 2017) to estimate the offset z and the extra-variance q that should be taken into account in order for the Gaia parallaxes to be consistent with these external estimates:

$$P(z, q|t, \sigma_t, \varpi_G, \sigma_{\varpi_G}) \propto \int_{\varpi} \mathcal{N}\left[t, -5\ln\bar{\varpi} - 5, \sigma_t\right] \mathcal{N}\left[\varpi_G + z, \bar{\varpi}, \sqrt{\sigma^2{}_{\varpi_G} + q}\right] \, d\bar{\varpi} \tag{3.1}$$

where t and σ_t are the external distance modulus and its uncertainty, ϖ_G and σ_{ϖ_G} the Gaia parallax and its uncertainty, and $\bar{\varpi}$ is the range of possible parallaxes within 5σ confidence interval:

$$\bar{\varpi} \in \left[\mathrm{Max}\left[\varpi - 5\sigma, 0\right], \varpi + 5\sigma\right]$$

For DR1 we used 1987 stars of the APOKASC (Apogee + Kepler) catalogue, which already provides distance modulus calculated by Rodrigues et al. (2014) using Padova isochrones relations. This gave us 984 Tycho sources with precision better than 0.1 mas (APOKASC median $\sigma < 0.02$). As described in Arenou et al. (2017) we

*Stellar Seismic Indices: `http://ssi.lesia.obspm.fr/`

obtained a global bias zero-point of -0.060 ± 0.006 for the APOGEE stars, in agreement with other validation indicators (e.g. QSOs) detailed in the same article (see their Table 2). Our method, which takes into account the non-normal distribution of parallax errors in the distance modulus space, allows to find a much smaller offset than the one found in other studies (e.g. ~ 0.3 mas in De Ridder et al. 2016).

In parallel, the same test allowed to highlight a variation of parallax with magnitude. This could come, for instance, from a feature of stellar evolution models or from bolometric corrections. Both APOKASC and APOGEE showed a correlation between magnitude and colour, but while for APOKASC the brighter stars appeared bluer than the fainter ones (due to extinction effects on RC populations), for the APOGEE stars it was the opposite. In both cases though, the colour did not allow to explain the systematics seen in magnitude.

For Gaia DR2 we will be able to use the new homogeneous asteroseismic distances derived for the SSI database (Section 3.1) as input for this parallax zero-point verification.

4 Conclusions

We used Gaia Data Release 1 to derive fully empirical calibrations for colours, effective temperatures, absolute magnitudes and the extinction coefficient $k_{\rm G}$, by using the Gaia G band, the most up-to-date 3D extinction map of Capitanio et al. (2017) and spectroscopic information. We took care of selecting high quality data and implemented robust methods for each parameter to guarantee the accuracy of the results. The extended and detailed work of all these calibrations may be found in Ruiz-Dern et al. (2017) and Danielski et al. (in prep.).

As stated, to select the samples of our calibrations we took advantage of the 3D extinction map of Capitanio et al. (2017). Then, the empirical fits obtained were combined to derive different physical stellar parameters, such as effective temperatures and interstellar extinctions. In particular, they have been used to determine the photometric interstellar extinctions for all the APOGEE stars. This has allowed us to provide a new important input to the 3D extinction map of Capitanio et al. (2017), and thus improving the current precision of the map.

Moreover, while Gaia DR1 was the main ingredient to obtain those calibrations, these have turned to be an ingredient for the verification of Gaia DR2 parallaxes. Indeed, the combination of these relations together with asteroseismic constraints allow us to derive homogeneous distance modulus for an important number of stars (Ruiz-Dern et al. in prep.). They will be used to check the Gaia parallax zero-point and extra-variance of DR2.

So far asteroseismology allows to provide a more detailed HR diagram. However, the combination of Gaia and asteroseismology data, and specially the forthcoming Gaia releases, will allow a deeper study of the different HR observational features, such as the main and secondary RCs or the Red and Asymptotic Giant Branch Bumps.

This work has made use of data from the European Space Agency (ESA) mission *Gaia* (`https://www.cosmos.esa.int/gaia`), processed by the *Gaia* Data Processing and Analysis Consortium (DPAC, `https://www.cosmos.esa.int/web/gaia/dpac/consortium`). Funding for the DPAC has been provided by national institutions, in particular the institutions participating in the *Gaia* Multilateral Agreement. This publication makes use of data products from the Two Micron All Sky Survey, which is a joint project of the University of Massachusetts and the Infrared Processing and Analysis Center/California Institute of Technology, funded by the National Aeronautics and Space Administration and the National Science Foundation. We acknowledge financial support from the *Centre National d'Etudes Spatiales* (CNES) fellowship program, and from the *Agence Nationale de la Recherche* (ANR) through the STILISM project.

References

Arenou, F., Luri, X., Babusiaux, C., et al. 2017, A&A, 599, A50

Capitanio, L., Lallement, R., Vergely, J. L., Elyajouri, M., & Monreal-Ibero, A. 2017, ArXiv e-prints

Castelli, F. & Kurucz, R. L. 2003, in IAU Symposium, Vol. 210, Modelling of Stellar Atmospheres, ed. N. Piskunov, W. W. Weiss, & D. F. Gray, A20

Danielski, C., Babusiaux, C., Ruiz-Dern, L., Sartoretti, P., & Arenou, F. in prep.

De Ridder, J., Molenberghs, G., Eyer, L., & Aerts, C. 2016, A&A, 595, L3

Fitzpatrick, E. L. & Massa, D. 2007, ApJ, 663, 320

Plummer, M. 2008, Biostatistics, 9, 523

Rodrigues, T. S., Girardi, L., Miglio, A., et al. 2014, MNRAS, 445, 2758

Ruiz-Dern, L., Babusiaux, C., Arenou, F., Turon, C., & Lallement, R. 2017, ArXiv e-prints

Ruiz-Dern et al., L. in prep.

Schlegel, D. J., Finkbeiner, D. P., & Davis, M. 1998, ApJ, 500, 525

SDSS Collaboration, Albareti, F. D., Allende Prieto, C., et al. 2016, ArXiv e-prints

SEARCHING FOR COMETARY ACTIVITY IN CENTAURS OF THE OSSOS SURVEY

N. Cabral[1], P. Rousselot[1,] and A. Guilbert-Lepoutre[1,]

Abstract. To date, about 200 Centaurs have been detected of which only 29 are active and have a cometary designation. In order to better constrain the origin of Centaurs' cometary activity, it is necessary to increase the sample of studied targets. The Outer Solar System Origin Survey (OSSOS) observed a large sample of targets at large heliocentric distances, providing photometric and astrometric data. We implemented an automatized method to constrain the cometary activity of the OSSOS objects with heliocentric distances lower than 30 au. We describe here our image analysis method for one typical object. Our approach allows to compute the sky background, the surface brightness radial profile and the upper limit of the $Af\rho$ parameter.

Keywords: comets: general; Kuiper Belt; solar system: general; Centaurs

1 Introduction

Centaurs are an intermediate population between Jupiter Family Comets (JFCs) and trans-Neptunian Objects (TNOs). They are usually defined as bodies whose orbits have their perihelion, q, and their semi-major axis, a, larger than the semi-major axis of Jupiter ($a_{\rm J}$=5.2 au) and lower than the semi-major axis of Neptune ($a_{\rm N}$=30 au). Numerical simulations show that their orbits are chaotic and dynamically short-lived compared to the age of the solar system, with a median lifetime near 10 Myr (Tiscareno & Malhotra 2003). They are therefore believed to be recently escaped from the TNOs of the Kuiper Belt through gravitational scattering from giant planets (Levison & Duncan 1997; Horner et al. 2004; Volk & Malhotra 2008). They are potentially the key to understand the process that transforms TNOs to short period comets.

Despite the pivotal role of Centaurs, the sample of detected objects remains relatively small. Only about 200 Centaurs have been detected of which 29 are active and have a cometary designation. For our study, we selected targets from the release 8 of the OSSOS survey, with a simple criterion satisfying heliocentric distance r <30 au. This corresponds to a sample of 23 objects including 9 Centaurs, 8 resonant objects, 5 scattered objects and 1 non-classified object. In order to describe our method, we apply the latter to a typical object of this sample. We basically constrain the cometary activity by computing the upper limits of the $Af\rho$ parameter for the *o3e01* target. The tools developed here will be applied in future for the whole selected sample, which represents a total of 390 photometric images.

2 Cometary activity

2.1 The OSSOS survey

OSSOS is a Large Program on the Canada-France Hawaii Telescope surveying eight $\sim$21 deg^2 fields in r-band. Initially OSSOS was allocated for 8 semesters of the period 2013-2016, but it has been extended up to the beginning of 2017. The imaging observations of the survey were taken at the University of Hawaii with the MegaPrime camera on the 3.6 m Canada-France-Hawaii Telescope. The r-band observations used the 0.90 deg^2 field of view of the camera. A full description of OSSOS can be found in Bannister et al. (2016). The photometric data used in this work come from the release 8 of OSSOS.

[1] Institut UTINAM, CNRS UMR6213, Univ. Bourgogne Franche-Comté, OSU THETA Franche-Comté-Bourgogne, Observatoire de Besançon, BP 1615, 25010 Besançon Cedex, France

2.2 Data analysis

We developed routines to determine the brightness radial profile of a target, from which we can search for cometary activity by comparing it to the Point-Spread Function (PSF) radial profile adjusted in intensity. We did not manage to find any clear evidence of cometary activity in any image of the object *o3e01* but we tried to estimate an upper limit for the $Af\rho$ parameter (see section 2.3). All these steps are automatized to treat a large sample.

We basically proceed to 4 preparatory steps:

- *Centroid:* We use the IRAF* functions of the daophot package to determine the target centroid.
- *Sky background:* To determine the sky background we segment the image in squares of 30×30 pixels and we compute the median of pixel intensities. We use the minimum of these medians as the sky background.
- *Radial profile:* We compute the surface brightness profiles for the targets and we adjust the PSF. Fig. 1 shows a typical example of the radial profile for the target *o3e01*.
- *Upper limit for the coma flux:* Since there is no apparent cometary activity we can only put upper limit on the coma flux, in order to compute upper limit for the $Af\rho$ parameter (section 2.3).

In Fig. 1 we display the radial profile of the object *o3e01* observed during the night of 8 february 2013. At the time of observation, *o3e01* was located at 23.4 au from the Sun. The two profiles, the psf one (mauve line) and the target one (green points with errors bars) are very close, meaning there is no cometary activity detected.

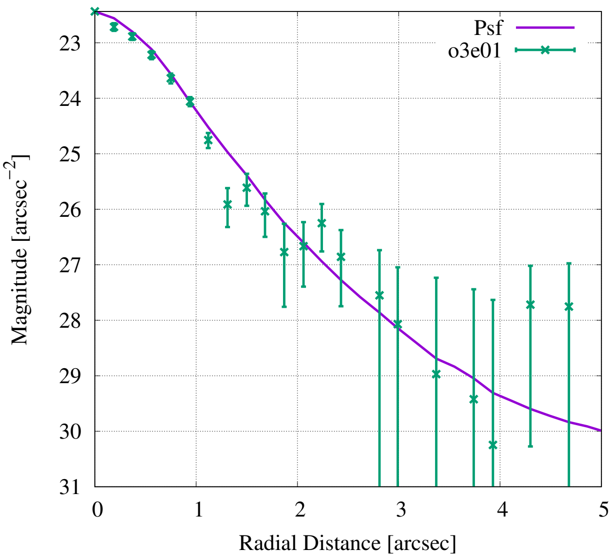

Fig. 1. Surface brightness profile for the target *o3e01* observed on 8 February 2013. Magnitude as a function of the radial distance for the target (green points with errors bars) and the psf (mauve line). Close Psf and target profiles indicates the target has no detectable cometary activity.

2.3 The $Af\rho$ parameter

The $Af\rho$ parameter has been introduced by A'Hearn et al. (1984), it enables to quantify the cometary activity. This parameter is more or less independant of unknown parameters such as grain albedo or grain size and independent of the field of view (if we assume that the radial profile follows a ρ^{-1} dependance). It is possible to

*Image Reduction and Analysis Facility `http://iraf.noao.edu/`.

	r(au)	Δ(au)	$Af\rho_{max}$(cm)	mjd
1	23.279	22.335	64	56387.56945
2	23.279	22.335	97	56387.57336
3	23.279	22.335	107	56387.57724
4	23.279	22.335	62	56387.58112
5	23.279	22.335	38	56387.58503
6	23.277	22.327	48	56388.60299

Table 1. $Af\rho_{max}$ and the corresponding heliocentric distance r, geocentric distance Δ, and the modified julian day mjd, for the observations of the *o3e01* OSSOS target. The orbital parameters for this object are: semi-major axis a=34.421 au, perihelion distance q=14.125 au, and eccentricity e=0.590.

compute $Af\rho$ with the magnitude of the Sun and the magnitude of the coma in the same band (Korsun et al. 2014):

$$Af\rho = [2.4686 \times 10^{19} \times r^2 \times \Delta \times 10^{0.4(m_{\odot} - m_{\rm coma})}]/D \tag{2.1}$$

where r is the heliocentric distance (expressed in au), Δ is the geocentric distance (in au), $m_{\odot}$ is the magnitude of the Sun, $m_{\rm coma}$ the global magnitude of the coma and D the apparent diameter of the field of view in arcsec. The resulting $Af\rho$ is expressed in cm.

Because we did not manage to detect any cometary activity around our targets we computed only upper limits for the $Af\rho$ parameter. Our estimate of this upper limit is based on the radial profile, and based on a three steps computation:

1. We compute lower limits for the magnitude per square arcsec in a range of radial distance outside the inner part of the radial profile (i.e. typically around 2 to 3 arcsec). This lower limit is computed from the radial profile minus the errorbar (see Fig. 1) and converted in units of flux. We subtract, then, the corresponding flux of the PSF profile. We obtain, consequently, the flux value for a range of radial distance outside the center and inside the region where the sky background is important.
2. We extrapolate this flux for the other radial distances on the basis of a $1/\rho$ law, ρ being the radial distance. We sum all the resulting flux in order to get the maximum possible flux.
3. This maximum possible flux is converted in an overall coma magnitude and this magnitude is used in the above formula (Eq. 2.1) to compute $Af\rho_{\rm max}$.

Table 2.3 summarizes the upper limits with corresponding orbital parameters and date of observation for a sample of observations of the *o3e01* target. The values of the $Af\rho_{\rm max}$ parameter refer to the upper limit.

3 Conclusions

The few number of known Centaurs prevents a statistical analysis crucial to constrain cometary models. Hence, the ultimate goal of this work is to increase the number of Centaurs with constrained cometary activity. Here, we implemented a methodology to determine the upper limit of the $Af\rho$ parameter. We described our analysis focusing on the *o3e01* target from the release 8 of the OSSOS survey. We did not find evidence of cometary activity for this object. In a forthcoming paper we will pursue this study with the whole sample of the OSSOS survey (for r <30 au).

References

A'Hearn, M. F., Schleicher, D. G., Millis, R. L., Feldman, P. D., & Thompson, D. T. 1984, AJ, 89, 579

Bannister, M. T., Kavelaars, J. J., Petit, J.-M., et al. 2016, AJ, 152, 70

Horner, J., Evans, N. W., & Bailey, M. E. 2004, MNRAS, 355, 321

Korsun, P. P., Rousselot, P., Kulyk, I. V., Afanasiev, V. L., & Ivanova, O. V. 2014, Icarus, 232, 88

Levison, H. F. & Duncan, M. J. 1997, Icarus, 127, 13

Tiscareno, M. S. & Malhotra, R. 2003, AJ, 126, 3122

Volk, K. & Malhotra, R. 2008, ApJ, 687, 714

SF2A 2017
C. Reylé, P. Di Matteo, F. Herpin, É. Lagadec, A. Lançon, Z. Meliani, F. Royer (eds)

ON AN ALLAN VARIANCE APPROACH TO CLASSIFY VLBI RADIO-SOURCES ON THE BASIS OF THEIR ASTROMETRIC STABILITY

C. Gattano[1], S. Lambert[1] and C. Bizouard[1]

Abstract. In the context of selecting sources defining the celestial reference frame, we compute astrometric time series of all VLBI radio-sources from observations in the International VLBI Service database. The time series are then analyzed with Allan variance in order to estimate the astrometric stability. From results, we establish a new classification that takes into account the whole multi-time scales information. The algorithm is flexible on the definition of "stable source" through an adjustable threshold.

Keywords: astrometry, VLBI, source stability, allan variance

1 Introduction

During the 90s, the celestial reference system leaves a stellar definition to an extragalactic definition. During the XXI$^{\text{st}}$ International Astronomical Union (IAU) general assembly (IAU 1991), it was recommended that a list of extragalactic radio-sources observed by the Very Long Baseline Interferometry (VLBI) technique is provided to realize the system, following International Earth Rotation Service (IERS) works (Arias et al. 1995). Those sources, mostly quasars, are called defining sources because they define the axis of the realized celestial reference frame. This new system, called the International Celestial Reference System (ICRS, Arias et al. 1995) and its first realization, the International Celestial Reference Frame (ICRF1, Ma et al. 1998) are approved by IAU (1997).

In principle, extragalactic sources should not present any variation of their position on the sky. In one way, this is the case because quasars are at such a distance that their proper motion and parallax are undetectable. But sources are not point-like and the apparent structure of their flux have an effect on their apparent position depending on the baseline orientation (Charlot 1990). This apparent structure for a given source is dependent of the frequency and evolves with time. This is the main reason why VLBI sources well-monitored present instabilities on their position records and one should be careful in its defining sources selection process. Precisely define the stability of the observed sources on the basis of the 37 years of VLBI observation is the goal of this paper. Since 1998, several methods were elaborated in this goal. Amongst other criteria, two variances has been used successively in order to estimate the source stability from time series: the classical variance was used by ICRF (Ma et al. 1998) and ICRF2 (Ma et al. 2009; Fey et al. 2015) working groups as well as other authors (Lambert & Gontier 2009; Liu et al. 2017) whereas the Allan variance (Allan 1966) was introduced by a group of researchers (Feissel et al. 2000; Gontier et al. 2001; Feissel-Vernier 2003; Feissel-Vernier et al. 2005) and taken up in more recent years (Le Bail & Gordon 2010; Le Bail et al. 2016; Liu et al. 2017). Chronologically, selected sources define celestial frames that proved to be more and more stable, from $\sim 20\mu$as to $\sim 5\mu$as, even if the selection process changes. This means that new observations have a dominant improvement of the axis stability. But Feissel-Vernier (2003) challenges both variances at the same epoch and shows best performance with the Allan variance. Nevertheless, authors restrict the Allan variance to a unique time-scale whereas it could provide multi-time scales information as revealed by Le Bail & Gordon (2010) without exploiting it in the selection process.

In our study, we propose a new method to determine the stability of VLBI radio-sources based on the multi-time scales Allan variance information. We begin with a short review of the current data available. Then we develop first the method used to build the astrometric time series and second the way to classify sources with respect to their stability. We conclude with the overview of our classification.

[1] SYRTE, Observatoire de Paris, PSL Research University, CNRS, Sorbonne Universités, UPMC Univ. Paris 06, LNE, 61 avenue de l'Observatoire, 75014 Paris, France

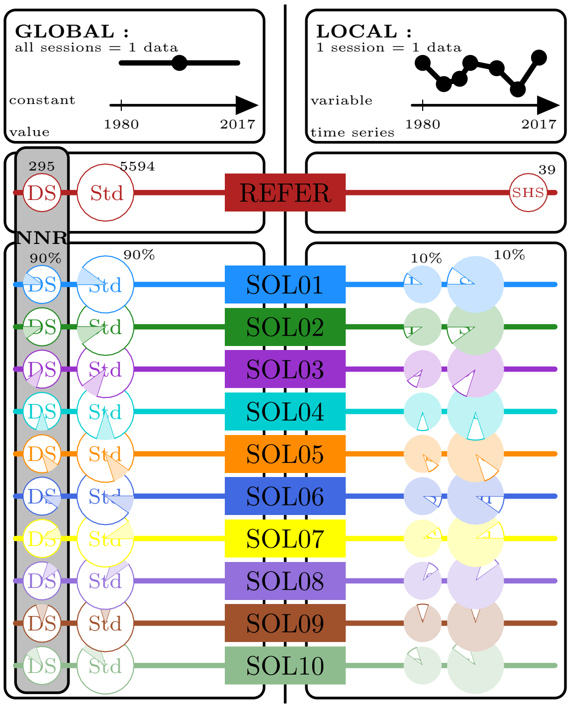

Figure 1: Illustration of the astrometric part in VLBI analysis strategy for each adjustment that determines sources astrometric time series. NNR = subset of sources on which a no-net rotation constraint is applied during the least squares adjustment.

2 Set of Data used

We use 6 327 diurnal geodetic VLBI sessions available on the IVS database in Mars 2017, in which 5 928 sources were observed. VLBI is a powerful astrometric technique in radio that takes advantage from interferometry on Earth-scaled baseline. It needs to process a complex data treatment involving several effects that need to be modelled and/or corrected: light deflection in the solar system, atmospheric corrections, Earth motion and deformation, thermal antenna and other instrumental corrections. The observation occurence for each sources is highly inhomogeneous. Most of the sources are observed a few times whereas less than 100 sources benefit from more than 1 000 observation sessions.

Only sources that have a large observational history can be characterized by means of studying their position time series. In our stability study, we reduce our set of data to 710 sources observed in 10 sessions or more with an observation history larger than 2 years.

3 Determine astrometric time series

Our first task is to determine astrometric time series for all VLBI sources. To this aim, we build a composite solution of 11 different adjustments inspired from Ma et al. (1998). The method is classical and used in several references cited in introduction. Here we only explain the astrometric part of the analysis strategy[1] illustrated on Fig. 1.

From a first adjustment, called `REFER`, we retrieve the astrometric time series for the 39 ICRF2 special handling sources (Ma et al. 1998) that are recommended to be adjusted locally (see Fig. 1) whereas the set of 295 ICRF2 defining sources is constrained during the least squares adjustment to not rotate, assuring the stability of the celestial frame. This is the important reason why defining sources should be stable, because any apparent motion due to, e.g., structure evolution will be transfered to other parameters such as the Earth orientation parameters because of this necessary constraint.

[1]The whole details of the analysis strategy not mentioned below can be found in the OPA technical file → `ftp://ivsopar.obspm.fr/vlbi/ivsproducts/eops/opa2017a.eops.txt`

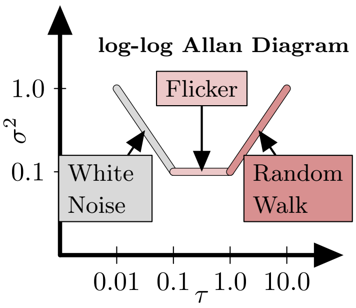

	Drift in Allan diagram
Red noise also called Random walk	1
Pink noise also called Flicker noise	0
White noise	-1

Figure 2: Illustration of an Allan diagram for a perfect artificial noisy signal with three different types of noise, each one dominating at different time scales.

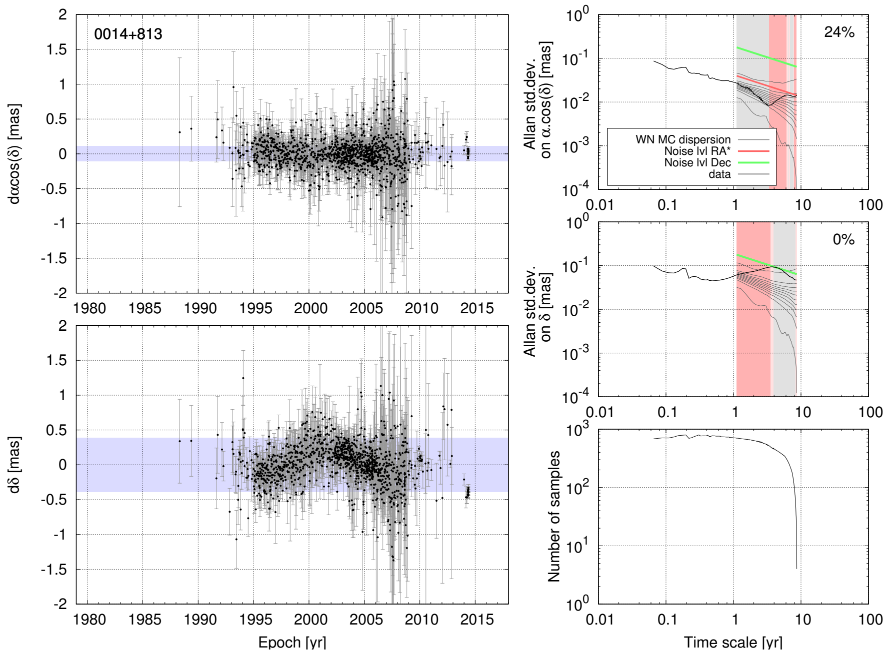

Figure 3: Example of 0014+813 astrometric instabilities and its corresponding Allan diagrams on $\Delta\alpha\cos\delta$ and $\Delta\delta$. Colored backgrounds indicate the type of noise respecting the Fig. 2 color scheme. Green and red straight lines show the minimum white noise level necessary too hide all other colored noise effects. The grey dispersion curves are a Monte-Carlo-based statistical validation test (see the text for more details).

Then, in each additional adjustment (`SOL01` to `10`), 10% of all the other sources adjusted globally in `REFER`, are adjusted locally (see Fig. 1). Consequently, the no-net rotation constraint is applied to 90% of the ICRF2 defining sources. By doing so, we reduce the noise level of the produced time series by a factor of two in mean with respect to time series obtained to a straightforward solution in independent mode in which all sources are estimated locally.

4 Estimate sources astrometric stability

We use the Allan variance (Allan 1966; Rutman 1978) to quantify the stability of each sources. This statistical tool allows us to discriminate different natures of noise within the time series and estimate their levels at perceptible time scales through Allan diagrams (see Fig. 2). The Allan variance estimator is

$$\sigma^2(t,\tau) = \frac{\sum^{k} 1/2\,(\bar{y}_k - \bar{y}_{k+1})^2}{N}$$

where t is the epoch of the first observation, τ is the measurements period and N their number. We compute both Allan diagrams on $\Delta\alpha\cos\delta$ and $\Delta\delta$ for the 710 sources observed in more than 10 sessions spread on more than 2 years (see Fig. 3 for an example). Then, we analyse the noise at each time scale.

Our classification is built on three categories. The first one, referred to as `AV0` are sources dominated by a white noise at most of the time scales or by flicker noise otherwise. The second one, referred to as `AV1`, are

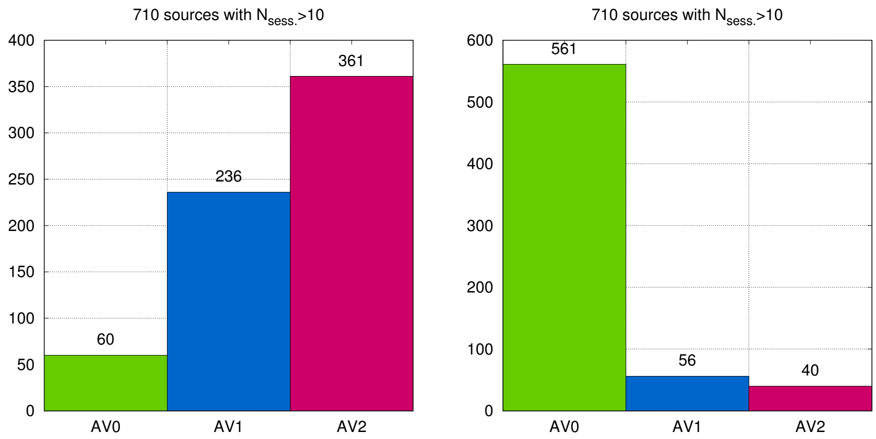

Figure 4: Classification overview in the most pessimistic scenario (left), where the statistical threshold was fixed at 100%, and the most optimistic scenario (right), where the statistical threshold was fixed at 0%.

sources that can present a red noise behaviour at intermediate time scale, but not at long time scale where it is dominated by white noise. Finally, the last class, referred to as `AV2`, are all others sources showing an unstable behaviour, i.e., red noise at long time scale.

Our estimation of sources stability includes the determination of the lowest white noise level that returns a pessimist limit on the source potential as defining sources (its corresponding Allan diagram maximizes the computed Allan diagrams built on the observations). It means that the potential of the considered source to define a stable axis direction will be better than this hypothetical purely white noise source on all perceptible time-scales. This information can be used to roughly resume the noise level of the source without consideration of the noises combination within the data.

Finally, and because our method appears to be too severe in determining stable sources (`AV0`), we implement a statistical validation test based on Monte Carlo analysis. The result of the test may rehabilitate `AV1` and `AV2` sources into the `AV0` class. For a given source, the test consists of simulating white noise on the data sampling and computing the corresponding Allan variance, repeating the operation over 1 000 random draws. Because of the irregular, finite sampling, a white noise can show false drifts from the expected −1-slope in its Allan diagram, especially at the longest time scales. Consequently, we computed a scatter plot of all the 1 000 Allan diagrams and superimposed it to the real Allan diagrams of the sources. Then we retrieve a percentage of white noises that drift more than the Allan diagrams of the source. The bigger the percentage, the better the chance than the observed drifts on the source Allan diagrams are not statistically significant.

Without the MC validation test, our method returns a very pessimistic overview of only 60 stable sources over the 710 well observed and 361 unstable. Nevertheless when we apply the validation test with the loosest threshold, the number of stable sources increases to 561. So, our classification established an adjustable hierarchy that can be used in the context of selecting defining sources. Within each category, the noise level enables to sort out the sources.

5 Conclusion

We establish a new classification of VLBI radio-sources on the basis of their astrometric time series analysed by Allan variance. Three classes are composing the solution : sources `AV0` with a stable behaviour, sources `AV2` with an unstable long-term behaviour and intermediate sources `AV1`. The distribution of the sources in this classification is user-dependent throught a threshold that can be modified in order to restrict or loosen a statistical constraint defining the border of stable/unstable behaviours.

This classification brings accurate additional information for the selection of defining sources in the realization of a celestial reference frame. For example, after fixing the threshold for the validation test, one can select only the `AV0` sources. A preferable strategy would be to combine the `AV` classes and the noise level information in order to select a set of candidates sources to define the celestial frame axis. Moreover the astrometric variability defined by the time series that we compute accurately is also rich on astrophysical information about active galactic nuclei (AGN) plasma jet. Their detailed study may answer some questions such as the origin of the instabilities or help to understand physical particularities of sources that are well-suited for geodetic observations and that should be preferred in the VLBI scheduling.

References

Allan, D. W. 1966, IEEE Proceedings, 54, 221

Arias, E. F. et al. 1995, A&A, 303, 604

Charlot, P. 1990, AJ, 99, 1309

Feissel, M., Gontier, A.-M., & Eubanks, T. M. 2000, A&A, 359, 1201

Feissel-Vernier, M. 2003, A&A, 403, 105

Feissel-Vernier, M. et al. 2005, A&A, 438, 1141

Fey, A. L. et al. 2015, AJ, 150, 58

Gontier, A.-M. et al. 2001, A&A, 375, 661

IAU. 1991, XXIst General Assembly

IAU. 1997, XXIIIrd General Assembly

Lambert, S. B. & Gontier, A.-M. 2009, A&A, 493, 317

Le Bail, K. & Gordon, D. 2010, in Sixth International VLBI Service for Geodesy and Astronomy. Proceedings from the 2010 General Meeting, "VLBI2010: From Vision to Reality". Held 7-13 February, 2010 in Hobart, Tasmania, Australia. Edited by D. Behrend and K.D. Baver. NASA/CP 2010-215864., p.280-284, ed. S. Rogstad, C. E. Goodhart, J. E. Clark, S. Finley, G. E. Lanyi, L. A. White, & C. S. Jacobs, 280–284

Le Bail, K., Gordon, D., & Ma, C. 2016, in International VLBI Service for Geodesy and Astrometry 2016 General Meeting Proceedings: "New Horizons with VGOS", Eds. Dirk Behrend, Karen D. Baver, Kyla L. Armstrong, NASA/CP-2016-219016, p. 288-291, ed. D. Behrend, K. D. Baver, & K. L. Armstrong, 288–291

Liu, N., Liu, J.-C., & Zhu, Z. 2017, MNRAS, 466, 1567

Ma, C. et al. 1998, AJ, 116, 516

Ma, C. et al. 2009, IERS Technical Note, 35

Rutman, J. 1978, IEEE Proceedings, 66, 1048

SF2A 2017
C. Reylé, P. Di Matteo, F. Herpin, É. Lagadec, A. Lançon, Z. Meliani, F. Royer (eds)

TRACING THE HERCULES STREAM WITH GAIA AND LAMOST: NEW EVIDENCE FOR A FAST BAR IN THE MILKY WAY

G. Monari[2, 1]

Abstract. The length and pattern speed of the Milky Way bar are still controversial. Photometric and spectroscopic surveys of the inner Galaxy, as well as gas kinematics, favour a long and slowly rotating bar, with corotation around a Galactocentric radius of 6 kpc. On the other hand, the existence of the Hercules stream in local velocity space was classically interpreted as the signature of a short and fast bar with corotation around 4 kpc. This follows from the fact that the Hercules stream looks like a typical signature of the outer Lindblad resonance of the bar. Here, by combining the TGAS catalogue of the Gaia DR1 with LAMOST radial velocities, Monari et al. have confirmed that the position of Hercules in velocity space as a function of radius in the outer Galaxy is very well described by fast bar models with a pattern speed no less than 1.8 times the circular frequency at the Suns position.

Keywords: Galaxy: kinematics and dynamics, Galaxy: disc, Galaxy: structure

1 Introduction

To a first approximation, axisymmetric dynamical models (e.g. Cole & Binney 2017) describe the distribution and kinematics of stars in the Milky Way. However, it is now well established that the Milky Way contains prominent non-axisymmetric structures, in particular the bar and the spiral arms in the Galactic disc. The presence of non-axisymmetries reflects also in the velocity distribution of stars. In particular, in the Solar neighbourhood this would appear as an homogeneous ellipsoid, with a tail for low tangential velocity stars, if the Galaxy were a pure axisymmetric disc in differential rotation. However, substructures in local velocity space space have been known for a very long time and called 'moving groups'. It has been shown (e.g. Famaey et al. 2005) that the most prominent of these moving groups are not disrupted open clusters keeping coherence in velocity space. Therefore, alternative mechanisms have to be invoked for their formation like the resonant interaction between the stars and the bar or the spiral arms. In particular, Dehnen (2000) has shown that the Hercules moving group, could be a direct consequence of the Sun being located just outside of the bar's outer Lindblad resonance (OLR). This resonance occurs at the radius $R_{\rm OLR}$ where stars make two epicyclic oscillations while making one retrograde rotation in the frame of the bar, hence

$$\kappa + 2\,(\Omega - \Omega_{\rm b}) = 0, \tag{1.1}$$

where $\Omega(R)$, $\kappa(R)$, and $\Omega_{\rm b}$ are the Galaxy's circular frequency, epicyclic frequency, and the bar's pattern speed respectively (see Binney & Tremaine 2008).

This is at odds with new studies of the stellar photometry (Wegg & Gerhard 2013; Wegg et al. 2015) and stellar and gas kinematics (Portail et al. 2015; Sormani et al. 2015; Li et al. 2016; Portail et al. 2016) of the Galactic centre which favour a long bar (extending to $R \sim 5$ kpc), oriented at an angle of $\phi_b \sim 27°$, and with a pattern speed $\Omega_{\rm b} \sim 40$ km s^{-1} kpc^{-1}, placing the bar corotation at about 6 kpc from the Galactic centre (Portail et al. 2016), and the OLR way beyond the Solar neighbourhood.

A way to check whether the OLR or CR explanation holds is to investigate how the Hercules feature in velocity space varies with the position in the Galaxy (e.g. Antoja et al. 2014). The Gaia mission provides a

[1] The Oskar Klein Centre for Cosmoparticle Physics, Department of Physics, Stockholm University, AlbaNova, 10691 Stockholm, Sweden
[2]Leibniz Institut für Astrophysik Potsdam (AIP), An der Sterwarte 16, D-14482 Potsdam, Germany

unique opportunity to test this in the Galactic disc. One first step is to cross-match the recent Gaia DR1/TGAS catalogue with existing spectroscopic surveys and trace the position of Hercules in velocity space as a function of Galactocentric radius. In particular Monari et al. (2017c) combine TGAS with the LAMOST DR2 catalogue (Liu et al. 2014). I summarise this work in this contribution. In Sect.

2 Cross matching TGAS and LAMOST

Monari et al. (2017c) cross match the TGAS catalogue (providing Right Ascension α, the declination δ, the parallax π, and the proper motions μ_α and μ_δ) with the LAMOST DR2 A, F, G and K type stars catalogue (Liu et al. 2014), from which we obtain the line–of–sight velocity $v_{\rm los}$. They select stars with fractional parallax error $\sqrt{\sigma_\pi^2 + (0.3\text{mas})^2}/\pi < 0.2$, (where the use of the 0.3 mas systematic uncertainty is recommended in Gaia Collaboration et al. 2016), obtaining a total 49,075 stars, mostly distributed towards the anti–centre of the Milky Way (while, the spectroscopic survey RAVE, for example, focuses on the central parts).

3 Analysis

The observables $(\alpha, \delta, \pi, \mu_\alpha, \mu_\delta, v_{\rm los})$ are transformed to the cylindrical Galactocentic coordinates $(R, \phi, z, v_R, v_\phi, v_z)$ using fundamental parameters of our Galaxy derived by Reid et al. (2014), and a value of the radial motion of the Sun with the respect of the Local Standard of Rest of $U_\odot = 10$ km s^{-1} (e.g. Bovy et al. 2015).

It is then studied the distribution of stars in the (R, v_ϕ) plane, shown in Fig. 1 (left panel). In this space, Hercules appears as the clump of stars localized between $v_\phi \sim 190$ km s^{-1}, and $v_\phi \sim 200$ km s^{-1}, slightly detached from the main velocity mode at higher v_ϕ. The valley between Hercules and the main velocity mode (the 'gap'), appears only for stars with $v_R > 0$ (right panel). This is due to the fact that Hercules is composed by stars moving outwards in the Galaxy (e.g. Dehnen 1998; Famaey et al. 2005).

Assuming that the Hercules gap in the (R, v_ϕ) plane corresponds to stars with guiding radii at the position of the OLR ($R_{\rm OLR}$), one can write how the tangential velocity of these stars ($v_{\rm OLR}$) as

$$v_{\rm OLR} = \frac{R_{\rm OLR} v_{\rm c}(R_{\rm OLR})}{R}, \tag{3.1}$$

where $v_{\rm c}(R_{\rm OLR})$ is the circular speed of the Galaxy at the OLR. As we move outwards in R, $v_{\rm OLR}$ becomes lower, and the number of stars that is affected by the OLR becomes smaller, which eventually leads to the disappearance of the Hercules moving group. This is in good agreement with theoretical models of perturbed disc DF described by Monari et al. (2016, 2017b). Hercules, however, can be traced it at larger R and lower $v_{\rm OLR}$, using the v_ϕ distribution shown in Fig. 2.

One can describe the circular velocity curve as a power-law $v_{\rm c}(R) = v_0(R/R_0)^\beta$. In the right panel of Fig. 1 the corresponding $v_{\rm OLR}(R)$ for three values of $R_{\rm OLR}$ was overplot, using $\beta = -0.3, 0, 0.3$, and $\Omega_{\rm b} = 1.89\Omega_0$. This value of the pattern speed $\Omega_{\rm b}$ was found by Antoja et al. (2014) using the RAVE catalogue which mostly probes regions with $R < R_0$, and still nicely follow the shape of the gap even for $R > R_0$, without *any* tuning of the parameters to obtain a good fit. This is also confirmed when looking at the saddle points in the v_ϕ distributions in Fig. 2.

4 Conclusion

The traditional explanation that the Hercules moving group is a signature in local stellar kinematics of the Galactic bar's OLR (Dehnen 2000) is at odds with the slowly rotating long bar models favoured by stellar and gas kinematics in the inner Galaxy. This would mean that an alternative explanation, e.g. based on spiral arms or the bar's corotation (Pérez-Villegas et al. 2017) is necessary.

One way to test whether Hercules is indeed linked to the OLR of the bar is to trace its position and shape in velocity space as a function of position in the Galaxy. Monari et al. (2017c) made a first step in this direction, combining the TGAS and LAMOST DR2 catalogues, and found out that the rotational velocity of the Hercules moving group is indeed closely following the prediction of older models (obtained with different data) placing the Sun just outside the OLR of the bar. At this pattern speed, the corotation of the bar is close to $R \sim 4$ kpc, and its OLR is at $R \sim 7$ kpc.

Alternative explanations, necessary to account for a slowly rotating bar with corotation around $R \sim 6$ kpc, should also reproduce the position of Hercules in velocity space and its variation with position in the Galaxy

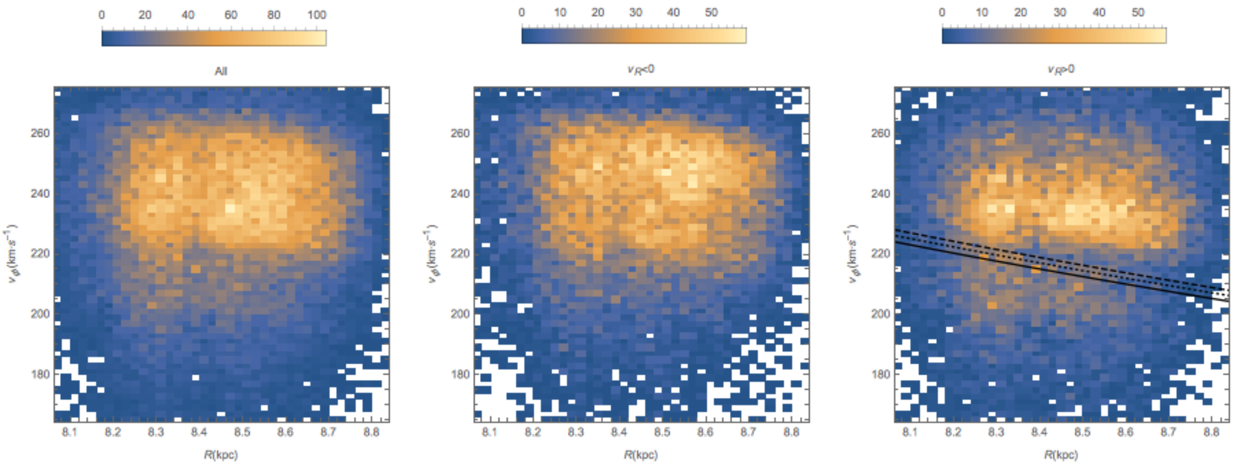

Fig. 1. Distribution of stars in TGAS+LAMOST in the (R, v_ϕ) plane from Monari et al. (2017c). Stars with parallax accuracy $\sqrt{\sigma_\pi^2 + (0.3\ \mathrm{mas})^2}/\pi < 0.2$ are selected. The bin size is 20 pc in R, and 2 km s^{-1} in v_ϕ, and the units of the color bar indicate the number of stars per bin (the white bins are empty). The left panel represents the whole sample, the central panel stars with $v_R < 0$, and the right panel stars with $v_R > 0$. The different curves in the right panel correspond to different models of v_{OLR} with $\Omega_\mathrm{b} = 1.89\Omega_0$: the solid curve has a flat $v_\mathrm{c}(R)$ ($\beta = 0$), the dashed curve has an increasing $v_\mathrm{c}(R)$ ($\beta = 0.3$), and the dotted curve a decreasing $v_\mathrm{c}(R)$ ($\beta = -0.3$).

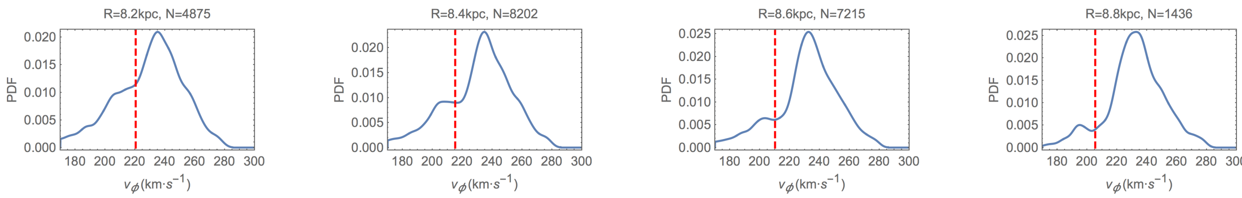

Fig. 2. Distribution of stars in v_ϕ, for stars with $v_R > 0$ and $R_i - \Delta R < R < R_i + \Delta R$, where $R_i = 8.2$ kpc, 8.4 kpc, 8.6 kpc, and 8.8 kpc, and $\Delta R = 0.1$ kpc. The PDFs are obtained using Gaussian kernels of bandwidth 3 km s^{-1}. The red dashed line corresponds to $v_{\mathrm{OLR}}(R_i)$ for $\Omega_\mathrm{b} = 1.89\Omega_0$, and $\beta = 0$, indicating the theoretical gap between the high- and low-velocity modes in v_ϕ. From Monari et al. (2017c)

as the fast bar models do. The way that the position of the Hercules gap in v_ϕ varies in R indicates its origin linked to a single resonance radius. This excludes models of perturbers with varying pattern speed with radius, like the corotating spiral arms.

Models of the star counts in the inner Galaxy shows the existence of a long, flat structure reaching out to $R \sim 5$ kpc. If the bar is fast, this structure could for example be a loosely wound spiral coupled to the end of the bar.

The debate on the origin of the Hercules moving group is yet to be settled, as recent N-body models (Pérez-Villegas et al. 2017) suggest that Hercules could also have an origin related to orbits trapped to the bar's corotation. To settle this debate, the upcoming Gaia data releases will have the greatest importance, to trace precisely the shape of the velocity distribution of the stars at different locations in a large volume of the Galaxy. Necessary will also be the use of more refined models to describe the star's distribution function under the effect of non-axisymmetric perturbers, especially in the vicinity of resonances (Monari et al. 2017a).

References

Antoja, T., Helmi, A., Dehnen, W., et al. 2014, A&A, 563, A60
Binney, J. & Tremaine, S. 2008, Galactic Dynamics: Second Edition (Princeton University Press)
Bovy, J., Bird, J. C., García Pérez, A. E., et al. 2015, ApJ, 800, 83
Cole, D. R. & Binney, J. 2017, MNRAS, 465, 798
Dehnen, W. 1998, AJ, 115, 2384

Dehnen, W. 2000, AJ, 119, 800
Famaey, B., Jorissen, A., Luri, X., et al. 2005, A&A, 430, 165
Gaia Collaboration, Prusti, T., de Bruijne, J. H. J., et al. 2016, A&A, 595, A1
Li, Z., Gerhard, O., Shen, J., Portail, M., & Wegg, C. 2016, ApJ, 824, 13
Liu, C., Deng, L.-C., Carlin, J. L., et al. 2014, ApJ, 790, 110
Monari, G., Famaey, B., Fouvry, J.-B., & Binney, J. 2017a, MNRAS, 471, 4314
Monari, G., Famaey, B., & Siebert, A. 2016, MNRAS, 457, 2569
Monari, G., Famaey, B., Siebert, A., et al. 2017b, MNRAS, 465, 1443
Monari, G., Kawata, D., Hunt, J. A. S., & Famaey, B. 2017c, MNRAS, 466, L113
Pérez-Villegas, A., Portail, M., Wegg, C., & Gerhard, O. 2017, ApJ, 840, L2
Portail, M., Gerhard, O., Wegg, C., & Ness, M. 2016, arXiv:1608.07954
Portail, M., Wegg, C., Gerhard, O., & Martinez-Valpuesta, I. 2015, MNRAS, 448, 713
Reid, M. J., Menten, K. M., Brunthaler, A., et al. 2014, ApJ, 783, 130
Sormani, M. C., Binney, J., & Magorrian, J. 2015, MNRAS, 454, 1818
Wegg, C. & Gerhard, O. 2013, MNRAS, 435, 1874
Wegg, C., Gerhard, O., & Portail, M. 2015, MNRAS, 450, 4050

SF2A 2017
C. Reylé, P. Di Matteo, F. Herpin, É. Lagadec, A. Lançon, Z. Meliani, F. Royer (eds)

IMPACT OF GAIA ON UNDERSTANDING MILKY WAY EVOLUTION

G. Kordopatis[1]

Abstract. Gaia space mission has published in September 2016 its first data release. In the years to come, exquisite astrometry, photometry and spectroscopy will be available for hundreds of millions of targets, opening a new era of discoveries in galactic archaeology. In this proceeding, I review some key aspects, such as kinematic and metallicity gradients in the Galaxy, that are linked to the internal and external mechanisms that influence Galaxy evolution and that have already started to be clarified with GDR1.

Keywords: Milky Way, stellar content, evolution

1 Introduction

In the context of a Λ-Cold Dark Matter Universe, disc galaxies are formed from the successive accretion of smaller galaxies (Springel et al. 2006). This paradigm, though very successful explaining the large structures in the Universe, has met a number of issues on smaller scales (of the order of the $\sim$Mpc), such as the missing satellite problem, the absence of classical bulges in the galaxies, and the age and size of galactic discs (Bullock & Boylan-Kolchin 2017). The thorough and detailed study of individual stars in our Galaxy, the Milky Way, can help us understand to a great extent the mechanisms that come into play in galaxy evolution. Indeed, internal processes such as stellar radial migration, galactic fountains, dynamical heating, chemical enrichment, as well as gas and star accretions and responses of the disc to those accretions are encoded in the stellar kinematics, chemistry and age (Freeman & Bland-Hawthorn 2002).

2 Galactic archaeology and Gaia performances

The fossils that are used in Galactic archaeology are *(i)* stellar distance and position on the sky (to identify stellar streams and characterise the morphology of the galactic structures), *(ii)* proper motions and radial velocities (to identify old accretions and moving groups through the obtention of the 3D kinematics of the stars, and assuming a Galactic potential, infer their orbit), and *(iii)* the stellar atmospheric parameters, including the metallicity and chemical abundances in order to perform chemical tagging of the stars (e.g. Tolstoy et al. 2009), and infer an age estimation (Soderblom 2010; Kordopatis et al. 2015b). The combination of all this information will in return allow to infer star formation histories at different regions and epochs of the Galaxy, and highlight indirect signatures of evolution (see next sections).

The difficulty of this endeavour is that data *(i)* to *(iii)* are of increasing difficulty to obtain, and that one needs to collect this data for at least several hundreds of thousand of stars. This is were the Gaia space mission comes into play (Gaia Collaboration et al. 2016b). By the end of its mission, Gaia will provide parallaxes up to $G \sim 20.7$, with 10% uncertainty at 10 kpc from the Sun (depending on the colour of the star), transversal velocities with uncertainties better than a few 100 $\mathrm{m\,s^{-1}}$ for $d < 2$ kpc, and a few $\mathrm{km\,s^{-1}}$ up to $d \sim 5$ kpc. T_{eff}, $\log g$ and [M/H] will be derived from both the Blue and Red spectrophotometers (BP/RP) for most of the targets and the Radial Velocity Spectrometer (RVS) for $\sim 10^7$ stars brighter than $G_{\mathrm{RVS}} < 14.5$ mag (Bailer-Jones et al. 2013). Radial velocities will be obtained for $\sim 10^8$ stars with $G_{\mathrm{RVS}} < 16$ mag, with $\sigma_{V_{\mathrm{rad}}} \sim 2.5$ $\mathrm{km\,s^{-1}}$ (see proceeding of D. Katz, this volume). Finally, coarse stellar parameterisation (including [α/Fe] estimations) will be obtained spectroscopically for $\sim 10^7$ stars brighter than $G_{\mathrm{RVS}} < 14.5$ (though with $\sigma_{[\alpha/\mathrm{Fe}]}$ getting significantly degraded for stars fainter than $G_{\mathrm{RVS}} > 11$ mag), and individual element abundances for Fe, Ca, Mg, Ti and Si for the stars brighter than $G_{\mathrm{RVS}} \approx 11$ mag (Recio-Blanco et al. 2016).

[1] Université Côte d'Azur, Observatoire de la Côte d'Azur, CNRS, Laboratoire Lagrange, France

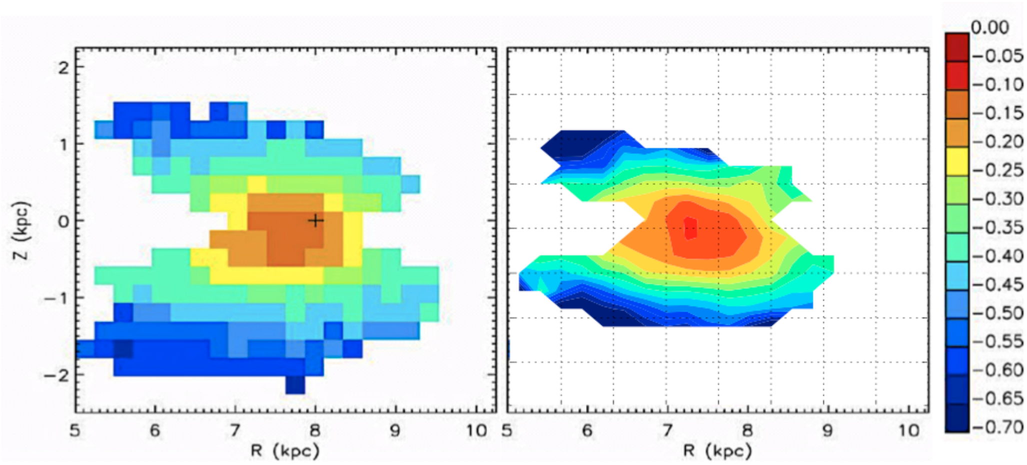

Fig. 1. Metallicity maps before Gaia (left, obtained with RAVE data, taken from Kordopatis et al. 2013b), and after Gaia (right, courtesy of I. Carrillo). The plot on the right is obtained for a smaller volume, since TGAS has a magnitude limit which is brighter than the RAVE one. Nevertheless, smoother structures in the extended Solar neighbourhood can be seen with the updated dataset.

3 Galactic Maps and gradients

A first glimpse of Gaia's potential has been given with its first data release (Gaia Collaboration et al. 2016a). In particular its sub-catalogue TGAS (Tycho-Gaia Astrometric Solution, Lindegren et al. 2016) published 2 million parallaxes and proper motions for stars brighter than the 11th magnitude, which can be combined with past or on-going ground-based spectroscopic surveys in order to get the radial velocities and chemical abundances of the stars. RAVE's fifth data release (Kunder et al. 2017), in particular, has the largest overlap with TGAS, with $\sim 2 \cdot 10^5$ stars in common. RAVE, when associated with distance estimates taking into account Gaia's parallaxes (provided by, for example, Astraatmadja & Bailer-Jones 2016 or McMillan et al. 2017), allow us to have much clearer (and smoother) view of the change of the stellar properties (velocities, metallicities) across the Galaxy. Figure 1 shows the updated metallicity map obtained with the Astraatmadja & Bailer-Jones (2016) distance set and the RAVE metallicities; even though the volume is smaller on the right hand-side figure, the vertical and radial gradients are now much smoother, due to sounder distances. Similar plots can be obtained for the different velocity fields too, see Carrillo et al. (2017). In the next subsection, I discuss some preliminary results regarding the metallicity distribution functions in the Galaxy and the spatial distribution of the super metal-rich stars.

4 Metallicity distribution functions and super-solar metallicity stars

The metallicity distribution function (MDF) of the stellar components of the Milky Way hold valuable information regarding the processes that have taken place in the evolution of our Galaxy. Up to recently, the study of the MDFs with precise stellar locations (via parallax measurements) for FGK stars could be done only up to a few 100 pc from the Sun, i.e. within the Hipparcos volume. To go beyond this limit, so-called spectroscopic distances projecting on isochrones the stellar atmospheric parameters were used (e.g.: Pont & Eyer 2004).

Figure 2 shows preliminary results taken from Kordopatis et al. (in prep). The box-plots represent the metallicity distributions as a function of height above the Galactic plane, at different galactic radii (different panels), using the RAVE-DR5 metallicities and the McMillan et al. (2017) distances. Excluding the $Z-$bins closest to the plane (which are suffering from selection biases and completeness issues that differ from one $R-$bin to the other, see Wojno et al. 2017), we measure the following vertical metallicity gradients, $\partial[\mathrm{M/H}]/\partial|Z|$, for the four 1 kpc-wide radial bins: $-0.27, -0.34, -0.33$ and $-0.19 dex$ kpc^{-1}, going from 6 kpc to 10 kpc, respectively. These values are compatible, within the errors (of the order of $0.07 dex$ kpc^{-1}), with the ones of Schlesinger et al. (2014) of $-0.243 \pm 0.05 dex$ kpc^{-1}, obtained using SEGUE G dwarfs. We note, however, that our measurements should be considered more reliable compared to previous studies, thanks to the improved distances that are being used here.

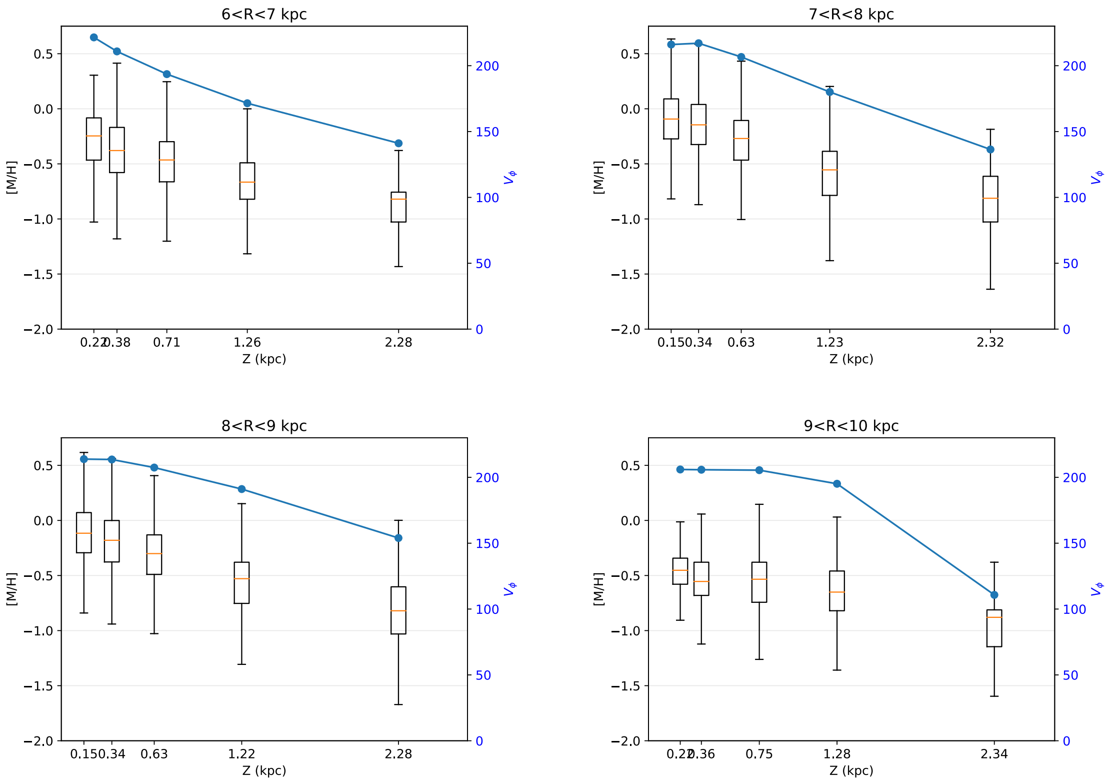

Fig. 2. Box plots representing the median metallicity (orange line) as a function of absolute distance from the Galactic plane, Z, for different radial ranges, R, from the Galactic centre. The actual boxes enclose the metallicity value of the first and third quartile, whereas the sizes of the bar span 99 per cent of the distribution. The median V_ϕ value, in $\mathrm{km\,s^{-1}}$, for each spatial bin is also represented in blue (and right-hand-side y-axis).

Regarding the skewness of the MDFs, no particular changes are noticed as a function of R; this is illustrated with the lack of change of the relative position of the median line within a box from one $R-$bin to another, at a fixed Z. This is not in agreement with the inversion of the MDF's skewness highlighted in Hayden et al. (2015) using APOGEE data. Nevertheless, we note that in Hayden et al. (2015) the skewness changes for the bins closest to the plane, regions where RAVE is potentially biased. A more thorough analysis, taking into account the completeness of our sample, needs therefore to be performed in order to confirm this statement.

Compared to results obtained without Gaia information (using the RAVE-DR4 parameters and distances, see Kordopatis et al. 2013a), we do not find any significant change on the mean of the MDFs. That said, the updated tails of the MDFs make more sense using the Gaia data: many super metal-rich stars ([M/H] > 0, noted SMR hereafter) found previously to occupy large distances from the Galactic plane are found to be closer to the disc, whereas metal-poor stars are also shifted to higher Z. We note, however, that few SMR stars can still be detected, up to 1 kpc from the Galactic plane, confirming previous studies (see, for example, Kordopatis et al. 2015a). The majority of these SMR stars, even though they have updated eccentricities, are found to be in majority on circular orbits ($e < 0.2$), therefore having radially migrated from the inner parts of the disc through mechanisms involving co-rotation resonances with the spiral arms (e.g. Sellwood & Binney 2002).

Finally, it should be highlighted that we find a remarkably flat trend for the mean V_ϕ (obtained using UCAC5 proper motions, see Zacharias et al. 2017) as a function of Z for our outermost radial bin ($9 < R < 10$ kpc). Up to almost 750 pc from the plane, we find stars to have $< V_\phi >\approx 220\ \mathrm{km\,s^{-1}}$, i.e. associated to a stellar population dominated by the thin disc. This seems to confirm the thin disc flaring and the absence of the thick disc at the outer Galaxy, as already suggested by other studies (Bensby et al. 2011; Minchev et al. 2014; Bovy et al. 2016; Kordopatis et al. 2017), but now clearly indicated with the sole kinematics.

5 Signatures of accretion

Past accretion events can be identified directly in either the stellar positions (stellar streams), or energy-angular momentum space, or indirectly, by the dynamical effect that such accretions can have on the disc (Gómez et al. 2013).

Helmi et al. (2017) selected the metal-poor halo stars in the RAVE-TGAS sample in order to identify, in phase-space, over-densities associated with old accretions. Their work – which represents a first attempt of what will later be possible to achieve with better kinematics, distances and larger statistics– contains at least two important results. The first is that the selected halo stars that are identified as the less bound are in general in retrograde orbits, which is something that they evaluate not likely to happen in a smooth distribution, and the second is the identification of ten over-densities, an amount consistent with haloes formed purely by accretions. Future Gaia data-releases will allow to confirm this result, which at the moment is still hampered, to some extent, by low number statistics, and non-negligible uncertainty in stellar distance.

Carrillo et al. (2017) investigated the stellar motions in the galactic disc. The authors compared their results with the ones of Widrow et al. (2012) and Williams et al. (2013), where a wave-like pattern in the mean vertical velocity of stars near the Sun had been identified and been interpreted either as a vibration of the galactic plane due to the last major merger of the Milky Way, or as a dynamical signature of the potential of spiral arms on the stellar orbits, due to the inter-spiral arm position of the Sun (Faure et al. 2014; Monari et al. 2016). The new analysis, even though obtained in a smaller volume (limiting magnitude of TGAS $\sim 11\,\mathrm{mag}$ compared to $\sim 12\,\mathrm{mag}$ for RAVE), seem to suggest that the inner disc exhibits a breathing mode (provoked by either the accretion of a satellite or presence of the spiral arms), and that the outer disc exhibits a bending mode, solely explained by an accretion event (see their Figures 4 and 14). However, as the authors suggest, the error budget in the stellar kinematics, is still too large to make robust conclusions, and more accurate parallaxes and proper motions, together with (most importantly) a larger volume coverage by the future Gaia data-releases will allow to draw a definitive conclusion on the vibration modes of the disc.

6 Perspectives: Gaia and future ground-based spectroscopic surveys

Gaia DR2 is estimated to be released in April 2018. This data release will be a significant improvement over GDR1, since it will have better calibrations of the astrometry and the photometry, and will provide parallaxes and proper motion measurements up to $G \sim 20$ (i.e. up to 9 magnitudes fainter than TGAS), as well as radial velocities up to $G_{\mathrm{RVS}} \sim 12\,\mathrm{mag}$. The entire APOGEE, Gaia-ESO, LAMOST, GALAH and RAVE surveys, will be able to be crossmatched with GDR2, leading to a catalogue of $\sim 2 \cdot 10^6$ stars with metallicity and abundance measurements (and V_{rad} measurements for the faintest targets, for which the RVS will not get spectra). This fact, from itself constitutes an important milestone in galactic archaeology (as we have seen in the previous sections with just the crossmatch with RAVE), but the inhomogeneity of the chemical abundances, derived by different teams and different methods, might still be a limiting factor to achieve major breakthroughs in the field.

On the other hand, Gaia-DR3 (estimated to be released in mid-2020) will be the largest homogeneous spectroscopic catalogue ever available. Despite being derived from medium resolution spectra ($R \sim 11500$), the metallicities, radial velocities and abundances that will be published based on an homogeneous method, will be a huge leap towards investigating the relative abundances of the stellar populations, highlighting their chemo-dynamical differences and hence deciphering the evolution of our galaxy.

Finally, Gaia's potential will be even further increased thanks to WEAVE (Dalton et al. 2012), MOONS (Cirasuolo et al. 2011) and 4MOST (de Jong 2011), three spectroscopic surveys that will not start observing before the end of 2018, 2019 and 2022. WEAVE and 4MOST, in particular, will eventually provide high-resolution (up to $V \sim 15-16\,\mathrm{mag}$) and medium-resolution spectra (up to $V \sim 18-19\,\mathrm{mag}$) for tens of millions of stars and allow to map the Solar neighbourhood (up to $\sim$ 1 kpc), thought to contain stars coming from wide regions across the disc and halo, with unprecedented details thanks to the abundance measurements of several chemical elements of different nucleosynthetic families and kinematic accuracies of a few 100 $\mathrm{m\,s^{-1}}$. In addition, those surveys will allow to obtain spectra up to the magnitudes where Gaia will have proper motions and parallax measurements but no RVS spectra, leading to chemodynamical catalogues of stars with a precision that can be achieved nowadays only up to a couple of kpc away from the Sun.

G.K. would like to thank the PNCG for financial support.

References

Astraatmadja, T. L. & Bailer-Jones, C. A. L. 2016, ApJ, 833, 119

Bailer-Jones, C. A. L., Andrae, R., Arcay, B., et al. 2013, A&A, 559, A74

Bensby, T., Alves-Brito, A., Oey, M. S., Yong, D., & Meléndez, J. 2011, ApJ, 735, L46

Bovy, J., Rix, H.-W., Schlafly, E. F., et al. 2016, ApJ, 823, 30

Bullock, J. S. & Boylan-Kolchin, M. 2017, ARA&A, 55, 343

Carrillo, I., Minchev, I., Kordopatis, G., et al. 2017, ArXiv e-prints

Cirasuolo, M., Afonso, J., Bender, R., et al. 2011, The Messenger, 145, 11

Dalton, G., Trager, S. C., Abrams, D. C., et al. 2012, in Proc. SPIE, Vol. 8446, Ground-based and Airborne Instrumentation for Astronomy IV, 84460P

de Jong, R. 2011, The Messenger, 145, 14

Faure, C., Siebert, A., & Famaey, B. 2014, MNRAS, 440, 2564

Freeman, K. & Bland-Hawthorn, J. 2002, ARA&A, 40, 487

Gaia Collaboration, Brown, A. G. A., Vallenari, A., et al. 2016a, A&A, 595, A2

Gaia Collaboration, Prusti, T., de Bruijne, J. H. J., et al. 2016b, A&A, 595, A1

Gómez, F. A., Minchev, I., O'Shea, B. W., et al. 2013, MNRAS, 429, 159

Hayden, M. R., Bovy, J., Holtzman, J. A., et al. 2015, ApJ, 808, 132

Helmi, A., Veljanoski, J., Breddels, M. A., Tian, H., & Sales, L. V. 2017, A&A, 598, A58

Kordopatis, G., Binney, J., Gilmore, G., et al. 2015a, MNRAS, 447, 3526

Kordopatis, G., Gilmore, G., Steinmetz, M., et al. 2013a, AJ, 146, 134

Kordopatis, G., Gilmore, G., Wyse, R. F. G., et al. 2013b, MNRAS, 436, 3231

Kordopatis, G., Wyse, R. F. G., Chiappini, C., et al. 2017, MNRAS, 467, 469

Kordopatis, G., Wyse, R. F. G., Gilmore, G., et al. 2015b, A&A, 582, A122

Kunder, A., Kordopatis, G., Steinmetz, M., et al. 2017, AJ, 153, 75

Lindegren, L., Lammers, U., Bastian, U., et al. 2016, A&A, 595, A4

McMillan, P. J., Kordopatis, G., Kunder, A., et al. 2017, ArXiv e-prints

Minchev, I., Chiappini, C., Martig, M., et al. 2014, ApJ, 781, L20

Monari, G., Famaey, B., Siebert, A., et al. 2016, MNRAS, 461, 3835

Pont, F. & Eyer, L. 2004, MNRAS, 351, 487

Recio-Blanco, A., de Laverny, P., Allende Prieto, C., et al. 2016, A&A, 585, A93

Schlesinger, K. J., Johnson, J. A., Rockosi, C. M., et al. 2014, ApJ, 791, 112

Sellwood, J. A. & Binney, J. J. 2002, MNRAS, 336, 785

Soderblom, D. R. 2010, ARA&A, 48, 581

Springel, V., Frenk, C. S., & White, S. D. M. 2006, Nature, 440, 1137

Tolstoy, E., Hill, V., & Tosi, M. 2009, ARA&A, 47, 371

Widrow, L. M., Gardner, S., Yanny, B., Dodelson, S., & Chen, H.-Y. 2012, ApJ, 750, L41

Williams, M. E. K., Steinmetz, M., Binney, J., et al. 2013, MNRAS, 436, 101

Wojno, J., Kordopatis, G., Piffl, T., et al. 2017, MNRAS, 468, 3368

Zacharias, N., Finch, C., & Frouard, J. 2017, AJ, 153, 166

SF2A 2017
C. Reylé, P. Di Matteo, F. Herpin, É. Lagadec, A. Lançon, Z. Meliani, F. Royer (eds)

DISC KINEMATICS FROM GAIA DR1

A. C. Robin[1], O. Bienaymé[2], J. G. Fernández-Trincado[1] and C. Reylé[1]

Abstract. The complementarity of radial velocity survey RAVE with Gaia first data release (TGAS) gives the opportunity to study the full 3D velocity space in a wide solar neighbourhoud. Using a revised version of the Besançon Galaxy Model, we simulate the kinematics of stellar populations to be compared with those new data. In modelling the kinematics, we account for the asymmetric drift computed from fitting a Stäckel potential to orbits (Bienaymé et al. 2015). We show that this model is able to reproduce the kinematics of the local discs in great detail for both the thin and thick discs. The $U_\odot$ and $W_\odot$ components of the Solar motion agree well with previous studies. However we revise significantly the previous estimates of $V_\odot$ velocity, with a value of 1 km/s, thanks to the new proper motions from Gaia, the inclusion of the variation of the asymmetric drift with distance to the plane, and to the method used where model parameters are fitted in the space of observables.

Keywords: Galaxy:evolution, Galaxy:dynamics, Galaxy:disk, Galaxy:kinematics, Galaxy: formation, Galaxy: stellar content

1 Introduction

The Gaia mission, launched in December 2013, is expected to revolutionize our view of the Milky Way, specially from the measurements of exquisite proper motions and parallaxes. Since the first data release (Gaia Collaboration et al. 2016) it has provided accurate transversial velocities for nearby stars, by combining the first months of observations, with previous Tycho-2 positions. On the other hand, The RAVE (RAdial Velocity Experiment, Kordopatis et al. 2013; Kunder et al. 2017) has provided exquisit radial velocities, with an accuracy of 1-2 km/s for a large sample of stars in a wide solar neighbourhood. This is a good opportunity to question our knowledge about the kinematics in the solar neighbourhood, at larger distances than Hipparcos allowed to do.

In this study we use a revised version of the Besançon Galaxy Model to compare with these new data sets and reconsider the velocity ellipsoids and age-velocity dispersion relations of the thin and thick disc as well as the solar motion.

2 Description of the data set

We make use of the RAVE DR4 (Kordopatis et al. 2013). The stars are randomly selected in fields covering the southern hemisphere, avoiding the Galactic plane. Hence this is a sample which is adequate for a statistical analysis of the stellar populations and their kinematics. Stars are selected from their magnitude and are all part of the Tycho-2 catalogue (Hoeg et al. 1997). In our analysis we select stars with temperatures between 4000 and 8000 K, and at latitudes $|b| > 25°$.

The Gaia first data release (TGAS)(Lindegren et al. 2016; Gaia Collaboration et al. 2016), has provided proper motions and parallaxes for stars in Tycho-2 catalogue, based on a the scheme proposed by Lindegren et al. (2016). This first release provides positions, parallaxes with an accuracy of about 1 mas and proper motions for single stars at the level of 1 mas/yr, using the first 11 months of the mission, using the positions measured 25 years ago by Tycho-2. However this first release suffers from some systematics, depending on the number of time the star has been observed, which varies with sky position. This is for this reason, and because

[1] Institut Utinam, CNRS UMR6213, Univ. Bourgogne Franche-Comté, OSU THETA , Observatoire de Besançon, BP 1615, 25010 Besançon Cedex, France
[2] Observatoire Astronomique de Strasbourg, Université de Strasbourg, CNRS, 11 rue de l'Université, F-67000 Strasbourg, France

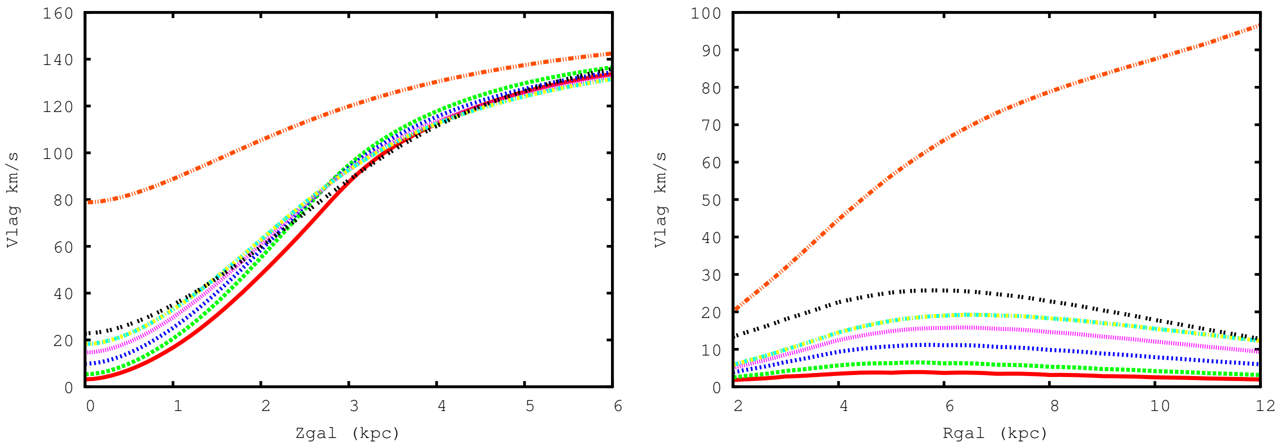

Fig. 1. Asymmetric drift computed from the Stäckel approximation of the BGM for subcomponents 2 to 7 (thin disk, with increasing ages plotted in solid red, long dashed green, short dashed blue, dotted magenta, dashed yellow and cyan), and for the young (dot-dashed black) and old (dot-dot-dashed red) thick disks. **Left panel:** as a function of $R_{\rm gal}$ for $z_{\rm gal}$=0; right panel: as a function of $z_{\rm gal}$ for $R = R_\odot$.

the accuracy is limited to stars within a small solar neighbourhood, that we choose in this study not to use the parallax information, but only the proper motions.

We analyse the combined sample RAVE+GaiaDR1 (TGAS) by comparison of these data with model simulations which are provided by the Besançon Galaxy Model, as described below, in the space of observables (magnitude, metallicity, radial velocity, proper motions).

3 The Besançon Galaxy Model

In this study we use the version of the model described in Czekaj et al. (2014) where the stars are drawn from chosen initial mass function and star formation rate for the thin disc population. This scheme takes into account the expected binary fraction, mass ratio and semi-major axis distributions as seen in observations, as described in Arenou (2011). The thin disc population is modeled by the sum of 7 sub-populations of different ages, assumed to be each isothermal. The metallicity is also a function of age (Haywood 2008). The Galactic potential is computed from the mass distributions of the stellar populations, where the interstellar matter and dark halo are added up (Robin et al. 2003). In Bienaymé et al. (2015) this potential has been approximated by a Stäckel potential, which allows to compute the third integral of motions and self-consistent analytical solutions for the distribution functions. This method is used to compute the exact value of the asymmetric drift and its variation with R and z for each isothermal sub-population. Figure 1 show the variations of the asymmetric drift as a function of Galactocentric cylindrical coordinates. For simplicity for the time being, the densities are Einasto laws, as in previous models (Robin et al. 2003).

In this model, the thick disc is modelled as described in Robin et al. (2014), that is a sum of two episodes of formation, at 10 Gyr ago (the young thick disc) and 12 Gyr (old thick disc). These two components have different density distributions on the sky, the young thick disc being more concentrated to the Galactic center and the Galactic plane (see Robin et al. 2014, for details).

We attempted to define the kinematics of the thick disc in this study, trying to see whether the contraction of the thick disc with time (from the old to the young, as found previously) was also seen in their kinematics, expecting the velocity dispersion of the young component to be smaller than the older one.

To test the sensitivity of the data to the choice of a given rotation curve, we consider alternatively Caldwell & Ostriker (1981) and Sofue (2015) rotation curves.

4 Model fitting method and results

The ABC-MCMC scheme was used to determine the free parameters of the model. Namely : the solar motion, the age-velocity dispersion V_z of the thin disc, and the ratios V_z/V_x and V_y/V_z assumed not varying with time, the full velocity ellipsoid for the young and old thick discs, a vertex deviation depending linearly on age. To evaluate each model, the goodness-of-fit parameter was the one used by Bienaymé et al. (1987). An ABC (Approximate Bayesian Computation) method allowed to compute the likelihood for each model realization, because it is not possible to compute an analytic bayesian probability distribution function for our complex model.

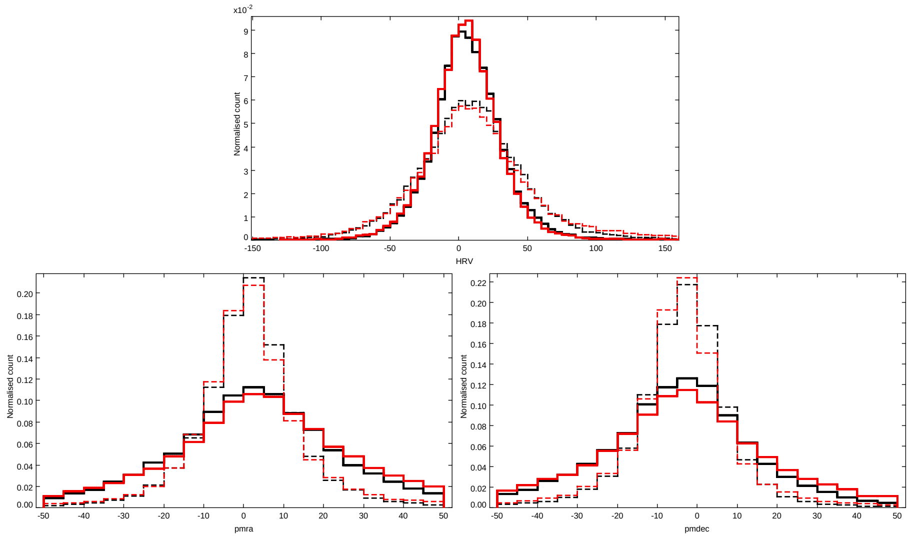

Fig. 2. Histograms of RAVE radial velocity distributions, and proper motions from Gaia DR1, for hot (solid lines) and cool (dashed lines) stars. Data are shown as black lines, and the best-fit model is shown as red lines.

The ABC-MCMC algorithm, using the Metropolis-Hasting sampling, was used in 15 independent runs of 200,000 iterations each. We checked the correlations between parameters in the solutions, and that the standard deviation in each run was compatible between independent runs. Table 1 shows the resulting model parameters obtained by averaging the solutions of different runs, together with the uncertainties, assuming that the variation of the σ_W with age in Gyr follows a polynomial of coefficients A,B,C.

5 Conclusions

The complementarity of the RAVE radial velocities with the Gaia proper motions gives a unique opportunity to trace and characterize the kinematics in a wide solar neighbourhood. The sample is much larger than the ones used in previous studies, such as the Geneva-Copenhaguen survey, used in Schönrich et al. (2010), and the accuracies and precisions are incomparable. Hence, we believe that our results are more robust that previous ones. We determined the variation of the velocity ellipsoid of the thin disc as a function of time, which we find in good agreement with Gómez et al. (1997) and with the model of Bovy et al. (2012); the velocity ellipsoid of the thick disc is shown to also vary with time, with the young thick disc having a lower velocity dispersion than the old thick disc, in agreement with our scenario of contraction during the thick disc episode (Robin et al. 2014).

We find the Solar motion to be U, V, W=(12.75,0.93,7.10) km/s slightly different from previous studies, probably due to the fact that we account for the variations of the asymmetric drift with position from the Galactic plane, that we fit in the observable parameter space, avoiding biases introduced by the inversion method, thanks to the exquisite precisions of Gaia data.

The new model can be used for simulations at this address: `http://model2016.obs-besancon.fr/`. It is also available through a web service, for automatic uses and downloads from workflows.

BGM simulations were executed on computers from the Utinam Institute of Université de Franche-Comté, supported by the Région de Franche-Comté. This study was supported by Programme National Cosmologie et Galaxies (PNCG) and INSU. JGFT acknowledges the support from CNES (Centre National d'Etudes Spatiales) and Région de Franche-Comté. We acknowledge the use of the *RAVE* survey (`https://www.rave-survey.org`). This work has made use of data from the European Space Agency (ESA) mission *Gaia* (`https://www.cosmos.esa.int/gaia`), processed by the *Gaia* Data Processing and Analysis Consortium (DPAC,

Table 1. Best values of fitted parameters obtained by the mean of the last third of eight independent chains and standard deviation assuming Caldwell & Ostriker (1981) and Sofue (2015) rotation curves. Units are km/s for velocities, pc for the scale lengths, and radians for the vertex deviation, which is given for stars younger than 1 Gyr (VD_a) and older than 1 Gyr (VD_b). A, B, and C are the coefficients of the polynomial describing the variation of σ_W with age in Gyr.

Parameter	Caldwell	Sofue
Solar motion		
$U_\odot$	12.75 ± 1.26	11.88± 1.38
$V_\odot$	0.93 ± 0.30	0.91± 0.26
$W_\odot$	7.10 ± 0.16	7.07± 0.16
Thin disk		
A	5.69 ± 0.37	5.69± 0.41
B	2.48 ± 0.30	2.33± 0.28
C	−0.0966 ± 0.0404	−0.0774± 0.0362
σ_V/σ_U	0.57 ± 0.03	0.58± 0.03
σ_W/σ_U	0.46 ± 0.03	0.46± 0.02
h_{σ_U}	13176. ± 6908.	9534.± 3982.
h_{σ_W}	15919. ± 8609.	10414.± 6299.
Thick disk		
σ_U	40.02 ± 1.74	41.58± 1.51
σ_V	31.86 ± 1.55	30.95± 1.50
σ_W	27.89 ± 1.26	27.02± 1.00
Old thick disk		
σ_U	75.64 ± 8.58	79.64± 7.96
σ_V	55.41 ± 8.74	57.55± 8.51
σ_W	66.43 ± 3.95	62.15± 6.62

`https://www.cosmos.esa.int/web/gaia/dpac/consortium`). Funding for the DPAC has been provided by national institutions, in particular the institutions participating in the *Gaia* Multilateral Agreement.

References

Arenou, F. 2011, in American Institute of Physics Conference Series, Vol. 1346, American Institute of Physics Conference Series, ed. J. A. Docobo, V. S. Tamazian, & Y. Y. Balega, 107–121

Bienaymé, O., Robin, A. C., & Crézé, M. 1987, A&A, 180, 94

Bienaymé, O., Robin, A. C., & Famaey, B. 2015, A&A, 581, A123

Bovy, J., Allende Prieto, C., Beers, T. C., et al. 2012, ApJ, 759, 131

Caldwell, J. A. R. & Ostriker, J. P. 1981, ApJ, 251, 61

Czekaj, M. A., Robin, A. C., Figueras, F., Luri, X., & Haywood, M. 2014, A&A, 564, A102

Gaia Collaboration, Brown, A. G. A., Vallenari, A., et al. 2016, A&A, 595, A2

Gómez, A. E., Grenier, S., Udry, S., et al. 1997, in ESA Special Publication, Vol. 402, Hipparcos - Venice '97, ed. R. M. e. a. Bonnet, 621–624

Haywood, M. 2008, MNRAS, 388, 1175

Hoeg, E., Bässgen, G., Bastian, U., et al. 1997, A&A, 323, L57

Kordopatis, G., Gilmore, G., Steinmetz, M., et al. 2013, AJ, 146, 134

Kunder, A., Kordopatis, G., Steinmetz, M., et al. 2017, AJ, 153, 75

Lindegren, L., Lammers, U., Bastian, U., et al. 2016, ArXiv e-prints

Robin, A. C., Reylé, C., Derrière, S., & Picaud, S. 2003, A&A, 409, 523

Robin, A. C., Reylé, C., Fliri, J., et al. 2014, A&A, 569, A13

Schönrich, R., Binney, J., & Dehnen, W. 2010, MNRAS, 403, 1829

Sofue, Y. 2015, PASJ, 67, 75

Session 07

Models and interpretation of stellar populations

SF2A 2017
C. Reylé, P. Di Matteo, F. Herpin, É. Lagadec, A. Lançon, Z. Meliani, F. Royer (eds)

DETECTION OF SPECTROSCOPIC BINARIES IN THE GAIA-ESO SURVEY

M. Van der Swaelmen[1], T. Merle[1], S. Van Eck[1] and A. Jorissen[1]

Abstract. The Gaia-ESO survey (GES) is a ground-based spectroscopic survey, complementing the Gaia mission, in order to obtain high accuracy radial velocities and chemical abundances for 10^5 stars. Thanks to the numerous spectra collected by the GES, the detection of spectroscopic multiple system candidates (SBn, $n \geq 2$) is one of the science case that can be tackled. We developed at IAA (Institut d'Astronomie et d'Astrophysique) a novative automatic method to detect multiple components from the cross-correlation function (CCF) of spectra and applied it to the CCFs provided by the GES. Since the bulk of the Milky Way field targets has been observed in both HR10 and HR21 GIRAFFE settings, we are also able to compare the efficiency of our SB detection tool depending on the wavelength range. In particular, we show that HR21 leads to a less efficient detection compared to HR10. The presence of strong and/or saturated lines (Ca II triplet, Mg I line, Paschen lines) in the wavelength domain covered by HR21 hampers the computation of CCFs, which tend to be broadened compared to their HR10 counterpart. The main drawback is that the minimal detectable radial velocity difference is $\sim 60\,\mathrm{km\,s^{-1}}$ for HR21 while it is $\sim 25\,\mathrm{km\,s^{-1}}$ for HR10. A careful design of CCF masks (especially masking Ca triplet lines) can substantially improve the detectability rate of HR21. Since HR21 spectra are quite similar to the one produced by the RVS spectrograph of the Gaia mission, analysis of RVS spectra in the context of spectroscpic binaries can take adavantage of the lessons learned from the GES to maximize the detection rate.

Keywords: Surveys: Gaia-ESO Survey, Stars: binaries: spectroscopic, Methods: data analysis, Techniques: radial velocities, Techniques: spectroscopic

1 Introduction

Merle et al. (2017) presented a (semi-automated) pipeline, Detection Of Extrema (Doe), and applied it to the fourth data release (iDR4) of the Gaia-ESO Survey (Gilmore et al. 2012; Randich et al. 2013). We quickly repeat the principles of Doe: 1/ a cross-correlation function (CCF) is simultaneously smoothed by a Gaussian kernel and derived three times; 2/ first and third derivatives are used to look for local maxima and/or inflexion points; 3/ the positions of those remarkable points provide the velocity of the stellar components forming the suspected multiple stellar system; 4/ multi-epoch and multi-setting observations are used to qualitatively (with flags: probable, possible or tentative) estimate the probability that the stellar multiplicity is real.

Merle et al. (2017) noted that the SB2 detection efficiency (here, we mean the smallest detectable velocity difference between the two stellar components) strongly depends on the setting. In order to investigate this sensitivity, we generate Monte-Carlo HR10 and HR21 spectra ($R \sim 21500$ and $R \sim 18000$, resp.) of a pair of twin (non-rotating) stars for various levels of S/N and radial velocity separations $\Delta v_{\rm rad}$. We then build the maps of SB2 detection efficiency for both setups (Fig. 1) by running the Doe pipeline on the simulated spectra. In Fig. 1, the green dots (respectively the red triangles) indicate ($\Delta v_{\rm rad}$, S/N) conditions when Doe is able to detect the two expected peaks in more than 95% of cases (resp., conditions when Doe failed at detecting two expected peaks in more than 95% of cases). Blue plusses represent intermediate cases making detection efficiency dependent of the noise: (i) due to the noise, spurious peaks may appear or (ii) thanks to the noise, the two peaks have different height (despite being a pair of twins) and become discernible to Doe. Our simulations show that HR10 allows a more efficient detection, with a good detection rate as soon as S/N ≥ 2 and $\Delta v_{\rm rad} \geq 25\,\mathrm{km\,s^{-1}}$. On the other hand, HR21 allows the detection of SB2 with $\Delta v_{\rm rad} \geq 45\,\mathrm{km\,s^{-1}}$ and S/N ≥ 5. In their full analysis of GES DR4 spectra, Merle et al. (2017) noted that the smallest detected $\Delta v_{\rm rad}$ is $25\,\mathrm{km\,s^{-1}}$ for HR10 and $60\,\mathrm{km\,s^{-1}}$ for HR21, in rather good agreement with our predictions.

[1] Institut d'Astronomie et d'Astrophysique, Université Libre de Bruxelles, Belgium

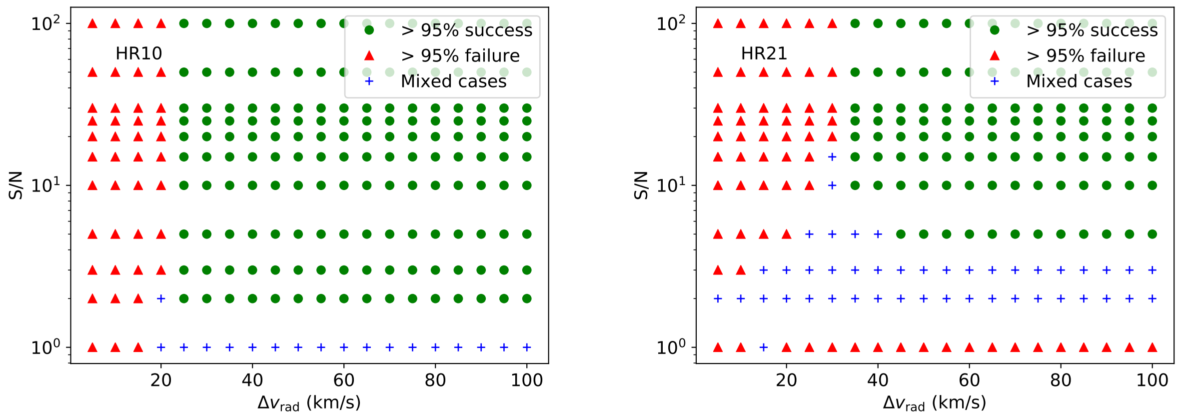

Fig. 1. SB2 detection efficiency for HR10 and HR21 GIRAFFE setups

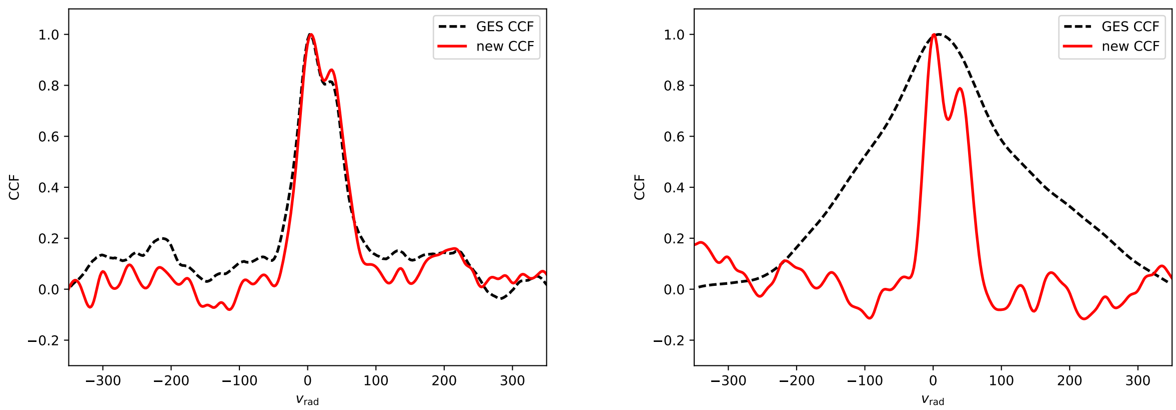

Fig. 2. HR10 (left) and HR21 (right) CCF of 07272578-0310066 at MJD 57032.153726 and 57032.247332 (resp.). Black dashed curve is the GES/CASU CCF, red solid curve is the newly computed CCF.

Fig. 2 exhibits a puzzling case. The same object, namely 07272578-0310066, is observed twice during the same night, once with the HR10 grating, once with the HR21 grating. The black curves in Fig. 2 display the CCFs provided by the GES/CASU: while the binary nature is clearly visible in the HR10 CCF, it is not the case in the HR21 CCF. This kind of disagreement between HR10 and HR21 CCFs has motivated our effort to recompute the GES CCFs.

2 Method

In order to improve the HR21 CCFs, we selected a set of weakly-blended lines in the range [8430 Å, 8990 Å] and used them to compute HR21 synthetic masks. Though we do not expect to significantly improve the computation of HR10 CCFs (detection is already very efficient), we apply the same procedure to recompute new HR10 synthetic masks: HR10 will serve to validate our method. We then recompute the CCFs by cross-correlating the GES spectra and our HR10/HR21 synthetic masks.

Fig. 2 compares the GES/CASU CCF (black curves) to our new CCF (red curves) for the object 07272578-0310066. As expected, our new CCFs give the same results for HR10, showing that the method is robust and that our new mask allows to retrieve already known SB2s. However, unlike the GES CCF, the new HR21 CCF has narrower peaks and now also indicates the SB2 nature. The presence of strong saturated lines (Ca II triplet, strong Mg line, Paschen lines) in the range [8430 Å, 8990 Å] tends to broaden HR21 CCFs. Therefore, binary systems with small $\Delta v_{\rm rad}$ tend to have their components hidden in the unique broad peak of their HR21 CCF. Since our masks do not include such lines, we get narrower CCFs.

3 Conclusion

We performed preliminary tests on a subset (72 objects) of SB2s identified by Merle et al. (2017) for which the SB2 nature is detected in HR10 GES CCFs but not in HR21 ones. Our new CCFs now allow to detect the SB2 nature of $\sim 35\%$ objects based on their HR21 CCFs (26 objects out of 72). With the new HR21 CCFs we are also able to detect systems with a $\Delta v_{\rm rad}$ as low as $25\,\mathrm{km\,s^{-1}}$, to be compared to the smallest $\Delta v_{\rm rad}$ reported in Merle et al. (2017) ($60\,\mathrm{km\,s^{-1}}$).

Our work shows that very low S/N spectra ($>\sim 3$) are still usable in the context of radial velocity measurement and moreover, for SB detection. Since the HR21 spectral domain resembles that of the Gaia RVS, RVS CCFs may suffer from similar broadening issues and may benefit from a careful design of correlating masks.

MVdS deeply thanks the SF2A for its financial support to attend "Les Journées de la SF2A". MVdS benefits from a "Fondation ULB" fellowship.

References

Gilmore, G., Randich, S., Asplund, M., et al. 2012, The Messenger, 147, 25

Merle, T., Van Eck, S., Jorissen, A., et al. 2017, ArXiv e-prints

Randich, S., Gilmore, G., & Gaia-ESO Consortium. 2013, The Messenger, 154, 47

SF2A 2017
C. Reylé, P. Di Matteo, F. Herpin, É. Lagadec, A. Lançon, Z. Meliani, F. Royer (eds)

CONSTRAINING THE ORIGIN OF MULTIPLE STELLAR POPULATIONS IN GLOBULAR CLUSTERS WITH N-BODY SIMULATIONS

A. Mastrobuono-Battisti[1] and H. B. Perets[2]

Abstract. Globular Clusters (GCs) are composed by multiple stellar populations whose origin is still unknown. Second population (SP) stars are currently thought to arise from gas ejected by first population (FP) stars, which is then accreted into the primordial GC core. Such gas forms a stellar disk whose long-term evolution and effects on the embedding cluster can be followed by means of N-body simulations. Here, we find that as the SP disk relaxes, the old, first stellar population flattens and develops a significant radial anisotropy, making the GC structure become more elliptical. The second stellar population is characterized by a lower velocity dispersion, and a higher rotational velocity, compared with the primordial population. The strength of these signatures increases with the relaxation time of the cluster and with the mass ratio between the SP and FP mass stars. We conclude that GC ellipticities and rotation constitute fossil records that can be used as observational proxies to unveil the origin of multiple stellar populations.

Keywords: Milky Way, globular clusters, multiple populations, formation, dynamical evolution, observational signatures

1 Introduction

Recent observations revealed the complex nature of globular clusters (GCs). These dense stellar systems, historically considered the prototype of single stellar populations, are in fact composed by several stellar populations characterized by chemical inhomogeneities in light elements and by a strong anti-correlation between Na and O (Gratton et al. 2012). Second population (SP) stars are thought to account for ∼30%-70% of the total number of stars (D'Antona & Caloi 2008; Carretta et al. 2009; Pancino et al. 2010; Bastian & Lardo 2015). The origin of SP stars is still unknown and one of the possible formation channels is through FP gas accreted into the GC core. Possible sources for this gas is material ejected by FP asymptotic giant branch (AGB) stars (Ventura et al. 2001; D'Ercole et al. 2008), interacting massive FP binaries (de Mink et al. 2009; Bastian et al. 2013), very massive stars (Denissenkov & Hartwick 2014) or fast rotating massive stars (Decressin et al. 2007; Krause et al. 2013). Material ejected at sufficiently low velocities (lower than the escape velocity from the GC) can be retained in the cluster, concentrate at its center and mix with the leftover pristine gas and then fragment to form new stars (see Gratton et al. 2012, and references therein). In all the self-enrichment scenarios, the initial spatial and kinematical configuration of the younger stellar population strongly depends on the original gas configuration. (Bekki 2010, 2011) recently studied the case of dissipative accretion of material lost through AGB winds. In their simulations, they found that if the gas inherits even only a small amount of the orbital angular momentum of the progenitor stars, it will then produce a disk rather than a spherical distribution of gas. Such process leads to the formation of a SP stellar disk embedded in the FP spherical cluster. As we found in Mastrobuono-Battisti & Perets (2013) , the evolution of such embedded disks in an ω Cen-like cluster, significantly impact the evolution of the system leaving behind kinematical and morphological signatures on its structure. Here and in Mastrobuono-Battisti & Perets (2016) we generalize this analysis and study the evolution of embedded SP disks with a range of masses and we follow their long-term effects on the cluster structure, and the dependence of the properties of the cluster on the fractional mass of the SP stellar population. We also compare these results to the case of SP stars formed in an embedded spherical sub-structure rather than a disk configuration. In Section 2 we describe the methods and simulations used in our analysis. The results obtained are shown in Section 3. We draw our conclusions in Section 4.

[1] Max-Planck Instiut für Astronomie, Königstuhl 17, D-69117 Heidelberg, Germany
[2] Department of Physics, Technion, Israel Institute of Technology, Haifa 32000, Israel

2 Methods and simulations

We follow the evolution of massive second population disks embedded in initially spherical clusters, by means of high-precision N-body simulations. To do so we use ϕGPU (Berczik et al. 2011), a direct N-body code running on graphic processing units (GPUs). We run our simulations both on the cluster Tamnun at the Technion and on the cluster Cytera in Cyprus. In order to smooth close encounters between particles we adopt a softening length of 10^{-3} pc. The relative energy variations at the end of the simulations are smaller than $\Delta E/E = 0.01$. The initial spherical, FP, component of the cluster is a single mass King (1966) model, similar to the best fit model of the density profile of ω Cen (Meylan 1987), with $W_0 = 6$, core radius $r_c = 4.4$ pc and tidal radius $r_t = 80$ pc. This system is sampled using $N = 50000$ particles, whose mass is 20 $M_{\odot}$, accounting for a total mass of $M = 10^6$ $M_{\odot}$. We begin our simulations after the cluster has already lost a large fraction of the FP stars. We embed the SP disk in the spherical FP component and we let the disk relax until it reaches a quasi-stable state, which is then considered to be the initial configuration of the system. During the pre-initial stage a fraction of the SP stars in the disk are expelled from the system, and are removed from the N-body simulation, leaving behind a disk whose mass corresponds to 19% (S19), 24% (S24), 29% (S29), 33% (S33) and 50% (S50) of the total stellar mass of the system, in the different models considered (see Table 1 in Mastrobuono-Battisti & Perets 2016, for more details). The choice of using particles masses larger than those of individual stars – justified by computational reasons – affects the dynamical time-scales, thus we rescale the simulation time to the relaxation time of the corresponding real system, using the procedure described in Mastrobuono-Battisti & Perets (2013). We assume an average stellar mass of $\langle m_* \rangle = 0.5$ $M_{\odot}$ and we evolve each system for 12Gyr of rescaled simulation time. The dynamics of stars born in a disk can give rise to different signatures observable in the cluster structure, compared with the effects of SP stars born in a spherical sub-cluster. In order to compare these two different initial configurations, we run an additional simulation where the SP stars are distributed inside the core radius of the FP population with a King profile with the same shape used for the FP stars. This comparison case is simulated only for a SP population comprising 50% of the total mass of the cluster (S50s, including both FP and SP stars). In this study we neglect tidal effects due to the Galaxy and stellar evolution. We use single mass particles, however we note that massive stars are short lived and low mass stars, whose mass range is limited, will dominate the evolution of the cluster.

3 Results

We analyzed the morphological and kinematical properties of the system after 12Gyr in order to find how the initial presence of a disk modifies the structure of the whole cluster, leaving behind long term observable signatures. The isodensity contours of each simulated stellar disk at the beginning of the simulation and after 3, 6, 9 and 12Gyr are shown in Figure 1. The second generation stars always remain confined within the central 10-20 pc without completely mixing with the FP population (see also Mastrobuono-Battisti & Perets 2013; Vesperini et al. 2013). The 19, 24 and 29% disks, at the end of the simulation, are almost spherical while the 33% and the 50% disks are still significantly flattened. We also note that the 50% disk is unstable and forms a central bulge that could lead to a faster angular momentum exchange with the FP population through collective effects rather than two-body relaxation (see also Mastrobuono-Battisti & Perets 2013). The left panel of Figure 2 shows the axial ratios of the whole system at the end of each simulation. The 19% disk is slightly prolate, with all axial ratios ~ 1, while the other systems are oblate. As shown in Mastrobuono-Battisti & Perets (2016), the projected axial ratios strongly depend on the viewing angle and increase with the mass of the SP disk. However, statistical analysis and future observations, e.g., potentially provided by the GAIA mission, could give more detailed information on the spatial structure of GCs, allowing a quantitative comparison between the theoretical expectations and the observations. The c/a axial ratio is smaller for larger disks, the 50% disk is almost perfectly oblate while the clusters with lower mass disks are more triaxial. The cluster is flattened at any radius, but the effect is larger in the central 10-20pc, where most of the disk stars reside. In contrast, the spherical SP system (model S50s) and its host cluster system do not show any significant flattening, as expected. Additionally, we found that the FP stars show a larger velocity dispersion compared with the SP stars. This anisotropy correlates with the mass of the disk. However, the same difference is also found when the SP has an initially spherical configuration. The anisotropy is thus a tracer of the mass of the second generation and not of its initial configuration. The right panel of Figure 2 shows the azimuthal velocity v_θ of the FP and SP stars as a function of the radius. In all the cases the FP stars show a mild central rotation with velocity between 0.5 and 1 km/s. The SP stars, regardless of the mass of the disk, rotate with v_θ between 0.5 and 2km/s (within the central $\sim$ 20pc). The rotation initially increases, up to ~ 3 pc, and then decreases at larger distances from

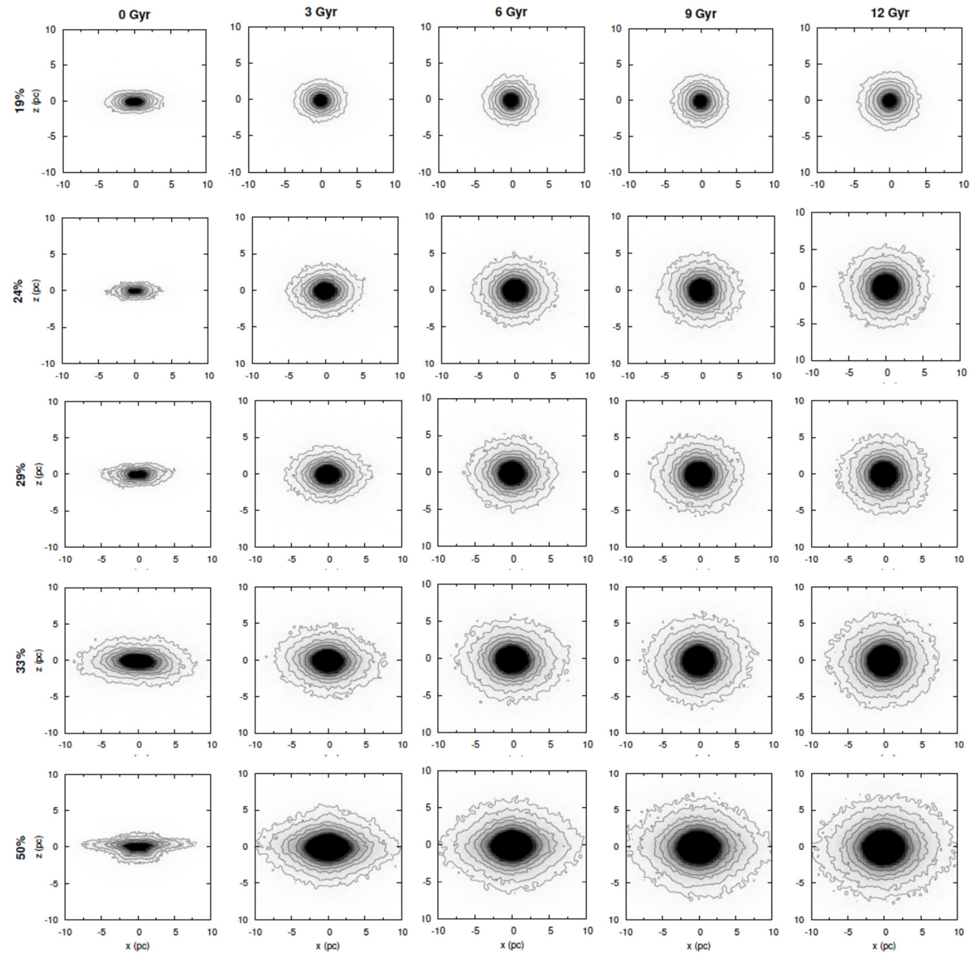

Fig. 1. The evolution of the SP simulated disks with time. The isodensity contours are given at 0, 3, 6, 9 and 12Gyr (going from the left to the right) and for the 19%, 24%, 29%, 33%, 50% mass fraction disks (going from top to bottom). The density contour levels are 50, 100, 200, 300, 500 and 1000 $M_{\odot}/\mathrm{pc}^3$. The z axis is parallel to the L_z component of the disk angular momentum. The disks clearly inflate with time, becoming almost spherical after 12Gyr. Different systems have different relaxation times so their final configuration slightly depends also on this factor. From Mastrobuono-Battisti & Perets (2016).

the center of the cluster. As expected (see also Hénault-Brunet et al. 2015), the spherical case does not show any significant rotation. Thus, in the AGB model or in any model where the SP stars form in a disk, the rotation, which is actually observed in many Galactic GCs (Kamann et al. 2017), can be potentially explained as the result of angular momentum exchange between an initially flattened and slowly rotating second stellar population and an initially spherical first stellar population.

4 Conclusions

We explored the long-term evolution of massive SP disks embedded in an initially spherical cluster composed of primordial, FP stars. We also compared these results with the case of SP stars in a spherical configuration. The presence of the disk imprints kinematic and structural signatures in the cluster properties whose strength is correlated with the SP population mass fraction and depend on the relaxation time of the system, but all the signatures are evident even after 12Gyr in any of the simulated cases. The presence and the strength of differential radial anisotropy between populations can be used as a tracer of the mass fraction of SP stars, while flattening and differential rotation are a clear consequence of an initial disk-like configuration of the younger

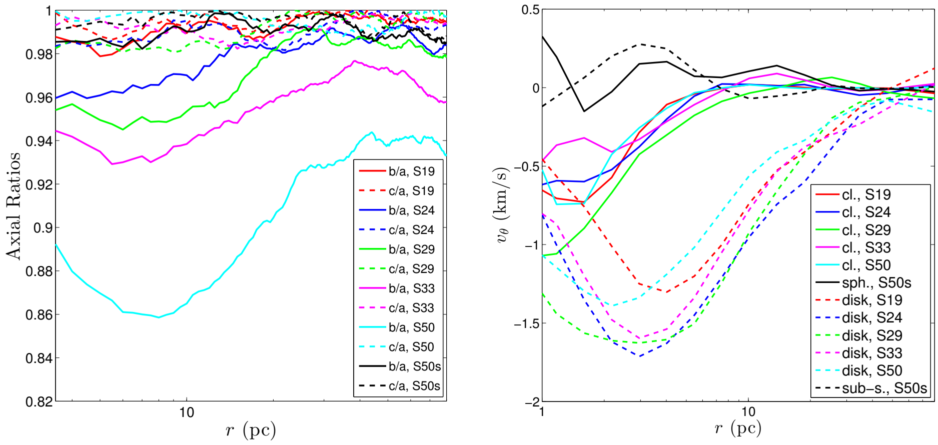

Fig. 2. The axial ratios of both first and second generation populations after 12Gyr of evolution (left panel) and the azimuthal velocity (right panel) for all the systems. The solid lines are for the initially spherical component, the dashed lines are instead for the flattened or spherical second generation population. From Mastrobuono-Battisti & Perets (2016).

population. The presence of the disk speeds-up the core collapse of the clusters because it reduces the relaxation time of the GC. We conclude that only the contemporary observation of flattening, lower velocity dispersion for the SP stars, radial anisotropy and SP rotation could point to an initially disk-like configuration of the younger, light-element enriched populations. The strength of these signatures could provide information on the dynamical age of the clusters and also on the fraction of SP stars present in the system.

We acknowledge the Cyprus Institute under the LinkSCEEM/Cy-Tera project.

References

Bastian, N., Lamers, H. J. G. L. M., de Mink, S. E., et al. 2013, MNRAS, 436, 2398

Bastian, N. & Lardo, C. 2015, MNRAS, 453, 357

Bekki, K. 2010, ApJL, 724, L99

Bekki, K. 2011, MNRAS, 412, 2241

Berczik, P., Nitadori, K., Zhong, S., et al. 2011, in International conference on High Performance Computing, Kyiv, Ukraine, October 8-10, 2011., 8–18

Carretta, E., Bragaglia, A., Gratton, R. G., et al. 2009, A&A, 505, 117

D'Antona, F. & Caloi, V. 2008, MNRAS, 390, 693

de Mink, S. E., Pols, O. R., Langer, N., & Izzard, R. G. 2009, A&A, 507, L1

Decressin, T., Meynet, G., Charbonnel, C., Prantzos, N., & Ekström, S. 2007, A&A, 464, 1029

Denissenkov, P. A. & Hartwick, F. D. A. 2014, MNRAS, 437, L21

D'Ercole, A., Vesperini, E., D'Antona, F., McMillan, S. L. W., & Recchi, S. 2008, MNRAS, 391, 825

Gratton, R. G., Carretta, E., & Bragaglia, A. 2012, A&ARr, 20, 50

Hénault-Brunet, V., Gieles, M., Agertz, O., & Read, J. I. 2015, MNRAS, 450, 1164

Kamann, S., Husser, T.-O., Dreizler, S., et al. 2017, ArXiv e-prints

King, I. R. 1966, AJ, 71, 64

Krause, M., Charbonnel, C., Decressin, T., Meynet, G., & Prantzos, N. 2013, A&A, 552, A121

Mastrobuono-Battisti, A. & Perets, H. B. 2013, ApJ, 779, 85

Mastrobuono-Battisti, A. & Perets, H. B. 2016, ApJ, 823, 61

Meylan, G. 1987, A&A, 184, 144

Pancino, E., Rejkuba, M., Zoccali, M., & Carrera, R. 2010, A&A, 524, A44

Ventura, P., D'Antona, F., Mazzitelli, I., & Gratton, R. 2001, ApJL, 550, L65

Vesperini, E., McMillan, S. L. W., D'Antona, F., & D'Ercole, A. 2013, MNRAS, 429, 1913

SF2A 2017
C. Reylé, P. Di Matteo, F. Herpin, É. Lagadec, A. Lançon, Z. Meliani, F. Royer (eds)

STUDY OF THE STRUCTURE AND FORMATION OF THE THICK DISC FROM STELLAR POPULATION MODELLING

G. Nasello[1], A.C. Robin[1], C. Reylé[1] and N. Lagarde[1]

Abstract. The thick disc is a major component of the Milky Way but, its characteristics and history are still not yet well constrained. The use of a population synthesis model, based on a scenario of formation and evolution of the Galaxy, a star formation history, and a set of stellar evolution models, is a way to improve the constraints on this population. For this reason, we use the Besançon Galaxy Model (BGM, Robin et al. (2003)). This model in constant evolution has been, thanks to Lagarde et al. (2017), implemented with new evolutionary tracks (STAREVOL, Lagarde et al. (2012)) to provide global asteroseismic and surface chemical properties along the evolutionary stages. Thanks to this updated Galaxy model and the Markov Chain Monte Carlo fitting method (MCMC) we will be able to constrain the thick disc structure and history. We show preliminary results applying this MCMC method to analyse the 2MASS photometric survey.

Keywords: Galaxy: disk, Galaxy: stellar content

1 Introduction

The Milky Way disc is, due to our particular position, difficult to study. Gilmore & Reid (1983) distinguished two disc populations, an old thick disc and a young thin disc. Thanks to the recent spectroscopic survey (such as APOGEE, Gaia-ESO) we can now recognize the thin and thick discs with their chemical properties. In early studies, only kinematical properties allowed to distinguish them.
Some studies (Snaith et al. (2014),Snaith et al. (2015), Haywood et al. (2013),Haywood et al. (2016) Robin et al. (2014), Hayden et al. (2015), Kordopatis et al. (2015), Guiglion et al. (2015)) are in favor of a thick disk formation at high redshift (z between 1 and 2) when the gas turbulence was high enough to form stars at a large distance from the plane. During this period, the thick disc can slightly contract (Robin et al. 2014). Other scenarios considere a thick disc formed by heating of the thin disc, for example by satellite accretion (Quinn et al. 1993) or from radial migration (Sellwood & Binney 2002). Even so, the thick disc nature, its history and relation to the thin disc are still under debate.
In this work, we try to constrain the thick disc structure and age distribution with the help of a Markov Chain Monte Carlo method (MCMC).

2 Method and preliminary results

We make use of the same method as Robin et al. (2014). We fit photometric observations varying thick disc parameters in the simulations. The fitted parameters and their boundaries are listed in table 1. We assume that the thick disc covers the age range from 8 to 12 Gyrs and attempt to derive the relative density in 4 age bins of 1 Gyr width.

Contrarily to Robin et al. (2014), we do not use isochrones (Bergbusch & Vandenberg 1992) to simulate the thick disc, but a grid of stellar models computed with STAREVOL (Lagarde et al. 2012). This grid allows us to test multiple thick disc's age distribution to constrain the thick disc star formation history that could give us a clue for the scenarios of formation of the thick disc.

[1] UTINAM Institute, University of Bourgogne-Franche-Comté, UMR CNRS 6213, 41 bis avenue de l'Observatoire BP 1615 25010 Besançon Cedex

	Scale length (pc)	Scale height (pc)	flare slope	flare radius (pc)	Relative density per age bin
Minimum value	1500	250	-0.1	0	0
Maximum value	4000	1200	0.2	16000	6

Table 1. List of thick disc parameters constrained by the MCMC and their boundaries. The thick disc is divided into 4 age bins of 1 Gyr width.

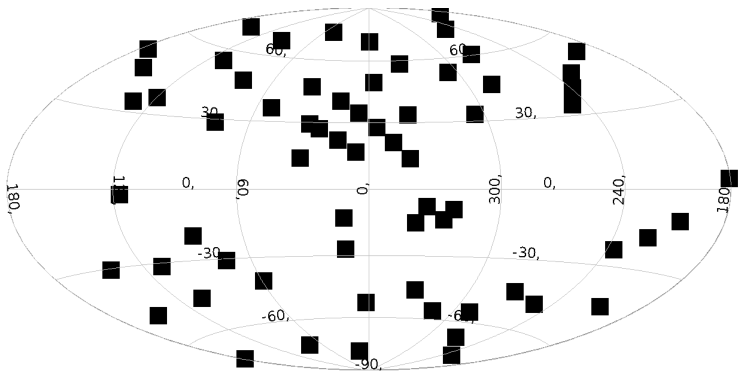

Fig. 1. 2MASS fields used to adjust the model in galactic coordinates

The new grid allows to compute extra stellar parameters, such as asterosismic quantities and chemical abundances.
We compare our simulations with 80 2MASS intermediate and high galactic latitude fields of 16 sq deg each (those fields are shown in figure 1).

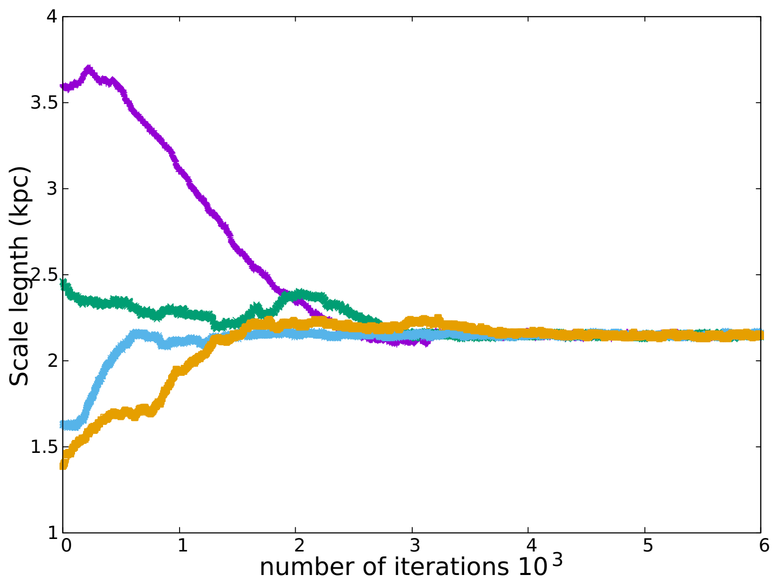

Fig. 2. Evolution of the thick disc scale length during the MCMC fitting process, for 5 MCMC independent runs with randomly chosen initial values. The scale length converges at about 2 kpc after 4 000 iterations.

To constrain the thick disc parameters, we maximize the log of the reduced likelihood (see eq. 2.1. where N_{sim} and N_{obs} are the numbers of simulated and observed stars present in a given color magnitude bin) using

	Scale length (pc)	Scale height (pc)	flare slope	flare radius (pc)	Relative density per age bin (in Gyrs)
Value of the best fit	2147.79 ± 7.40	576.48 ± 1.98	0.14 ± 0.04	9206.66 ± 31.01	[8;9]: 1.07±0.02; [9;10]: 0.81±0.03 [10;11]: 0.32±0.03; [11;12]: 0.30±0.02

Table 2. Thick disc parameters and their uncertainties obtained after averaging over 4 independent MCMC runs. The errors presented in this table do not take into account the correlations.

a MCMC scheme, starting with randomly chosen parameters within fixed boundaries given in table 1.

$$Lr = N_{sim} - N_{obs} + N_{sim} \times log(\frac{N_{obs}}{N_{sim}}) \tag{2.1}$$

Except for the flare, the thick disc parameters generally converge towards the same thick disc from one MCMC run to another: a thick disc younger than 11 Gyr with an increasing star formation rate from 11 to 8 Gyr, as also proposed by Snaith et al. (2014). We also find a short scale length, in agreement with previous results (Bensby et al. (2011) and Robin et al. (2014)), and a scale height similar to Robin et al. (2014).
The values of the best fit are listed on table 2. Those parameters and their uncertainties are obtained after averaging over 4 independent MCMC runs. The errors do not take into account the correlations.
Figure 2 shows an example of the convergence for the thick disc scale length. For each MCMC launched, the scale length converges towards 2 kpc which is in agreement with values found in Robin et al. (2014), Bensby et al. (2011) and Cheng et al. (2012). The quality of the fit can be illustrated in figure 3 that shows for a 2MASS field the histograms of J-K in several K magnitude bins for the observations and best fitting model.

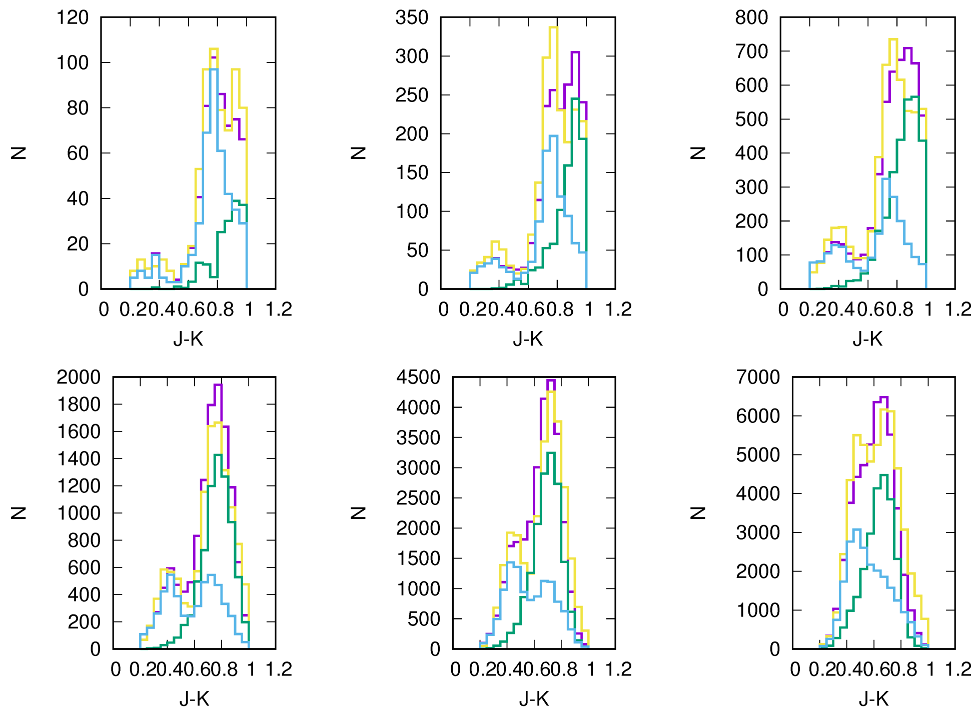

Fig. 3. Histogram of the J-K color for 6 K magnitude bins ([8;9], [9;10], [10;11], [11;12], [12;13], [13;14], [14;15]) the observations are in yellow, the simulations in purple, the thin disc in blue and the thick disc in green. This field is centered at galactic longitude of 11 ° and galactic latitude of -12 ° .

3 Conclusions

The results presented here were obtained with a fixed thick disc's average metallicity of -0.5 dex and a standard deviation of 0.3 dex. The initial mass function (IMF) was also fixed. It is planned to run MCMC on simulations with different thick disc metallicities, (in particular by adding an age metallicity relation for the thick disc) to observe their impact.

Focusing on 2MASS survey allowed us to test the thick disc without having to constrain the halo (its contribution is negligible at these magnitudes). However the lack of high latitude deep magnitude fields can bias the results obtained. To improve our results, we shall incorporate new observations from SDSS survey (Shadab et al. 2015), CFIS survey at CFHT (Ibata et al. 2017), and from Pan-STARRS (Chambers et al. 2017). To constrain the flare, it is also planned to add anticenter fields.

In the near future we plan to test the reliability of our results on the thick disc star formation history with detailed spectroscopic and asteroseismic data, such as the APOKASC data set (a combination of APOGEE spectroscopy and *Kepler* asterosismology, Pinsonneault et al. (2014)), CoroGEE (Anders et al. 2017), and CoRoT-GES (Valentini et al. 2016), allowing to get better constraints on its formation scenario.

We acknowledge the financial support from "Programme National Cosmologie et Galaxies" (PNCG) and from "Programme National de Physique Stellaire" (PNPS) of CNRS/INSU, France. BGM simulations were executed on computers from the Utinam Institute of the Université de Franche-Comté, supported by the Région de Franche-Comté and Institut des Sciences de l'Univers (INSU).

References

Anders F. et al. (2017) A& A, 597, A30, 27
Bensby T., Alves-Brito A., Oey M. S., Yong D., Meléndez J. (2011) ApJL, 735, 2, L46, 6
Bergbusch P.A., Vandenberg D. A., ApJS, 81, 163-220
Bovy, J., Rix H., Schlafly E., Nidever D., Holtzman J., Shetrone M., Beers T. (2016) ApJ, 823, 1, 30, 20
Chambers K.C., Pan-STARRS team (2017) AAS 229, 223.03
Cheng, J. Y. et al (2012) ApJ, 752, 1, 51, 12
Guiglion, G. et al. (2014) A & A, 583, A91
Gilmore G., Reid N. (1983), MNRAS, 202, 1025
Hayden M. R. et al. (2015) APJ, 808, 2,132
Haywood M., Di Matteo P., Lehnert M., Katz D., Gmez A. (2013) A&A, 560, A109, 18
Haywood M., Lehnert M. D., Di Matteo P., Snaith O., Schultheis M., Katz D., Gmez A. (2016) A & A, 589, A66
Ibata R. et al. (2017) eprint arXiv:1708.06356
Kordopatis G. et al. (2015) A & A, 582, A122
Lagarde N., Robin A.C., Reylé C., and Nasello G. (2017) A&A, 601, A27, 8
Lagarde N. et al (2012) A&A, 543, A108, 14
Pinsonneault M.H. et al (2014) ApJS, 215, 2, 19, 23
Quinn P. J., Hernquist Lars, Fullagar D. P. (1993) ApJ, 403, 1, 74-93.
Robin A.C., Reylé C., Derrière S., Picaud S.(2003) A&A, 409, 523-540
Robin A.C., Reylé C., Fliri J., Czekaj M., Robert C., Martins A. (2014) A&A, 569, A13, 26
Sellwood J., Binney J. (2002) MNRAS, 336, 3, 785-796
Shadab, A et al. (2015) ApJS, 219, 1, 12, 27
Snaith O., Haywood M., Di Matteo P., Lehnert M. D., Combes F., Katz D., Gmez A., (2014), ApJL 781, 2, L31
Snaith O., Haywood M., Di Matteo P., Lehnert M. D., Combes F., Katz D., Gmez A. (2015),A & A, 578, A87
Valentini M. et al. (2016), AN, 337, 8-9, 970.

Session 08

Space missions with exobiology interest

SF2A 2017
C. Reylé, P. Di Matteo, F. Herpin, É. Lagadec, A. Lançon, Z. Meliani, F. Royer (eds)

MODELING OF EXOPLANETS INTERIORS IN THE FRAMEWORK OF FUTURE SPACE MISSIONS

B. Brugger[1], O. Mousis[1] and M. Deleuil[1]

Abstract. Probing the interior of exoplanets with known masses and radii is possible via the use of models of internal structure. Here we present a model able to handle various planetary compositions, from terrestrial bodies to ocean worlds or carbon-rich planets, and its application to the case of CoRoT-7b. Using the elemental abundances of an exoplanets host star, we significantly reduce the degeneracy limiting such models. This further constrains the type and state of material present at the surface, and helps estimating the composition of a secondary atmosphere that could form in these conditions through potential outgassing. Upcoming space missions dedicated to exoplanet characterization, such as PLATO, will provide accurate fundamental parameters of Earth-like planets orbiting in the habitable zone, for which our model is well adapted.

Keywords: Earth — planets and satellites: composition — planets and satellites: interiors — planets and satellites: individual (CoRoT-7b)

1 Introduction

Despite the huge diversity of detected exoplanets, in terms of orbital and physical properties, our knowledge regarding their composition remains limited. Overcoming this limitation is essential, namely to better understand the formation of the planetary systems we discover (but also our solar system), or to investigate the potential habitability of these extrasolar worlds. Beyond the simple approximation given by an exoplanet's mean density (inferred from its measured fundamental parameters), models of planetary interiors are able to probe the composition of such bodies, based on our knowledge of the interior of the Earth and other solar system bodies (Valencia et al. 2006; Sotin et al. 2007; Seager et al. 2007; Zeng & Seager 2008; Dorn et al. 2015). Such models are however inherently limited by the existence of degeneracies on the investigated compositions, as two planetary bodies of the same size and mass may have different compositions.

The interior model described and applied here aims at breaking this degeneracy by using additional parameters of the studied exoplanets. This model has been developed to handle solid planetary compositions, as all terrestrial planets of the solar system, with possible addition of water in solid and/or liquid phase (Brugger et al. 2017, *submitted*). By making the assumption that the bulk Fe/Si and Mg/Si ratios of a planet are similar to that of its host star, we are able to significantly reduce the degeneracy on the planet's composition, and in particular on the metallic core size. To illustrate this, we apply our model to the well-known Super-Earth CoRoT-7b. We do not investigate here the possibility that this planet is surrounded by a thick gaseous atmosphere.

2 Model and parameters

2.1 Planetary interiors model

Our approach is based on the work by Sotin et al. (2007): a planet in our model can be made from three main layers, namely a metallic core, a silicate mantle, and a hydrosphere. Following our knowledge about the Earth's interior, as well as other solar system bodies, the silicate mantle and the hydrosphere may be divided into two sublayers each. Therefore, we can simulate a planet made of up to five concentric and fully differentiated layers

[1] Aix Marseille Univ, CNRS, LAM, Laboratoire d'Astrophysique de Marseille, Marseille, France (e-mail: `bastien.brugger@lam.fr`)

(see Figure 1). The masses of the three main layers (in terms of fraction of the total planet mass) allow to set the composition of a planet, since the boundaries between two sublayers are directly computed by phase change laws of the corresponding material. By mass conservation, the core and water mass fractions only (hereafter CMF and WMF, respectively) allow to fix the composition. The compositional parameter space of a planet is then completely described by the variations of the CMF and WMF, which can be represented by a ternary diagram, as on Figure 2. Via the use of an equation of state adapted to high-pressures (the Vinet EoS), we are able to provide more accurate radius estimations compared to previous studies. Further details about our approach, as well as about other compositional parameters, can be found in Brugger et al. (2016) and Brugger et al. (2017, *submitted*).

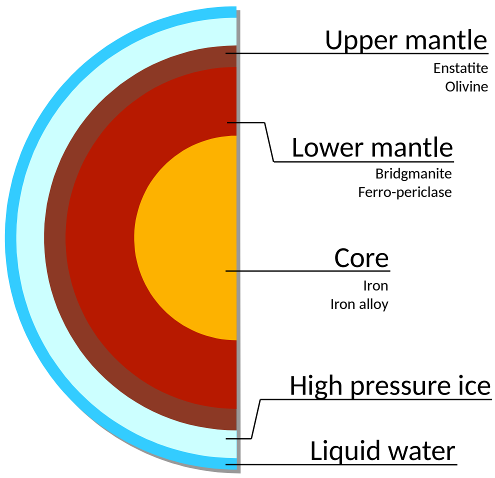

Fig. 1. Schematic view of the different concentric layers that compose our interior model: metallic core, lower and upper silicate mantles, high-pressure water ice, and liquid water. Depending on the mass of the water layers, the upper mantle or the high pressure ice layer may be absent.

2.2 *Physical limitations on planetary compositions*

Valencia et al. (2007) suggested two physical limitations to be placed on the composition of studied exoplanets, both taken from solar system formation conditions. From this, they exclude values of the CMF and WMF that are over 65% and 77%, respectively. In our work, we lower the limit on the WMF to 50%, based on the composition of large icy satellites in our solar system (Brugger et al. 2016). However these considerations are only valid if we assume that all studied exoplanets formed in the same conditions as in our solar system, which is an important limitation. Placing constraints on the composition of exoplanets from the chemical abundances of their host star is more adapted, since these abundances rule the composition of the protoplanetary disk from which these planets formed. Using a model of planet formation, Thiabaud et al. (2015) indeed showed that the Fe/Si and Mg/Si ratios of a star are retrieved in the planets that formed around it. With this assumption, and by incorporating the bulk Fe/Si ratio of a planet into our code, we show that this parameter can be linked to the CMF and WMF of the planet (see Figure 2). This significantly reduces the set of compositions compatible with the planet's fundamental parameters.

3 Results and discussion

CoRoT-7b is a well-known exoplanet, representative of the Super-Earth family, with a mass and radius of $3.72 \pm 0.42\ M_{\oplus}$ and $1.47 \pm 0.03\ R_{\oplus}$, respectively (Barros et al. 2014; Haywood et al. 2014). Its composition and interior have been studied by Valencia et al. (2010), who concluded that the planet was not compatible with an Earth-like composition, and that it should present a significant depletion in iron in order to remain rocky. Here, we apply our model to CoRoT-7b, with the use of the planet's Fe/Si ratio, estimated from the host-star abundances to be 0.826 ± 0.419 (Brugger et al. 2017, submitted). With these parameters, we investigate the composition of CoRoT-7b in the entire ternary diagram, assuming that the surface conditions of the planet are

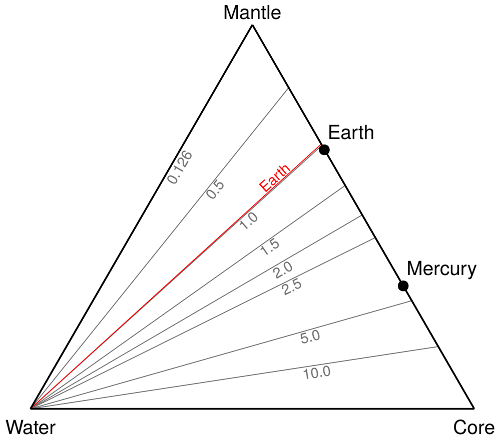

Fig. 2. Isolines of constant planetary Fe/Si ratio in the ternary diagram. The Earth's value is shown in red.

Earth-like. Our results are shown on Figure 3. From the mass and radius of CoRoT-7b, we constrain its CMF in the 0–50% range, showing that this data is compatible with an Earth-like composition (32.5% CMF). By incorporating the Fe/Si ratio of this planet, this range is significantly reduced, to 13–37%, which still includes an Earth-like composition. The WMF of CoRoT-7b, on the other hand, can be estimated to be 31% at maximum from the same data, and is not significantly modified by the incorporation of the Fe/Si ratio. This latter result is however strongly overestimated given the planet's high equilibrium temperature, since water on the surface of CoRoT-7b would rather be in the vapor (or supercritical) phase.

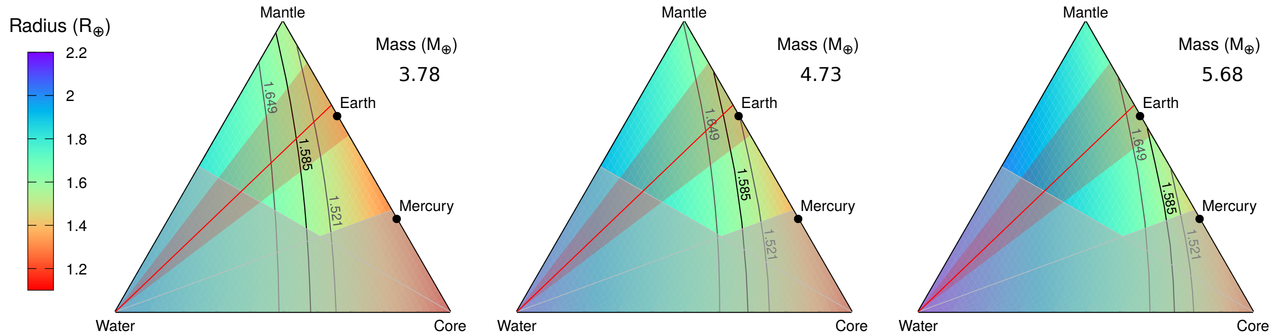

Fig. 3. Ternary diagrams displaying the investigated compositional parameter space of a cold water-rich CoRoT-7b for the minimum, central, and maximum masses inferred by Haywood et al. (2014), using 1σ uncertainties. Also shown are the isoradius curves denoting the planet radius measured by Barros et al. (2014) with the 1σ extreme values. Two areas of the diagrams are excluded from the study, based on assumptions on the solar system's present properties (Brugger et al. 2017, submitted). The Fe/Si ratio assumed for CoRoT-7b, with its associated uncertainties, delimit a line and an area represented in red.

We showed here that our model is able to constrain the compositional parameter space of a given exoplanet from its mass and radius measurements only, and that this space can be even more restrained if we use the bulk Fe/Si ratio of the planet (taken equal to the stellar value, following planet formation models). In the case of CoRoT-7b, we show in particular that this planet is compatible with an Earth-like composition, unlike in previous studies, which strengthens its Super-Earth status. Our model is not yet adapted to the case of hot water-rich exoplanets that orbit close to their star, even if it still can be used to derive the maximum water amount of the planet. However, in the future, space missions as PLATO will be dedicated to the search of Earth-like candidates orbiting within their host star's habitable zone, where water can be stable in the liquid phase. Our model is thus well prepared to the study of such planetary interiors.

The project leading to this publication has received funding from Excellence Initiative of Aix-Marseille University - A*MIDEX, a French "Investissements d'Avenir" program. O.M. and M. D. also acknowledge support from CNES.

References

Barros, S. C. C., Almenara, J. M., Deleuil, M., et al. 2014, A&A, 569, A74
Brugger, B., Mousis, O., Deleuil, M., & Deschamps, F. 2017, *Submitted to ApJ*
Brugger, B., Mousis, O., Deleuil, M., & Lunine, J. I. 2016, ApJ, 831, L16
Dorn, C., Khan, A., Heng, K., et al. 2015, A&A, 577, A83
Haywood, R. D., Collier Cameron, A., Queloz, D., et al. 2014, MNRAS, 443, 2517
Seager, S., Kuchner, M., Hier-Majumder, C. A., & Militzer, B. 2007, ApJ, 669, 1279
Sotin, C., Grasset, O., & Mocquet, A. 2007, Icarus, 191, 337
Thiabaud, A., Marboeuf, U., Alibert, Y., Leya, I., & Mezger, K. 2015, A&A, 574, A138
Valencia, D., Ikoma, M., Guillot, T., & Nettelmann, N. 2010, A&A, 516, A20
Valencia, D., O'Connell, R. J., & Sasselov, D. 2006, Icarus, 181, 545
Valencia, D., Sasselov, D. D., & O'Connell, R. J. 2007, ApJ, 665, 1413
Zeng, L. & Seager, S. 2008, PASP, 120, 983

SF2A 2017
C. Reylé, P. Di Matteo, F. Herpin, É. Lagadec, A. Lançon, Z. Meliani, F. Royer (eds)

HIGH-CONTRAST IMAGING WITH THE JWST-NIRSPEC INTEGRAL FIELD UNIT

M. Ygouf[1], C. Beichman,[1], K. Hodapp[2] and T. Roellig[3]

Abstract. With its integral field unit, the near-infrared spectrograph Nirspec on Jwst will allow to measure high-resolution spectra into the $3 - 5\,\mu$m range with an increased sensitivity over ground-based systems. This capability will considerably extend our knowledge of brown dwarfs and bright exoplanets at large separations from their host star. But because there is not any coronagraph on Nirspec , the performance in term of contrast at close separation will be extremely limited. In this communication, we explore possibilities to further push this limitation by exploiting the wavelength diversity offered by the spectral differential imaging strategy.

Keywords: Jwst , Nirspec , Ifu , Exoplanets, Brown Dwarfs, Direct Imaging, Post-Processing, Spectral Differential Imaging

1 Introduction

The integral field units (Ifu s) on board of Jwst (Gardner et al. 2009) offer a chance to measure high-resolution spectra of brown dwarfs and bright exoplanets in the near-Ir for Nirspec (Ferruit et al. 2012) and in the mid-Ir for Miri (Wright et al. 2008). To achieve this, there is a need for techniques of post-processing to subtract the starlight while preserving the flux from the companion. This can be done by implementing observing strategies that introduce diversity in the data.

The spectral differential imaging (Sdi) strategy exploit the wavelength diversity offered by an Ifu . Empirical methods of post-processing have been used to subtract the starlight from coronagraphic or non-coronagraphic images in the focal plane (Sparks & Ford 2002; Lafrenière et al. 2007; Soummer et al. 2012). These methods are entirely based on starlight calibration in the focal plane, which cause part or totality of the planet signal to be subtracted in the process. To avoid this, there have been some attempts to model the off-axis Psf , using forward modelling (Soummer et al. 2012; Pueyo et al. 2014). Although this approach is useful for characterization (Pueyo et al. 2014; Ygouf et al. 2015), it can only work with Sdi if there is a high correlation between the pattern of starlight residuals at different wavelengths. Even though the residual instrumental aberrations are responsible for these starlight residuals, none of these post-processing methods use a model of imaging that takes these aberrations as parameters. As a consequence, prior information inferred from our knowledge of the instrument can not be used as an input for post-processing.

An optimal post-processing technique would handle these limitations of the current techniques of post-processing. Ygouf et al. (2013) have developed the technique called Medusae (*Multispectral Exoplanet Detection Using Simultaneous Aberration Estimation*) in a Bayesian framework, based on an analytical model of multispectral coronagraphic imaging and an inversion algorithm, to estimate jointly the instrumental aberrations and the circumstellar scene in order to separate these two contributions (Ygouf et al. 2013; Ygouf 2013). The inversion algorithm is based on a maximum-a-posteriori estimator, which measures the discrepancy between the multispectral data from an Ifu and the imaging model. It is then possible to retrieve, from multispectral images, an estimation of the aberration map and of the position and flux of the companions at each wavelength and thus their spectra.

For the first time, we applied the Medusae technique on non-coronagraphic Jwst Nirspec Ifu images. In the following sections, we describe two Nircam Gto programs that will make use of the Nirspec Ifu

[1] IPAC, Caltech, 1200 E. California Blvd., Pasadena, CA 91125, USA
[2] Institute for Astronomy, University of Hawaii, 640 N. Aohoku Place, Hilo, HI 96720, USA
[3] NASA Ames Research Center, MS 245-6, Moffett Field, CA 94035-1000, USA

to further characterize known exoplanets and brown dwarfs with the Nirspec Ifu ; we present the Medusae technique before describing our simulated data; finally, we implement the technique on these simulated data to estimate jointly the instrumental aberrations and some injected point sources.

2 Direct Imaging of Exoplanet and Brown Dwarfs in the NIRCam GTO Program

The Nircam Gto team (Pi : Marcia Rieke) designed two programs to image directly exoplanet and brown dwarfs with the Nirspec Ifu :

- The *Spectroscopy of Young, Widely Separated Planets* led by Klaus Hodapp. The goal of this program is to understand the spectra of self-luminous, fairly young objects below the deuterium burning limit throughout their contraction and cooling.
- The *Y Dwarf Observations with* Jwst led by Tom Roellig. The goal of this program is to understand the nature of the coolest brown dwarfs - their formation, their atmospheres, including their composition, temperature, pressure structures, and the nature of any clouds that may be present.

The methodology for these two programs is to obtain Nirspec Ifu R=2700 spectra to allow direct imaging and spectroscopy. The use of Nirspec will thus extend the measurements into the $3-5\,\mu\mathrm{m}$ range with a substantial sensitivity advantage over competing ground-based systems. In the following, we apply for the first time the Medusae technique on non-coronagraphic images for the preparation of Gto -Nircam observations with Nirspec .

3 The MEDUSAE technique

Medusae was developed in the context of a coronagraphic instrument and is thus based on an analytical model of multispectral coronagraphic imaging (Ygouf et al. 2013). Here, in the context of the Nirspec Ifu , we slightly change the model to deal with non-coronagraphic images. We assume that, for an image at the wavelength λ, the direct model is the following sum of three terms, separating the contributions of the star, the circumstellar source and noise n_λ:

$$i_\lambda(\alpha) = f^*_\lambda \cdot h^{nc}_\lambda(\alpha) + [o_\lambda \star h^{nc}_\lambda](\alpha) + n_\lambda(\alpha), \tag{3.1}$$

where $i_\lambda(\alpha)$ is the data, f^*_λ is the star flux at wavelength lambda and $h^{nc}_\lambda(\alpha)$, the non-coronagraphic point spread function (Psf). The expression of the non-coronagraphic Psf is $h^{nc}_\lambda = A_n A^*_n$, with $A_n(\alpha) = \mathrm{TF}^{-1}\left[\mathcal{P}(\rho)\, e^{j\phi(\rho)}\right]$, $\mathcal{P}(\rho)$ the telescope pupil and the Opd map $\phi(\rho) = 2\pi\frac{\delta(\rho)}{\lambda}$. TF [.] denotes the Fourier Transform.

Following the Bayesian inverse problem approach, solving the inverse problem consists in finding the unknowns, firstly the object characteristics $o(\alpha,\lambda) = \{o_\lambda(\alpha)\}_\lambda$, secondly the parameters the Psf $h^{nc}_\lambda(\delta)$ (namely the Opd map) and $f^*(\lambda) = \{f^*_\lambda\}_\lambda$, which are the most likely given the data and our prior information about the unknowns. This boils down to minimizing the following criterion:

$$J(o, f^*, \delta) = \sum_\lambda \sum_\alpha \frac{1}{2\sigma^2_{n,\lambda}(\alpha)} \left| i_\lambda - f^*_\lambda \cdot h^{nc}_\lambda(\delta) - o_\lambda \star h^{nc}_\lambda(\delta) \right|^2 (\alpha) + R_o + R_{f^*} + R_\delta + \cdots. \tag{3.2}$$

This criterion is the sum of two terms: the data fidelity term, which measures the distance between the data and the imaging model, and a non-exhaustive list of regularization terms on our unknowns R_o, R_{f^*}, R_δ. The structure of the joint criterion of Eq. (3.2) prompted us to adopt an estimation of wavefront and object that alternates between estimation of the aberrations, assuming that the object is known (multispectral *phase retrieval*) and estimation of the object assuming that the aberrations are known (*multispectral deconvolution*). To minimize the criterion, we used the Variable Metric with Limited Memory and Bounds (VMLM-B) (Thiébaut 2002). More information about the regularization terms, constraints and minimization scheme can be found in Ygouf et al. (2013).

4 Simulations

Using the image formation model of equation (3.1), we simulate a data cube of 30 images typical of the Nirspec instrument. We choose pixel indicator functions as the basis for the phase rather than, e.g., a truncated basis

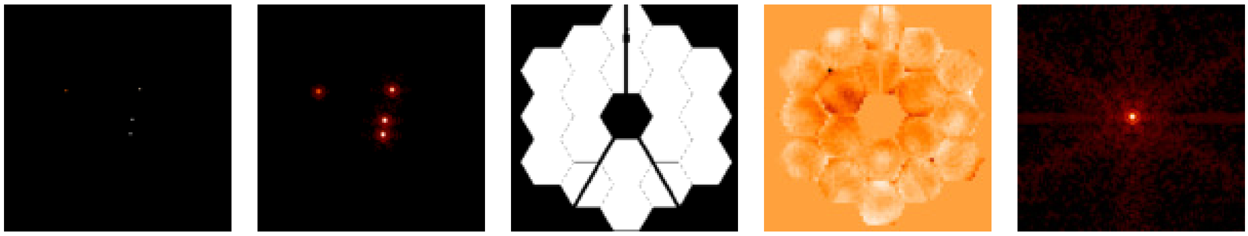

(a) Object map with four planets (b) Image of the object map in the focal plane (c) JWST pupil (d) Aberration map (e) Image of the NIRSPEC PSF

Fig. 1. Simulations of NIRSpec-like images at $\lambda = 3\,\mu$m. (a) Simulated object map and (b) associated image in the focal plane – the image in the focal plane is obtained by convolving the object map o_λ by the non-coronagraphic PSF h^{nc}_λ – (c) JWST pupil, (d) simulated aberrations and (e) associated PSF in the image focal plane.

of Zernike polynomials, in order to model and reconstruct phases with a high spatial frequency content. The hypothesis are typical of a NIRSPEC -like instrument: JWST pupil file (pupil_RevV.fits publicly available from the WEBBPSF package (Perrin et al. 2014)), OPD δ simulated with standard deviation of 125 nm (OPD file OPD_RevV_nirspec_125.fits publicly available from the WEBBPSF package (Perrin et al. 2014)), and a spectral range spanning from 3 to 5 µm. Photon noise is added to the data. We use 128×128 pixels to simulate our images, with an oversampling of 2 (0.05215 arcsec/pixel to be compared to 0.1 arcsec/pixel of the NIRSPEC detector). The number of unknowns to estimate for the aberration map is about 3×10^3. If we add the unknowns to estimate for the object map, which is 16×10^3, the total number of unknowns is about 2×10^4. Figure (1) shows the simulated object map (1(a)) and the associated image in the focal plane (1(b)). Figure 1(d) shows the simulated aberration map and the associated image of the speckle field in the focal plane (1(e)). Figure 2 shows the evolution of the NIRSPEC PSF with the wavelength. For an easier visualization, we represent the images in the focal plane and not the object map in the following.

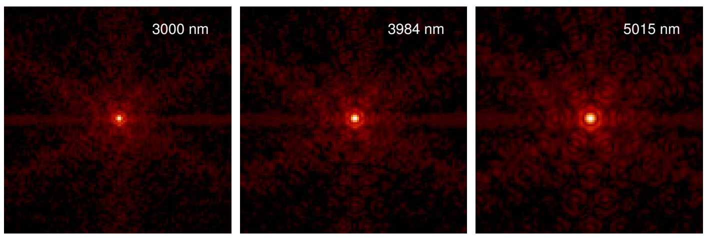

Fig. 2. Evolution of the NIRSpec-like PSF with the wavelength. Simulated images at 3, 4 and 5 µm. The two point sources that are closer to the star are completely buried in stellar halo. The two other point sources are barely visible. The dynamic range is adapted to the visualization.

5 Post-processing: preliminary results

From the simulated data cube we jointly estimate the OPD and the object maps using the MEDUSAE algorithm that we modified to deal with non-coronagraphic images. The results can be seen on Figure 3. For both the object and the OPD maps we compare the estimated map to the simulated one. The star halo is almost completely subtracted. Some starlight residuals can be observed. The four point sources are recovered but there is a non-negligible error on the object estimation. This error is all the more important as the point source is close to the star, which is a completely normal behavior of the algorithm. The global structure of the OPD is relatively well estimated. The residuals mostly comes from the error in planet flux estimation (sinusoidal structure). However, a few structures are not perfectly recovered. In Fig. 4 we plotted the contrast after post-processing with MEDUSAE . Contrast gain is comprised between 20 and 300 for separations spanning from 0.5 to 3".

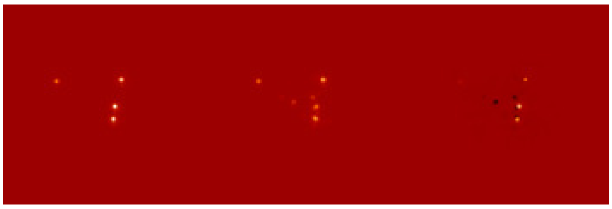

(a) Object estimation

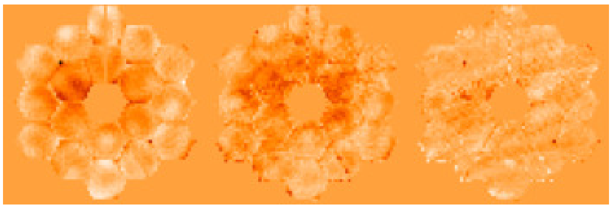

(b) OPD estimation

Fig. 3. Estimation of object and OPD maps (a) [Left] Simulated image in the focal plane of the object map, [center] estimated image and [right] difference between the simulated and estimated images at $\lambda = 3\,\mu m$. (b) [Left] Simulated OPD map, [center] estimated OPD map and [right] difference between the simulated and estimated images. The dynamic range is adapted to the visualization.

6 Conclusions and perspectives

We applied for the first time the MEDUSAE technique on non-coronagraphic images for the preparation of GTO - NIRCAM observations with NIRSPEC . The preliminary results are promising, demonstrating contrast gains up to 300 after post-processing as well as the ability to reconstruct the instrumental aberration map. The aberration map reconstruction shows the potential of the MEDUSAE technique for wavefront sensing and control of JWST . In future tests, we will consider simulation hypothesis that closer reflect the observing strategy we plan to implement in our NIRCAM -GTO programs and we will compare the performance of MEDUSAE to other observing strategies and corresponding post-processing techniques.

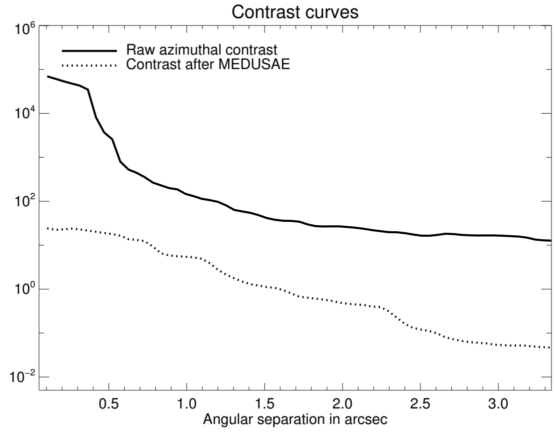

Fig. 4. Contrast curves before and after post-processing. Contrast curves are plotted by measuring the azimuthal 1-σ level of residual starlight.

This research has made use of the WEBBPSF python package (Perrin et al. 2014). Most of the figures in this work were created using Matplotlib, a Python graphics environment (Hunter 2007).

References

Ferruit, P., Bagnasco, G., Barho, R., et al. 2012, in SPIE Astronomical Telescopes+ Instrumentation, International Society for Optics and Photonics, 84422O–84422O

Gardner, J. P., Mather, J. C., Clampin, M., et al. 2009, Astrophysics in the Next Decade, 1

Hunter, J. D. 2007, Computing In Science & Engineering, 9, 90

Lafrenière, D., Marois, C., Doyon, R., Nadeau, D., & Artigau, É. 2007, Astrophys. J., 660, 770

Perrin, M. D., Sivaramakrishnan, A., Lajoie, C.-P., et al. 2014, in Space Telescopes and Instrumentation 2014: Optical, Infrared, and Millimeter Wave, Vol. 9143, International Society for Optics and Photonics, 91433X

Pueyo, L., Soummer, R., Hoffmann, J., et al. 2014, ArXiv e-prints

Soummer, R., Pueyo, L., & Larkin, J. 2012, Astrophys. J. Lett., 755, L28

Sparks, W. B. & Ford, H. C. 2002, Astrophys. J., 578, 543

Thiébaut, E. 2002, in Society of Photo-Optical Instrumentation Engineers (SPIE) Conference Series, Vol. 4847, Society of Photo-Optical Instrumentation Engineers (SPIE) Conference Series, ed. J.-L. Starck & F. D. Murtagh, 174–183

Wright, G., Reike, G., Barella, P., et al. 2008, in Space Telescopes and Instrumentation 2008: Optical, Infrared, and Millimeter, Vol. 7010, International Society for Optics and Photonics, 70100T

Ygouf, M. 2013, PhD thesis, Université de Grenoble

Ygouf, M., Mugnier, L. M., Mouillet, D., Fusco, T., & Beuzit, J.-L. 2013, Astronomy & Astrophysics, 551, A138

Ygouf, M., Mugnier, L. M., Mouillet, D., Fusco, T., & Beuzit, J.-L. 2013, Astron. Astrophys., 551, A138

Ygouf, M., Pueyo, L., Soummer, R., et al. 2015, in Soc. Photo-Opt. Instrum. Eng., Vol. 9605, Techniques and Instrumentation for Detection of Exoplanets VII, 96050S

Session 09

SPHERE: three years of operations at VLT

SF2A 2017
C. Reylé, P. Di Matteo, F. Herpin, É. Lagadec, A. Lançon, Z. Meliani, F. Royer (eds)

SHINE, THE SPHERE INFRARED SURVEY FOR EXOPLANETS

G. Chauvin[1,2], S. Desidera[3], A.-M. Lagrange[1], A. Vigan[4], M. Feldt[5], R. Gratton[2], M. Langlois[4,6], A. Cheetham[7], M. Bonnefoy[1], M. Meyer[8] and the SHINE team

Abstract. The SHINE survey for SPHERE High-contrast ImagiNg survey for Exoplanets, is a large near-infrared survey of 400-600 young, nearby stars and represents a significant component of the SPHERE consortium Guaranteed Time Observations consisting in 200 observing nights. The scientific goals are: i) to characterize known planetary systems (architecture, orbit, stability, luminosity, atmosphere); ii) to search for new planetary systems using SPHERE's unprecedented performance; and finally iii) to determine the occurrence and orbital and mass function properties of the wide-orbit, giant planet population as a function of the stellar host mass and age. Combined, the results will increase our understanding of planetary atmospheric physics and the processes of planetary formation and evolution.

Keywords: Imaging and spectroscopy - Planets: physical parameters, atmospheres and formation

1 Introduction

Our understanding of the origin and evolution of extrasolar planets has drastically transformed in the last decade. Current theories favor the formation of planets within a protoplanetary disk by accretion of solids, building up a 3 to 10 $M_\oplus$ core followed by rapid accumulation of gas, or by gravitational instability of the gas (Helled et al. 2014). The planets could either migrate toward or away from the star by disk-planet interactions (Kley & Nelson 2012) or by planet-planet interactions (Dawson & Murray-Clay 2013), which will alter the original semi-major axis distribution. A wide range of potential planet masses, sizes, locations and compositions results from this diverse set of physical processes. A major goal for exoplanetary science of the next decade is a better understanding of these mechanisms. In this context, the role of observations is crucial to provide constraints that will help to understand the diversity of exoplanetary properties. The main observables are the occurrence of exoplanets, including the physical and orbital characteristics (composition, mass, radius, luminosity, distribution of mass, period and eccentricity), as well as the properties of the planet themselves (luminosity, mass, effective temperature, composition...). The main statistical constraints on exoplanets originally came from the radial velocity and transit techniques. More than 3000 exoplanets have been now confirmed, featuring a broad range of physical (mass) and orbital (P, e) characteristics around different stellar hosts (Howard et al. 2010; Mayor et al. 2011; Burke et al. 2015). Despite the success of both techniques, the time spans explored limit the studies to the close ($\leq 5-6$ AU) exoplanets. Within the coming years, direct imaging represents the only viable technique distinct from microlensing for probing the existence of exoplanets and brown dwarf companions at large ($\geq 5-10$ AU) separations. This technique is also unique for the characterization of planetary atmospheres that are not strongly irradiated by the planetary host, as well as for the connection of the exoplanets with their

[1] Univ. Grenoble Alpes, CNRS, IPAG, F-38000 Grenoble, France
[2] Unidad Mixta Internacional Franco-Chilena de Astronomía, CNRS/INSU UMI 3386 and Departamento de Astronomía, Universidad de Chile, Casilla 36-D, Santiago, Chile
[3] INAF - Osservatorio Astronomico di Padova, Vicolo dell Osservatorio 5, 35122, Padova, Italy
[4] Aix Marseille Université, CNRS, LAM (Laboratoire d'Astrophysique de Marseille) UMR 7326, 13388 Marseille, France
[5] Max Planck Institute for Astronomy, Königstuhl 17, D-69117 Heidelberg, Germany
[6] CRAL, UMR 5574, CNRS, Universit de Lyon, Ecole Normale Suprieure de Lyon, 46 Alle d'Italie, F-69364 Lyon Cedex 07, France
[7] Geneva Observatory, University of Geneva, Chemin des Mailettes 51, 1290 Versoix, Switzerland
[8] Institute for Astronomy, ETH Zurich, Wolfgang-Pauli-Strasse 27, 8093 Zurich, Switzerland

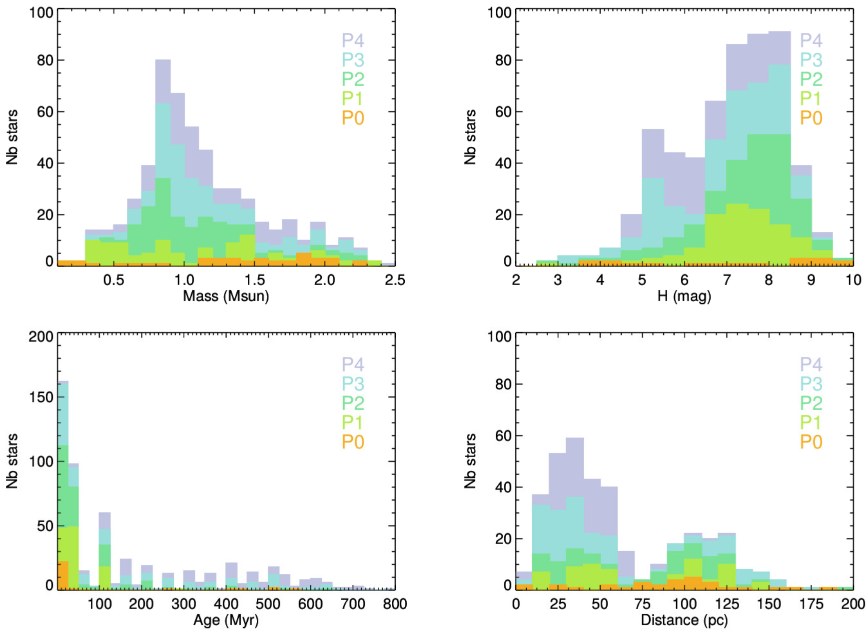

Fig. 1. Histogram of main properties (mass, age, distance and magnitude) of the SHINE target sample. Science priorities are reported with different color codes. P0 targets represent the top priority targets of the SHINE sample.

birth environment. In this context, the SpHere INfraed survey survey for Exoplanets (SHINE) is a major program of the SPHERE consortium Guaranteed Time Observations consisting in 200 observing nights spread over 5 years to conduct the largest near-infrared survey of 400-600 young, nearby stars. The science goals are to characterize known planetary systems (architecture, orbit, stability, luminosity, atmosphere), to search for new planetary ones, ultimately to determine the occurrence and orbital and mass function properties of the wide-orbit, giant planet population as a function of the stellar host mass and age. In Section 2, we describe the approach followed to build the SHINE target sample. In Section 3, are presented the observing strategy and the data reduction. In Section 4, we finally present early-scientific results illustrating the spectrophotometric and astrometric performances achieved.

2 Sample selection

The SHINE target list with flagged priorities has been selected from a target database of more than a thousand young, nearby stars catalogued with their most relevant stellar properties for the selection: coordinates, age, distance, spectral type, kinematics, activity and association membership. The final list was optimized by performing MonteCarlo simulations of planet detectability (Bonavita et al. 2012) for a variety of input planet populations, then ensuring the expectation of several detections and the potential for disentangling between different planet parameter distributions. As prerequesite, we considered stars with R-band magnitude limit set at $R \sim 12$ to ensure a good-XAO correction. Spectroscopic and close visual binaries (stellar companions within SPHERE field of view) are also excluded to have a sample suited for comparison of planet frequency as derived from RV surveys, which also typically excluded multiples. Members of nearby young groups (e.g, β Pic, Tuc-Hor, Columba etc.) represent a major source of targets. A sample of early-type stars from Sco-Cen groups is included, allowing the exploration of planet frequency on young moderately massive stars. Finally, a few individual targets which are outside the statistical sample as defined above were added to the GTO list for their special interest (signature in the disks suggesting the presence of planets, a couple of stars with RV planets potentially detectable with SPHERE if they are actually brown dwarfs companions, etc.). The main target properties (mass, age, distance, magnitude) are shown in Fig. 1.

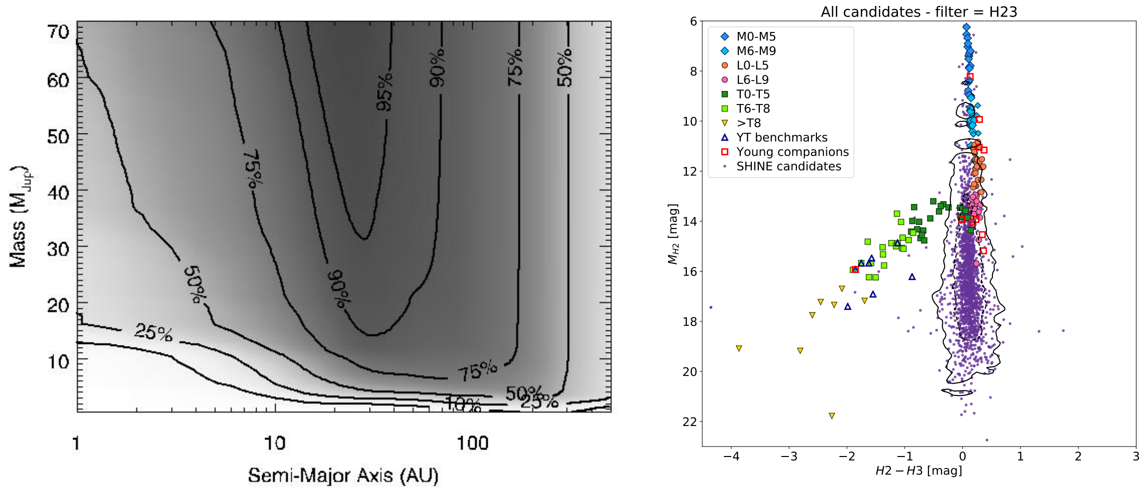

Fig. 2. *Left:* Detection probabilities given in planetary masses as a function of the semi-major axis for the first hundred stars oberved during SHINE. SHINE is sensitive in the planetary mass regime between 10 and 100 au. *Right:* Color-magnitude diagramme in H_2H_3 showing the cloud of SHINE candidates together with the predicted sequence of young late-M, L, T and Y brown dwarfs and giant planets.

3 Observations & Data reduction

The SPHERE planet-finder instrument installed at the VLT (Beuzit et al. 2008) is a highly specialized instrument, dedicated to high-contrast imaging and spectroscopy of young giant exoplanets. It is based on the SAXO extreme adaptive optics system (Fusco et al. 2006; Petit et al. 2014; Sauvage et al. 2010), which controls a 41×41 actuators deformable mirror, and 4 control loops (fast visible tip-tilt, high-orders, near-infrared differential tip-tilt and pupil stabilization). The common path optics employ several stress polished toric mirrors (Hugot et al. 2012) to transport the beam to the coronagraphs and scientific instruments. Several types of coronagraphic devices for stellar diffraction suppression are provided, including apodized pupil Lyot coronagraphs (Soummer 2005) and achromatic four-quadrants phase masks (Boccaletti et al. 2008). The instrument has three science subsystems: the infrared dual-band imager and spectrograph (IRDIS; Dohlen et al. 2008), an integral field spectrograph (IFS; Claudi et al. 2008) and the Zimpol rapid-switching imaging polarimeter (ZIMPOL; Thalmann et al. 2008).

Standard SHINE data are acquired in IRDIFS pupil-tracking mode with the 185 mas diameter apodized-Lyot coronograph (Carbillet et al. 2011; Guerri et al. 2011), using IRDIS in dual-band imaging mode with the H_2H_3 filters ($\lambda_{H_2} = 1.593\pm0.055\,\mu$m; $\lambda_{H_3} = 1.667\pm0.056\,\mu$m), and the IFS integral field spectrograph simultaneously in $Y-J$ ($0.95-1.35\,\mu$m, $R_\lambda = 54$) mode. This combination enables the possible use of angular differential and/or spectral imaging technics to improve the contrast perfomances at the sub-arcseconds level.

A uniform data processing of the whole dataset of the SHINE survey is already implemented within the SPHERE Data Centre (DC), hosted by IPAG, with contribution by members of the whole SPHERE Consortium, which have the possibility to remotely work on the data reduction and processing via the DC tools. During each GTO observing run, raw data are retrieved and properly archived at DC. The complete SHINE data reduction and analysis procedures are based on the combination of: i/ the SPHERE Data Reduction and Handling (DRH) automated pipeline Pavlov et al. (2008) to correct each datacube for bad pixels, dark current, flat field, sky background, frame recentering (and cross-talk and wavelength calibration in addition for IFS), and ii/ the use of dedicated post-processing procedures using the Specal pipeline (Galicher et al., in prep) ensuring the proper astrometric and photometric calibration of the reduced datacubes and the angular and spectral differential imaging processing with various algorithms, including TLOCI (Marois et al. 2014) and PCA (Soummer et al. 2012; Amara & Quanz 2012; Mesa et al. 2015), to optimally suppress the stellar right and detect and characterize the planetary signal. The final data products include reduced images of the IRDIS and IFS datacubes, positions, magnitudes and spectra of the detected point sources and circumstellar disks in the field of view, detection limits for faint companions and extended sources around each targets.

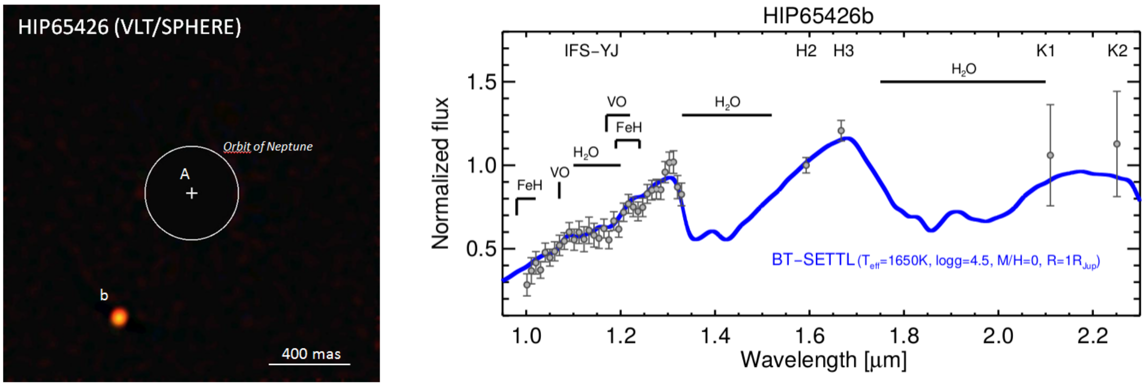

Fig. 3. *Left:* First planet discovery with SPHERE around the young star HIP 65426 (Chauvin et al. 2017). *Right:* SPHERE near-infrared spectrum of HIP 65426 b compared to BT-Settl atmospheric models for $T_{eff} = 1650\,K$, $log(g) = 4.5$ and solar-metallicity.

4 Scientific results

The performance of the instrument in terms of detectability of exoplanets, brown dwarfs and disks at very small separation fully agrees with expectations achieving 5σ detection limits of 15 mag at 300 mas. SHINE is particularly sensitive to giant planets between 10 and 100 au as shown with the survey mean detection probabilities in Fig 2 (*Left*). A specific focus has been dedicated to the characterization of several known systems at the beginning of the survey to highlight the SPHERE detection, astrometric and spectrophotmetric performances and its versatility. Among the systems characterized, we can list: the brown dwarf companions around GJ 758 (Vigan et al. 2016), PZ Tel (Maire et al. 2016), HD206893 (Delorme et al. 2017), GJ 504 (Bonnefoy et al., submitted), the giant planet 51 Eri b (Samland et al. 2017) or the multiple-planet system HR8799 (Zurlo et al. 2016; Bonnefoy et al. 2016) and the young Solar-Analogue HD 95086 (Chauvin et al., submitted). The first discovery of a warm, dusty Jovian planet with SPHERE at VLT in the course of SHINE has been in addition rcently announced (Chauvin et al. 2017) (see Fig. 3). To date, more than 1900 planetary candidates have been detected as illustrated by the color-magnitude diagramme of Fig. 2 (*Right*). Second-epoch observations are required to confirm the physical association of the most promising candidates to their central stars. While focused on detection of giant planets, SHINE program is also contributing significantly to the detection and characterization of circumstellar disks. Several disks were spatially resolved for the first time. They include the new disk discoveries around HD 106906 (Lagrange et al. 2016), RXJ1615.3-3255 (de Boer et al. 2016) or HIP 73145 (Feldt et al. 2017). Since the beginning of the SPHERE GTO operation in February 2015, 25 papers exploiting SHINE data have been accepted for publications in journals (Science, ApJ, MNRAS and A&A). A serie of three papers presenting the early-statistical analysis of the first 200 SHINE targets is foreseen for 2018, before the final analysis that will be carried out at the horizon 2020 when the survey will be completed.

We acknowledge financial support from the Programme National de Planétologie (PNP) and the Programme National de Physique Stellaire (PNPS) of CNRS-INSU. This work has also been supported by a grant from the French Labex OSUG@2020 (Investissements davenir ANR10 LABX56). The project is supported by CNRS, by the Agence Nationale de la Recherche (ANR-14-CE33-0018). This work has made use of the the SPHERE Data Centre, jointly operated by OSUG/IPAG (Grenoble), PYTHEAS/LAM/CESAM (Marseille), OCA/Lagrange (Nice) and Observtoire de Paris/LESIA (Paris). SPHERE also received funding from the European Commission Sixth and Seventh Framework Programmes as part of the Optical Infrared Coordination Network for Astronomy (OPTICON) under grant number RII3-Ct-2004-001566 for FP6 (20042008), grant number 226604 for FP7 (20092012) and grant number 312430 for FP7 (20132016). Part of this work has been carried out within the frame of the National Centre for Competence in Research PlanetS supported by the Swiss National Science Foundation (SNSF).

References

Amara, A. & Quanz, S. P. 2012, MNRAS, 427, 948

Beuzit, J.-L., Feldt, M., Dohlen, K., et al. 2008, in Proc. SPIE, Vol. 7014, Ground-based and Airborne Instrumentation for Astronomy II, 701418

Bonavita, M., Chauvin, G., Desidera, S., et al. 2012, A&A, 537, A67

Bonnefoy, M., Zurlo, A., Baudino, J. L., et al. 2016, A&A, 587, A58
Burke, C. J., Christiansen, J. L., Mullally, F., et al. 2015, ApJ, 809, 8
Carbillet, M., Bendjoya, P., Abe, L., et al. 2011, Experimental Astronomy, 30, 39
Chauvin, G., Desidera, S., Lagrange, A.-M., et al. 2017, A&A, 605, L9
Claudi, R. U., Turatto, M., Gratton, R. G., et al. 2008, in Proc. SPIE, Vol. 7014, Ground-based and Airborne Instrumentation for Astronomy II, 70143E
Dawson, R. I. & Murray-Clay, R. A. 2013, ApJ, 767, L24
de Boer, J., Salter, G., Benisty, M., et al. 2016, A&A, 595, A114
Delorme, P., Schmidt, T., Bonnefoy, M., et al. 2017, ArXiv e-prints
Dohlen, K., Langlois, M., Saisse, M., et al. 2008, in Proc. SPIE, Vol. 7014, Ground-based and Airborne Instrumentation for Astronomy II, 70143L
Feldt, M., Olofsson, J., Boccaletti, A., et al. 2017, A&A, 601, A7
Fusco, T., Rousset, G., Sauvage, J.-F., et al. 2006, Optics Express, 14, 7515
Guerri, G., Daban, J.-B., Robbe-Dubois, S., et al. 2011, Experimental Astronomy, 30, 59
Helled, R., Bodenheimer, P., Podolak, M., et al. 2014, Protostars and Planets VI, 643
Howard, A. W., Marcy, G. W., Johnson, J. A., et al. 2010, Science, 330, 653
Hugot, E., Ferrari, M., El Hadi, K., et al. 2012, A&A, 538, A139
Kley, W. & Nelson, R. P. 2012, ARA&A, 50, 211
Lagrange, A.-M., Langlois, M., Gratton, R., et al. 2016, A&A, 586, L8
Maire, A.-L., Bonnefoy, M., Ginski, C., et al. 2016, A&A, 587, A56
Marois, C., Correia, C., Véran, J.-P., & Currie, T. 2014, in IAU Symposium, Vol. 299, Exploring the Formation and Evolution of Planetary Systems, ed. M. Booth, B. C. Matthews, & J. R. Graham, 48–49
Mayor, M., Marmier, M., Lovis, C., et al. 2011, ArXiv e-prints
Mesa, D., Gratton, R., Zurlo, A., et al. 2015, A&A, 576, A121
Pavlov, A., Möller-Nilsson, O., Feldt, M., et al. 2008, in Proc. SPIE, Vol. 7019, Advanced Software and Control for Astronomy II, 701939
Petit, C., Sauvage, J.-F., Fusco, T., et al. 2014, in Proc. SPIE, Vol. 9148, Adaptive Optics Systems IV, 91480O
Samland, M., Mollière, P., Bonnefoy, M., et al. 2017, A&A, 603, A57
Sauvage, J.-F., Fusco, T., Petit, C., et al. 2010, in Proc. SPIE, Vol. 7736, Adaptive Optics Systems II, 77360F
Soummer, R., Pueyo, L., & Larkin, J. 2012, ApJ, 755, L28
Thalmann, C., Schmid, H. M., Boccaletti, A., et al. 2008, in Proc. SPIE, Vol. 7014, Ground-based and Airborne Instrumentation for Astronomy II, 70143F
Vigan, A., Bonnefoy, M., Ginski, C., et al. 2016, A&A, 587, A55
Zurlo, A., Vigan, A., Galicher, R., et al. 2016, A&A, 587, A57

SF2A 2017
C. Reylé, P. Di Matteo, F. Herpin, É. Lagadec, A. Lançon, Z. Meliani, F. Royer (eds)

,

THE SYSTEM OF HD169142 SEEN BY SPHERE/VLT

R. Ligi[1], A. Vigan[1], R. Gratton[2], J. de Boer[3], M. Benisty[4], A. Boccaletti[5], S. P. Quanz[6], M. Meyer[6 7], C. Ginski[3], E. Sissa[2], C. Gry[1], T. Henning[8] and SPHERE GTO

Abstract. Young stellar objects are perfect targets to unveil the mechanisms of planetary formation. We present new observations of HD169142, a young Herbig Ae star surrounded by a succession of rings. Interestingly, several previous direct imaging observations showed two point-like structures that were interpreted as substellar companions, one of 28 to 80 M_{Jup} at a separation of 110-156 mas, and the other of 8-15 M_{Jup} at 180 mas from the star. We used the high-contrast capabilities of SPHERE/VLT to investigate the nature of these detected companions. Our new observations reveal a bright ring at 180-200 mas, that is confirmed by polarised images. We also show that the companion detected at 180 mas is actually a part of this ring and follows the disk in a Keplerian movement. Finally, we marginally detect a structure at 93 mas from the star that could also correspond to an undiscovered ring in the innermost part of the system.

Keywords: Stars: individual: HD169142, Planets and satellites: detection and formation, Techniques: high angular resolution, Protoplanetary disc

1 Introduction: a complex disc structure

Young stellar objects are adequate laboratories to study planetary formation processes. In particular, transitional discs are interesting because they constitute the intermediate step between gas-rich protoplanetary discs and dusty debris discs. HD169142 is a Herbig Ae star surrounded by a nearly face-on pre-transitional disc. A succession of rings have been detected in this disc with polarimetric observations with NaCo (Quanz et al. 2013), later confirmed by Monnier et al. (2017) with GPI: a ring stands at 20 au*, followed by an annular gap at 32-56 au, the surface brightness smoothly decreasing after 66 au. More interestingly, Biller et al. (2014) detected with NaCo in the L' band a point-like structure of Δmag=6.4±0.2 at a positional angle (PA) of 0±14° and a separation ρ=110±30 mas, that could correspond to a 60-80 M_{Jup} substellar companion. In turn, Reggiani et al. (2014) discovered with the same instrument an emission source of Δmag=6.5±0.5 at ρ=156±32 mas and PA=7.4±1.3°, compatible with a 28-32 M_{Jup} companion. However, none of these detections were confirmed by/in follow-up observations. Biller et al. (2014) detected another point-like structure around HD169142 using the MagAO/MCT in 2013. It is located at ρ=180 mas and PA=33°, and would correspond to a 8-15 M_{Jup} substellar companion, although it was not initially detected in the L' band with NaCo.

We tried to investigate the nature of these point-like detections using SPHERE/VLT instrument. SPHERE has primarily been designed to image and characterise exoplanets, but it is also a powerful instrument for probing the dusty surface of protoplanetary discs. These new observations aim at bringing light to the complex disc structure of HD169142, and are fully described in Ligi et al. (2018).

[1] Aix Marseille Univ, CNRS, LAM, Laboratoire d'Astrophysique de Marseille, Marseille, France
[2] INAF – Osservatorio Astronomico di Padova, Vicolo dell'Osservatorio 5, I-35122, Padova, Italy
[3] Leiden Observatory, Leiden University, PO Box 9513, 2300 RA Leiden, The Netherlands
[4] Univ. Grenoble Alpes, CNRS, IPAG, 38000 Grenoble, France
[5] LESIA, Observatoire de Paris, PSL Research University, CNRS, Sorbonne Universités, UPMC Univ. Paris 06, Univ. Paris Diderot, Sorbonne Paris Cité
[6] Institute for Astronomy, ETH Zurich, Wolfgang-Pauli-Strasse 27, 8093 Zurich, Switzerland
[7] Department of Astronomy, University of Michigan, 1085 S. University Ave, Ann Arbor, MI 48109-1107, USA
[8] Max Planck Institute for Astronomy, Königstuhl 17, D-69117 Heidelberg, Germany
*the separations in mas have been converted to au using the Gaia distance, 117 pc (Gaia Collaboration 2016).

Table 1. Observing log of SPHERE SHINE data for HD169142. A more detailed table is given in Ligi et al. (2018).

UT Date	MJD [day]	Coro-nagraph	Instr. & Band	Exposure time [s]	Field rotation [deg]	Mean seeing ["]
2015-06-07	57180.17	Y	IFS YJ IRDIS $H2H3$	91.7 102.4	45.82	1.57
2015-06-28	57201.12	Y	IFS YJH IRDIS $K1K2$	69.3 85.33	36.42	1.00
2016-04-21	57499.34	Y	IFS YJ IRDIS $H2H3$	82.1 90.67	145.0	1.88
2016-06-27	57566.15	N	IFS YJH IRDIS $K1K2$	64.8 64.22	149.9	0.67
2017-04-30	57873.30	N	IFS YJH IRDIS $K1K2$	61.2 78.10	98.82	0.62

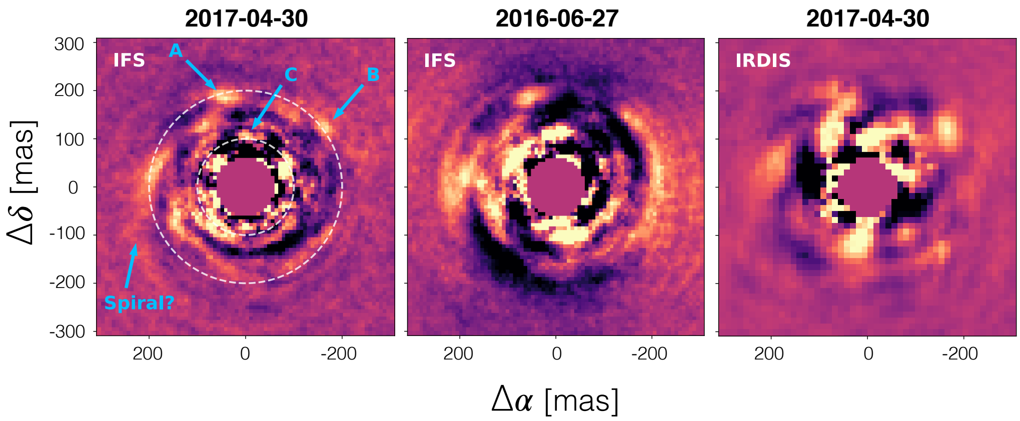

Fig. 1. Results of the PCA analysis in the YJ (left), H (middle) and K (right) bands. For the IFS and IRDIS data, 50 modes were subtracted. The bright structures which we are particularly interested in are indicated with the blue arrows. North is up and East is left.

2 SPHERE/VLT observations and data analysis

2.1 Observations

We performed observations of HD169142 from 2015 to 2017 using SPHERE/VLT with IRDIS and IFS instruments in pupil-stabilised mode in order to enable angular differential imaging (ADI, Marois et al. 2006). These observations were part of the GTO program aimed at detecting and characterising exoplanets using the direct imaging technique. The observations made use of either the `IRDIS` or the `IRDIS_EXT` modes, both with the dual-band imaging mode. For the first observations, a coronagraph was used but not for the two recent ones, in order to image the very inner part of the system of HD169142. A summary of the observations is given in Tab. 1. The data reductions were made using several pipelines in order to check the consistency of the results. We used the LAM-ADI pipeline (Vigan et al. 2015), the SPHERE Data Center pipeline, the `PYPOINT` pipeline (Amara & Quanz 2012) for the IRDIS data only, and the pipeline described in Mesa et al. (2015) (ASDI-PCA algorithm) for the IFS data only.

2.2 Data analysis: PCA and RDI reductions

We analysed the data using the Principal Component Analysis (PCA) and the Reference Differential Imaging (RDI). The first method is based on the formalism described by Soummer et al. (2012). The modes are calculated over the full sequence at separations up to 500 mas, and are subtracted to the total number of modes. The images are then rotated to a common orientation and averaged. The RDI method (Soummer et al. 2014) consists in subtracting one or several reference images to the target image. This allows to subtract speckle patterns

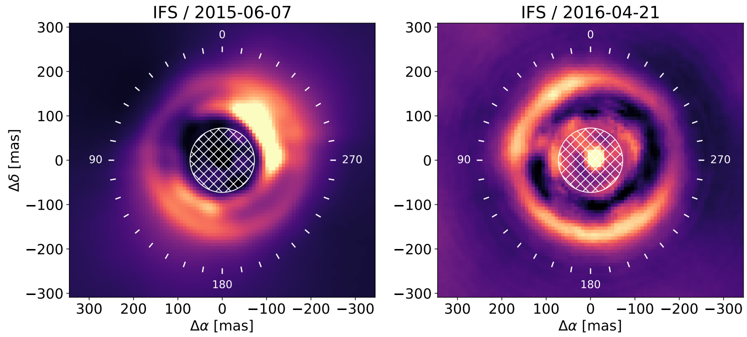

Fig. 2. Results of the RDI analysis of the IFS data. We clearly see en inhomogeneous bright ring at ∼180 mas, and possibly another inner ring. North is up and East is left.

while limiting the self-subtraction effects usually affecting ADI data, in particular for extended structures like discs (e.g. Milli et al. 2012).

With the PCA reduction (Fig. 1), point-like (in particular in the YJ and K bands) and extended (especially in the H band) bright structures appear at 180-200 mas, particularly at PA=20° (structure A), 90° and 310° (structure B). Other structures appear at ∼150 mas (PA=320°) and 100 mas (PA=355°, structure C). In the YJ band, we also see an arm-like structure that looks like a faint spiral in the IFS data. Structures A, B and C are detected at positions close to previous detections of point-like structures (see Sec. 1). We thus try to investigate if the previous and our detections are the same objects.

The RDI reduction (Fig. 2) shows a possible double-ring structure, with one located at ∼180 mas and the other one at ∼100 mas separation. The ring at 180 mas has an inhomogeneous brightness: it is darker at PA∼20°, while several brightness enhancements are visible in the north-west and south-west directions. The inner ring also is homogeneous, with a brighter region in the north-west direction. However, this ring is not detected in each reduction.

3 An inhomogeneous ring at 180 mas

3.1 Simulationof cADI reduction with PDI data

Observations of Polarimetric Differential Imaging (PDI) data from 2015 show a bright inhomogeneous ring at ∼180 mas (Fig. 3; see Pohl et al. 2017, for a complete analysis of these data), that is very similar to our detection. Brightness enhancements are particularly obvious at 20°, 90°, 180°, and at a lesser extent at 310°. Interestingly, these are the locations were we find regions of enhanced brightness structures in our IRDIFS PCA images. We also clearly see a cavity inside the ring thanks to the small coronagraph used. We thus try to understand if there is a link between this ring, in one hand, and the point-like detections from our IRDIFS data and the previous NaCo detections, in another hand.

We perform a simulation of ADI reduction using the IRDIS PDI intensity image. First, we create a copy of 1709 images[†] of the PDI image, with each of the images being rotated to match the pupil offset rotation and the PA of the observations. We apply the classical ADI (cADI) reduction to these images, and rotate them back to a common orientation and mean-combine them. We see a strong correlation between the main structures seen in the IRDIFS images using PCA, and the result of this simulation, where the shapes of the features at 20° and 90° are almost identical to those in the IFS image. The same bright spot at a PA of 310° is also clearly visible.

This result shows that the main structures in the IRDIFS reductions and in the simulation have been spatially filtered by the ADI processing. This effect has already been encountered in the study of several objects (HD100456, T Cha, e.g.), and studied by Milli et al. (2012) who show that ADI has a strong impact on the flux and morphology of discs, up to the point of creating artificial features. Moreover, planets are not supposed to emit polarised light, in particular when embedded in a disc because their emission would be too low (Berdyugina et al. 2008, 2011). The consistency between the ring seen in polarized light and our non-

[†]which corresponds to the number of frames after selection using the LAM-ADI pipeline.

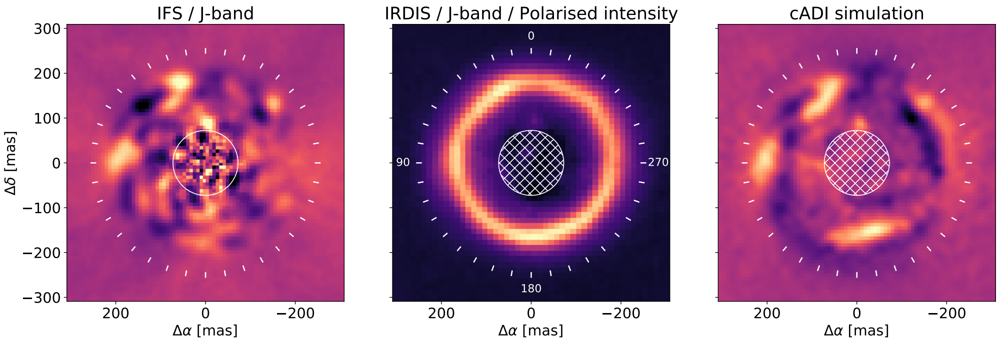

Fig. 3. Left: IFS image in the J band with 50 PCA modes subtracted. Middle: IRDIS PDI polarised intensity image in the J band, which shows a bright irregular ring. Right: Result of a cADI simulation using the polarised intensity image as input. The circular grid at the centre represents the centre star covered by coronagraphic mask in the PDI data. North is up and east is left. See Ligi et al. (2018) for details.

polarised ring indicates that we are observing bright structure tracing a ring and not substellar companions as first suggested by Biller et al. (2014) and Reggiani et al. (2014).

3.2 Keplerian anaysis

To confirm ou statement, we analyse the positions of structures A and B according to the observing period. The object detected by Biller et al. (2014) was at PA=33° and ρ=180 mas. Considering the stellar distance (117 pc, Gaia Collaboration 2016), mass (1.65 $M_\odot$ Blondel & Djie 2006) and inclination of the disc (13±1°, Panić et al. 2008), this object should have an orbital period of 78.5 years if in the disc plane. It should have moved of 13.7° from 2013 June to 2016 June which would bring it to PA=19.3° with a clockwise motion, that is, at a position similar to structure A. Besides, the position of structures A and B as a function of the MJD is consistent with a Keplerian motion in a clockwise direction, while the separation to the parent star remains constant. Thus, the blobs trace the bright ring in the disc, and they rotate in a clockwise direction with a Keplerian velocity. Combining our result with ALMA data (Fedele et al. 2017), we see that the northern part of the disc is moving faster toward us while the southern part is moving slower, with the western side closer to the observer.

3.3 Origins of the blobs

The nature of the detected blobs remains to be investigated. However, two hypothesis seem compatible with our observations. The first possibility invokes intrinsic disc variations in density and temperature. The dust concentration might trace the maximum density in the gas profile, that could trigger the formation of vortices by the Rossby wave instability. Since these vortices could be favourable places to initiate planet formation (Barge & Sommeria 1995), HD169142 could be the site of on-going planet formation at an earlier stage than previously expected. However, SPHERE images only show the surface of discs, thus we cannot confirm that our blobs have the spatial extend of vortices. Moreover, ALMA data, that trace the mid-plane layer of the disc, would not be able to resolve the structures we detect at this scale.

The second hypothesis concerns illumination variations because of azimuthally asymmetric optical depth variations through an inner disc closer to the star. Pohl et al. (2017) found azimuthal variations of 25% at 180 mas that could be caused by such effects. Moreover, the inner disc at ~0.3 present a variable SED. However, this hypothesis would be difficult to prove since the Keplerian movement that we found is not consistent with an origin from the inner structure of the disc.

4 A point-like structure at 100 mas?

Another structure in the disc draws attention: structure C, located at PA≈ 4° and ρ=105±6 mas. Indeed, its locations is close to that of the object detected by Biller et al. (2014) and is slightly offset but consistent with that of the object detected by Reggiani et al. (2014). While our detection seems robust when using the ASDI-PCA algorithm and the LAM-ADI pipeline, it is only marginally detected using the `PYNPOINT` pipeline.

Structure C appears quite extended in the H and K bands, whereas it appears point-like in the NaCo images. It also is detected in the PDI images, which means that it is light scattered by dust rather than emission from a planet photosphere. When considering the effect of a cADI reduction to a disc (see Sec. 3.1), we can consider that our detection is actually a yet undiscovered ring whose azimuthal component has been spatially filtered. The RDI images seem consistent with this assumption, althought we cannot verify it. Additional observations in polarised light without a coronagraph would bring a precious assess to understand this structure.

5 Conclusion

We used the SPHERE/VLT instrument to investigate the innermost parts of the system of HD169142. We found several interesting results:

- we detected several blobs at 180-200 mas separation from the star using the PCA algorithm. Comparing these detections to RDI and PDI images, that both show a bright ring at 180 mas, we find that these blobs are part of this ring. It is confirmed by the fact that we detect polarised (PDI) and scattered (IRDIFS) light from the dust at the surface of the disc, which is more compatible to disc structure than to planetary companions in formation. These blobs could be precursors of Rossby vortices, or (even if less plausible), the results of illumination variations from an inner disc.
- Analysing the movement of several blobs (structures A and B), we show that they follow a Keplerian motion, and thus trace the bright ring in the disc. Combining this result with ALMA data results leads to a better comprehension of its position, that is, the western-side is closer to us and the northern part is moving faster toward us.
- We also marginally detect a bright structure at PA$\approx$ 4° and ρ=105$\pm$6 mas, which is also visible in the polarised data. This structure could be a part of a yet undetected disc, that would have been filtered out by the ADI reduction.

Additional observations of HD169142 would certainly help better understanding the system of HD169142.

R. L. thanks CNES for financial support through its post-doctoral programme. The authors thank the ESO Paranal Staff for support for conducting the observations.

References

Amara, A. & Quanz, S. P. 2012, MNRAS, 427, 948
Barge, P. & Sommeria, J. 1995, A&A, 295, L1
Berdyugina, S. V., Berdyugin, A. V., Fluri, D. M., & Piirola, V. 2008, ApJ, 673, L83
Berdyugina, S. V., Berdyugin, A. V., Fluri, D. M., & Piirola, V. 2011, ApJ, 728, L6
Biller, B. A., Males, J., Rodigas, T., et al. 2014, ApJ, 792, L22
Blondel, P. F. C. & Djie, H. R. E. T. A. 2006, A&A, 456, 1045
Fedele, D., Carney, M., Hogerheijde, M. R., et al. 2017, A&A, 600, A72
Gaia Collaboration. 2016, VizieR Online Data Catalog, 1337
Ligi, R., Vigan, A., Gratton, R., et al. 2018, MNRAS, 473, 1774
Marois, C., Lafrenière, D., Doyon, R., Macintosh, B., & Nadeau, D. 2006, ApJ, 641, 556
Mesa, D., Gratton, R., Zurlo, A., et al. 2015, A&A, 576, A121
Milli, J., Mouillet, D., Lagrange, A.-M., et al. 2012, A&A, 545, A111
Monnier, J. D., Harries, T. J., Aarnio, A., et al. 2017, ApJ, 838, 20
Panić, O., Hogerheijde, M. R., Wilner, D., & Qi, C. 2008, A&A, 491, 219
Pohl, A., Benisty, M., Pinilla, P., et al. 2017, ApJ, 850, 52
Quanz, S. P., Avenhaus, H., Buenzli, E., et al. 2013, ApJ, 766, L2
Reggiani, M., Quanz, S. P., Meyer, M. R., et al. 2014, ApJ, 792, L23
Soummer, R., Perrin, M. D., Pueyo, L., et al. 2014, ApJ, 786, L23
Soummer, R., Pueyo, L., & Larkin, J. 2012, ApJ, 755, L28
Vigan, A., Gry, C., Salter, G., et al. 2015, MNRAS, 454, 129

SF2A 2017
C. Reylé, P. Di Matteo, F. Herpin, É. Lagadec, A. Lançon, Z. Meliani, F. Royer (eds)

CHARACTERISING EXOPLANET ATMOSPHERES WITH SPHERE: THE HR 8799 SYSTEM WITH EXO-REM AND NEMESIS

J.-L. Baudino[1], M. Bonnefoy[2], A. Vigan[3] and P.J. Irwin[1,]

Abstract. The characterisation of the exoplanets evolved recently thanks to the beginning of the second generation of direct imaging instruments, especially with SPHERE. The resolution and wavelength range available currently give access to an increase of accuracy and on the number of physical parameters that can be constrain.

One of the first target of SPHERE was the HR 8799 system. The four planets was characterised using four different forward models including *Exo-REM*. We complete this paper buy using *NEMESIS*, a retrieval code.

Keywords: planets and satellites: atmospheres, planets and satellites: gaseous planets, radiative transfer

1 Introduction

In this presentation we characterise the planets of the HR 8799 system, using the data coming from Zurlo et al. (2016). We constrained these observations with one atmospheric forward model *Exo-REM* and one retrieval code *NEMESIS*.

The Exoplanet Radiative-convective Equilibrium Model (*Exo-REM,* Baudino et al. 2015) is an atmospheric model computing the radiative-convective equilibrium taking into-account equilibrium or non-equilibrium chemistry (parametrised by the eddy coefficient K_{zz}). The model uses 10 molecular and atomic absorbers (H_2O, CH_4, NH_3, CO, CO_2, TiO, VO, PH_3, Na, K) and H_2-H_2, H_2-He CIA. *Exo-REM* takes also into-account cloud absorption of Fe and Mg_2SiO_4 (with some recent update, see also Benjamin Charnay presentation).

This model computes the atmospheric structure (abundance and temperature profiles) and the emission spectrum of a planet.

The Non-linear optimal Estimator for MultivariatE spectral analySIS (*NEMESIS,* Irwin et al. 2008) is a retrieval code using the radiative transfer code Radtrans. This code directly retrieves what is the best combination of parameters to reproduce the observations without physical constrain (no equilibrium, chemistry ...).

First, we compare models generated by Exo-REM with the observations. Then we define the priors of NEMESIS using the results of Exo-REM. Finally, we apply NEMESIS retrieval on the data.

2 Characterising

The two externals planets of the system (b and c) are outside the field of view of the spectroscopic mode of SPHERE (IFS). So the data are restrained to five photometric bands J, H2, H3, K1, K2 (of IRDIS). For the two internal planets (d and e), we use observations of the two instruments including IFS in mode Y-H.

[1] Department of Physics, University of Oxford, Oxford, UK
[2] Université Grenoble Alpes, IPAG, 38000 Grenoble, France
[3] Aix Marseille Univ, CNRS, LAM, Laboratoire d'Astrophysique de Marseille, 13000 Marseille, France

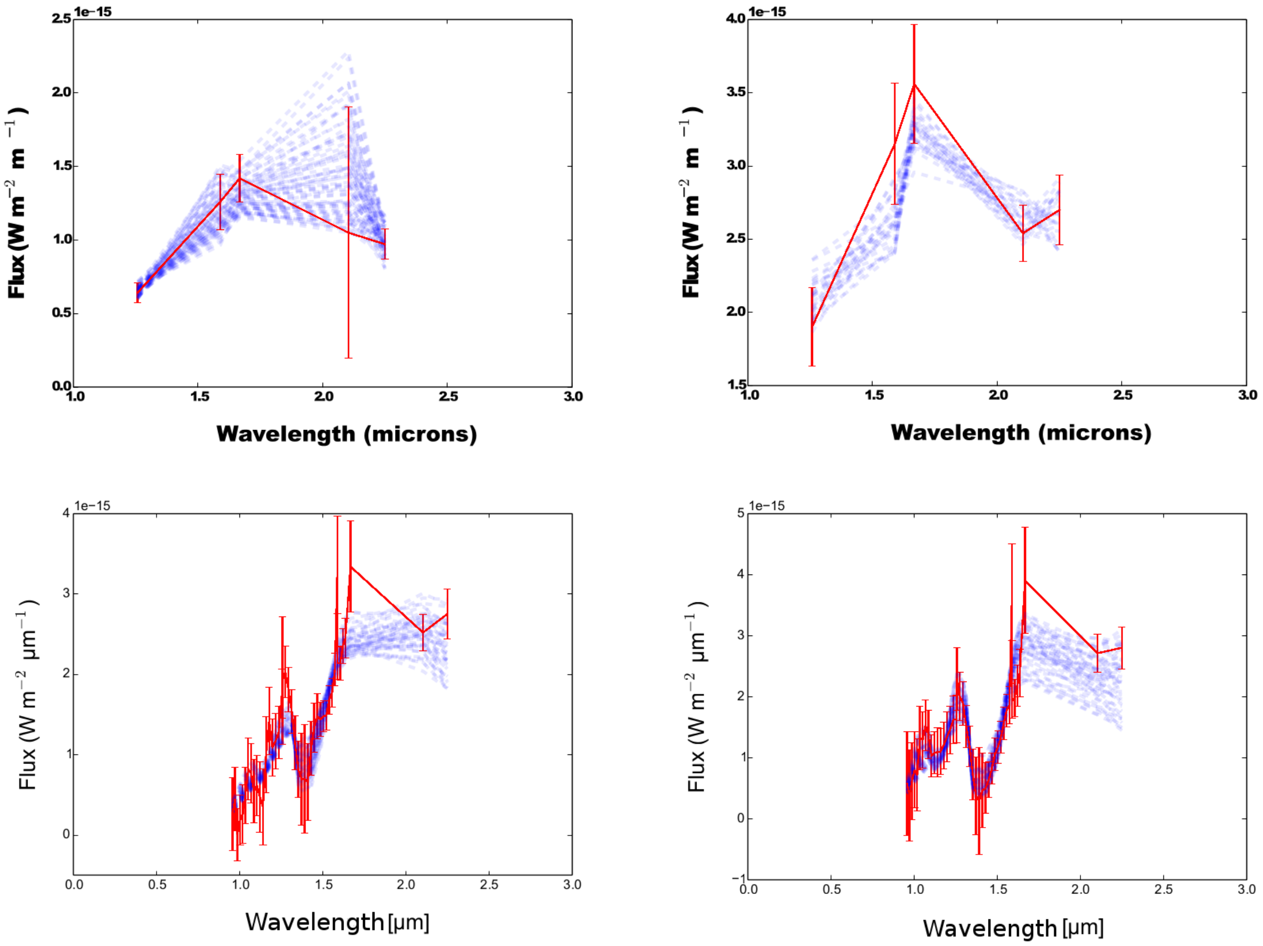

Fig. 1. Spectra corresponding to the best fits (< 2 sigma) using Exo-REM models (blue) compared to SPHERE observations (red) of the planets (from the left to the right and from the bottom to the top) HR 8799 b, c, d and e.

	b	c	d	e
$\log_{10}(g[cgs])$	4.8 ± 0.4	4.95 ± 0.45	5.0 ± 0.4	4.7 ± 0.7
$T_{\rm eff}$	975 ± 225 K	1125 ± 225 K	1125 ± 75 K	1200 ± 150 K

Table 1. Constrained surface gravity and effective temperature of HR 8799 b, c d and e with *Exo-REM* (2 σ).

2.1 Exo-REM

First we analyse the observations with *Exo-REM*, using the method described in Baudino et al. (2015), with grids exploring $T_{\rm eff}$ = 400-1850 K, and log10(g[cgs])= 2.5-5.4, at equilibrium of with non-equilibrium chemistry ($k_{\rm zz}$=10^8 cm^{2}s^{-1}), with clouds ($\tau_{\rm ref}$=0.5) or without, with a metallicity z=-0.4-1.5.

Fig. 1 shows the best result for each planet, the constrained parameters are listed in the Table 1. Additionaly to the $T_{\rm eff}$ and $\log(g)$ all the cases reproducing the observations are with clouds and non-equilibrium chemistry.

2.2 NEMESIS

As *NEMESIS* is a retrieval code, we need to define a prior. To do so we use the outputs of Exo-REM in an average case, i.e. the profiles generated by the atmospheric model.

The NEMESIS prior is $\log 10(g[cgs])$=4.8 $\pm$ 0.5 and $T_{\rm eff}$ = 1100 K. We use with also various clouds approaches: no clouds, grey clouds, same clouds as Exo-REM.

We retrieve the radius, gravity, location of the cloud, particule abundances, scale eight, and the abundances

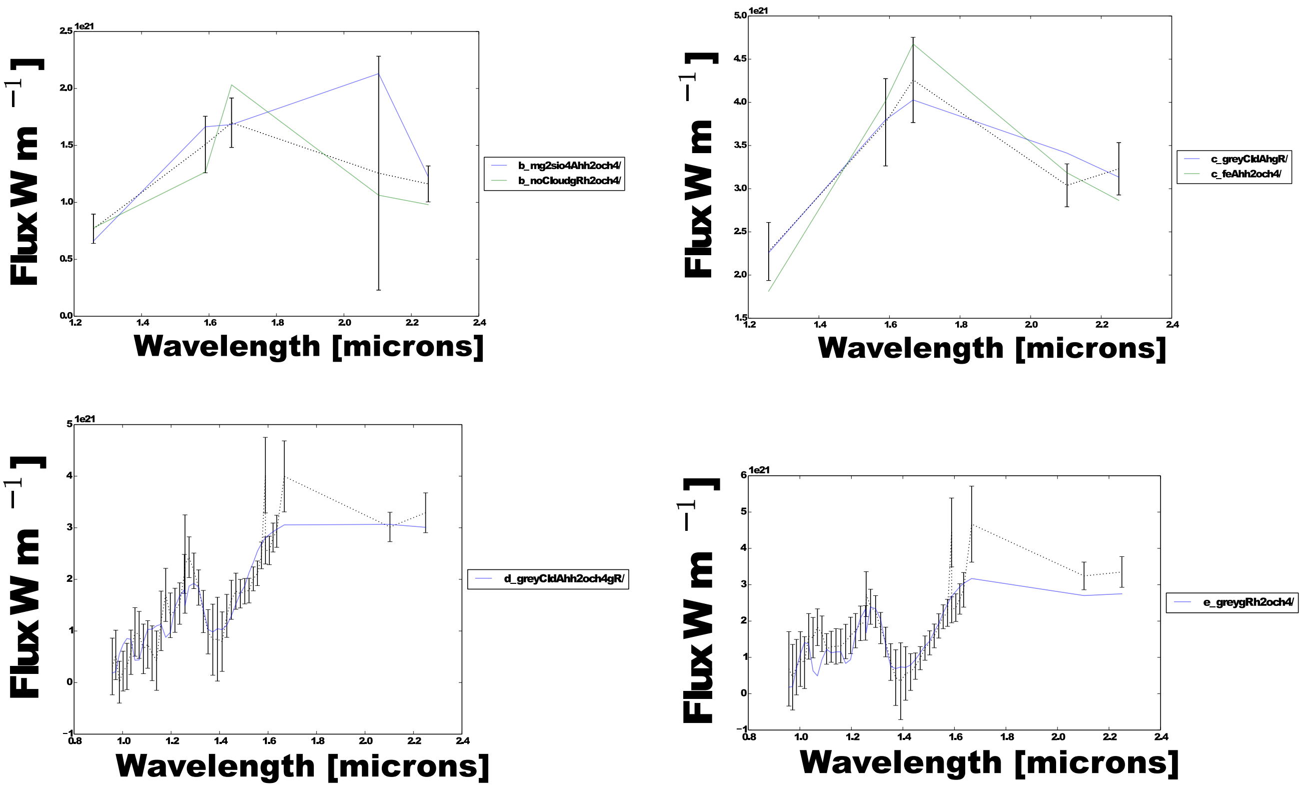

Fig. 2. Spectra corresponding to the best retrievals ($\chi^2 < 1$) on the data (black) of the planets (from the left to the right and from the bottom to the top) HR 8799 b, c, d and e with NEMESIS . For b the case in blue is with Mg_2SiO_4 cloud, the green is without cloud. For c the case in blue is with with grey cloud, the green is with Fe cloud. For d and e the case in blue is with with grey cloud.

	b	c	d	e
log10(g[cgs])	4.0 ± 0.2	5.1 ± 0.3	5.3 ± 0.2	5.1 ± 0.3
	$C/O_b < C/O_{sol}$	$C/O_b < C/O_c < C/O_{sol}$	$C/O_d < C/O_{sol}$	$C/O_e < C/O_{sol}$

Table 2. Constrained surface gravity and effective temperature of HR 8799 b, c d and e with *NEMESIS*

of H_20, CH_4, Na, K.

The temperature is not retrieved because *NEMESIS* needs to retrieve a temperature profile of 50 levels to do so properly, it corresponds to too much free parameters compared to the number of observations.

Fig. 2 shows the retrieved spectra of the four planets and the Table 2 shows the results. The low C/O of the planet b corresponds to what was announced in Barman et al. (2015).

3 Conclusion

The five IRDIS photometric points give already a first estimation (coming from the contrast between low and high wavelengths in H and K). SPHERE observations took into-account separately give a first idea of the temperature, surface gravity, and "reddening" (cloud effect). *Exo-REM* can be used to define prior of *NEMESIS*, such as a temperature profile as the radiative-convective equilibrium when the number of observation doesn't allow us to retrieve this profile. *NEMESIS* can give some information about H_2O and CH_4 abundances in the SPHERE wavelength (with similar results compared to studies using more high resolution data).

SPHERE targets are under study with *Exo-REM* and *NEMESIS*. We will publish the complete study of

HR8799 with NEMESIS. We benchmark and update *NEMESIS* using the protocol define in Baudino et al. (submitted to ApJ).

References

Barman, T. S., Konopacky, Q. M., Macintosh, B., & Marois, C. 2015, ApJ, 804, 61

Baudino, J.-L., Bézard, B., Boccaletti, A., et al. 2015, Astronomy & Astrophysics, 582, A83

Irwin, P., Teanby, N., de Kok, R., et al. 2008, Journal of Quantitative Spectroscopy and Radiative Transfer, 109, 1136

Zurlo, A., Vigan, A., Galicher, R., et al. 2016, Astronomy & Astrophysics, 587, A57

SF2A 2017
C. Reylé, P. Di Matteo, F. Herpin, É. Lagadec, A. Lançon, Z. Meliani, F. Royer (eds)

THE SPHERE DATA CENTER: A REFERENCE FOR HIGH CONTRAST IMAGING PROCESSING

P. Delorme[1], N. Meunier[1], D. Albert[1], E. Lagadec[2], H. Le Coroller[3], R. Galicher[4], D. Mouillet[1], A. Boccaletti[4], D. Mesa[5], J.-C. Meunier[2], J.-L. Beuzit.[1], A.-M. Lagrange[1], G. Chauvin[1], A. Sapone[3], M. Langlois[6], A.-L. Maire[7], M. Montargès[8], R. Gratton[5], A. Vigan[3], C. Surace[3], C Moreau[3] and T. Fenouillet[3]

Abstract. The objective of the SPHERE Data Center is to optimize the scientific return of SPHERE at the VLT, by providing optimized reduction procedures, services to users and publicly available reduced data. This paper describes our motivation, the implementation of the service (partners, infrastructure and developments), services, description of the on-line data, and future developments. The SPHERE Data Center is operational and has already provided reduced data with a good reactivity to many observers. The first public reduced data have been made available in 2017. The SPHERE Data Center is gathering a strong expertise on SPHERE data and is in a very good position to propose new reduced data in the future, as well as improved reduction procedures.

Keywords: High contrast imaging - SPHERE - Exoplanets - Circumstellar environment - Planetology

1 Introduction: Objectives of the service

1.1 The SPHERE instrument

The main goal of the SPHERE instrument (Spectro-Polarimetric High-Contrast Exoplanet REsearch, Beuzit et al. 2008) on the VLT is to detect and characterize young giant exoplanets orbiting nearby stars using direct imaging. SPHERE also allows to detect and characterize circumstellar disks where such exoplanets form. Other science cases include: stellar physics (massive stars, stars in clusters, stellar surface imaging), circumstellar environments (envelopes, jets, companions), planetology (asteroids, satellites), high energy objects, etc.

The detection of exoplanets using direct imaging is very challenging because they are forming close to their parent star and their luminosity is much lower (typically by a factor of at least 10^5). The conception of SPHERE was therefore constrained by the necessity to obtain the largest contrast possible in the close environment of these young stars. As a consequence, SPHERE combines several sophisticated techniques to achieve this goal: extreme Adaptive Optics, coronagraphy, polarimetry, low resolution spectroscopy, differential imaging in the visible and near-IR and spectro-imaging in the near-IR. SPHERE is composed of three instruments fed by a common path: IRDIS (differential imaging, long-slit spectroscopy and polarimetry in the near infra-red), IFS (integral field spectrograph, also in the near infra-red), and ZIMPOL (differential polarimetric imaging in the visible). These instruments provide large quantities of heterogeneous data needing specific data processing to maximize the contrast and more generally in order to derive the best performances in terms of detection and characterization of the astronomical signal.

[1] Univ. Grenoble Alpes, CNRS, IPAG, F-38000 Grenoble, France
[2] Université Côte d'Azur, Observatoire de la Côte d'Azur, CNRS, Lagrange, France
[3] Aix Marseille Univ, CNRS, LAM, Marseille, France
[4] LESIA, Observatoire de Paris, PSL Research University, CNRS, Sorbonne Universités, UPMC Univ. Paris 06, Univ. Paris Diderot, Sorbonne Paris Cité
[5] INAF - Osservatorio Astronomica di Padova, Vicolo dell'Osservatorio 5, I-32122 Padova, Italy
[6] CRAL, UMR 5574, CNRS, Université Lyon 1, Saint Genis Laval Cedex, France
[7] Max-Planck-Institut für Astronomie, Königstuhl 17, 69117, Heidelberg, Germany
[8] Institute of Astronomy, KU Leuven, Celestijnenlaan 200D B2401, 3001 Leuven, Belgium

1.2 Motivations : short- and long-term strategy

Given the complexity of the instrument and of the data calibration specifically required to a variety of observing modes, it was necessary to implement a service that would allow to optimise the scientific return of the instrument, by helping the PI to process their data adequately, and by providing some state-of-the-art reduced data to the whole community. In parallel, the way to optimally combine data and self-calibrate the stellar residual is still an active field of research, and new solutions are regularly proposed in the literature: the development of dedicated tools and the build-up of a centralized expertise on massive Adaptive Optics imaging data reduction provide the community with a support by experienced users who are likely to have already met the same issue and to have already developed a solution. Beside this scientific return optimization, the database format containing massive amount of data and processing them consistently allows to develop in the near future unique complementary capabilities such as the coupling between wavefront sensor information and the actual detection limits on the final reduced images, the building of a massive reference library of SPHERE coronagraphic images for use in advanced reference differential imaging techniques as well as to explore the opportunity to use deep-learning techniques in AO analysis.

Our objective is to build-up a reference center on high-contrast imaging and gather the community to foster data reduction through centralized user-feedback and to continuously strengthen this community. On a long-term basis, such services could be extended to future instruments, in line with our ongoing service to provide reduced data for (older) Adaptive Optics instruments other than SPHERE (such as NACO and NICI for instance) in the DIVA archive (see Sect. 4.4).

2 Implementation of the service

2.1 Partners

The SPHERE Data Center have been developed by four partners, with infrastructures localized on two sites:

- OSUG (Observatoire des Sciences de l'Univers de Grenoble)/ IPAG (Institut de Planetologie et d'Astrophysique de Grenoble): The processing center (hereafter PC) is implemented in Grenoble. The most voluminous data (especially large data cubes) are available there, and this center also provides data reduction services. It is part of the OSUG Data Center*.

- PYTHEAS (Observatoire des Sciences de l'Univers de Marseille) / LAM (Laboratore d'Astrophysique de Marseille): A database of high-level data, called the Target Data Base (hereafter TDB) has been developed in Marseille, and receives data from the processing center in Grenoble, to which some complementary data are added. It is part of CeSAM†.

- OCA (Observatoire de la Côte d'Azur) / LAGRANGE laboratory: This partner contributes to the operation of the processing center.

- Observatoire de Paris Meudon / LESIA (Laboratoire d'Etudes Spatiales et d'Instrumentation en Astrophysique): This partner contributes to the software development used by the processing center.

Additional informal support was provided by members of the SPHERE Consortium who provided some of the algorithms used at the DC as well as contributed to debugging of the software.

2.2 Local infrastructures and developments

The SPHERE Data Center is organized around two main tools, the Processing Center (PC) and the Target DataBase (TDB). The PC is oriented toward data processing and reduced data distribution organized around observations and instruments while the TDB is oriented toward the distribution of advanced data products organized around targets and surveys. In the mid-term future, the TDB will be the main SPHERE Data Center link to the Virtual Observatory.

*http://datacenter.osug.fr/
†https://www.lam.fr/cesam/

2.2.1 The Processing Center

The objective of the Processing Center was first to provide an infrastructure allowing a reduced team to easily process large amount of data in an homogeneous manner, and with a proper tracking system of the used data reduction parameters and algorithm versions. This data processing can be performed either on request with a good reactivity (since 2015), or systematically in a second phase of the project (started in 2017). It is therefore necessary to develop a complex database to archive many informations (and not only the information necessary for public data release) as well as a functional interface with many functionalities. We summarize the different components developed at the Processing Center:

- *A relational database*: The MySQL relational database contains raw and processed data and headers informations, processing parameters, processes which have been applied to the data, code version ...

- *A user interface*: The interface allows the team to manage the operations: data import from ESO (manual after data retrieving, automatic for the calibrations) with file type identification, data browsing and processing, data validation, extraction of information for the instrument monitoring, visualisation tools, ... This is illustrated in Fig. 1. It also allows access to services and data (see fourth point below). We used the jMCS framework developed by the JMMC (available at https://github.com/JMMC_OpenDev/jMCS).

- *The pipeline and workflows*: The pipeline is based on the DRH (Data Reduction and Handling) pipeline delivered by the SPHERE consortium to ESO (Pavlov et al. 2008), with a number of significant additions and corrections. It is indeed possible to add any new routine easily. The additionnal tools have been developed in Grenoble and Paris (SpeCal pipeline, Galicher et al., 2017) and are routinely used; more tools will be added in the future (see Sect. 5). The notion of workflows has been implemented, with standard workflows which are easy to use during processing operations: a significant effort has been dedicated to automatically associate the most relevant calibrations for each dataset.

- *A user manual*: It is possible for external users to connect to the interface to work on their own data, using our application and hardware. Data is organized into workspaces for data protection and rights management. The interface therefore includes a user identification. A public username has been created for public data, which are located in specific workspaces, as illustrated in Fig. 2. Additionnally, the SPHERE Data Center user manual is a valuable source of information for any user willing to reduce SPHERE data.

- *Instrument monitoring*: Dedicated routines have been developed to extract useful information (Strehl ratio, seeing, coherence time, wave front sensor information) to monitor the instrument, based on the very large amount of data available. The SPHERE Data Center allows to quantitatively link such observational metadata to the final quality of the reduced products (see Sect. 5 for more details).

- *Infrastructure*: Up to now a dedicated server was used for the software and data processing, associated to a data storage at Grenoble Alpes University (SUMMER). We are currently implementing a new server, dedicated to heavy data processing: this server will be part of a grid (LUKE) developed by the high performance computing mesocenter CIMENT at University Grenoble Alpes, with dedicated high performance storage disks. The SUMMER storage will continue to be used and will be extended over time, and an additional virtual server will then be implemented for the database at the OSUG Data Center (OSUG-DC) to manage the database and other operations.

- *Administration tools*: A number of functionalities used to administrate the data center have been developed, such as (not exhaustive) user access and rights, logs, algorithm to recognize star names from SIMBAD at the CDS, monitoring tools (tasks progression, batchs, system health), reporting tools (data statictics, quality control reports), management tools (ESOrex pipeline versions, local DC recipes, workflows, users and security)

- *Connection with the TDB*: The PC prepares advanced reduced data products gathering all necessary information that is automatically sent to the Target Data Base (TDB).

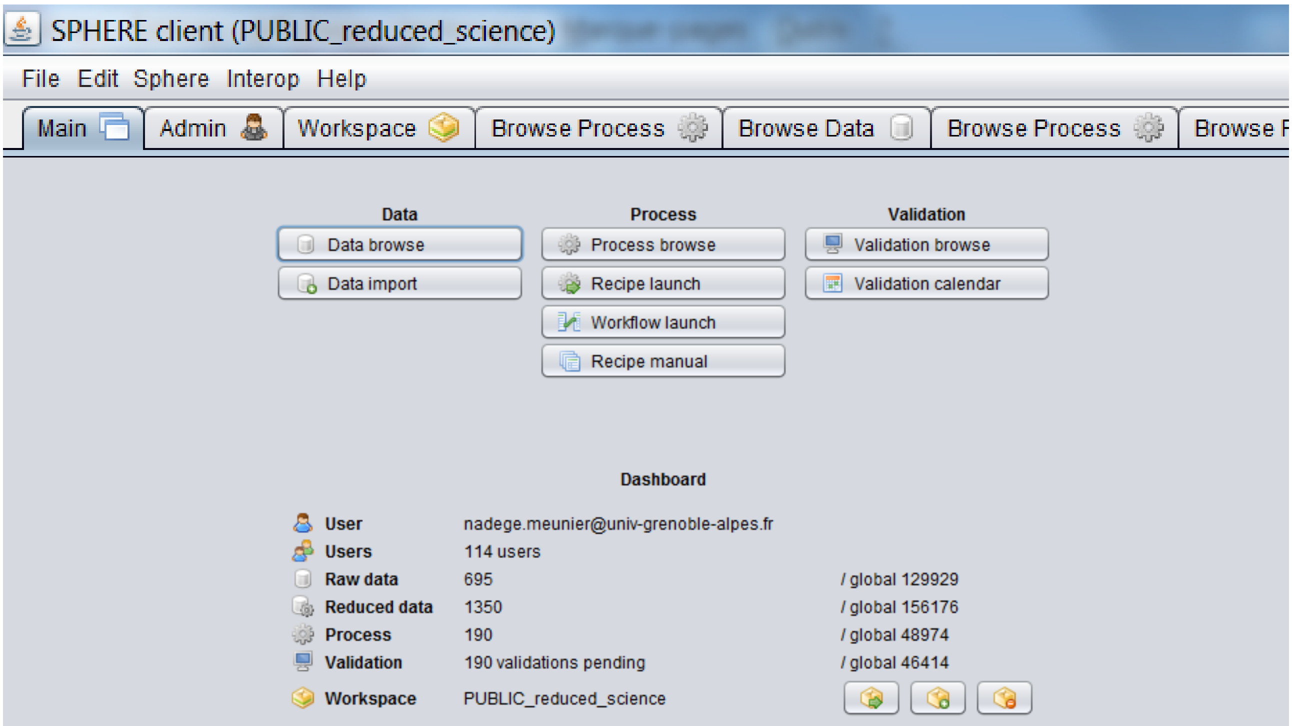

Fig. 1. Example of the main menu on the Processing Center client interface (seen by administrators) and showing the different functionalities.

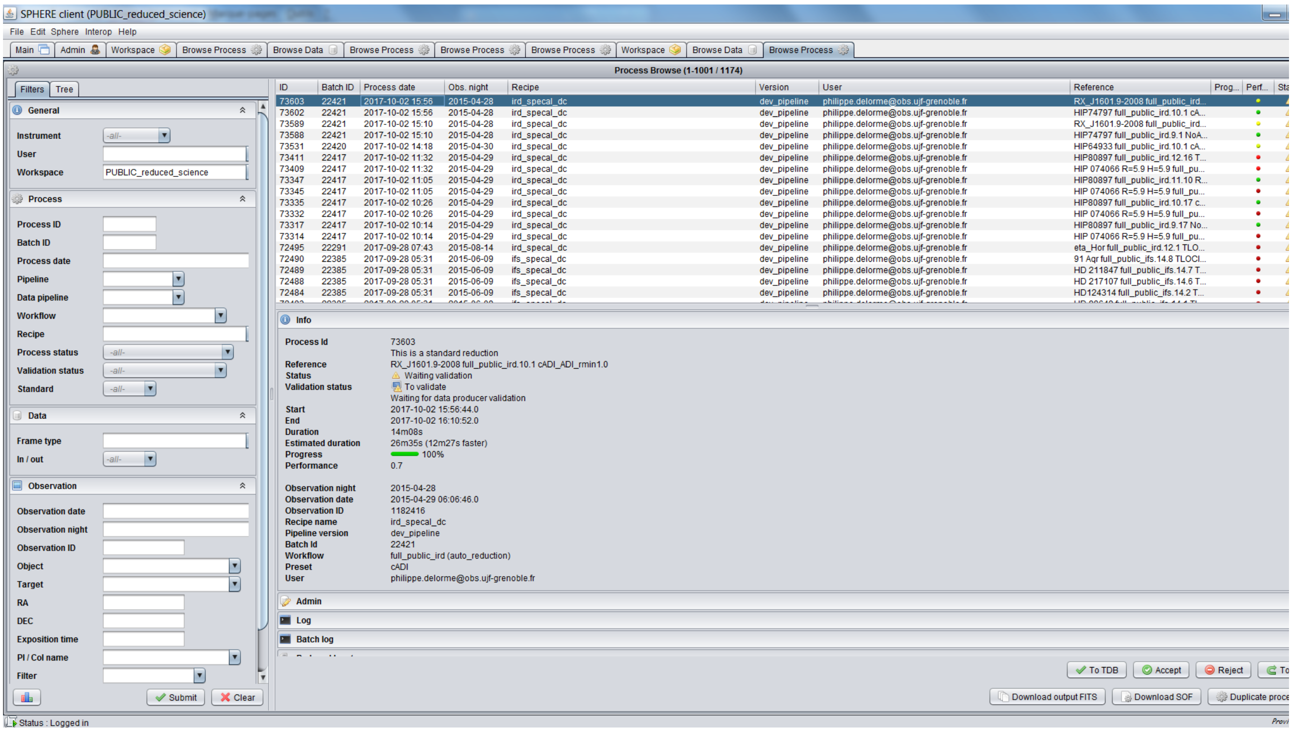

Fig. 2. Example of the process browse functionality on the public reduced data, showing the main request criteria.

2.2.2 The Target Data Base (TDB)

The Target Data Base, at http://cesam.lam.fr/spheretools/, has been developed in a very generic way, with the goal to provide access to high level data as well as dedicated tools to analyze them. In this section, we summarize the different components developed at the Target Data Base:

- *A relational database*: The TDB is based on a hierarchical design (Observations → Reductions → Detections[‡]). A relational PostgreSQL database contains all the tables required to store science products of high-contrast imaging surveys. The main tables and columns of this database are described in the Annexe A. In this structure, an observation is unique, and we can import as many reductions related to this observation as needed, as well as detections found in each reduction made by the PC.
- *Data import and conneion to other databases*: A generic code has been developed in the TDB to import these data from a hierarchic json file[§]. This file format notably allows to import data from various surveys even if some columns are missing (the surveys are not homogeneous, and sometime astrometry or photometry informations are missing). Such files are used to transfer data from the PC to the TDB (see Sect. 4 and 5 for the data description). The TDB also contains a lot of informations on the observed targets such as their astrometry (coordinates, proper motion, parallax), photometry (B, V, R, I, J , H, K magnitudes) and ages. An algorithm of the TDB recognizes star names from SIMBAD at the CDS coupled to an internal dictionary for objects not referenced in SIMBAD, and astro-photometry of a new target is automatically retrieved from SIMBAD.
- *The web portal and tools:* The web portal (http://cesam.lam.fr/spheretools/) is mainly based on Python Django, and some pages use the ANIS framework (Moreau et al. 2015) developed by the CeSAM in Marseille. It allows requests on the database using forms (for example such as in Fig. 3) with a large number of criteria and allowing crossing of informations: star age and mass, number of detections, confirmed companion candidates, reductions type, observation dates, etc. Request forms using the whole potential of the TDB relational data base will be developed in the future. In addition, tools such as dynamic charts have been developed for Level 3 data (see more details in Sect. 5.2).
- *Rights management*: A fine-grained rights management interface has been developed, based on Django. Depending on the rights of the users (public, in one or several surveys), it is possible to access different tools and/or data (see Sect. 5 for discussion).
- *Virtual Observatory*: We plan to implement later Virtual Observatory service to give access to table data (service TAP=Table Access Protocol) and reference this service in the VO Registry. It will enable access to target and detection data by programs such as python scripts.

3 Services

3.1 Services currently available

- *Data processing on request*: the Data Center team reduces PI data on demand and also carries out early data analysis steps, notably providing ADI analysis and detection limits. This service is provided to the PI (or their coI) of the observation. *For IRDIS, IFS and ZIMPOL*
- *Access to the SPHERE Data Center application to process private data*: This service is an alternative to the first service. The user can access our application and process its own data through it. This service is open with some conditions: limited time for a given dataset (1 week), outside of intensive run periods (either GTO or systematic processing), so that we can control the charge on our server. This could evolve in the future depending on the needs and available infrastructures. *For IRDIS and IFS*

[‡]detections are objects (either companions or background stars) identified in the field of coronographic observations (see Sect. 5.2 for more details)

[§]JavaScript Object Notation, file with an open-standard format allowing the storage and transfer of data structures and objects.

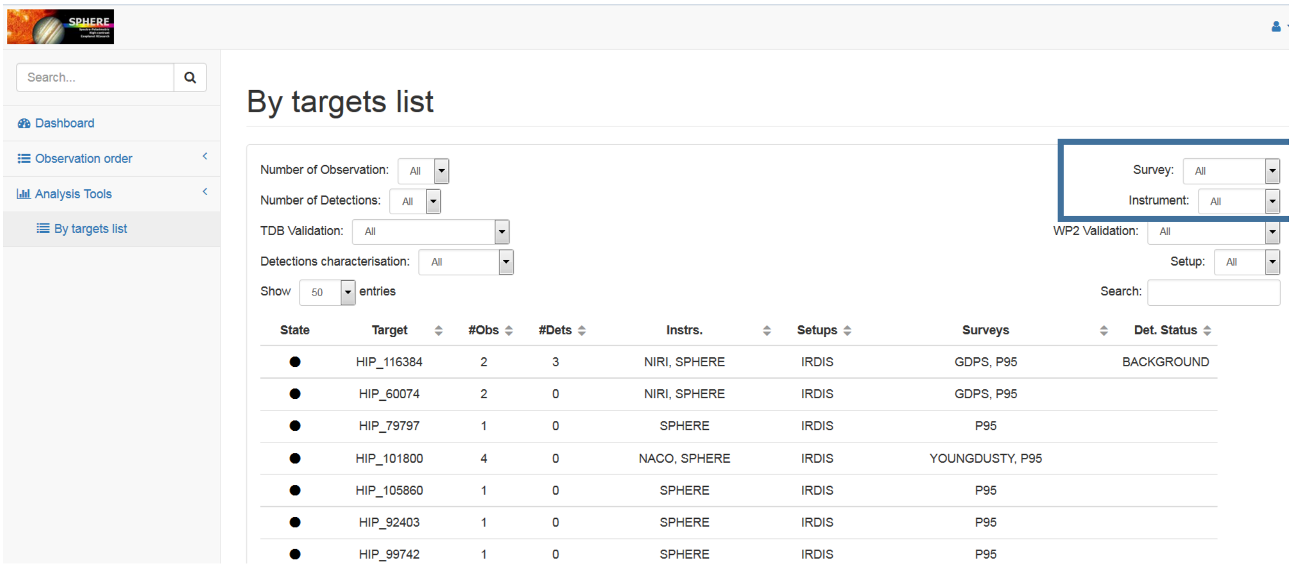

Fig. 3. Request form at the TDB.

- *Support to SPHERE surveys*: Surveys or Large Programs may have specific needs. For example the SHINE survey of the SPHERE consortium has complementary needs in term of routines and organization, in order to organize data processing within H+24 of the actual observations. *For IRDIS and IFS*

- *Reduced calibration on-line*: Reduced SPHERE calibrations are put online less than two days after observation and can be easily downloaded with the public login. *For IRDIS, IFS and ZIMPOL*

- *Reduced observations on-line after a certain period*: Scientific SPHERE data are reduced, notably providing ADI analysis and associated detection limits. As of now most of P95 IFS and IRDIS science data is reduced and can be easily downloaded from the PC and TDB with the public login. Note that individual PIs have the possibility to delay the public release of reduced data obtained from their public raw data if this would endanger a publication in preparation and jeopardize their program, notably in case of the possible detection of a candidate companion at a first epoch, now public, for which the PIs are expecting a second epoch confirmation (this concerns a minority of observations). In the future we will strive to provide public reduced data of SPHERE science data one year after the raw data has been made public by ESO, so 2 years after the science observations in most cases. *For IRDIS and IFS*

3.2 Practical information

Information on the SPHERE Data Center are available on our website at http://sphere.osug.fr/spip.php?rubrique 16&lang=en and will be regularly updated (Fig. 4). They include (not exhaustive):

- Information on data access, including a direct link to the TDBi¶ and to DIVA‖.

- A FAQ with useful informations and tips.

- A description of the available data.

¶http://cesam.lam.fr/spheretools/search
‖http://cesam.lam.fr/diva/

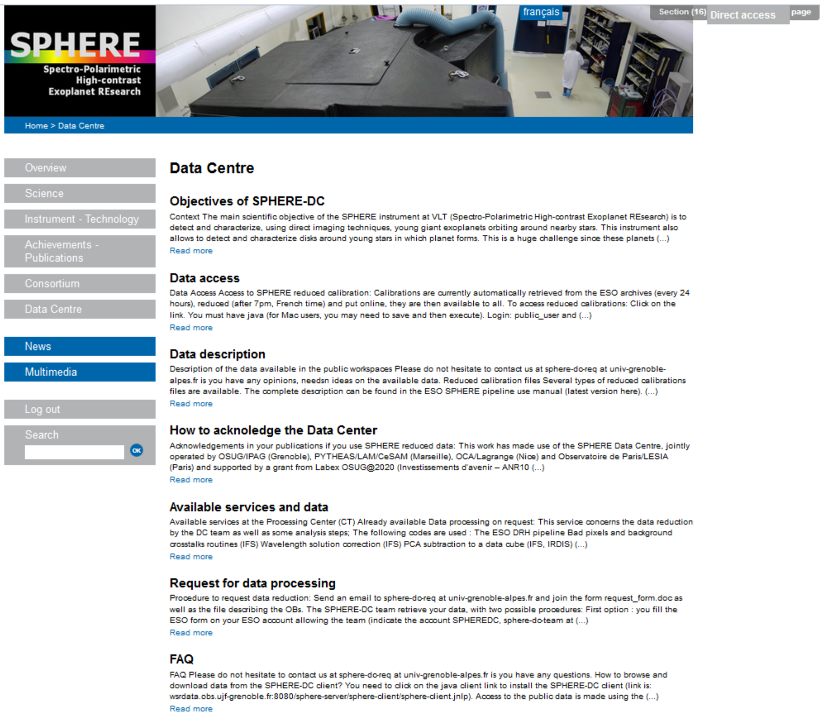

Fig. 4. Website of the SPHERE Data Center illustrating a subsample of the available information.

4 On-line data: description of the data levels

4.1 *Reduced calibrations*

In 2017 we have implemented an automatic retrieval procedure (from the ESO archive) to process all calibration files. They are retrieved every 24 hours. The reduction automatically starts at 7pm CET. These reduced calibration files are then publicly available in the PC database. Older calibration files will shortly be retrieved and processed as well.

4.2 *Level 1 data*

For IRDIS data, the first reductions steps (dark, flat, and bad pixel correction) rely on the SPHERE Data Reduction and Handling (DRH) pipeline (Pavlov et al. 2008) provided by the consortium to ESO. The star centering is obtained through observations with coronagraph with waffle mode (a small fixed waffle pattern is applied to the deformable mirror to create four unsaturated crosswise echoes of the PSF) or with unsaturated exposures without coronagraph. The quality of this centering is automatically controlled and if the centering is too bad (error larger than 0.7pixel or 8.6mas) the workflows use a homemade centering routine to try to improve it and keep the most accurate result.

For IFS data the SPHERE Data Center complements the DRH pipeline with additional steps that improve the wavelength calibration, bad pixel correction, and the cross-talk correction (Mesa et al. 2015). The astrometric calibration, computation of parallactic angles (see below) are also done using routines external to the DRH.

For both IRDIS and IFS data, we automatically associate the calibrations that are the nearest in time (usually within 12hr of the observations) and use the same coronagraph, filter, neutral density, readout mode and exposure time (when relevant) as the science data. To perform the astrometric calibration of the IRDIS and IFS dataset on sky, we use both the fixed instrumental corrections (0° for IRDIS in field tracking mode, 135.99° in pupil tracking mode, and -100.48° for IFS) and the on-sky calibration by Maire et al. (2016) leading to a True North correction value of $-1.75 \pm 0.08°$ and a plate scale of 12.255 ± 0.009 milliarcseconds/pixel for IRDIS and 7.46 ± 0.02 milliarcseconds/pixel for IFS.

The resulting master reduced data cube, that stores one reduced frame per Detector Integration Time in a given observing block, is associated with the following metadata:

- A vector containing the accurate parallactic angle for each frame. The raw headers have this information but with a coarser sampling (two per NDIT), so this vector is a prerequisite for using ADI algorithms for observations in pupil tracking mode.

- A vector containing the wavelength calibration for each channel (2 for IRDIS and 39 for IFS).

- If flux calibration data (unsaturated exposures of the out-of-coronagraph target star) are available, the Data Center reduces them and provides them together with the science data, for use as flux calibration or as PSF models.

- In the near future, a table will be added that provides the essential information from the wavefront sensor (seeing, coherence time, wind speed and image quality estimator: Strehl ratio) derived with a frame by frame time-sampling, within the limit of the temporal sampling of recorded wavelength sensor statistical data: up to now every 20s, currently in discussion with ESO to improve to 10s.

The resulting Level 1 reduced data are available through the PC, with the public login for public data or with private login for PI data. Examples of Level 1 images are shown on Fig. 5.

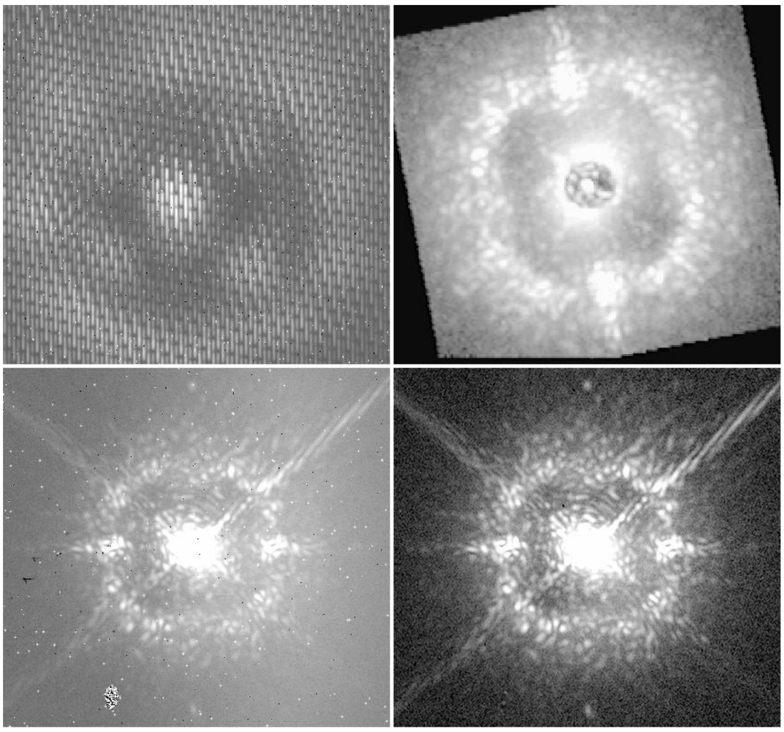

Fig. 5. Raw (left) and Level 1 reduced images (right) of HD206893B (Delorme et al. 2017), for IFS images (upper panels) and IRDIS (lower panels).

4.3 Level 2 data

The Level 1 reduced master cubes are then used as input for high contrast imaging post-processing. We use the Speckle Calibration (SpeCal) package, described by Galicher et al. (2017), which implements several types of differential imaging strategies: ADI (Angular Differential Imaging), SDI (Spectral Differential Imaging), ASDI (Angular and Spectral Differential Imaging), and RSDI (Reference Star Differential Imaging). Various algorithms are offered in conjunction with the aforementioned strategies: cADI (Marois et al. 2006), LOCI (Lafrenière et al. 2007), T-LOCI (Marois et al. 2010), PCA (Soummer et al. 2012). Direct stacking and

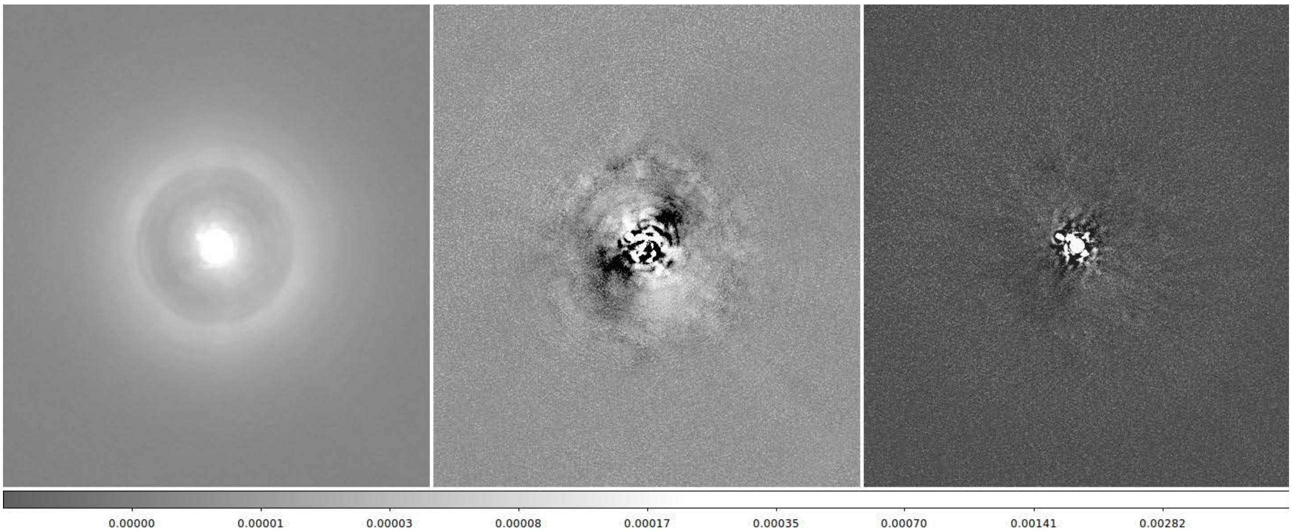

Fig. 6. Level 2 reduced residual of HD206893B (Delorme et al. 2017) with various algorithms. From left to right: No ADI, Classical ADI, TLOCI-ADI. the substellar companion is visible on the upper left (North East) of the star center.

subtraction of an azimuthally averaged profile are also available. The package applies similarly to IRDIS and IFS data cubes.

For all these algorithms the outputs follow the same rationale and include:

- A final image using one of the algorithms, in which all wavelength channels are stacked.
- The same final image corrected from flux loss caused by ADI-induced self-subtraction of companion flux
- A final cube, similar to the final image, but without stacking it in the wavelength dimension (with one frame per wavelength)
- The corresponding signal to noise ratio map (one map for each wavelength)
- Detection limits: contrast curve at 5 sigma in each wavelength as a function of the angular separation

Full Level 2 data are available from the PC and a subset of images (final reduced median image, contrast curve, SNR maps) are available at the TDB. In both cases public data are accessible with the public login and private data with private login. Examples of Level 2 images are shown on Fig. 6.

4.4 The DIVA archive

The DIVA (Direct Imaging Virtual Archive) has been built for reduced data for Adaptive Optics imaging instruments other than SPHERE (NaCo, HST, Keck, Gemini, Subaru, LBT) and contains astrometry and photometry of the detections as well as images. They include a large part of pre-SPHERE surveys. The procedure and data are described by Vigan et al. (2017). Note that the DIVA and SPHERE data are in the same relational database (as described in Sect. 2.2.2); their portal are currently different but we plan to merge these two sites in the near future.

5 Future developments

5.1 Overcoming our current limitations

Though we strive to provide a very comprehensive service of SPHERE data reduction, we do not yet cover all kind of data that this very versatile instrument can provide. Our main current limitations are listed below. We are currently working to resolve each of the following issue, the time scale depending on the manpower available at SPHERE-DC to continue developing our tools, beyond data production and existing tools maintenance.

- ZIMPOL: we do not yet have a fully automated pipeline for ZIMPOL and this will be implemented beginning of 2018. As of now we can only reduce ZIMPOL data for PIs on a case by case basis, using two sets of routines: i/ Part of the reduction is performed using the ESO DRH pipeline. Because of the stripe mask on the ZIMPOL detector, all recipes include a pre-processing step that re-orders the image rows into logical and viewable images. In imaging mode, the pre-processed imaging science frames are then calibrated (for each camera) by subtracting the master imaging bias and the master imaging dark, and divided by the corresponding intensity imaging flat field. The calibrated frames are de-dithered and de-rotated and then saved as intermediate products. The final step combines all these calibrated, de-dithered and de-rotated frames, using a standard mean algorithm, to produce one reduced image per detector. ii/ For the polarisation data, the same processes are applied to the different measurement groups with regards to each Stokes parameters (Q [Q+, Q-] and/or or U [U+, U-], then homemade routines are applied to provide polarisation maps (intensity, degree of linear polarisation, polarisation angle, polarized flux). What remain to be done is the integration of all these recipes as a workflow associated to associating rules in the PC.
- IRDIS Polarimetry: we only provide the basic reduction steps that are common between non-polarimetric and polarimetric scientific data. The reduction of polarimetric IRDIS data with procedures taking into account as much as possible instrumental effects will therefore be soon implemented.
- IRDIS Long Slit Spectroscopy: we only provide the basic reduction steps that are common between imaging and spectroscopic scientific data, i.e. similar to the ESO pipeline. Further analysis remains to be defined and implemented and may depend on the scientific case. Our current approach is to implement the routines developed by Vigan (2016) for the specific reduction of IRDIS data acquired in the long-slit spectroscopy mode. These routines consist in a combination of the standard DRH recipes with custom IDL routines designed to simplify the reduction and analysis of LSS data, going from the raw data to a set of clean, aligned image cubes that can be analyzed with speckle-subtraction techniques adapted to LSS data (e.g. Vigan et al. 2008).
- IRDIS Observations without star centering sequence or observations with saturated or otherwise invalid star centering sequence are currently only reduced to Level 1.

5.2 Level 3 data

Data with more added value will be provided in the future, mostly through the TDB. While some Level 2 data were part of the ESO pipeline (although we propose more added value), Level 3 data are completely outside the scope of the ESO pipeline and different added value data may be produced depending on the scientific cases. We plan to produce the Level 3 data described below, which concerns detections associated to their property and tools to visualize them, but more will be produced in the future for other science cases.

We recall that detection are objects identified in the field of view of coronagraphic images when searching for exoplanets: they can be either bounded companions, background stars. Data of Level 3 would then be all informations related to the detections found in such Level 2 images, in particular their astrometric and photometric characterization. These data can already be produced by the SpeCalcharac (Galicher et al., 2017) algorithm included in the DC. The algorithm however requests a visual identification of candidate companions and therefore cannot be applied in an automatic workflow yet. We are developing automated detection algorithms compatible with SpeCalcharac, but their current ratio of true positive over false positive detections is still less reliable than human analysis. The TDB is already able to deal with these data of Level 3: The tools developed at the TDB allows the users to determine whether the detections are background objects or possible companions. It is also possible to use forms in the TDB to search and sort by criteria (ex: stars that have bound objects, etc.).

To help the users to determine the nature of the detections (background stars or bound companions), we have therefore developed several dynamics charts using Aladin tools and javascript libraries such as plotly.js** and chart.js††. For example, it is possible to show one detection, or all the detections found around one star, or all the detections in the TDB, in color magnitude diagrams: MH2[mH2- mH3], MK1[mk1-mk2], etc., which are crucial to determine their nature. Reference points of known cold objects are super-imposed on these graphics. An other tool of astrometry allows to visualize all the detections at all the epochs of observation around a selected star (as illustrated for example in Fig. 7), and to superimpose the astrometric curve of the background stars. An admin tool allows to regroup the detections observed at several dates so that the users can see graphically the detections nature (i.e. put in a same group) around one star (background stars, bound objects, etc.). the TDB shows all its power, by plotting all together, on the same graphic, data that come from any surveys (NaCO, SPHERE, Keck, Hubble, etc.).

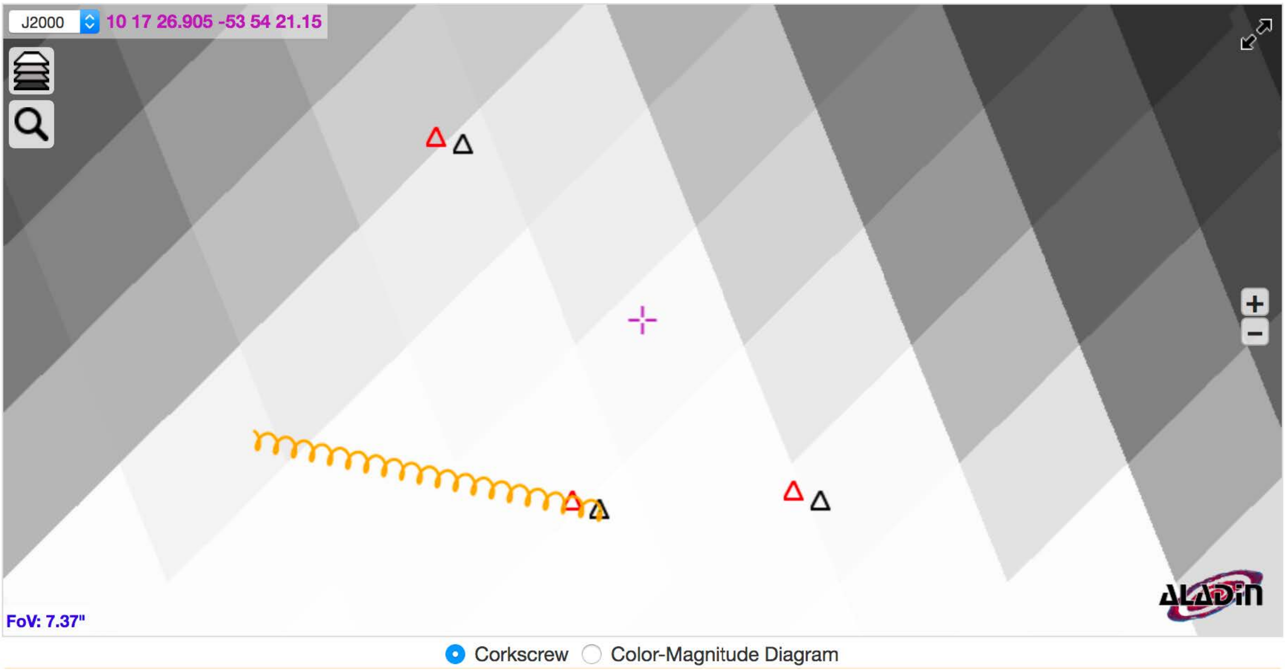

Fig. 7. Three detections around a star of the DIVA project (NACO and NICMOS instruments) at two different dates (dark and red). The astrometry curve of the background stars is shown in yellow.

Future work will therefore include an automatisation of the detection procedure and the develoment of other graphics, and statistical tools to provide this Level 3 data.

5.3 New algorithms for Level 2 data and frame sorting

We plan to regularly add state-of-the-art differential imaging algorithms to our toolbox to follow the fast development of such routines in the high-contrast imaging community. Beyond striving to provide such up-to-date algorithms, we also want to explore the unique opportunities opened by coupling a direct imaging reduction center to a massive database taking advantage of Reference star Differential Imaging while avoiding self-subtraction inherent to ADI, SDI or ASDI. Using a large library of coronagraphic images will allow to perform in a more efficient way as it was done recently for HST NICMS (Choquet et al. 2016).

Another issue concerns frame selection, i.e. the elimination of low quality images before going from Level 1 to Level 2 (and above) data: which frames in a given science sequence were affected by poor AO correction ?

**https://plot.ly/javascript/
††http://www.chartjs.org/

This is currently investigated using science data cubes and wavefront sensors data (see Sect. 5.4) and will lead to complementary Level 2 data after frame selection, in addition to information on the data quality.

5.4 Exploitation of observatory metadata

Apart from science detector data, the system archives some contemporary statistics of the wavefront sensors data. This provides direct information on the outer turbulence conditions and the achieved AO correction quality. Temporal sampling for these statistical data is typically every 30s up to now, and on-going discussions with ESO currently push to increase this sampling rate to every 10s.

On a statistical manner, such information is useful to monitor the instrument performance and also to help and predict what performance to expect according to conditions. Such an analysis motivates some current change at ESO to modify the user-specified constraints to execute given OBs (ESO Observing Blocks) in service mode according to turbulence speed rather than seeing, which appear much more relevant to guarantee the desired performance level (Milli et al. 2017).

On an a posteriori data reduction perspective, we have started development to extract relevant information and associate then directly to the science data product with the following interests and goals:

- *Night and/or program overviews*: the AO data provide a nice overview of the conditions and image quality obtained during a night or a program, which is much more relevant than the generic ESO seeing monitor. It includes both the seeing and turbulence speed and the achieved image quality correponding to the science data (Fig. 8).

- *Data selection for a given data set reduction, or building classes of PSF libraries*: The coronagraphic images by construction hide the stellar PSF core and direct indication of the AO quality SR is lost. The AO sensor data provide this in real time. Also, the turbulence speed is directly correlated to the coronagraphic flux leaks (especially in the direction of the wind), as illustrated in Fig. 9. The AO data are thus very valuable to guide the image selection among data cube that are often heterogeneous. These AO data are currently being associated to reduced science frames. It will be used to support the optimal selection of frames to obtain the best contrast of a given data set; it will also guide the construction and classification of large PSF libraries according to conditions and support the choice of the best PSF among this library to enhance the power of reference star differential imaging (RSDI Gerard & Marois 2016; Wahhaj et al. 2016).

5.5 Data format and tools

The data available at the TDB will soon be also available in a HCI-FITS format (Choquet et al. 2014; Hagan et al. 2017) as aready done for the DIVA project[‡‡] (see Sect. 4.4).

Other tools may also be available in the future, for example tools to prepare survey observations. For example, the coordinators of the SHINE survey can prepare their observation catalogues directly from the TDB. This option, in discussion, could be developed for other surveys and PIs but might require to be adapted to deal with a lot more instrumental configurations.

5.6 Virtual Observatory layer

We plan to develop an interoperability layer for both databases, with a Virtual Observatory (VO) access to the public data. This will allow direct requests on the database. The typical fields will be : coordinates, target name, instrument (to be completed). This layer will be implemented for both PC and TDB databases. On a longer term basis, it may be possible to implement our catalogue at the CDS: this would allow easier cross-identification with other catalogues at CDS.

[‡‡]http://cesam.lam.fr/diva/index/format

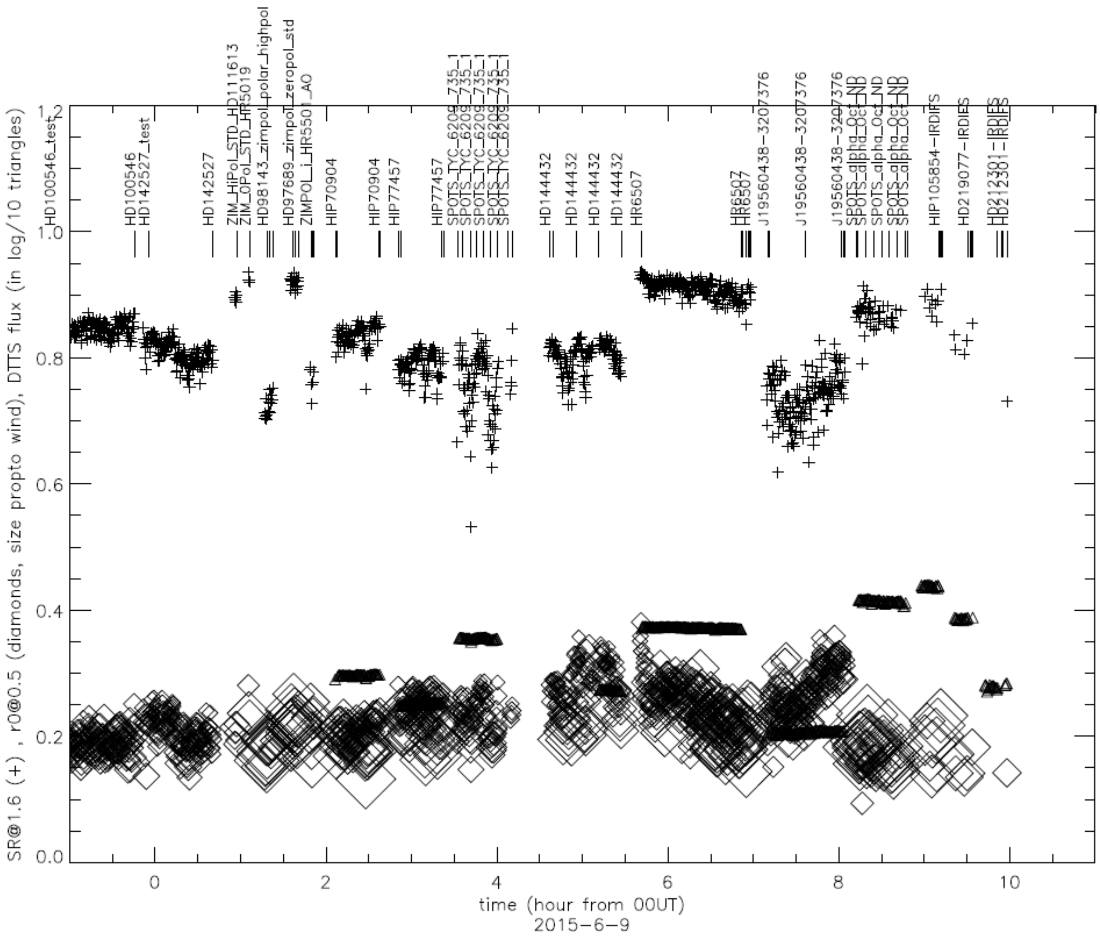

Fig. 8. Example of the night conditions overview as extracted from AO data. It includes an estimate of the achieved AO image quality (Strehl ratio at 1.6 mic imaging wavelength), spatial and temporal scale of the turbulence (r_0 and t_0).

6 Conclusion

The SPHERE Data Center has been operational for more than two years, with success. It allowed to provide reduced data with a good reactivity to many observers, and the first public reduced data have been made recently available through the PC and TDB interface (corresponding to a major subset of ESO P95 period, i.e. April-September 2015), for Levels 1 and 2. The SPHERE Data Center is gathering a strong expertise on SPHERE data and is in a very good position to propose new reduced data in the future, as well as improved reduction procedures. Some tools to extend the coverage and provide new added value are currently being developed, and some of the functionalities are almost ready (for example concerning the Level 3 data "detection", functionality already existing at the TDB). This position opens interesting perspectives for future instruments (for example high contrast instruments on the E-ELT).

Acknowledgement: We thank the colleagues from the SPHERE consortium who have helped us with feedback on our services and by providing some tools, special thanks to Janis Hagelberg. The SPHERE Data Center received support from the LabEx OSUG@2020 (Investissement d'avenir - ANR10 LABX56). We thank the OSUG-DC and CIMENT teams and in particular Françoise Roch, Bruno Bzeznik, Bernard Boutherin, Jean-Charles Augereau. We used the jMCS framework developed by the JMMC and available at https://github.com/JMMC_OpenDev/jMCS. We thank Gilles Duvert for his help in using GDL. This work has made use of the SIMBAD database and ALADIN tools operated at the CDS, Strasbourg, France. We thank the CeSAM for its support. We thank the computer department at IPAG for its support as well as the administrative support both at IPAG and OSUG. This project has received funding from the European Unions Horizon 2020 research and innovation programme under the Marie Skodowska-Curie Grant agreement No. 665501 with the research Foundation Flanders (FWO) ([PEGASUS] 2 Marie Curie fellowship 12U2717N awarded to MM.

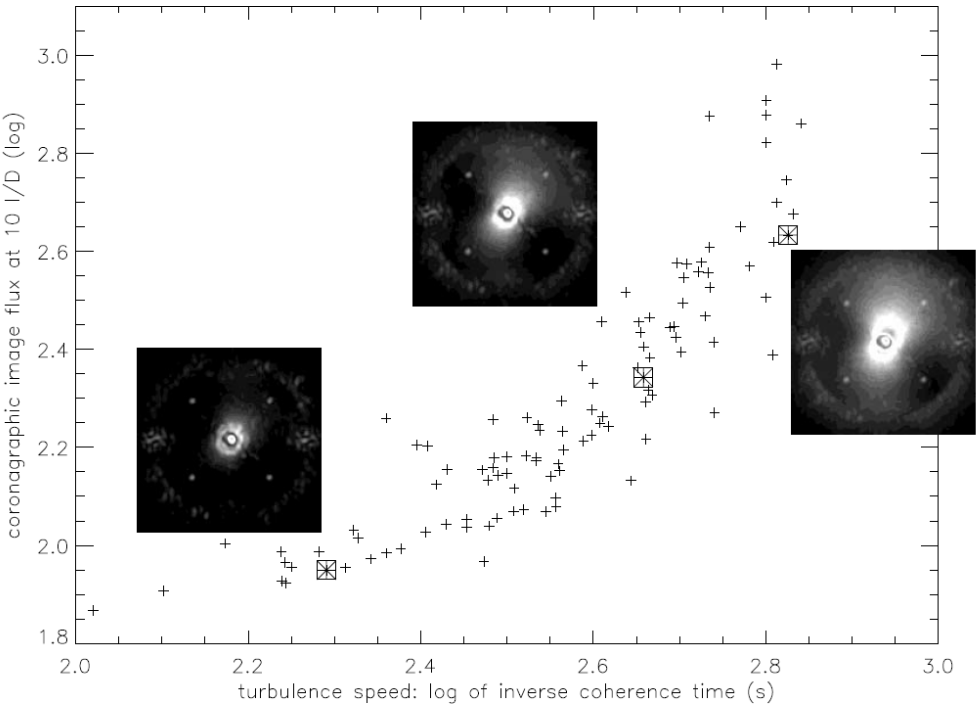

Fig. 9. Correlation between the coronagraphic image intensity over an annulus at 10 λ/D vs the AO sensor estimate of the turbulence speed (log of the inverse coherence time expressed in s), along a 1-hour sequence on a bright object, in variable conditions. The turbulence speed estimator is a very good proxy for the coronagraphic flux leaks.

References

Beuzit, J.-L., Feldt, M., Dohlen, K., et al. 2008, in Society of Photo-Optical Instrumentation Engineers (SPIE) Conference Series, Vol. 7014, Society of Photo-Optical Instrumentation Engineers (SPIE) Conference Series

Choquet, É., Perrin, M. D., Chen, C. H., et al. 2016, ApJ, 817, L2

Choquet, É., Vigan, A., Soummer, R., et al. 2014, in Proc. SPIE, Vol. 9147, Ground-based and Airborne Instrumentation for Astronomy V, 914751

Delorme, P., Schmidt, T., Bonnefoy, M., et al. 2017, ArXiv e-prints

Galicher, R. & et al. 2017, in preparation for A&A

Gerard, B. L. & Marois, C. 2016, in Proc. SPIE, Vol. 9909, Adaptive Optics Systems V, 990958

Hagan, J., Choquet, E., Soummer, R., & Vigan, A. 2017, submitted to ApJ

Lafrenière, D., Marois, C., Doyon, R., Nadeau, D., & Artigau, É. 2007, ApJ, 660, 770

Maire, A.-L., Langlois, M., Dohlen, K., et al. 2016, in Proc. SPIE, Vol. 9908, Society of Photo-Optical Instrumentation Engineers (SPIE) Conference Series, 990834

Marois, C., Lafrenière, D., Doyon, R., Macintosh, B., & Nadeau, D. 2006, ApJ, 641, 556

Marois, C., Macintosh, B., & Véran, J.-P. 2010, in Society of Photo-Optical Instrumentation Engineers (SPIE) Conference Series, Vol. 7736, Society of Photo-Optical Instrumentation Engineers (SPIE) Conference Series

Mesa, D., Gratton, R., Zurlo, A., et al. 2015, A&A, 576, A121

Milli, J., Mouillet, D., Fusco, T., et al. 2017, ArXiv e-prints

Moreau, C., Agneray, F., & Gimenez, S. 2015, in Astronomical Society of the Pacific Conference Series, Vol. 495, Astronomical Data Analysis Software an Systems XXIV (ADASS XXIV), ed. A. R. Taylor & E. Rosolowsky, 433

Pavlov, A., Möller-Nilsson, O., Feldt, M., et al. 2008, in Proc. SPIE, Vol. 7019, Advanced Software and Control for Astronomy II, 701939

Soummer, R., Pueyo, L., & Larkin, J. 2012, ApJ, 755, L28

Vigan, A. 2016, SILSS: SPHERE/IRDIS Long-Slit Spectroscopy pipeline, Astrophysics Source Code Library

Vigan, A., Bonavita, M., Biller, B., et al. 2017, A&A, 603, A3

Vigan, A., Langlois, M., Moutou, C., & Dohlen, K. 2008, A&A, 489, 1345

Wahhaj, Z., Milli, J., Kennedy, G., et al. 2016, A&A, 596, L4

A Description of the tables in the Target Data Base

The main tables of the data base are described below (not exhaustive). We find this hierarchical logic (Observations → Reductions → Detections) in all the web site and notably in the json files used to import the reduced products from any surveys.

Observation:

observation date (JD) instrument name
telescope name
survey name
target name (simbad)
true north (deg)
true north error (deg) filter name
parallactic angle (deg)
pixel scale on the CCD (mas/pixel)
pixel scale error on the CCD (mas/pixel)
observing setup (generic name for all the config. Ex: IRDIFS)
unique observation id

Reductions:

validation flag
software name used for the reduction
version of the software
algorithm used (PCA, TLOCI, etc.)
Date of the reduction (JD)
Address of the reduction on the DC
Unique id number of reduction

Detections:

Detection 0:
wavelength (micron)
magnitude
magnitude error
signal to noise
x position (mas)
x position error (mas)
y position (mas)
y position error (mas)
separation (mas)
separation error (mas)
position angle (deg from North)
position angle error (deg)
Detection 1:
etc.

Session 10

Fundamental physics from space data

ACES MWL DATA ANALYSIS CENTER AT SYRTE

F. Meynadier[1], P. Delva[1], C. le Poncin-Lafitte[1], C. Guerlin[2], P. Laurent[1] and P. Wolf[1]

Abstract. The ACES-PHARAO mission aims at operating a cold-atom caesium clock on board the International Space Station, and performs two-way time transfer with ground terminals, in order to allow highly accurate and stable comparisons of its internal timescale with those found in various metrology institutes. Scientific goals in fundamental physics include tests of the gravitational redshift with unprecedented accuracy, and search for a violation of the Lorentz local invariance.

As launch is coming closer we are getting ready to process the data expected to come from ACES Microwave Link (MWL) once on board the International Space Station. Several hurdles have been cleared in our software in the past months, as we managed to implement algorithms that reach target accuracy for ground/space desynchronisation measurement.

I will present the current status of data analysis preparation, as well as the activities that will take place at SYRTE in order to set up its data processing center.

Keywords: General Relativity, Atomic Clocks, Tests of Fundamental Physics, Relativistic Time and Frequency Transfer, Data Analysis, Space Mission

1 Introduction

This talk reports on the current status of the ACES-PHARAO mission preparation at SYRTE, where our team is currently building a Data Analysis Center (SYRTE-DAC) for ACES Micro Wave Link (MWL). This preparation spans a long time range, hence this status report follows several previous ones, e.g. Meynadier et al. (2012) which describes the mission in general as well as measurement principle.

2 The SYRTE DAC

The need for a specific Data Analysis Center appeared gradually in the last couple of years. As ground segment implementation unfolded, it became clear that the initial plan (i.e. full processing chain running on CADMOS premises with little or no operator interaction) would be difficult to achieve, because of the complexity of some of the processing required to reach ACES goals.

It was thus requested by ESA that SYRTE should take on from CADMOS for the scientific stages of data processing and analysis, and would then return processed results within the ACES archive. This is illustrated on Fig. 1.

Figure 2 shows the location of the MWL ground terminals across the world. ACES Ground Segment will process their data up to the L2/L3 level on a routine basis. ACES Investigators Working Group (IWG) will then prioritize which data will be further processed, and SYRTE DAC will then proceed accordingly, generating the L4 data that contains physical values of interest for the community (i.e. desynchronisation between round and space clocks and some by-products, namely Total Electron Content (TEC) of the ionosphere and pseudo-ranges).

The core software of the DAC has been developed at SYRTE for roughly ten years, from the very first ideas and prototype codes, to the present python code that powers data processing (whose implementation began in 2011). Simulation software has been developed in parallel, taking care to isolate has much as possible both

[1] LNE-SYRTE, Observatoire de Paris, PSL Research University, CNRS, Sorbonne Universités, UPMC Univ. Paris 06, 61 avenue de l'Observatoire, 75014 Paris, France

[2] Laboratoire Kastler Brossel, ENS-PSL Research University, CNRS, UPMC-Sorbonne Universités, Collège de France, 75005 Paris, France

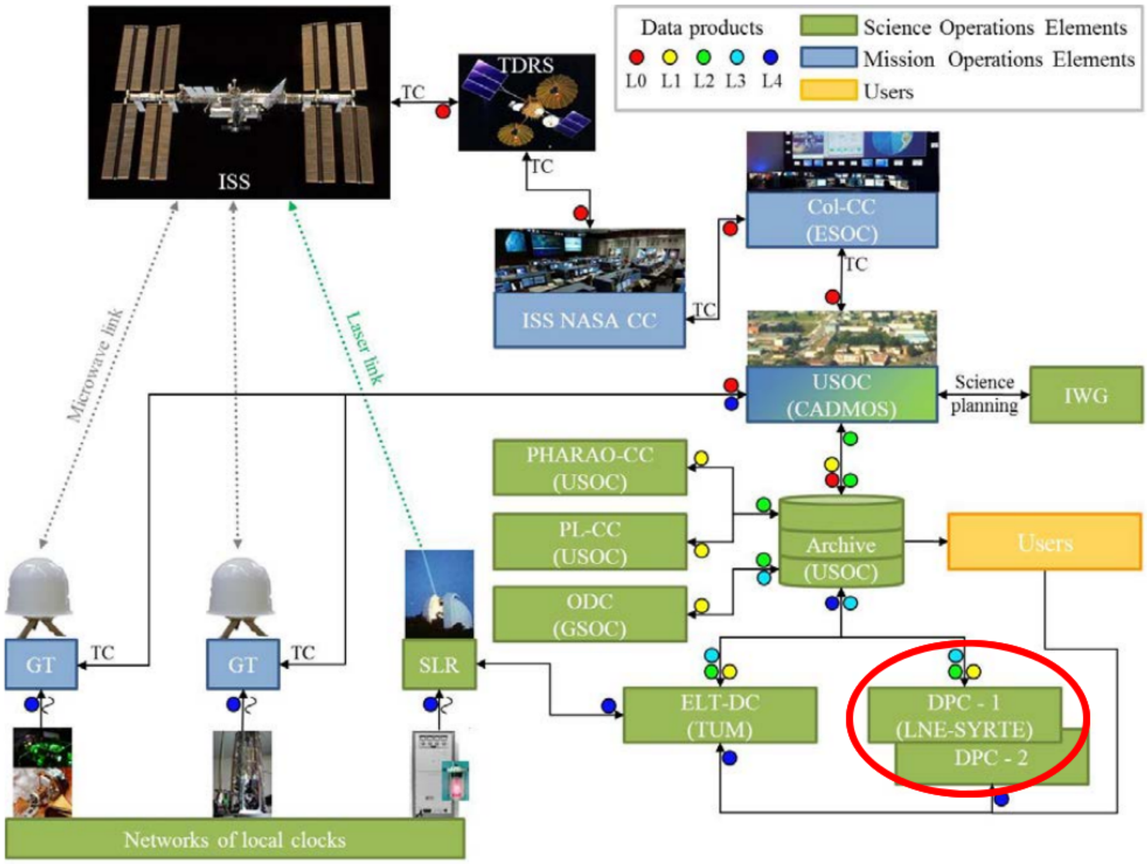

Fig. 1. The ACES ground segment organization. Red ellipse highlights the position of the Syrte DAC within the processing chain. Note that SYRTE will also host a ground Terminal (GT) but there will be no direct connection between DAC and GT, all data will go through CADMOS archive and SYRTE GT will be just another GT from DAC perspective.

codes (different languages, different developers). Our simulation is now the most complete simulation software for MWL data, and serves as benchmark for other pieces of software developed for the ground segment by the industrial contractor (Airbus D&S). It is highly flexible and allows to test almost any imaginable configuration, realistic or not, while mimicking as well as possible the kind of data that we expect to receive at the L1 level.

3 Processing of simulated data

Figure 3 shows typical results from our analysis software, when fed with simulated data. In this context we can compare the input values to the output and determine what errors are introduced by the measurement principle and its implementation. Note that, in the absence of any other noise, we are limited by the measurement method which is based on counters, which introduces a truncation in the measured values. Signal is composed of a carrier carrying a code : both can be used for measurement, the code giving absolute desynchronisation values with a 20 ps spread, while carrier has only 0.5 ps spread but have an offset which will be unknown (but constant as long as the MWL is switched on).

One of the major breakthroughs in the past year as been the implementation of a method which allows to recover this “unknown but constant” offset between successive ISS visibility period, enabling us to reach the expected specifications. This achievement is demonstrated on Fig. 4.

In the end, we have now demonstrated our ability to simulate data for long durations (more than expected ACES uninterrupted run durations, i.e. 20 days at most), and recover desynchronisation and other parameters at the expected level through data analysis. Work is ongoing to encapsulate the core software into an integrated DAC infrastructure which will automatize as much as possible the data analysis, easing the mandatory validation

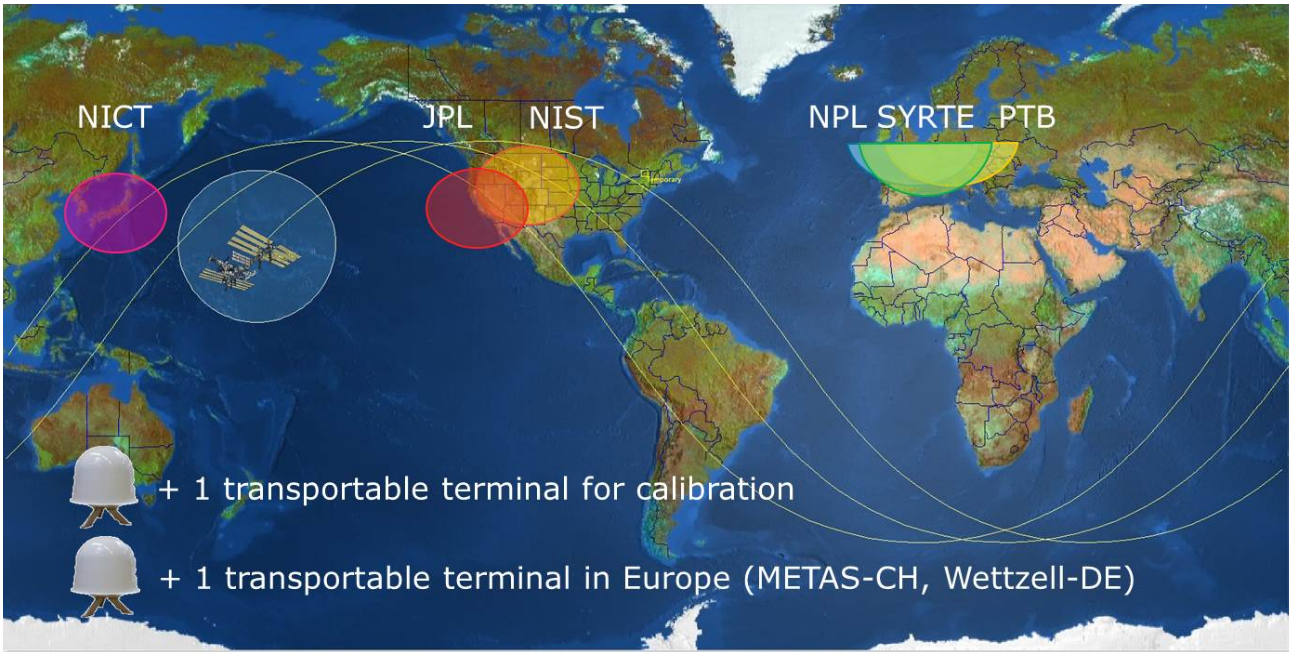

Fig. 2. Location of ACES MWL ground terminal, with visibility zones of the ISS showing possibilities for common-view operations (source : ESA)

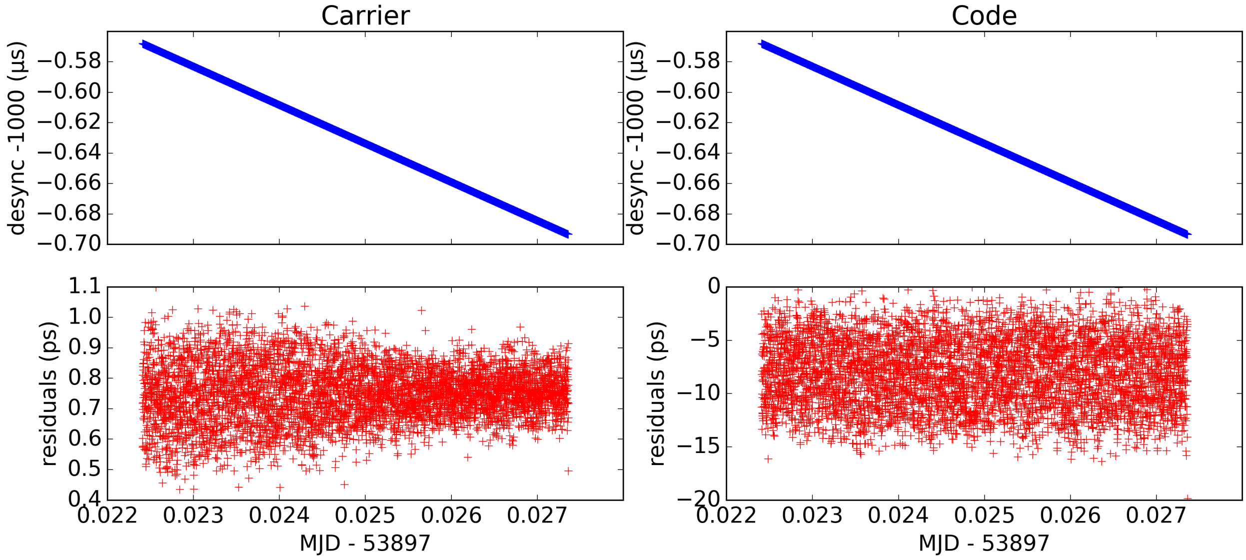

Fig. 3. Typical output from the analysis of simulated data. Top = input theoretical values of desynchronisation, bottom = residuals between those values and the ones coming out of the analysis. Noise caused by counter quantization (no other noise source simulated here), so this is the noise floor of this mesurement.

steps that will be performed while in flight.

4 Estimation of ISS position uncertainty impact

Our simulation/analysis combination can also be used to assert the impact of various factors on the measurement. A first application is to measure the impact of ISS orbitography uncertainty. First theoretical estimates (Duchayne et al. 2009) pointed out that this was a major contributor to the global error on desynchronisation determination, and Duchayne (2008) proposes a method to cancel it at first order by interpolating data such

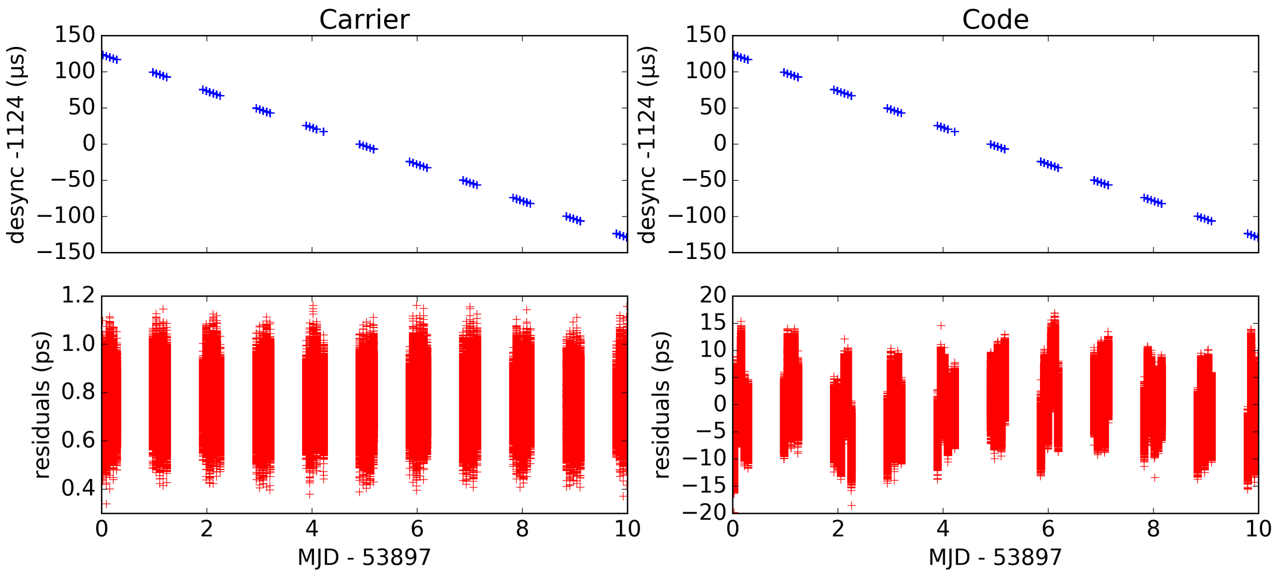

Fig. 4. 10 days ($\simeq$ 50 ISS passes) of data. Drift in desynchronisation corresponds to what is expected from General Relativity. For each pass, code data mean residuals stay within ± 10 ps but shows jitter, whereas carrier data residuals stay within a few tenths of ps around a common arbitrary offset.

that downlink signal leaves the ISS exactly as the same time as the uplink signal arrives (dubbed "lambda configuration").

In 2006 a study on ISS orbit determination used positioning data from 2 devices, one being the regular position and attitude sensor (SIGI), the other one being a more precise GNSS receiver. By combining both measurements we were able to estimate the position uncertainty we should expect from SIGI measurements, and also were able to generate synthetic orbitography with tunable yet realistic uncertainty. By feeding the correct orbitography to our simulation, then using its modified counterpart for the analysis, we were able to show how our limited knowledge of the ISS position can impact the ACES measurements.

Our conclusion is that even a factor 10 on the ISS position uncertainty will still allow to be well within specifications as long as individual desynchronisation determination is concerned. More details will be available in an article that is currently submitted.

5 Conclusion

The Syrte DAC core software is now close to completion, and we are currently setting up the infrastructure that will run it. Next step is to implement the interface with the main database at CADMOS and ensure smooth operation. This task is under way and should be operational as soon as the rest of the ground segment is.

However we expect a lot of adjustments to become necessary when real data comes out of scheduled end-to-end tests. Those first batches of real data are eagerly wanted to finish the validation of this work and fine-tune the DAC for the operational phase of the ACES-PHARAO mission

We thank Oliver Montenbruck (DLR) for providing ISS orbit data. This work was supported by CNES.

References

Duchayne, L. 2008, PhD thesis, Observatoire de Paris, France

Duchayne, L., Mercier, F., & Wolf, P. 2009, A&A, 504, 653

Meynadier, F., Delva, P., Le Poncin-Laffite, C., Laurent, P., & Wolf, P. 2012, in Journées de La SF2A 2012, 149–154

SF2A 2017
C. Reylé, P. Di Matteo, F. Herpin, É. Lagadec, A. Lançon, Z. Meliani, F. Royer (eds)

A TEST OF THE ONE-WAY ISOTROPY OF THE SPEED OF LIGHT FROM THE T2L2 SPACE EXPERIMENT

A. Belli[1], P. Exertier[1,] and E. Samain[1,]

Abstract.
The Time Transfer by Laser Link (T2L2) space experiment that is currently flying on-board Jason-2 (1335 km of altitude) provides an opportunity to make a test of the isotropy of the speed of light using one-way propagation on a non-laboratory scale. Following the general framework given by Mansouri & Sexl (1977), which permits violations of Einstein special relativity, we study the problem of deducing the isotropy of the speed between two clocks as the orientation path varies relative to an inertial reference frame. The short term stability of the T2L2 ground-to-space time transfer has been established at 5-6 ps at 60 seconds between a hydrogen maser and the on-board oscillator on use for the Jason-2 satellite. Nevertheless, during the satellite pass above a laser ranging station (of around 1000 seconds), the stability of the space oscillator is decreasing in $\tau^{3/2}$ that clearly impacts the expected performance of the present test. We thus give insights into certain modelling issues and processes, including time transfer problems which have a bearing on the global error budget. Our goal is to achieve an accuracy of $\frac{\delta c}{c} \approx 2 - 3.10^{-9}$ locally with a scope for improvement by cumulating numerous passes over the same laser ranging station.

Keywords: Isotropy of the speed of light, free space laser, clocks.

1 Introduction

The Newtonian universal law of gravity and mechanics form the framework of what we need to compute and measure in Newtonian systems. All systems of coordinates we use are equivalent or interchangeable, as long as they move with a constant velocity; furthermore, transformations between time scales and coordinate systems are linear functions or angular rotations. Einstein proposed the theory of Special Relativity (SR) to explain several effects that seemed to contradict Newtonian physics and mechanics. It deals with motions in inertial reference frames. He generalised the principle by stating that all inertial frames are totally equivalent for the performance of all physical experiments. The constancy (isotropy) of the velocity of light in inertial reference frames, which was first tested in the classic Michelson-Morley experiment, is a fundamental postulate of the SR theory.

Advances in technology have made possible new experimental tests; in particular, clock comparison is one major category of experiments for probing the SR theory and Lorentz invariance. Additionally, space is one of the most likely places where some manifestations, i.e. anisotropy of the one-way velocity of light, or variation of fundamental constants may be investigated. While providing access to greater variation of gravitational potentials, greater velocities, and full orientation coverage, space also mimics the well-understood and controlled laboratory environment. Thus, clock experiments in space will set new limits on Einstein's gravitational redshift and fundamental Lorentz symmetry; clocks enable science and open the door of chronometric geodesy.

In order to study the significance of a given experimental test of relativity, it is useful to employ a general framework. The work of Mansouri & Sexl (1977) gives a kinematic background, which assumes the existence of a preferred frame S' where space and light speed are isotropic while, in an inertial frame S moving with velocity w with respect to S', the one-way speed of light is no longer isotropic. From this formalism, the goal is to express one-way propagation from a source to a receiver (where the coordinates are expressed in the frame S) in terms of measurable quantities. The Time Transfer by Laser Link (T2L2) instrument, which was launched

[1] CNRS-UCA-OCA Géoazur UMR 7329 250 Rue Albert Einstein 06560 Valbonne France

in 2008 on-board the altimeter satellite Jason-2 (altitude of 1335 km), is one of the space experiments that actually enables both two-way and one-way laser ranging (Samain et al. 2008). Considering the design of the mission (repeatability, altitude, etc.) and technological aspects both on the ground and on board − very short laser pulses (20 ps), ground hydrogen maser(s), and picoseconds resolution and precision of event timers −, we study the potential performance of T2L2.

In Section 2, we start explaining the principle of T2L2 experiment then we discuss the main limiting factors of the present test of SR, notably about the stability induced by the on-board oscillator. We discuss the overall accuracy, of $\frac{\delta c}{c} \approx 2 - 3.10^{-9}$, that we expect from T2L2 data once modeled the behavior of the oscillator.

2 Time Transfer by Laser Ranging

The optical space time transfer allows to synchronise remote ground clocks that equip laser ranging stations of the ILRS (International Laser Ranging Service) network (Pearlman et al. 2002). A series of space missions have embarked a detector (mostly at 532 nm) and a sub-nanosecond event timer in addition to the reference clock of the spacecraft in view of very different objectives: navigation, fundamental physics and Time & Frequency (TF) metrology. Examples of time transfer by laser ranging mission that may be given include: LAser Synchronization from Stationary Orbit (LASSO) (Fridelance & Veillet 1995) and more recently Laser Time Transfer (LTT) (Fumin et al. 2008). Depending on the mission, the embarked clock can be a Rubidium, as e.g. on GNSS-Beidou or an Ultra Stable Oscillator (USO) as it is the case on the Lunar Reconnaissance Orbiter spacecraft orbiting the Moon (Mao et al. 2014) or on T2L2/Jason-2 (Samain et al. 2008). Additionally in 2018, the ESA project ACES on the ISS is the only one project which will deploy a cold atom clock in space together with a high accurate optical link (European Laser Transfer, ELT) in a single photon mode (Schreiber et al. 2009).

In all these experiments, the principle consists in measuring the propagation time of a light signal transmitted from one point on the ground to another in space; it is measured directly by comparing the phases of both clocks using the adopted laser time transfer system. Behind, the expected result of the potential test of SR simply lies in the ratio $\delta c/c$, where δc corresponds to the deviation of the speed (in the moving geocentric frame) in a preferred direction of space.

The pass of the satellite above a given laser ranging station, which potentially provides many directions of measurement, from the beginning to the end of the pass (around 140 degrees), is thus by itself a realisation of the test of SR.

The readings of a short laser pulse event (i) of around 20-30 ps is made by a H-maser (Hydrogen-maser) at emission (t_E) and reception (t_R) whereas the space clock records the arrival time of that pulse (τ_i) which thus is a proper time (Exertier et al. 2010). Einstein's second postulate would require that, for a series of measurements, the difference between the up and down links should be equal to a constant Δ_0 (initial clock offset) independent of the spatial orientation of each of the individual links. In that way, the time transfer equation is :

$$\Delta_i^E(t) = \tau_i - (t_E + 1way) + \Delta_0 + C + \Delta r \tag{2.1}$$

Where :

C are geometric and instrumental corrections

$1way$ is given by: $\frac{1}{2}(t_R - t_E - \Delta t_{Sagnac})$. The present Sagnac delay is caused by the motion of the receiver on the surface of the Earth due to the Earth's rotation during the time when the signal is on its way from the satellite. This delay is given by:

$$\Delta t_{Sagnac} = \frac{\bar{v}_E \bar{D}}{c^2}$$

Where :

- $\bar{v_E}$ the angular motion of the Earth
- $\bar{D}$: ground to spacecraft distance

Δr are relativistic corrections; for precision navigational systems operating in space on artificial satellites, three major systematic relativistic effects also need to be considered with regard to using the broadcast timing signal. Time dilation refers to the effect of the clock's velocity on its frequency; the effect of time dilation is given by:

$$\Delta t' = \frac{\Delta t}{\sqrt{1 - \frac{v^2}{c^2}}}$$

Where :

- v is the velocity of the satellite
- c the speed of light in the vacuum.

Because the clocks, at an altitude of thousands of km, experience a gravity field less than clocks on Earth, the gravitational red shift causes them to run fast. This effect can be estimated roughly, assuming circular orbits for the satellites, from:

$$\Delta t' = \Delta t\,\frac{\Delta\Phi}{c^2} = \Delta t\,\frac{1}{c^2}\left[\frac{GM_E}{r} - (\frac{GM_E}{a_E})\right]$$

Where :

- $\Delta\phi$ is the difference of potential between spacecraft and ground station,
- $\frac{GM_E}{r}$ the potential at the satellite
- $\frac{GM_E}{a_E}$ the geopotential of the Earth.

In order to precisely convert the elapsed on-board proper time to be compared to the ground time coordinate, these corrections have been integrated on a pass-by-pass level. The resulting stability of the ground-to-space time transfer link in addition to the typical propagation time are the primary parameters that constraint the performance of the SR test (Wolf 1995). As an example, when the T2L2 mission actually flights at 1335 km altitude, comparing to 450 km for ELT (on the ISS), it is not obvious that the ground-to-space stability of the latter has been improved by a factor 3 comparing to the former. On the other hand, the stability of the overall experiment (over a complete satellite pass above a laser ranging station) clearly depends on the on-board oscillator, which is an USO in case of T2L2/Jason-2 (3-5 10^{-13} between 10-100s, with an evolution in $\tau^{3/2}$ (Auriol & Tourain 2010)). Because of the small quantity we are looking for (an overall signal of a few ps) during the SR test, a deterministic model of the USO frequency is added to the above explained integration process (Belli et al. 2015). This model is essentially controlled by external data, such as temperature and level of particles flux (of around 85 MeV) both quantities being measured on-board. This avoids any empirical parameters that could absorb the SR test signal. An other source of instability which comes from the laser technology itself (pulse width, temperature of the optical bench, etc.) during a complete ground-to-space pass has been investigated by (Samain et al. 2014, 2015); the resulting analysis gave an error budget of 10-15 ps without bias. Thus, we will take into account at least three months of data from a dedicated laser ranging station, which roughly provides 60 passes per month.

Now the idea is to compare the phase readings of both clocks during a pass. Following the theoretical context given by Mansouri & Sexl (1977), to the lowest order in the velocity w of S relative to S' (CMB), the one-way experiment discussed here measures variation or anisotropy controlled by the amplitude:

$$A = \alpha w \cos\theta$$

where α is the coefficient in the expansion of the function in power of w^2, and θ is the angle between w and a direction relevant to the experiment in question, such as the propagation direction of light or the velocity vector of a moving clock. In SR, $\alpha = 0$, so that the anisotropy vanishes. For the velocity w, it is natural to choose the velocity of the Earth relative to the CMB; its amplitude and direction have been published many times. We will use the formalism:

$$c(\theta, w) = c\left[1 - \frac{(1+2\alpha)w}{c}\cos\theta + \mathcal{O}(c^3)\right] \tag{2.2}$$

3 Conclusion

Challenges of space deployment impose additional requirements on the reliability of the instruments and put pressure to minimise their mass, volume, and power requirements. A proposal for a new T2L2 instrument on the proposed E-GRASP mission (ESA, EE-9) takes place through the concerted efforts to be deployed for miniaturisation and space qualification.

Some other missions and projects have been designed to search for a variation of the fine-structure constant. The European Atomic Clock Ensemble in Space (ACES) is the only remaining space experiment based on clock tests, and is scheduled for launch in 2018. More recently, optical clocks have shown the potential for even greater precision than their microwave counterparts. Several mission proposals using optical clocks have already been proposed in the ESA Cosmic Vision program. In Europe, there is currently a great deal of work underway for potential future ESA projects on optical clocks and atom interferometry.

We wish to thank the French agency CNES for providing on-board T2L2/Jason-2 data for years, and additionally the laser ranging stations of the ILRS network for their corresponding efforts to provide the tracking Full Rate data. We thank also the Labex FIRST-TF and the GRGS for its support.

References

Auriol, A. & Tourain, C. 2010, Advances in Space Research, 46, 1484 , dORIS: Precise Orbit Determination and Applications to Earth Sciences

Belli, A., Exertier, P., Samain, E., et al. 2015, Advances in Space Research, 58, , scientific Applications of DORIS in Space Geodesy

Exertier, P., Samain, E., Bonnefond, P., & Guillemot, P. 2010, Advances in Space Research, 46, 1559 , dORIS: Precise Orbit Determination and Applications to Earth Sciences

Fridelance, P. & Veillet, C. 1995, Metrologia, 32, 27

Fumin, Y., Peicheng, H., Zhongping, Z., et al. 2008, in Proceedings of the 16th International Workshop on Laser Ranging, Poznan Poland, 12–17

Mansouri, R. & Sexl, R. U. 1977, General Relativity and Gravitation, 8, 515

Mao, D., Sun, X., Skillman, D., et al. 2014, in AGU Fall Meeting Abstracts, Vol. 1, 0503

Pearlman, M., Degnan, J., & Bosworth, J. 2002, Advances in Space Research, 30, 135

Samain, E., Exertier, P., Courde, C., et al. 2015, Metrologia, 52, 423

Samain, E., Vrancken, P., Guillemot, P., Fridelance, P., & Exertier, P. 2014, Metrologia, 51, 503

Samain, E., Weick, J., Vrancken, P., et al. 2008, International Journal of Modern Physics D, 17, 1043

Schreiber, U., Prochazka, I., Lauber, P., et al. 2009, in 2009 IEEE International Frequency Control Symposium Joint with the 22nd European Frequency and Time forum, 594–599

Wolf, P. 1995, Physical Review A, 51, 5016

Session 11

Galaxies decadence: theory and observation

RAM PRESSURE STRIPPING VERSUS TIDAL INTERACTIONS IN THE ABELL CLUSTERS A85 AND A496

F. Durret[1], H. Bravo-Alfaro[2], Y. Venkatapathy[2], Y. D. Mayya[3], C. Lobo[4], J. H. van Gorkom[5] and M. Lopez-Gutierrez[2]

Abstract.
We have undertaken a multi-wavelength survey of several nearby clusters of galaxies to compare the effects of ram pressure stripping to those of gravitational interactions and their role in galaxy evolution. We present here preliminary results for Abell 85 and Abell 496, based on optical, near infrared and HI imaging, as well as X-ray temperature maps.

Keywords: galaxies: clusters: individual: A85, A496

1 Introduction

Galaxy evolution is known to be influenced by environment, and galaxies in clusters may evolve differently than isolated ones. In particular, ram pressure can strip galaxies from their HI gas, thus reducing the star formation rate of cluster spirals. Other phenomena such as single or multiple tidal interactions (galaxy harassment), may also modify galaxy properties in clusters, in particular transforming late type into early type galaxies.

We have selected a sample of nearby clusters (redshift $z \leq 0.2$) with different masses, X-ray luminosities and stages of relaxation, to see how the cluster environment influences the galaxies. Our data include imaging in the optical, near-infrared (NIR) and in the HI 21 cm line. These observations are then compared to X-ray emissivity, temperature and metallicity maps, which give informations on the overall cluster properties and history. We present here preliminary results on two very different clusters: Abell 85 (hereafter A85), at redshift $z = 0.055$, which is known to have undergone and still be undergoing mergers, and Abell 496 (A496), at $z = 0.033$, a typical relaxed cluster.

The basic hypothesis we want to test is the following: if the HI component is perturbed but the stellar disk is not, it is most probable that ram pressure stripping causes the perturbations in the gas distribution; on the other hand, if both the HI component and the stellar disk are perturbed, then gravitational mechanisms such as mergers or galaxy harassment are most probably at stake.

2 The data

• In A85, we observed 68 galaxies in NIR (JHK') within 26 fields; ten of these fields cover HI detections reported by Bravo-Alfaro et al. (2009), and other zones containing pairs or groups of galaxies. Details on the observations and data reduction can be found in Venkatapathy et al. (2017). These data were combined with images in the ultraviolet (GALEX) and g band (CFHT/Megacam). HI data cubes were obtained with the NRAO-VLA.
• For A496, the HI images were also obtained with the NRAO-VLA. Optical imaging was obtained with the CFHT/Megacam in several bands and NIR with the CFHT/WIRCam.

[1] UPMC Université Paris 06, UMR 7095, Institut d'Astrophysique de Paris, 98bis Bd Arago, 75014 Paris, France
[2] Departamento de Astronomía, Universidad de Guanajuato, Apdo. Postal 144, Guanajuato 36000, Mexico
[3] Instituto de Astrofísica, Óptica y Electrónica. Luis Enrique Erro # 1, Puebla 72840, México
[4] Instituto de Astrofísica e Ciências do Espaço, Universidade do Porto, CAUP, Rua das Estrelas, PT4150-762 Porto, Portugal; Departamento de Física e Astronomia, Faculdade de Ciências, Universidade do Porto, Rua do Campo Alegre 687, PT4169-007 Porto, Portugal
[5] Department of Astronomy, Columbia University, New York, NY 10027, USA

We developed a new asymmetry index $\alpha_{\rm An}$ and applied it to our NIR images (Venkatapathy et al. 2017), showing that out of 41 bright galaxies 10 show mild to strong asymmetries. This suggests that tidal interactions must be playing an important role driving galaxy evolution in A85.

3 Results

3.1 The cluster A85

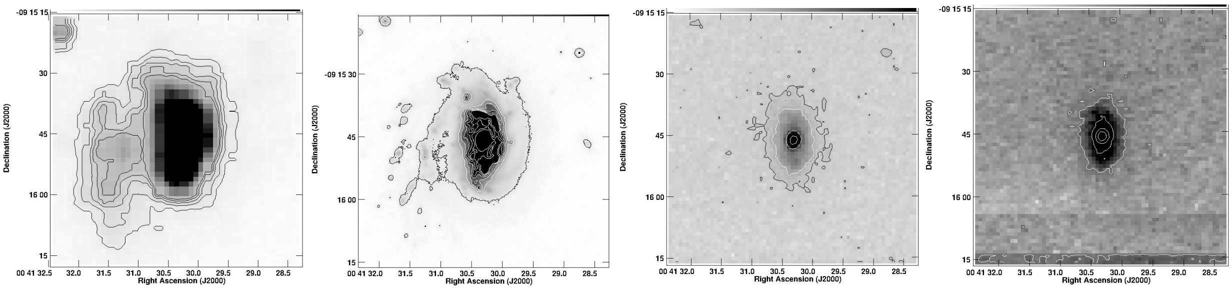

Fig. 1. From left to right: NUV, g, J and H band images of one of the jellyfish galaxies we observed, KAZ 364. The disrupted arms seen in the UV and blue bands are depleted of old stars (see the J and H bands), suggesting that ram pressure stripping is the mechanism responsible for the disruption (see text).

Among the galaxies studied in NIR in A85, three display long filaments in the blue bands; two of them are reported as "jellyfish" galaxies (see e.g. Poggianti et al. 2016). Interestingly, no old stars are found in our deep NIR images along the filaments, implying that the blue stars in these structures must be formed *in situ* and that ram pressure stripping is very active in A85 too. The most extreme case of a jellyfish galaxy (KAZ 364) is shown in Fig. 1.

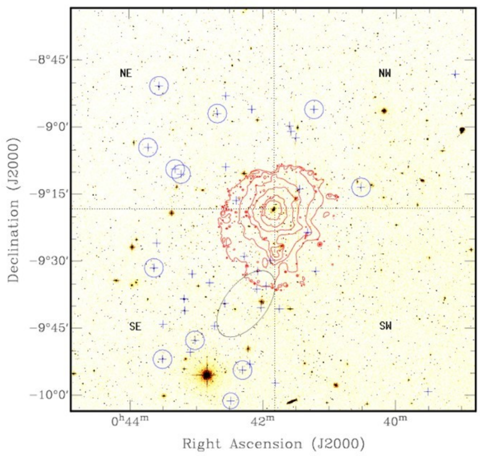

Fig. 2. Distribution of blue galaxies in A85 (crosses) superimposed on the optical image, with the galaxies detected in HI circled. The X-ray contours from ROSAT are in red. The blue ellipse southeast of the cluster shows the position of the X-ray filament (taken from Bravo-Alfaro et al. 2009).

The strong influence of ram pressure stripping in A85 is confirmed by the spatial distribution of the galaxies where HI is detected. As seen in Fig. 2, ten of them are in the east half of the cluster, while only two are detected in the west half. One hypothesis to explain this picture is that ram pressure stripping must have been much stronger in the west half of the cluster. X-ray maps allow to understand better what has happened, as explained below.

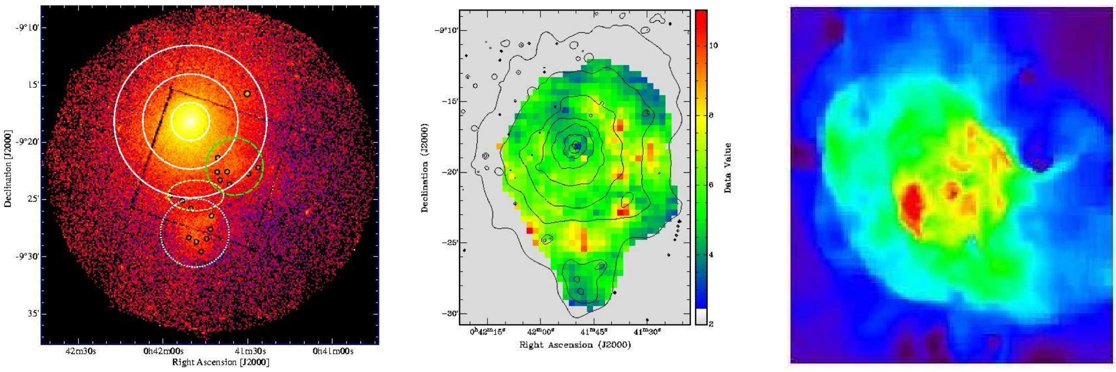

Fig. 3. From left to right: emissivity, temperature map of the X-ray gas in A85, and temperature map obtained from a hydrodynamical simulation by Bourdin et al. (2004).

In X-rays, A85 appears to be strongly perturbed. Figure 3 shows the emissivity and the temperature map of the X-ray gas in A85, derived from XMM-Newton observations (see Durret et al. 2005). This temperature map can be compared with that obtained from a hydrodynamical simulation by Bourdin et al. (2004) where a small cluster coming from the northwest has merged with the main cluster. The similarities between the temperature map observed for A85 and the simulation strongly suggest that a merger has taken place about 3–4 Gyr ago coming from the west or northwest. This can explain why ram pressure has been more efficient in the west half of the cluster, leading to a deficit of HI detections in this zone. An X-ray filament was also detected southeast of A85 and is believed to be made of groups falling onto the cluster, implying that a second merger is presently taking place, the impact region being hotter (Durret et al. 2003; Bravo-Alfaro et al. 2009).

3.2 The cluster A496

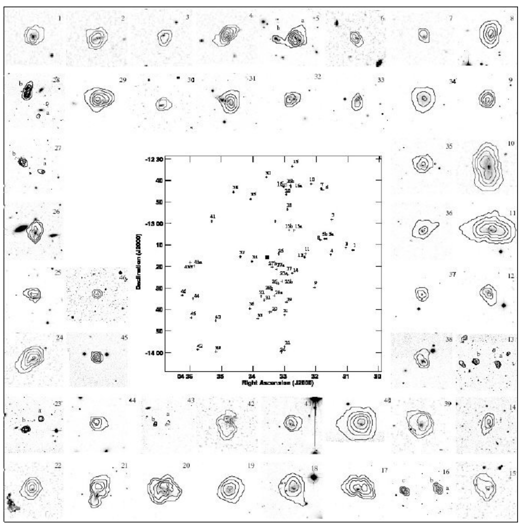

Fig. 4. Distribution of the galaxies detected in HI in A496 and corresponding individual HI maps (from Bravo-Alfaro et al., in preparation).

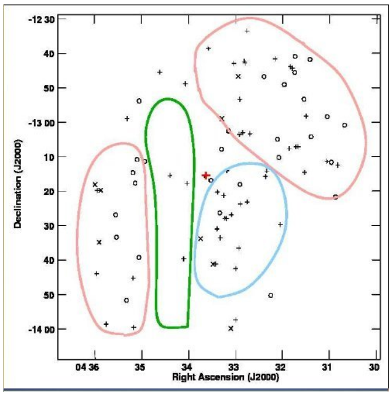

Fig. 5. Spatial distribution of the bright spiral galaxies ($B_T < 17.5$) in A496: in the pink zones, the galaxies are perturbed in HI but show a normal stellar disk in the NIR, while the blue zone is dominated by galaxies perturbed both in HI and NIR. The green region is unexpectedly depleted of spirals.

We fully mapped A496 in HI and detected 58 galaxies, many more than in A85 (Fig. 4). Out of those 58 galaxies between 20% and 30% show disruptions in HI, either with gas deficiency and/or asymmetries and offsets between HI and optical positions. Therefore, ram pressure stripping must play a less important role in A496 than in A85, as expected by the relaxed nature of A496. However, if we compare the distributions of the galaxies detected in HI with the galaxies showing asymmetries in the NIR, we find some surprising results: some galaxies appear somehow disrupted in HI but have rather normal stellar disks, and some are perturbed at both wavelengths. Interestingly, A496 does not display the expected pattern of HI-rich spirals projected at higher radius, and HI-deficient galaxies closer to the cluster core. Fig. 5 shows a rather complex spatial distribution of the brightest spiral galaxies and their various kinds of asymmetries. We can see that they are segregated spatially. It is very likely that the "pink" zones, where the galaxies are perturbed in HI but have a normal stellar disk, are zones where ram pressure stripping dominates. On the other hand, in the "blue" region, there are galaxies perturbed both in HI and NIR, where tidal interactions must dominate. The green zone appears nearly depleted of spirals. A detailed analysis of the HI properties of the A496 galaxies is under study (Bravo-Alfaro et al. in preparation).

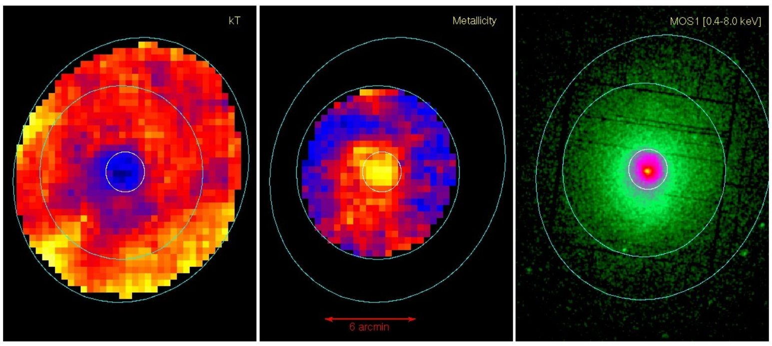

Fig. 6. From left to right: temperature, metallicity, and emissivity maps of the X-ray gas in A496. The two ellipses show the regions where the number of X-ray photons was sufficient to compute the temperature and metallicity maps.

The X-ray emissivity map of A496, which appears quite smooth and relaxed, contrary to A85, suggests that it is a relaxed cluster (Fig. 6). However, the temperature and metallicity maps are not perfectly symmetrical: the gas is hotter in the south part of the cluster, and a metallicity excess is also detected south of the cluster center. This suggests that a minor merger may have come from the south, the merging group or small cluster being of relatively small mass, since we do not see patches of hot gas in the temperature map as was the case in A85. However, this scenario is difficult to put together with the picture drawn by the very complex distribution of spiral galaxies and their HI content, that suggest recent falling of groups (or subclusters).

4 Conclusions

The study of asymmetries in the gas component (HI) and in the old stellar distribution (NIR) of spirals in A85 and A496, shows that in these clusters both mechanisms (ram pressure stripping and tidal interactions) are playing a role in galaxy evolution. By combining these techniques with X-ray maps we begin to disentangle the effects produced by each physical mechanism and we understand better the dynamical history of the clusters. In particular we link the cluster merger history with the zones where different physical mechanisms dominate the transformation of galaxy morphology.

References

Bourdin H., Sauvageot, J.-L., Slezak E., Bijaoui A., Teyssier R. et al. 2004, A&A 414, 429

Bravo-Alfaro H., Caretta C.A., Lobo C. et al. 2009, A&A 495, 379

Durret F., Lima Neto G.B., Forman W., Churazov E. 2003, A&A 403, L29

Durret F., Lima Neto G.B., Forman W. 2005, A&A 432, 809

Poggianti B., Fasano G., Omizzolo A. et al. 2016, AJ 151, 78

Venkatapathy Y., Bravo-Alfaro H., Mayya Y.D. et al. 2017, AJ in press, arXiv:1709.06681

F.D. acknowledges long term support from CNES. HBA acknowledges support from DAIP and CONACyT. CL acknowledges support by Fundação para a Ciência e a Tecnologia (FCT, Portugal) through national funds (UID/FIS/04434/2013) and by FEDER through COMPETE2020 (POCI-01-0145-FEDER-007672).

CALIBRATING THE PLANCK CLUSTER MASS SCALE WITH CLUSTER VELOCITY DISPERSIONS

S. Amodeo[1], S. Mei[1, 2], S. A. Stanford[3], J. G. Bartlett[4], C. L. Lawrence[5], R. R. Chary[6], H. Shim[7], F. Marleau[8] and D. Stern[5]

Abstract. The potential of galaxy clusters as cosmological probes critically depends on the capability to obtain accurate estimates of their mass. This will be a key measurement for the next generation of cosmological surveys, such as Euclid. The discrepancy between the cosmological parameters determined from anisotropies in the cosmic microwave background and those derived from cluster abundance measurements from the *Planck* satellite calls for careful evaluation of systematic biases in cluster mass estimates. For this purpose, it is crucial to use independent techniques, like analysis of the thermal emission of the intracluster medium (ICM), observed either in the X-rays or through the Sunyaev-Zeldovich (SZ) effect, dynamics of member galaxies or gravitational lensing. We discuss possible bias in the *Planck* SZ mass proxy, which is based on X-ray observations. Using optical spectroscopy from the Gemini Multi-Object Spectrograph of 17 *Planck*-selected clusters, we present new estimates of the cluster mass based on the velocity dispersion of the member galaxies and independently of the ICM properties. We show how the difference between the velocity dispersion of galaxy and dark matter particles in simulations is the primary factor limiting interpretation of dynamical cluster mass measurements at this time, and we give the first observational constraints on the velocity bias.

Keywords: Cosmology: cosmic background radiation, Cosmology: observations, Galaxies: clusters: general, Galaxies: distances and redshifts

1 Introduction

Within the standard cosmological model, the formation of structures takes place from the gravitational collapse of small perturbations in a quasi-homogeneus Universe dominated by cold dark matter. In this frame, galaxy clusters are the largest nearly virialised collapsed objects in the observable Universe, and they are also the last to form. Therefore, they are fundamental tools to test the cosmological scenario and for understanding the formation and evolution of cosmic structures. The potential of galaxy clusters as cosmological probes depends on the capability to obtain accurate estimates of their mass (Allen et al. 2011). However, mass is not directly observable, it can be estimated through many methods based on different physical properties. Clusters are composed by about the 85% of dark matter, 10% of gas and 5% of galaxies. All these components can be investigated with multi-wavelenght observations. Methods to estimate the mass are based on the analysis of the thermal emission of the intracluster medium (ICM), observed either in the X-rays or through the Sunyaev-Zeldovich (SZ) effect, or from optical observations through the dynamics of member galaxies or gravitational lensing. Each method is affected by systematic effects, so a comparison of the estimates obtained with different techniques is a critical check on the reliability of each method under different conditions, and also a test of the cosmological scenario.
We present here the relation between velocity dispersion and mass for a sample of clusters detected by *Planck* and followed-up with spectroscopic observations at the Gemini telescopes, with the aim to calibrate the mass-observable scaling relation.

[1] LERMA, Observatoire de Paris, PSL Research University, CNRS, Sorbonne Universités, UPMC Univ. Paris 06, F-75014 Paris, France
[2] Université Paris Denis Diderot, Université Paris Sorbonne Cité, 75205 Paris Cedex13, France
[3] Department of Physics, University of California Davis, One Shields Avenue, Davis, CA 95616, USA ; Institute of Geophysics and Planetary Physics, Lawrence Livermore National Laboratory, Livermore, CA 94550, USA
[4] APC, AstroParticule et Cosmologie, Université Paris Diderot, CNRS/IN2P3, CEA/lrfu, Observatoire de Paris, Sorbonne Paris Cité, 10 rue Alice Domon et Léonie Duquet, 75205, Paris Cedex 13, France
[5] Jet Propulsion Laboratory, California Institute of Technology, 4800 Oak Grove Drive, Pasadena, California, USA
[6] Infrared Processing and Analysis Center, California Institute of Technology, Pasadena, CA 91125, USA
[7] Department of Earth Science Education, Kyungpook National University, Republic of Korea
[8] Institute of Astro and Particle Physics, University of Innsbruck, 6020, Innsbruck, Austria

2 The Planck mass bias

We have selected a subsample of 17 *Planck* clusters in the last PSZ2 catalog (Planck Collaboration et al. 2016), in a broad range of mass measured by *Planck*, $2 \times 10^{14} M_{\odot} \lesssim M \lesssim 10^{15} M_{\odot}$, in the redshift range $0.16 < z < 0.44$. These targets were followed-up for spectroscopic observations with Gemini (GMOS-N and GMOS-S), from which we could typically confirm $\sim$ 20 (10-40) galaxies in each cluster, and get average cluster redshifts and velocity dispersions (see Amodeo et al. 2017, for a detailed description of the sample selection and the spectroscopic analysis).

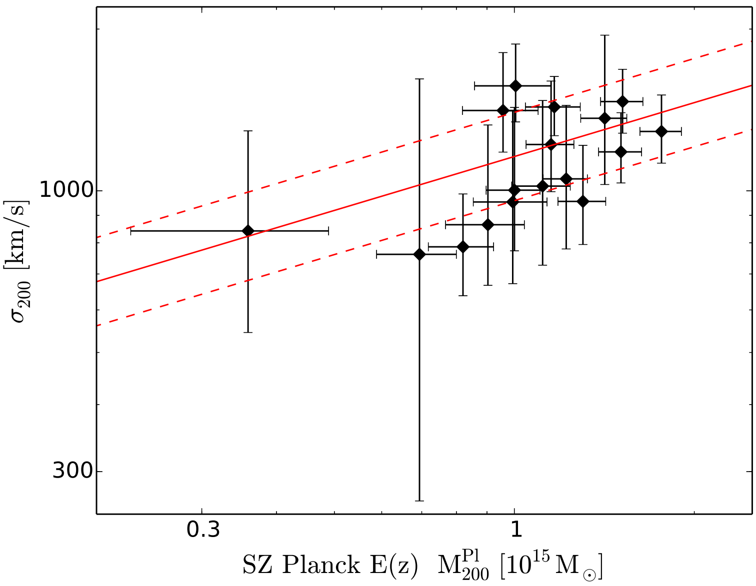

Fig. 1. Relation between the *Planck* SZ mass proxy and velocity dispersion for our sample of 17 galaxy clusters observed with Gemini (diamonds). The solid red line shows the best fit to the functional form of Eq. (2.1) in log-space, where the slope is set to 1/3, with the dashed lines delineating the dispersion of the data about the best-fit line.

Figure 1 plots the velocity dispersions that we obtained versus the mass estimated by *Planck*. The red curve is the fit to the data of the following power-law relation predicted for complete virialization*:

$$\sigma_{200} = A \left[\frac{h(z)\, M_{200}}{10^{15} M_{\odot}} \right]^{1/3} . \tag{2.1}$$

The normalization A is the only free parameter in the fit, while the slope is fixed to 1/3, which is the value predicted for a virial relation and confirmed by simulations.
Planck mass estimates are based on a combination of *Planck* data and an X-ray scaling relation established with XMM-Newton (Planck Collaboration et al. 2014). Any possible systematic due to this assumption or to the X-ray analysis, and more generally, any difference between mass determined by *Planck* and the true halo mass is expressed in terms of the bias factor $(1 - b) = M_{200}^{\mathrm{Pl}}/M_{200}$. In order to estimate this bias, we compare the fit of our observed relation to Eq. (2.1) with the relation predicted by Evrard et al. (2008) from DM simulations, accounting for effects due to GMOS finite aperture, Eddington bias and correlated scatter between velocity dispersion and the *Planck* mass proxy. The details of this analysis are discussed in Amodeo et al. (2017). The main problem in calibrating the $\sigma - M$ relation with simulations is that galaxies may have a different velocity dispersion than their dark matter host because they inhabit special locations within the cluster (e.g., subhalos). While the scaling relation is very well constrained for simulations of dark matter particles, it is not as well understood for galaxies, as discordant results in the literature demonstrate (e.g. Munari et al. 2013; Caldwell et al. 2016). We find that the unknown velocity bias of the member galaxy population, quantified by the ratio between the galaxy and the DM velocity dispersions, is the largest source of uncertainty in our result on the mass bias parameter:

*Estimates of mass and velocity dispersion are quoted at a radius R_{200}, within which the cluster density is 200 times the critical density of the universe at the cluster's redshift.

$(1-b) = (0.51 \pm 0.09) b_{\rm v}^3$. Using a baseline value of $b_{\rm v} = 1.08$ from Munari et al. (2013), we find $(1-b) = (0.64 \pm 0.11)$, consistent within weak lensing results and within 1σ of the value $(1-b) = (0.58 \pm 0.04)$ needed to reconcile the *Planck* cluster counts with the primary CMB.
Turning the analysis around, we propose to obtain observational constraints on the velocity bias by combining accurate mass estimates from weak lensing measurements with velocity dispersion measurements. Assuming a prior on the mass bias from Penna-Lima et al. (2017), we derive $b_{\rm v} = 1.12 \pm 0.07$, i.e., $b_{\rm v} \gtrsim 0.9$ at 3σ.

3 Conclusions

We have measured the *Planck* cluster mass bias using velocity dispersions of a subsample of 17 *Planck*-detected clusters. We have achieved a precision of 17% on the mass bias measurement with our limited sample. On the other hand, we have provided the first observational constraints on the velocity bias combining accurate mass estimates from weak lensing with velocity dispersion measurements. Assuming that simulations and observations will eventually settle on a value for the velocity bias, this motivates continued effort to increase our sample size to produce a 10% or better determination, comparable to recent weak lensing measurements.

Based on observations obtained at the Gemini Observatory (Programs GN-2011A-Q-119, GN-2011B-Q-41, and GS-2012A-Q-77; P.I. J.G. Bartlett), which is operated by the Association of Universities for Research in Astronomy, Inc., under a cooperative agreement with the NSF on behalf of the Gemini partnership: the National Science Foundation (United States), the National Research Council (Canada), CONICYT (Chile), Ministerio de Ciencia, Tecnologa e Innovacin Productiva (Argentina), and Ministrio da Cincia, Tecnologia e Inovao (Brazil).

References

Allen, S. W., Evrard, A. E., & Mantz, A. B. 2011, ARA&A, 49, 409
Amodeo, S., Mei, S., Stanford, S. A., et al. 2017, ApJ, 844, 101
Caldwell, C. E., McCarthy, I. G., Baldry, I. K., et al. 2016, MNRAS, 462, 4117
Evrard, A. E., Bialek, J., Busha, M., et al. 2008, ApJ, 672, 122
Munari, E., Biviano, A., Borgani, S., Murante, G., & Fabjan, D. 2013, MNRAS, 430, 2638
Penna-Lima, M., Bartlett, J. G., Rozo, E., et al. 2017, A&A, 604, A89
Planck Collaboration, Ade, P. A. R., Aghanim, N., et al. 2014, A&A, 571, A29
Planck Collaboration, Ade, P. A. R., Aghanim, N., et al. 2016, A&A, 594, A27

SF2A 2017
C. Reylé, P. Di Matteo, F. Herpin, É. Lagadec, A. Lançon, Z. Meliani, F. Royer (eds)

QUENCHING OF THE STAR FORMATION ACTIVITY OF GALAXIES IN DENSE ENVIRONMENTS

A. Boselli[1]

Abstract. The nearby Universe is an ideal laboratory to study the effects of the environments on galaxy evolution. We have analysed the multifrequency properties of galaxies in the nearby clusters Virgo, Coma, and A1367. We have shown that the HI gas content and the activity of star formation of the late-type galaxies start to gradually decrease inwards $\sim$ one virial radius. We have also shown that late-type galaxies in these clusters have truncated HI, H_2, dust, and star forming discs once the HI gas content is removed by the harsh environment. Some of these galaxies also exibit spectacular tails of atomic neutral, ionised, or hot gas without any counterpart in the stellar component. All this evidence favors ram pressure stripping as the dominant mechanism responsible for the gas removal from the disc, and for the following quenching of the star formation activity.

Keywords: Galaxies: evolution, galaxies: interactions, galaxies: ISM, galaxies: star formation

1 Introduction

It is now well established that the main drivers of galaxy evolution are the total mass of galaxies (Cowie et al. 1996; Gavazzi et al. 1996; Boselli et al. 2001) and the environment in which galaxies resides (Boselli & Gavazzi 2006, 2014). The simple analysis of a colour-magnitude relation done on a large sample of local objects indicates that galaxies form two main sequences, one composed of red passive objects and one of blue star forming systems. The fraction of red objects increases with increasing stellar mass of the system and with the density of objects within the Universe (Peng et al. 2010; Gavazzi et al. 2010).

Different physical processes have been invoked to explain this observational evidence. Merging (e.g. Kauffmann et al. (1993)), AGN feedback (e.g. Kauffmann et al. (2003)), or secular evolution (Gavazzi et al. 1996; Boselli et al. 2001; Boissier & Prantzos 2000; Boissier et al. 2001), including the modulation induced by bars on the star formation activity of rotating systems (Gavazzi et al. 2015; Consolandi et al. 2017a), have been proposed to explain the increase of red galaxies with stellar mass (mass quenching). The morphology-segregation effect (Dressler 1980), as well as the decrease of the star formation activity of galaxies in dense regions (environmental quenching), have been explained with other mechanism. These can be devided in two main families, those related to the gravitational interactions expected in high density regions (galaxy-galaxy - Merritt (1983); galaxy-cluster - Byrd & Valtonen (1990); harassment - Moore et al. (1998)), and those due to the interaction of the interstellar medium (ISM) of galaxies moving at high velocity ($\sim$ 1000 km s^{-1}) within the hot (10^7-10^8 K) and dense ($\rho_{ICM} \sim 10^{-3}$ cm^{-3}; Sarazin (1986)) intracluster medium (ICM) trapped within the potential well of clusters (ram pressure - Gunn & Gott (1972); viscous stripping - Nulsen (1982); thermal evaporation - Cowie & Songaila (1977); starvation - Larson et al. (1980)). All these processes can start to be active well before galaxies enter rich clusters, when they aggregate in small groups that will later infall into the most massive sturctures observed in the local Universe (pre-processing, Dressler (2004); Cortese et al. (2006)).

The identification of the dominant quenching process is crucial to tune cosmological simulations and semi-analytic models of galaxy evolution. This exercise, however, is very difficult, since different quenching mechanisms are expected to dominante in different environments, at different epochs, and on galaxies of different mass.

[1] Aix Marseille Université, CNRS, LAM (Laboratoire d'Astrophysique de Marseille), UMR 7326, F-13388, Marseille, France

2 Environmental quenching

The dominant quenching mechanism in high density regions can be identified by combining the multifrequency analysis of complete samples of galaxies selected according to strict criteria, or the detailed study of representative objects, with the predictions of tuned models and simulations. The statistical analysis of complete samples can be used to derive observationally the typical angular scales and timescales on which the perturbation is active, and compare them to the predictions of models and simulations. Indeed, gravitational perturbations, such as galaxy harassment, are expected to be efficient well within the virial radius of the high density region where the density of galaxies is sufficiently high (e.g. Moore et al. (1998)), and require long timescales (several Gyr) to allow multiple fly-by encounters to occur. Starvation (the gentle consumtion of the cold gas located on the disc of the galaxy via star formation once infall of fresh gas is stopped), on the contrary, starts to be active at several virial radii, when the galaxy becomes for the first time satellite of the cluster halo (Larson et al. 1980). Starvation also requires several Gyr to totally quench the star formation activity of the perturbed galaxies given the large amount of gas available on their discs (Boselli et al. 2006, 2014d,b,c). Models and simulations indicate that ram pressure is much more efficient since it is able to remove most of the gas from the disc in a few hundreds Myr, and totally quench the activity of star formation in ≤ 1.5 Gyr (Roediger & Hensler 2005; Tonnesen & Bryan 2009). Furthermore, the observations of peculiar galaxies with extended tails of gas, witnessing an ongoing stripping process, well outside the virial radius suggest that this mechanism start to be efficient even at the periphery of clusters (Chung et al. 2007; Scott et al. 2012).

Other clear imprints of the different mechanisms are the presence of asymmetric low surface brightness tails of gas and stars in gravitational perturbations, combined with an enached nuclear star formation activity, and the presence of truncated stellar discs and bars (e.g. Mastropietro et al. (2005)). An homogeneous fading of the star formation rate along the disc of the perturbed galaxies, with possibly an increase of the contribution of the nuclear feedback, is instead expected in a starvation scenario. Gaseous tails with a cometary shape without any old stellar counterpart, as well as truncated discs in the different components of the ISM (gas - dust) and in the youngest stellar populations are produced by the outside-in stripping of the gas in a ram pressure stripping event.

3 The nearby Universe

In the last years we have done a huge effort to identify the dominant perturbing mechanism in nearby clusters of galaxies. This effort has been done both observationaly, collecting data at different frequencies to map the distribution of the different components of the ISM (cold gas: HI, H_2; ionised gas: Halpha; hot gas: X-rays; dust: infrared) and of the different stellar populations in representative nearby clusters such as Virgo, Coma, and A1367 (Boselli et al. 2014d; Gavazzi et al. 2010, 2013), and through the developement of tuned models and simulations expressely tailored to take into account the effects of the different perturbing mechanisms typical of rich environments (Boselli et al. 2006, 2008a,b). All results consistently indicate ram-pressure as the dominant mechanism in nearby clusters of mass 10^{14}-10^{15} $M_\odot$. Indeed we have observed that the the stripping of the ISM, which occurs on HI (Gavazzi et al. 2005, 2006, 2013; Boselli et al. 2014d), H_2 (Fumagalli et al. 2009; Boselli et al. 2014b; Scott et al. 2015), and dust (Cortese et al. 2010, 2012b), is able to quench the activity of star formation of galaxies up to $\simeq$ the virial radius of the cluster. We have also shown that the stripping of all the difference phases of the ISM is outside-in, producing truncated HI, H_2 and dust discs (Fig. 1; Cayatte et al. (1994); Cortese et al. (2010); Boselli et al. (2014b)). As a consequence, the activity of star formation in the perturbed galaxies continues only in the inner disc, while the outer disc is dominated by an old stellar populations (Boselli & Gavazzi 2006; Boselli et al. 2006, 2015; Koopmann et al. 2006; Cortese et al. 2012a; Fossati et al. 2013). There is also clear evidence that a large fraction of late-type galaxies in these and other nearby clusters have extended cometary tails of stripped gas witnessing an ongoing ram pressure stripping event. These tails have been observed in radio continuum (Gavazzi et al. 1995), HI (Chung et al. 2007; Scott et al. 2012), X-rays (Sun et al. 2007), but are becoming more and more evident in very deep Hα narrow-band imaging now made possible thanks to large panoramic detectors coupled to 4-8 metre class telescopes (Gavazzi et al. 2001a; Yoshida et al. 2002; Yagi et al. 2007, 2010, 2017; Kenney et al. 2008; Fossati et al. 2012, 2016; Fumagalli et al. 2014; Boselli et al. 2016a). These results are at the origin of the Virgo Environmental Survey Tracing Ionised Gas Emission (VESTIGE; Boselli et al. in prep.), a narrow-band Hα imaging survey of the Virgo cluster that we are undertaking at the CFHT.

More recently we have tried to quantify the typical timescale for the quenching of the star formation activity of late-type galaxies in the Virgo cluster (Ciesla et al. 2016; Boselli et al. 2016b). We have done this exercice

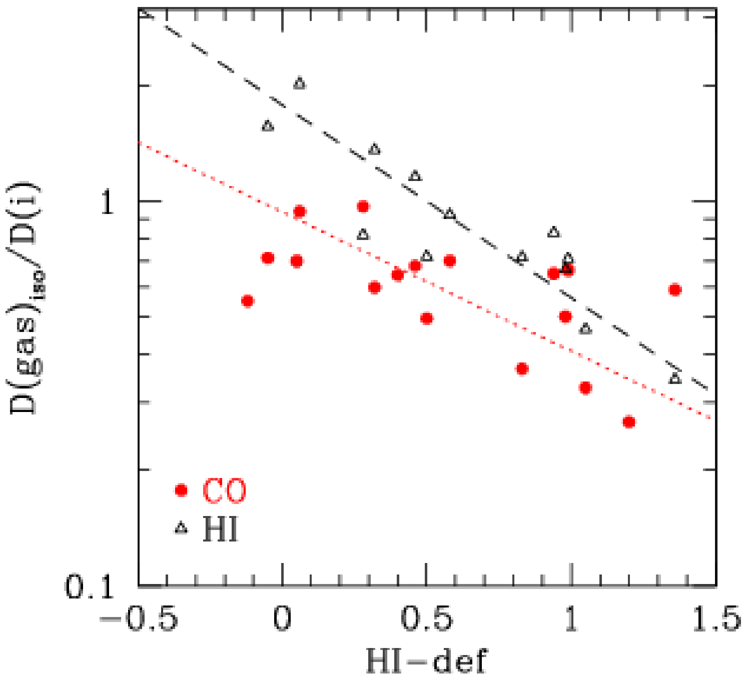

Fig. 1. Relationship between the gas-to-stellar (i-band) isophotal diameter ratio and the HI-deficiency parameter for galaxies of the Herschel Reference Survey, a stellar mass-selected, volume-limited sample including the Virgo cluster (Boselli et al. 2010). Red filled dots are for CO data, black open triangles for HI data. The red dotted and black dashed lines indicate the best fit to the molecular and atomic gas data, respectively. Adapted from Boselli et al. (2014b)

by fitting the observed UV-to-far infrared spectral energy distribution (SED) of ~ 300 galaxies in the Herschel Reference Survey (HRS; Boselli et al. (2010)) with the CIGALE SED fitting code (Noll et al. 2009). To better constrain the typical quenching timescale we have added to the available 20 photometric bands the integrated spectra of the galaxies (Boselli et al. 2013) which includes several age-sensitive absorption lines from the Balmer series, and the narrow-band Hα imaging sensitive to the youngest stellar populations ($< 10^7$ yr; Boselli et al. (2009)). To reproduce the quenching episode we have used truncated star formation histories characterised by a secular evolution (indicised on the velocity rotation of the galaxy, available from HI spectra, Boselli et al. (2014a)), where the only free parameters are the epoch of the quenching and the quenching factor. This star formation history well matches the observed SED of perturbed galaxies (Boselli et al. 2016b). The analysis of this sample indicated that in most of the HI-deficient galaxies of the Virgo cluster the activity of star formation has been quenched only recently, ≤ 250 Myr, as depicted in Fig. 2, and thus that the quenching episod has been rapid, as expected in a ram pressure stripping scenario (Boselli et al. 2016b).

Although ram pressure seems the dominant mechanism perturbing galaxies in these nearby clusters, there are also examples of objects undergoing other kinds of perturbations. A clear example is the galaxy NGC 4438 in Virgo, where the presence of extended tidal tails in the stellar component are a clear sign of a gravitational perturbation (Combes et al. 1988; Boselli et al. 2005; Vollmer et al. 2005). In other objects gravitational perturbations can contribute to make ram pressure stripping more efficient such as in the three galaxies CGCG 97-73, 97-79, and 97-87 in A1367 (Gavazzi et al. 2001a,b; Consolandi et al. 2017b), or in NGC 4654 in Virgo (Vollmer 2003). Among these the most spectacular case is certainly the Blue Infalling Group in A1367 (BIG) first discovered by Sakai et al. (2002) and Gavazzi et al. (2003) and then studied in detail by Cortese et al. (2006). Indeed, this is the best example of pre-processing in a nearby cluster.

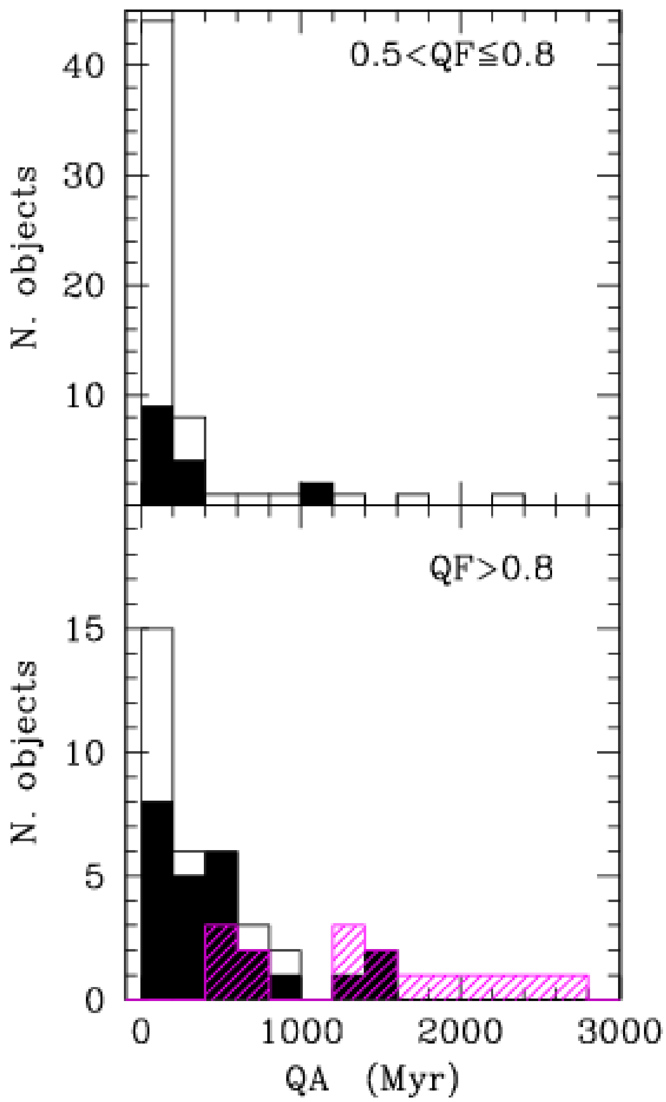

Fig. 2. Distribution of the quenching age parameter (QA) with a quenching factor 0.5<QF<0.8 upper panel) and QF>0.8 (lower panel). The magenta histogram is for early-type galaxies, the empty histogram for all late-type galaxies, and the black shaded histogram for HI-deficient late-type systems. Adapted from Boselli et al. (2016b)

4 Conclusions

The multifrequency analysis of late-type galaxies in the nearby clusters Virgo, Coma, and A1367, the detailed study of representative objects, and the results of models and simulations tailored to reproduce the observed properties of representative objects consistently indicate ram pressure stripping as the dominant mechanism modulating the star formation history in rich environments. These results, however, are in apparent disagreement with those found by the analysis of other larger samples of local or high-z galaxies with optical data which rather suggest a gentle decrease of the star formation activity over ~ 5 Gyr followed by a rapid decrease in the last 0.5 Gyr (pre-processing; e.g. Wetzel et al. (2012, 2013); Fossati et al. (2017)), or a slow decrease of the star formation activity (starvation: e.g. McGee et al. (2009); Haines et al. (2015)). They also disagree with the prediction of semi-analytic models of galaxy evolutions or cosmological simulations, which generally overpredict the number of quiescent galaxies with respect to observations (e.g. Hirschmann et al. (2014)). An important effort by observers and modelers is still necessary if we want to fully understand the role of the environment on galaxy evolution.

I would like to thanks all my collaborators with whom I had the pleasure to work during these years. This work has been partly supported by the French national program PNCG

References

Boissier, S., Boselli, A., Prantzos, N., & Gavazzi, G. 2001, MNRAS, 321, 733
Boissier, S. & Prantzos, N. 2000, MNRAS, 312, 398
Boselli, A., Boissier, S., Cortese, L., et al. 2009, ApJ, 706, 1527
Boselli, A., Boissier, S., Cortese, L., & Gavazzi, G. 2008a, ApJ, 674, 742
Boselli, A., Boissier, S., Cortese, L., & Gavazzi, G. 2008b, A&A, 489, 1015
Boselli, A., Boissier, S., Cortese, L., et al. 2005, ApJ, 623, L13
Boselli, A., Boissier, S., Cortese, L., et al. 2006, ApJ, 651, 811
Boselli, A., Cortese, L., & Boquien, M. 2014a, A&A, 564, A65
Boselli, A., Cortese, L., Boquien, M., et al. 2014b, A&A, 564, A67
Boselli, A., Cortese, L., Boquien, M., et al. 2014c, A&A, 564, A66
Boselli, A., Cuillandre, J. C., Fossati, M., et al. 2016a, A&A, 587, A68
Boselli, A., Eales, S., Cortese, L., et al. 2010, PASP, 122, 261
Boselli, A., Fossati, M., Gavazzi, G., et al. 2015, A&A, 579, A102
Boselli, A. & Gavazzi, G. 2006, PASP, 118, 517
Boselli, A. & Gavazzi, G. 2014, A&A Rev., 22, 74
Boselli, A., Gavazzi, G., Donas, J., & Scodeggio, M. 2001, AJ, 121, 753
Boselli, A., Hughes, T. M., Cortese, L., Gavazzi, G., & Buat, V. 2013, A&A, 550, A114
Boselli, A., Roehlly, Y., Fossati, M., et al. 2016b, A&A, 596, A11
Boselli, A., Voyer, E., Boissier, S., et al. 2014d, A&A, 570, A69
Byrd, G. & Valtonen, M. 1990, ApJ, 350, 89
Cayatte, V., Kotanyi, C., Balkowski, C., & van Gorkom, J. H. 1994, AJ, 107, 1003
Chung, A., van Gorkom, J. H., Kenney, J. D. P., & Vollmer, B. 2007, ApJ, 659, L115
Ciesla, L., Boselli, A., Elbaz, D., et al. 2016, A&A, 585, A43
Combes, F., Dupraz, C., Casoli, F., & Pagani, L. 1988, A&A, 203, L9
Consolandi, G., Dotti, M., Boselli, A., Gavazzi, G., & Gargiulo, F. 2017a, A&A, 598, A114
Consolandi, G., Gavazzi, G., Fossati, M., et al. 2017b, ArXiv e-prints
Cortese, L., Boissier, S., Boselli, A., et al. 2012a, A&A, 544, A101
Cortese, L., Ciesla, L., Boselli, A., et al. 2012b, A&A, 540, A52
Cortese, L., Davies, J. I., Pohlen, M., et al. 2010, A&A, 518, L49
Cortese, L., Gavazzi, G., Boselli, A., et al. 2006, A&A, 453, 847
Cowie, L. L. & Songaila, A. 1977, Nature, 266, 501
Cowie, L. L., Songaila, A., Hu, E. M., & Cohen, J. G. 1996, AJ, 112, 839
Dressler, A. 1980, ApJ, 236, 351
Dressler, A. 2004, Clusters of Galaxies: Probes of Cosmological Structure and Galaxy Evolution, 206
Fossati, M., Fumagalli, M., Boselli, A., et al. 2016, MNRAS, 455, 2028
Fossati, M., Gavazzi, G., Boselli, A., & Fumagalli, M. 2012, A&A, 544, A128
Fossati, M., Gavazzi, G., Savorgnan, G., et al. 2013, A&A, 553, A91
Fossati, M., Wilman, D. J., Mendel, J. T., et al. 2017, ApJ, 835, 153
Fumagalli, M., Fossati, M., Hau, G. K. T., et al. 2014, MNRAS, 445, 4335
Fumagalli, M., Krumholz, M. R., Prochaska, J. X., Gavazzi, G., & Boselli, A. 2009, ApJ, 697, 1811

Gavazzi, G., Boselli, A., Mayer, L., et al. 2001a, ApJ, 563, L23
Gavazzi, G., Boselli, A., van Driel, W., & O'Neil, K. 2005, A&A, 429, 439
Gavazzi, G., Consolandi, G., Dotti, M., et al. 2015, A&A, 580, A116
Gavazzi, G., Contursi, A., Carrasco, L., et al. 1995, A&A, 304, 325
Gavazzi, G., Cortese, L., Boselli, A., et al. 2003, ApJ, 597, 210
Gavazzi, G., Fumagalli, M., Cucciati, O., & Boselli, A. 2010, A&A, 517, A73
Gavazzi, G., Fumagalli, M., Fossati, M., et al. 2013, A&A, 553, A89
Gavazzi, G., Marcelin, M., Boselli, A., et al. 2001b, A&A, 377, 745
Gavazzi, G., O'Neil, K., Boselli, A., & van Driel, W. 2006, A&A, 449, 929
Gavazzi, G., Pierini, D., & Boselli, A. 1996, A&A, 312, 397
Gunn, J. E. & Gott, III, J. R. 1972, ApJ, 176, 1
Haines, C. P., Pereira, M. J., Smith, G. P., et al. 2015, ApJ, 806, 101
Hirschmann, M., De Lucia, G., Wilman, D., et al. 2014, MNRAS, 444, 2938
Kauffmann, G., Heckman, T. M., Tremonti, C., et al. 2003, MNRAS, 346, 1055
Kauffmann, G., White, S. D. M., & Guiderdoni, B. 1993, MNRAS, 264, 201
Kenney, J. D. P., Tal, T., Crowl, H. H., Feldmeier, J., & Jacoby, G. H. 2008, ApJ, 687, L69
Koopmann, R. A., Haynes, M. P., & Catinella, B. 2006, AJ, 131, 716
Larson, R. B., Tinsley, B. M., & Caldwell, C. N. 1980, ApJ, 237, 692
Mastropietro, C., Moore, B., Mayer, L., et al. 2005, MNRAS, 364, 607
McGee, S. L., Balogh, M. L., Bower, R. G., Font, A. S., & McCarthy, I. G. 2009, MNRAS, 400, 937
Merritt, D. 1983, ApJ, 264, 24
Moore, B., Lake, G., & Katz, N. 1998, ApJ, 495, 139
Noll, S., Burgarella, D., Giovannoli, E., et al. 2009, A&A, 507, 1793
Nulsen, P. E. J. 1982, MNRAS, 198, 1007
Peng, Y.-j., Lilly, S. J., Kovač, K., et al. 2010, ApJ, 721, 193
Roediger, E. & Hensler, G. 2005, A&A, 433, 875
Sakai, S., Kennicutt, Jr., R. C., van der Hulst, J. M., & Moss, C. 2002, ApJ, 578, 842
Sarazin, C. L. 1986, Reviews of Modern Physics, 58, 1
Scott, T. C., Cortese, L., Brinks, E., et al. 2012, MNRAS, 419, L19
Scott, T. C., Usero, A., Brinks, E., et al. 2015, MNRAS, 453, 328
Sun, M., Donahue, M., & Voit, G. M. 2007, ApJ, 671, 190
Tonnesen, S. & Bryan, G. L. 2009, ApJ, 694, 789
Vollmer, B. 2003, A&A, 398, 525
Vollmer, B., Braine, J., Combes, F., & Sofue, Y. 2005, A&A, 441, 473
Wetzel, A. R., Tinker, J. L., & Conroy, C. 2012, MNRAS, 424, 232
Wetzel, A. R., Tinker, J. L., Conroy, C., & van den Bosch, F. C. 2013, MNRAS, 432, 336
Yagi, M., Komiyama, Y., Yoshida, M., et al. 2007, ApJ, 660, 1209
Yagi, M., Yoshida, M., Gavazzi, G., et al. 2017, ApJ, 839, 65
Yagi, M., Yoshida, M., Komiyama, Y., et al. 2010, AJ, 140, 1814
Yoshida, M., Yagi, M., Okamura, S., et al. 2002, ApJ, 567, 118

Session 13

Exploitation of GRAVITY at VLTI

SF2A 2017
C. Reylé, P. Di Matteo, F. Herpin, É. Lagadec, A. Lançon, Z. Meliani, F. Royer (eds)

VLTI/GRAVITY OBSERVATIONS OF THE YOUNG STAR β PICTORIS

D. Defrère[1]

Abstract. The nearby young star β Pictoris is surrounded by the archetypal debris disc, which provides a unique window on the formation and early evolution of terrestrial planets. While the outer disc has been extensively studied since its discovery in 1984, very little is currently known about the inner planetary system (<4AU). Recently, accurate squared visibilities obtained with VLTI/PIONIER revealed the presence of resolved circumstellar emission with an integrated brightness amounting to approximately 1.4% of the stellar brightness in H band. However, it is not clear whether this excess emission originates from thermal emission, reflected light from hot dust grains located in the innermost regions of the planetary system, or is simply due to forward scattering by dust grains located further away (but still within the PIONIER field-of-view, i.e., close to the line of sight). In this paper, we present medium-resolution K-band observations of β Pic obtained with VLTI/GRAVITY during science verification. The goals of these observations are to better constrain the temperature of the grains (and hence their location and chemical composition) and to showcase the high-precision capabilities of GRAVITY at detecting faint, close-in circumstellar emission.

Keywords: Exoplanet, planet formation, exozodiacal dust, β Pic, interferometry, VLTI.

1 Introduction

The young ($\sim 12^{+8}_{-4}$ Myr, Zuckerman et al. 2001) A6V-type star β Pic (HD 39060, A6V, 19.3 pc) is surrounded by a famous planetary system, which is a prime target for understanding planetary system formation and evolution. Since its discovery (Smith & Terrile 1984), successive generations of telescopes have reported the detection of an edge-on debris disc with several distinctive features suggestive of a multiple-belt system (Telesco et al. 2005), star-grazing comets ("falling evaporating bodies", Beust et al. 1990), circumstellar gas (e.g., Hobbs et al. 1985; Roberge et al. 2006), and a 9-$M_{\rm Jup}$ planetary companion orbiting at a projected distance of approximately 4.3 AU (Lagrange et al. 2009). The existence of other planets seems likely (Freistetter et al. 2007) and might explain several asymmetries identified in the debris disc, including a warp at $\sim$50 AU (Mouillet et al. 1997; Augereau et al. 2001) inclined by $\sim 4^\circ$ with respect to the outer disc (Lagrange et al. 2012).

Over the past few years, the close environment ($\lesssim$ a few AU) of β Pic has been the focus of several studies trying to detect a putative sub-stellar companion. In particular, closure phase measurements with VLTI/AMBER and VLTI/PIONIER excluded the presence of companions a few hundred times as faint as the central star at angular separations up to about 100 mas (i.e., a brown dwarf of about 30 $M_{\rm Jup}$ at β Pic's age, Absil et al. 2010). Whereas no companion has been detected at the current precision level, accurate squared visibilities obtained with VLTI/PIONIER revealed the presence of resolved circumstellar emission with an integrated brightness amounting to approximately 1.4% of the stellar brightness in H band (see left part of Fig. 1, Defrère et al. 2012). An attractive scenario to explain the spectral shape of the measured excess is the scattering of stellar light in the outer disc seen edge-on. However, current models fail at reproducing the total value of this excess and hot material in the innermost region of the planetary system must also be present. The prevailing scenario is the presence of hot exozodiacal dust as proposed for older A-type stars (e.g., Absil et al. 2013; Ertel et al. 2014). However, the exact amount of hot dust, its location, and chemical properties remain unclear, particularly because of the lack of multi-wavelength information.

[1] Space sciences, Technologies & Astrophysics Research (STAR) Institute, University of Liège, Liège, Belgium

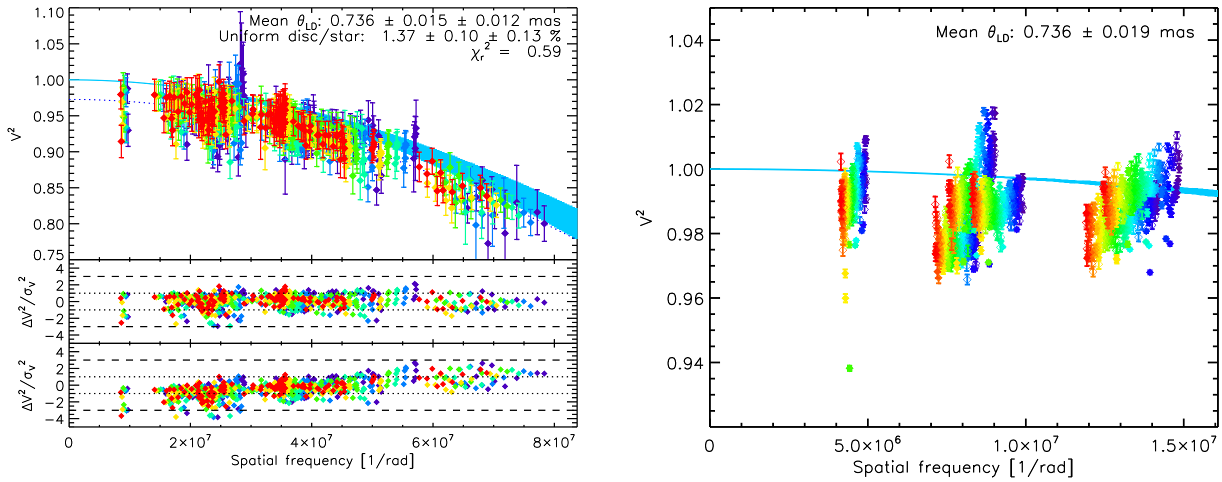

Fig. 1. Left: initial detection of a near-infrared excess around β Pic with VLTI/PIONIER (Defrère et al. 2012). The measured squared visibilities (one colour per spectral channel) are clearly below the expected squared visibility of the limb darkened photosphere (blue solid line). The best-fit model is represented by the dotted blue line with the residuals of the fit given in the middle panel. It corresponds to a limb-darkened photosphere of 0.736 ± 0.015 ± 0.012 mas in diameter surrounded by a uniform circumstellar emission of 1.37 ± 0.10 ± 0.13% in the H band. The bottom panel gives the residuals obtained by fitting only the stellar diameter (no circumstellar emission). **Right:** detection of a hot excess emission around β Pic with VLTI/GRAVITY (data obtained on September 12th, 2016, during science verification). The presence of an excess can be identified as a drop of squared visibility compared to that expected from the limb-darkened photosphere (blue solid line). Unlike previous observations of this excess obtained at H band with VLTI/PIONIER (Defrère et al. 2012), the K-band excess detected by GRAVITY depends on the wavelength and the baseline orientation. This provides crucial data to reveal the puzzling nature of β Pic's inner planetary system (modelling under progress).

In this paper, we present the first K-band interferometric observations of β Pic obtained with VLTI/GRAVITY during science verification and a preliminary data analysis. Our final goal is to better constrain the morphology and nature of the hot excess resolved around β Pic with VLTI/PIONIER. This will be presented in an upcoming paper.

2 Observations and data reduction

Medium-resolution VLTI/GRAVITY observations of the young star β Pic (HD 39060, A6V, 19.3 pc, $\sim 12^{+8}_{-4}$ Myr) were obtained on September 12th, 2016 using the compact VLTI configuration (A0-B2-C1-D0). Observations of β Pic were interleaved with observations of reference stars to calibrate the instrumental contribution in the observed quantities. Calibrators were chosen close to β Pic, in terms of both position and magnitude, from the catalogue of Mérand et al. (2005). Data were reduced and calibrated using the Python data visualization and reduction tools developed by the GRAVITY consortium (see `http://www.eso.org/sci/facilities/paranal/instruments/gravity/tools.html`). In the following, we focus on the squared visibilities ($\mathcal{V}^2$) to search for circumstellar material using a stellar angular diameter of 0.736 ± 0.019 mas measured by VLTI/PIONIER (Defrère et al. 2012). After binning the spectral channels by groups of 5, the final calibrated data set ($\mathcal{V}^2$) is shown in the right part of Fig. 1.

3 Data analysis

Figure 1 shows that the measured dispersed squared visibilities are clearly below the expected values from the limb-darkened photosphere (blue solid line). This suggests that VLTI/GRAVITY confirms the presence of a near-infrared excess emission around β Pic. The spectral shape of this excess is however puzzling and suggests that the excess emission is either barely resolved or much fainter at short wavelengths. Further analyses of these data are currently under progress to validate the accuracy and spectral behavior of GRAVITY at this level. If validated, the variation of the squared visibilities with respect to the wavelength and the baseline orientation will be crucial to constrain the morphology and nature of the excess emission.

4 Conclusions

In this paper, we have presented VLTI/GRAVITY observations of β Pic obtained during science verification. This data set confirms the presence of a faint near-infrared excess emission previously detected by VLTI/PIONIER and suggests that the accuracy achieved by GRAVITY is suitable to carry out an exozodiacal dust disk survey. Further analyses are currently under progress to determine whether the measured spectral shape is real or due to unknown instrumental effects.

The author thanks the National Scientific Research Fund (F.R.S.-FNRS) for its support. This work was partly funded by the French Community of Belgium through an ARC grant for Concerted Research Action.

References

Absil, O., Defrère, D., Coudé du Foresto, V., et al. 2013, A&A, 555, A104

Absil, O., Le Bouquin, J.-B., Lebreton, J., et al. 2010, A&A, 520, L2

Augereau, J. C., Nelson, R. P., Lagrange, A. M., Papaloizou, J. C. B., & Mouillet, D. 2001, A&A, 370, 447

Beust, H., Vidal-Madjar, A., Ferlet, R., & Lagrange-Henri, A. M. 1990, A&A, 236, 202

Defrère, D., Lebreton, J., Le Bouquin, J.-B., et al. 2012, A&A, 546, L9

Ertel, S., Absil, O., Defrère, D., et al. 2014, A&A, 570, A128

Freistetter, F., Krivov, A. V., & Löhne, T. 2007, A&A, 466, 389

Hobbs, L. M., Vidal-Madjar, A., Ferlet, R., Albert, C. E., & Gry, C. 1985, ApJ, 293, L29

Lagrange, A.-M., Boccaletti, A., Milli, J., et al. 2012, A&A, 542, A40

Lagrange, A.-M., Gratadour, D., Chauvin, G., et al. 2009, A&A, 493, L21

Mérand, A., Bordé, P., & Coudé Du Foresto, V. 2005, A&A, 433, 1155

Mouillet, D., Larwood, J. D., Papaloizou, J. C. B., & Lagrange, A. M. 1997, MNRAS, 292, 896

Roberge, A., Feldman, P. D., Weinberger, A. J., Deleuil, M., & Bouret, J.-C. 2006, Nature, 441, 724

Smith, B. A. & Terrile, R. J. 1984, Science, 226, 1421

Telesco, C. M., Fisher, R. S., Wyatt, M. C., et al. 2005, Nature, 433, 133

Zuckerman, B., Song, I., Bessell, M. S., & Webb, R. A. 2001, ApJ, 562, L87

Session 15

Mauna Kea Spectroscopic Explorer

SF2A 2017
C. Reylé, P. Di Matteo, F. Herpin, É. Lagadec, A. Lançon, Z. Meliani, F. Royer (eds)

THE MAUNAKEA SPECTROSCOPIC EXPLORER STATUS AND SYSTEM OVERVIEW

S. Mignot[1], R. Murowinski[2], K. Szeto[2], A. Blin[3] and P. Caillier[4]

Abstract. The Maunakea Spectroscopic Explorer (MSE) project explores the possibility of upgrading the existing CFHT telescope and collaboration to turn it into the most powerful spectroscopic facility available in the years 2020s. Its 10 meter aperture and its 1.5 hexagonal field of view will allow both large and deep surveys, as complements to current (Gaia, eRosita, LOFAR) and future imaging (Euclid, WFIRST, SKA, LSST) surveys, but also to provide tentative targets to the TMT or the E-ELT. In perfect agreement with INSU's 2015-2020 prospective, besides being well represented in MSE's science team (23/105 members), France is also a major contributor to the Conceptual Design studies with CRAL developing a concept for the low and moderate spectrographs, DT INSU for the prime focus environment and GEPI for systems engineering.

Keywords: astronomical observatories, maunakea, multiobject spectroscopy, survey, optical fibres, large telescope, CFHT

1 Introduction

Although always very competitive in terms of the number of scientific publications, the future of the 3.6 m Canada-France-Hawaii telescope, operational since 1979, has been discussed as early as 1996, when the Scientific Advisory Council of CFHT set up a working group to envisage possible evolution of the telescope and the observatory. This led to a proposal to replace the telescope by another with a 12-16 m aperture within the same dome (Grundmann 1997). More recently Canada set up a team for addressing the same subject as part of the LRP2010. Their convincing ngCFHT (new generation CFHT) design and case led the CFHT corporation to kick-off the MSE project in 2014.

MSE targets being the most efficient spectroscopic facility available in the years 2020s. Efficiency is to be understood as capable of conducting large scale surveys in terms of area on the sky, completeness down to magnitude 24 and resolution ranging from 3000 to 40000. As a comparison, MSE will produce 7 million spectra every year and yield as much science as the Sloan Digital Sky Survey every 4 months.

With the purpose of contributing spectroscopic observations to published imaging data from Gaia, eRosita and LOFAR, MSE aims at being on the sky by 2025. To this end, as well as for cost reasons, MSE is a risk-adverse, success-driven project aiming at building on existing technology and know-how. A clear example is the decision to make its primary mirror a segmented one, building on W. M. Keck's experience and available feedback thanks to geographic proximity, with segments whose dimensions would allow TMT partners to also fabricate or polish segments for MSE.

Figure 1 illustrates the transformation of the CFHT into MSE. The key element is to reuse the concrete pier on which the current telescope is anchored to support the new one. Comparison of their respective masses and the capabilities of the pier show that this is possible. Another key element is the dome, which expanded by 10% only will host the telescope and its prime focus instrument. The combination of these two facts mean that MSE will not need to go through the complex paper work required to obtain a building permit – the element which has been blocking the construction of TMT for the last 2 years.

[1] GEPI, Observatoire de Paris, PSL Research University, CNRS, 61 Avenue de l'Observatoire, 75014 Paris, France
[2] Canada France Hawaii Telescope, 65-1238 Mamalahoa Hwy, Kamuela, HI USA 96743
[3] Division Technique, Institut National des Sciences de l'Univers, CNRS, 1 place Aristide Briand, 92195 MEUDON cedex, France
[4] Univ Lyon, Univ Lyon1, Ens de Lyon, CNRS, Centre de Recherche Astrophysique de Lyon, UMR5574, F-69230, Saint-Genis-Laval, France

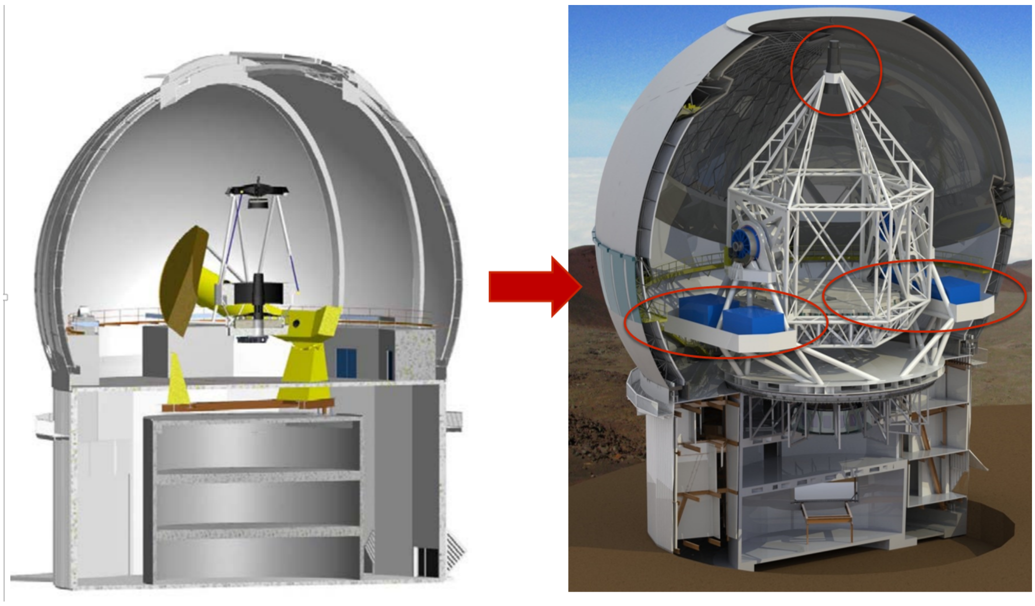

Fig. 1. Artist's conception of the transition between the existing CFHT (**Left**) and MSE (**Right**).

2 Partnership

It 10 meter aperture and its 1.5 hexagonal field of view will allow both large and deep surveys, as complements to current (Gaia, eRosita, LOFAR) and future imaging (Euclid, WFIRST, SKA, LSST) surveys, but also to provide tentative targets to the TMT or the E-ELT. In perfect agreement with INSU's 2015-2020 prospective, besides being well represented in MSE's science team (23/105 members), France is also a major contributor to the Conceptual Design studies with CRAL developing a concept for the low and moderate spectrographs, DT INSU for the prime focus environment and GEPI for systems engineering.

There are at least two reasons for expanding the existing partnership for MSE. One is to gather partners to benefit from their expertise in the design, another is to gather forces, either directly with in-kind contributions, or via funding for a project with a cost cap of $300,000 2018 US dollars. Technical collaboration (1) with Australia for the fiber positioners, (2) with China for the eventual polishing of MSE's mirror segments in Nanjing and the design of the high resolution spectrograph, (3) with Spain for a proposal on the fiber positioner technology, (4) and India's interest in mirror segment geometry has quite naturally resulted in putting them in the loop. "In the loop" refers to having them join the Manangement Group, which is the decision-making committee for MSE and which is expected to eventually turn into MSE's board of directors.

The composition of the Management Group (Tab. 1) reflects the amount of effort each partner invests in the project. Activities funded by the project lead to reduced representation in the Management Group as opposed to volunteered ones. Thanks to its investing significant work force in the project, France earns 2 votes.

Australia	Andrew Hopkins
Canada	Greg Fahlman & Pat Hall
China	Suijian Xue& Xuefei Gong
France	Guy Perrin & Jean Gabriel Cuby (chair)
India	G.C. Anupama
Spain	Eva Villaver
UHawaii	Bob McLaren & Len Cowie

Table 1. Composition of the Management Group in 2017 (in alphabetical order, members are appointed for two years).

Beyond the financial and technical activities, MSE is also working on making the project a success with the local community. For years the observatories have had outreach activities, but the group of inhabitants blocking the construction of the TMT has shown that it was not enough or that the community did not feel they owned the observatories or that they in turn served them well. Since 2015, considerable efforts have been devoted to change the way the observatories, grouped as the "MaunaKea Observatories", are perceived and work together to deliver more to the local community.

3 Baseline design

MSE has an alt-azimuthal mount which is very advantageous in terms of the overall mass compared the CFHT's equatorial mount and thereby makes the substitution possible. As represented in Fig. 1, the baseline telescope is of yoke type. It features a single focus located at the prime focus, similar to MegaPrime in intent, which is to offer a wide field of view and remain accessible. Being dedicated to spectroscopic surveys, MSE operates with low, medium and high resolution spectrographs, possibly simultaneously. These spectrographs are built in the project in the sense that MSE's requirements optimize the whole range of the observatory's constituents, from the building, the telescope all the way to the spectrographs' properties.

The French contribution in terms of design focuses on systems engineering, the Top End Assembly (TEA) and the Low and Moderate Resolution spectrographs (LMR) which are the subject of the following sections.

3.1 Systems engineering

All of MSE's WBS elements have or will soon be reviewed in order for the project to move from the concept design phase to the preliminary design phase. Internal modifications to the building, software and system design are to be found among the last.The system design review includes examining the requirement flow-down from the Science Requirements Document (SRD) to the Observatory Architecture Document (OAD), the Operations Concept Document (OCD) down to the Observatory Requirements Document (ORD). This organization is similar to the structure adopted by TMT. The intent is to rationalize the flow-down so that the OAD and OCD elaborate on the SRD and the ORD is built to serve as the unique reference for all subsystems. France is an active part of this requirement engineering process with Shan Mignot contributing to the systems budgets.

3.2 Top End Assembly

The DT INSU has been working on TEA since 2016*. They have been developing a mechanical environment supporting the prime focus: a barrel to maintain the relative alignment of the optics, a hexapod to align the optics as a whole versus the telescope, and a rotator in charge of compensating the field rotation†.

They have chosen to subcontract the rotator and the hexapod which need not be specialized from MSE and have focused on the design of the wide-field corrector and atmospheric dispersion corrector barrel. They propose a modular approach with the use of spacers giving great flexibility on where to place the optics which is in line for the tolerance analysis for the optical system. An identified risk in this approach, however, is accumulating the position errors of modules resulting in failing to maintain the optics with the required absolute precision.

3.3 Low and Moderate Resolution spectrographs

Building on their experience with MUSE on the VLT and the low resolution spectrographs for 4MOST, CRAL is involved in the development of MSE's LMR. The LMR is summarized in Table 2. One of the very challenging aspects of the LMR design is the need to observe two wavelength ranges alternatively (either J or H). Indeed the cryogenics constraints resulting from the addition of the H band can prove critical as the mechanism used to operate the LMR in one mode or the other. This comes in addition to running the LMR in low or moderate resolution. A original optical design was proposed for the LMR CoDR. The panel recommended assessing the risks through a sensitivity analysis.

4 Conclusions

The French involvement in MSE, as part of the science or as part of the engineering teams is significant. The TEA and LMR teams are currently taking into account the recommendations made by the review panels in order to complete the Conceptual Design Phase. These activities are in perfect agreement with INSU's 2015-2020 prospective.

---

*Together with a local optics engineer (David Horville from GEPI) to derive mechanical requirements from the optical design.

†Which is an unavoidable result of the alt-azimuthal mount.

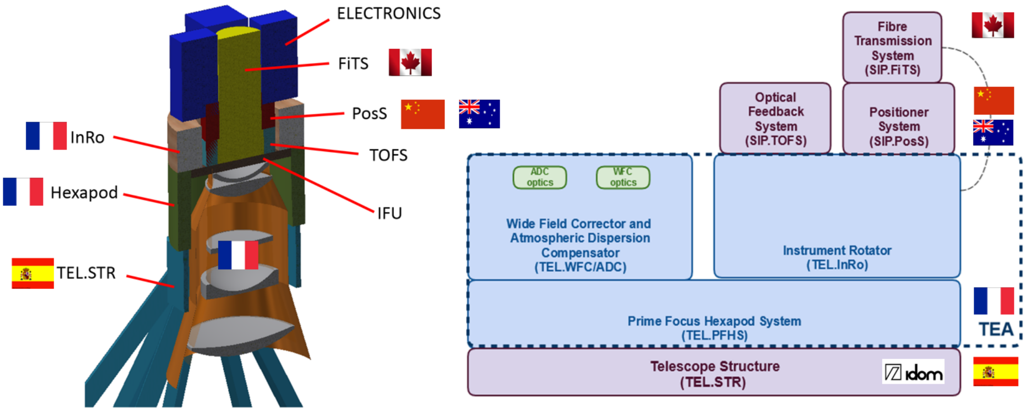

Fig. 2. Cut through TEA (**Left**) indicating its different components, compared to its functional block diagram (**Right**), with the indication of the ownership of the WBS elements to illustrate that TEA is at a critical location by both the number and the owners of its interfaces.

Modes	Low		Moderate
Wavelenth range	0.36 - 0.95 m	J, H bands	0.36 - 0.95 m
Spectral resolution $R = \lambda_c/d\lambda$	2500 (3000)	3000 (5000)	6000
Multiplexing		> 3200	
Spectral windows	Full		Half
Sensitivity	m=24@SNR=2		m=23.5 @ SNR=2
Velocity precision	20km/s@SNR=5		9 km/s @ SNR=5
Spectrophotometic		accuracy < 3 (relative)	

Table 2. Requirements on the LMR (from the SRD).

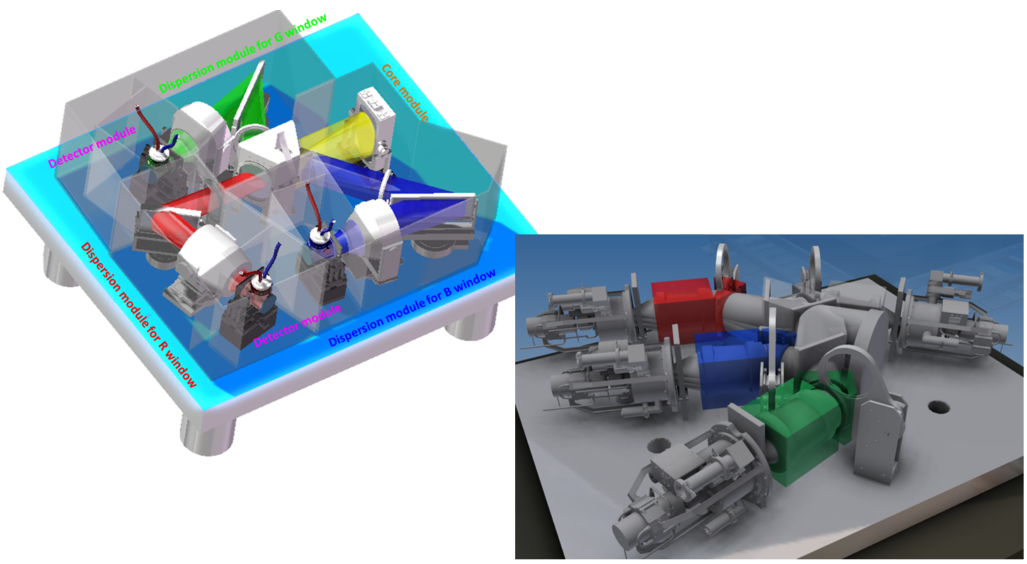

Fig. 3. Left Optical design of the LMR, **Right** corresponding mechanical design.

The French involvement in the next phase is pending on INSU's directives to pursue the effort or stop. In the long term such a decision implies having France leaving the CFHT corporation and losing access to a privileged observing site. INSU's decision partly depends on the cost of the project and its ability to make the funding effort minimum by accreting more partners and with averaging the expenses over the years

Whatever may INSU's decision be, MSE ,as it is, is an exciting project both scientifically and technically.

References

SF2A 2017
C. Reylé, P. Di Matteo, F. Herpin, É. Lagadec, A. Lançon, Z. Meliani, F. Royer (eds)

THE SCIENCE ENABLED BY THE MAUNAKEA SPECTROSCOPIC EXPLORER

N. F. Martin[1], C. Babusiaux[2] and the MSE Science Team

Abstract. With its unique wide-field, multi-object, and dedicated spectroscopic capabilities, the Maunakea Spectroscopic Explorer (MSE) is a powerful facility to shed light on the faint Universe. Built around an upgrade of the Canada-France Hawaii Telescope (CFHT) to a 11.25-meter telescope with a dedicated ~ 1.5 deg^2, 4,000-fiber wide-field spectrograph that covers the optical and near-infrared wavelengths at resolutions between 2,500 and 40,000, the MSE is the essential follow-up complement to the current and next generations of multi-wavelength imaging surveys, such as the LSST, Gaia, Euclid, eROSITA, SKA, and WFIRST, and is an ideal feeder facility for the extremely large telescopes that are currently being built (E-ELT, GMT, and TMT). The science enabled by the MSE is vast and would have an impact on almost all aspects of astronomy research.

Keywords: astronomical observatories, Maunakea, multi-object spectroscopy, survey, large telescope, CFHT

1 Introduction

Following in the foot steps of dedicated spectroscopic facilities like the multiple iterations of the transformative Sloan Digital Sky Surveys (e.g., Blanton et al. 2017), the MSE is the realization of the long-held ambition of the international astronomy community for highly multiplexed, large aperture, optical and near-infrared spectroscopy on a dedicated facility. In this era of all-sky panoptic surveys (Pan-STARRS1, Gaia, soon Euclid, eROSITA or SKA), such a facility is the most glaringly obvious and important missing capability in the international portfolio of astronomical facilities. MSE is built around an upgrade of the CFHT to an 11.25-meter telescope and a dedicated set of heavily multiplexed spectrographs that are envisioned to be running for at least a decade on large spectroscopic surveys. The breadth of the science enabled by such a facility is vast and would impact all fields of astronomy, from the detailed characterization of exoplanet hosts to the next generation of cosmological surveys, via the ultimate Galactic archaeology survey and the definitive Gaia follow-up.

This quick overview of the science envisioned with MSE is developed in much greater details in "A concise overview of the Maunakea Spectroscopic Explorer" (McConnachie et al. 2016b) and in "The detailed science case for the Maunakea Spectroscopic Explorer" (McConnachie et al. 2016a), which have both been developed through contributions of the large MSE Science Team under the guidance of the MSE Project Scientist, Alan McConnachie.

2 MSE capabilities

The system architecture of MSE and its major sub-systems are presented in Figure 1 and its envisioned capabilities are summarized in Figure 2. Compared to operating or planned facilities, MSE is unique in its:

1. *Survey speed and sensitivity:* its étendue is more than twice that of its closest 8-meter competitor (149 vs. 66 m^{2}deg^2 for Subaru/PFS) while the excellent Maunakea site ensures efficient observations of the faintest objects.

[1] Université de Strasbourg, CNRS, Observatoire astronomique de Strasbourg, UMR 7550, F-67000 Strasbourg, France
Max-Planck-Institut für Astronomie, Königstuhl 17, D-69117 Heidelberg, Germany
[2] GEPI, Observatoire de Paris, PSL Research University, CNRS UMR 8111 - 5 Place Jules Janssen, 92190 Meudon, France
Univ. Grenoble Alpes, CNRS, IPAG, 38000 Grenoble, France

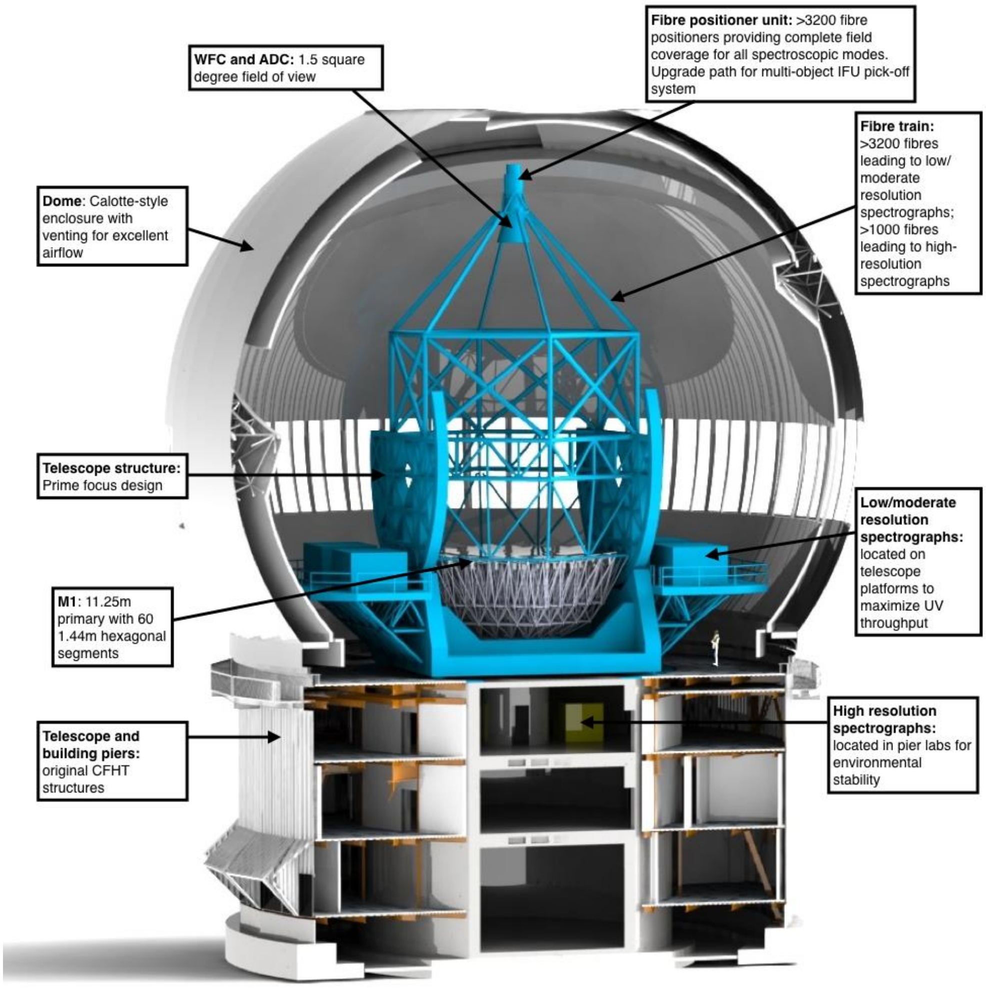

Fig. 1. Cut-away of the MSE revealing the system architecture and major sub-systems. Credit: McConnachie et al. (2016b).

2. *Dedicated operations:* the MSE's specialized capabilities enable a vast range of new science. In particular, they enable very long surveys of millions of target stars or galaxies and allow for time-domain programs with multiple cadences that are difficult to schedule at other facilities.

3. *Spectral performance:* the extensive wavelength coverage of the MSE from the UV ($0.36\,\mu$m) to the H-band ($1.8\,\mu$m) uniquely enables the same tracers to be used to study galaxy and black-hole growth at all redshifts to beyond cosmic noon. More locally, the very high resolution mode of MSE (R=40,000) opens the realm of chemical tagging and detailed Galactic archaeology across the full luminosity range of Gaia targets.

3 MSE science

As mentioned above, the science enabled by the MSE is described in great detail in McConnachie et al. (2016a). These proceedings only aim at a succinct summary of the vast amount of new science such a facility would open for investigation.

Accessible sky	30000 square degrees (airmass<1.55)						
Aperture (M1 in m)	11.25m						
Field of view (square degrees)	1.5						
Etendue = FoV x π (M1 / 2)^2	149						
Modes	**Low**		**Moderate**	**High**			**IFU**
Wavelength range	0.36 - 1.8 μm		0.36 - 0.95 μm	0.36 - 0.95 μm ♯			IFU capable; anticipated second generation capability
	0.36 - 0.95 μm	J, H bands		0.36 - 0.45 μm	0.45 - 0.60 μm	0.60 - 0.95 μm	
Spectral resolutions	2500 *(3000)*	3000 *(5000)*	6000	40000	40000	20000	
Multiplexing	>3200		>3200	>1000			
Spectral windows	Full		≈Half	$\lambda_c/30$	$\lambda_c/30$	$\lambda_c/15$	
Sensitivity	m=24 *		m=23.5 *	m=20.0 ♮			
Velocity precision	20 km/s ♪		9 km/s ♪	< 100 m/s ★			
Spectrophotometric accuracy	< 3 % relative		< 3 % relative	N/A			

♯ Dichoric positions are approximate

* SNR/resolution element = 2 ♪ SNR/resolution element = 5

♮ SNR/resolution element = 10 ★ SNR/resolution element = 30

Fig. 2. Summary of major science capabilities of the MSE. Credit: McConnachie et al. (2016b).

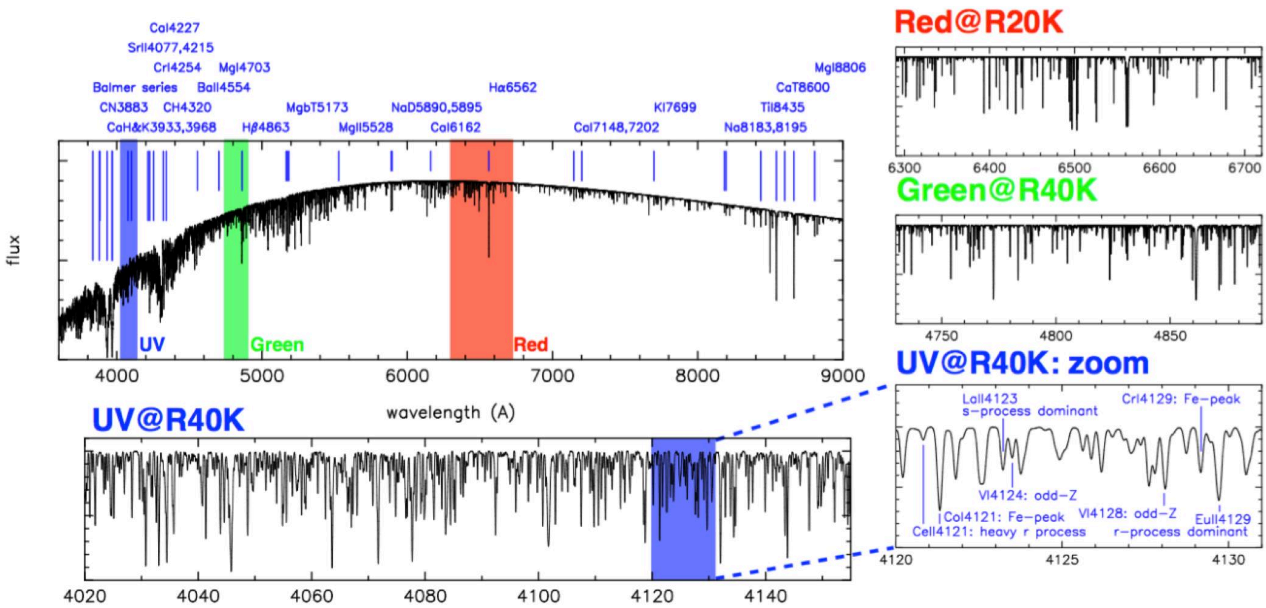

Fig. 3. The main panel shows the relative flux of a synthetic spectrum of a metal-poor red-giant star at the intermediate MSE spectral resolution of $R \sim 6,000$), along with some of the strong-line stellar diagnostics accessible at this resolution. Highlighted regions show the normalized flux in three windows observable with the high resolution mode of MSE. A magnified region of the UV window shows examples of the species that will be identified at high resolution. MSE chemical tagging surveys will identify species sampling a large and diverse set of nucleosynthetic pathways and processes. Credit: McConnachie et al. (2016b).

3.1 Exoplanets and stellar astrophysics

MSE will provide spectroscopic characterization at high resolution and high SNR of the faint end of the PLATO target distribution ($g \sim 16$), to allow for statistical analysis of the properties of planet-hosting stars as a function of stellar and chemical parameters. With high velocity accuracy and stability, MSE time domain spectroscopic programs will allow for highly complete, statistical studies of the prevalence of stellar multiplicity into the regime of hot Jupiters for this and other samples and also directly measure binary fractions away from the Solar neighborhood. MSE will also investigate links between the interstellar medium and the stellar formation history and follow up rare objects and LSST transients.

3.2 Chemical tagging in the outer Galaxy: the definitive Gaia follow-up

MSE will have an unmatched capability for chemical tagging experiments. Recent work in this field has started to reveal the dimensionality of chemical space and has shown the potential for chemistry to be used in addition to, or instead of, phase space, to reveal the stellar associations that represent the remnants of the building blocks of the Galaxy. MSE will push these techniques forward and will focus on understanding the outer components of the Galaxy — the halo, thick disk and outer disk — where dynamical times are long and whose chemistry is inaccessible from 4-m class facilities. These components will be decomposed into their constituent star formation events by measuring abundances of chemical species that trace a large number of nucleosynthetic pathways. This includes rare species and heavy elements at blue wavelengths (Figure 3). *MSE is the only facility capable of high resolution studies of stars across the full luminosity range of Gaia targets.*

3.3 The Dark Matter Observatory

MSE is the ultimate facility for probing the dynamics of dark matter over all spatial scales. For Milky Way dwarf galaxies, MSE will obtain complete samples of tens of thousands of member stars to very large radius and with multiple epochs to remove binary stars. Such analyses will allow the internal dark matter profile of the systems to be derived with high accuracy. In the Galactic halo, high precision radial velocity mapping of stellar streams will reveal the extent of their heating through interactions with dark sub-halos and place strong limits on the mass function of dark sub-halos around an L* galaxy. On cluster scales, MSE will use galaxies, planetary nebulae and globular clusters as dynamical tracers to provide a fully consistent portrait of dark-matter halos across the mass function.

3.4 The connection between galaxies and the large scale structure of the Universe

Within the ΛCDM paradigm, it is fundamental to understand how galaxies evolve and grow relative to the dark matter structure in which they are embedded. This requires mapping the distribution of stellar populations and supermassive black holes to the dark matter halos and filamentary structures that dominate the mass density of the Universe, and to do so over all mass and spatial scales. MSE will provide a breakthrough in extragalactic astronomy by linking the formation and evolution of galaxies to the surrounding large-scale structure, across the full range of relevant spatial scales (from kpc to Mpc). A local galaxy survey with MSE out to 100 Mpc could sample our neighborhood down to the lowest detectable masses of $3 \times 10^5\,\mathrm{M}_\odot$ allowing for a complete census of mass in the local Universe. A deep near infrared selected spectroscopic survey will be able to measure velocity dispersion masses for systems analogous to the Milky Way, M31, or M33 to $z = 1$, providing a direct measurement of dark matter assembly for $> 10^{12}\,\mathrm{M}_\odot$ halos over half the age of the Universe. MSE will follow galaxy evolution across the peak in star-formation and merger activity, and trace the transition from merger-dominated spheroid formation to the growth of disks.

4 Conclusions

With the breadth of the science it enables combined to its capability as a follow-up machine for the upcoming large surveys of the sky, MSE will enable transformational science in areas as diverse as exoplanetary host characterization; stellar monitoring campaigns; tomographic mapping of the interstellar and intergalactic media; the in-situ chemical tagging of the distant Galaxy; connecting galaxies to the large scale structure of the Universe; measuring the mass functions of cold dark matter sub-halos in galaxy and cluster-scale hosts; reverberation mapping of supermassive black holes in quasars. MSE is the largest ground based optical and near infrared telescope in its class, and it will occupy a unique and critical role in the emerging network of astronomical facilities active in the 2020s and beyond.

This contribution builds heavily on the work of the MSE Science Team and the MSE Project Office.

References

Blanton, M. R., Bershady, M. A., Abolfathi, B., et al. 2017, AJ, 154, 28
McConnachie, A., Babusiaux, C., Balogh, M., et al. 2016a, ArXiv e-prints, arXiv:1606.00043
McConnachie, A. W., Babusiaux, C., Balogh, M., et al. 2016b, ArXiv e-prints, arXiv:1606.00060

Lunch session 03

Outreach

SF2A 2017
C. Reylé, P. Di Matteo, F. Herpin, É. Lagadec, A. Lançon, Z. Meliani, F. Royer (eds)

2101, SCIENCES & FICTION: A WAY OF DEVELOPING TEENAGERS' INTEREST FOR SCIENCE

I. Vauglin[1] and P. Chiuzzi[2]

Abstract. Since nearly 30 years, many european studies have demonstrated a worrying decline of young people's interest in science and technical studies. Despite the number of efforts and programs made to reverse the trend, there are still few signs of improvement. We must step up our efforts otherwise this will impact the long-term innovation capacities of our country. We have tried to participate to these efforts with the creation of a digital and interactive comics *"2101, Science & Fiction"*, created by Chromatiques, that explores the connections between reality of science and science fiction. It takes advantage of the new opportunities opened by digital technology and is another way of developing interest in learning sciences. Free access on: `http://2101.fr` !

The goal is to create an new opportunity to popularize science and attract the young generation in different fields of technology and science.

L'e-poster présentant cette BD numérique interactive en français est disponible à cette adresse : `http://sf2a.eu/semaine-sf2a/2017/posterpdfs/294_224_66.pdf`

Keywords: scientific education, digital technologies, outreach

1 Introduction

The growing evidences showing that young people are losing interest in key science studies are all the more worrying that it concerns all European countries. This leads to a decreasing number of students in technical and scientific studies and consequently to a lack of engineers and researchers. So far, the programs developed to foster the young generation have had rather modest results compared to the efforts developed.

Yet, in the coming years, the technological and scientific challenges to be met to guarantee the survival of

[1] Centre de Recherche Astrophysique de Lyon, UMR 5574, F-69230, Saint-Genis Laval, France, Université Lyon1, Université de Lyon, F-69622, Lyon, France
[2] Chromatiques Production, 69006 Lyon, France

humanity will be enormous. Thus, it's of vital importance to ensure the next generation of scientists. We think that we must harness the power of digital systems to raise young people interest in studying technology or science. That's the case of this digital comics. The goal is to enhance and share humanity's scientific achievements.
Science-fiction work, *"2101, Science & Fiction"* propels the reader in the following century. But the scenario relies on current knowledge and interviews scientists to complete each episode with the aim of giving young people a chance to discover different fields of sciences.

2 Benefit from the potential of digital technology

"2101, Science & Fiction" is a digital, interactive and documentary comics opening to sciences and current research. It includes and exploit the full potential of new technologies to catch the curiosity of young people (targeted to the 15-25 year age group), trying to arouse their interest for scientific fields.
The story? it is a free adaptation of the legend of Faust, looking to the future: we are in Paris in 2101, a dramatic climatic environment leaves few future to humanity. Banished from the scientific community, the astrophysicist Fosto lives alone with the artificial intelligence Pandora. Against all odds, the University of Palerme offers him to restart working on the exoplanet Eden 1024, he claimed to be habitable.
The "reader" is driven in the 26-episode story by Pandora, the speaking artificial intelligence of the fiction, materialized by a moving blue sphere on which one must click to trigger the following content. Several interactive elements included in the comics strips take the reader along the story and propose an audiovisual and transmedia journey allowing him to watch short interviews of experts and longer scientific documentaries to learn more and investigate the matter.

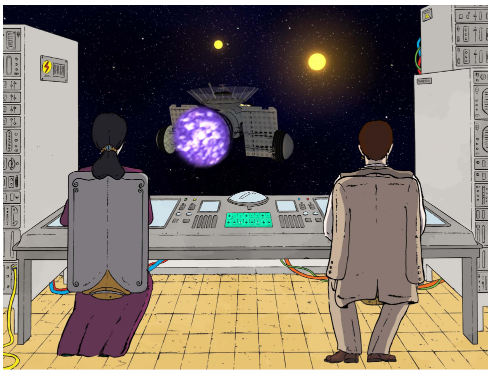

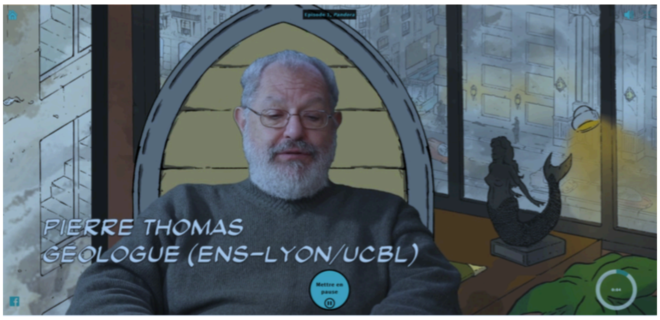

Fig. 1. Left: drawing board of the comics. **Right:** scientist interview.

3 broadening the openness toward sciences

Space travels and extra-terrestrial life is one of the most popular topics in science fiction. With its strong multidisciplinary character and powerful public appeal, astronomy play an important role in modern science education. Hence an important part is given to astronomy in the comics explaining for example the search and detection of exoplanets, the difficulties of interstellar travels due to the distances in the universe, the (im)possibility for human beings to reach potentially habitable planets...
Each episode includes a number of web-docs such as 2-3 min videos in which a scientist gives his-her point of view on the story and assesses the current state of research on the topic. He or she also imagines how his-her domain will have evolved in 2101. The interview ends with a "Need More Info?" section which contains deepening videos on the topics developed in the episode.

Numerous scientific questions are addressed by specialists, around five main domains:

- Earth science: geophysics, sismology, climatology, energies, ...
- Astrophysics: exoplanets, extra-terrestrial life, astrochemistry, ...
- robotics: autonomous vehicles, drones, ...
- life sciences: DNA, cellular aging, genetics, ...
- computer science: computers for the future, holograms, data transmission, ...

Experts are interviewed to capitalise on scientific and technological progress in each domain, important for tomorrow's society. P. Chiuzzi pushed them to imagine innovating concepts and why they are not yet reachable: because of technological barrier or theoretical one?
Then, in longer videos "readers" can discover scientific points of view in area including climate changes, energies of the future, genetic modification, space travels employing ionic propulsion systems, time-reversal physical process, etc. They can obtain information on the most recent technological developments in many different domains leading to major advances in everyday life such as: what would become our travels with autonomous vehicles, what could be the capacities of the future computers, which possibilities we can imagine with genetics to repaire human bodies' damages of the old age...

4 outreach dissemination

"2101, Science & Fiction" has been financially supported by an ESTIM grant (Egalité d'accès aux sciences et techniques, à l'innovation et au multimédia) from Universciences and is available via a total free access website since June 2016 : `http://2101.fr`
Universciences provides also free access to the videos via its scientific webTV pages:
`http://www.universcience.tv/video-2101-sciences-et-fiction-8635.html`

Science plays a major role in our society, both economically, socially and culturally. It's important to give a wide access to all citizens to reliable scientific background and inform the public about the latest advances. We hope that this comics, using digital technologies they like, would impact young people having little interest in, and sometimes a total rejection of, science studies and would contribute to change their mind. Our aim was to stimulate or create their interest in technology and science. The long-term objective is to ensure the existence of a pool of young qualified engineers and scientists because we need them to guarantee our innovation capabilities. With a large number of pages viewed on 2101 website, we hope we have reached our target.

The web comics is nominated in the 17-20 age group category of the 2017 Roberval Prize, an international francophone competition rewarding audiovisual work which goal is to contribute to a better understanding of sciences amoung young audience.

Chromatiques produced also a feature film screened at the Cannes Festival Film Market. The trailer can be watched from this address: `https://www.youtube.com/watch?v=3LfioCM9VE4&feature=youtu.be`

We thank Universcience for its financial support.

Author Index